forests

Special Issue Reprint

Advances in Plant Science Research

Celebrating Nanjing Forestry University's 120th Anniversary

Edited by
Yanming Fang, Fuyuan Zhu and Yong Yang

mdpi.com/journal/forests

MDPI

Advances in Plant Science Research: Celebrating Nanjing Forestry University's 120th Anniversary

Advances in Plant Science Research: Celebrating Nanjing Forestry University's 120th Anniversary

Guest Editors

Yanming Fang
Fuyuan Zhu
Yong Yang

MDPI

Basel • Beijing • Wuhan • Barcelona • Belgrade • Novi Sad • Cluj • Manchester

Guest Editors

Yanming Fang
College of Life Sciences
Nanjing Forestry University
Nanjing
China

Fuyuan Zhu
College of Life Sciences
Nanjing Forestry University
Nanjing
China

Yong Yang
College of Life Sciences
Nanjing Forestry University
Nanjing
China

Editorial Office
MDPI AG
Grosspeteranlage 5
4052 Basel, Switzerland

This is a reprint of the Special Issue, published open access by the journal *Forests* (ISSN 1999-4907), freely accessible at: www.mdpi.com/journal/forests/special_issues/6XYGC9ZXT8.

For citation purposes, cite each article independently as indicated on the article page online and using the guide below:

Lastname, A.A.; Lastname, B.B. Article Title. *Journal Name* **Year**, *Volume Number*, Page Range.

ISBN 978-3-7258-2810-4 (Hbk)
ISBN 978-3-7258-2809-8 (PDF)
https://doi.org/10.3390/books978-3-7258-2809-8

© 2025 by the authors. Articles in this book are Open Access and distributed under the Creative Commons Attribution (CC BY) license. The book as a whole is distributed by MDPI under the terms and conditions of the Creative Commons Attribution-NonCommercial-NoDerivs (CC BY-NC-ND) license (https://creativecommons.org/licenses/by-nc-nd/4.0/).

Contents

Preface . . . . . **vii**

Fenghou Shi, Zhujing Pan, Pengfei Dai, Yongbao Shen, Yizeng Lu and Biao Han
Effect of Waterlogging Stress on Leaf Anatomical Structure and Ultrastructure of *Phoebe sheareri* Seedlings
Reprinted from: *Forests* **2023**, *14*, 1294, https://doi.org/10.3390/f14071294 . . . . . **1**

Chunping Xie, Lin Chen, Meng Li, Dawei Liu and Chi-Yung Jim
Spatial–Temporal Distribution Pattern of *Ormosia hosiei* in Sichuan under Different Climate Scenarios
Reprinted from: *Forests* **2023**, *14*, 1261, https://doi.org/10.3390/f14061261 . . . . . **24**

Kaiyue Hong, Zhenyu Chen, Yasmina Radani, Renhua Zheng, Xueyan Zheng and Yong Li et al.
Establishment of PEG-Mediated Transient Gene Expression in Protoplasts Isolated from the Callus of *Cunninghamia lanceolata*
Reprinted from: *Forests* **2023**, *14*, 1168, https://doi.org/10.3390/f14061168 . . . . . **39**

Yu Wu, Chenyin Peng, Xiangyu Yu and Yongbao Shen
Biochemical Changes during Fruit and Seed Development in Nanjing Linden (*Tilia miqueiana* M.)
Reprinted from: *Forests* **2023**, *14*, 969, https://doi.org/10.3390/f14050969 . . . . . **54**

Yurong Li, Haifei Xia, Ying Liu, Lintao Huo, Chao Ni and Binli Gou
Detection of Moisture Content of *Pinus massoniana* Lamb. Seedling Leaf Based on NIR Spectroscopy with a Multi-Learner Model
Reprinted from: *Forests* **2023**, *14*, 883, https://doi.org/10.3390/f14050883 . . . . . **67**

Lu Wang, Yao Li, Na He, Ye Peng, Yanming Fang and Xingwang Zhang et al.
Comparative Chloroplast Genome Analysis of Chinese Lacquer Tree (*Toxicodendron vernicifluum*, Anacardiaceae): East-West Divergence within Its Range in China
Reprinted from: *Forests* **2023**, *14*, 818, https://doi.org/10.3390/f14040818 . . . . . **82**

Haiyan Chen and Yongbao Shen
Investigation of Water Distribution and Mobility Dynamics in Recalcitrant *Quercus acutissima* Seeds during Desiccation Using Magnetic Resonance Methods
Reprinted from: *Forests* **2023**, *14*, 738, https://doi.org/10.3390/f14040738 . . . . . **100**

Chaohe Tang, Yuran Dong and Lingfeng Mao
Optimized Plant Diversity and Carbon Storage for Priority Protection Areas in China
Reprinted from: *Forests* **2023**, *14*, 621, https://doi.org/10.3390/f14030621 . . . . . **114**

Chenxue Lin, Wanyi Zhao, Zaixiong Chen, Qiang Fan and Kewang Xu
Ilex danxiaensis (Aquifoliaceae), a Distinct New Tree Species Endemic to Danxia Mountain in Guangdong Province, China, Based on Molecular and Morphological Evidence
Reprinted from: *Forests* **2023**, *14*, 583, https://doi.org/10.3390/f14030583 . . . . . **126**

Huihui Liu, Cheng Zhang, Yanqiong Meng, Fengyu Zhang, Nuo Huang and Jianan Wang et al.
Hydraulic and Economical Traits in Short- and Long-Shoot Leaves of *Ginkgo biloba* Males and Females
Reprinted from: *Forests* **2023**, *14*, 535, https://doi.org/10.3390/f14030535 . . . . . **138**

Kaidong Huang, Cheng Xu, Zhuangzhuang Qian, Kang Zhang and Luozhong Tang
Effects of Pruning on Vegetation Growth and Soil Properties in Poplar Plantations
Reprinted from: *Forests* **2023**, *14*, 501, https://doi.org/10.3390/f14030501 . . . . . **154**

Zhi Yang, David Kay Ferguson and Yong Yang
Plastome Phylogeny and Taxonomy of *Cinnamomum guizhouense* (Lauraceae)
Reprinted from: *Forests* **2023**, *14*, 310, https://doi.org/10.3390/f14020310 . . . . . **170**

Yu Duan, Tengyun Ye, Daiquan Ye and Jian Zhou
Seed Distribution and Phenotypic Variation in Different Layers of a Cunninghamia Lanceolata Seed Orchard
Reprinted from: *Forests* **2023**, *14*, 240, https://doi.org/10.3390/f14020240 . . . . . **181**

Xiao Zhang, Lintao Huo, Ying Liu, Zilong Zhuang, Yutu Yang and Binli Gou
Research on 3D Phenotypic Reconstruction and Micro-Defect Detection of Green Plum Based on Multi-View Images
Reprinted from: *Forests* **2023**, *14*, 218, https://doi.org/10.3390/f14020218 . . . . . **199**

Chen-Long Fu, Chun-Ping Xie, Muhammad Idrees, Xian-Gui Yi, Xian-Rong Wang and Meng Li
The Species Richness-Environment Relationship for Cherries (*Prunus* subgenus *Cerasus*) across the Northern Hemisphere
Reprinted from: *Forests* **2023**, *14*, 193, https://doi.org/10.3390/f14020193 . . . . . **215**

Yinghu Zhang, Lu Wang, Wenqi Zhang, Zhenming Zhang and Mingxiang Zhang
Quantification of Root Systems and Soil Macropore Networks Association to Soil Saturated Hydraulic Conductivity in Forested Wetland Soils
Reprinted from: *Forests* **2023**, *14*, 132, https://doi.org/10.3390/f14010132 . . . . . **228**

Jinlong Wang, Meijia Zhou, Haibo Hu, Jie Kuai, Xia Wang and Lei Chu
Effects of Soil Warming on Soil Microbial Metabolism Limitation in a *Quercus acutissima* Forest in North Subtropical China
Reprinted from: *Forests* **2022**, *14*, 19, https://doi.org/10.3390/f14010019 . . . . . **244**

Yuan Yang, Meng Hu, Mingyang Fan, Lu Wang, Ting Lv and Huanchao Zhang et al.
Inter- and Intraspecific Variation Patterns of Leaf Phenotypic Traits in Two Sympatric Pine Species
Reprinted from: *Forests* **2022**, *13*, 2014, https://doi.org/10.3390/f13122014 . . . . . **258**

Cunxin Ruan, Haibo Hu, Can Cheng, Pei Fang, Xichuan Jia and Zhaoming Wu et al.
Photosynthetic Processes and Light Response Model Fitting of *Quercus acutissima Carruth.* and *Quercus variabilis Bl.* in the Changjiang River Delta, China
Reprinted from: *Forests* **2022**, *13*, 2010, https://doi.org/10.3390/f13122010 . . . . . **271**

Yan-Feng Song, Qing-Hua Yang, Xian-Gui Yi, Zhao-Qing Zhu, Xian-Rong Wang and Meng Li
Comparative Analysis of Codon Usage Patterns in Chloroplast Genomes of Cherries
Reprinted from: *Forests* **2022**, *13*, 1891, https://doi.org/10.3390/f13111891 . . . . . **287**

Xuejie Huo, Zhi Yang, Yinfeng Xie and Yong Yang
Tempo and Mode of Floristic Exchanges between Hainan Island and Mainland Asia: A Case Study of the *Persea* Group (Lauraceae)
Reprinted from: *Forests* **2022**, *13*, 1722, https://doi.org/10.3390/f13101722 . . . . . **300**

Wenbin Deng, Xia Wang, Haibo Hu, Mengdie Zhu, Jianyu Chen and Shuai Zhang et al.
Variation Characteristics of Soil Organic Carbon Storage and Fractions with Stand Age in North Subtropical *Quercus acutissima* Carruth. Forest in China
Reprinted from: *Forests* **2022**, *13*, 1649, https://doi.org/10.3390/f13101649 . . . . . **309**

Meijia Zhou, Haibo Hu, Jinlong Wang, Ziyi Zhu and Yuanyuan Feng
Nitric Acid Rain Increased Bacterial Community Diversity in North Subtropical Forest Soil
Reprinted from: *Forests* **2022**, *13*, 1349, https://doi.org/10.3390/f13091349 . . . . . **323**

Preface

To celebrate the 120th Anniversary of NJFU, *Forests* invited distinguished scholars who have long been engaged in plant science to conduct a systematic review and advanced study of the progress in different subfields, such as dendrology, forest ecology and biodiversity, plant taxonomy, woody plant growth and development, plant resource utilization, plant systematics and evolution. In addition, we also invited well-known experts to publish their scientific and academic views on current topics of interest such as the inter- and intraspecific variation patterns in Pine species, the establishment of a transient gene expression system in *Cunninghamia lanceolata*, the new tree species *Ilex danxiaensis* (Aquifoliaceae), the taxonomy of *Cinnamomum guizhouense* (Lauraceae), and plant diversity and carbon storage in priority protection areas in China.

We hope that the publication of this Special Issue will provide an overview of recent systematic advances in plant science research in China, particularly within forestry research, introduce in-depth perspectives on future developments, and provide a tribute to the 120th anniversary of NJFU. NJFU, as the national "Double First-Class" initiative university featuring modern forestry science, aims to strengthen major national strategies such as biological breeding, ecological civilization construction, rural revitalization, carbon peaks and carbon neutrality, and healthy China, as well as to support high-quality development with high levels of scientific and technological self-reliance. After 120 years of development, Nanjing Forestry University is not only a distinguished and important institution of higher learning with a strong heritage, but also a place where profound ideas converge. NJFU continues to maintain its revolutionary legacy and ecofriendly focus, committed to building a world-class university with a focus on forestry and distinctive characteristics.

Yanming Fang, Fuyuan Zhu, and Yong Yang
Guest Editors

forests

MDPI

Article

Effect of Waterlogging Stress on Leaf Anatomical Structure and Ultrastructure of *Phoebe sheareri* Seedlings

Fenghou Shi [1,*], Zhujing Pan [1], Pengfei Dai [1], Yongbao Shen [1], Yizeng Lu [2] and Biao Han [2]

[1] Collaborative Innovation Centre of Sustainable Forestry in Southern China, College of Forestry, Nanjing Forestry University, Nanjing 210037, China; panzj@njfu.edu.cn (Z.P.); xd007@njfu.edu.cn (P.D.); ybshen@njfu.edu.cn (Y.S.)

[2] Shandong Provincial Center of Forest and Grass Germplasm Resources Resources, Jinan 250102, China; luyizeng@shandong.cn (Y.L.); hanbiaok831228@163.com (B.H.)

* Correspondence: shifenghou@njfu.edu.cn

Abstract: *Phoebe sheareri* is an excellent roadside tree with a wide distribution range and high ornamental value. Excessive moisture can affect the external morphology, the microstructure, and the ultrastructure of the leaf. Little is known at present regarding the leaf structure of *P. sheareri* under waterlogging stress. In this paper, the external morphology of leaves, the microstructure of leaf epidermis, and the ultrastructure of mesophyll cells of *P. sheareri* seedlings under waterlogging stress and drainage were dynamically observed. Waterlogging stress contributed to the yellowing and wilting of *P. sheareri* seedling leaves, the gradual closing of leaf epidermal stomata, increasing density of leaf stomata, gradual loosening of the arrangement of leaf cell structure, and merging of leaf palisade tissue cells. Waterlogging stress forced the structure of the chloroplast membranes to blur, gradually causing swelling, and deformation, with plasmolysis occurring in severe cases. During waterlogging, the basal lamellae were disorganized, and the mitochondrial membrane structure was damaged. The damaged state of the leaves was not relieved after drainage. Waterlogging stress not only inhibited the growth of leaves, but also accelerated the closure of stomata, disordered the arrangement of palisade tissue and spongy tissue gradually, and damaged the internal organelles of mesophyll cells.

Keywords: *Phoebe sheareri*; waterlogging stress; leaf anatomical structure; leaf ultrastructure

check for updates

Citation: Shi, F.; Pan, Z.; Dai, P.; Shen, Y.; Lu, Y.; Han, B. Effect of Waterlogging Stress on Leaf Anatomical Structure and Ultrastructure of *Phoebe sheareri* Seedlings. *Forests* **2023**, *14*, 1294. https://doi.org/10.3390/f14071294

Academic Editor: Claudia Cocozza

Received: 20 May 2023
Revised: 17 June 2023
Accepted: 20 June 2023
Published: 23 June 2023

Copyright: © 2023 by the authors. Licensee MDPI, Basel, Switzerland. This article is an open access article distributed under the terms and conditions of the Creative Commons Attribution (CC BY) license (https://creativecommons.org/licenses/by/4.0/).

1. Introduction

Climate change affects atmospheric precipitation, leading to extreme weather events and an increase in the frequency and duration of floods [1,2]. During the plum rain season in the middle and lower reaches of the Yangtze River, China, there are extended periods of continuous heavy rainfall, which severely hinder seedling growth [3]. Moisture is one of the essential elements in the growth of seedlings, but waterlogging stress can arise from saturation or even excessive water in the soil [4]. Excessive water directly affects the diffusion of oxygen in plant tissue, forming an oxygen-deficient environment, and heavily impairing gas exchange between plants and the atmosphere [5]. Prolonged waterlogging and hypoxic environments ultimately lead to the accumulation of toxic metabolites and the increase of reactive oxygen species, affecting the physiological and biochemical processes of seedlings, and hindering the growth of seedlings, and, thus, eventually leading to cell death and plant senescence [6–8]. Although most plants perform poorly when waterlogged, they can resist waterlogging stress by changing their morphological structures, physiological characteristics, cell structures, etc. [5,9].

Under waterlogging conditions, the appearance of leaves may show signs of wilting, curling, or even abscission [10]. When 15~25-cm-tall *Celosia argentea* and *Melampodium paludosum* were waterlogged for ten days, the leaf of *M. paludosuma* appeared to droop

after three days, and those of *C. argentea* appeared to droop after 7 days, and both had no ornamental value after the waterlogging treatment ended [11].

The effects of waterlogging stress on seedlings are not only reflected in the changes in external morphology, but also in changes in the internal cell structure of seedling leaves, such as the destruction of cell membrane structure, swelling and deformation of chloroplasts, loose arrangement of grana lamellae, and extravasation of mitochondrial contents [12–14]. Seedlings can cope with waterlogging stress by controlling stomatal closure level and leaf gas exchange rate, which can be reflected in the dynamic changes of leaf anatomical structure [15]. In the previous study, after seedlings of *Sorghum bicolor* were waterlogged for two weeks, leaf thickness significantly decreased, mainly due to changes in the thickness of the upper epidermal and mesophyll cells [16]. When *Avicennia marina* was waterlogged by means of experimentally simulated semidiurnal tides, it was observed that, with increasing duration of waterlogging, leaf thickness, mesophyll thickness, palisade parenchyma thickness, palisade–spongy ratio, and hypodermis thickness decreased, but the mesophyll to leaf thickness ratio increased [17]. After deep waterlogging treatment (with a waterlogging depth exceeding 20 cm of the soil layer), the leaf structure of *Quercus shumardii* blurred, some palisade tissue cells became irregular, becoming almost round or oval, the gap of sponge tissue cells became larger, and some lower epidermal cells disintegrated [18].

In addition, the morphology and structure of organelles. such as chloroplasts and mitochondria, in mesophyll cells change under waterlogging stress, which plays an important role in leaf photosynthesis [4]. In the study, a waterlogged pool of *Zea mays* was maintained at 2–3 cm above the soil surface. During the different waterlogging stages, the cytoderm structure of *Z. mays* became incomplete and exhibited indistinct gradation, irregular chloroplast configuration, reduction in chloroplast numbers in mesophyll cells, and dimming of the mitochondrial outer membrane. Fine-grained substance exosmosis occurred and structures became diluted after exposure to waterlogging [12]. Under waterlogging treatment, there were almost no substances in the cells of *Chionanthus virginicus* leaves, due to the chloroplasts degrading, starch particles accumulating in large quantities, and severe damage to the structure of the cells [19]. The chloroplasts of *Carya illnoinensis* showed similar changes after waterlogging for 30 days, in that the chloroplasts were swollen and rounded, the number of osmophilic particles increased, and the lamella structure began to loosen [20]. Thus, it is important to investigate the effects of waterlogging on leaves in terms of external morphology, anatomical structure and ultrastructure.

As an evergreen *Phoebe* tree in the Lauraceae family, *Phoebe sheareri* is suitable for places with warm, humid climates and fertile soil. *P. sheareri* has a long growth cycle, a tall and beautiful tree shape, and dense branches and leaves, and is an excellent shade tree and roadside tree with high ornamental value [21,22]. In addition, *P. sheareri* wood is hard, straight textured, corrosion-resistant, and durable, and has a special fragrance. It is is an excellent material for high-end furniture, architecture, and wooden utensils, and is the royal building material of choice for palaces, and tombs and for their gardens [23]. The phenomenon of waterlogging often occurs in the Yangtze River Delta region, which is an area where *P. sheareri* is widely distributed, so it is important to study the response of *P. sheareri* seedling leaves to waterlogging [24]. Currently, studies on the stress resistance of *P. sheareri* have mainly focused on low-temperature stress [25] and drought stress [26], and less research has been connducted on waterlogging stress.

Few studies have reported on the effects of different durations of waterlogging and drainage on the leaf morphology and structure of *P. sheareri*. In this study, we used the "double pot method" to artificially simulate the waterlogging experimental environment. The aims were the following: (1) to measure changes in the leaf morphology, leaf epidermal stomata, leaf anatomical structure and ultrastructure of *P. sheareri* under waterlogging and drainage; (2) to understand the changes and coping mechanisms of the leaf structure of *P. sheareri* seedlings in a waterlogging environment; (3) to provide basic waterlogging informational support for the promotion and application of the *P. sheareri* species.

Based on the results of the above-related studies, before the experiment began, we speculated that, during waterlogging treatment, the leaf morphology of *Phoebe sheareri* seedlings would exhibit gradual yellowing, falling off, and even dying. The leaf anatomical structure would gradually change, with the width and opening and closing degrees of the leaf epidermal layer becoming smaller, the palisade tissue cells becoming irregular and nearly round or oval, the cell spaces becoming larger, and the leaf thickness decreasing. In leaf ultrastructure, the chloroplast and mitochondrial organelles would be damaged, the chloroplast shape would change, gradually swelling and becoming round, the lamellar structure would gradually loosen, the mitochondrial membrane would be damaged, and the contents would exude. We further speculated that the damaged states of leaf morphology, anatomical structure and ultrastructure might not improve after drainage treatment of *Phoebe sheareri* seedlings after the waterlogging.

2. Materials and Methods

2.1. Plant Materials

The experimental materials were 2-year-old container seedlings of *P. sheareri*. The seeds were collected from the wild population of Qionglong Mountain, Suzhou, Jiangsu Province. In the middle of June 2020, container seedlings, with basically the same growth, were selected for pot change transplanting. The transplanting container was a plastic flowerpot with a height of 20 cm, an upper diameter of 23 cm, and a lower diameter of 19 cm, The seedling substrate was produced by Jiangsu Xingnong Substrate Technology Co., Ltd., (Zhenjiang, China) with a dry bulk density of 0.4 g/cm^3, total porosity of 64%, large to small porosity ratio of 1:5, pH 7.6, EC 3.2, organic matter content of 41%, and total nitrogen, phosphorus, and potassium content of 3.8%. When transplanting, the seedling substrate from the original containers was gently washed away to preserve the entire root system of the seedlings as much as possible; An equal amount of seedling substrate was put into each plastic flowerpot, and one seedling transplanted to each container. Sufficient root fixing water was poured in. After transplanting, the seedlings were placed in the greenhouse of Baima Teaching and Scientific Research Base of Nanjing Forestry University (Baima Town, Lishui District, Nanjing, China) for slow seedling growth, during which normal water and fertilizer management was carried out.

2.2. Waterlogging Treatment

To explore the leaf morphology, anatomical structure and ultrastructure changes in *P. sheareri* under waterlogged and waterlogged–drainage conditions, we used the "double pot method" to artificially simulate the waterlogging environment.

This experiment adopted a single factor completely randomized block design and consisted of two parts: a waterlogging experiment and a waterlogging–drainage experiment. A total of 180 plants, with roughly the same growth potential, were used in the two-part experiment, from which 30 seedlings were randomly selected for each treatment, and three biological replicates were applied. A total of 120 seedlings were divided into four waterlogging experiments. A total of 60 seedlings participated in the drainage process, being waterlogged for 12 days and drained for 6 days and 12 days, respectively. The seedlings under normal management and without waterlogging treatment were used as the control group (Table 1).

Table 1. Each treatment of *P. sheareri* seedlings for waterlogging and waterlogging-drainage experiments.

Experiment	Treatment
Part 1 Waterlogging treatment	Control group (without waterlogging treatment) Waterlogging stress for 6 days Waterlogging stress for 12 days Waterlogging stress for 18 days
Part 2 Waterlogging-drainage treatment	Control group (without waterlogging treatment) Waterlogging stress for 12 days Waterlogging stress for 12 days and drainage for 6 days Waterlogging stress for 12 days and drainage for 12 days

Three biological replicates were applied for each treatment.

The waterlogging treatment began on 11 September 2020, named the 0-day for waterlogging stress. In adopting the "double pot method", the seedlings of *P. sheareri* were placed in a lotus basin together with a plastic pot, and tap water was poured in to obtain a water level approximately 2–5 cm above the substrate (Figure 1). Throughout the test, the water level change was observed, and timely replenishment maintained the submergence level. The waterlogging-drainage treatment involved removing seedlings treated with waterlogging for 12 days from their lotus pots and draining the substrate naturally without water.



Figure 1. Schematic diagram of "double pot method".

2.3. Indicator Determination

Plant sampling: we observed and photographed the overall shape and morphological changes of seedlings during the treatment of waterlogging stress and drainage. At 9:00 a.m. on the sampling day, 3–5 standard plants were selected, and the 3rd to 5th intact functional leaves from the bottom to the top of the seedlings were collected, and washed with tap water several times to remove any dirt and dust accumulated on their surfaces. Small circular pieces, about 0.5 cm wide, from the central part of the leaves (avoiding the main veins), were taken as samples, put into glutaraldehyde fixative solution, and stored at 4 °C, so as to observe the changes in the stomata, anatomical structure and microstructure of the seedling leaves.

Seedling leaf morphological observation: we observed the morphological changes of *P. sheareri* seedlings and their leaves, and took pictures to record the growth status of seedlings and leaves under different waterlogging and drainage periods.

Stomata and anatomical structure of seedling leaf epidermis: referring to the method of Jain et al. [27], the leaf stomata and anatomical structure of *P. sheareri* seedlings were observed, recorded and photographed using Scanning Electron Microscopy (SEM).

The samples were taken out of the glutaraldehyde, and rinsed to remove traces of glutaraldehyde. The fixed samples were dehydrated through a series of dehydrating solutions (gradually dehydrated at 30%, 70%, 80%, and 90% ethanol gradients), and subjected to critical point drying. The dehydrated samples were fixed on an adhesive platform and sputtered with a film of gold using an ion-beam sputter coater. The samples were examined under an FEI Quanta 200 Scanning Electron Microscope (USA) at Nanjing forestry university, Nanjing, China. The stomatal length, stomatal width, stomatal opening rate, and stomatal number per unit area were observed and photographed under a 600× microscope, and were measured by Image J (a free, Java-based image-processing package, version 1.8.0.112). This process was repeated 3 times, and 5 visual fields were randomly observed to calculate the average value.

Microstructure of seedling mesophyll cells: referring to the method of Salah et al. [28], the internal ultrastructure of mesophyll cells of *P. sheareri* was observed, recorded and photographed with a transmission electron microscope.

The samples were taken out and washed 3 times with 100 mmol/L phosphoric acid buffer at pH 7.4. They were fixed in 1% buffered osmium tetroxide for 1 h (this process was carried out in a fume hood) and then cleaned 3 times for 10 min each time. Then, the samples were placed in ethanol of different concentration gradients (30%, 45%, 60%, 75%) for dehydration treatment. Finally, the samples were treated with anhydrous ethanol and pure acetone for 30 min. After the above dehydration treatment, the samples were soaked in Spurr's epoxy resin (Sigma-Aldrich, St. Louis, MO, USA) for 12 h, and kept in a dark environment. Using an ultra-thin slicer, the samples were sliced into 50 nm sections. After staining, the samples were observed and photographed under transmission electron microscopy (JEM 2100 High-Resolution Transmission Electron Microscopy, Tokyo, Japan). This was repeated 3 times, and 3 visual fields randomly observed.

2.4. Statistical Analysis

A Shapiro–Wilk test, one-way analysis of variance (ANOVA) data analyses and Duncan multiple comparisons were performed with SPSS version 22.0, which were used to assess data normality and to analyze the differences in the waterlogging and waterlogging–drainage treatments, respectively. Comparisons with p values less than 0.05 were considered significantly different (expressed in lowercase letters), and those with less than 0.01 were considered extremely significantly different (expressed in uppercase letters). The correlation analyses were performed with the Pearson model two-tail test.

3. Results

3.1. Changes in Leaf Morphology of Phoebe sheareri Seedlings during Waterlogging Stress and Drainage

With the extension of waterlogging stress time, the leaf morphology of *P. sheareri* seedlings changed (Table 2). New leaves sprouted on the seedlings of *P. sheareri* after 6 days of waterlogging stress. Under waterlogging stress for 12 days, some leaves drooped for a short time at noon or dusk, but the droop disappeared at night and early morning. However, after 18 days of waterlogging, the leaves wilted continuously and did not recover, which indicated that the leaves were severely damaged. The seedlings that had been waterlogged for 12 days were drained. When they were drained for 6 days, the leaves drooped, wilted, and became chlorotic. Nearly 50% of the seedlings died. When the seedlings were drained for 12 days, 50% of the leaf lost green coloring and turned yellow, 50% of the leaf withered and fell off, 83% of the *P. sheareri* seedlings died, the leaves did not recover to their states before waterlogging and showed more serious damage.

Table 2. Changes in leaf morphology of *Phoebe sheareri* seedlings under waterlogging stress.

Experimental Treatment	Leaf Morphology
Control group	The seedlings grew normally with green leaves and no wilting and drooping phenomenon;
Waterlogging stress for 6 days	The seedlings and their leaves grew well with 2–3 new leaves on the top;
Waterlogging stress for 12 days	About 30% of the leaves appeared with yellow spots, and 50% of the leaves appeared with a temporary wilting phenomenon;
Waterlogging stress for 18 days	All leaves of the seedling wilted and drooped, and all of the terminal bud and basal leaves of the seedlings turned yellow and fell off;
Waterlogging stress for 12 days and drainage for 6 days	Nearly 50% of the leaves drooped, and 50% of the leaves lost green coloring and turned yellow
Waterlogging stress for 12 days and drainage for 12 days	All leaves withered and drooped, 50% of the leaves lost green coloring and turned yellow, and 50% of the leaves withered and fell off.

3.2. Changes in Leaf Epidermal Stomata of Phoebe sheareri Seedlings during Waterlogging Stress and Drainage

3.2.1. Effects of Waterlogging Stress on Leaf Epidermis Stomata of *Phoebe sheareri* Seedlings

The stomata of *P. sheareri* seedling leaves are concentrated in the lower epidermis of the leaves, are mostly oval or nearly round, and the stomata apparatus is composed of two kidney-shaped guard cells (Figure 2a). The observation of stomata in the leaf epidermis of *P. sheareri* under waterlogging stress showed that, with the extension of stress time, stomata in the leaf epidermis gradually closed, and its opening degree gradually decreased (Figure 2).

With the extension of waterlogging stress time, the stomatal length in the leaves of *P. sheareri* seedlings did not change significantly, and the stomatal width showed a gradually decreasing trend (Tables 3 and A1). The stomatal width of seedlings under waterlogging stress for 6 days had extremely significant differences from those of other treatments ($p < 0.01$). Compared to waterlogging stress for 12 days and 18 days, the stomatal width increased by 2.56 μm and 2.85 μm, respectively, during waterlogging stress for 6 days. The effect of waterlogging stress on leaf stomatal opening rate reached an extremely significant level ($p < 0.01$) and gradually decreased with the extension of waterlogging time. Compared with the control group, the stomatal opening rate decreased by 14.52% after 18 days of waterlogging treatment. At 18 days of waterlogging stress, the stomatal width and stomatal opening rate of *P. sheareri* seedlings were the lowest, at 2.67 μm and 13.03%, respectively. Under the condition of waterlogging stress, the stomatal density of *P. sheareri* seedlings increased gradually, and there were extremely significant differences among different treatments ($p < 0.01$). The order, from large to small, was the following: waterlogging stress for 18 days > waterlogging stress for 12 days > waterlogging stress for 6 days > Control group).

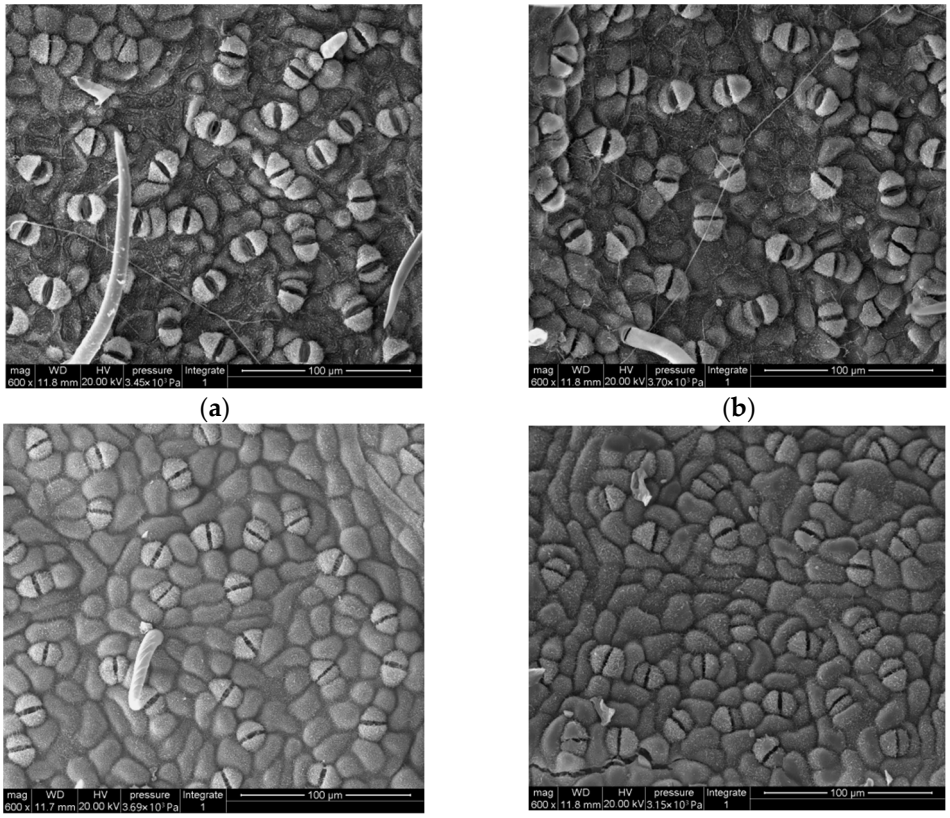


Figure 2. Changes in leaf epidermal stomata of seedlings under waterlogging stress. (**a**): Control group; (**b**): Waterlogging stress for 6 days; (**c**): Waterlogging stress for 12 days; (**d**): Waterlogging stress for 18 days.

Table 3. Determination results of leaf epidermal stomata of seedlings under waterlogging stress.

Treatment	Stomatal Length (μm)	Stomatal Width (μm)	Stomatal Opening Rate (%)	Stomatal Density (n/mm^2)
Control group	13.35 ± 0.49 Aa	7.35 ± 0.34 Aa	27.55 ± 0.34 Aa	2082 ± 22.47 Dd
Waterlogging stress for 6 days	14.18 ± 0.38 Aa	5.52 ± 0.28 Bb	22.91 ± 0.06 Bb	2336 ± 12.96 Cc
Waterlogging stress for 12 days	14.58 ± 0.33 Aa	2.96 ± 0.20 Cc	17.41 ± 0.76 Cc	3298 ± 75.58 Bb
Waterlogging stress for 18 days	14.71 ± 0.66 Aa	2.67 ± 0.11 Cc	13.03 ± 0.25 Dd	3467 ± 5.59 Aa

Note: Different capital letters indicated extremely significant differences between treatments ($p < 0.01$), and different lowercase letters indicated significant differences between treatments ($p < 0.05$). The same applies to the below.

3.2.2. Effect of the Waterlogging-Drainage Process on Leaf Epidermal Stomata of *Phoebe sheareri* Seedlings

With the extension of drainage time, the stomatal opening degree and the number of stomata per unit area witnessed gradual decrease (Figure 3c,d). The leaf stomatal length of *P. sheareri* seedlings showed gradual increase after drainage (Tables 4 and A2), among which, the leaf stomatal length of the seedlings drained for 12 days had extremely significant differences from that of the control seedlings ($p < 0.01$), and had significant differences from that of the seedlings waterlogged for 12 days and drained for 6 days ($p < 0.05$). After waterlogging stress for 12 days and drainage for 12 days, leaf stomatal length reached a maximum (16.16 μm), with an increase of 2.81 μm compared with the control group.

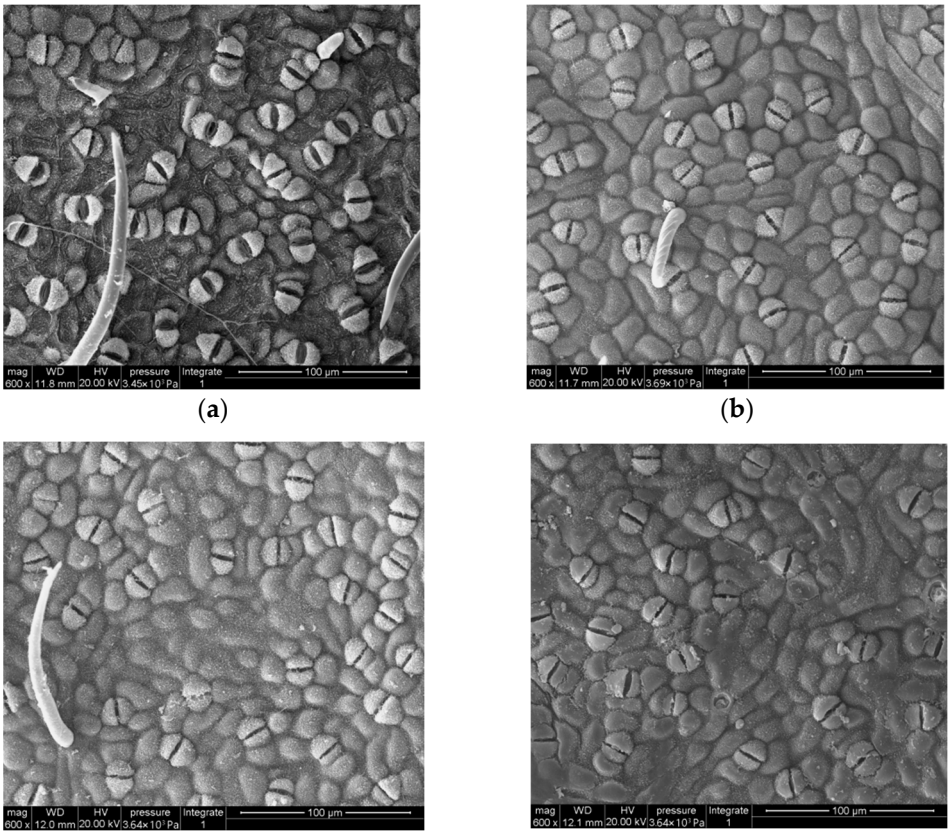


Figure 3. Changes in leaf epidermal stomata of seedlings during the waterlogging-drainage process. (**a**): Control group; (**b**): Waterlogging stress for 12 days; (**c**): Waterlogging stress for 12 days and drainage for 6 days; (**d**): Waterlogging stress for 12 days and drainage for 12 days.

Table 4. Determination results of leaf epidermal stomata of *Phoebe sheareri* seedlings during the waterlogging-drainage process.

Treatment	Stomatal Length (μm)	Stomatal Width (μm)	Stomatal Opening Rate (%)	Stomatal Density (n/mm^2)
Control group	13.35 ± 0.49 Bb	7.35 ± 0.34 Aa	27.55 ± 0.34 Aa	2082 ± 22.47 Cc
Waterlogging stress for 12 days	14.58 ± 0.33 ABb	2.96 ± 0.20 Bb	17.41 ± 0.76 Bb	3298 ± 75.58 Aa
Waterlogging stress for 12 days and drainage for 6 days	14.68 ± 0.53 ABb	2.96 ± 0.14 Bb	15.91 ± 0.36 BCbc	3272 ± 53.80 Aa
Waterlogging stress for 12 days and drainage for 12 days	16.16 ± 0.44 Aa	3.04 ± 0.19 Bb	15.22 ± 0.44 Cc	2644 ± 70.95 Bb

Compared with 12 days of waterlogging treatment, there was no significant change in leaf stomatal width after 6 days and 12 days of drainage. After drainage, the stomatal opening rate of seedlings decreased with the extension of drainage time. The stomatal opening rate of the *P. sheareri* seedlings drained for 12 days was extremely significantly lower than that of the control seedlings and of the seedlings under waterlogging stress for 12 days ($p < 0.01$). In terms of leaf stomatal density, there was an extremely significant difference between that of seedlings waterlogged for 12 days and that of seedlings drained for 12 days ($p < 0.01$), with a difference of 654 n/mm^2, but no significant differences between that of seedlings waterlogged for 12 days and that of seedlings drained for 6 days.

3.3. Changes in Leaf Anatomical Structure of Phoebe sheareri Seedlings during Waterlogging Stress and Drainage Process

3.3.1. Effects of Waterlogging Stress on Leaf Anatomical Structure of *Phoebe sheareri* Seedlings

With the extension of waterlogging stress time, the internal structure of *P. sheareri* leaves changed (Figure 4). The upper and lower epidermis cells of the control seedlings were arranged neatly and closely, the palisade tissue cells were plump and arranged neatly in a long column, and the spongy tissue cells were nearly round and arranged loosely (Figure 4a). There were no obvious changes in the anatomical structure of *P. sheareri* seedling leaves when they were waterlogged for 6 days (Figure 4b). After 12 days of waterlogging stress, palisade tissue cells of seedling leaves fused with unclear boundaries and loose arrangements, and the spongy tissue cells became smaller (Figure 4c). After 18 days of waterlogging stress, due to the narrowing of lower epidermis cells and the widening of upper epidermis cells, the palisade tissue cells shortened with increased intercellular spaces, and disorderly arranged spongy tissue cells (Figure 4d).

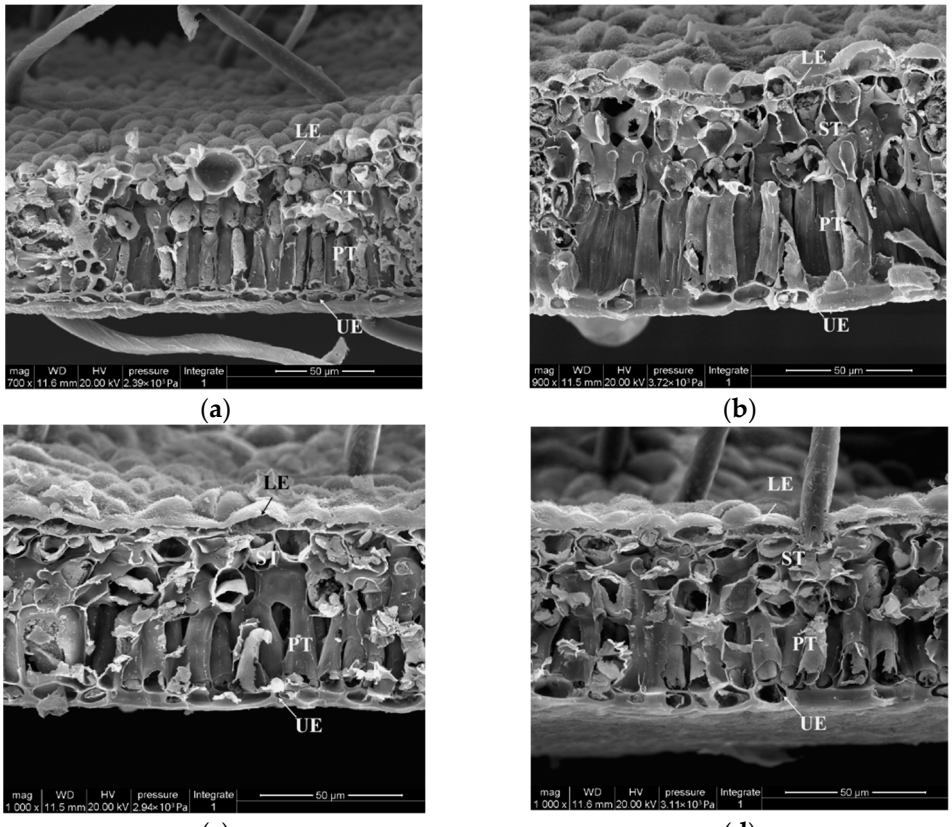


Figure 4. Changes in leaf anatomical structure of seedlings under waterlogging stress. (**a**): Control group; (**b**): Waterlogging stress for 6 days; (**c**): Waterlogging stress for 12 days; (**d**): Waterlogging stress for 18 days; LE: Lower epidermis; ST: Spongy tissue; PT: Palisade tissue; UE: Upper epidermis.

With the extension of waterlogging stress time, the total leaf thickness of *P. sheareri* seedlings witnessed an initial increase and then a decrease (Tables 5 and A3). The total leaf thickness of *P. sheareri* seedlings reached the maximum (88.58 μm) under waterlogging stress for 6 days, presenting a significant difference compared with those of seedlings at other waterlogging stress time nodes ($p < 0.01$).

Table 5. Determination results of leaf anatomical structure of seedlings under waterlogging stress.

Treatment	Total Blade Thickness (μm)	The Thickness of the Upper Epidermis (μm)	The Thickness of the Lower Epidermis (μm)	Palisade Tissue Thickness (μm)	Spongy Tissue Thickness (μm)	The Ratio of Palisade Tissue to the Spongy Tissue
Control group	77.15 ± 0.66 Bb	5.94 ± 0.50 Aa	9.10 ± 0.47 Aa	28.49 ± 0.27 Bbc	32.31 ± 1.01 BCb	0.88 ± 0.02 Bb
Waterlogging stress for 6 days	88.58 ± 1.40 Aa	6.82 ± 0.76 Aa	9.00 ± 0.17 Aa	41.56 ± 0.52 Aa	37.05 ± 0.99 Aa	1.12 ± 0.03 Aa
Waterlogging stress for 12 days	63.67 ± 0.43 Cc	5.36 ± 0.18 Aa	4.75 ± 0.70 Bb	29.07 ± 0.41 Bb	26.73 ± 0.87 Cd	1.09 ± 0.05 Aa
Waterlogging stress for 18 days	62.62 ± 0.75 Cc	6.62 ± 0.48 Aa	4.29 ± 0.67 Bb	27.18 ± 0.78 Bc	29.53 ± 0.47 Cc	0.92 ± 0.02 Bb

In the process of waterlogging stress, the upper epidermis thickness of *P. sheareri* seedling leaves did not change significantly. At 6 days of waterlogging stress, the thickness of the upper epidermis reached the maximum value (6.82 μm), with a difference of 0.88 μm compared with the control group. Compared to that of the control seedlings, the thickness of the lower epidermis of the seedlings' leaves under waterlogging stress showed a decreasing trend, during which the difference between the lower epidermal thickness of the seedlings waterlogged for 6 days and those of the seedlings enduring waterlogged stress for 12 days and 18 days reached a very extremely significant level ($p < 0.01$).

The leaf palisade tissue thickness of *P. sheareri* seedlings at the different waterlogging times was in the following order: waterlogging stress for 6 days > Control group > waterlogging stress for 12 days > waterlogging stress for 18 days. The palisade tissue thickness reached the maximum at 6 days after waterlogging treatment, and there was an extremely significant difference between other treatments ($p < 0.01$). The thicknesses of leaf spongy tissue among different treatments experienced significant differences ($p < 0.05$), and showed a trend of initial increase and subsequent decrease with the extension of stress time. Compared with the control group, the palisade tissue thickness increased by 4.74 μm after 6 days of waterlogging treatment, with extremely significant differences ($p < 0.01$).

The thickness ratio of palisade tissue to the spongy tissue of *P. sheareri* seedling leaves treated with waterlogging was larger than that of the control, and decreased gradually with the extension of waterlogging stress time. The ratio of palisade tissue to spongy tissue reached the maximum value at waterlogging stress for 6 days, and was extremely significantly higher than those at 18 days of waterlogging treatment and the control group ($p < 0.01$).

3.3.2. Effect of Waterlogging-Drainage Process on the Anatomical Structure of *Phoebe sheareri* Seedling Leaves

After 6 days of drainage, the cross-sections of upper epidermal cells on the leaf surface became wider and were nearly rectangular (Figure 5c). The cross-sections of lower epidermal cells become narrower with palisade tissues arranged loosely and the spongy tissue cells thickened (Figure 5c). After 12 days of drainage, the degree of damage of cells in each part of the seedling leaves was aggravated, the upper epidermis cells became narrower, and the palisade tissue cells became shorter, and, thus, the cell gap increased, the palisade tissue and spongy tissue cells fused with blurred boundaries, increased layer number and enlarged thickness of spongy tissue cells (Figure 5d).

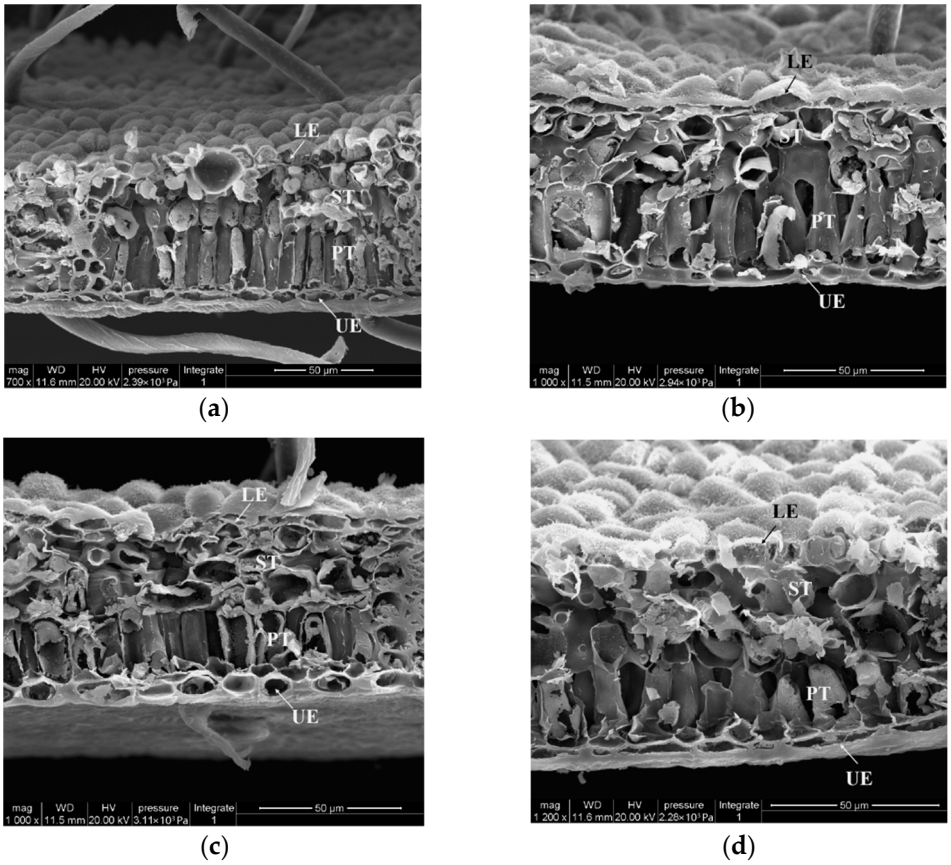


Figure 5. Changes in leaf anatomical structure of seedlings during the waterlogging-drainage process. (**a**): Control group; (**b**): Waterlogging stress for 12 days; (**c**): Waterlogging stress for 12 days and drainage for 6 days; (**d**): Waterlogging stress for 12 days and drainage for 12 days; LE: Lower epidermis; ST: Spongy tissue; PT: Palisade tissue; UE: Upper epidermis.

The total leaf thickness of the seedlings decreased gradually after drainage, and there was no significant difference between the seedlings after 12 days of waterlogging (Tables 6 and A4). The upper epidermal thickness of the leaves of *P. sheareri* seedlings showed a trend of increasing and then decreasing after drainage; in contrast, the lower epidermal thickness of the leaves showed a trend of decreasing and then increasing. The thickness of the upper epidermis reached its minimum value at 12 days of drainage, which was significantly different from other treatments ($p < 0.01$). The thickness of the lower epidermis reached the minimum value at 6 days of drainage, which decreased by 1.08 μm compared to 12 days of waterlogging stress and by 5.43 μm compared to the control. There was an extremely significant difference between the thicknesses of the lower epidermal layers of the leaves of *P. sheareri* seedlings drained for 6 days and those drained for 12 days ($p < 0.01$).

With the extension of drainage time, the thickness of leaf palisade tissue of *P. sheareri* seedlings decreased initially and then increased, and the thickness of palisade tissue of seedling leaves treated with drainage was extremely significantly smaller than those of the control seedlings and the 12-day-waterlogged seedlings ($p < 0.01$). The thickness of spongy tissue in the leaves of *P. sheareri* seedlings increased first and then decreased after drainage, which was extremely significantly different from that of the control seedlings ($p < 0.01$). Compared with waterlogging stress for 12 days, the spongy tissue thickness increased after 12 days and 18 days of drainage, by 3.12 μm and 2.47 μm, respectively.

Table 6. Determination results of leaf anatomical structure of seedlings during the waterlogging-drainage process.

Treatment	Total Blade Thickness (μm)	The Thickness of the Upper Epidermis (μm)	The Thickness of the Lower Epidermis (μm)	Palisade Tissue Thickness (μm)	Spongy Tissue Thickness (μm)	The Ratio of Palisade Tissue to the Spongy Tissue
Control group	77.15 ± 0.66 Aa	5.94 ± 0.50 Aa	9.10 ± 0.47 Aa	28.49 ± 0.27 Aa	32.31 ± 1.01 Aa	0.88 ± 0.02 Bb
Waterlogging stress for 12 days	63.67 ± 0.43 Bb	5.36 ± 0.18 Aa	4.75 ± 0.70 BCbc	29.07 ± 0.41 Aa	26.73 ± 0.87 Bc	1.09 ± 0.05 Aa
Waterlogging stress for 12 days and drainage for 6 days	63.16 ± 0.64 Bb	6.08 ± 0.31 Aa	3.67 ± 0.40 Cc	22.92 ± 0.38 Bb	29.85 ± 0.80 BCb	0.77 ± 0.03 Bc
Waterlogging stress for 12 days and drainage for 12 days	61.73 ± 0.74 Bb	3.00 ± 0.14 Bb	6.37 ± 0.73 Bb	23.26 ± 0.69 Bb	29.20 ± 0.80 BCbc	0.80 ± 0.03 Bbc

The thickness ratio of palisade tissue to spongy tissue in seedling leaves drained for 6 days was significantly different from that of control seedlings ($p < 0.05$), but the thickness ratio of palisade tissue to spongy tissue in leaves was not significantly different between the seedlings drained for 12 days and the control seedlings. The ratio of palisade tissue to spongy tissue decreased by 41.56% and 36.25%, respectively, after drainage for 12 days and 18 days, compared with waterlogging stress for 12 days.

3.4. Ultrastructural Changes in Mesophyll cells of Phoebe sheareri Seedlings during Waterlogging Stress and Drainage

3.4.1. Effect of the Ultrastructure of Leaf Mesophyll Cells of *Phoebe sheareri* Seedlings under Waterlogging Stress

With the extension of waterlogging stress time, the organelle structures, such as the structures of chloroplasts and mitochondria, in the leaves of *P. sheareri* seedlings changed to different degrees (Figure 6).

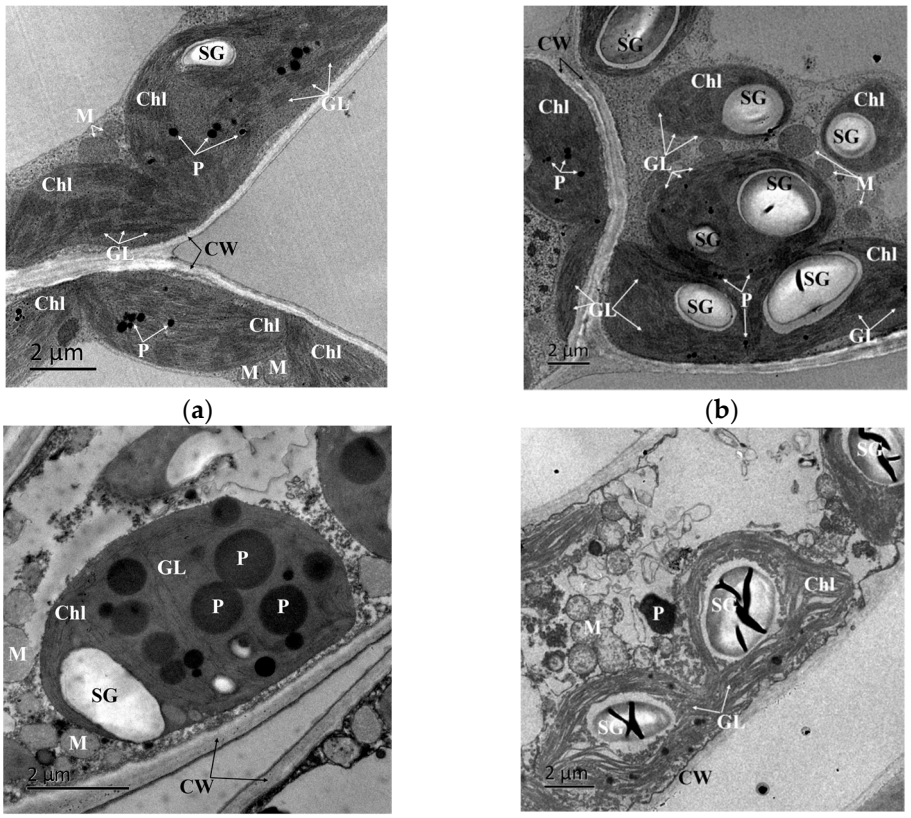


Figure 6. Ultrastructural changes of mesophyll cells of *Phoebe sheareri* seedlings under waterlogging stress. (**a**): Control group; (**b**): Waterlogging stress for 6 days; (**c**): Waterlogging stress for 12 days; (**d**): Waterlogging stress for 18 days; CW: Cell wall; Chl: Chloroplast; M: Mitochondrion; P: Plastoglobule; SG: Starch granule; GL: Granum lamella.

The cell walls of seedling leaves without waterlogged treatment were smooth, clear, and complete, and the cytoplasmic membrane was intact without folds (Figure 6a). The structure of the inner and outer membranes of the chloroplast was visible. It was fusiform and distributed in the inner membrane of the plasma membrane along its long axis with the thylakoids packed tightly, the grana lamellae arranged neatly, and a few plastid pellets and starch grains randomly distributed in the chloroplast. The mitochondrial structure was normal and complete, and its capsule visible, which was circular and distributed near the chloroplast with many inclusions.

After 6 days of waterlogging stress, the structure of the chloroplast membrane in seedling leaves was still clear and intact, but the chloroplasts were swollen in oval shapes, some chloroplasts had separated from the cell wall and moved toward the center of the cell, and the thylakoids were still stacked but not obviously so, the arrangement of the lamellae of some basal grains had changed, which might have been caused by the extrusion of starch grains (Figure 6b). The starch grains gradually became larger, some of them appeared with bright and dark stripes, and the mitochondrial structure was normal, distributed near chloroplasts, without obvious changes.

After 12 days of waterlogging stress, the chloroplast outer membrane of seedling leaf cells was no longer clear and there were impurities attached (Figure 6c). The chloroplast had clearly swelled, from spindle shapes to irregular ellipses. Plasmolysis appeared with blurred thylakoid structure and disorderly arranged grana lamellae. The plastid pellets had clearly swelled and increased. The outer membranes of the mitochondria were damaged, broken and incomplete, the contents of the mitochondria had spilled out, the matrix had become thinner, and the inner crest structure had vanished.

After 18 days of waterlogging stress, the chloroplast membrane of seedling leaf cells was wavy with rough edges, loose basal lamellae and partial dissolution (Figure 6d). Holes had appeared, and the starch grains in the chloroplast cells were irregular in shape, and distributed with many bright and dark stripes. Meanwhile, the plastid pellets were irregular and round. The mitochondrial outer membrane rupture was incomplete with impurities attached, some of the mitochondria merged, and some mitochondria had formed small vacuoles due to the break of the outer membrane and the outflow of the contents.

3.4.2. Effect of the Waterlogging-Drainage Process on the Ultrastructure of Leaf Mesophyll Cells of *Phoebe sheareri* Seedlings

The chloroplast outer membranes of leaf cells became rough with attached impurities when the seedlings were waterlogged for 12 days and drained for 6 days (Figure 7c). The chloroplasts swelled and distorted to an irregular oval shape. Meanwhile, their quantity decreased, and plasmolysis occurred. The thylakoid and grana inside the cells were blurred due to the disappearance of compact structure and the disorder of grana lamellae. The color of plastid pellets became lighter and dark patches appeared. The outer membranes of mitochondria were damaged, broken, and incomplete, and, thus, phenomena like the outflow of mitochondria inclusions, thinned matrix, and the disappearance of the inner crest structure occurred.

After 12 days of drainage, the leaf mesophyll cells were severely atrophied, and the outer membranes of the chloroplasts were wavy with impurities attached (Figure 7d). With intensified plasmolysis, the volume of plastid pellets became larger, the number and volume of starch grains increased, and some starch grains showed irregular shapes, due to the extrusion of plastid pellets. Impurities were attached to the outer membranes of mitochondria, and the structure of the inner crest disappeared.

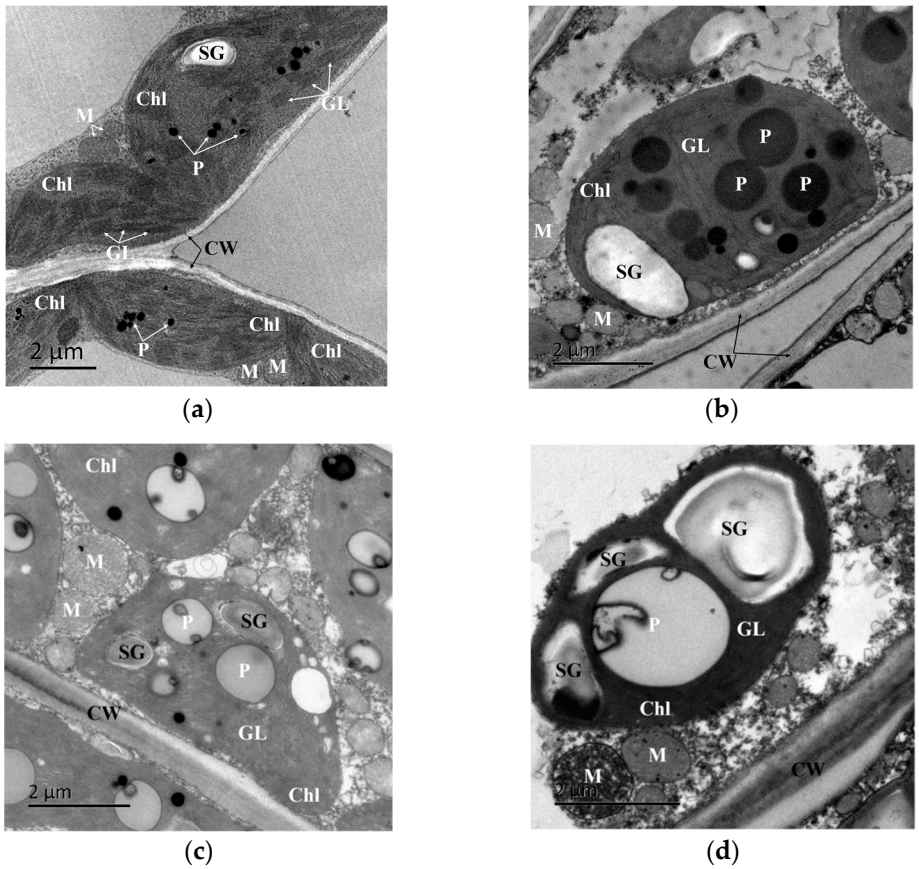


Figure 7. Ultrastructural changes of mesophyll cells of *Phoebe sheareri* seedlings during the waterlogging-drainage process. (**a**): Control group; (**b**): Waterlogging stress for 12 days; (**c**): Waterlogging stress for 12 days and drainage for 6 days; (**d**): Waterlogging stress for 12 days and drainage for 12 days; CW: Cell wall; Chl: Chloroplast; M: Mitochondrion; P: Plastoglobule; SG: Starch granule; GL: Granum lamella.

3.5. Correlation Analysis of Leaf Structure Indexes of Phoebe sheareri Seedlings during Waterlogging Stress and Drainage

When the seedlings were drained after 12 days of waterlogging, the leaf anatomical structure of the seedlings witnessed significant change, which affected photosynthesis, respiration, and transpiration of leaves, as well as the growth and physiological metabolism of the seedlings. To investigate the relationship of leaf anatomical structure, correlation analysis was performed on related indicators of *P. sheareri* seedling leaves during waterlogging stress and the drainage process, respectively (Tables 7 and 8).

When *P. sheareri* seedlings were treated with drainage after waterlogging, there was a certain correlation between the stomatal structure and anatomical structure of leaves (Table 8). There was a significant negative correlation between leaf stomatal density and thinner epidermis thickness ($0.01 < p < 0.05$). The leaf stomatal opening rate was significantly positively correlated with the stomatal width ($0.01 < p < 0.05$). The total leaf thickness had an extremely significant positive correlation with the stomatal width and the stomatal opening ($p < 0.01$).

Table 7. Correlation analysis of leaf anatomical structure indexes of *Phoebe sheareri* seedlings under waterlogging stress.

	X1	X2	X3	X4	X5	X6	X7	X8	X9	X10
X1	1									
X2	−0.970 *	1								
X3	−0.945	0.973 *	1							
X4	0.907	−0.981 *	−0.970 *	1						
X5	−0.560	0.744	0.740	−0.856	1					
X6	0.085	0.095	−0.071	−0.174	0.490	1				
X7	−0.841	0.947	0.934	−0.990 **	0.919	0.273	1			
X8	−0.063	0.298	0.337	−0.477	0.855	0.540	0.589	1		
X9	−0.344	0.557	0.584	−0.707	0.966 *	0.494	0.794	0.959 *	1	
X10	0.421	−0.266	−0.103	0.089	0.307	−0.014	0.005	0.702	0.534	1

X1: Stomatal length (μm), X2: Stomatal width (μm), X3: Stomatal opening rate (%), X4: Stomatal density (n/mm^2), X5: Total Blade thickness (μm), X6: The thickness of the upper epidermis (μm), X7: The thickness of the lower epidermis (μm), X8: palisade tissue thickness (μm), X9: Spongy tissue thickness (μm), X10: The ratio of palisade tissue to the spongy tissue; ** indicates correlation at 0.01 level, * indicates correlation at 0.05 level, the same below.

Table 8. Correlation analysis of leaf anatomical structure indexes of *Phoebe sheareri* seedlings during the waterlogging–drainage process.

	X1	X2	X3	X4	X5	X6	X7	X8	X9	X10
X1	1									
X2	−0.767	1								
X3	−0.846	0.985 *	1							
X4	0.336	−0.862	−0.779	1						
X5	−0.843	0.991 **	0.997 **	−0.790	1					
X6	−0.861	0.378	0.472	0.127	0.484	1				
X7	−0.423	0.890	0.841	−0.974 *	0.835	−0.077	1			
X8	−0.674	0.510	0.637	−0.223	0.579	0.397	0.430	1		
X9	−0.494	0.813	0.719	−0.799	0.768	0.265	0.692	−0.077	1	
X10	−0.226	−0.099	0.055	0.315	−0.019	0.158	−0.095	0.804	−0.654	1

** indicates correlation at 0.01 level, * indicates correlation at 0.05 level.

Under conditions of waterlogging stress, a certain correlation existed between leaf stomatal structure and leaf anatomical structure indices of *P. sheareri* seedlings (Table 7). There was an extremely significant negative correlation between stomatal density and the thickness of the lower epidermis ($p < 0.01$), the reason being that the stomatal density of *P. sheareri* concentrates in the lower epidermis, and change of stomatal density is closely related to change in lower epidermis thickness. The stomatal opening rate of the leaf epidermis was significantly positively correlated with stomatal width ($p < 0.05$), and significantly negatively correlated with stomatal density ($0.01 < p < 0.05$), indicating that the stomatal opening degree of *P. sheareri* seedlings was mainly affected by stomatal width and stomatal density during the waterlogging process. The thickness of spongy tissue was significantly positively correlated with the thickness of palisade tissue ($p < 0.05$).

4. Discussion

In the waterlogged environment, on the one hand, seedlings maintain their metabolic activity by consuming carbon reserves to facilitate the development of aerenchyma, adventitious roots, and hypertrophied lenticels, and, on the other hand, they decrease their metabolisms to preserve compounds for use in post-hypoxic conditions [29]. Waterlogging stress leads to hypoxia in the root system of seedlings, which, in turn, causes damage to the above-ground parts of seedlings, including leaves and other tissues and organs, through the accumulation of oxidation products [30,31].

4.1. Leaf Morphology

Under adverse circumstances, the change of leaf morphology is the most intuitive manifestation of the physiological state of seedlings. Changes in leaf shape can be environmentally induced, demonstrating that leaves are capable of responding to the surrounding climate conditions in a flexible manner [30]. Under conditions of waterlogging stress, the morphology of seedlings changes adaptively, the formation and growth of new leaves is blocked, the seedlings gradually age and fall off, and the growth of seedlings slows down [11]. Due to waterlogging stress, the leaves of *Pterocarya stenoptera* [32] and *Morus alba* [33] seedlings turned yellow, wilted, withered, and fell off. However, some studies have found that different plant species exhibit varying degrees of waterlogging symptoms due to their waterlogging tolerance. For example, after 18 days of waterlogging stress treatment, the lower leaves of *Populus* seedlings sensitive to waterlogging stress showed obvious chlorosis, while those tolerant to waterlogging stress had no significant change [34]. This paper demonstrates that, with the extension of waterlogging stress time, the leaves of *P. sheareri* seedlings gradually wilted, withered, and even fell off, which was similar to the research results of Kumutha et al. [35], Geng et al. [36], etc. In the early stage of waterlogging, the seedlings of *P. sheareri* grew new leaves and showed a short-term and recoverable wilting phenomenon. With the extension of waterlogging time, the wilting phenomenon of seedlings continued and could not be recovered. This was because the short-term waterlogging environment made *P. sheareri* seedlings mobilize their stress resistance mechanism to produce a large amount of energy and maintain the normal physiological metabolism of the seedlings, which was more conducive to the growth of *P. sheareri* seedlings. Waterlogging also had no significant effect on the growth and morphology of *Malus hupehensis* (Pamp.) Rehd. at the beginning of waterlogged treatment [37]. However, a long-term continuous waterlogging environment led to hypoxia in the roots of the seedlings, which made it impossible to synthesize and transform more energy to support growth, which was similar to the results of *Cerasus campanulata* after being waterlogged [38]. Consequently, the damaged metabolic mechanism in the seedlings blocked the synthesis of organic matter, inhibited the normal physiological metabolic process, affected the leaf morphology, and even led to leaf abscission [39].

This paper found that after waterlogging stress was relieved, the seedlings did not return to the state when waterlogged or before waterlogging. After 12 days of drainage, the seedlings appeared with the phenomenon of leaf abscission, and the survival rate declined steadily, which was different from *Taxodium* 'Zhongshansha 407', which survived without obvious symptoms of damage after relief of waterlogging [40]. The discrepancy results from *Taxodium* 'Zhongshansha 407' being a strong water-tolerant plant, maintaining a static watering-resistant strategy during the watering-out process [41,42]. However, it has also been shown that during the follow-up observation, grass plants, such as *Cynodon dactylon*, began to sprout new buds after the waterlogging environment was relieved, indicating that long-term waterlogging did not seriously affect their normal physiological functions, and the seedlings could recover growth through self-repair after the waterlogging stress was relieved [43]. The reason is that, although the leaf structures and functions of the seedlings were damaged under the condition of long-time continuous hypoxia, the overall growth of the seedlings was not affected, and survival could be guaranteed by adjusting the material and energy distribution of organs [40]. This suggests that the recovery process mainly depends on the type of species and nutrient reserves [44,45]. Plants with low levels of nutrient reserves cannot survive and grow with reserve substances under waterlogging for a long time [41].

4.2. Stomata and Anatomical Structure of Leaf Epidermis

The response of leaf epidermal structure to waterlogging stress is mainly reflected in the shape and arrangement of leaf epidermal cells, stomatal conductance, and stomatal density. The seedlings exchange gas, water, and signals with the external environment through the adjustment of stomatal size and density, which play an important role in the

regulation of stress resistance [46,47]. Leaves respond to stress by changing stomatal size, degrees of opening and closing, and density [48]. Leaf stomata are sensitive to the leaf water status. Stomata close actively to reduce water evaporation and increase waterlogging tolerance [12,49]. In this paper, it was found that waterlogging stress reduced the activity of guard cells in leaves of *P. sheareri* seedlings, and contributed to change of stomatal morphology and movement, increase in the ratio of length to width for stomata in the lower epidermis and stomatal density, as well as decreased stomatal opening degree, similar to the results of Gu et al. [50]. It is an adaptive strategy for plants, and under waterlogging conditions, plants growing in permanently damp environments have more stomata than those growing in dry habitats [49]. To maintain normal gas exchange and energy balance, the leaves quickly close part of the stomata, which may reduce leaf transpiration and the damage of waterlogging stress [51]. At the same time, the smaller the stomata, the higher the water use efficiency under conditions of favorable water supply [52]. The leaf stomatal status of *P. sheareri* seedlings gradually recovered after the waterlogging stress was relieved, but could not be restored to the state before waterlogging. The reason for this is that the waterlogging stress seriously damaged the stomatal state of the leaves and the internal cell structure, and even with drainage the stomatal status could not be recovered.

The leaf is the main organ for photosynthesis, respiration and transpiration of seedlings, and the unification of morphological structural change and function is the biological basis for seedlings to adapt to the growth environment [53,54]. It was found that under the condition of waterlogging, the upper epidermal cells, lower epidermal cells and palisade tissue cells of *P. sheareri* leaves transformed from a tight and neat arrangement to a loose arrangement. At the later stage of stress, the palisade tissue cells fused, the gaps became larger, and spongy tissue cells became smaller and were disorderly in arrangement, similar to the research results of Ren et al. [12]. Yin et al. [51] observed that intercellular spaces increased significantly in *Chrysanthemum zawadskii* leaves under waterlogged conditions, which facilitated rapid gas exchange. Intercellular spaces appeared in the leaf structure, which represented another positive adaptation to waterlogging, which could improve the capacity for oxygen capture, and help to store and exchange gases within the waterlogged tissues [55,56]. With the extension of stress time, the thickness of the upper epidermis and palisade tissue, and the ratio of the palisade tissue to spongy tissue of *P. sheareri* leaves experienced an initial increase and a subsequent decrease. This finding was different from that reported by Zhang et al. [16], who observed that the leaf thickness of *Sorghum bicolor* decreased under waterlogging stress, mainly due to changes in the thickness of the upper epidermal and mesophyll cells. The leaf thickness and its components increased differently after 6 days of waterlogging, which indicated that the stress-resistant mechanism of seedlings could respond quickly in a short time to maintain the normal growth of seedlings through leaf thickening, promoting the development of seedling leaves to a certain extent, similar to the results for *Chrysanthemum zawadskii* [49]. At the later stage of waterlogging stress, the leaf thickness was thinner due to decreased turgor pressure, which caused the enlargement of the cell gap and the loose arrangement of cells affecting the thickness of leaves [16].

After being relieved of waterlogging stress, the anatomical structure of *P. sheareri* seedling leaves confirmed that the degree of damage to all parts of the cells was aggravated, in that the upper epidermis cells became narrow, palisade tissue and spongy tissue cells were fused with blurred boundaries, the thickness of leaves and their components were not much different from those of the waterlogged seedlings, and even showed signs of gradual thinning. The reason is that although they grew in a normal water environment after drainage, the leaf structure of *P. sheareri* seedlings had been seriously and irreversibly damaged during the waterlogging process.

4.3. Mesophyll Cell Ultrastructure

Photosynthesis is directly influenced by the morphology and ultrastructure of chloroplasts, and in adverse circumstances, the obvious organelles in plant mesophyll cells are

chloroplasts and mitochondria [28]. Their morphologies and internal structures change with the external environment [12]. This paper found that under the conditions of waterlogging stress, the chloroplast membrane structure of seedling leaf cells ruptured gradually, the chloroplasts swelled continuously, deforming from spindles to irregular ellipses and separating from the cell wall with a tendency to move towards the center of the cell. The grana and thylakoids lost their compact and orderly arrangements and the grana lamellae gradually twisted. Thylakoid membrane degradation and lipid accumulation increased the number and volume of plastid pellets. Such changes also occurred in the waterlogging stress experiments of *Zea mays* and *Sorghum bicolor* [12,14]. The chloroplasts of *Kosteletzkya virginica* became spherical and their volume decreased under waterlogging. Moreover, the lamellae of thylakoids swelled, and chloroplast inclusions decreased [13]. Waterlogging damages the ultrastructure of mesophyll cells and reduces the photosynthetic capacity of the leaf [57]. The breakdown of membrane systems caused by waterlogging on mesophyll cells results in apoptosis and the loss of photosynthetic potential [58].

Compared with the seedlings waterlogged for 12 days, the ultrastructure of mesophyll cells in the seedlings drained for 6 days did not change significantly and did not show obvious signs of recovery. After 12 days of drainage, the chloroplast structure of leaf cells was further damaged, the outer membranes of chloroplasts blurred, the swelling of chloroplasts was aggravated, the separation of plasma wall was obvious, and a large amount of starch accumulated to form large starch granules, indicating that 12 days after the stress was relieved, the damage to chloroplasts was more serious than that caused by waterlogging. The reason is that the waterlogging environment caused irreversible damage to the chloroplast structure of *P. sheareri* seedlings. The chloroplast membrane gradually disintegrated, and grana and starch grains piled up together, resulting in the decline of the photosynthetic areas and hindering normal photosynthesis. The chloroplast structure could not be restored to the normal state after the stress was relieved [59]. In addition, this paper confirmed that there was a certain correlation between the abnormality of chloroplast structure and leaf color of *P. sheareri* seedlings during waterlogging progression. When waterlogged for 12 days, the young leaves of *P. sheareri* seedlings wilted, curled, and turned yellow. Among the chloroplast ultrastructures over the same period, it was observed that the thylakoid had a fuzzy structure, and the number and volume of plastid pellets increased, which was similar to the research results of Sun et al. [60] and Liu et al. [61].

As important organelles in respiration, mitochondria can not only provide energy for various life activities, but also participate in processes such as cell differentiation, cell information transmission, and cell apoptosis, with the ability to regulate cell growth and cell cycle [62]. Furthermore, certain mitochondria grow longer and become dysfunctional with time, and their membranes disintegrate [57]. After 12 days of waterlogging stress, the mitochondrial structure of *P. sheareri* seedling leaf cells began to change significantly, as the outer membranes broke and degraded, and contents flowed out. With the extension of stress time, the mitochondrial damage intensified, the membrane structure was damaged and degraded gradually, and the mitochondria fused. The phenomenon of mitochondria gradually swelling and finally disintegrating under waterlogging also occurred in *Kosteletzkya virginica* [11]. After the stress was relieved, the ultrastructure of mitochondria in leaf cells was not significantly improved, and the structure was still loose and fuzzy, indicating that the respiratory function of *P. sheareri* seedlings was damaged after drainage. Observation of *Cabernet sauvignon* cells found that vitamin C in mitochondria may flow out together with the contents, thereby causing programmed cell death (PCD), resulting in partial mitochondrial apoptosis and the formation of small vacuoles [63]. Some studies have also found that cell necrosis caused by programmed cell death of chloroplasts and mitochondria may be one of the mechanisms by which *Ammodendron argenteum* and *Triticum aestivum* seedlings adapt to water stress [64,65].

Under stress conditions, two organelles, the chloroplasts and the mitochondria, interact with each other. After the mitochondrial structure is destroyed, the metabolism of the seedling is disordered, unable to provide energy for the transport of photosynthetic

products and, thus, affecting the transport of photosynthetic products in the chloroplasts for seedling survival [66]. As a result, a large amount of starch accumulates in the chloroplasts, which cannot be transported in time. When the number of starch grains reaches a certain amount, it causes mechanical damage to the thylakoid structure, thereby affecting chloroplast photosynthetic rate and photosynthetic activity [57,67]. This paper confirmed that chloroplasts and mitochondria have different response times and degrees of response to stress. Chloroplasts began to respond in the early stage of stress in *P. sheareri* by changing their shape, size and membrane structure, and their systems became disordered and scattered, whereas mitochondria began to rupture the outer membrane, release contents and form small vacuoles in the late stage of stress. This asynchronous stress response alleviates the damage and ensures that *P. sheareri* seedlings can carry out physiological adjustments in a short time to maintain normal physiological metabolic functions. This pattern was also observed in *Populus simonii* under waterlogging stress, where chloroplasts were sensitive to stress, while mitochondrial structures were relatively stable [66]. This mechanism can only cope with stress for a short time and cannot play a role in a long-term continuous waterlogging environment. However, some studies have found that in the process of stress, mitochondria are less sensitive, and their stress response occurs later than that of chloroplasts since mitochondria need to provide senescent leaves with the energy required for various life activities, such as the transfer and transportation of nutrients [28].

Leaves are sensitive to environmental changes with strong plasticity, and the changes in their external morphology and anatomical structural characteristics can better reflect the adaptability of plants to waterlogging [17]. With the extension of waterlogging time, the balance between the organelles of *P. sheareri* seedlings was gradually broken, the chloroplasts were deformed, the plasma walls separated, the mitochondrial membranes were damaged, the inclusions were exuded, and the grainy lamellae were gradually distorted, resulting in leaf thickness changes [55,68]. The thickness of leaf components of *P. sheareri* gradually decreased under waterlogging conditions, especially the lower epidermis thickness. In addition, due to the influence of waterlogging environment on gas exchange, the stomatal opening of leaves also decreased gradually [48]. Under the influence of these factors, the leaf external morphology showed gradual wilting. When waterlogging stress causes irreversible damage to leaf cells, leaf stomata and leaf thickness gradually decrease, and organelles, such as chloroplasts and mitochondria, gradually disintegrate and cavitate, eventually causing leaf morphology to wither and seedling death [69,70].

Taken together, these results showed that leaf morphology, anatomical structure and ultrastructure associated with increasing waterlogging treatment respond differently. Nevertheless, leaf physiology or molecular mechanisms can further reveal the correlation between seedling leaves and changes in the external moisture environment. Additional measurements of leaf physiology, internal structure and moisture should be made in future studies to obtain further information.

5. Conclusions

This paper confirmed that waterlogging stress affects the external morphology of the leaves of *P. sheareri* seedlings, mainly reflected in aspects such as the inhibition of the growth of new leaves, gradual yellowing and wilting of leaves, and leaf abscission in severe cases. Further observation of the microstructure of the leaf epidermis illustrated that waterlogging stress leads to stomatal closure and increased stomatal density of the leaf epidermis, anda long-term waterlogging environment reduces the thickness of leaves and their components. Waterlogging stress mainly affects organelles such as chloroplasts and mitochondria, causing damage to chloroplast outer membranes, changes in shape, plasmolysis, disarray of grana lamellae arrangements, decrease of mitochondrial matrix concentrations, and disappearance of inner crest structures. After *P. sheareri* seedlings were treated with drainage, their leaf morphology, stomata, epidermal structure and mesophyll cells did not improve significantly, which was attributed to the fact that the seedlings suffered irreversible damage during the waterlogging process, and their internal metabolic

mechanism was seriously injured and could not be recovered. Based on the leaf morphology and various indices, the seedlings of *P. sheareri* performed best in several aspects such as leaf morphology, leaf epidermis microstructure and mesophyll cell ultrastructure when they were waterlogged for 6 days, which indicated that a short-term waterlogging treatment can promote better development of the leaves and their internal mechanisms in *P. sheareri* seedlings. However, under conditions of long-term waterlogging, the damage became increasingly serious.

This paper focused on preliminary observations of the changes in the external morphology of leaves, the microstructure of leaf epidermis, and the ultrastructure of mesophyll cells of *P. sheareri* seedlings under waterlogging stress and during the waterlogging–drainage process, but lacked deep exploration on the differences in the waterlogging resistance mechanisms among the internal organelles of *P. sheareri* seedlings and the dynamic changes in the internal metabonomics and molecular mechanisms of *P. sheareri* seedlings under waterlogging stress. In the future, it is still necessary to conduct in-depth research on the linkage mechanism of cell structure and function of seedling leaves in adverse environments, as well as on metabolomics and the molecular mechanisms.

Author Contributions: F.S. contributed to conceptualization, investigation, supervision, writing—review and editing. Z.P. contributed to conceptualization, data curation and visualization, writing—original draft, writing—review and editing. P.D. contributed to conceptualization, investigation, data curation and visualization, writing—review and editing. Y.S. contributed to supervision, conceptualization, review and editing. Y.L. and B.H. contributed to supervision, review and editing. All authors have read and agreed to the published version of the manuscript.

Funding: This research was funded by the subject of Key R&D Plan of Shandong Province (Major Scientific and Technological Innovation Project): Mining and Accurate Identification of Forest Tree Germplasm Resources (2021LZGC023); Jiangsu Agriculture Science and Technology Innovation Fund (CX (19) 2123).

Data Availability Statement: All data relevant to the study are included in the article.

Conflicts of Interest: The authors declare no conflict of interest.

Appendix A

Table A1. ANOVA of leaf epidermal stomata of seedlings under waterlogging stress.

Index	Square Sum	Degree of Freedom	Mean Square	F Value	*p* Value
Stomatal length	5.647	3	1.882	1.617	0.225
Stomatal width	74.140	3	24.713	80.535	0.000
Stomatal opening rate	0.060	3	0.020	210.754	0.000
Stomatal density	6,649,454.502	3	2,216,484.834	106.044	0.000

Table A2. ANOVA of leaf epidermal stomata of seedlings during the waterlogging-drainage process.

Index	Square Sum	Degree of Freedom	Mean Square	F Value	*p* Value
Stomatal length	20.998	3	6.99	6.491	0.004
Stomatal width	67.621	3	22.540	72.143	0.000
Stomatal opening rate	0.052	3	0.017	312.298	0.000
Stomatal density	3,949,174.521	3	131,631.507	122.422	0.000

Table A3. ANOVA of leaf anatomical structure of seedlings under waterlogging stress.

Index	Square Sum	Degree of Freedom	Mean Square	F Value	*p* Value
Total blade thickness	2271.940	3	757.313	193.140	0.000
The thickness of the upper epidermis	6.616	3	2.205	1.618	0.225
The thickness of the lower epidermis	103.091	3	34.364	23.120	0.000
Palisade tissue thickness	674.194	3	224.731	163.064	0.000
Spongy tissue thickness	289.756	3	96.585	25.908	0.000
The ratio of palisade tissue to the spongy tissue	0.219	3	0.073	14.275	0.000

Table A4. ANOVA of leaf anatomical structure of seedlings during the waterlogging-drainage process.

Index	Square Sum	Degree of Freedom	Mean Square	F Value	*p* Value
Total blade thickness	802.069	3	267.356	93.849	0.000
The thickness of the upper epidermis	30.688	3	10.229	20.753	0.000
The thickness of the lower epidermis	83.573	3	27.858	15.861	0.000
Palisade tissue thickness	146.466	3	48.822	29.286	0.000
Spongy tissue thickness	78.828	3	26.276	6.895	0.003
The ratio of palisade tissue to the spongy tissue	0.301	3	0.100	15.970	0.000

References

1. Chen, H.; Wu, Q.; Ni, M.; Chen, C.; Han, C.; Yu, F. Transcriptome analysis of endogenous hormone response mechanism in roots of *Styrax tonkinensis* under waterlogging. *Front. Plant Sci.* **2022**, *13*, 896850. [CrossRef]
2. Arnell, N.W.; Gosling, S.N. The impacts of climate change on river flood risk at the global scale. *Clim. Change* **2016**, *134*, 387–401. [CrossRef]
3. Pan, L.; Xue, L. Plant physiological mechanisms in adapting to waterlogging stress: A review. *Chin. J. Ecol.* **2012**, *31*, 2662–2672. (In Chinese) [CrossRef]
4. Pan, J.; Sharif, R.; Xu, X.; Chen, X. Mechanisms of waterlogging tolerance in plants: Research progress and prospects. *Front. Plant Sci.* **2021**, *11*, 627331. [CrossRef] [PubMed]
5. Zhou, W.G.; Chen, F.; Meng, Y.J.; Chandrasekaran, U.; Luo, X.F.; Yang, W.Y.; Shu, K. Plant waterlogging/flooding stress responses: From seed germination to maturation. *Plant Physiol. Biochem.* **2020**, *148*, 228–236. [CrossRef] [PubMed]
6. Wei, W.L.; Li, D.H.; Wang, L.H.; Ding, X.; Zhang, Y.X.; Gao, Y.; Zhang, X.R. Morpho-anatomical and physiological responses to waterlogging of sesame (*Sesamum indicum* L.). *Plant Sci.* **2013**, *208*, 102–111. [CrossRef] [PubMed]
7. Kaur, G.; Vikal, Y.; Kaur, L.; Kalia, A.; Mittal, A.; Kaur, D.; Yadav, I. Elucidating the morpho-physiological adaptations and molecular responses under long-term waterlogging stress in maize through gene expression analysis. *Plant Sci.* **2021**, *304*, 110823. [CrossRef] [PubMed]
8. Zhang, P.; Lyu, D.; Jia, L.; He, J.; Qin, S. Physiological and de novo transcriptome analysis of the fermentation mechanism of *Cerasus sachalinensis* roots in response to short-term waterlogging. *BMC Genom.* **2017**, *18*, 649. [CrossRef] [PubMed]
9. Doupis, G.; Kavroulakis, N.; Psarras, G.; Papadakis, I. Growth, photosynthetic performance and antioxidative response of 'Hass' and 'Fuerte' avocado (*Persea americana* Mill.) plants grown under high soil moisture. *Photosynthetica* **2017**, *55*, 655–663. [CrossRef]
10. Wu, J.; Wang, J.; Hui, W.; Zhao, F.; Wang, P.; Su, C.; Gong, W. Physiology of plant responses to water stress and related genes: A review. *Forests* **2022**, *13*, 324. [CrossRef]
11. Yang, W.C.; Lin, K.H.; Wu, C.W.; Chang, Y.J.; Chang, Y.S. Effects of waterlogging with different water resources on plant growth and tolerance capacity of four herbaceous flowers in a bioretention basin. *Water* **2020**, *12*, 1619. [CrossRef]
12. Ren, B.Z.; Zhang, J.W.; Dong, S.T.; Liu, P.; Zhou, B. Effects of waterlogging on leaf mesophyll cell ultrastructure and photosynthetic characteristics of Summer Maize. *PLoS ONE* **2016**, *11*, e0161424. [CrossRef]
13. Zhou, J.; Wan, S.W.; Li, G.; Qin, P. Ultrastructure changes of seedlings of *Kosteletzkya virginica* under waterlogging conditions. *Biol. Plant.* **2011**, *55*, 493–498. [CrossRef]
14. Zhang, R.D.; Zhou, Y.F.; Yue, Z.X.; Chen, X.F.; Cao, X.; Xu, X.X.; Xing, Y.F.; Jiang, B.; Ai, X.Y.; Huang, R.D. Changes in photosynthesis, chloroplast ultrastructure, and antioxidant metabolism in leaves of sorghum under waterlogging stress. *Photosynthetica* **2019**, *57*, 1076–1083. [CrossRef]
15. Li, C.; Wan, Y.; Shang, X.; Fang, S. Responses of microstructure, ultrastructure and antioxidant enzyme activity to PEG-Induced drought stress in *Cyclocarya paliurus* Seedlings. *Forests* **2022**, *13*, 836. [CrossRef]

16. Zhang, R.D.; Zhou, Y.F.; Yue, Z.X.; Chen, X.F.; Cao, X.; Ai, X.Y.; Jiang, B.; Xing, Y.F. The leaf-air temperature difference reflects the variation in water status and photosynthesis of sorghum under waterlogged conditions. *PLoS ONE* **2019**, *14*, e0219209. [CrossRef]
17. Xiao, Y.; Jie, Z.L.; Wang, M.; Lin, G.H.; Wang, W.Q. Leaf and stem anatomical responses to periodical waterlogging in simulated tidal floods in mangrove *Avicennia marina* seedlings. *Aquat. Bot.* **2009**, *91*, 231–237. [CrossRef]
18. Yang, J.; He, K.Y.; Li, X.C.; Huang, L.B. Influences of waterlogging stress on the growth and leaf anatomical structures of two oak species. *J. For. Eng.* **2008**, *110*, 34–37. (In Chinese)
19. Zhao, X.Y.; Han, L.X.; Zhang, G.X. Physiological characteristics and leaf structure of *Chionanthus virginicus* seedlings under flooding stress. *Acta Bot. Boreali-Occident. Sin.* **2023**, *43*, 410–420. (In Chinese)
20. Liu, G.Q.; Zhu, H.J.; Zhou, B.B.; Sheng, J.Y.; Zang, X. Effects of drought and flooding stress on photosynthetic characteristics of pecan *Carya illinoinensis* Wangenh. and ultrastructure of its chloroplast. *Jiangsu J. Agric. Sci.* **2012**, *28*, 1429–1433. (In Chinese)
21. Ye, Z.H.; Huang, S.L.; Zhu, J.; Zou, H.H.; Tan, G.W. Propagation, maintenance and landscape application of four ornamental plant species of *Phoebe*. *Guangdong Landsc. Archit.* **2016**, *38*, 48–51. (In Chinese)
22. Wang, Y.; Ma, X.H.; Lu, Y.F.; Hu, X.E.; Lou, L.H.; Tong, Z.K.; Zhang, J.H. Assessing the current genetic structure of 21 remnant populations and predicting the impacts of climate change on the geographic distribution of *Phoebe sheareri* in southern China. *Sci. Total Environ.* **2022**, *846*, 157391. [CrossRef]
23. Wang, Z.; Dong, Z. Research on the development and utilization of plant resources in the genus *Phoebe*. *Heilongjiang Agric. Sci.* **2008**, *180*, 119–121. (In Chinese)
24. Shi, H.; Deng, Y.; Liu, S.; Li, M. Container seedling cultivation techniques of *Phoebe sheareri* in Wuhan area. *Hubei For. Sci. Technol.* **2020**, *49*, 83–84. (In Chinese)
25. Wang, Z.M.; Zhou, T.T.; Xue, L.; Xu, J.X. Effect of low temperature stress on physiological characteristics of seedlings of four landscape species. *J. Anhui Agric. Univ.* **2016**, *43*, 209–214. (In Chinese)
26. Li, G.F.; Li, Y.Z.; Zhu, Y.Z.; Zheng, W.J.; Li, M.X.; Hu, J.L.; Fei, Y.J.; Zhu, S.J. Exogenous application of melatonin to mitigate drought stress-induced oxidative damage in *Phoebe sheareri* seedlings. *PeerJ* **2023**, *11*, e15159. [CrossRef]
27. Jain, R.; Singh, A.; Singh, S.P.; Chandra, A.; Pathak, A.D. Morphological and anatomical aberrations induced by waterlogging in sugarcane. *J. Environ. Biolog.* **2019**, *40*, 634–640. [CrossRef]
28. Salah, A.; Zhan, M.; Cao, C.G.; Han, Y.L.; Ling, L.; Liu, Z.H.; Li, P.; Ye, M.; Jiang, Y. Gamma-Aminobutyric acid promotes chloroplast ultrastructure, antioxidant capacity, and growth of waterlogged maize seedlings. *Sci. Rep.* **2019**, *9*, 484. [CrossRef]
29. Bhusa, N.; Kim, H.S.; Han, S.G.; Yoon, T.M. Photosynthetic traits and plant-water relations of two apple cultivars grown as bi-leader trees under long-term waterlogging conditions. *Environ. Exp. Bot.* **2020**, *176*, 104111. [CrossRef]
30. Zhou, P.Y.; Qian, J.; Yuan, W.D.; Yang, X.; Di, B.; Meng, Y.; Shao, J.Z. Effects of interval flooding stress on physiological characteristics of Apple leaves. *Horticulturae* **2021**, *7*, 331. [CrossRef]
31. Jimenez, J.D.; Cardoso, J.A.; Dominguez, M.; Fischer, G.; Rao, I. Morpho-anatomical traits of root and non-enzymatic antioxidant system of leaf tissue contribute to waterlogging tolerance in Brachiaria grasses. *Grassl. Sci.* **2015**, *61*, 243–251. [CrossRef]
32. Xu, L.P.; Pan, Y.L.; Yu, F.Y. Effects of water-stress on growth and physiological changes in *Pterocarya stenoptera* seedlings. *Sci. Hortic.* **2015**, *190*, 11–23. [CrossRef]
33. Rao, L.Y.; Li, S.Y.; Cui, X. Leaf morphology and chlorophyll fluorescence characteristics of mulberry seedlings under waterlogging stress. *Sci. Rep.* **2021**, *11*, 1337. [CrossRef] [PubMed]
34. Peng, Y.J.; Zhou, Z.X.; Zhang, Z.; Yu, X.L.; Zhang, X.Y.; Du, K.B. Molecular and physiological responses in roots of two full-sib poplars uncover mechanisms that contribute to differences in partial submergence tolerance. *Sci. Rep.* **2018**, *8*, 12829. [CrossRef] [PubMed]
35. Kumutha, D.; Ezhilmathi, K.; Sairam, R.K.; Srivastava, G.C.; Deshmukh, P.S.; Meena, R.C. Waterlogging induced oxidative stress and antioxidant activity in pigeonpea genotypes. *Biol. Plant.* **2009**, *53*, 75–84. [CrossRef]
36. Geng, R.N.; Zhang, X.Y.; Fan, X.P.; Hu, Q.; Ni, T.H.; Du, K.B. Waterlogging tolerance evaluation of fifteen poplar clones cultivated in the Jianghan Plain of China. *Not. Bot. Horti Agrobot. Cluj Napoca* **2021**, *49*, 12421. [CrossRef]
37. Liu, X.; Peng, Y.; Fan, J.J.; Zhang, W.X.; Li, X.; Zou, X. Effects of waterlogging stress on growth and physiological characteristics in *Malus hupehensis*. *Nonwood For. Res.* **2018**, *36*, 35–42. (In Chinese) [CrossRef]
38. Lu, R.H.; Xu, L.X.; Zhou, X.X.; Sheng, S.H.; Feng, C.; Chen, C.; Tang, L. Effects of flooding stress on growth and photosynthesis of *Cerasus campanulate* seedlings. *Acta Agric. Univ. Jiangxiensis* **2022**, *44*, 871–881. (In Chinese) [CrossRef]
39. Tong, M.Y.; Huang, J.Q.; Li, C.J. Effects of waterlogging on morphology and chlorophyll fluorescence characteristics of cherry tomato at seedling stage. *J. Irrig. Drain.* **2019**, *38*, 8–15. (In Chinese) [CrossRef]
40. Hua, J.F.; Han, L.W.; Wang, Z.Q.; Shi, Q.; Yin, Y.L. The growth and photosynthesis characters of *Taxodium* hybrid'Zhongshanshan 407' following the de-submergence. *J. Nanjing For. Univ. Nat. Sci. Ed.* **2017**, *41*, 191–196. (In Chinese)
41. Tanaka, K.; Masumori, M.; Yamanoshita, T.; Tange, T. Morphological and anatomical changes of *Melaleuca cajuputi* under submergence. *Trees* **2011**, *25*, 695–704. [CrossRef]
42. Yu, X.Q.; Luo, N.; Yan, J.P.; Tang, J.C.; Liu, S.W.; Jiang, Y.W. Differential growth response and carbohydrate metabolism of global collection of perennial ryegrass accessions to submergence and recovery following de-submergence. *J. Plant Physiol.* **2012**, *169*, 1040–1049. [CrossRef] [PubMed]
43. Feng, Y.L.; Xian, X.D. Preliminary observation on the growth recovery of five grass plants after long-term flooding. *South China Agric.* **2012**, *6*, 18–21. (In Chinese) [CrossRef]

44. Voesenek, L.A.C.J.; Colmer, T.D.; Pierik, R.; Millenaar, F.F.; Peeters, A.J.M.; Peeters, A. How plants cope with complete submergence. *New Phytol.* **2006**, *170*, 213–226. [CrossRef]
45. Bailey-Serres, J.; Voesenek, L.A.C.J. Flooding stress: Acclimations and genetic diversity. *Annu. Rev. Plant Biol.* **2008**, *59*, 313–339. [CrossRef] [PubMed]
46. Florez-Velasco, N.; Balaguera-Lopez, H.E.; Restrepo-Diaz, H. Effects of foliar urea application on lulo (*Solanum quitoense* cv. *septentrionale*) plants grown under different waterlogging and nitrogen conditions. *Sci. Hortic.* **2015**, *186*, 154–162. [CrossRef]
47. Luan, H.Y.; Guo, B.J.; Pan, Y.H.; Lv, C.; Shen, H.Q.; Xu, R.G. Morpho-anatomical and physiological responses to waterlogging stress in different barley (*Hordeum vulgare* L.) genotypes. *Plant Growth Regul.* **2018**, *85*, 399–409. [CrossRef]
48. Yin, D.M.; Zhang, Z.G.; Luo, H.L. Anatomical responses to waterlogging in *Chrysanthemum zawadskii*. *Sci. Hortic.* **2012**, *146*, 86–91. [CrossRef]
49. Malik, A.I.; Colmer, T.D.; Lambers, H.; Schortemeyer, M. Changes in physiological and morphological traits of roots and shoots of wheat in response to different depths of waterlogging. *Aust. J. Plant Physiol.* **2001**, *28*, 1121–1131. [CrossRef]
50. Gu, X.B.; Xue, L.; Lu, L.H.; Song, G.H.; Xie, M.; Zhang, H.Q. Characteristics of the response of *Actinidia polygama* to long-term waterlogging stress. *J. Fruit Sci.* **2019**, *36*, 327–337. (In Chinese) [CrossRef]
51. Rood, S.B.; Nielsen, J.L.; Shenton, L.; Gill, K.M.; Letts, M.G. Effects of flooding on leaf development, transpiration, and photosynthesis in narrowleaf cottonwood, a willow-like poplar. *Photosynth. Res.* **2010**, *104*, 31–39. [CrossRef] [PubMed]
52. Blanke, M.M.; Cooke, D.T. Effects of flooding and drought on stomatal activity, transpiration, photosynthesis, water potential and water channel activity in strawberry stolons and leaves. *Plant Growth Regul.* **2004**, *42*, 153–160. [CrossRef]
53. Li, G.; Hu, S.; Zhao, X.Y.; Kumar, S.; Li, Y.X.; Yang, J.J.; Hou, H.W. Mechanisms of the morphological plasticity induced by phytohormones and the environment in plants. *Int. J. Mol. Sci.* **2021**, *22*, 765. [CrossRef] [PubMed]
54. Chitwood, D.H.; Sinha, N.R. Evolutionary and environmental forces sculpting leaf development. *Curr. Biol.* **2016**, *26*, R297–R306. [CrossRef] [PubMed]
55. Wang, W.Q.; Xiao, Y.; Chen, L.Z.; Lin, P. Leaf anatomical response to periodical waterlogging in simulated semidiurnal tides in mangrove *Bruguiera gymnorrhiza* seedlings. *Aquat. Bot.* **2007**, *86*, 223–228. [CrossRef]
56. Yin, D.M.; Chen, S.M.; Chen, F.D.; Guan, Z.Y.; Fang, W.M. Morpho-anatomical and physiological responses of two *Dendranthema* species to waterlogging. *Environ. Exp. Bot.* **2010**, *68*, 112–130. [CrossRef]
57. Sharma, S.; Bhatt, U.; Sharma, J.; Kalaji, H.M.; Mojski, J.; Soni, V. Ultrastructure, adaptability, and alleviation mechanisms of photosynthetic apparatus in plants under waterlogging: A review. *Photosynthetica* **2022**, *60*, 430–444. [CrossRef]
58. Bertamini, M.; Muthuchelian, K.; Nedunchezhian, N. Shade effect alters leaf pigments and photosynthetic responses in Norway spruce (*Picea abies* L.) grown under field conditions. *Photosynthetica* **2006**, *44*, 227–234. [CrossRef]
59. Qi, H.Y.; Liu, Y.; Liu, H.T. Effect of water deficit on stomatal characteristics and ultrastructure of chloroplast in tomato leaves. *Acta Bot. Boreali-Occident. Sin.* **2009**, *29*, 9–15. (In Chinese)
60. Sun, W.W.; Meng, X.M.; Xu, X.Y.; Wu, M.H.; Qin, M.Y.; Lin, M.M.; Zhang, X.Y.; Yue, G.Z. Contents of pigments and anatomical structure in the leaves of *Forsythia koreana* 'Sun Gold'. *Bull. Bot. Res.* **2020**, *40*, 321–329. (In Chinese)
61. Shao, G.C.; Lan, J.J.; Yu, S.E.; Liu, N.; Guo, R.Q.; She, D.L. Photosynthesis and growth of winter wheat in response to waterlogging at different growth stages. *Photosynthetica* **2013**, *51*, 429–437. [CrossRef]
62. Navarro, A.; Boveris, A. The mitochondrial energy transduction system and the aging process. *Am. J. Physiol. Physiol.* **2007**, *292*, C670–C686. [CrossRef]
63. Shen, J.; Zhang, Z.W. Cytomorphological studies of programmed cell death in Cabernet sauvignon induced by artificial drought stress. *J. Northwest A F Univ. (Nat. Sci. Ed.)* **2009**, *37*, 125–132. (In Chinese) [CrossRef]
64. Jiang, Z.; Song, X.F.; Zhou, Z.Q.; Wang, L.K.; Li, J.W.; Deng, X.Y.; Fan, H.Y. Aerenchyma formation: Programmed cell death in adventitious roots of winter wheat (*Triticum aestivum*) under waterlogging. *Funct. Plant Biol.* **2010**, *37*, 748–755. [CrossRef]
65. Xu, P.; Li, J.; Lv, H.Y.; Li, Y.J.; Li, J.; Ma, C.L. Effects of drought stress on ultrastructure of chloroplasts and mitochondria and membrane lipid peroxidation of *Ammodendron argenteum* seedlings. *Arid Zone Res.* **2016**, *33*, 120–130. (In Chinese) [CrossRef]
66. Du, K.B.; Xu, L.; Tu, B.K.; Shen, B.X. Influences of soil flooding on ultrastructure and photosynthetic capacity of leaves of one-year old seedlings of two poplar clones. *Sci. Silvae Sin.* **2010**, *46*, 58–64, 183. (In Chinese)
67. Vassileva, V.; Simova-Stoilova, L.; Demirevska, K.; Feller, U. Variety-specific response of wheat (*Triticum aestivum* L.) leaf mitochondria to drought stress. *J. Plant Res.* **2009**, *122*, 445–454. [CrossRef]
68. Hu, J.; Ren, B.Z.; Dong, S.T.; Liu, P.; Zhao, B.; Zhang, J.W. Phosphoproteomic and physiological analysis revealed 6-benzyladenine improved the operation of photosynthetic apparatus in waterlogged summer maize. *Environ. Exp. Bot.* **2021**, *193*, 104679. [CrossRef]
69. Peng, Y.J.; Zhou, Z.X.; Tong, R.G.; Hu, X.Y.; Du, K.B. Anatomy and ultrastructure adaptations to soil flooding of two full-sib poplar clones differing in flood-tolerance. *Flora* **2017**, *233*, 90–98. [CrossRef]
70. Du, K.B.; Xu, L.; Wu, H.; Tu, B.K.; Zheng, B. Ecophysiological and morphological adaption to soil flooding of two poplar clones differing in flood-tolerance. *Flora* **2012**, *207*, 96–106. [CrossRef]

Disclaimer/Publisher's Note: The statements, opinions and data contained in all publications are solely those of the individual author(s) and contributor(s) and not of MDPI and/or the editor(s). MDPI and/or the editor(s) disclaim responsibility for any injury to people or property resulting from any ideas, methods, instructions or products referred to in the content.

forests

MDPI

Article

Spatial–Temporal Distribution Pattern of *Ormosia hosiei* in Sichuan under Different Climate Scenarios

Chunping Xie [1], Lin Chen [2], Meng Li [2], Dawei Liu [3] and Chi-Yung Jim [4,*]

[1] College of Sciences, Qiongtai Normal University, Haikou 571127, China; xcp@mail.qtnu.edu.cn
[2] Co-Innovation Center for the Sustainable Forestry in Southern China, College of Biology and the Environment, Nanjing Forestry University, Nanjing 210037, China; clinechen@njfu.edu.cn (L.C.); limeng@njfu.edu.cn (M.L.)
[3] Faculty of Criminal Science & Technology, Nanjing Forest Police College, Nanjing 210023, China; dwliu@nfpc.edu.cn
[4] Department of Social Sciences, Education University of Hong Kong, Tai Po, Hong Kong, China
* Correspondence: cyjim@eduhk.hk

Abstract: *Ormosia hosiei* is an endemic plant in China listed as a national grade II key protected wild plant with important scientific, economic, and cultural values. This study was designed to predict the potential suitable distribution areas for *O. hosiei* under current and future climate change and to provide a reference to enhance the species' conservation and utilization. Based on the actual geographical locations of *O. hosiei* in Sichuan, we applied two species distribution models (BIOCLIM and DOMAIN) to predict its current and future potential suitable areas and future change patterns. We also analyzed the major climatic variables limiting its geographical distribution with principal component analysis. The results indicated that *O. hosiei* was mainly distributed in the eastern region of Sichuan and concentrated in the middle subtropical climate zone at relatively low elevations. The principal component analysis identified two critical factors representing temperature and moisture. The temperature was the most critical factor limiting *O. hosiei* distribution in Sichuan, especially the effect of extreme low temperatures. Both models' simulation results of potential suitable areas under the current climate scenario showed that the excellent suitable habitat was consistent with the current actual distribution, remaining in the eastern region of Sichuan. Under the future climate scenario with doubled CO_2 concentration (2100), both models predicted a sharp decrease in the areas of excellent and very high suitable habitats. The findings can inform strategies and guidelines for *O. hosiei* research, conservation, nursery production, and cultivation in Sichuan.

Keywords: bioclimate; suitable area; *Ormosia hosiei*; species distribution model; BIOCLIM; DOMAIN

check for updates

Citation: Xie, C.; Chen, L.; Li, M.; Liu, D.; Jim, C.-Y. Spatial–Temporal Distribution Pattern of *Ormosia hosiei* in Sichuan under Different Climate Scenarios. *Forests* **2023**, *14*, 1261. https://doi.org/10.3390/f14061261

Academic Editor: Juan A. Blanco

Received: 24 May 2023
Revised: 15 June 2023
Accepted: 15 June 2023
Published: 19 June 2023

Copyright: © 2023 by the authors. Licensee MDPI, Basel, Switzerland. This article is an open access article distributed under the terms and conditions of the Creative Commons Attribution (CC BY) license (https://creativecommons.org/licenses/by/4.0/).

1. Introduction

The Quaternary glaciation and interglacial periods provide evidence of the influence of climate change on the geographical distribution patterns of plants. They indicate climate as the primary and crucial factor of species distribution [1]. Analyzing the current species distribution patterns can identify the key climatic factors restricting their distribution [2]. Meanwhile, species' current endangered status, diversity, specialization, historical evolutionary patterns, and future potential distribution can be explored through their geographical distribution [3].

Global warming poses a severe threat to human beings and biodiversity [4], especially to rare and endangered species, exacerbating the risk of extinction [5]. The continuous increase in CO_2 emissions and irreversible climate warming necessitate predicting species' responses to current and future climatic scenarios. Such studies can reveal changes in their suitable habitats, providing the basis to formulate species conservation strategies.

The profound impact of global climate warming on species' geographical distribution is regarded as indisputable [6]. The spatial research questions can be assessed with GIS technology combined with ecological models to predict climate change impacts on species

distribution. Species distribution models (SDMs) are one of the most effective ways to predict current and future species distribution changes [7]. Common models include MaxEnt, BIOMOD, DOMAIN, BIOCLIM, and CLIMEX [8]. They are widely applied in many fields, such as delineating conservation areas of rare and endangered species, managing diversity of forest species, predicting invasive plant distribution, identifying introduction and cultivation areas of economic and medicinal plants, and evaluating climate warming impacts on regional biodiversity [1,9].

BIOCLIM is the pioneering species distribution model [10], which paved the way for developing other SDMs [11]. For example, the model was applied to predict the distribution of *Euryale ferox* under future climate change scenarios in 2050 and 2070 in India. In response to rising temperatures, the species' range is expected to contract completely in some regions [12]. BIOCLIM was employed to predict the suitable distribution area of *Jacaranda mimosifolia* D. Don in China. The low temperature is the key factor limiting the species from spreading north [13].

The DOMAIN is also a widely used SDM, which calculates potential species distribution based on range standardization and a point-to-point similarity algorithm. It provides a simple, robust method to simulate a species potential distribution [14]. The principle of continuous similarity function offers a heuristic tool with considerable flexibility. This model can investigate endangered species and the selection of protected areas [15]. Comparing the potential suitable areas of *Pseudolarix amabilis* (J. Nelson) Rehder predicted by different niche models, DOMAIN yielded results similar to GARP and MaxEnt. The AUC value exceeded 0.9, indicating good results in predicting species suitable habitats [16]. The BIOCLIM and DOMAIN models have been embedded in the DIVA-GIS [17] to facilitate SDM studies and boost their adoption by researchers.

Ormosia hosiei Hemsl. et Wils., a member of the Leguminosae family, is listed as a second-class national protected plant in China [18]. The tree is sporadically distributed in eastern, central, and southwestern China, including Zhejiang, Jiangsu, Jiangxi, Hunan, Hubei, Guizhou, and Sichuan provinces [19]. The species is the northernmost and the most cold-resistant tree species in the genus *Ormosia* [18]. *O. hosiei* has high ornamental, medicinal, and timber value [20]. Inherent reproductive limitations and external disturbances have sharply reduced its natural population, calling for urgent protection efforts [21]. Most studies of *O. hosiei* focus on genetic diversity [19,22], phytochemical composition [23,24], seedling cultivation [25,26], and ecology [27], furnishing a rich empirical and theoretical basis for species protection. However, phytogeography studies are lacking [28].

In contemporary urban forestry practice, using native plants is widely supported [29]. *O. hosiei* was first found and studied in Chengdu [30]. Therefore, it has special value for the city of Sichuan regarding biodiversity conservation. This study aims to apply the BIOCLIM and DOMAIN models to achieve the following objectives: (1) To identify and evaluate the crucial climatic factors shaping the present distribution of *O. hosiei*, (2) to forecast the optimal areas for the future growth of *O. hosiei* based on its current distribution data, and (3) to predict and determine the most suitable areas for *O. hosiei* growth under different climate-change scenarios. This study is envisaged to provide a reference for studies on selecting and breeding tree species for urban greening in Sichuan and other places.

2. Materials and Methods

2.1. Study Area

Sichuan is located in southwest China (26°03′–34°19′ N, 97°21′–108°12′ E) (Figure 1) with an area of 486,000 km^2. The large province is marked by complex topography, including mountains, hills, plains, basins, and plateaus, and the origin and passage of major rivers. Its unique climate types include the humid subtropical of central Asia, the semi-humid subtropical of southwestern and northwestern Sichuan, and the high-altitude and cold climate of the plateau.

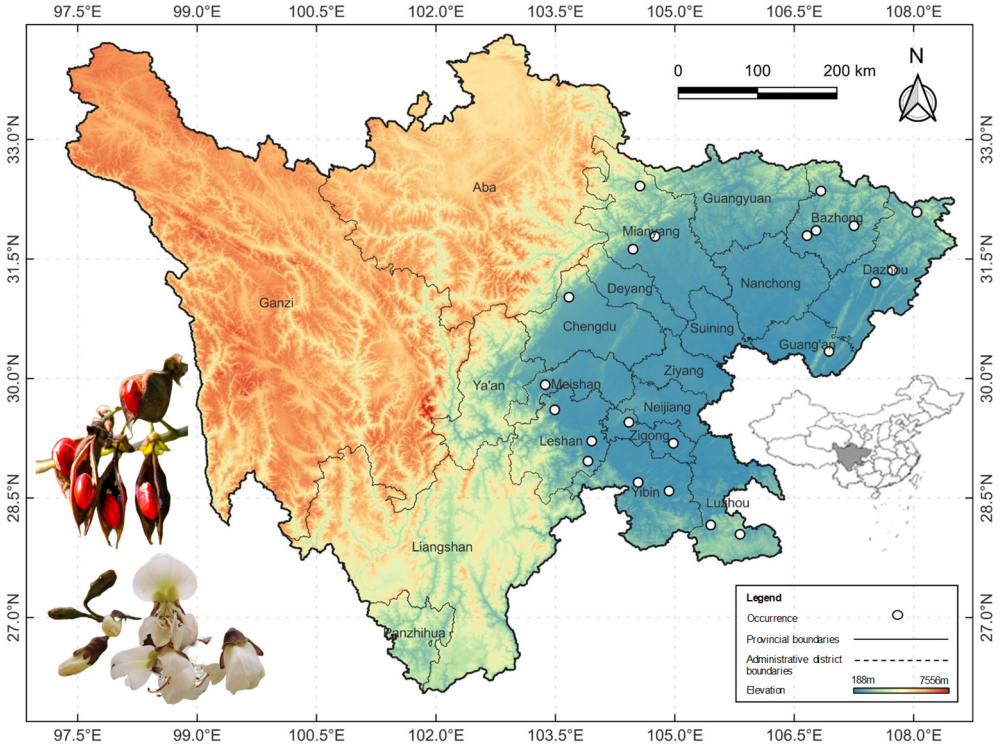


Figure 1. Locations of 22 collected occurrence records (shown by white dots) of *Ormosia hosiei* in Sichuan and images of its flowers and fruits (photographed by Chenghui Nan).

O. hosiei is mainly distributed in eastern Sichuan, which includes the Sichuan Basin and surrounding mountains. The distribution area has a humid subtropical climate with oceanic characteristics. The warm and humid climate offers an average annual temperature of 16–18 °C, 240–280 days with a daily temperature ≥10 °C, an annual accumulated temperature of 4000–6000 °C, a small diurnal temperature range, and a large annual temperature range. The winters are warm, and summers are hot with 230–340 days of frost-free period. The annual precipitation reaches 900–1200 mm.

The complex topography and abundant water and heat resources have nurtured a rich plant diversity in this region. Some rare and endangered plants, such as *Alsophila spinulosa* (Wall. ex Hook.) R. M. Tryon, *Torreya fargesii* Franch., *Phoebe zhennan* S. Lee et F. N. Wei, *Davidia involucrata* Baill., *Acer amplum* subsp. *catalpifolium* (Rehder) Y. S. Chen, *Tetracentron sinense* Oliv., *Magnolia sinensis* (Rehd. et Wils.) Stapf, etc., have been found. The region has the most intensive economic development and human activities in Sichuan, which has exerted impacts on the survival of rare and endangered plants.

2.2. Data Collection

2.2.1. Geographical Data

The distribution data of *O. hosiei* in Sichuan were acquired from literature records, online specimen databases, and field investigations. The online databases mainly included the Chinese National Museum of Natural History (http://www.cfh.ac.cn/, accessed on 3 December 2022), Chinese Virtual Herbarium (http://www.cvh.org.cn/, accessed on 4 December 2022), National Specimen Platform (http://www.nsii.org.cn, accessed on 7 December 2022), and Teaching Specimen Resource Sharing Platform (http://mnh.scu.edu.cn/, accessed on 11 November 2022). The distribution occurrences explicitly indicated at or below the county level were retained, and the others were deleted. Finally, 22 valid county-level distribution points were obtained, and the latitudes and longitudes were obtained from the coordinate acquisition system (http://aqsc.shmh.gov.cn/gis/getpoint.htm, accessed on 12 March 2023).

2.2.2. Bioclimatic Data

Currently, 19 bioclimatic data variables are commonly used for species distribution and related ecological modeling. Our modeling used climate data extracted from the DIVA-GIS 7.5 software (sourced from the WorldClim database, http://www.worldclim.org/, accessed on 20 May 2020) [31]. They included annual mean temperature (bio1), annual precipitation (bio12), extreme high temperature (bio5), extreme low temperature (bio6), precipitation of warmest quarter (bio18), precipitation of coldest quarter (bio19), etc. (the parameters are listed in Table 1) [32]. Derived from monthly temperature and precipitation values, these bioclimatic factors are biologically meaningful, representing annual trends and seasonal and extreme or limiting environmental factors. Future climate data were generated using the CCM3 model of the National Center for Atmospheric Research (NCAR) in the United States. It simulates the 2100 climate scenario after doubling the atmospheric CO_2 concentration [33,34]. The spatial resolution of 2.5 min was used in the current and future climate data.

Table 1. The factor loadings of the first five principal components concerning the 19 bioclimatic variables for *Ormosia hosiei*.

Bioclimatic Variable	Factor Loading				
	PC1	**PC2**	**PC3**	**PC4**	**PC5**
bio1 Annual mean temperature	**0.29**	−0.06	−0.11	0.26	0.03
bio2 Mean diurnal range [a]	−0.28	0.04	0.00	0.06	0.54
bio3 Isothermality [b]	−0.17	0.25	−0.31	−0.03	0.63
bio4 Temperature seasonality [c]	−0.19	−0.23	**0.44**	0.14	−0.09
bio5 Max. temperature of warmest month	0.20	−0.29	0.20	0.24	0.27
bio6 Min. temperature of coldest month	**0.30**	−0.02	−0.13	0.03	0.02
bio7 Annual temperature range [d]	−0.24	−0.19	0.32	0.13	0.18
bio8 Mean temperature of wettest quarter	0.25	−0.17	−0.03	0.26	0.24
bio9 Mean temperature of driest quarter	**0.29**	0.01	−0.20	0.16	0.07
bio10 Mean temperature of warmest quarter	0.23	−0.22	0.15	0.38	0.02
bio11 Mean temperature of coldest quarter	**0.29**	0.01	−0.20	0.16	0.07
bio12 Annual precipitation	0.16	0.27	**0.47**	−0.06	0.17
bio13 Precipitation of wettest month	0.10	**0.40**	0.23	0.14	0.00
bio14 Precipitation of driest month	0.27	−0.07	0.08	−0.36	0.08
bio15 Precipitation seasonality [e]	−0.07	**0.37**	−0.19	0.38	−0.28
bio16 Precipitation of wettest quarter	0.10	**0.39**	0.27	0.09	0.02
bio17 Precipitation of driest quarter	0.28	−0.01	0.08	−0.36	0.07
bio18 Precipitation of warmest quarter	0.14	**0.38**	0.19	0.07	0.02
bio19 Precipitation of coldest quarter	0.28	−0.01	0.08	−0.36	0.07
Eigenvalue	10.65	4.86	1.61	1.19	0.54
Variance %	56.05	25.59	8.46	6.25	2.84
Cumulative variance %	56.05	81.64	90.10	96.34	99.18

(1) Bold and underlined values indicate the most influential variables of the first four principal components. (2) [a] Mean diurnal range = mean of monthly (max. temp − min. temp); [b] isothermality = (bio2/bio7) × 100; [c] temperature seasonality = standard deviation × 100; [d] annual temperature range = bio5 − bio6; [e] precipitation seasonality = coefficient of variation.

To avoid collinearity among the 19 bioclimatic variables, those with Spearman rank correlation coefficients less than 0.8 were kept using correlation analysis and variance inflation factors (VIF) [35]. We also considered the result of the principal component analysis, selecting the top four and top two factors with the largest loadings for the first principal component and second principal component, respectively. Ultimately, six bioclimatic variables were kept: bio1, bio6, bio9, bio11, bio13, and bio16. The environmental limiting factors for *O. hosiei* distribution in Sichuan were evaluated with principal component analysis using the PAST 4.09 software [36].

2.3. Models Analysis

The BIOCLIM and DOMAIN models were used to simulate the suitable habitats for *O. hosiei* in Sichuan. The BIOCLIM model uses environmental data from known species distribution points to determine the climate scenario suitable for species occurrence. The percentile distribution of each climate variable in each grid of the species distribution area is used for multivariate analysis. If the range of all climate variables in the grid falls within the range suitable for the species, the location is suitable [10,11].

DOMAIN uses point-to-point similarity measures based on Gower distance, a method for creating a distance matrix from a set of species features. DOMAIN assigns a suitability index classification value to each potential location based on its proximity to the most similar occurrence location in the environmental space. Then, the suitability threshold is selected to determine the distribution boundary of the species' ecological niche [15,37].

Both models were analyzed in the Modeling-Bioclim/Domain module of the DIVA-GIS 7.05 software [17]. The generated simulation maps of the suitable habitats (in .bmp format) were imported into QGIS 3.20 for corresponding raster calculations [38], resulting in the current and future changes in the distribution area of *O. hosiei* under different climate scenarios.

The suitable habitats were classified into excellent, very high, high, medium, low, and unsuitable and differentiated by color in DIVA-GIS 7.05 [17]. The two models differ notably in defining the suitable habitats' class thresholds. BIOCLIM defines unsuitable to excellent as "Unsuitable", 0%–2.5%, 2.5%–5.0%, 5.0%–10.0%, 10.0%–20.0%, and 20.0%–46.0%. DOMAIN uses the evaluation index to define the unsuitable to excellent classes as −210–50, 51–90, 91–95, 96–97, 98–99, and 100 based on [39].

We assigned 75% of the distribution points to the training set and the remaining 25% to the test set. Model accuracy was evaluated using the area under the receiver operating characteristic curve (AUC). An AUC value close to 1 signifies a higher prediction accuracy. The values 0.5–0.6, 0.6–0.7, 0.7–0.8, and >0.9 represent the fair, good, very good, and excellent prediction results, respectively. AUC < 0.5 means failed prediction [40].

3. Results

3.1. Geographic Distribution Pattern

Based on field investigations, online specimen data, and the literature, *O. hosiei* was mainly distributed in Sichuan's eastern region, which can be divided into northeastern and southeastern Sichuan. In southeastern Sichuan, the distribution included Gulian, Xuyong, Yibin, Changning, and other places. In northeastern Sichuan, the main occurrences were Tongjiang, Nanjiang, Dazhou, Jiange, and Cangxi. The high-altitude areas, such as Garze, Aba, and Liangshan prefectures in western Sichuan and the cities of Panzhihua, Neijiang, and Nanchong, had no *O. hosiei* record. In addition, *O. hosiei* was mostly distributed in middle and low-altitude areas, concentrated in the 200–900 m range. The communities accommodating *O. hosiei* were mainly secondary forests disturbed by some factors located mainly in sunny areas, such as valleys, mountain slopes, and stream banks.

3.2. Restrictive Climatic Factors

The bioclimatic data of *O. hosiei* in different distribution areas in Sichuan were evaluated using principal component analysis (Table 1). The first four axes with eigenvalues >1 were the main principal components (PCs). The contributions of the first three principal components (PC1 to PC3) were 56.05%, 25.59%, and 8.46%, respectively, reaching a cumulative value of 90.10% (>75%). Therefore, the climatic profile affecting the geographic distribution of *O. hosiei* could largely be reflected by the first three PCs. In PC1, bio6 (0.30), bio1 (0.29), bio9 (0.29), and bio11 (0.29) ranked in the top four. Therefore, the dominant distribution factor was temperature, and extreme low temperature was the most crucial factor. In PC2, bio13 (0.40), bio16 (0.39), bio18 (0.38), and bio15 (0.37) ranked in the top four. Therefore, PC2 reflected the impact of precipitation on distribution with the average precipitation of the wettest month as the most important factor. PC3 had a relatively limited

influence on distribution compared with PC1 and PC2. The two most important factors were bio12 (0.47) and bio4 (0.44). The contributions of the remaining PCs were <10%, indicating a weak impact on distribution.

Descriptive statistical analysis was performed on the major bioclimatic factors selected with principal component analysis (Table 2). The average annual temperature was approximately 17 °C, fluctuating in the 16.36–17.40 °C range, which falls within the annual average temperature range (16 °C to 20 °C) observed in China's subtropical region. Therefore, *O. hosiei* can be considered a subtropical species based solely on annual average temperature. The average precipitation during the wettest month was 617.27 mm, fluctuating in a 547.04–687.50 mm range. However, the annual average precipitation in the region is approximately 1000 mm, mainly concentrated in the summer months (June to September), indicating uneven temporal spread. The coefficients of variation (CV) of these five key climatic factors were 14.51% (bio1), 1.58% (bio6), 5.05% (bio11), 3.26% (bio13), and 3.90% (bio16). Generally, for a climatic factor, a smaller CV signifies a greater limiting effect on species distribution [2]. Therefore, extreme low temperature (bio6) is the most critical factor of *O. hosiei* distribution in Sichuan, consistent with the results of principal component analysis (with the highest loading on PC1). In addition, the range of precipitation during the wettest month (bio13) and wettest quarter (bio16) was 202.35–266.10 mm and 547.04–687.50 mm, respectively, indicating the impact of summer precipitation on *O. hosiei* growth.

Table 2. Descriptive statistics of the main bioclimatic parameters in the distribution areas of *Ormosia hosiei* in Sichuan.

Bioclimatic Variable	Minimum	Maximum	Mean ± SD	Coefficient of Variation	95% Confidence Interval
bio1 Annual mean temperature	13.84	18.53	16.88 ± 1.16	14.51	16.36~17.40
bio6 Min. temperature of coldest month	−1.00	5.80	3.06 ± 1.93	1.58	2.20~3.92
bio9 Mean temperature of driest quarter	3.91	9.72	7.41 ± 1.57	6.15	6.22~7.81
bio11 Mean temperature of coldest quarter	3.93	9.42	7.36 ± 1.46	5.05	6.72~8.01
bio13 Precipitation of wettest month	165.00	447.00	234.23 ± 71.89	3.26	202.35~266.10
bio16 Precipitation of wettest quarter	481.00	1099.00	617.27 ± 158.39	3.90	547.04~687.50

3.3. Current Potential Distribution

The potential distribution of *O. hosiei* in Sichuan under the current climate scenario simulated by the BIOCLIM and DOMAIN models is shown in Figure 1. Overall, the two models' simulation results share a similar structure with a concentrated distribution in the eastern region of Sichuan spreading in a "C" shape, consistent with the actual *O. hosiei* distribution. However, BIOCLIM yielded a more concentrated pattern for high to excellent suitable habitats, while DOMAIN was more scattered. Secondly, the two models were largely consistent in predicting the unsuitable habitat. The western plateau areas of Aba, Ganzi, and Liangshan in Sichuan had extensive gray or dark green areas, indicating that high-altitude and cold areas were unsuitable. BIOCLIM demarcated the areas of high, very high, and excellent suitable habitats to be 28,717 km^2, 50,832 km^2, and 42,218 km^2, totaling 121,767 km^2. DOMAIN's results were 51,569 km^2, 30,304 km^2, and 738 km^2, totaling 82,611 km^2. The two models generated considerable differences in the excellent suitable habitat. This divergence could be attributed to the different algorithms and definitions used by the models to define suitable habitats. DOMAIN requires a stringent value of 100 for the excellent class. However, both models predicted that the eastern region of Sichuan contains the most suitable habitats for *O. hosiei* growth under the current climate scenario.

The potential suitability areas of *O. hosiei* in Sichuan under the current climate scenario obtained by the BIOCLIM and DOMAIN models are shown in Figure 2. For BIOCLIM, the top three areas with the highest proportion of excellent suitable habitat were Suining (64.14%), Deyang (63.66%), and Ziyang (59.81%) followed closely by Nanchong (49.56%), Neijiang (42.81%), Mianyang (38.86%), and Chengdu (38.48%). The proportion of excellent

habitat in other regions was <30%. For DOMAIN, the top three areas with the highest proportion of excellent habitat were Zigong (3.36%), Mianyang (0.72%), and Bazhong (0.59%). The excellent suitable habitat in Yibin (0.57%), Dazhou (0.55%), Luzhou (0.46%), and Leshan (0.44%) ranked fourth to seventh. The proportion of excellent suitable habitat in other areas was <0.3%. Despite some differences in the proportion of excellent suitable habitat obtained by the two models, several areas, such as Deyang, Nanchong, and Mianyang, had a consistently high proportion. Therefore, these areas have a great potential for protection, cultivation, and introduction of *O. hosiei* in the future.

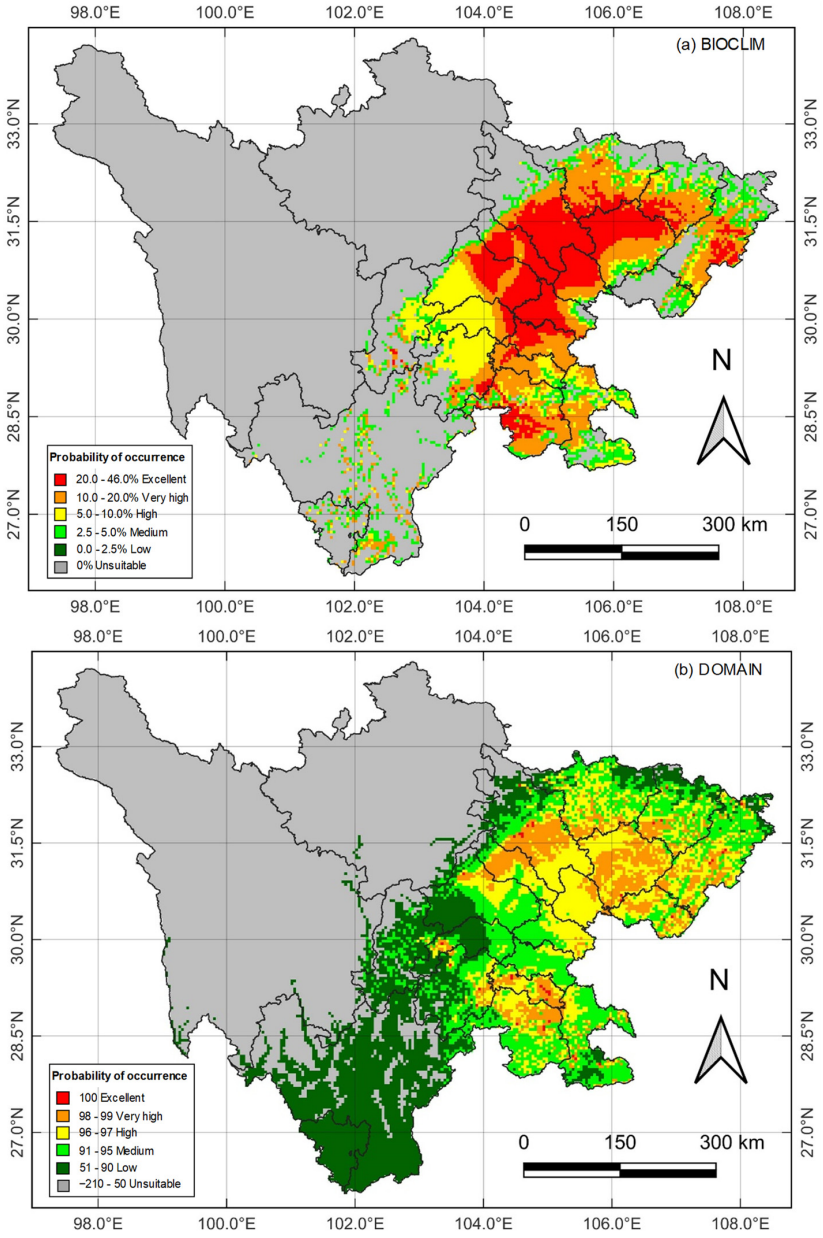


Figure 2. Potential suitability areas of *Ormosia hosiei* under the current climate scenario (1970–2000) generated by the (**a**) BIOCLIM model and (**b**) DOMAIN model. They are divided into six categories based on the calculated habitat suitability index, as explained in the legend.

Under the current climatic scenario, the models found some differences in the environmental factors limiting *O. hosiei* distribution in Sichuan (Figure 3). BIOCLIM demarcated large white areas representing unsuitable and excluded them from assessing the limiting factors. The most significant factor of *O. hosiei* growth in Chengdu, Meishan, Leshan, and Nanchong was rainfall during the wettest season, highlighting the impact of summer rain.

Extreme low temperatures greatly impacted Luzhou, Yibin, and Guangyuan. DOMAIN found the influence of the annual average precipitation covering a larger part of Sichuan followed by the wettest season precipitation, which generated more scattered distribution in Luzhou, Neijiang, Chengdu, and Nanchong. In addition, the limiting effect of extreme low temperatures was more prominent in Garze, Aba, Liangshan, Panzhihua, and the Chengdu Plain. Overall, the environmental limiting factors in eastern Sichuan were more complex than in western Sichuan.

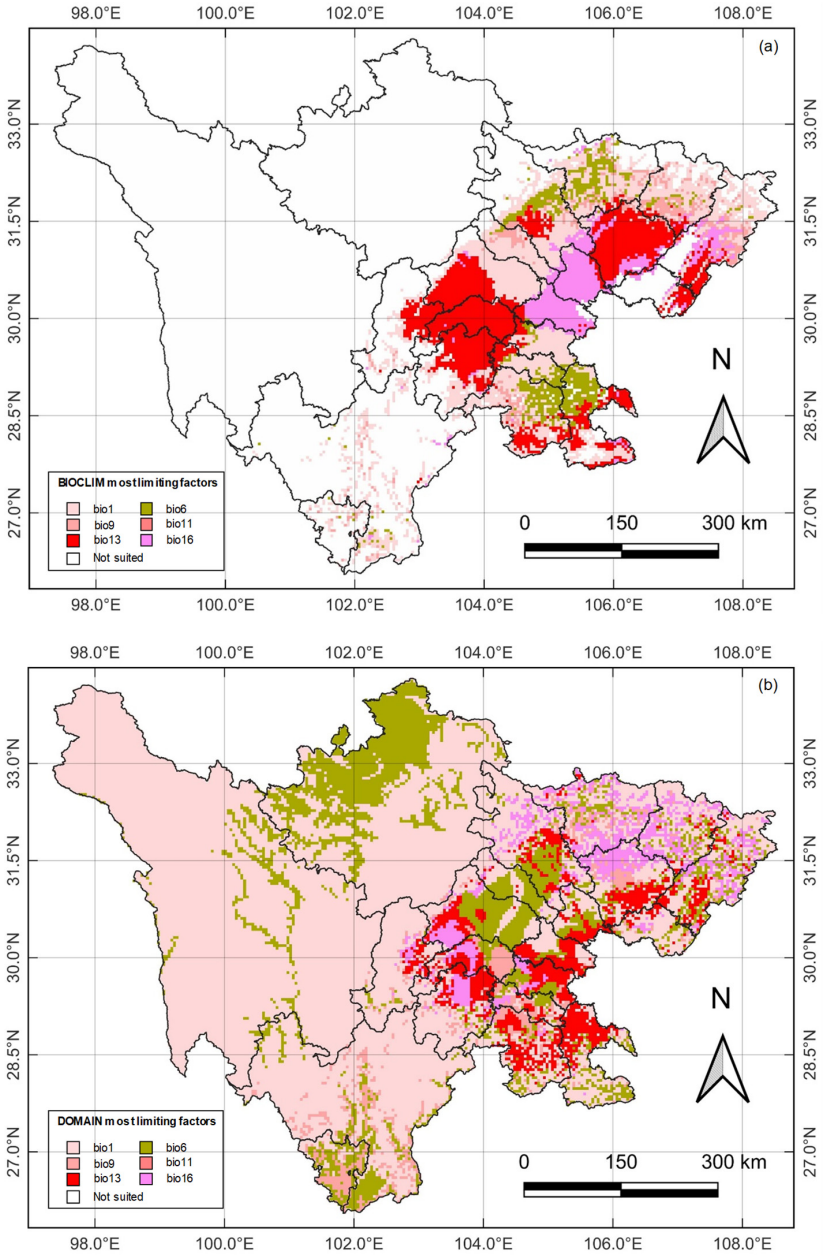


Figure 3. Distribution patterns of the limiting factors shaping the distribution areas of *Ormosia hosiei* generated by the (**a**) BIOCLIM model and (**b**) DOMAIN model. The selected six bioclimatic variables, shown in different colors, had the greatest impact on predicting suitable habitats in the distribution area. Refer to Table 1 for the meaning of the bioclimatic variables.

3.4. Predicting Changes in Suitable Habitats

The potential distribution area of *O. hosiei* in Sichuan was predicted under the future climate scenario with doubled CO_2 concentration in 2100, shown in Figure 4. Both models predicted a notable reduction in excellent and very high suitable habitats (the red and

orange areas). The BIOCLIM results showed that the originally contiguous red area had been significantly fragmented. DOMAIN also yielded more scattered and fragmented orange patches. QGIS software was used to count the raster cells for each suitable habitat class (Table 3). The total area of excellent suitable habitat predicted by BIOCLIM and DOMAIN decreased from 42,218 km^2 and 738 km^2 to 30,709 km^2 and 728 km^2, respectively, denoting a 27.26% and 1.36% reduction. Compared with the current potential distribution, the center of excellent suitable habitat shifted to the east, while most of western Sichuan remained unsuitable.

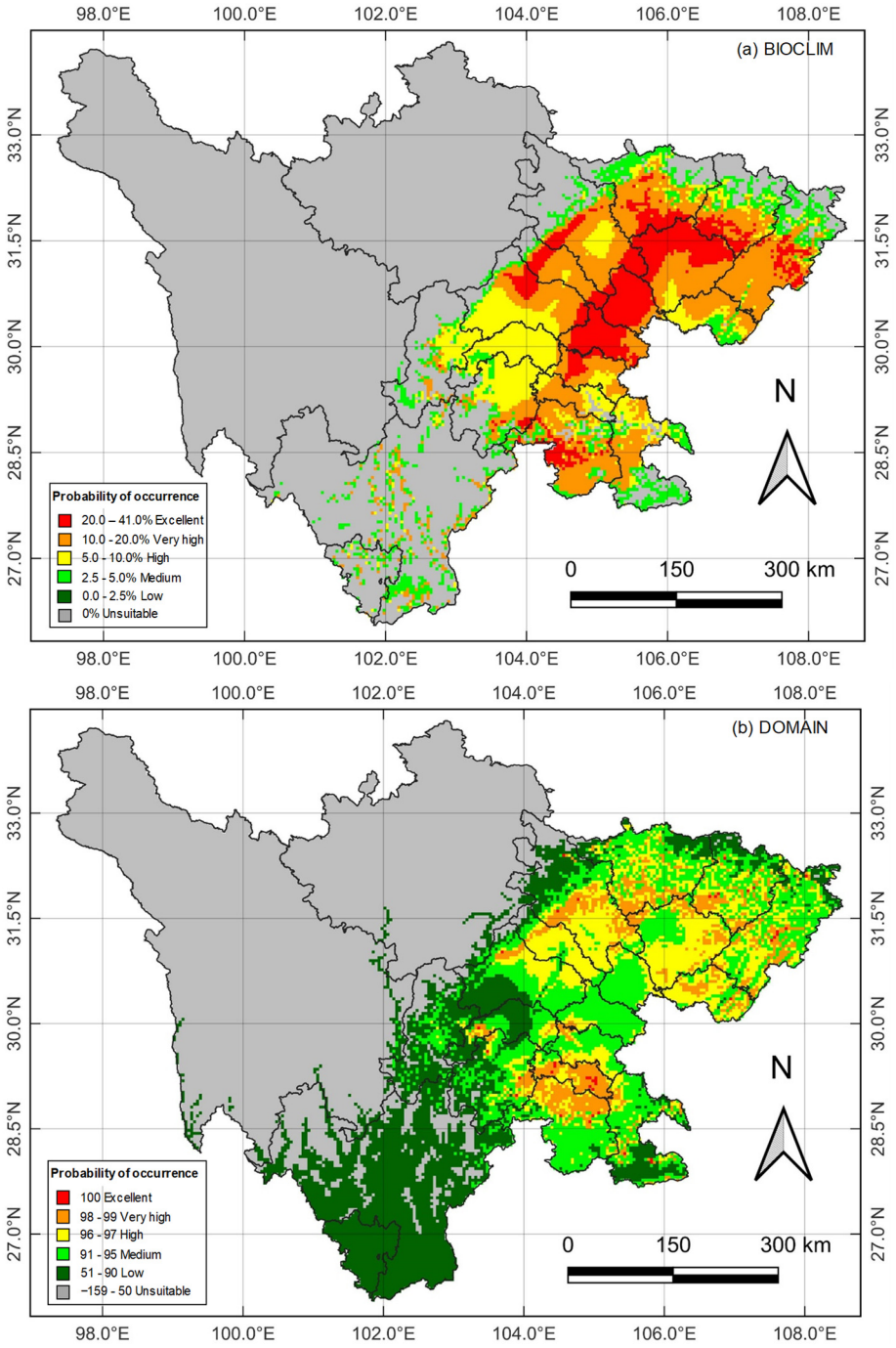


Figure 4. Potential suitable habitats of *Ormosia hosiei* under the climate change scenario (double CO_2 concentration) in 2100 generated by the (**a**) BIOCLIM model and (**b**) DOMAIN model. The six categories of potential suitability habitats are explained in the legend.

Table 3. Predicted suitable areas (km^2) for *Ormosia hosiei* under the current and future climate scenarios are classified into six suitability categories generated by the BIOCLIM and DOMAIN models.

Suitability Category	BIOCLIM			DOMAIN		
	Current	Future	Area Change %	Current	Future	Area Change %
Excellent	42,218	30,709	−27.26	738	728	−1.36
Very high	50,832	63,909	25.73	30,304	23,387	−22.82
High	28,717	34,048	18.56	51,569	47,456	−7.98
Medium	26,762	27,943	4.41	58,265	67,597	16.02
Low	0	0	0.00	87,056	90,984	4.51
Unsuitable	337,470	329,392	−2.39	258,069	255,847	−0.86

Both models indicated that the excellent suitable habitat of *O. hosiei* under the future climate scenario in Aba, Ganzi, Liangshan, and Panzhihua had 0 or nearly 0 values (Table 3 and Figure 4). Such results indicated that these areas could not provide excellent suitable habitat despite climatic warming. BIOCLIM predicted an increase in excellent suitable habitat in six areas, including Bazhong, Dazhou, and Guangyuan. However, ten areas, including Chengdu, Deyang, and Leshan, would encounter a reduction. DOMAIN also found an increase or decrease in excellent suitable habitat in five and nine areas, respectively. Despite some differences in the predicted changes in excellent suitable habitat in various parts of Sichuan obtained by the two models, the overall reduction trend in excellent suitable habitat was consistent.

3.5. Model Accuracy

The BIOCLIM and DOMAIN models were applied to predict the suitable habitats of *O. hosiei* in Sichuan under the current and future climate scenarios. The results showed that the AUC values of both models were 0.881 and 0.873, and 0.871 and 0.867, respectively, under the current and future climate scenarios. These AUC values were significantly higher than the random distribution model (0.5). Thus, the models were tested to be accurate, indicating that the predicted potential distribution areas were very close to the actual distribution areas, and the research results were reliable.

4. Discussion

Exploring the response of rare and endangered species to the current and future climate can enhance the understanding of their survival risks with substantial scientific value to formulate targeted conservation strategies [4,41]. This study used the geographical distribution points of *O. hosiei* in Sichuan to predict its potential suitable distribution under current and future climate change scenarios based on the BIOCLIM and DOMAIN models. Moreover, the alternative areas for *O. hosiei* growth were predicted, providing a scientific reference for conservation management, introduction area selection, and sustainable utilization of its wild resources.

Both models predicted consistent outcomes for very high and excellent suitable habitats and the same species distribution concentration in the eastern Sichuan region. However, some differences in specific results at the local scale were generated. First, the DOMAIN and BIOCLM models output different values, producing classification confidence rather than species suitable habitat probability [15,39]. After obtaining this value, the suitable threshold needs to be customized according to the study's actual situation. In this study, if the results of the suitable habitat classification were automatically assigned by DOMAIN, almost no excellent suitable habitat could be found in Sichuan (Table 3), which is inconsistent with actual investigations. Therefore, we suggested that it is unnecessary to be too harsh when analyzing the DOMAIN modeling results. Instead, the top two high and excellent classes can be considered together. Secondly, the two models' algorithms are fundamentally different. BIOCLIM belongs to the "environmental envelope" type [42,43], which identifies and determines the locations where the environmental values occur within the range of

measured values. Additionally, it uses the 5–95% probability envelope as the boundary to ignore the lowest and highest 5% of each climatic index to reduce the outliers' impact on the prediction results [10]. DOMAIN derives a point-to-point similarity measure and assigns a value to the potential distribution point based on the degree of similarity between it and the most similar point in the environmental space. It then uses the sum of the standardized distances between the two points of each environmental prediction variable to quantify the similarity between two distribution points [15,44]. Therefore, judging from the prediction map, the excellent regional assignment of the DOMAIN model is significantly less than the BIOCLIM model (Figure 2).

Temperature is a crucial limiting factor for species distribution, especially extreme low temperatures (bio6) (Table 2 and Figure 3). The effects of extreme low temperatures on species distribution depend on the natural environment, domestication status, and species growth form. The organs and tissues of different plants have dissimilar low-temperature tolerances, which vary by season and life-cycle phase [45]. For example, tropical plants never experience temperatures below 0 °C and could be killed at 0–10 °C [46]. The study of European linden (*Tilia cordata* Mill.) distribution in the UK concerning temperature found that low temperature significantly affected the distribution by limiting the ability to flower or reducing the ability of embryos to fertilize [47]. The evergreen cultivated shrub *Vaccinium bracteatum* Thunb. is significantly less cold-tolerant than heat-tolerant. Therefore, low temperature may be a key factor limiting its spread to high-latitude areas in north China [48]. Similar situations also occur in plants such as *Rhodomyrtus tomentosa* (Ait.) Hassk. [40] and *J. mimosifolia* [13].

Our principal component analysis showed that extreme low temperature (bio6) had the largest loading among the 19 bioclimatic factors (Table 1), indicating its considerable impact on *O. hosiei* distribution in Sichuan. The current geographical distribution of *O. hosiei* extends from the eastern coastal areas of Fujian, Zhejiang, and Jiangsu to western areas, such as Guizhou, Sichuan, and Shaanxi, covering China's central subtropical and north subtropical climatic zones. The national distribution pattern indicates that *O. hosiei* has a relatively high temperature demand. The lack of natural distribution in western Sichuan supports that low temperature is a key factor limiting its westward spread to higher elevations (Figure 2). In addition, the first principal component explains over 50% of the variance. Its high-ranking factors are related to temperature, indicating that temperature factors impact *O. hosiei* distribution in Sichuan more than precipitation factors.

The Intergovernmental Panel on Climate Change (IPCC) Sixth Assessment Report (AR6) clearly states that, by 2050, all climate scenarios could cause global warming to rise by 1.5 °C [49]. If greenhouse gas emissions do not significantly decrease, global surface temperatures are expected to increase by at least 2.1 °C by 2100 compared to 1850–1900 [50]. Current research also indicates that, when global warming reaches 1.5 °C, 4%–8% of species worldwide will be at risk of extinction. If the temperature increases to 2 °C and 3.2 °C, the percentage of species facing extinction will rapidly increase to 8%–18% and 26%–49%, respectively [5].

When global warming exceeds 1.5 °C, the natural global climate control solutions will become ineffective, and ecosystems will reach their absolute adaptation limit [51]. Therefore, the impact of climate change on biodiversity distribution patterns is profound. The geographical distribution pattern of species echoes the products of the evolutionary performance of adaptation to the environment [52]. However, the accelerating global warming process over the past century has induced the lagging of species evolution behind the pace of the temperature rise [53]. Consequently, their suitable habitats have been greatly reduced in recent years, especially rare and endangered species sensitive to temperature [54]. For example, according to the MaxEnt model prediction, the suitable distribution area of the sal tree (*Shorea robusta* C. F. Gaertner) in Purba Bardhaman, Bangladesh, will decrease by more than 20% by 2070 [55]. A rare endangered plant, *Manihot walkerae* Croizat, in Central and North America is expected to lose 9% and 14% of its suitable habitat by 2050 and 2070, respectively [56]. The temperature-sensitive *Rosa arabica* Crép. in Egypt will disappear

below 1500 m above sea level and migrate to higher altitudes [35]. Most species that lack effective and rapid migration capabilities will struggle to find suitable habitats to permit range shifts and face aggravated extinction risk [57].

Our modeling results implied that the excellent suitable habitat for *O. hosiei* in Sichuan had significantly decreased (Figure 4). The pattern generated by DOMAIN was more fragmented than BIOCLIM, indicating a telltale sign of a declining species population. These degradation changes align with the response of endangered plants to climate change observed in other regions of the world. Therefore, specific strategies should be developed to address the potential impact of climate change on the adaptive habitat of *O. hosiei* in Sichuan.

A study of the potential distribution area of *O. hosiei* at a larger scale (the whole of China) showed that the range of *O. hosiei* declined by 35.9% from the Last Glacial Maximum to the Mid-Holocene using MaxEnt, losing 54.1% of suitable habitats. Under future climate scenarios, the area of suitable habitats shrank sharply compared to the current climate scenario (decline by 49.3%–49.5% under RCP 8.5, and 14.1%–17.4% under RCP 2.6) [28]. Moreover, the predicted results obtained by our two models (BIOCLIM and DOMAIN) showed a notable reduction in the suitable area of *O. hosiei* in Sichuan. Therefore, with the validation of the three models, the decline of the suitable habitats of *O. hosiei* under the climate warming scenario could be considered an indisputable fact.

The accuracy of predictions from various SDMs has been debated. It is generally believed that the MaxEnt model is superior to DOMAIN, DK-GARP, and BIOCLIM [14]. All SDM prediction methods show a certain degree of model-specific bias. Some algorithms such as DOMAIN produce rather embracive predictions, while others such as BIOCLIM present more restrictive predictions [7]. However, the DOMAIN model has been found to perform well once sensitivity and omission errors are taken into account [58]. The evaluation by the ROC curve verified that the BIOCLIM model predicted the distribution of *Cerasus schneideriana* (Koehne) Yü et Li in China accurately and reliably (AUC = 0.998) [59]. Combining the results of this and previous studies [28], we believe that the prediction results of DOMAIN and BIOCLIM on the potential distribution of *O. hosiei* in Sichuan are reliable.

The holotype of *O. hosiei* collected from Chengdu has special significance in taxonomy. It also carries a profound traditional Chinese cultural connotation, regarded as the "longing" tree by Chinese people since time immemorial. Therefore, we suggest the following scientific and practical measures to enhance the conservation of *O. hosiei* resources in Sichuan: (1) Research institutions can strengthen the collection of germplasm resources and establish important resource sites. Knowledge of the geographical distribution of *O. hosiei* could identify suitable sites for collecting germplasm materials from its wild populations in different regions. The same knowledge base could allow precision relocation of the species and protect individuals with excellent traits. (2) Researchers can strengthen the conservation biology studies of *O. hosiei*. The critical reasons for the endangerment of *O. hosiei* include its low fruiting rate, poor dispersal ability [21,27], and susceptibility to human interference. Therefore, targeted research on the reproductive biology, seed germination, and seedling establishment of *O. hosiei* should be boosted. The findings can inform complementary strategies for the conservation of wild populations. (3) Relevant government departments should increase the introduction and promotion of *O. hosiei* in suitable areas in Sichuan. As a native species, *O. hosiei* has a beautiful form, strong adaptability to the local environment, and a special Chinese cultural undertone. Therefore, relevant government entities in Sichuan should provide scientific guidance to the seedling production nurseries to increase the breeding, domestication, and production of meritorious planting materials for *O. hosiei*. The species can be more vigorously promoted for planting in courtyards, streets, parks, squares, and other suitable urban sites.

5. Conclusions

O. hosiei is mainly distributed in the eastern region of Sichuan with the characteristics of a tree species in Central Asia's subtropical humid climate zone. The temperature has a greater impact on the distribution of *O. hosiei* in Sichuan than precipitation, and extreme low temperatures are the key limiting factor. Precipitation factors reflected the climate profile of *O. hosiei*, preferring warm and humid conditions, but it was not the key limiting factor for its geographical distribution. The simulation results of the species distribution models under the current climatic scenario illustrated that the potential suitable area in Sichuan was similar to the current natural distribution pattern, and the eastern part of Sichuan would remain the main distribution area. However, a significant reduction trend in the distribution area was detected under the future climate scenario of doubling CO_2 concentration. Therefore, specific conservation measures are urgently needed to strengthen the conservation and expand the planting program of *O. hosiei* in Sichuan.

Author Contributions: Data curation, C.X., L.C. and M.L.; Methodology, C.X.; Software, C.X., C.-Y.J. and M.L.; Writing—original draft, C.X.; Validation, C.X. and C.-Y.J.; Formal analysis, C.-Y.J.; Writing—review and editing, C.-Y.J.; Visualization, D.L. and C.X.; Investigation, L.C., M.L. and D.L. All authors have read and agreed to the published version of the manuscript.

Funding: This research was funded by the Natural Science Foundation of Hainan Province (grant number: 423MS061), the Education Department of Hainan Province (project number: Hnky2023ZD-17), the National Natural Science Foundation of China (grant number: 32071782), and Tropical Biodiversity and Bioresource Utilization Laboratory, Qiongtai Normal University (grant number: QTPT21-5).

Data Availability Statement: The data presented in this study are available on request from the corresponding author.

Acknowledgments: We are grateful to Chenghui Nan for providing the photos of *O. hosiei* for this article.

Conflicts of Interest: The authors declare no conflict of interest.

References

1. Shitara, T.; Fukui, S.; Matsui, T.; Momohara, A.; Tsuyama, I.; Ohashi, H.; Tanaka, N.; Kamijo, T. Climate change impacts on migration of *Pinus koraiensis* during the Quaternary using species distribution models. *Plant Ecol.* **2021**, *222*, 843–859. [CrossRef]
2. Fang, J.; Lechowicz, M.J. Climatic limits for the present distribution of beech (*Fagus* L.) species in the world. *J. Biogeogr.* **2006**, *33*, 1804–1819. [CrossRef]
3. Wang, F.; Xiong, Z.; Yan, X.; Dai, X.; Wang, L.; Li, Y. Geographical distribution pattern of species diversity of the genus *Populus* L. in China. *Acta Ecol. Sin.* **2018**, *38*, 282–290. [CrossRef]
4. Sintayehu, D.W. Impact of climate change on biodiversity and associated key ecosystem services in Africa: A systematic review. *Ecosyst. Health Sustain.* **2018**, *4*, 225–239. [CrossRef]
5. Warren, R.; Price, J.; Graham, E.; Forstenhaeusler, N.; VanDerWal, J. The projected effect on insects, vertebrates, and plants of limiting global warming to 1.5 °C rather than 2 °C. *Science* **2018**, *360*, 791–795. [CrossRef] [PubMed]
6. Ramírez-Preciado, R.P.; Gasca-Pineda, J.; Arteaga, M.C. Effects of global warming on the potential distribution ranges of six *Quercus* species (Fagaceae). *Flora* **2019**, *251*, 32–38. [CrossRef]
7. Sarquis, J.A.; Cristaldi, M.A.; Arzamendia, V.; Bellini, G.; Giraudo, A.R. Species distribution models and empirical test: Comparing predictions with well-understood geographical distribution of *Bothrops alternatus* in Argentina. *Ecol. Evol.* **2018**, *8*, 10497–10509. [CrossRef]
8. Yang, J.; Jiang, P.; Huang, Y.; Yang, Y.; Wang, R.; Yang, Y. Potential geographic distribution of relict plant *Pteroceltis tatarinowii* in China under climate change scenarios. *PLoS ONE* **2022**, *17*, e0266133. [CrossRef] [PubMed]
9. Dyderski, M.K.; Paź, S.; Frelich, L.E.; Jagodziński, A.M. How much does climate change threaten European forest tree species distributions? *Glob. Chang. Biol.* **2018**, *24*, 1150–1163. [CrossRef]
10. Booth, T.H.; Nix, H.A.; Busby, J.R.; Hutchinson, M.F. Bioclim: The first species distribution modelling package, its early applications and relevance to most current MaxEnt studies. *Divers. Distrib.* **2014**, *20*, 1–9. [CrossRef]
11. Booth, T.H. Why understanding the pioneering and continuing contributions of BIOCLIM to species distribution modelling is important. *Austral Ecol.* **2018**, *43*, 852–860. [CrossRef]

12. Semwal, D.P.; Pandey, A.; Gore, P.G.; Ahlawat, S.P.; Yadav, S.K.; Kumar, A. Habitat prediction mapping using BioClim model for prioritizing germplasm collection and conservation of an aquatic cash crop 'makhana' (*Euryale ferox* Salisb.) in India. *Genet. Resour. Crop Evol.* **2021**, *68*, 3445–3456. [CrossRef]
13. Xie, C.; Zhang, G.; Jim, C.; Liu, X.; Zhang, P.; Qiu, J.; Liu, D. Bioclimatic suitability of actual and potential cultivation areas for *Jacaranda mimosifolia* in Chinese cities. *Forests* **2021**, *12*, 951. [CrossRef]
14. Wisz, M.S.; Hijmans, R.J.; Li, J.; Peterson, A.T.; Graham, C.H.; Guisan, A.; Group, N.P.S.D.W. Effects of sample size on the performance of species distribution models. *Divers. Distrib.* **2008**, *14*, 763–773. [CrossRef]
15. Carpenter, G.; Gillison, A.N.; Winter, J. DOMAIN: A flexible modelling procedure for mapping potential distributions of plants and animals. *Biodivers. Conserv.* **1993**, *2*, 667–680. [CrossRef]
16. Wang, G.; Gen, Q.; Xiao, M.; Zhang, M.; Zhang, Y.; Wang, Z. Predicting *Pseudolarix amabilis* potential habitat based on four Niche models. *Acta Ecol. Sin.* **2020**, *40*, 6096–6104. [CrossRef]
17. Hijmans, R.J.; Guarino, L.; Cruz, M.; Rojas, E. Computer tools for spatial analysis of plant genetic resources data: 1. DIVA-GIS. *Plant Genet. Resour. Newsl.* **2001**, *127*, 15–19.
18. Chu, X.; Fu, Y.; Yan, W. Genetic conservation for rare plant of *Ormosia hosiei* and research progress in its fine silviculture. *Chin. Wild Plant Resour.* **2021**, *40*, 61–65. [CrossRef]
19. Zhang, R.; Zhou, Z.; Du, K. Genetic diversity of natural populations of endangered *Ormosia hosiei*, endemic to China. *Biochem. Syst. Ecol.* **2012**, *40*, 13–18. [CrossRef]
20. Zhai, D.; Fang, Z.; Wu, J.; Yao, Q.; Bai, X.; Yang, L.; Gao, Q.; Zhang, Y. Analysis on the character diversity of *Ormosia hosiei* seeds from different producing regions. *J. Nanjing For. Univ. (Nat. Sci. Ed.)* **2019**, *62*, 63–69. [CrossRef]
21. Liu, P.; Que, S.; Liu, L.; Huang, X. Research status and endangered conservation strategy of *Ormosia hosiei*. *Subtrop. Plant Sci.* **2017**, *46*, 96–100. [CrossRef]
22. Zhang, J.-Q.; Jiang, M.-Y.; Zhu, D.-D.; Zhang, J.-L.; Zheng, J.-Z.; Deng, C.-Y. Characterization of the complete chloroplast genome of an endemic species of pea family in China, *Ormosia hosiei* (Fabaceae). *Conserv. Genet. Resour.* **2019**, *11*, 443–446. [CrossRef]
23. Xu, H.; Qiu, Y.; Chen, J.; Shi, Y.; Zhang, X.; Song, Q.; Huang, M.; Wu, Z.; Ni, L. Chemical constituents and their activities from the seeds of *Ormosia hosiei*. *Nat. Prod. Commun.* **2019**, *14*, 1–4. [CrossRef]
24. Pouny, I.; Batut, M.; Vendier, L.; David, B.; Yi, S.; Sautel, F.; Arimondo, P.B.; Massiot, G. Cytisine-like alkaloids from *Ormosia hosiei* Hemsl. & E.H. Wilson. *Phytochemistry* **2014**, *107*, 97–101. [CrossRef] [PubMed]
25. Chu, X.; Luo, X.; Zhou, Z. Exponential fertilization on red-seed tree (*Ormosia hosiei*) seedlings subjected to contrasting light conditions: Do we really need intensive nutrient loading? *Not. Bot. Horti Agrobot. Cluj-Napoca* **2021**, *49*, 12244. [CrossRef]
26. Xiao, D.; Deng, Z.; Luo, Q.; Xu, Z.; Shen, B.; Chen, H.; Xu, H.; Zhou, Z. Growth and form-quality traits diversity analysis of young *Ormosia hosiei* family. *For. Res.* **2021**, *34*, 152–157. [CrossRef]
27. Liu, X.; Wang, Z.; Xiao, Z. Patterns of seed predation and dispersal of an endangered rare plant *Ormosia hosiei* by Edward's long-tailed rats and Chinese white-bellied rats. *Biodivers. Sci.* **2011**, *19*, 93–96. [CrossRef]
28. Qiu, H.; Sun, J.; Xu, D.; Jiao, J.; Xue, M.; Yuan, W.; Shen, A.; Jiang, B.; Li, S. The distribution dynamics of *Ormosia hosiei* under different climate change scenarios since the Last Glacial Maximum. *Acta Ecol. Sin.* **2020**, *40*, 3016–3026. [CrossRef]
29. Almas, A.D.; Conway, T.M. The role of native species in urban forest planning and practice: A case study of Carolinian Canada. *Urban For. Urban Green.* **2016**, *17*, 54–62. [CrossRef]
30. Wu, Z.; Raven, P.H. *Flora Reipublicae Popularis Sinicae*; Science Press: Beijing, China, 1994; Volume 40.
31. Fick, S.E.; Hijmans, R.J. WorldClim 2: New 1-km spatial resolution climate surfaces for global land areas. *Int. J. Climatol.* **2017**, *37*, 4302–4315. [CrossRef]
32. Bazzato, E.; Rosati, L.; Canu, S.; Fiori, M.; Farris, E.; Marignani, M. High spatial resolution bioclimatic variables to support ecological modelling in a Mediterranean biodiversity hotspot. *Ecol. Model.* **2021**, *441*, 109354. [CrossRef]
33. Rodríguez-Núñez, J.R.; Campos-Rojas, E.; Andrés-Agustín, J.; Alia-Tejacal, I.; Ortega-Acosta, S.A.; Peña-Caballero, V.; Madera-Santana, T.J.; Núñez-Colín, C.A. Distribution, eco-climatic characterisation, and potential growing regions of *Annona cherimola* Mill. (Annonaceae) in Mexico. *Ethnobiol. Conserv.* **2021**, *10*, 1–17. [CrossRef]
34. Huang, Z.; Xie, L.; Wang, H.; Zhong, J.; Li, Y.; Liu, J.; Ou, Z.; Liang, X.; Li, Y.; Huang, H.; et al. Geographic distribution and impacts of climate change on the suitable habitats of *Zingiber* species in China. *Ind. Crops Prod.* **2019**, *138*, 111429. [CrossRef]
35. Abdelaal, M.; Fois, M.; Fenu, G.; Bacchetta, G. Using MaxEnt modeling to predict the potential distribution of the endemic plant *Rosa arabica* Crép. in Egypt. *Ecol. Inform.* **2019**, *50*, 68–75. [CrossRef]
36. Hammer, Ø.; Harper, D.A.; Ryan, P.D. PAST: Paleontological statistics software package for education and data analysis. *Palaeontol. Electron.* **2001**, *4*, 9.
37. Duan, R.-Y.; Kong, X.-Q.; Huang, M.-Y.; Fan, W.-Y.; Wang, Z.-G. The predictive performance and stability of six species distribution Models. *PLoS ONE* **2014**, *9*, e112764. [CrossRef] [PubMed]
38. Moyroud, N.; Portet, F. Introduction to QGIS. In *QGIS and Generic Tools*; John Wiley & Sons, Inc.: Hoboken, NJ, USA, 2018; pp. 1–17.
39. Sheng, Q.; Wang, C.; Wang, L.; Liu, Y.; Geng, X.; Zhu, Z. Prediction of suitable habitat of *Paeonia suffruticosa* Andr. in China by DIVA-GIS. *Nonwood For. Res.* **2022**, *40*, 205–213, 248. [CrossRef]
40. Xie, C.; Huang, B.; Jim, C.Y.; Han, W.; Liu, D. Predicting differential habitat suitability of *Rhodomyrtus tomentosa* under current and future climate scenarios in China. *For. Ecol. Manag.* **2021**, *501*, 119696. [CrossRef]

41. Foden, W.B.; Young, B.E.; Akçakaya, H.R.; Garcia, R.A.; Hoffmann, A.A.; Stein, B.A.; Thomas, C.D.; Wheatley, C.J.; Bickford, D.; Carr, J.A.; et al. Climate change vulnerability assessment of species. *WIREs Clim. Chang.* **2019**, *10*, e551. [CrossRef]
42. Santika, T.; Hutchinson, M.F. The effect of species response form on species distribution model prediction and inference. *Ecol. Model.* **2009**, *220*, 2365–2379. [CrossRef]
43. Hijmans, R.J. Cross-validation of species distribution models: Removing spatial sorting bias and calibration with a null model. *Ecology* **2012**, *93*, 679–688. [CrossRef] [PubMed]
44. Hernandez, P.A.; Graham, C.H.; Master, L.L.; Albert, D.L. The effect of sample size and species characteristics on performance of different species distribution modeling methods. *Ecography* **2006**, *29*, 773–785. [CrossRef]
45. Körner, C. Significance of temperature in plant life. *Plant Growth Clim. Chang.* **2006**, *100*, 48–66.
46. Strimbeck, G.R.; Schaberg, P.G.; Fossdal, C.G.; Schröder, W.P.; Kjellsen, T.D. Extreme low temperature tolerance in woody plants. *Front. Plant Sci.* **2015**, *6*, 884. [CrossRef] [PubMed]
47. Woodward, F.I.; Fogg, G.E.; Heber, U.; Laws, R.M.; Franks, F. The impact of low temperatures in controlling the geographical distribution of plants. *Philos. Trans. R. Soc. London B Biol. Sci.* **1997**, *326*, 585–593. [CrossRef]
48. Zhang, M.; Chen, Q.; Huang, J.; Zhou, P. Geographic distribution and potential distribution of *Vaccinium bracteatum*. *J. Jiangsu For. Sci. Technol.* **2019**, *46*, 1–8. [CrossRef]
49. Matthews, H.D.; Wynes, S. Current global efforts are insufficient to limit warming to 1.5 °C. *Science* **2022**, *376*, 1404–1409. [CrossRef] [PubMed]
50. Ming, A.; Rowell, I.; Lewin, S.; Rouse, R.; Aubry, T.; Boland, E. *Key Messages from the IPCC AR6 Climate Science Report*; Cambridge University Press: Cambridge, UK, 2021. [CrossRef]
51. Mycoo, M.A. Beyond 1.5 °C: Vulnerabilities and adaptation strategies for Caribbean Small Island Developing States. *Reg. Environ. Chang.* **2018**, *18*, 2341–2353. [CrossRef]
52. Rangel, T.F.; Edwards, N.R.; Holden, P.B.; Diniz-Filho, J.A.F.; Gosling, W.D.; Coelho, M.T.P.; Cassemiro, F.A.S.; Rahbek, C.; Colwell, R.K. Modeling the ecology and evolution of biodiversity: Biogeographical cradles, museums, and graves. *Science* **2018**, *361*, eaar5452. [CrossRef]
53. Lippmann, R.; Babben, S.; Menger, A.; Delker, C.; Quint, M. Development of wild and cultivated plants under global warming conditions. *Curr. Biol.* **2019**, *29*, R1326–R1338. [CrossRef] [PubMed]
54. Kempel, A.; Bornand, C.N.; Gygax, A.; Juillerat, P.; Jutzi, M.; Sager, L.; Bäumler, B.; Eggenberg, S.; Fischer, M. Nationwide revisitation reveals thousands of local extinctions across the ranges of 713 threatened and rare plant species. *Conserv. Lett.* **2020**, *13*, e12749. [CrossRef]
55. Shishir, S.; Mollah, T.H.; Tsuyuzaki, S.; Wada, N. Predicting the probable impact of climate change on the distribution of threatened *Shorea robusta* forest in Purbachal, Bangladesh. *Glob. Ecol. Conserv.* **2020**, *24*, e01250. [CrossRef]
56. Garza, G.; Rivera, A.; Venegas Barrera, C.S.; Martinez-Ávalos, J.G.; Dale, J.; Feria Arroyo, T.P. Potential effects of climate change on the geographic distribution of the endangered plant species *Manihot walkerae*. *Forests* **2020**, *11*, 689. [CrossRef]
57. Varol, T.; Canturk, U.; Cetin, M.; Ozel, H.B.; Sevik, H. Impacts of climate change scenarios on European ash tree (*Fraxinus excelsior* L.) in Turkey. *For. Ecol. Manag.* **2021**, *491*, 119199. [CrossRef]
58. Natale, E.; Zalba, S.M.; Reinoso, H. Presence—Absence versus invasive status data for modelling potential distribution of invasive plants: Saltcedar in Argentina. *Ecoscience* **2013**, *20*, 161–171. [CrossRef]
59. Zhu, H.; You, L.; Li, Y.; Wang, H.; Wang, X. Modeling the geographical distribution pattern and climatic limited factors of *Cerasus schneideriana*. *J. Trop. Subtrop. Bot.* **2017**, *25*, 315–322. [CrossRef]

Disclaimer/Publisher's Note: The statements, opinions and data contained in all publications are solely those of the individual author(s) and contributor(s) and not of MDPI and/or the editor(s). MDPI and/or the editor(s) disclaim responsibility for any injury to people or property resulting from any ideas, methods, instructions or products referred to in the content.

forests

MDPI

Article

Establishment of PEG-Mediated Transient Gene Expression in Protoplasts Isolated from the Callus of *Cunninghamia lanceolata*

Kaiyue Hong [1,†], Zhenyu Chen [1,†], Yasmina Radani [1], Renhua Zheng [2], Xueyan Zheng [3], Yong Li [3], Jinhui Chen [1,*] and Liming Yang [1,*]

[1] State Key Laboratory of Tree Genetics and Breeding, Co-Innovation Center for Sustainable Forestry in Southern China, Nanjing Forestry University, Nanjing 210037, China; awzh18252056628@163.com (K.H.); aiyou9@njfu.edu.cn (Z.C.); radani.yasmina@gmail.com (Y.R.)
[2] The Key Laboratory of Timber Forest Breeding and Cultivation for Mountainous Areas in Southern China, Fujian Academy of Forestry, Fuzhou 350012, China; zrh08@126.com
[3] National Germplasm Bank of Chinese Fir, Fujian Yangkou Forest Farm, Shunchang 353211, China; zxy0553@163.com (X.Z.); yklcliuong@163.com (Y.L.)
* Correspondence: chenjh@njfu.edu.cn (J.C.); yangliming@njfu.edu.cn (L.Y.)
† These authors contributed equally to this work.

Abstract: *Cunninghamia lanceolata* (*C. lanceolata*) is an important timber tree species in southern China that requires gene function studies to understand its traits. In this study, we investigated the callus induction rates of immature zygotic embryos from reciprocal hybrids between genotypes B46 and B49. With zygotic embryo development, the callus induction rates showed an increasing trend, followed by a decreasing trend. Moreover, the rate of callus induction in genotype B46 × B49 immature zygotic embryos was greater than in genotype B49 × B46. Callus from *C. lanceolata* with genotype B46 × B49 was selected as the donor material for protoplast isolation. By using an enzymatic digestion solution containing cellulase, macerozyme, and pectinase, combined with an osmotic stabilizer, we obtained 9.76×10^6 protoplasts/mL with 92.7% viability. We subsequently transformed plasmids into *C. lanceolata* callus protoplasts and observed the location of the H2B-eYFP fusion protein in the nucleus. To achieve transient transfection of *C. lanceolata* callus protoplasts, we compared transfection efficiencies at different concentrations of PEG4000, PEG6000, or PEG8000 in a modified MMg solution. We found that 20% (*w*/*v*) PEG6000 mediated the transient transfection of *C. lanceolata* callus protoplasts with a 6.70% efficiency. This study provides a technical foundation for future research on transient transfection and functional analysis of *C. lanceolata* genes.

Keywords: *Cunninghamia lanceolata*; callus induction; protoplast preparation; transient transfection

check for updates

Citation: Hong, K.; Chen, Z.; Radani, Y.; Zheng, R.; Zheng, X.; Li, Y.; Chen, J.; Yang, L. Establishment of PEG-Mediated Transient Gene Expression in Protoplasts Isolated from the Callus of *Cunninghamia lanceolata*. *Forests* **2023**, *14*, 1168. https://doi.org/10.3390/f14061168

Academic Editor: David Lee

Received: 22 April 2023
Revised: 24 May 2023
Accepted: 29 May 2023
Published: 6 June 2023

Copyright: © 2023 by the authors. Licensee MDPI, Basel, Switzerland. This article is an open access article distributed under the terms and conditions of the Creative Commons Attribution (CC BY) license (https://creativecommons.org/licenses/by/4.0/).

1. Introduction

Cunninghamia lanceolata is a valuable species found in the Yangtze River Basin and the south of the Qinling Mountains in China [1]. It is known for its rapid growth, wind resistance, soot tolerance, and abundant material, making it both economically and ecologically important [2]. However, *C. lanceolata*, like many other perennial woody gymnosperms, has a long sexual reproduction cycle, making it difficult to conserve its superior traits. Additionally, available regeneration systems are time-consuming, and obtaining transgenic plants is challenging. As a result, researchers often express *C. lanceolata* genes in the model plant *Arabidopsis thaliana* to explore their function; however, due to major genetic variations between the two species, this approach may not yield satisfactory results. They are members of different families and have diverged evolutionaryly over time. As a result, their genetic makeup and regulatory mechanisms may change dramatically, influencing the function of the expressed genes in the heterologous host. For example, in *Arabidopsis thaliana*, the regulatory elements that control gene expression in *C. lanceolata* may not function properly,

resulting in incorrect or incomplete expression of the gene of interest. Alternatively, the protein products of the expressed genes may be incompatible with the cellular machinery of *Arabidopsis thaliana*, leading to protein misfolding or degradation. Overall, genetic variations between *C. lanceolata* and *Arabidopsis thaliana* can lead to significant differences in the function and behavior of expressed genes, limiting the utility of heterologous expression as a tool for studying gene function. To address this issue, transient transfection of protoplasts (TTPs) has been widely used for gene function identification, protein interaction analysis, subcellular localization, gene editing, plant regeneration, and vaccine preparation [3–8]. As a result, we investigated and established TTP technology in *C. lanceolata* to facilitate gene-function studies. Due to its speed and efficiency, TTP technology holds great potential for improving our understanding of the functional genomics of *C. lanceolata*.

Different transient transfection methods have been employed in gymnosperms, such as agrobacterium-mediated transient transfection systems in *Pinus armandii*, *Pinus elliottii*, *Pinus taeda*, *Picea mariana*, and *Pinus sylvestris* [9–13]. Gene gun-mediated transient transfection systems have been applied to *P. armandii*, *Pinus radiate*, and *Picea glauca*, whereas electroporation-mediated transient transfection systems have been established for *P. taeda* [14–17]. However, protoplasts are ideal recipients for genetic transfection since they lack a cell wall, making it easier for them to absorb exogenous genetic material. Polyethylene glycol (PEG)-mediated TTP has the advantage of being easy to operate as it achieves chemical binding by a simple mixing reaction at room temperature. This process does not require any special equipment and may be conducted with standard laboratory equipment. Therefore, PEG-mediated TTP technology is simple to use, does not require expensive or complex instrumentation, and can be conducted in a variety of laboratory and industrial settings [18,19]. Established systems for mediating TTP in mesophyll cells of *Liriodendron chinense*, *Hevea brasiliensis*, *Populus* L., and *Elaeis guineensis* make exploring the potential of PEG-mediated TTP for *C. lanceolata* extremely appealing [20–23].

Protocols for preparing protoplasts from secondary xylem, needle leaves [24], and suspension cells of *C. lanceolate* have been reported [25]. Callus cells are usually derived by taking a small piece of tissue from a plant body and culturing it in an appropriate medium. These tissues are typically cultured in a laboratory where environmental factors such as temperature, humidity, and light can be controlled. In contrast, other types of plant cells, such as leaf or root cells, must be collected from the natural environment and are thus subject to seasonal changes such as temperature and daylight hours. As a result, callus cells can be cultured at any time, regardless of the season. In particular, callus tissue inducted from immature zygotic embryos (IZEs) exhibits lower contamination rates than callus obtained from stem segments or needle leaves [26]. Previous studies have demonstrated that in gymnosperms, maternal genotypes have a stronger influence on callus induction than male parent genotypes, as seen in *P. taeda* [27]. Therefore, it is important to investigate the ability of *C. lanceolata* reciprocal hybrid IZEs to produce callus tissue. Exploring the use of IZE-induced callus for protoplast preparation could be an interesting avenue to pursue. However, there have been limited studies on the use of IZE-induced callus from *C. lanceolata* for protoplast preparation.

In this study, our primary objective was to compare the induction rate of embryogenic callus derived from IZE in reciprocal hybrids of *C. lanceolata*. Specifically, we focused on comparing the induction rates between genotypes B49 × B46 and B46 × B49 at various developmental phases. We also aimed to investigate the impact of varying mannitol concentrations on the degree of plasmolysis in *C. lanceolata* callus cells. Additionally, we analyzed the yield and viability of callus protoplasts (CPs) prepared with various enzymatic solutions containing mannitol as an osmotic stabilizer. Finally, we investigated the efficacy of PEG-mediated callus TTP at different PEG concentrations and molecular weights. By examining these various factors, our study provides a valuable technical platform for TTPs isolated from gymnosperm species, as well as functional analysis of *C. lanceolata* genes, and presents new ideas for their preparation.

2. Materials and Methods

2.1. Plant Materials and Plasmids

Cones from the superior genotypes B49×B46 and B46×B49 of the *C. lanceolata* species were carefully collected at different developmental phases in 2020. Based on previous research [28], the 24 June, 2 July, 12 July, 15 July, and 18 July 2020 sampling dates were classified as developmental phases 1, 2, 3, 4, and 5, respectively. The developmental phases of the collected seeds were categorized as cleavage polyembryony, dominant embryo, columnar embryo, or early cotyledonary. To ensure the materials' sterility, immature seeds were gently removed from the cones and placed in conical flasks containing detergent. The flasks were carefully sealed with gauze and rinsed for 30 min with tap water.

Following that, the seeds were prepared for sterilization. The conical flask was drained of tap water, and then alcohol was added. The flasks were shaken for 30 s before removing the alcohol using a 150-mesh sieve (Sangon Biotech, Shanghai, China). After adding sodium hypochlorite, the flask was shaken for 8 min before removing sodium hypochlorite using a 150-mesh sieve (Sangon Biotech, Shanghai, China). Sterile water was then added, and the seeds were rinsed three times; the 150-mesh sieve was used to remove sterile water. Finally, the sterilized material was stored at 4 °C in a sterile conical flask until use.

Tiangen High Pure Maxi Plasmid Kit (DP116) (Tiangen, Beijing, China) was used to extract the plasmids, which were then diluted to 1.0 μg/μL in 20 μL aliquots for subsequent experiments. Figure 1 depicts the expression framework of the fusion protein reporter gene, comprising H2B and eYFP fluorescent proteins on the plasmid, as visualized using the ApE software (v3.1.3, 11 November 2022). The basic backbone of the plasmid is pjit166 [20], named pjit166-H2B-eYFP, which encompasses an expression framework that enables the synthesis of a fusion protein reporter gene comprising H2B and eYFP fluorescent proteins. This framework can be described as follows: A promoter sequence is present near the plasmid's starting point (promoter region), which can be recognized by transcription factors within the cell, hence initiating gene transcription. The coding region of the H2B gene follows immediately downstream of the promoter, encompassing the DNA sequence responsible for encoding the histone H2B protein. A terminator codon is placed at the 3′ end of the H2B coding sequence, signaling the termination of the transcription process. Subsequent to the terminator, in the downstream region, lies the coding sequence of the eYFP (enhanced yellow fluorescent protein) gene, which encodes the fluorescent protein. In summary, the pjit166 plasmid contains a promoter for gene transcription, a coding sequence for the H2B protein, and a coding sequence for the eYFP fluorescent protein. This expression framework allows the synthesis of a fusion protein consisting of H2B and eYFP, thereby facilitating specific research or analysis purposes in experimental studies [29].

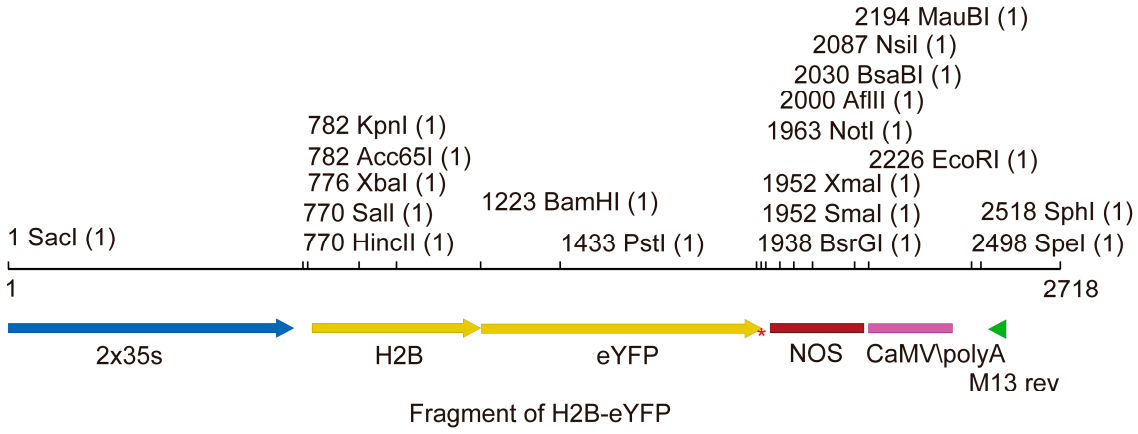


Figure 1. Gene expression framework of the H2B-eYFP fusion protein. 2 × 35s: duplication of the cauliflower mosaic virus (CaMV) 35S promoter. H2B: histone H2B protein; eYFP: enhanced yellow fluorescent protein. NOS: NOS terminator. *: Stop codon. Green triangle: universal sequencing primers m13 rev.

2.2. Experimental Procedures

2.2.1. Callus Induction and Protoplast Preparation

C. lanceolata immature seeds were sterilized and placed on a bench. After cutting open the seed coats and removing the IZEs, a transverse incision was made across the endosperms, and the wound sites were pressed firmly against the modified basal medium DCR induction medium to induce callus formation [30]. The growth of the callus was observed using a microscope, and the material for protoplast preparation was chosen based on the genotype with the best growth rate. To prepare the protoplasts, we optimized the solutions and procedures based on a previously reported method for *A. thaliana* [31]. First, we treated the callus samples (1 g) for 6 h with a 0.3~0.6 M mannitol solution. Using a Zeiss Axio Imager D2 fluorescence microscope (Carl Zeiss, Jena, Germany), we then counted the number of cells in which the plasmalemma was effectively separated from the cell wall and measured the distances between them. After 4–5 h of enzymatic digestion, we obtained isolated protoplasts by centrifugation and calculated the yield with a 0.1 mm × 400 mm hemocytometer (Qiujing, Shanghai, China). The protoplast suspension was stained with fluorescein diacetate (FDA) (Sigma-Aldrich, St. Louis, MO, USA), and protoplasts with high green fluorescence were considered viable. Before transfection, the *C. lanceolata* protoplasts were placed in an ice bath with W5 solution (154 mM NaCl, 125 mM $CaCl_2$, 5 mM KCl, and 2 mM MES at pH 5.7) [31]. We monitored the protoplast viability using the FDA stain protocol every 6 h from 0 to 24 h.

2.2.2. Mediation of TTP by PEG of Varying Molecular Weights Prepared at Different Concentrations

To prepare *C. lanceolata* protoplasts for transfection, a few modifications were made. Before transfection, the protoplasts were first incubated for 15 min in a modified MMg solution, followed by thorough mixing. This solution consisted of 0.5 M mannitol, 15 mM $MgCl_2$, and 4 mM MES at pH 5.7. Different concentrations (10%, 15%, and 20% w/v) of PEG with varying molecular weights were prepared as storage solutions. After transfection, the protoplasts were centrifuged at 100× *g* for 2 min, and the supernatant was discarded. The pellets were resuspended in the modified MMg solution and diluted to a 1×10^5 cells/mL concentration. Transfection was carried out using the H2B-eYFP plasmid, a transient expression vector where the H2B gene is ligated with the enhanced yellow fluorescent protein (eYFP) tag gene [32]. The eYFP fluorescence signal was observed using a Zeiss Axio Imager D2 fluorescence microscope. To carry out transfection, protoplasts and PEG were mixed sequentially in a centrifuge tube and incubated at 23 °C for 15 min. After adding four times the volume of W5 for dilution, the protoplasts were collected by centrifugation at 100× *g* for 2 min. Finally, the protoplasts were resuspended with W5 and incubated in a 6-well cell culture plate for 16 h at 20~25 °C. Following that, the protoplasts were sampled and photographed for observation.

2.3. Data Analysis

C. lanceolata genotypes B46 × B49 and B49 × B46 were extracted from the same batch and inoculated using DCR media [33] (with five statistical replicates) at a rate of nine induced zygotic embryo explants per petri dish (with nine biological replicates). Table 1 presents the formulation of the callus induction medium for *Cunninghamia lanceolata*. Table 2 outlines the formulation of the subculture medium for *Cunninghamia lanceolata* callus. Table 3 provides the formula for the mother liquor of the DCR medium.

Table 1. Formulation of callus induction medium for *Cunninghamia lanceolata*.

Pharmaceutical	Culture Medium Number 01	Culture Medium Number 02
	Quantity of Ingredients Used for Preparing 1 L	Quantity of Ingredients Used for Preparing 1 L
Mother liquor with a high concentration of elements	50 mL	50 mL
Mother liquor containing micronutrition	10 mL	10 mL
Organic	10 mL	10 mL
Iron salt	10 mL	10 mL
2,4-D	20 mL	10 mL, 20 mL, 30 mL
6-BA	5 mL	5 mL
KT	5 mL	5 mL
VC	10 mL	10 mL
Casein acid hydrolysate	0.5 g/L	0.5 g/L
Sucrose	20 g/L	20 g/L
Active charcoal	3 g/L	3 g/L
Glutamine	0.45 g/L	0.45 g/L
Inositol	0.1 g/L	0.1 g/L

Table 2. Formulation of the subculture medium for the callus of *Cunninghamia lanceolata*.

Pharmaceutical	Culture Medium Number 03
	Quantity of Ingredients Used for Preparing 1 L
Mother liquor with a high concentration of elements	50 mL
Mother liquor containing micronutrition	10 mL
Organic	10 mL
Iron salt	10 mL
2,4-D	10 mL
6-BA	5 mL
KT	5 mL
VC	10 mL
Casein acid hydrolysate	0.5 g/L
Sucrose	20 g/L
Active charcoal	3 g/L
Glutamine	0.45 g/L
Inositol	0.1 /L

Table 3. Formula of the mother liquor of DCR medium.

Pharmaceutical	Elements	g/L
Mother liquor with a high concentration of elements	KNO_3	0.34
	$Ca(NO_3)_2 \cdot 4H_2O$	0.556
	$MgSO_4 \cdot 7H_2O$	0.37
	NH_4NO_3	0.4
	KH_2PO_4	0.17
	$CaCl_2$	0.064/0.085
Mother liquor containing micronutrition	KI	0.00083
	H_3BO_3	0.0062
	$MnSO_4 \cdot 4H_2O$	0.0294
	$ZnSO_4 \cdot 7H_2O$	0.0086
	Na_2MoO_4	0.00025
	$CuSO_4 \cdot 5H_2O$	0.00025
	$CoCl_2 \cdot 6H_2O$	0.000025
	$NiCl_2$	0.000025

Table 3. *Cont.*

Pharmaceutical	Elements	g/L
Iron salt	$FeSO_4 \cdot 7H_2O$	0.0278
	EDTA	0.0373
Organic	Inositol	0.2
	Glycine	0.002
	Niacin	0.0005
	VB1 (Thiamine hydrochloride)	0.001
	VB6 (Pyridoxine HCL)	0.0005
VC		1
2,4-D		0.1
6-BA		0.1
KT		0.1

Equation (1) was then used to calculate the *C. lanceolata*-induced callus induction rate (CIR).

$$\text{CIR} = \frac{\text{Number of IZEs with induced callus}}{\text{Total number of IZEs}} \times 100\% \quad (1)$$

Statistical data processing was performed using Microsoft Office Excel, and the degree of *C. lanceolata* CP (protoplasts with cell walls removed) plasmolysis under 0.3~0.6 M mannitol solutions was analyzed using ANOVA in OriginPro2021 student version (OriginLab Corporation, Northampton, MA, USA). Box plots were generated to determine the appropriate mannitol concentration for plasmolysis of *C. lanceolata* callus cells. The viability of the obtained *C. lanceolata* CPs was calculated using Equation (2); the TTP (transformation and transfection protocol) efficiency of *C. lanceolata* callus was calculated using Equations (3) and (4) was used to calculate the yield of *C. lanceolata* CPs. *C. lanceolata* CP yield, viability, and TTP efficiency were measured three times, and the mean values were calculated.

$$\text{Protoplasts viability} = \frac{\text{Number of viable protoplasts}}{\text{Total number of protoplasts}} \times 100\% \quad (2)$$

$$\text{TTP efficiency} = \frac{\text{Total number of fluorescent protoplasts}}{\text{Total number of protoplasts}} \times 100\% \quad (3)$$

$$\text{Protoplast yield} = \frac{\text{Protoplast density} \times \text{total volume of suspension}}{\text{The fresh weight of the material (e.g., plant tissue) used for isolating protoplasts.}} \times 100\% \quad (4)$$

3. Results

3.1. Callus Induction from Immature Embryos of Different Developmental Phases

Reciprocal hybrids of *C. lanceolata* genotypes B46 and B49 were subjected to callus induction from IZEs. One week following preparation, the resultant embryos became swollen and enlarged, and calluses formed after two weeks. Although the callus induction rate (CIR) varied, the appearance of the callus induced by the reciprocal hybrid IZE hydration was similar across all samples, with a loose, white texture. (Figure 2). The callus obtained from reciprocal hybrids requires three consecutive passages. The CIR for *C. lanceolata* genotype B46 × B49 IZE was greater than for genotype B49 × B46 IZE. The CIR of genotype B49 × B46 IZEs at developmental phase 1 was 30%, but those at developmental phases 2–5 did not induce callus tissue. Conversely, callus formation was seen in genotype B46 × B49 IZEs harvested during developmental phases 1–3. Specifically, genotype B46 × B49 IZEs obtained during developmental phase 1 exhibited a 20% CIR, while those obtained at developmental phase 2 showed the highest CIR (30%). However, genotype B46 × B49 IZEs collected at developmental phase 4 resulted in the formation of roots or shoots, with only a 15% rate of induced callus cells. At developmental phase 5,

genotype B46 × B49 IZEs did not induce any callus but only roots or shoots. Overall, the CIR tended to increase and then decrease with the IZE developmental phase (Figure 2).

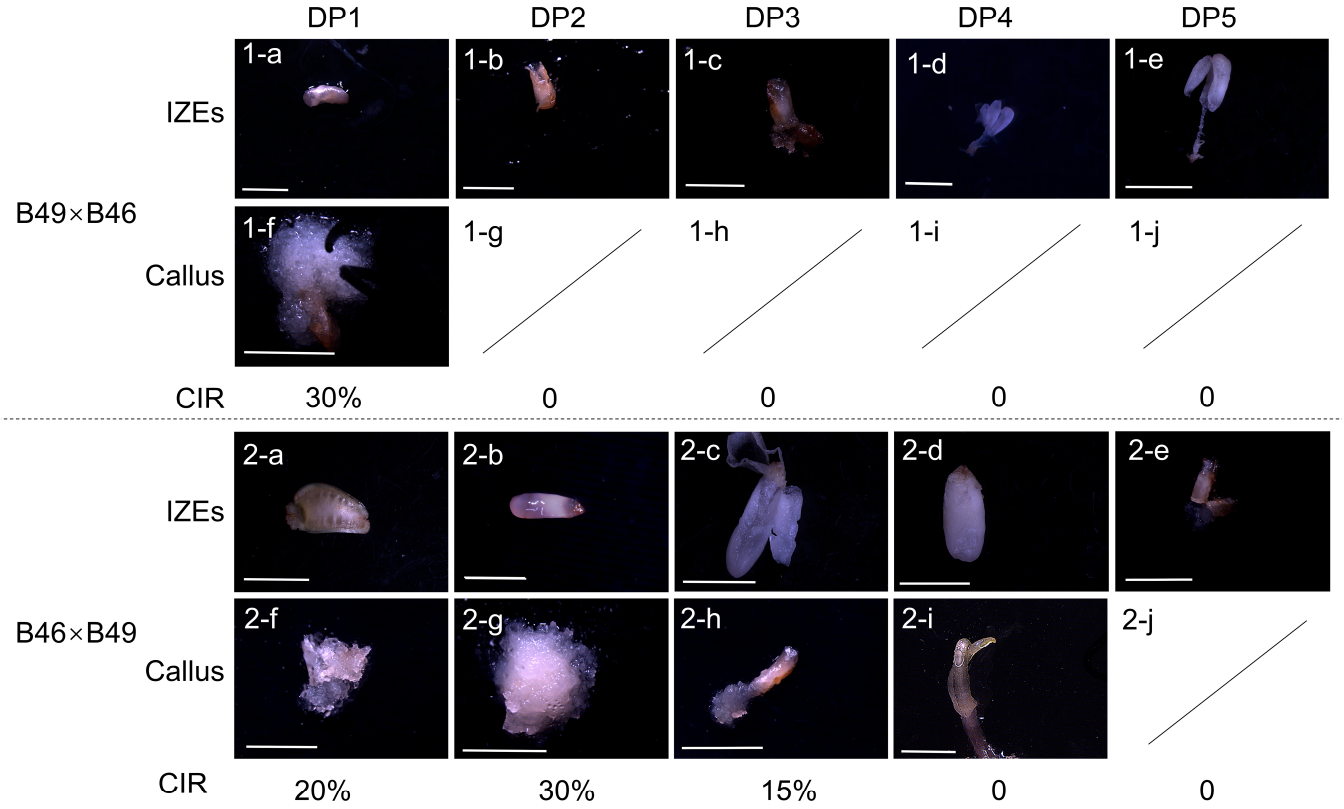


Figure 2. Callus induction of IZEs from the reciprocal hybrid of *C. lanceolata* at different developmental phases. B49 × B46 and B46 × B49: collection of fruits from reciprocal crosses of *C. lanceolata*. IZEs: immature zygotic embryos. CIR: callus induction rate. DP: developmental phase. (**1-a**–**e**,**2-a**–**e**): IZEs were cleaned, sterilized, and placed on DCR induction medium. (**1-f**–**j**,**2-f**–**j**): images of callus induced from IZEs. (**2-i**): only buds were induced without callus. (**1-g**–**j**): no callus was induced. Bar = 0.5 cm.

3.2. Preparation of Protoplasts

3.2.1. Mannitol Concentration Screening

Plasmolysis levels were clearly visible in callus cells induced by IZE treatment at mannitol concentrations of 0.4 M and 0.5 M, but not at 0.3 M (Figures 3 and 4). The degree of plasmolysis in callus cells of genotype B49 × B46 varied with increasing mannitol concentration. Our data analysis revealed that the impact of 0.3 M to 0.6 M mannitol concentrations on the level of plasmolysis in callus cells of genotype B49 × B46 was statistically significant at a probability level of 0.01 (Figure 3), with the highest level of significance observed in the 0.6 M mannitol treatment group. As such, plasmolysis in callus cells was not immediately apparent at low mannitol concentrations; conversely, at high mannitol concentrations, the protoplasts shrank, and clumped together, making recovery difficult. Based on the degree and distribution of plasmolysis across the different mannitol concentrations, we selected 0.4 M mannitol as the optimal concentration for osmotic stabilization during CP preparation.

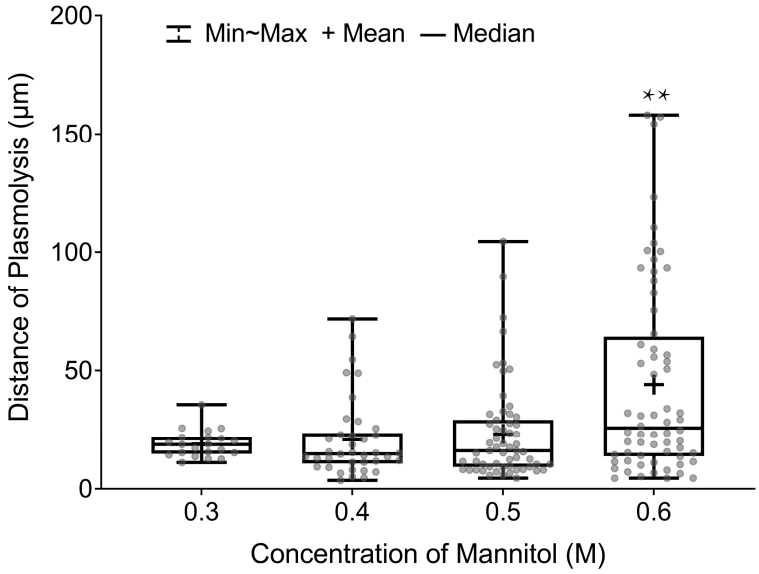


Figure 3. Plasmolysis of *C. lanceolata* callus at different concentrations of mannitol solutions. The callus samples were treated with a 0.3~0.6 M mannitol solution for 6 h, and the distance of plasmolysis was measured by the software of the Zeiss microscope after taking photos. ** above the box of the 0.6 M mannitol treatment group indicates significant differences between treatments on any other variable at $p < 0.01$.

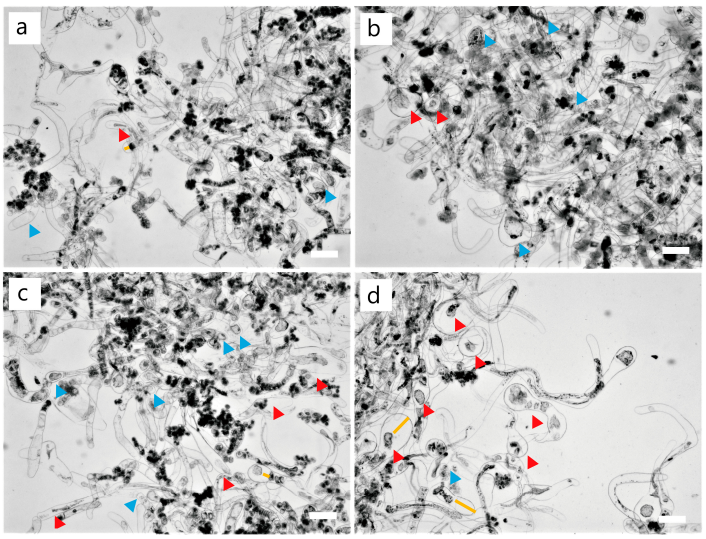


Figure 4. Microscopic observations of *C. Lanceolata* callus at different mannitol concentrations. (**a**): 0.3 M, (**b**): 0.4 M, (**c**): 0.5 M, and (**d**): 0.6 M. Scale = 100 μm. Red arrows indicate excessive separation of the mass walls. Blue arrows indicate moderate separation of the bulk walls. Yellow lines show the measurement method for the mass wall separation distance.

3.2.2. Screening of Enzymatic Digestion Conditions

Upon subculturing the *C. lanceolata* callus in solid medium, a bright translucent structure with a white appearance was observed, and the cells appeared to be rich in water (Figure 5a). Microscopic analysis revealed that the embryoid pedicel mass was composed of the embryo head and long rod-shaped embryo stem cells, with elongated cell clusters on the cell surface, corresponding to embryoid callus. (Figure 6a). Following the preparation of the *C. lanceolata* callus protoplasts, three types were identified: those with few inclusions (Figure 6b), those with a small number of conspicuous inclusions (Figure 6c), and those with full-filled conspicuous inclusions (Figure 6d).

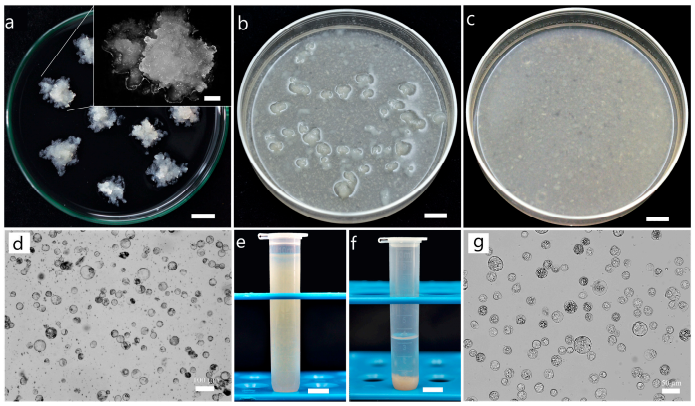


Figure 5. Purification of protoplasts from *C. Lanceolata* calluses. (**a**): Callus on solid medium; the small picture is a close-up of a single piece of callus. (**b**): Initiation of enzymatic digestion of *C. lanceolata* callus. (**c**): Enzymatic digestion after 3~4 h. (**d**): Protoplasts before purification. (**e**): Protoplasts being washed with W5 solution for purification. (**f**): Protoplasts collected by centrifugation after washing. (**g**): Protoplasts after purification. Scale without labeled distance is 1 cm.

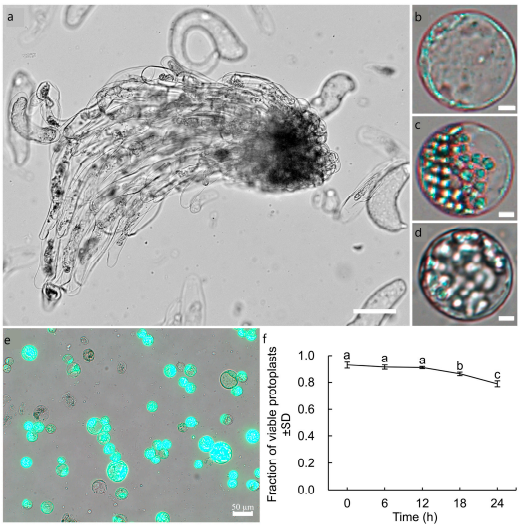


Figure 6. Microscopic observation and viability assessment of *C. Lanceolata* protoplasts. (**a**,**c**): *C. Lanceolata* callus, scale = 100 µm. (**b**–**d**): Protoplast type, scale = 5 µm. (**e**): FDA staining to detect the viability of protoplasts by FITC channel, scale = 50 µm. (**f**): Percentages of viable protoplasts after standing on ice for different periods of time. Means sharing with ±SD, and common letter do not differ significantly at $p \leq 0.05$ according to ANOVA with the Duncan test.

Among the four enzymatic solutions tested for protoplast preparation, enzymatic combination C, which consisted of 2% (w/v) Cellulase R-10, 0.2% (w/v) Macerozyme R-10, 0.1% (w/v) Pectolyase Y-23, and 5 mM mercaptoethanol, yielded the highest number of protoplasts with 9.76×10^6 cells/mL (Figure 7 and Table 4). Therefore, this combination was chosen for the preparation of *C. lanceolata* CPs. During enzymolysis of the *C. lanceolata* callus, the enzymolysis liquid gradually changed from clear to milky, and complete digestion of the callus to obtain the protoplast crude extract was achieved in 3 to 4 h (Figure 5b,c). The protoplasts obtained from enzymatic digestion with 0.4 M mannitol as the osmotic stabilizer exhibited similar shape and size, clear edges, more inclusions, and fewer fragments (Figure 5d). The crude extract of protoplasts was then filtered using a 0.7-micrometer cell strainer to effectively remove the incompletely dissociated *C. lanceolata* callus. After centrifugation, collection, and washing with W5 solution (Figure 5e,f), purified protoplasts from *C. lanceolata* calluses were obtained (Figure 5g).

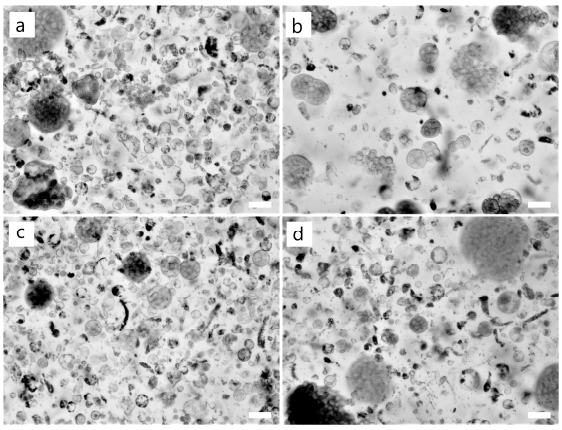


Figure 7. Visual representation of enzymatic solutions for protoplast isolation. (**a**–**d**) represent formulas a–d of enzymatic solutions, respectively, in Table 4. Scale = 100 µm.

Table 4. Protoplasts prepared under different enzymatic solutions from *C. lanceolata* callus.

N.	Cellulase R-10	Macerozyme R-10	Pectolyase Y-23	Yield (Cells/mL)	Whether to Add Mercaptoethanol
a	1.5%	0.1%	0.1%	2.47×10^6	yes
b	2%	0.2%	0.1%	5.24×10^5	no
c	2%	0.2%	0.1%	9.76×10^6	yes
d	3%	0.1%	0.2%	1.38×10^6	yes

After purification, the viability of *C. lanceolata*'s CPs was originally 92.7%, but it gradually decreased with increasing duration in ice incubation, particularly after 12 h (Figures 6e,f and S1). After 24 h, there was an increase in contamination and fragments within the microscope field, which led to an irregular morphology of the protoplasts. As a result, the viability of CPs was reduced to 79.0%.

3.3. Different Concentrations and Molecular Weights of PEG Were Used to Mediate the Transient Gene Expression from C. lanceolata Callus

Our results indicate that the H2B-eYFP fusion protein is targeted to the nucleus of *C. lanceolata* CPs (Figure 6), which is consistent with prior studies on *Arabidopsis thaliana* [34]. Moreover, the findings demonstrate that PEG at various concentrations and molecular weights can facilitate transient gene expression in *C. lanceolata* calluses and allow for the localization of H2B-eYFP to the nucleus (Figure 8). Specifically, the highest efficiencies were observed with 20% (*w*/*v*) PEG6000-mediated transient transfection efficiency, which peaked at 6.70%, and 15% (*w*/*v*) PEG8000-mediated transient transfection efficiency, which peaked at 8.99%. Considering the potential adhesions and breakage of transfected protoplasts, we recommend the use of 20% (*w*/*v*) PEG6000 for mediating TTP of *C. lanceolata* callus (Figure 9).

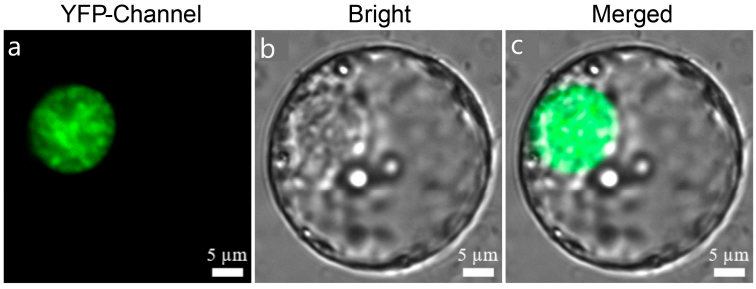


Figure 8. Subcellular location of the H2B-eYFP recombinant protein in protoplasts of *C. lanceolata* callus. (**a**) The image represents the YFP channel fluorescence. (**b**) The image is captured in bright-

field illumination. (**c**) The image is a merged composite, combining different channels or modalities. YFP-Channel: the photo was taken using Filter 46-YFP of the Zeiss fluorescence microscope with excitation wavelength λex = 426–446 nm and emission wavelength λem = 520–550 nm.

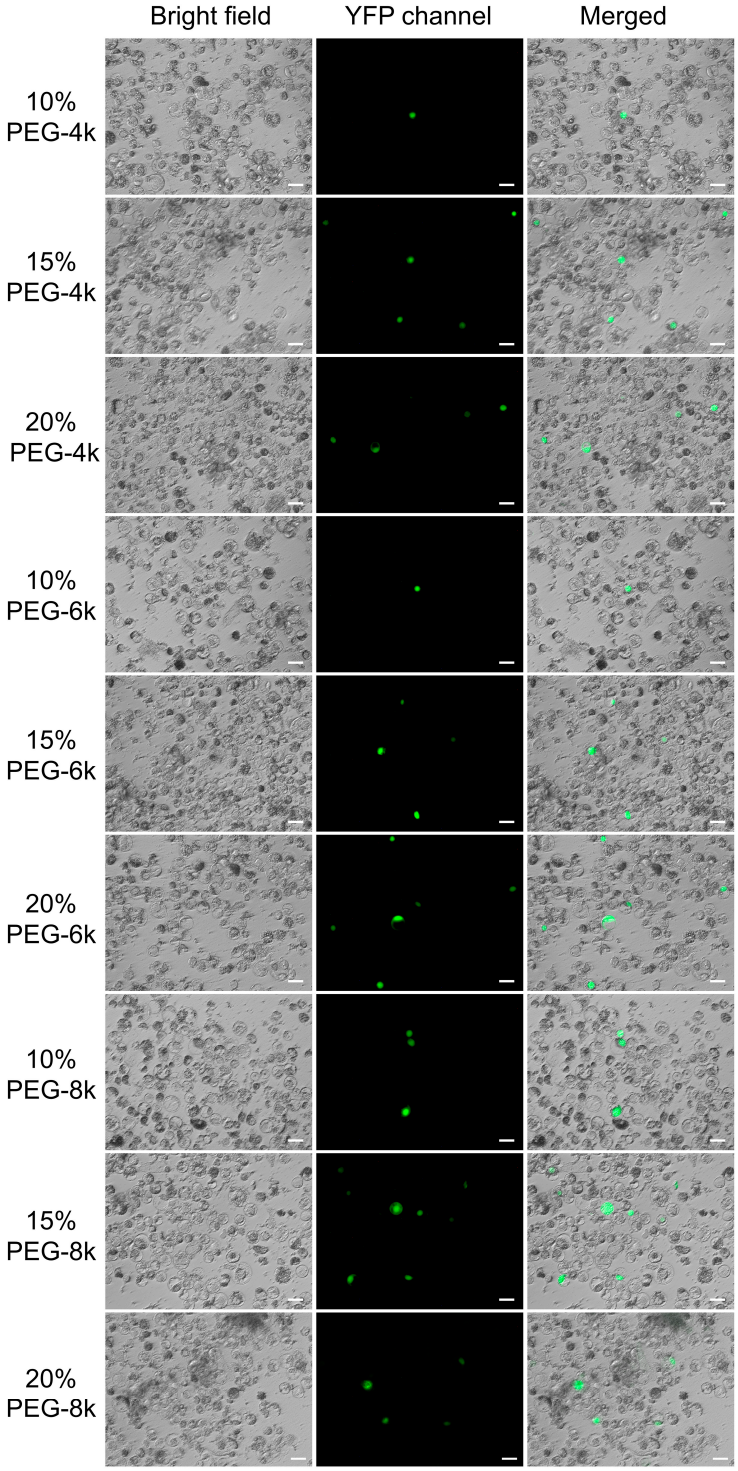


Figure 9. Optimizing transfection efficiency in *C. lanceolata* callus protoplasts by PEG solutions with varying molecular weights and concentrations. Working concentrations of weight/volume (*w*/*v*): 10%/15%/20%. PEG-4k/6k/8k: polyethylene glycol (PEG) with a molecular weights of 4000/6000/8000. Bar = 50 μm.

4. Conclusions

One of the critical steps in plant TTP studies is the preparation of high-quality protoplasts. Gymnosperm protoplasts can be derived from various sources such as callus (*Picea abies* [35], *Akjesfabri*, *Pinus lambertiana* [36]), needle leaves (*C. lanceolata*, *Platycladus orientalis* [37]), and suspension cells (*P. taeda* L., *C. lanceolata*, *P. lambertiana*, *P. mariana*, *Larix gmelinii* [38]). Among these sources, enzymatic digestion of *C. lanceolata* callus is comparatively easier than needle leaves [39]. The suspension cell system requires a long experiment cycle, and stem segments have a high contamination rate; therefore, *C. lanceolata* callus was selected to prepare protoplasts in our study. To obtain abundant protoplasts, the first step is to optimize the conditions for callus induction. Callus induction is known to be affected by the degree of IZE development and genotype [40]. Our study found that the CIR of *C. lanceolata* IZE increased and then decreased with the developmental phase, which is consistent with previous observations on *Pinus koraiensis* [41,42], *P. elliottii* [43], *Pinus thunbergii* [44], and *P. taeda* L. [45]. Furthermore, we found that genotype has a major influence on callus induction [46], with significant differences observed in the CIR of IZE of *C. lanceolata* reciprocal hybrids between genotypes B46 and B49 collected at the same developmental phase. Studies on *P. aspoerata*, *P. sylvestris*, and *P. taeda* L. have also revealed that the maternal genotype has a greater effect on embryonic callus induction than the paternal genotype [47].

Currently, mannitol is widely used as an osmotic stabilizer during protoplast preparation [48]. However, the osmotic stabilizer concentration must be carefully controlled to avoid damaging the protoplasts. The protoplasts can break apart if the concentration is too low, and they can shrink or contract if the concentration is too high. Previous studies have indicated that 0.4 M mannitol is the optimal concentration for protoplast isolation from various plant species, including *C. lanceolata* callus, *Populus* L., *Quercus palustris*, and *Camellia sinensis* leaves [49]. Enzymes such as Cellulase R-10, Macerozyme R-10, and Pectolyase Y-23 are commonly used in protoplast preparation protocols; however, the optimal combination of enzymes varies depending on the plant species. In *Onobrychis taneitica*, for example, viable protoplasts were obtained using only Cellulase R-10 and *Pectolyase* Y-23 [50], while in *Lotus corniculatus* L., increasing the concentration of Macerozyme R-10 improved protoplast production [51]. In this study, we found that increasing the concentration of Cellulase R-10 alone did not significantly improve the yield or viability of *C. lanceolata* protoplasts. However, increasing both Cellulase R-10 and Macerozyme R-10 concentrations led to a significant increase in protoplast yield. After screening various enzyme combinations, we identified a final enzymatic cocktail containing Cellulase R-10, Macerozyme R-10, Pectolyase Y-23, and 5 mM mercaptoethanol, which enabled us to obtain a high yield of *C. lanceolata* protoplasts with minimal cell debris. TTP efficiency is influenced by several factors. A high protoplast concentration can make cells sticky and unfavorable for observation; conversely, a low concentration can lead to transient transfection failure. To ensure high transfection efficiency, the protoplast concentration should be controlled within the range of 0.5 to 2×10^5 cells/mL [51]. In our study, we used CPs of *C. lanceolata* genotype B49×B46 at a concentration of 1×10^5 cells/mL as the recipient for PEG-mediated transient transfection. The highest efficiency was obtained with 25% (w/v) PEG-mediated TTP in *Triticum aestivum* L. [52]; while in *Zea mays* and *Sorghum bicolor*, 30% (w/v) PEG-mediated leaf TTP yielded the best results [53,54]. However, we found that the TTP efficiency of *C. lanceolata* callus initially increased and then decreased as the PEG concentration increased. Moreover, TTP efficiency is also affected by PEG molecular weight [55]. For example, in *Citrus reticulata*, *Phalaenopsis aphrodite*, and *Carica papaya* L., the highest mesophyll TTP efficiency was achieved with PEG4000, PEG6000, and PEG8000, respectively [56,57]. In our study, we found that 15% PEG8000 mediated the highest TTP efficiency in *C. lanceolata* callus, although this resulted in severe damage to some protoplasts. As a result, we selected 20% (w/v) PEG6000 as the optimal medium for TTP transfection in *C. lanceolata* calluses. Additionally, in *Manihot esculenta*, longer transfection periods were associated with higher protoplast damage by PEG [58]. In *Chenopodium quinoa*, the highest protoplast

transfection efficiency was observed at a transfection duration of 15 min [59]. Similarly, we observed that the TTP efficiency of *C. lanceolata* callus initially improved and then dropped as transfection time increased, with many protoplasts fragmenting after 30 min. Therefore, we selected 15 min as the optimal transfection duration.

Here, IZEs from the *C. lanceolata* genotype B49×B46 were utilized to induce callus, and a *C. lanceolata* CP transient transfection system was established. These significant findings lay a solid foundation for gene localization studies, functional analysis, and germplasm innovation related to this important species.

Supplementary Materials: The following supporting information can be downloaded at: https://www.mdpi.com/article/10.3390/f14061168/s1. Figure S1: Viability test of protoplasts of *C. lanceolata* callus from 0 to 24 h.

Author Contributions: J.C. and L.Y. conceived, planned, coordinated the project, and finalized the manuscript. K.H. performed the experiments, performed the data analysis, and wrote the draft. Z.C. validated and contributed to data analysis and curation and revised the manuscript. Y.R. has made edits and polished the language of this text. R.Z., X.Z. and Y.L. reviewed and edited the manuscript. J.C. coordinated, contributed to data curation, finalized, and funded this research. All authors have read and agreed to the published version of the manuscript.

Funding: This research was funded by the Seed Industry Innovation and Industrialization Project of Fujian Province, grant number ZYCX-LY-202101, the Research Startup Fund for High-Level and High-Educated Talents of Nanjing Forestry University, and the Priority Academic Program Development of Jiangsu Higher Education Institutions (PAPD).

Data Availability Statement: Not applicable.

Acknowledgments: We thank Wei Jianhua for supplying PtoMYB148-eYFP. Transient expression vectors of eYFP-tagged fusions of PtoMYB148-eYFP were provided by Jianhua Wei, Beijing Agro-Biotechnology Research Center. We recombined the H2B-eYFP fusion protein into the instantaneous protein expression plasmid vector PJIT-166 preserved in our laboratory. It was used to assess the ability of the expression system to target the product of an exogenously introduced gene to the nucleus.

Conflicts of Interest: The authors declare no conflict of interest.

References

1. Jiang, Y.; Zhang, X.; Chhin, S.; Zhang, J. A Bimodal Pattern and Age-Related Growth of Intra-Annual Wood Cell Development of Chinese Fir in Subtropical China. *Front. Plant Sci.* **2021**, *12*, 757438. [CrossRef] [PubMed]
2. Xu, R.; Wang, L.; Zhang, J.; Zhou, J.; Cheng, S.; Tigabu, M.; Ma, X.; Wu, P.; Li, M. Growth Rate and Leaf Functional Traits of Four Broad-Leaved Species Underplanted in Chinese Fir Plantations with Different Tree Density Levels. *Forests* **2022**, *13*, 308. [CrossRef]
3. Ma, W.; Yi, F.; Xiao, Y.; Yang, G.; Chen, F.; Wang, J. Isolation of leaf mesophyll protoplasts optimized by orthogonal design for transient gene expression in *Catalpa bungei*. *Sci. Hortic.* **2020**, *274*, 109684. [CrossRef]
4. Priyadarshani, S.; Hu, B.; Li, W.; Ali, H.; Jia, H.; Zhao, L.; Ojolo, S.P.; Azam, S.M.; Xiong, J.; Yan, M.; et al. Simple protoplast isolation system for gene expression and protein interaction studies in pineapple (*Ananas comosus* L.). *Plant Methods* **2018**, *14*, 95. [CrossRef]
5. Mackon, E.; Ma, Y.; Jeazet Dongho Epse Mackon, G.C.; Li, Q.; Zhou, Q.; Liu, P. Subcellular localization and vesicular structures of anthocyanin pigmentation by fluorescence imaging of black rice (*Oryza sativa* L.) stigma protoplast. *Plants* **2021**, *10*, 685. [CrossRef] [PubMed]
6. Bahariah, B.; Masani, M.Y.A.; Rasid, O.A.; Parveez, G.K.A. Multiplex CRISPR/Cas9-mediated genome editing of the *FAD2* gene in rice: A model genome editing system for oil palm. *J. Genet. Eng. Biotechnol.* **2021**, *19*, 86. [CrossRef]
7. Lin, C.; Hsu, C.; Yang, L.; Lee, L.; Fu, J.; Cheng, Q.; Wu, F.; Hsiao, H.; Zhang, Y.; Zhang, R.; et al. Application of protoplast technology to CRISPR/Cas9 mutagenesis: From single-cell mutation detection to mutant plant regeneration. *Plant Biotechnol. J.* **2018**, *16*, 1295–1310. [CrossRef]
8. Spiegel, H.; Boes, A.; Voepel, N.; Beiss, V.; Edgue, G.; Rademacher, T.; Sack, M.; Schillberg, S.; Reimann, A.; Fischer, R. Application of a scalable plant transient gene expression platform for malaria vaccine development. *Front. Plant Sci.* **2015**, *6*, 1169. [CrossRef]
9. Ma, Z.; Liu, J.-J.; Zamany, A.; Williams, H. Transient gene expression in western white pine using agroinfiltration. *J. For. Res.* **2019**, *31*, 1823–1832. [CrossRef]

10. Wei, T.; Caroline, L. Overexpression of zinc finger transcription factor ZAT6 enhances salt tolerance. *Open Life Sci.* **2020**, *50*, 199–209. [CrossRef]
11. Tang, W. Additional virulence genes and sonication enhance *Agrobacterium tumefaciens*-mediated loblolly pine transformation. *Plant Cell Rep.* **2003**, *21*, 555–562. [CrossRef] [PubMed]
12. Liu, Y.; Liu, K.; Wang, J. Research Progress on Agrobacterium Mediated Genetic Transformation of Conifer Species. *Heilongjiang Agric. Sci.* **2021**, *44*, 136–141. [CrossRef]
13. Rafique, M.; Paasela, T.; Lim, K.-J.; Sayed, H.; Teeri, T. Promoter analysis in Scots pine (*Pinus sylvestris*) via transient expression of luciferase fusions. *New Biotechnol.* **2012**, *29*, S135–S136. [CrossRef]
14. Fernando, D.; Owens, J.; Misra, S. Transient gene expression in pine pollen tubes following particle bombardment. *Plant Cell Rep.* **2000**, *19*, 224–228. [CrossRef] [PubMed]
15. Rey, M.; González, M.V.; Ordás, R.J.; Tavazza, R.; Ancora, G. Factors affecting transient gene expression in cultured radiata pine cotyledons following particle bombardment. *Physiol. Plant.* **1996**, *96*, 630–636. [CrossRef]
16. Tian, L.; Brown, D.; Sibbald, S.; Latoszek-Green, M. Extraction buffer effects on detection of transient gene expression in white spruce. *Plant Mol. Biol. Report.* **2012**, *21*, 175. [CrossRef]
17. Gupta, P.; Dandekar, A.; Durzan, D. Somatic proembryo formation and transient expression of a luciferase gene in Douglas fir and loblolly pine protoplasts. *Plant Sci.* **1988**, *58*, 85–92. [CrossRef]
18. Wu, S.; Zhu, H.; Liu, J.; Yang, Q.; Shao, X.; Bi, F.; Hu, C.; Huo, H.; Chen, K.; Yi, G. Establishment of a PEG-mediated protoplast transformation system based on DNA and CRISPR/Cas9 ribonucleoprotein complexes for banana. *BMC Plant Biol.* **2020**, *20*, 425. [CrossRef]
19. Mao, J.; Li, J.; Wang, H.; Rui, M.; Zhai, W. Preparation and regeneration method of fusarium oxysporum protoplast in melon. *Mol. Plant Breed.* **2021**, *36*, 202–208. [CrossRef]
20. Huo, A.; Chen, Z.; Wang, P.; Yang, L.; Wang, G.; Wang, D.; Liao, S.; Cheng, T.; Chen, J.; Shi, J. Establishment of transient gene expression systems in protoplasts from Liriodendron hybrid mesophyll cells. *PLoS ONE* **2017**, *12*, e0172475. [CrossRef]
21. Zhang, X.; Wang, L.; He, C.; Luo, H. An efficient transient mesophyll protoplast system for investigation of the innate immunity responses in the rubber tree (*Hevea brasiliensis*). *Plant Cell Tissue Organ Cult. PCTOC* **2016**, *126*, 281–290. [CrossRef]
22. Wang, H.-L.; Wang, T.; Yang, Q.; Yin, W.; Xia, X.; Guo, H.; Li, Z. Preparation and Transfection of Populus tomentosa Mesophyll Protoplasts. *Bio-Protocol* **2021**, *11*, e4220. [CrossRef]
23. Wang, Y.; Liu, X.; Zhang, Q.; Zheng, Y.; Li, D. Isolation of oil palm mesophyll protoplasts and establishment of transient transformation system. *J. Huazhong Agric. Univ.* **2021**, *40*, 154–159. [CrossRef]
24. Tang, J.; Lin, E.; Huang, H.; Tong, Z.; Lou, X. Isolation and total RNA extraction of leaf protoplasts in Chinese fir. *Sci. Silvae Sin.* **2018**, *54*, 38–48. [CrossRef]
25. Zhuge, Q.; Que, G. Establishment of cell suspension culture and isolation of protoplast of Chinese fir. *For. Res.* **1992**, *6*, 628–632. [CrossRef]
26. Jin, L.; Yi, X.; Cao, H. Research progress on somatic embryogenesis of oil palm. *Jiangsu Agric. Sci.* **2021**, *49*, 29–35. [CrossRef]
27. Newton, R.; Sen, S.; Puryear, J. Free proline changes in *Pinus taeda* L. callus in response to drought stress. *Tree Physiol.* **1986**, *1*, 325–332. [CrossRef] [PubMed]
28. Shi, J.; Zhen, Y.; Zheng, R.H. Proteome profiling of early seed development in *Cunninghamia lanceolata* (Lamb.) Hook. *J. Exp. Bot.* **2010**, *61*, 2367–2381. [CrossRef]
29. Davis, M.; Jorgensen, E. ApE, a plasmid editor: A freely available DNA manipulation and visualization program. *Front. Bioinform.* **2022**, *2*, 818619. [CrossRef]
30. Nasseri, E.; Kalantari, S.; Naderi, R. The effect of culture media type and species on embryogenic tissue induction in somatic embryogenesis of pine genus. *Iran. J. For. Poplar Res.* **2012**, *20*, 670–690. [CrossRef]
31. Yoo, S.; Cho, Y.; Sheen, J. Arabidopsis mesophyll protoplasts: A versatile cell system for transient gene expression analysis. *Nat. Protoc.* **2007**, *2*, 1565–1572. [CrossRef]
32. Cheng, Z.; Chen, Y.; Zhang, J.; Wang, H.; Wei, J. Isolation and characterization of PtoMYB148 transcription factor expressing preferentially in developing xylem in *Populus tomentosa*. *Biotechnol. Bull.* **2013**, *11*, 69–74. [CrossRef]
33. Zhou, X.; Zhang, Y.; Li, M.; Zhao, F.; Chen, J.; Zheng, R.; Xiao, H.; Huang, J.; Zhang, Z.; Li, Y. Studies on factors influencing rooting efficiency from mature Chinese fir superior clones in vitro. *J. Nanjing For. Univ.* **2013**, *56*, 169. [CrossRef]
34. Boisnard-Lorig, C.; Colon-Carmona, A.; Bauch, M.; Hodge, S.; Doerner, P.; Bancharel, E.; Dumas, C.; Haseloff, J.; Berger, F. Dynamic analyses of the expression of the HISTONE::YFP fusion protein in arabidopsis show that syncytial endosperm is divided in mitotic domains. *Plant Cell* **2001**, *13*, 495–509. [CrossRef]
35. Zhang, L.; Peiwang, L.; Huang, Z.; Li, C. Advances in preparation system of woody plants protoplast. *J. Cent. South Univ. For. Technol.* **2011**, *31*, 102–107. [CrossRef]
36. Ji, K.; Wang, P.; Wang, J.; Ruan, Q.; Pan, T.; Zhu, P.; Guo, T.; Liu, J. Review on in vitro culture of tree species in Pinaceae. *J. Nanjing For. Univ. Nat. Sci. Ed.* **2015**, *39*, 142–148. [CrossRef]
37. Zhou, Q.; Jiang, Z.; Li, Y.; Zhang, T.; Zhu, H.; Zhao, F.; Zhao, Z. Mesophyll protoplast isolation technique and flow cytometry analysis of ancient Platycladus orientalis (Cupressaceae). *Turk. J. Agric. For.* **2019**, *43*, 275–287. [CrossRef]
38. Korlach, J.; Zoglauer, K. Developmental patterns during direct somatic embryogenesis in protoplast cultures of european larch (*Larix decidua* Mill.). *Plant Cell Rep.* **1995**, *15*, 242–247. [CrossRef]

39. Maeda, E.; Hagiwara, T. Enzymatic isolation of protoplasts from the rice leaves and callus cultures. *Jpn. J. Crop Sci.* **1974**, *43*, 68–76. [CrossRef]
40. Ramarosandratana, A.; Van Staden, J. Tissue position, explant orientation and naphthaleneacetic acid (NAA) affect initiation of somatic embryos and callus proliferation in Norway spruce (*Picea abies*). *Plant Cell Tissue Organ Cult.* **2003**, *74*, 249–255. [CrossRef]
41. Gao, F.; Peng, C.; Wang, H.; Shen, H.; Yang, L. Selection of culture conditions for callus induction and proliferation by somatic embryogenesis of *Pinus koraiensis*. *J. For. Res.* **2020**, *32*, 483–491. [CrossRef]
42. Yang, F.; Xia, X.; Ke, X.; Ye, J.; Zhu, L. Somatic embryogenesis in slash pine (*Pinus elliottii* Engelm): Improving initiation of embryogenic tissues and maturation of somatic embryos. *Plant Cell Tissue Organ Cult. PCTOC* **2020**, *143*, 159–171. [CrossRef]
43. Xu, K.; Cheng, Q.; Yang, C.; Gu, Z.; Ding, W.; Li, H. Induction and proliferation of embryogenic callus on improved varieties of fast-growing *Pinus elliottii*. *Guihaia* **2021**, *41*, 283–291. [CrossRef]
44. Sun, T.; Yi, J.; Wu, X.; Zhu, L.; Wu, J.; Liang, F. Induction of Embryonic Callus from *Pinus thunbergii* for Resistance to Pine Wilt Disease. *J. Northeast. For. Univ.* **2015**, *43*, 96–99. [CrossRef]
45. Shin, H.; Kim, Y. Somatic embryogenesis of *Pinus rigida* × *P. taeda* and the relationship between the initiation of embryogenic tissue and zygotic embryo development. *Plant Biotechnol. Rep.* **2012**, *6*, 175–181. [CrossRef]
46. Gao, F.; Chen, S.; Qin, C.; Cai, J.; Wang, C.; Dong, H.; Tao, J. Optimization of somatic embryogenesis system and cryopreservation of *Picea koraiensis*. *J. Nanjing For. Univ. Nat. Sci. Ed.* **2021**, *45*, 100–108. [CrossRef]
47. Wang, C.; Xu, L. Analysis on the influencing factors of somatic embryogenesis of coniferous tree species. *J. Jilin For. Sci. Technol.* **2021**, *50*, 31–32. [CrossRef]
48. Wu, D.; Wei, T.; Gao, D.; Zang, R.; Xu, H.; Guo, P. Application of plant protoplast culture technology in medicinal plants. *Life Sci. Res.* **2021**, *25*, 176–182. [CrossRef]
49. Peng, Z.; Tong, H.-R.; Liang, G.-L.; Shi, Y.-Q.; Yuan, L.-Y. Protoplast isolation and fusion induced by PEG with leaves and roots of tea plant (*Camellia sinensis* L. O. Kuntze). *Acta Agron. Sin.* **2018**, *44*, 463–470. [CrossRef]
50. Zhao, H.; Zhang, B.; Chen, A.; Li, P.; Xiao, Y. Effects of different enzymolysis conditions on the cotyledons protoplast isolation of alfalfa. *Acta Agrestia Sin.* **2008**, *1*, 50–53. [CrossRef]
51. Yang, L.; Liu, S.; Li, Y.; Lin, R. Methods for examining transcription factor-DNA Interaction in plants. *Chin. Bull. Bot.* **2020**, *55*, 468–474. [CrossRef]
52. Xi, H.; Ai, K.; Tong, S. The optimization of isolation method for mesophyll protoplast from common wheat (*Triticum aestivum*) seedlings. *Biotechnol. Bull.* **2016**, *32*, 68–73. [CrossRef]
53. Lei, H.; Bai, F.; Feng, Y.; Guo, Y.; Qiao, N. Preparation of Maize Leaf Protoplasts and Establishment of Transient Transformation System. *J. Chang. Univ.* **2018**, *35*, 11–14. [CrossRef]
54. Zheng, G.; Cheng, Y.; Han, S.; Lü, Y.; Lu, Y.; Zhou, C.; Zhang, D.; Shen, X. The establishment of protoplasts isolation and transient expression system of sorghum cultivar BTx623. *Biot. Resour.* **2018**, *43*, 42–49. [CrossRef]
55. Huo, P.; Yan, P.; Shen, W.; Zhou, P. Establishment of gene transient expression system mediated by polyethylene glycol in *Carica papaya* L. mesophyll protoplasts. *Mol. Plant Breed.* **2015**, *13*, 808–815. [CrossRef]
56. Song, L.; Hou, Z.; Ren, Y.; Yan, J.; Zeng, A.; Xu, Y.; Zhang, C. Detection of gene editing efficiency in broccoli by PEI-SWNT mediated transient transformation. *Jiangsu Agric. Sci.* **2021**, *49*, 56–59. [CrossRef]
57. Xiao, Z.; Xu, Y.; Luo, N.; Zhou, Y. Application of plant protoplasts in molecular and cell biology research. *Guihaia* **2020**, *40*, 576–582. [CrossRef]
58. Chen, Y.; Lu, J. Application of CRISPR/Cas9 mediated gene editing in trees. *Hereditas* **2020**, *42*, 657–668. [CrossRef]
59. Xu, Y.; Chen, Z.; Jia, L.; Weng, X. Advances in understanding of the biosynthetic pathway and regulatory mechanism of triterpenoid saponins in plants. *Sci. Sin. Vitae* **2021**, *51*, 525–555. [CrossRef]

Disclaimer/Publisher's Note: The statements, opinions and data contained in all publications are solely those of the individual author(s) and contributor(s) and not of MDPI and/or the editor(s). MDPI and/or the editor(s) disclaim responsibility for any injury to people or property resulting from any ideas, methods, instructions or products referred to in the content.

forests

MDPI

Article

Biochemical Changes during Fruit and Seed Development in Nanjing Linden (*Tilia miqueiana* M.)

Yu Wu [1,2,†], Chenyin Peng [1,2,†], Xiangyu Yu [3] and Yongbao Shen [1,2,*]

1 College of Forestry, Nanjing Forestry University, Nanjing 210037, China
2 Co-Innovation Center for Sustainable Forestry in Southern China, Southern Tree Inspection Center National Forestry Administration, Nanjing 210037, China
3 School of Life Sciences, University of Sussex, Brighton BN1 9PX, UK
* Correspondence: ybshen@njfu.edu.cn
† These authors contributed equally to this work.

Abstract: In China, the wild population of Nanjing Linden (*Tilia miqueliana* M.) is experiencing a drastic decline, primarily due to high levels of empty seeds. This study aimed to measure the biochemical and physiological changes during fruit and seed development in *T. miqueliana* to determine the developmental mechanism. The weight method and photosynthetic respiration were used to determine the biological aspects of both fruits and embryos, while transmission electron microscopy and the anthrone colorimetric method were used to determine the endosperm content, including sugar, starch, protein, and fat. Enzyme-linked immunosorbent assays were conducted to determine the levels of endogenous plant hormones such as indole-3-acetic acid (IAA), gibberellic acid 3 (GA_3), zeatin riboside (ZR), and abscisic acid (ABA). The nonlinear least-squares method was used to fit the model of nutrient and hormone levels, revealing that fruit size expanded from the 5th to the 65th day and that fruit moisture content exhibited a downward trend, along with a decrease in fruit respiration intensity. Embryos were found to be fully developed between 35 DAF and 65 DAF, while the nutrients in the endosperm, i.e., sugar, starch, protein, and fat, continuously accumulated after 50 DAF. Additionally, ABA, IAA, GA_3, and ZR contents were found to synergistically regulate seed development and maturation.

Keywords: cell structure and morphology development process; endogenous hormones; endosperm contents; maturation; moisture content; seed embryo

check for updates

Citation: Wu, Y.; Peng, C.; Yu, X.; Shen, Y. Biochemical Changes during Fruit and Seed Development in Nanjing Linden (*Tilia miqueiana* M.). *Forests* **2023**, *14*, 969. https://doi.org/10.3390/f14050969

Academic Editor: Jorge Manuel P.L. Canhoto

Received: 10 April 2023
Revised: 25 April 2023
Accepted: 3 May 2023
Published: 8 May 2023

Copyright: © 2023 by the authors. Licensee MDPI, Basel, Switzerland. This article is an open access article distributed under the terms and conditions of the Creative Commons Attribution (CC BY) license (https://creativecommons.org/licenses/by/4.0/).

1. Introduction

The distribution range of Nanjing linden (*Tilia miqueiana* M.), a species used for timber, honey, and ornamental trees, covers most of the southeastern parts of China. In recent decades, the populations of *T. miqueiana* have dramatically declined in size and number throughout its natural distribution regions. Now, *T. miqueiana* is an endangered tree species in China. The life history of a seed begins with flowering and pollination and proceeds through fertilisation, development, maturation, scattering, dormancy, and germination. This series of steps translates into a subtle, unique, and interconnected life course [1]. The embryos of *Ginkgo biloba* L. begin to grow on the 140th day after flowering (140 DAF) [2]. However, embryo development is closely related to seed nutrients and endogenous hormones in the developing endosperm. During seed development, the nutrients in the plant flow to the seed in a dissolved state and accumulate inside the seed. With the development of the seed, these nutrients are gradually converted into non-dissolved dry matter, mainly starch, protein, and fat with high molecular weights [3,4]. When the seeds of *Brassica napus* L. mature, soluble sugars first form and are later transformed into starch, protein, and fat [5], and rutin, protein, and starch contents gradually rise when *Fagopyrum tataricum* G. seeds mature [6].

In addition, the plant hormone auxin is closely involved in many aspects of plant development, including seed formation [7], such as the embryo, endosperm, and seed coat.

In fact, after anthesis and seed setting, as the embryo develops, there is an initial stage of cell division and tissue differentiation [8]. Especially after dormancy, the contents of ABA and GA are very important for seed germination [9]. The maturation period of *Araucaria angustifolia* (Bert.) O. seeds can be shortened by increased ABA synthesis and accumulation, whereas GA rapidly declines during seed development and maturation [10]. Additionally, it is possible that other plant hormones also play a vital role in the development and maturation of seeds. For instance, during the wheat (*Triticum aestivum* L.) seed maturation process, the levels of IAA and SA gradually decrease [11]. The seed-filling phase then begins with a constant or nearly constant gradient until the end and can therefore be represented by a straight-line relationship [12]. During seed filling, the embryo of most tree species gradually grows. Sometimes, the beginning and end of embryo development greatly differ between plant species.

The stamens of *T. miqueiana* are precocious and almost sterile, and they have to be cross-pollinated. Additionally, the flowering phase is brief—only a week—which frequently leads to differences in florescence, subsequent years of low fertility, and a low seed setting rate. The seed of *T. miqueiana* is abortive, and the seed setting rate is generally less than 10%, which happens when development stops midway due to unknown reasons after pollination and fertilisation, resulting in a low full-seed percentage [13]. Additionally, the seed of *T. miqueiana* has a hard and difficult-to-penetrate seed coat, causing deep mechanical and physiological dormancy, and it is difficult for seeds to sprout in the year they were sown without any treatment. After two or three years of sowing, the majority of seeds begin to sprout. So, deep seed dormancy has made it extremely difficult to reproduce naturally, putting it on the verge of extinction [14]. These factors seriously affect the *T. miqueiana* seed yield and seedling propagation. In addition, due to the lack of knowledge of the early stage and the influence of human activities on the living environment of *T. miqueiana* in the state of nature, there are only 2000 wild *T. miqueiana* trees in China [13]. Thus, it is an endangered and rare species protected under a national program. Previous research has focused on breaking the seed dormancy of *T. miqueiana* and assumed that the coat permeability might be an important cause of the seed dormancy, with the aim of elucidating the cause of this decline. Nevertheless, few studies have examined fruit and seed development, including the storage of nutrients, moisture content, embryo growth, and endogenous hormones. In this study, the physiological and biochemical changes during seed development in *T. miqueiana* were therefore analysed, and the mechanism of seed development was revealed.

2. Materials and Methods

2.1. Fruit (Seed) Collection

In September 2020, fruits of *T. miqueiana* were collected from a mature tree on Niushou Mountain in Nanjing City, Jiangsu Province, China. Niushou Mountain (118′74 E, 31′92 N) is 248 m high and is located in the northern subtropical monsoon climate zone. The annual average temperature is 16 °C, the frost-free period is 237 days, the annual average humidity is 77%, and average rainfall is 1005.7 mm. The pH value of the mountain's soil is 5.5–6.5 [15]. The fruits collected were staged by days after flowering (DAF) as follows: 5 DAF (15 June), 20 DAF (30 June), 35 DAF (15 July), 50 DAF (30 July), 65 DAF (15 August), 80 DAF (30 August), 100 DAF (20 September), and 120 DAF (10 October). The size, respiration rate, water content of fruits, and embryo length were measured immediately. At the same time, the endosperms were taken from the fruits and stored in a freezer at −80 °C (Forma™ 89000, Thermo Scientific, MA, USA).

2.2. Fruit Size

Three replicates (100 fruits per replicate) of fruits were analysed per sample after fruit collection. The transverse and longitudinal diameters of the fruit were measured with a vernier calliper. Because the fruit is approximately spherical, the following ellipsoid

formula was used to calculate its size: $V = \frac{4}{3} \times a^2 b\pi$, where a = $\frac{1}{2}$ transverse diameter and b = $\frac{1}{2}$ longitudinal diameter.

2.3. Fruit Moisture Content and Respiration Rate

The fruit moisture content (MC) was determined using the high-temperature drying method described by Ista [16]. Three replicates of each of the 100 samples were oven-dried at 130 °C for 4 h to constant weight (AX 60, Carbolite Gero, Germany). MC was calculated using the following equation: $MC = \frac{M2-M3}{M2-M1} \times 100$, where $M1$ = weight (g) of the container and cover; $M2$ = weight (g) of the container, cover, and contents before drying; and $M3$ = weight (g) of the container, cover, and contents after drying.

The respiration rate during fruit development was tested with a photosynthetic respirometer (Li-6400, Lincoln, NE, USA). The respiratory rate Pn ($\mu mol \cdot g^{-1} \cdot min^{-1}$) was expressed as the CO_2 released by the respiration of 1 g of seeds in 1 min. One gram of randomly selected seeds from each treatment group was examined at 5, 20, 35, 50, 65, 80, 100, and 120 days. The moisture on the surface of the seeds was absorbed with absorbent paper. Then, the seeds were placed in the sample chamber. The two ends of the sample chamber were connected to the air inlet and the air outlet. The measurement time was 2 min, and measurements were recorded every 2 s. The final figure is the average. The photosynthesis respirometer was in analytical mode (light intensity = 0, ambient temperature = 25 °C).

2.4. Embryo Growth

Embryos were taken out from the fruit, and their lengths were defined under a stereo microscope (Eclipse Ci; Nikon, Tokyo, Japan) with three replicates (100 seeds per replicate) of seeds during their development.

2.5. Ultrastructural Observation of Endosperm Cells

The endosperm cell morphologies of five fruits randomly selected from each test sample were observed using transmission electron microscopy (TEM) (HT7700, Hitachi, Japan). The endosperms were cut into 1 mm^3 pieces, immediately fixed in 2.5% glutaraldehyde aqueous fixative solution (Servicebio) for 2 h, then transferred to 1% OsO_4 for 5 h, dehydrated in an ethanol series, and embedded in acetone blocks. Acetone blocks were sectioned to a thickness of 60 nm on a microtome with a glass knife, and sections were stained with 5% uranyl acetate and 0.5% lead citrate and viewed under an HT7700 transmission electron microscope. TEM image processing and analysis were performed using Image J software (Java-based public image processing software developed by the National Institutes of Health).

2.6. Embryo Germination Test

The embryo germination test included immature and mature embryo groups. There were four replicates in each group with 100 embryos. The immature embryos were derived from the fruits at 50 DAF, while the mature fruit embryos were obtained from the fruits at 65 DAF. All taken embryos were placed on soaked cotton in a germination box and put in an incubator (25 °C, 1000 Lx for 12 h) (RH-500A, RunHua, JS, China) for 30 days. When the embryo grew into a normal seedling, the embryo was considered to have germinated. The embryo germination percentage was calculated using the formula proposed by ISTA [16]: $G = \frac{N}{A} \times 100$, where G = % germination, N = number of embryos germinated, and A = total number of embryos tested. The final percent germination represents the mean (±standard deviation) of four replicates.

2.7. Assessment of Sugar, Starch, Protein, and Fat Contents

Total starch and soluble sugar contents were assessed using the anthrone colorimetric method [17]. Soluble protein content was assessed using the method described by Bradford [18], and fat content was determined using Soxhlet extraction [19].

2.8. Quantification of Endogenous Hormones

We used enzyme-linked immunosorbent assays to extract, purify, and quantify the levels of endogenous gibberellic acid (GA), abscisic acid (ABA), indole-3-acetic acid (IAA), and zeatin riboside (ZR) following the protocols described by Zhao et al. [20] and Wang et al. [21]. The kit utilised in this study was kindly provided by the Laboratory of Plant Endogenous Hormones, China Agricultural University. To extract the hormones, we used 10 mL of cold 80% (v/v) methanol extraction medium containing 1 $mmol^{-1}$ butylhydroxytoluene as an antioxidant. The extract was then incubated at 4 °C for 4 h and centrifuged × g at 4 °C for 15 min. The resulting supernatant was prewashed with 10 mL of 100% (w/v) and 5 mL of 80% (v/v) methanol, respectively, through a Sep-Pak C18 column (Waters Corp., Milford, MA, USA). A total of 10 mL of 100% (v/v) methanol and 10 mL of ether-eluting hormone components were then extracted and dissolved in 2 mL of phosphate-buffered saline (PBS) containing Tween 20 and 0.1% (w/v) gelatin (pH 7.5) for ELISA detection. We repeated all experiments three times to calculate the mean and standard error.

GA antibodies were developed using GA_3 as a hapten. It cross-reacts with other GAs, such as GA_1, which has a similar structure to GA_3. Thus, the detected GA content is the sum of the GA content of GA_3 and other GAs that cross-react with GA antibodies.

3. Results

3.1. Morphological Characteristic Changes in the Fruit and Embryo

3.1.1. Changes in Fruit Size, Moisture Content, Respiration Rate, and Embryo Length

During fruit development, the size of the fruit clearly changed. In the early phase of development, the fruit size increased rapidly from 0.1 ± 0.02 cm^3 at 5 DAF to 0.39 ± 0.04 cm^3 at 35 DAF. After that, the fruit size exhibited a slow upward trend, although the difference in size was not significant until the fruits were fully mature (Figure 1).

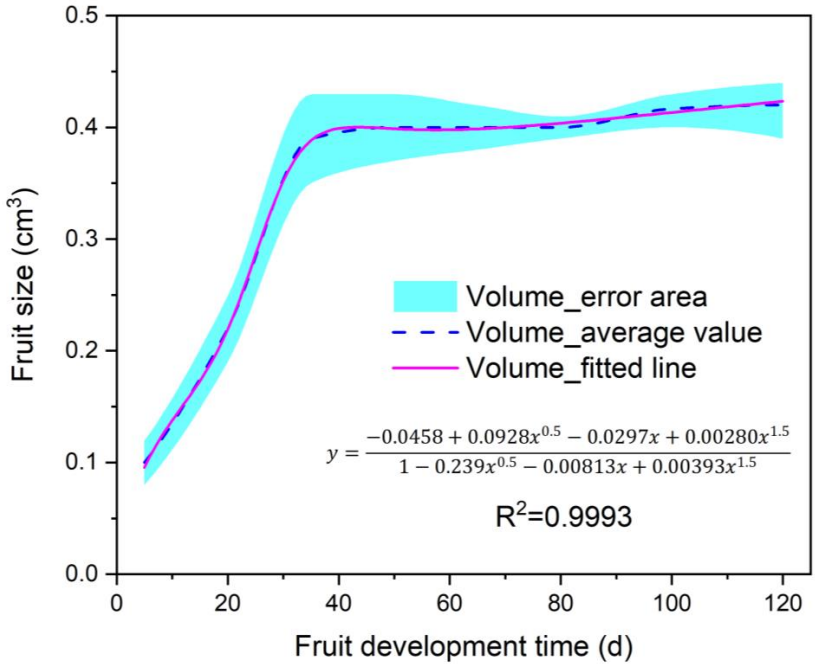


Figure 1. Changes in fruit size during fruit development process.

The fruit moisture content (MC) displayed a downward trend during fruit development (Figure 2), decreasing from 72.21% at 5 DAF to 13.98% at 120 DAF. There were two significant rapid water-loss stages: in the first stage from 5 DAF to 20 DAF, the MC dropped from 72.20% to 47.49%, and in the other stage from 50 DAF to 65 DAF, the MC dropped from 38.05% to 19.9%. On the other hand, the respiration rate of fruits basically had the same changes as the moisture content of fruits. Early in fruit

development (before 20 DAF), the respiration rate of fruits began to fall sharply from $38.72 \pm 1.02 \mu moL \cdot g^{-1} \cdot min^{-1}$ at 5 DAF to $13.46 \pm 0.63 \mu moL \cdot g^{-1} \cdot min^{-1}$ at 20 DAF. It gradually declined to $7.01 \pm 0.99 \mu moL \cdot g^{-1} \cdot min^{-1}$ at 65 DAF. After that, the fruit respiration rate remained basically unchanged until the fruit was fully mature (Figure 2).

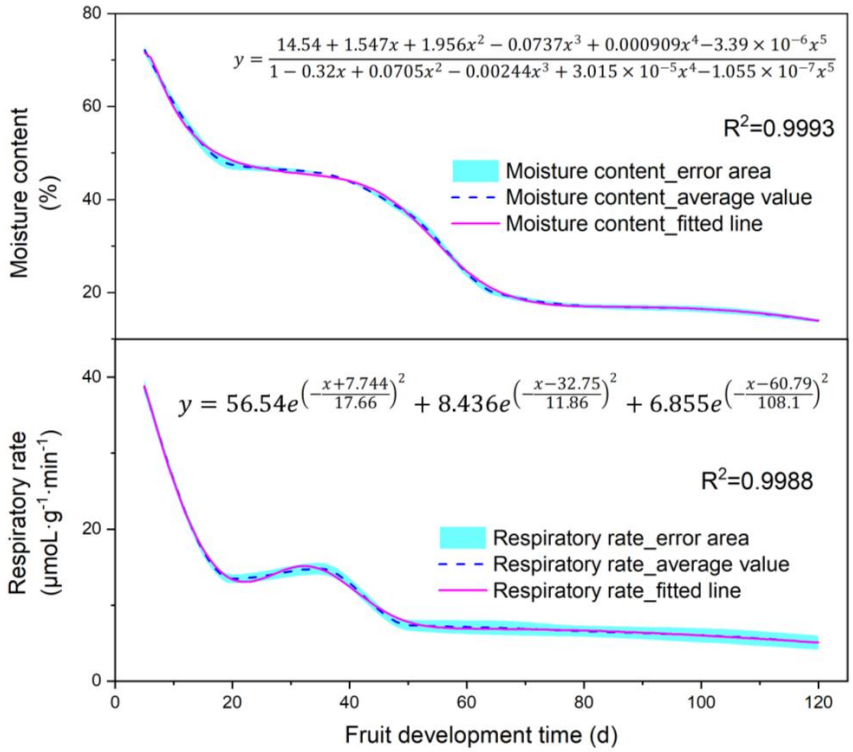


Figure 2. Changes in moisture content and respiratory rate during fruit development process.

The embryo began to substantially grow at 35 DAF. The average length of the immature embryo was 0.28 cm at 50 DAF (Figure 3), and its germination percentage was $23 \pm 0.02\%$ (Figure 4). At 65 DAF, the embryo was fully developed and reached 0.51 cm long. At this time, $97 \pm 0.01\%$ of isolated embryos were able to germinate. This result indicates that between 35 DAF and 65 DAF was the key period of embryo development. In only 30 days, the embryo had completed physiological maturation.

3.1.2. Changes in Fruit Structure and Embryo Morphology

During *T. miqueiana* fruit development, the morphological and anatomical structure of the fruit changed significantly (Figure 5). At 5 DAF, 10 seeds in each fruit arranged in two layers in a total of five chambers were clearly visible.

Young seeds containing a liquid substance were white and transparent and covered with a layer of a young seed coat. At 9 DAF or 12 DAF, the number of seeds in the fruit gradually decreased. At 20 DAF, the percentage of fruits with one seed decreased by up to 30%. This indicates that seed abortion in *T. miqueiana* mainly occurred from 9 DAF to 20 DAF. At 35 DAF, the fruit turned yellowish brown in colour. The mesocarp became a cork layer and was difficult to remove by hand. The seeds were enlarged with a white coat containing liquid substances. At 50 DAF, the pericarp was highly lignified and hard. The thickness of the seed coat became thinner, and the contents were pulpy. Young green embryos appeared. At 65 DAF, there were no further significant changes in fruit morphology, but endosperms became milky yellow, bulky, and solid. At 80 DAF, the fruit was completely mature and nut-like. The pericarp was highly lignified, the seed coat was black and thin, and the endosperm was milky white.

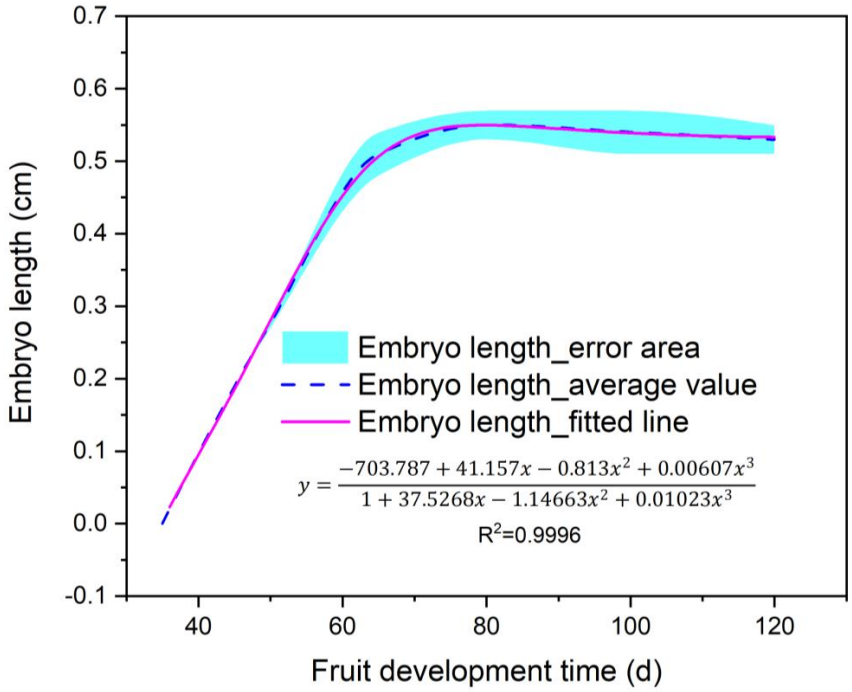


Figure 3. Changes in embryo length during fruit development process.

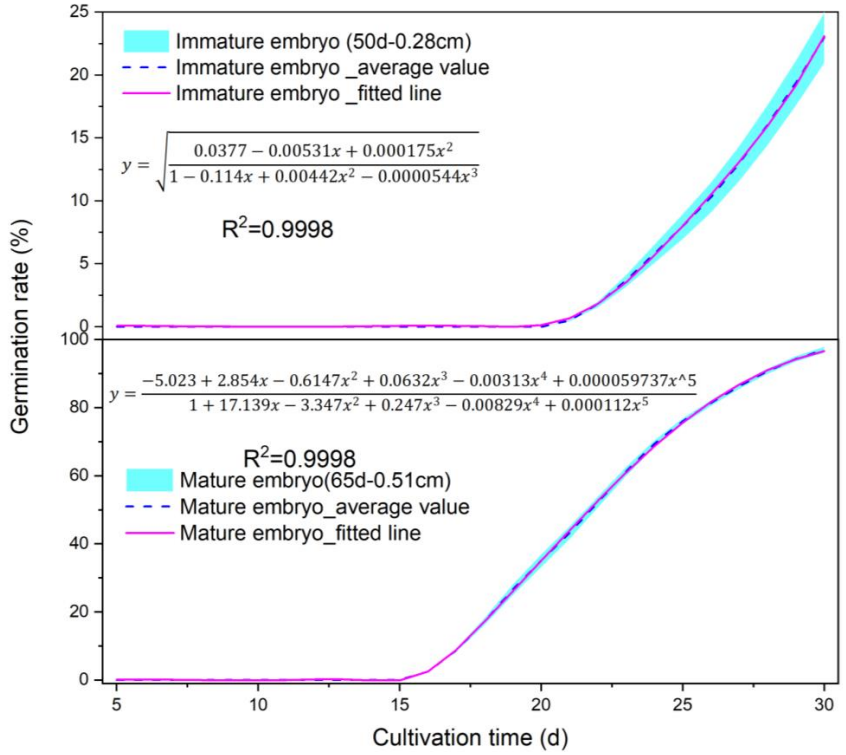


Figure 4. Germination of immature and mature embryos during cultivation time.

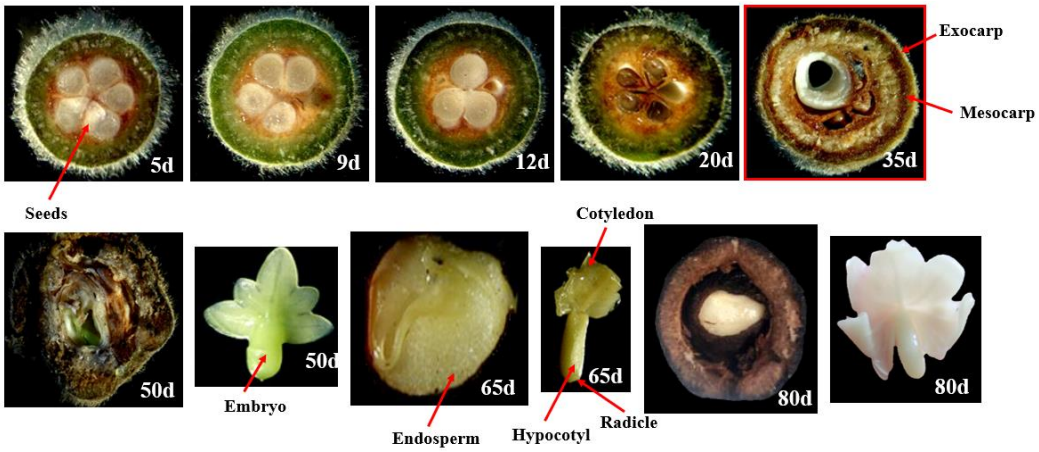


Figure 5. Cross-section of the fruit and embryo at 5 DAF, 9 DAF, 12 DAF, 20 DAF, 35 DAF, 50 DAF, 65 DAF, and 80 DAF.

3.2. Changes in the Morphology of Substances Contained in Endosperm Cells

The endosperm cells were composed of lipid droplets, a dense substance (covered with small cavities), and white vacuoles at 35 DAF and 50 DAF (Figure 6). At 65 DAF and 80 DAF, the number of lipid droplets increased markedly. Additionally, the pores on the dense substance became larger, and the white vacuoles disappeared completely. At 100 DAF and 120 DAF, the cells were densely covered with lipid droplets. Starch granules became larger, and the colour and size of the dense substance were considerably different.

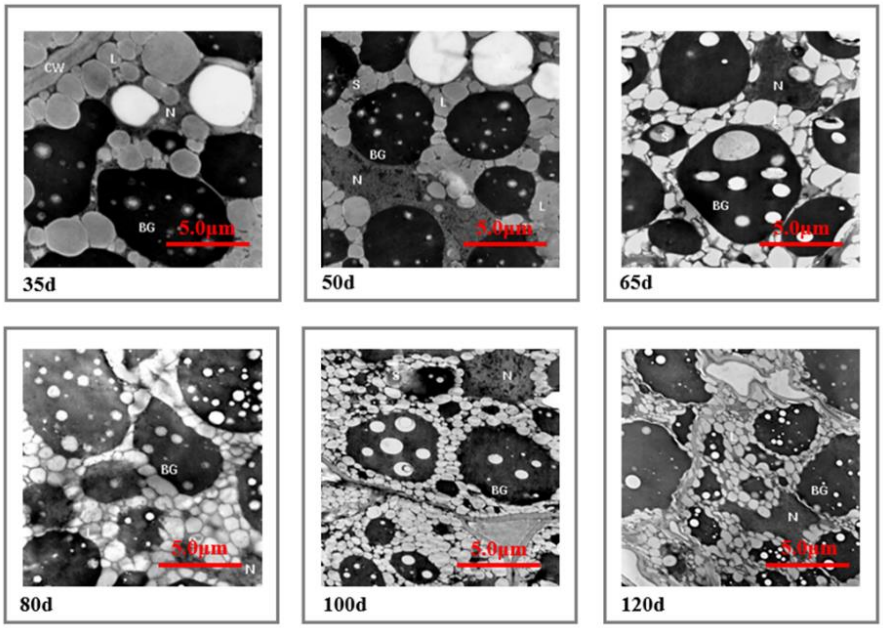


Figure 6. Morphological changes in the contents of endosperm cells. CW—cell wall; BG—dense substance; L—lipid droplet; N—cell nucleus; S—starch granule.

3.3. Changes in Contents of Sugar, Starch, Protein, and Fat in Endosperm

Especially early in fruit (seed) development, sugar showed a sharp upward trend and reached 66.3 mg·g^{-1} at 35 DAF (Figure 7). Then, it gradually decreased to 30.2 mg·g^{-1} at 80 DAF, during which much sugar was consumed for fast embryo growth. However, when the embryo was fully developed, the sugar remained at a relatively stable level. This indicates that in early seed development, sugars participated in the synthesis of storage substances, and their content increased. Shortly after, small-molecule sugars transformed into macromolecular substances, and their content decreased. Before 35 DAF, the contents

of starch, protein, and fat gradually rose. After that, starch and fat did not significantly change. However, based on fruit (seed) development, the protein slightly decreased when the embryo started to grow. It was presumed that during the development of the embryo, the degradation of the produced proteins provided materials for building the embryo structure. Thereafter, the protein, as seed storage material, began to increase to 32.42 mg·g^{-1} at 80 DAF. The fat content increased rapidly, but it markedly decreased to 13.2 mg·g^{-1} with embryo development. Afterwards, it increased slowly from 0 mg·g^{-1} to 202.6 mg·g^{-1} (at 120 DAF). Both of them increased slowly in the early stage (before 35 DAF) and then rapidly in the later stage (from 35 DAF to 120 DAF).

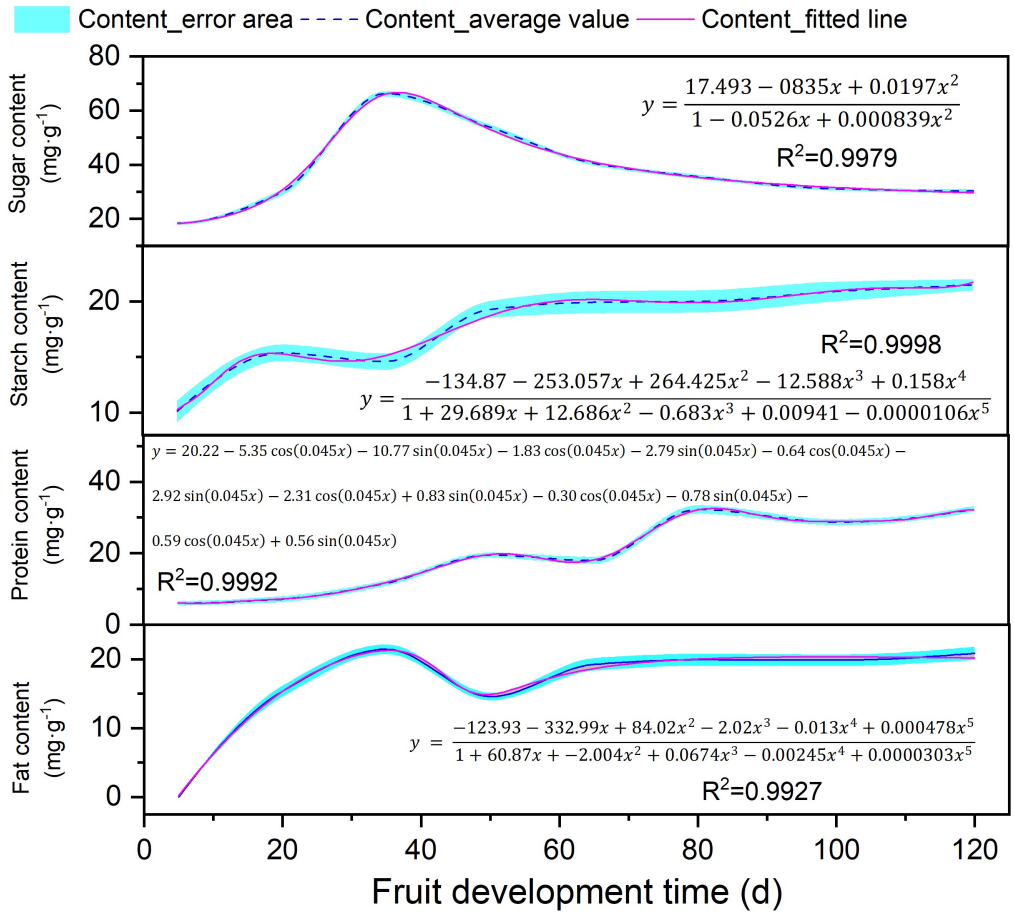


Figure 7. Changes in sugar, starch, protein, and fat contents during fruit development.

3.4. Changes in Levels of IAA, ZR, GA$_3$, and ABA in Endosperm

IAA, ZR, GA$_3$, and ABA are the most important during plant development, including fruit (seed) development. Changes in the contents of endogenous IAA, ZR, GA$_3$, and ABA are shown in Figure 8. At the beginning of fruit (seed) development, the contents of ABA in the endosperm were over 120 ng.g^{-1}FW, and the contents of IAA in the endosperm were over 65 ng·g^{-1}·FW. They were significantly higher than those of ZR and GA$_3$. Early in fruit (seed) development, each of them increased to different degrees, especially ABA and IAA. IBA increased from 124.17 ng·g^{-1}·FW to 133.14 ng·g^{-1}·FW, and IAA rose from 69.95 ng·g^{-1}·FW to the maximum value of 112.05 ng·g^{-1}·FW. However, GA$_3$ and ZR only slightly increased. During embryo development, the ABA level declined until the embryo was physiologically mature at 65 ADF, but GA$_3$ rose steadily from 15.23 ± 0.81 ng·g^{-1}·FW to 19.06 ± 0.95 ng·g^{-1}·FW. Furthermore, the ABA level was low and the GA level was high, promoting the rapid growth of the embryo. In addition, ZR and IAA levels had the same changes during embryo growth. For example, during the first half of embryo development, they kept declining, after which they rose until the embryo was well developed.

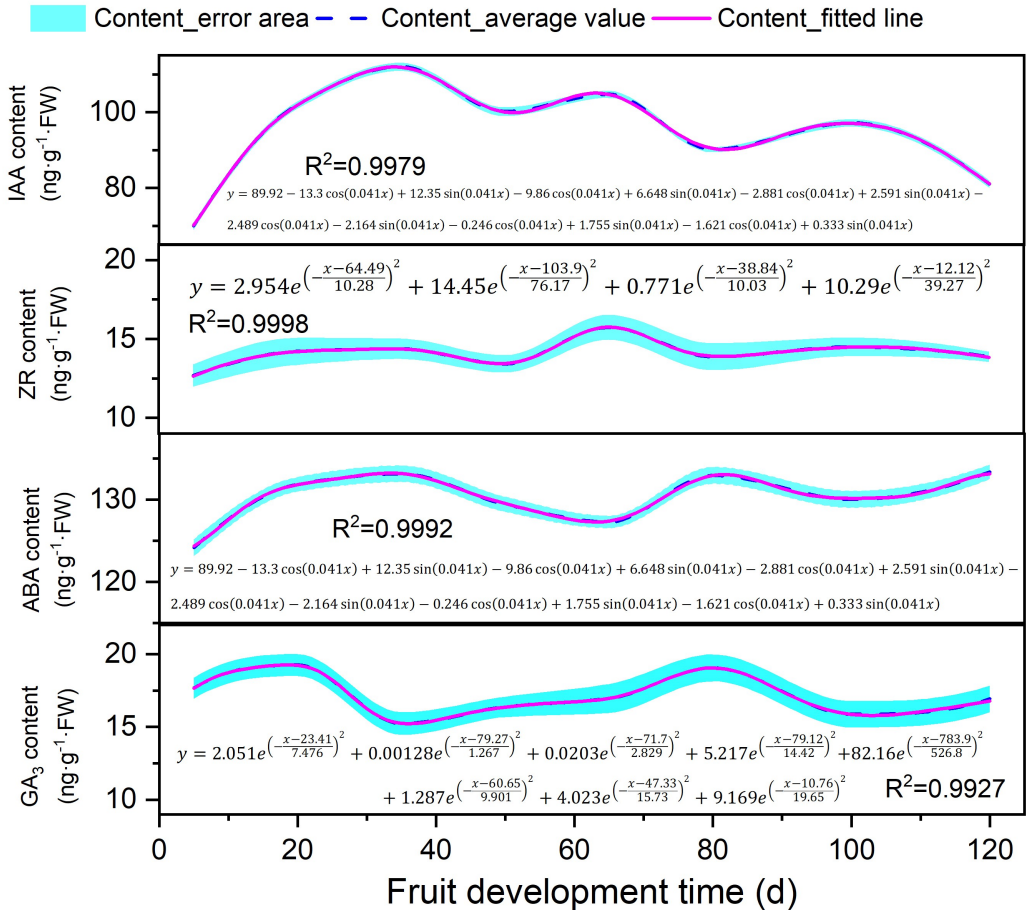


Figure 8. Changes in IAA, ZR, GA_3, and ABA contents of endosperm during fruit (seed) development.

4. Discussion

Seeds are composed of three main compartments, the embryo, endosperm, and seed coat, which originate from different cells of the ovule and have different maternal and paternal genome complements [22]. This study focused on the embryo and endosperm of the *T. miqueiana* seed. The aim was to achieve a better understanding of the mechanisms behind the low full-seed percentage of *T. miqueiana* by researching changes in biological characteristics, endosperm cell morphology, endosperm contents (sugar, starch, protein, and fat), and endogenous hormones (indole-3-acetic acid (IAA), gibberellic acid (GA_3), zeatin riboside (ZR), and abscisic acid (ABA)) during the fruit (seed) development phase. The most striking result is the progressive and drastic changes in fruit (seed) biological characteristics based on the study of the fruit (seed) different development phase.

4.1. Biological Characteristics of Fruit Development

During the fruit development process, dehydration was extensive, as the MC dropped from 72.2% (5 DAF) to 13.98% (120 DAF). At first, each fruit consisted of 10 seeds clearly arranged in two layers in a total of five chambers; unfortunately, only 30% of the fruits had one seed after 15 days, and the rest of the seeds became hollow kernels. There was significant abortion of *T. miqueiana* seeds before the morphological development of the embryo. Different plants have different phases of embryonic developmental arrest. Yang et al. [23] found that the number of aborted *Sorbus pohuashanesis* seeds significantly differed among different fruit (seed) developmental stages, with a higher abortion rate in the early stage compared to the later stage. According to embryo development in *T. miqueiana*, three phases could be determined: (a) pre-embryo development (35 days); (b) embryo development (30 days); (c) post-embryo development until ready for dispersal (over 60 days).

4.2. Changes in Cell Morphology in Endosperm

A build-up of nutrient reserves occurs in the later half of embryo maturation [24]. The number of lipid droplets increased, white vacuoles disappeared, and dense substances with different colours and sizes increased. This indicates that nutrients in the endosperm cells are constantly accumulating, which determines the size and quality of the seeds [25].

4.3. Changes in Endosperm Contents (Sugar, Starch, Protein, and Fat)

The contents of starch, protein, and fat all increased during the development process. This is consistent with observations for *Festuca arundinacea*, *Momordica charantia* L., and *Ginkgo biloba* L. seeds [26–28]. The sugar content increased during the early phase of development and decreased during the late stage. It is speculated that sugars are transformed into starch, protein, and fat, the contents of which play important roles in seed viability [29]. Insufficient starch accumulation results in low corn seed viability [30]. The integrity of the protein synthesis system is related to seed viability [31].

4.4. Changes in Endogenous Hormone Levels (IAA, ZR, GA_3, and ABA)

The plant hormone auxin is closely related to many aspects of plant development, including seed formation. Among the currently known higher plants, the most important auxin is IAA, which is initially biosynthesised from tryptophan [32]. Meanwhile, auxin levels have been linked to seed growth and development in many plant species. In *arabidopsis thaliana*, seed endosperm cell proliferation was positively correlated with increased auxin signalling, which was confirmed by auxin R2D2 sensor measurements [33]. In corn, the use of the DR5 auxin report gene [34] in the early stages of endosperm development detected the activity of auxin, which is associated with the accumulation of IAA in the maize endosperm; similar results were also observed in rice seeds. The IAA content is higher in the early stage and gradually decreases in the late stage of seed development [35,36]. This is consistent with the upward-downward trend of IAA during seed development in *T. miqueiana*.

Zein (Z) and ZR are the main active cytokinins in plants. Surface analyses in related studies showed that there were very high levels of Z and ZR in maize, rice, wheat, and barley grains [37]. Lulsdorf et al. [38] found that the cytokinin content peaked very early, at 4 days after anthesis, in *Cicer arietinum* and *Caryocolum anatolicum*, when the zygote was just developing into a spherical embryo and the cells were dividing rapidly. By day 8 after anthesis, the concentrations of these hormones were reduced, and by day 12, very little trans-ZR was present, except for trans-ZR in *C. anatolicum*. This is consistent with the upward-downward trend of ZR during seed development in *T. miqueiana*. Emery [39] correlated the predominance of ZR with pod abscission in white lupine. In legume species, flower and pod abortion is common, including in chickpea.

ABA is an important component of plant hormones and plays an important role in many stages of the plant life cycle, including seed development [40]. ABA regulates the accumulation of storage substances in seeds and their tolerance to dry conditions [41]. The ABA content in most seeds exhibits an upward trend during the early stage of embryo maturation and a downward trend during the later stage [42]. Embryo development in *T. miqueiana* was basically completed between days 35 and 65. The content of ABA exhibited an upward-downward trend from days 0 to 65. This is consistent with the trends in ABA content during embryonic development in *Pinus koraiensis* and *Rosa hybrida* [43,44]. An increase in ABA content is the basic characteristic of seed maturation [45]. The maturation of apple and *Rosa roxburghii* seeds is accompanied by an increase in ABA content [46,47]. This is consistent with observations for *T. miqueiana* seeds. High levels of ABA may promote seed dormancy during the mature period [48], which may be an important cause of *T. miqueiana* seed dormancy.

GAs indirectly promote seed development by promoting the synthesis of auxin [49]. The GA content during seed development in Korean pine is always low, exhibiting an upward-downward trend. It is speculated that the effect of GAs is not significant [44].

Accordingly, the role of GAs in *Picea glauca* seed development was not obvious [50]. The GA_3 content during *T. miqueiana* seed development did not change significantly, exhibiting a fluctuating upward-downward trend. It is speculated that GA_3 has no significant effect on seed development.

5. Conclusions

Changes in the biological characteristics, endosperm cell morphology, endosperm contents (sugar, starch protein, and fat), and endogenous hormones (IAA, GA_3, ZR, and ABA) of *T. miqueiana* seeds during their development process were studied, from which the mechanism of seed development was revealed. During seed development, the fruit size expanded from the 5th day to the 65th day. Fruit MC exhibited a downward trend along with the same changes in fruit respiration intensity. Embryos were fully developed between 35 DAF and 65 DAF. Nutrients continuously accumulated in the endosperm. Endosperm starch, protein, and fat exhibited an upward trend, whereas sugar exhibited a downward trend. The contents of the endogenous hormones ABA and IAA were significantly higher than those of GA_3 and ZR. The ABA content exhibited an overall upward trend, whereas IAA exhibited an overall downward trend. Overall changes in GA_3 and ZR contents were not pronounced. To sum up, the first 10 days of October, when the seeds are fully developed, is the best time to harvest *T. miqueiana*. The growth environment has a significant impact on the development of *T. miqueiana*, and the nutritional conditions are also essential for seed development.

Author Contributions: Conceptualisation, Y.S.; formal analysis, C.P.; investigation, Y.W.; methodology, X.Y.; project administration, Y.S.; resources, Y.W.; supervision, Y.S.; writing—original draft, Y.W.; writing—review and editing, C.P. All authors have read and agreed to the published version of the manuscript.

Funding: This work was supported by two projects. The project "Innovation and popularization of forest technology in Jiangsu Province, Long-term scientific research base for the in vitro conservation of ray native tree germplasm resources in Jiangsu Province: LYKJ [2001] 03" provided funds for most of the experimental costs. The projects "Priority Academic Program Development of Jiangsu Higher Education Institutions (PAPD)" and "Jiangsu Provincial Education Department, Jiangsu Postgraduate Training Innovation Project, KYCX20_0873" provided funds for the rest of the experimental costs.

Data Availability Statement: All data generated or analysed during this research are included in this published article.

Acknowledgments: We would like to thank the College of Forestry, Nanjing Forestry University, and Co-innovation Center for Sustainable Forestry in Southern China, Southern Tree Inspection Center National Forestry Administration.

Conflicts of Interest: The authors declare no conflict of interest.

References

1. Grundy, A.; Fenner, M. *Seeds: The Ecology of Regeneration in Plant Communities*, 2nd ed.; Centre for Agriculture and Bioscience International: Wallingford, UK, 2002.
2. Feng, J.; Shen, Y.; Shi, F.; Li, C. Embryo development, seed germination, and the kind of dormancy of *Ginkgo biloba* L. *Forests* **2018**, *9*, 700. [CrossRef]
3. Borisjuk, L.; Rolletschek, H.; Radchuk, R.; Weschke, W.; Wobus, U.; Weber, H. Seed development and differentiation: A role for metabolic regulation. *Plant Biol.* **2004**, *6*, 375–386. [CrossRef] [PubMed]
4. Norton, G.; Harris, J. Compositional changes in developing rape seed (*Brassica napus* L.). *Planta* **1975**, *123*, 163–174. [CrossRef] [PubMed]
5. Vigeolas, H.; van Dongen, J.T.; Waldeck, P.; Huhn, D.; Geigenberger, P. Lipid storage metabolism is limited by the prevailing low oxygen concentrations within developing seeds of oilseed rape. *Plant Physiol.* **2003**, *133*, 2048–2060. [CrossRef] [PubMed]
6. Liu, M.; Ma, Z.; Zheng, T.; Sun, W.; Zhang, Y.; Jin, W.; Zhan, J.; Cai, Y.; Tang, Y.; Wu, Q. Insights into the correlation between physiological changes in and seed development of tartary buckwheat (*Fagopyrum tataricum* Gaertn.). *BMC Genom.* **2018**, *19*, 648. [CrossRef]
7. Smit, M.E.; Weijers, D. The role of auxin signaling in early embryo pattern formation. *Curr. Opin. Plant Biol.* **2015**, *28*, 99–105. [CrossRef]

8. Bewley, J.D.; Black, M.; Halmer, P. *The Encyclopedia of Seeds: Science, Technology and Uses*; CABI: Wallingford, UK, 2006.
9. Kucera, B.; Cohn, M.A.; Leubner-Metzger, G. Plant hormone interactions during seed dormancy release and germination. *Seed Sci. Res.* **2005**, *15*, 281–307. [CrossRef]
10. Shibata, M.; Coelho, C.M.; de Garighan, J.A.; dos Santos, H.P.; Araldi, C.G.; Maraschin, M. Seed development of *Araucaria angustifolia*: Plant hormones and germinability in 2 years of seeds production. *New For.* **2021**, *52*, 759–775. [CrossRef]
11. Matsuura, T.; Mori, I.C.; Himi, E.; Hirayama, T. Plant hormone profiling in developing seeds of common wheat (*Triticum aestivum* L.). *Breed. Sci.* **2019**, *69*, 601–610. [CrossRef]
12. Ellis, R.; Pieta Filho, C. The development of seed quality in spring and winter cultivars of barley and wheat. *Seed Sci. Res.* **1992**, *2*, 9–15. [CrossRef]
13. Gao, F.; Shen, Y.B. Sporogenesis and development of male and female gametophytes in *Tilia miqueiana*. *J. For. Eng.* **2010**, *24*, 22–25.
14. Shi, F.H.; Zhu, C.C.; Shen, Y.B.; Shi, J.S. Germination and dormancy of *Tilia miqueiana* seeds. *J. Fujian Coll. For.* **2008**, *2008*, 48–51.
15. Tong, L.L.; Tang, G.G.; Xu, X.G. A Community Structure Analysis on *Tilia miqueliana* Maxim. Forest in Nanjing Mt.Niushou. *J. Nanjing For. Univ.* **2006**, *30*, 42–46.
16. International Seed Testing Association. *International Rules for Seed Testing*; International Seed Testing Association: Zurich, Switzerland, 1983.
17. DuBois, M.; Gilles, K.A.; Hamilton, J.K.; Rebers, P.t.; Smith, F. Colorimetric method for determination of sugars and related substances. *Anal. Chem.* **1956**, *28*, 350–356. [CrossRef]
18. Bradford, M.M. A rapid and sensitive method for the quantitation of microgram quantities of protein utilizing the principle of protein-dye binding. *Anal. Biochem.* **1976**, *72*, 248–254. [CrossRef] [PubMed]
19. De Castro, M.L.; Priego-Capote, F. Soxhlet extraction: Past and present panacea. *J. Chromatogr. A* **2010**, *1217*, 2383–2389. [CrossRef]
20. Zhao, J.; Li, G.; Yi, G.-X.; Wang, B.-M.; Deng, A.-X.; Nan, T.-G.; Li, Z.-H.; Li, Q.X. Comparison between conventional indirect competitive enzyme-linked immunosorbent assay (icELISA) and simplified icELISA for small molecules. *Anal. Chim. Acta* **2006**, *571*, 79–85. [CrossRef]
21. Wang, Y.; Li, B.; Du, M.; Eneji, A.E.; Wang, B.; Duan, L.; Li, Z.; Tian, X. Mechanism of phytohormone involvement in feedback regulation of cotton leaf senescence induced by potassium deficiency. *J. Exp. Bot.* **2012**, *63*, 5887–5901. [CrossRef]
22. Ohto, M.-A.; Stone, S.L.; Harada, J.J.; Bradford, K.; Nonogaki, H. Genetic control of seed development and seed mass. In *Seed Development, Dormancy, and Germination*; Blackwell Publishing: Oxford, UK, 2008; pp. 1–24.
23. Yang, L.; Li, Y.H.; Shen, H.L. Factors Influencing Seed Germination of *Sorbus pohuashanensis* Hedl. *Adv. Mater. Res.* **2011**, *393–395*, 758–761. [CrossRef]
24. Rock, C.D.; Quatrano, R.S. The role of hormones during seed development. *Plant Horm. Physiol. Biochem. Mol. Biol.* **1995**, 671–697. [CrossRef]
25. Zhang, X.; Jiang, W.; Pang, Y. Advances in the regulation mechanism of plant seed size. *Plant. Physiol. J.* **2016**, 998–1010.
26. Chunhui, M.; Jun, C.; Jianguo, H.; Jianxin, C.; Zhongliang, Y.; Yumin, D. Study on the dynamic changes of physiology and biochemistry during the seed development of tall fescue in Xinjiang. *Acta Prataculturae Sin.* **2002**, *11*, 76–80.
27. Lu, X.Q.; Pan, Y.; Lu, Y.; Wang, L. Study on the rule of nutrient accumulation during the development of endosperm in *Ginkgo biloba* L. *J. Anhui Agric. Sci.* **2009**, *37*, 2475–2476.
28. Zhang, M.; Huang, R.; Sun, D.; Luo, H. Changes in content of nutritional components and vigor of seed during fruit development of bitter gourd. *Guangxi Zhiwu/Guihaia* **2009**, *29*, 250–253.
29. Wang, S.; Shen, Y.; Bao, H. Morphological, physiological and biochemical changes in *Magnolia zenii* Cheng seed during development. *Physiol. Plant.* **2021**, *172*, 2129–2141. [CrossRef] [PubMed]
30. Cui, H.; Cheng, Z.; Li, P.; Miao, A. Prediction of sweet corn seed germination based on hyperspectral image technology and multivariate data regression. *Sensors* **2020**, *20*, 4744. [CrossRef] [PubMed]
31. Abdul-Baki, A.A. Biochemical aspects of seed vigor. *HortScience* **1980**, *15*, 765–771. [CrossRef]
32. Figueiredo, D.D.; Köhler, C. Auxin: A molecular trigger of seed development. *Genes Dev.* **2018**, *32*, 479–490. [CrossRef]
33. Liao, C.-Y.; Smet, W.; Brunoud, G.; Yoshida, S.; Vernoux, T.; Weijers, D. Reporters for sensitive and quantitative measurement of auxin response. *Nat. Methods* **2015**, *12*, 207–210. [CrossRef]
34. Chen, J.; Lausser, A.; Dresselhaus, T. Hormonal responses during early embryogenesis in maize. *Biochem. Soc. Trans.* **2014**, *42*, 325–331. [CrossRef]
35. Chourey, P.S.; Li, Q.-B.; Kumar, D. Sugar–hormone cross-talk in seed development: Two redundant pathways of IAA biosynthesis are regulated differentially in the invertase-deficient miniature1 (mn1) seed mutant in maize. *Mol. Plant* **2010**, *3*, 1026–1036. [CrossRef] [PubMed]
36. Abu-Zaitoon, Y.M.; Bennett, K.; Normanly, J.; Nonhebel, H.M. A large increase in IAA during development of rice grains correlates with the expression of tryptophan aminotransferase OsTAR1 and a grain-specific YUCCA. *Physiol. Plant.* **2012**, *146*, 487–499. [CrossRef] [PubMed]
37. Letham, D.; Palni, L. The biosynthesis and metabolism of cytokinins. *Annu. Rev. Plant Physiol.* **1983**, *34*, 163–197. [CrossRef]
38. Lulsdorf, M.M.; Yuan, H.Y.; Slater, S.M.; Vandenberg, A.; Han, X.; Zaharia, L.I.; Abrams, S.R. Endogenous hormone profiles during early seed development of *C. arietinum* and *C. anatolicum*. *Plant Growth Regul.* **2013**, *71*, 191–198. [CrossRef]
39. Emery, R. The forms and sources of cytokinins in developing *Lupinus albus* seeds and fruits. *Plant Physiol.* **2000**, *123*, 1–12. [CrossRef]

40. Seo, M.; Koshiba, T. Complex regulation of ABA biosynthesis in plants. *Trends Plant Sci.* **2002**, *7*, 41–48. [CrossRef]
41. Nonogaki, H. ABA responses during seed development and germination. In *Advances in Botanical Research*; Elsevier: Amsterdam, The Netherlands, 2019; Volume 92, pp. 171–217.
42. Silveira, V.; Balbuena, T.S.; Santa-Catarina, C.; Floh, E.I.; Guerra, M.P.; Handro, W. Biochemical changes during seed development in *Pinus taeda* L. *Plant Growth Regul.* **2004**, *44*, 147–156. [CrossRef]
43. Bosco, R.; Caser, M.; Ghione, G.G.; Mansuino, A.; Giovannini, A.; Scariot, V. Dynamics of abscisic acid and indole-3-acetic acid during the early-middle stage of seed development in *Rosa hybrida*. *Plant Growth Regul.* **2015**, *75*, 265–270. [CrossRef]
44. Liang, Y.; Shen, H.L. Content dynamics of endogenous hormones in different seed developmental stages of Korean Pine. *Sci. Silvae Sin.* **2016**, *52*, 105–111.
45. Shi, T.T.; Chen, W.T. Changes of endogenous hormone content during the growth and development of *Ginkgo biloba* seeds. *Seed Sci. Technol.* **2007**, *2007*, 39–42. (In Chinese)
46. Zou, Y.J.; Wang, Y.X. Research progress in the regulation of endogenous hormones on apple fruit growth and development. *Shaanxi Agric. Sci.* **2002**, *10*, 13–15.
47. Fan, W.G.; An, H.M.; Liu, G.Q.; He, S.T.; Liu, J.P. Changes of endogenous hormones contents in fruit, seeds and their effects on the fruit development of *Rosa roxburghii*. *Sci. Agric. Sin.* **2004**, *37*, 728–733.
48. Yan, X.; Tian, M.; Liu, F.; Wang, C.; Zhang, Y. Hormonal and morphological changes during seed development of *Cypripedium japonicum*. *Protoplasma* **2017**, *254*, 2315–2322. [CrossRef] [PubMed]
49. Rademacher, W. Growth retardants: Effects on gibberellin biosynthesis and other metabolic pathways. *Annu. Rev. Plant Biol.* **2000**, *51*, 501–531. [CrossRef] [PubMed]
50. Pullman, G.S.; Bucalo, K. Pine somatic embryogenesis: Analyses of seed tissue and medium to improve protocol development. *New For.* **2014**, *45*, 353–377. [CrossRef]

Disclaimer/Publisher's Note: The statements, opinions and data contained in all publications are solely those of the individual author(s) and contributor(s) and not of MDPI and/or the editor(s). MDPI and/or the editor(s) disclaim responsibility for any injury to people or property resulting from any ideas, methods, instructions or products referred to in the content.

forests

MDPI

Article

Detection of Moisture Content of *Pinus massoniana* Lamb. Seedling Leaf Based on NIR Spectroscopy with a Multi-Learner Model

Yurong Li †, Haifei Xia †, Ying Liu *, Lintao Huo, Chao Ni and Binli Gou

Jiangsu Co-Innovation Center of Efficient Processing and Utilization of Forest Resources, College of Mechanical and Electronic Engineering, Nanjing Forestry University, Nanjing 210037, China
* Correspondence: liuying@njfu.edu.cn
† These authors contributed equally to this work.

Abstract: The growth quality of *Pinus massoniana* (Lamb.) seedlings is closely related to the survival rate of afforestation. Moisture content detection is an important indicator in the cultivation of forest seedlings because it can directly reflect the adaptability and growth potential of the seedlings to the soil environment. To improve the accuracy of quantitative analysis of moisture content in *P. massoniana* seedlings using near-infrared spectroscopy, a total of 100 *P. massoniana* seedlings were collected, and their near-infrared diffuse reflectance spectra were measured in the range of 2500 to 800 nm (12,000 to 4000 cm^{-1}). An integrated learning framework was introduced, and a quantitative detection model for moisture content in *P. massoniana* seedlings was established by combining preprocessing and feature wavelength selection methods in chemometrics. Our results showed that the information carried by the spectra after multiple scattering correction (MSC) preprocessing had a good response to the target attribute. The stacking learning model based on the full-band spectrum had a prediction coefficient of determination R^2 of 0.8819, and the prediction accuracy of moisture content in *P. massoniana* seedlings could be significantly improved compared to the single model. After variable selection, the spectrum processed by MSC and feature selection with uninformative variable elimination (UVE) showed good prediction effects in all models. Additionally, the prediction coefficient of determination R^2 of the support vector regression (SVR)—adaptive boosting (AdaBoost)—partial least squares regression (PLSR) + AdaBoost model reached 0.9430. This indicates that the quantitative analysis model of moisture content in *P. massoniana* seedlings established through preprocessing, feature selection, and stacking learning models can achieve high accuracy in predicting moisture content in *P. massoniana* seedlings. This model can provide a feasible technical reference for the precision cultivation of *P. massoniana* seedlings.

Keywords: NIR spectroscopy; *Pinus massoniana* seedlings; non-destructive detection; multi-learner model

check for updates

Citation: Li, Y.; Xia, H.; Liu, Y.; Huo, L.; Ni, C.; Gou, B. Detection of Moisture Content of *Pinus massoniana* Lamb. Seedling Leaf Based on NIR Spectroscopy with a Multi-Learner Model. *Forests* **2023**, *14*, 883. https://doi.org/10.3390/f14050883

Academic Editor: Laurie Schimleck

Received: 2 March 2023
Revised: 19 April 2023
Accepted: 23 April 2023
Published: 25 April 2023

Copyright: © 2023 by the authors. Licensee MDPI, Basel, Switzerland. This article is an open access article distributed under the terms and conditions of the Creative Commons Attribution (CC BY) license (https://creativecommons.org/licenses/by/4.0/).

1. Introduction

Pinus massoniana (Lamb.) is highly adaptable and widely distributed, with a horizontal distribution spanning about 20° longitude and 12° latitude. It is a major afforestation species with high economic value in southern China [1,2]. The use of advanced technical tools for monitoring and quantitatively analyzing dynamic phenotypic changes in seedlings is crucial for achieving rapid and accurate evaluation of seedling vigor. This is particularly important for the cultivation of intensive industrial timber forests and the improvement of precise forestry management in China [3].

The moisture content of seedling leaves is an important indicator of vitality and plays an important role in photosynthesis, material transport, and the maintenance of physiological functions [4]. To improve the survival rate of *P. massoniana* plantations, leaf moisture content should be detected before seedling transplanting. Commonly used methods for

moisture content testing include the constant weight method, vacuum drying method, fixed temperature and time drying, and other chemical methods, etc. The mentioned testing methods are more accurate; however, they are cumbersome, have a long cycle time, and result in irreversible damage to seedling samples, leading to wastage of resources and not being conducive to the sustainable development of seedlings [5,6].

Near-infrared (NIR) spectroscopic imaging combines the advantages of spectroscopic and imaging techniques and is widely used as a mature non-destructive detection technique in the fields of agriculture and forestry, pharmaceuticals, food, petrochemicals, and tobacco [7–11]. There are information redundancy, noise, and background factors in the variables of spectral measurements. Extracting effective information from complex spectral data to identify component changes is a hot topic in spectral analysis research. NIR spectra (NIRS) were processed using discrete wavelet transforms (DWT), which decomposed the original spectrum into six layers of denoising. Information variables were then selected by reducing the dimensionality of sub-layer reconstruction spectra through the bootstrap soft shrinkage algorithm (BOSS), leading to the establishment of an effective non-destructive prediction model for tea moisture content [12]. Various preprocessing strategies and feature variable selection methods based on visible and near-infrared (Vis–NIR) technology, such as competitive adaptive reweighted sampling (CARS) and uninformative variable elimination (UVE), have been used to develop regression analysis models such as partial least squares regression (PLSR), support vector regression (SVR), and random forest (RF) to significantly improve the accuracy of predicting soil organic matter (SOM) content [13]. A model was established between leaf moisture content (LWC) and water index (WI) based on NIR reflectance, which provided a non-destructive and immediate measurement method for monitoring the water status of sunflower plants [14]. Moisture content detection and visualization of peanuts were achieved in the 900–1700 nm band, but only the weighted regression coefficient method was used to extract the characteristic wavelength [15]. The above studies show that NIR combined with different preprocessing, data dimension reduction, and feature extraction methods can achieve non-destructive detection of components.

Classical prediction models such as PLSR, SVR, back propagation neural network (BPNN), and RF are commonly used. However, to overcome the limitations of a single prediction model in various application scenarios, researchers have attempted to improve the accuracy and convergence speed of the model through two approaches: optimizing the core parameters of the algorithm or integrating different models. As a result, they have achieved good results [16–19]. The use of a radial basis function network (RBF) based on a self-organizing feature map (SOM) resulted in the successful prediction of key nutrient content in Lanzhou lily. This approach combined the self-organizing clustering features of SOM with the nonlinear approximation ability of RBF, leading to prediction results that were 5.6% higher than the correlation coefficient of prediction (Rp) obtained using the PLSR method [20]. Mixed linear regression and non-linear regression models, namely PLSR + general regression neural network (GRNN) and PLSR + BPNN, were used to predict the plant leaf nitrogen to phosphorus ratio (N/P). Both mixed models showed higher accuracy and stability as compared to PLSR, while also overcoming the overfitting problem of single regression models [21].

The aforementioned models can be classified into conventional regression models (PLSR, SVR), stacking learning models (RF), and neural network models (BPNN, GRNN). When dealing with high-dimensional and nonlinear spectral data, single regression models are no longer suitable due to their poor prediction performance and inability to effectively fit nonlinear or high-dimensional data. Combining multiple models and utilizing the stacking learning method can enable the mapping of data features from multiple perspectives, breaking the singularity of data domain analysis, and integrating the results of multiple learners to achieve more accurate predictions and higher robustness [22]. In this study, we utilized the NIRS data from *P. massoniana* seedlings as the primary source of information and integrated the stacking model to establish a quantitative analysis model for predicting the moisture content of *P. massoniana* seedlings. We compare and analyze our method with

the chemometric method of multiple corrections and address the issue of high-dimensional NIRS data by selecting the optimal feature variables. By comparing the prediction results, we choose a suitable system modeling method for predicting the moisture content of *P. massoniana* seedlings. This provides a new method for moisture content detection in the cultivation process of seedlings.

2. Materials and Methods

2.1. Experimental Materials

In this paper, all of the *P. massoniana* samples are obtained from Qingyuan Nursery, Yizhou District, Hechi City, Guangxi Province, China, for a total of 100 plants. These samples are all annual *P. massoniana* seedlings and the height of the seedlings ranges from 15 to 20 cm. Moreover, the selected samples are in good growth condition and are not infected with insects or diseases.

2.1.1. Spectral Data Acquisition

The diffuse reflection method is commonly used for collecting the NIR spectra of solid samples. In this method, NIR light enters the sample and undergoes several reflections, refractions, scatterings, and absorptions inside the sample. This process carries rich information about the sample's structure and tissue, and the resulting NIR signal is finally captured by the NIR spectrometer, completing the NIR spectral acquisition of the sample [23].

The spectral data of each *P. massoniana* sample were collected by a multi-purpose analyzer Fourier transform (MPA) NIR spectrometer (Figure 1a) equipped with a PbS detector in the wavelength range of 2500 to 800 nm (12,000 to 4000 cm^{-1}), with reflection mode and a spectral resolution of 4 cm^{-1}. The number of spectra per *P. massoniana* sample is 2203. The NIR optical fiber probe was aligned to the different parts of the *P. massoniana* samples to obtain the spectral data (Figure 1b). To avoid experimental errors as much as possible, the high, middle, and low areas of the *P. massoniana* seedling samples were selected for two repeated scans. We then took the average value of the data results from the six scans as the final value of the spectral data.



(**a**) (**b**) (**c**)

Figure 1. Equipment and collection process: (**a**) Bruker-MPA NIR spectrometer; (**b**) the process of spectral collection of *P. massoniana* seedlings; (**c**) HB43-S halogen moisture meter.

2.1.2. Moisture Content Determination

The moisture content of the leaves of *P. massoniana* was measured using the HB43-S halogen moisture meter (Figure 1c). This device determined the moisture contained in a sample by measuring the weight loss of the sample after heating and drying [24]. After placing the *P. massoniana* leaf samples into the sampling chamber, the temperature inside the instrument was increased to 125 °C, and the *P. massoniana* samples were heated by a halogen lamp until the sample mass no longer decreased, and then the moisture content of the samples was recorded.

2.2. Preprocessing and Feature Selection

2.2.1. Spectral Preprocessing

The raw spectral data may contain interference noise and irrelevant information generated under the influence of factors such as ambient temperature and humidity in the process of acquisition. Therefore, before model training, preprocessing operations are needed to be performed on the raw NIR spectral data to remove irrelevant noise that can interfere with the prediction results and improve the accuracy of the prediction model.

To reduce the random errors of the samples and filter out some systematic errors, five classical preprocessing methods are proposed in this experiment, including the moving window spectral matrix smoothing algorithm (Nirmaf), L2-normalize, multiple scattering correction (MSC), Savitzky–Golay smoothing (SG smoothing), and standard normal variate (SNV).

The Nirmaf preprocessing method uses a shifted average of individual sample data, thus denoising the data. The L2-normalize preprocessing method scales and pans the data so that they fall into a small, specific interval, which serves to remove the effect of data magnitude and make the data metrics comparable with each other. The L2-parametric normalization operation divides each dimension $(x_1, x_2, \ldots, x_n)$ of the spectral data X by the second parametric number $\|X\|_2$ of the vector X to obtain a new normalized vector, as shown in Equation (1):

$$X_{L2} = \left(\frac{x_1}{\sqrt{{x_1}^2 + {x_2}^2 + \ldots + {x_n}^2}}, \frac{x_2}{\sqrt{{x_1}^2 + {x_2}^2 + \ldots + {x_n}^2}}, \ldots, \frac{x_n}{\sqrt{{x_1}^2 + {x_2}^2 + \ldots + {x_n}^2}} \right) \quad (1)$$

MSC enhances the correlation between spectra and data [25]. SG smoothing has a strong filtering effect on noise points [26]. Additionally, SNV eliminates surface scattering and the effect of light range variation on diffuse reflectance spectra [27]. Considering the diversity of NIR spectral preprocessing results, MSC, SG smoothing, and SNV are also applied in this study. Spectral preprocessing operations are performed on MATLAB R2021b.

2.2.2. Feature Selection

The spectral data of *P. massoniana* seedlings contains a large number of spectral data features, including noise and a significant amount of unrelated information. Variable selection can be used to remove noise and interference variables that are unrelated to the target attribute from the spectral data. The proposed feature selection method not only reduces the number of model variables but also decreases the model's complexity, thereby improving the predictive performance and robustness of the model. Based on spectral preprocessing, we utilized five conventional methods, namely genetic algorithm (GA), successive projections algorithm (SPA), UVE, CARS, and least angle regression (LARS) [28–32], for variable selection of the spectral data. The goal was to select appropriate spectral variables to be used in the quantitative analysis of *P. massoniana* seedling moisture content. Spectral feature selection is performed on PyCharm 2022.2.

2.3. Model Selection and Optimization

The stacking integrated model is a multi-layer learning model, with the first layer being the base learner layer consisting of different regression models and the second layer being the final output meta-learner layer. The difference in the performance of the models is evident in the spectral data. Nevertheless, the stacking integrated model can further improve the model's prediction accuracy by combining the algorithmic strengths of each base learner and eliminating their respective prediction errors [33].

There are numerous ways to combine models in a stacking-integrated model. To select the appropriate learners for the stacking model, the prediction performance and correlation of every single model were compared and analyzed. Then, four candidate learners (adaptive boosting (AdaBoost), ExtraTree, PLSR, and SVR) are selected. Finally, the

optimal stacking model construction method for this study is selected by comparing different combinations. The hardware and software used in this study were as follows: operating system: Windows 10, CPU: Intel I7-11700F 2.50 GHz, GPU: Nvidia GeForce RTX 3080Ti (12 GB), and environment configuration: PyCharm+Pytorch1.8+Python 3.7.4+Cuda 12.1.

3. Results and Discussion

3.1. Sample Moisture Content Data

The experimental sample dataset in this study was divided into a training set and a test set using a division ratio of 8:2 through the sample set partitioning based on the joint X-Y distance sampling (SPXY) algorithm. This was conducted to ensure that each data set could characterize the sample distribution to the maximum extent, increase the variability and representativeness among the samples, and further improve the stability of the model. The results of leaf moisture content measurements of *P. massoniana* seedlings are shown in Figure 2.

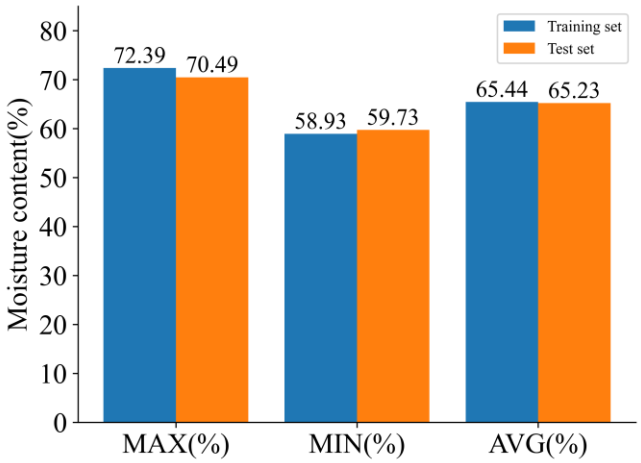


Figure 2. Statistics of the moisture content of *P. massoniana* samples. MAX (%) = the maximum value of moisture content in the training and test sets; MIN (%) = the minimum value of moisture content in the training and test sets; AVG (%) = the average value of moisture content in the training and test sets.

3.2. Raw Spectra and Spectral Preprocessing Results

The spectral data of *P. massoniana* measured by NIRS has certain noise and irrelevant information, so the raw spectral data needs to be preprocessed to eliminate them. The raw spectra and the NIR spectral curves after the five preprocessing methods of Nirmaf, L2-normalize, MSC, SG smoothing, and SNV are shown in Figure 3, in which the horizontal axis is the wavenumber (cm^{-1}) and the vertical axis is the absorbance (%). There are obvious absorbance peaks in the wavenumber 8000~4000 cm^{-1}, indicating that the use of NIR spectra to predict the moisture content of *P. massoniana* seedling samples is feasible [34,35].

As shown in Figure 3, the spectral curve becomes smoother after the preprocessing operation. To ensure the stability of the regression model and the accuracy of the prediction results, it is necessary to perform normalization on the preprocessed data and eliminate magnitude differences with the maximum–minimum normalization method. This is to avoid excessive differences in magnitude between data of different dimensions and improve the accuracy of the model.

PLSR was used to establish a prediction model for the leaf moisture content of *P. massoniana* seedlings. The coefficient of determination R^2 and root mean square error RMSE were used as the evaluation metrics of the prediction model. Furthermore, the number of potential factors of the optimal model was determined through manual tuning. The number of potential factors in the model was chosen in the range of 1 to 20. The

prediction results of the spectral data processed by each preprocessing algorithm in the PLSR model are shown in Table 1.

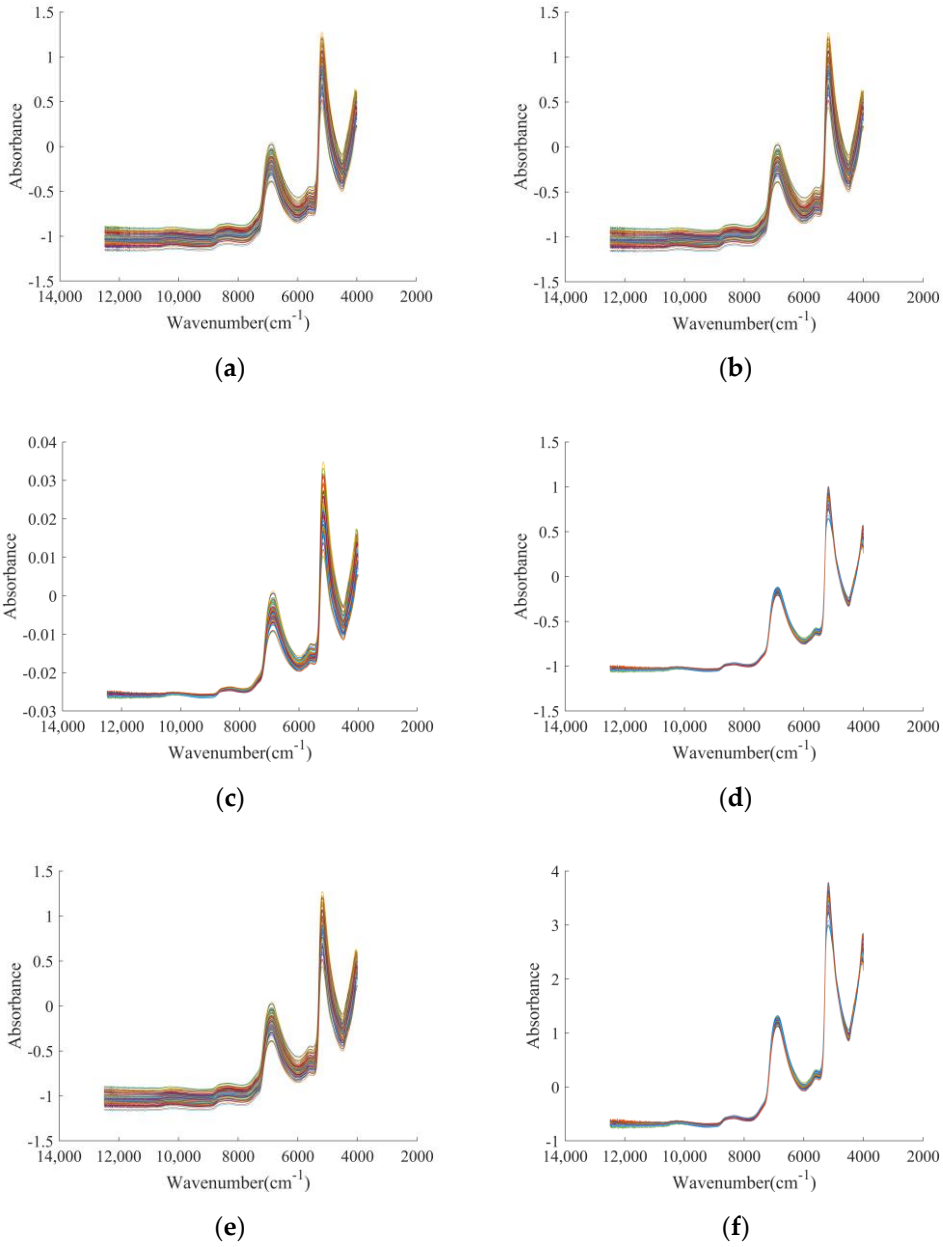


Figure 3. Spectral preprocessing effects: (**a**) raw spectrum; (**b**) Nirmaf−processed spectrum; (**c**) L2−normalize−processed spectrum; (**d**) MSC−processed spectrum; (**e**) SG smoothing−processed spectrum; and (**f**) SNV−processed spectrum.

Table 1. Comparison of PLSR-based preprocessing methods.

Preprocessing Methods	Number of Potential Factors	Training Set		Test Set	
		R^2	RMSE	R^2	RMSE
Raw data	10	0.8377	1.0040	0.7318	1.3384
Nirmaf	11	0.8447	0.9822	0.7513	1.2887
L2-normalize	10	0.9315	0.6523	0.7216	1.3637
MSC	10	0.8848	0.8458	0.8057	1.1391
SG smoothing	10	0.8150	1.0718	0.8009	1.1531
SNV	10	0.8848	0.8457	0.8011	1.1525

The coefficients of determination (R^2) of the raw spectral data and data processed by five preprocessing methods ranged from 0.7216 to 0.8057, and root mean square error (RMSE) ranged from 1.1391 to 1.3637 for the test set in the PLSR regression model. Generally, there is little difference in performance among PLSR models. The R^2 of the training and test sets of the MSC-PLSR are 0.8848 and 0.8057, respectively. The R^2 value of the training set is only 0.0467 lower than that of the L2-normalize-PLSR. Furthermore, the R^2 value of the test set improved by 0.0739 compared to the original spectrum, reaching 0.8057.

In contrast, other preprocessing methods, such as L2-normalize, reduce the original spectral modeling performance. Although this preprocessing has a higher R^2 in the training set than the other methods, it lacks robustness and does not significantly improve the model. Therefore, MSC is subsequently selected as the preprocessing method for the NIR spectra of *P. massoniana* seedlings.

3.3. Composition and Optimization of Stacking Integrated Model

The optimization of the prediction effect of the stacking integrated model depends on the selection of appropriate base learners and meta-learner, as well as the combination of different learners. In this study, the prediction performance of each single model and the Pearson correlation coefficient between each model were used to select the appropriate combination of base learner and meta-learner.

3.3.1. Selection of Base Learners

The component learners initially selected in this paper are AdaBoost, ExtraTree, RF, Ridge, PLSR, and SVR. Among them, AdaBoost and RF were improved with boosting and bagging integrated methods, respectively. Both of these models have a reasonable number of hyperparameters, and the practical application of these models does not require adjusting too many parameters. ExtraTree has a small number of key hyperparameters and reasonable heuristics for configuration parameters that can handle high-dimensional data. Ridge regression has high stability and can effectively improve the problem of model overfitting. PLSR is often used in spectral data, which can better handle data with dimensions much larger than the number of samples. The SVR algorithm is easy to implement and robust to outliers.

In integrated learning, the main challenge is how to synthesize multiple weak learners into one strong learner. In the initial selection of the base learner, two aspects need to be considered. Firstly, the learning strength of the base learner should be taken into account, and models with significant differences can be chosen as base learners to combine the advantages of different algorithms [36]. Secondly, the prediction performance of the base learner directly affects the overall performance of the stacking integrated model [37], so choosing base learners with better prediction performance can improve the integrated model's performance.

In testing the performance of a single model, the grid search method was used to select the optimal hyperparameters. The experimental results are shown in Table 2.

PLSR, SVR, and Ridge were more effective in predicting the moisture content of *P. massoniana* seedlings; Adaboost had the lowest test set R^2 of 0.6425 with weak performance; and the prediction accuracy of the remaining learners had little difference.

In this paper, the correlation between the prediction results of each model on the test set was measured using the Pearson correlation coefficient to analyze the difference between models. The correlation can be expressed using Equation (2):

$$\rho_{xy} = \frac{\sum_{i=1}^{n} (x_i - \mu_x)(y_i - \mu_y)}{\sqrt{\sum_{i=1}^{n} (x_i - \mu_x)^2} \sqrt{\sum_{i=1}^{n} (y_i - \mu_y)^2}} \quad (2)$$

where μ_x and μ_y are the predicted mean values of model x and model y, respectively. n denotes the number of test set samples. x_i, y_i denote the predicted values of the i-th sample of models x and y.

Table 2. Model optimal hyperparameters and prediction results.

Model	Optimal Hyperparameters	Training Set		Test Set	
		R^2	RMSE	R^2	RMSE
AdaBoost	n_estimators = 50	0.9125	0.7369	0.6425	1.5452
ExtraTree	min_samples_leaf = 7 max_depth = 5	0.7433	1.2626	0.7362	1.3272
RF	n_estimators = 8 max_leaf_nodes = 14	0.9000	0.7881	0.7336	1.3340
Ridge	alpha = 1.6 solver = sag	0.7939	1.1314	0.8054	1.1400
PLSR	n_components = 10	0.8848	0.8458	0.8057	1.1391
SVR	kernel = linear C = 1.25	0.8107	1.0842	0.7884	1.1888

The Pearson correlation coefficients of each single model are shown in Figure 4.



Figure 4. Correlation analysis of the prediction results of each model.

Different model algorithms extract features from different perspectives. Therefore, when constructing stacking models, it is essential to select models with a substantial difference to combine the advantages of various algorithms. As can be seen from Figure 4, the correlation between Ridge and SVR is the highest at 0.9966. This is because both models use L2 regularization terms and have similar hyperparameters, as well as the angles of the observed data being more similar. However, SVR has better robustness, so SVR is chosen as one of the candidate base learners. In contrast, AdaBoost and ExtraTree have large differences compared with other models, and the prediction results are less relevant. When constructing stacking models with large differences, the advantages between different model algorithms can be combined. Therefore, AdaBoost and ExtraTree are chosen as candidate-based learners. The prediction performance of the base learner directly affects the prediction performance of the stacking model. The candidate base learner was selected based on its prediction accuracy, and the PLSR with the highest accuracy was chosen as the base learner for the stacking model.

This paper selects AdaBoost, ExtraTree, PLSR, and SVR as the candidate base learners for the stacking model by combining the model prediction results and the correlation between the models. The mandatory base learners are chosen as the best and worst performers, PLSR and AdaBoost, respectively.

3.3.2. Comparison of Different Model Combinations in Stacking

As the hyperparameter of PLSR did not match the data structure, it was not used as the meta-learner in this paper. Instead, AdaBoost, ExtraTree, and SVR were used as meta-learners for comparison experiments to select the best combination of learners.

As can be observed from Table 3, there is a significant difference in the prediction of moisture content of *P. massoniana* seedlings for different combinations of stacking integrated models. Comparing the combination ways of numbers 1, 2, and 3 and numbers 4, 5, and 6, the stacking integrated model's overall performance improved when AdaBoost was used as the meta-learner. This is because AdaBoost considers the weight assignment of each base learner, reducing the risk of overfitting and improving the model's generalization ability. The overall prediction performance of the stacking integrated model was compared between the combinations of numbers 1 and 4, 2 and 5, and 3 and 6. It was found that using SVR, AdaBoost, and PLSR as base learners resulted in better performance than using ExtraTree, AdaBoost, and PLSR as base learners. Additionally, the inclusion of SVR was found to be more beneficial for improving the generalization ability of the model. Based on the above analysis, we can conclude that the combination of number 6 not only exhibits better prediction performance than each individual model, but it also achieves the best prediction performance among all the different combinations.

Table 3. Comparison of the combination method and performance of different learners.

Number	Base Learners	Meta-Learner	Training Set		Test Set	
			R^2	RMSE	R^2	RMSE
1	ExtraTree-AdaBoost-PLSR	SVR	0.9413	0.6039	0.7417	1.3135
2	ExtraTree-AdaBoost-PLSR	ExtraTree	0.7750	1.1819	0.7211	1.3647
3	ExtraTree-AdaBoost-PLSR	AdaBoost	0.9709	0.4253	0.8305	1.0639
4	SVR-AdaBoost-PLSR	SVR	0.9448	0.5856	0.7188	1.3705
5	SVR-AdaBoost-PLSR	ExtraTree	0.7740	1.1846	0.7708	1.2372
6	SVR-AdaBoost-PLSR	AdaBoost	0.9718	0.4187	0.8819	0.8879

Therefore, in this paper, we have chosen the combination of number 6, which includes SVR, AdaBoost, and PLSR as the base learners and AdaBoost as the meta-learner of the stacking integrated model. The stacking model framework and the complete training process are shown in Figure 5.

3.4. Feature Selection and Stacking Prediction Performance Analysis

Due to the large number of spectral bands in the raw spectral data of the leaves, the existence of interference information and redundant bands can result in a computationally intensive and less accurate prediction model. Therefore, it is necessary to perform feature band extraction on the raw spectral data to address this issue. The feature bands were selected by five feature selection algorithms: GA, SPA, UVE, CARS, and LARS (Figure 6).

Overall, SPA outputs more scattered feature bands and has the best dimensionality reduction effect, selecting 23 feature bands and reducing the number of bands by 98.96%; CARS has the second-best dimensionality reduction effect, with 46 feature bands, and a small number of overlapping bands can be seen when comparing CARS and SPA. UVE and LARS retain more features in the feature band selection process, mainly concentrated on 5500–4000 cm^{-1} and 12,500–8000 cm^{-1}, and the band reduction is 74.17% and 77.30%, respectively. GA has the worst dimensionality reduction effect, the features are uniformly scattered and dense, the discrimination of the strong interference information present in the spectral data is low, and the band reduction is 55.97%. The vibration generated by the O-H chemical bonds in plant water molecules is mainly in the 4600–4000 cm^{-1} interval [38], and the wavenumbers in this interval have a certain response relationship with plant moisture content. All five methods retained part of the wavelengths in this interval, which can be further analyzed.

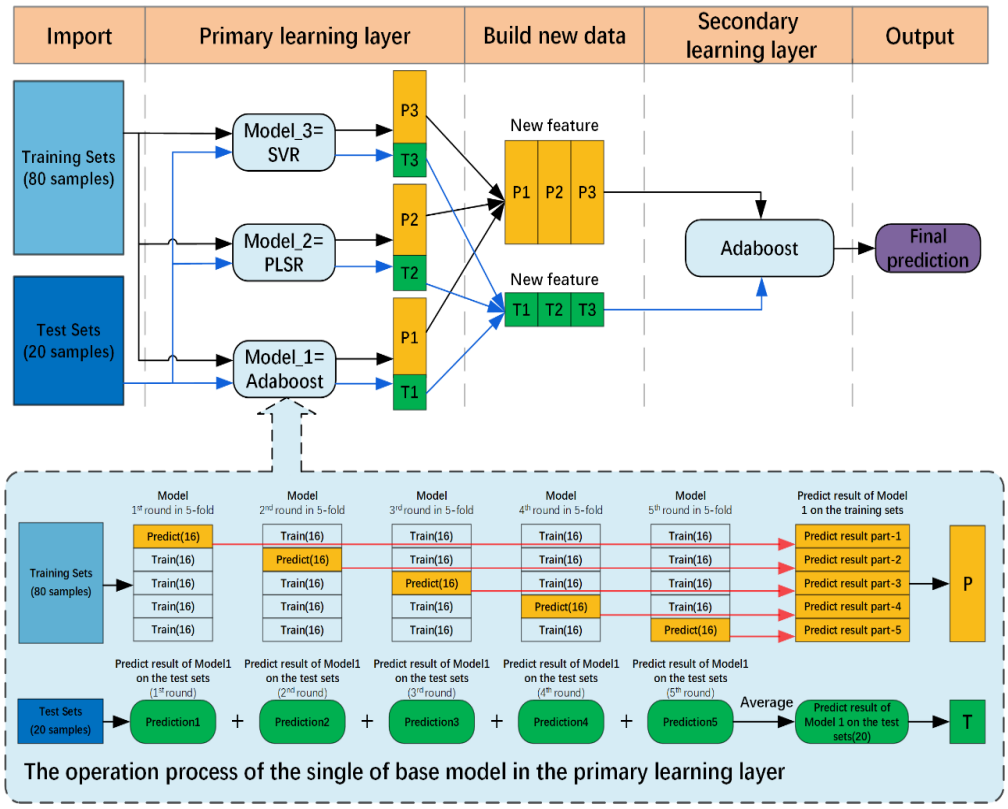


Figure 5. Moisture content prediction model of *P. massoniana* leaves based on the stacking integrated learning model.

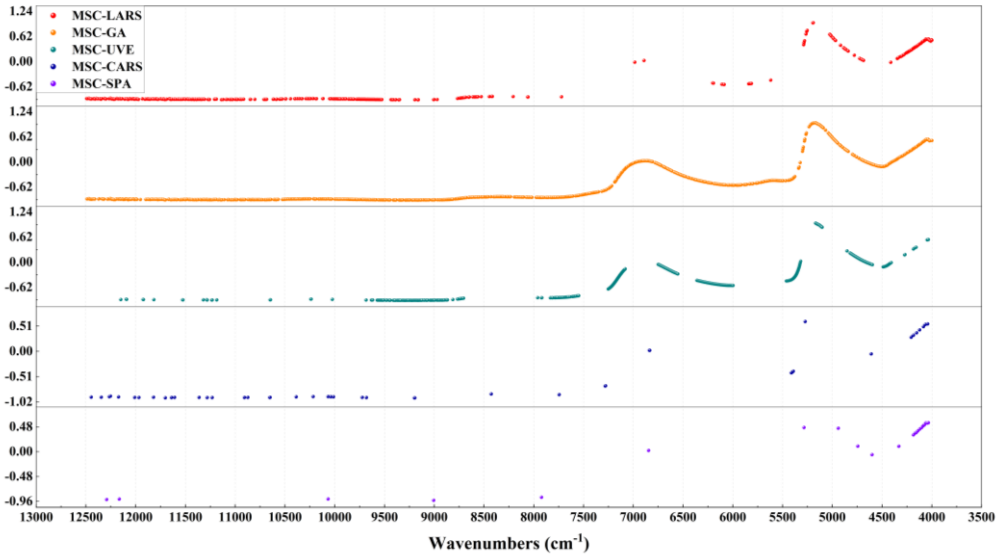


Figure 6. Spectral feature band selection effect. <Preprocessing> − <Feature Selection> = Spectral data after preprocessing and feature selection methods.

The PLSR, SVR, AdaBoost, and stacking integrated models for the moisture content of *P. massoniana* leaves were developed by using full-spectrum data and feature band spectral data, respectively. To ensure the best prediction results for each model, it is necessary to set the hyperparameters of each model. The model tuning process is conducted using the most widely used K-fold cross-validation, with K = 5. The final model hyperparameters are determined using a grid search method in combination with cross-validation. The prediction results of each model are shown in Table 4.

Table 4. Comparison of model results with different characteristic bands.

Feature Selection	Number of Wavenumbers	PLSR				SVR				AdaBoost				Stacking			
		Training Set		Test Set		Training Set		Test Set		Training Set		Test Set		Training Set		Test Set	
		R^2	RMSE	R^2	RMSE	R^2	RMSE	R^2	RMSE	R^2	RMSE	R^2	RMSE	R^2	RMSE	R^2	RMSE
MSC	2203	0.8848	0.8458	0.8057	1.1391	0.8107	1.0842	0.7884	1.1888	0.9125	0.7369	0.6425	1.5452	0.9718	0.4187	0.8819	0.8879
MSC-GA	970	0.8927	0.8163	0.8344	1.0518	0.7592	1.2228	0.7840	1.2011	0.9214	0.6988	0.7582	1.2709	0.9682	0.4443	0.8970	0.8293
MSC-SPA	23	0.8319	1.0216	0.8138	1.1151	0.5864	1.6025	0.6539	1.5204	0.9137	0.7322	0.6219	1.5890	0.9598	0.4999	0.8234	1.0862
MSC-UVE	569	0.9029	0.7764	0.7933	1.1749	0.7519	1.2413	0.7872	1.1921	0.8985	0.7941	0.6436	1.5428	0.9681	0.4448	0.8837	0.8814
MSC-CARS	46	0.9663	0.4575	0.9265	0.7008	0.5607	1.6516	0.5969	1.6408	0.8867	0.8389	0.7131	1.3843	0.9821	0.3349	0.9430	0.6168
MSC-LARS	500	0.9402	0.6091	0.7124	1.3860	0.7171	1.3254	0.7710	1.2367	0.9039	0.7725	0.6460	1.5375	0.9783	0.3673	0.8169	1.1059

Note: <Preprocessing> − <Feature Selection> = Spectral data after preprocessing and feature selection methods.

Upon longitudinal comparison of Table 4, it is evident that the model prediction accuracy of the feature bands selected by both the SPA and LARS algorithms significantly decreases compared to the full bands on the different models. The R^2 of the test set for the feature bands selected by SPA decreases on average by 6.47% compared to the full spectral data on each model, while the R^2 of the bands selected by LARS decreases on average by 5.16% compared to the full spectral data on each model. This indicates that these two methods failed to effectively extract the useful feature bands, resulting in lower prediction accuracy for each model. The prediction effect of the feature bands selected by the UVE algorithm on each model is closer to that of the full band, indicating that the use of noise to eliminate invalid variables in the spectral data is beneficial and retains a large amount of valid spectral information. GA and CARS perform better in extracting valid spectral data, leading to an improvement in model prediction accuracy to different degrees compared to the full band. Among them, the CARS algorithm shows the most significant improvement, with the highest R^2 improvement of 14.99% and RMSE reduction of 38.48% on PLSR and the highest R^2 of 0.9430 and RMSE of 0.6168 in the stacking model. Based on the results, it is evident that the method of adaptively weighting the spectral bands for the selection of feature bands in *P. massoniana* leaf spectral data is the most effective approach.

The comparison in Table 4 shows that the prediction accuracy of the Adaboost model in the training set is generally higher than that in the test set for each dataset, indicating that the model is more sensitive to data imbalance, resulting in decreased prediction accuracy. In contrast, the prediction accuracy of the SVR on both the training and test sets has a smaller fluctuation range, is robust to outliers, and has excellent generalization ability. However, the overall model's performance is low. It is possible that the low performance of the model is due to the excessive number of features. PLSR performed the best in the single model, especially in the MSC-CARS dataset, where R^2 reached 0.9265, and the MSC-CARS-Stacking model still had a 0.0165 improvement in R^2 in the same dataset. The stacking integrated learning model demonstrated improvement relative to the single model on each spectral dataset. The MSC-CARS-stacking model had the best overall improvement, with an average increase of 26.49% in R^2 and an average reduction of 50.34% in RMSE for the test set compared to the single learner. The worst performance improvement was observed in the MSC-GA-stacking integrated model, with an average test set R^2 improvement of 13.23% and an average RMSE reduction of 29.40%. This also confirms the effectiveness of the CARS method for spectral information extraction and the deficiency of the GA feature screening method. The CARS method selects the least number of feature bands in the interval of 4600–4000 cm^{-1}. It is seen that CARS selects the bands related to O-H chemical bonds well and filters the invalid information greatly. The number of overlapping feature waves between GA and CARS is 25, which is the highest among the overlapping wave statistics between CARS and SPA or UVE. However, GA has a large number of feature variables, which is 970, and the number of overlapping waves with CARS is only 2.5%. This suggests that GA contains a significant amount of invalid information. GA increases the complexity of spectral feature search, and its mutation and crossover information composition is not sufficient to traverse the solution space of large spectral data with complex information.

For the full-spectrum data and the spectral data of the characteristic bands selected by the five algorithms (GA, SPA, UVE, CARS, and LARS), the prediction accuracy of the stacking integrated model consisting of SVR, AdaBoost, and PLSR proposed in this paper is improved to different degrees compared with each single model. This is because the stacking integrated model first trains several weak learners in parallel to combine the advantages of multiple models, and then combines the different weak learners by training a meta-learner to output a final prediction result. This effectively overcomes the shortcomings of a single model in the training process, leading to improved prediction accuracy. The prediction results of the full-spectrum data and the spectral data of the feature bands selected by the five algorithms of GA (970), SPA (23), UVE (569), CARS (46), and LARS (500) in the stacking integrated model are shown in Figure 7.

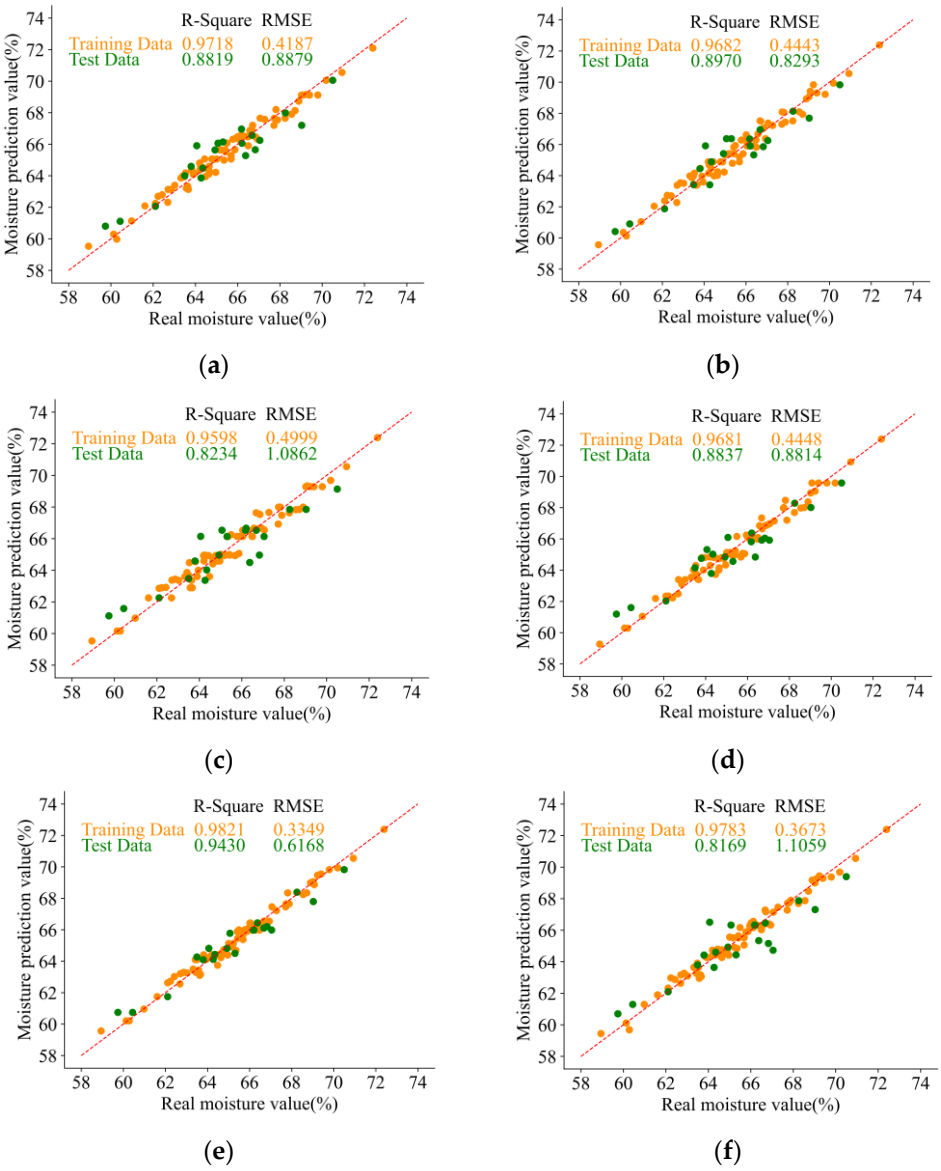


Figure 7. Model prediction effect under optimal combination. <Preprocessing> − <Feature Selection> − <Model> = Model results after preprocessing and feature extraction methods: (**a**) MSC-stacking; (**b**) MSC-GA-stacking; (**c**) MSC-SPA-stacking; (**d**) MSC-UVE-stacking; (**e**) MSC-CARS-stacking; and (**f**) MSC-LARS-stacking.

4. Conclusions

This study aims to develop a predictive model for the leaf moisture content of *P. massoniana* seedlings using near-infrared spectroscopy and multiple chemometric methods. Five preprocessing methods, including Nirmaf, L2-normalize, MSC, SG, and SNV, were employed to process the spectral data. A stacking learning framework was then introduced, and six models, namely AdaBoost, ExtraTree, RF, SVR, PLSR, and Ridge, were analyzed based on their predictive results. PLSR and AdaBoost were chosen as the candidate base learners for the stacking learning model, and the remaining four models were allocated to the base learners and meta-learners. The optimal combination of learners was determined by searching for all possible combinations. Furthermore, the SPA, CARS, UVE, GA, and LARS algorithms were utilized to select the wavelength variables, and the MSC full spectrum and MSC characteristic wavelength spectrum were used to establish a quantitative analysis model for the *P. massoniana* seedling moisture content based on the selected stacking learning model. The results show that the SVR-AdaBoost-PLSR+AdaBoost stack-

ing learning model in full-spectrum near-infrared spectroscopy can accurately quantify the moisture content of *P. massoniana* seedlings. As there are many spectral variables, the commonly used multivariate calibration methods in chemometrics are no longer applicable. The SVR-AdaBoost-PLSR+AdaBoost model still shows stable predictive performance in feature variable selection, indicating that the stacking learning model has good applicability and predictive performance in near-infrared spectroscopy quantitative analysis. As a result, this model holds significant potential for further research in the field of spectroscopy analysis. The modeling methods and procedures used in this study are also applicable to other forest seedlings. This provides a reference for the precise cultivation technology of *P. massoniana* seedlings and an effective and accurate modeling method for quantitatively analyzing seedling moisture content.

Author Contributions: Conceptualization, Y.L. (Yurong Li) and H.X.; methodology, Y.L. (Yurong Li) and H.X.; software, Y.L. (Yurong Li) and H.X.; validation, L.H. and B.G.; formal analysis, Y.L. (Yurong Li) and H.X.; investigation, B.G.; resources, C.N.; data curation, Y.L. (Yurong Li) and H.X.; writing—original draft preparation, Y.L. (Yurong Li) and H.X.; writing—review and editing, Y.L. (Ying Liu); visualization, Y.L. (Yurong Li), H.X. and C.N.; supervision, Y.L. (Ying Liu); project administration, Y.L. (Ying Liu); funding acquisition, Y.L. (Ying Liu). All authors have read and agreed to the published version of the manuscript.

Funding: This research was funded by the National Natural Science Foundation of China (NSFC: 31570714).

Data Availability Statement: The data are not publicly available because this study is still in progress.

Acknowledgments: We thank Zilong Zhuang, Wei Yu, Chenxi Zhou, Kaihao Ji, Qi Sun and Yinxi Shen for their help with field work.

Conflicts of Interest: The authors declare no conflict of interest.

References

1. Yang, R.; Meng, J. Using Advanced Machine-Learning Algorithms to Estimate the Site Index of Masson Pine Plantations. *Forests* **2022**, *13*, 1976. [CrossRef]
2. Chen, F.; Yuan, Y.-j.; Yu, S.-l.; Zhang, T.-w. Influence of climate warming and resin collection on the growth of Masson pine (*Pinus massoniana*) in a subtropical forest, southern China. *Trees-Struct. Funct.* **2016**, *30*, 1017. [CrossRef]
3. Dungey, H.S.; Dash, J.P.; Pont, D.; Clinton, P.W.; Watt, M.S.; Telferl, E.J. Phenotyping Whole Forests Will Help to Track Genetic Performance. *Trends Plant Sci.* **2018**, *23*, 854–864. [CrossRef] [PubMed]
4. Scharwies, J.D.; Dinneny, J.R. Water transport, perception, and response in plants. *J. Plant Res.* **2019**, *132*, 311–324. [CrossRef]
5. Wang, J.; Li, X.; Wang, W.; Wang, F.; Liu, Q.; Yan, L. Research on Rapid and Low-Cost Spectral Device for the Estimation of the Quality Attributes of Tea Tree Leaves. *Sensors* **2023**, *23*, 571. [CrossRef]
6. Aboulwafa, M.M.; Youssef, F.S.; Gad, H.A.; Sarker, S.D.; Nahar, L.; Al-Azizi, M.M.; Ashour, M.L. Authentication and discrimination of green tea samples using UV-vis, FTIR and HPLC techniques coupled with chemometrics analysis. *J. Pharm. Biomed. Anal.* **2019**, *164*, 653–658. [CrossRef]
7. Rebufa, C.; Pany, I.; Bombarda, I. NIR spectroscopy for the quality control of *Moringa oleifera* (Lam.) leaf powders: Prediction of minerals, protein and moisture contents. *Food Chem.* **2018**, *261*, 311–321. [CrossRef]
8. Zhang, H.; Ge, Y.; Xie, X.; Atefi, A.; Wijewardane, N.K.; Thapa, S. High throughput analysis of leaf chlorophyll content in sorghum using RGB, hyperspectral, and fluorescence imaging and sensor fusion. *Plant Methods* **2022**, *18*, 60. [CrossRef]
9. Shi, G.; Cao, J.; Li, C.; Liang, Y. Compression strength prediction of Xylosma racemosum using a transfer learning system based on near-infrared spectral data. *J. For. Res.* **2020**, *31*, 1061–1069. [CrossRef]
10. Falcioni, R.; Moriwaki, T.; Antunes, W.C.; Nanni, M.R. Rapid Quantification Method for Yield, Calorimetric Energy and Chlorophyll a Fluorescence Parameters in Nicotiana tabacum L. Using Vis-NIR-SWIR Hyperspectroscopy. *Plants* **2022**, *11*, 2406. [CrossRef] [PubMed]
11. Zhang, K.; Jiang, H.; Zhang, H.; Zhao, Z.; Yang, Y.; Guo, S.; Wang, W. Online Detection and Classification of Moldy Core Apples by Vis-NIR Transmittance Spectroscopy. *Agriculture* **2022**, *12*, 489. [CrossRef]
12. Zhang, M.; Guo, J.; Ma, C.; Qiu, G.; Ren, J.; Zeng, F.; Lu, E. An Effective Prediction Approach for Moisture Content of Tea Leaves Based on Discrete Wavelet Transforms and Bootstrap Soft Shrinkage Algorithm. *Appl. Sci.* **2020**, *10*, 4839. [CrossRef]
13. Li, C.; Zhao, J.; Li, Y.; Meng, Y.; Zhang, Z. Modeling and Prediction of Soil Organic Matter Content Based on Visible-Near-Infrared Spectroscopy. *Forests* **2021**, *12*, 1809. [CrossRef]

14. Neto, A.J.S.; Lopes, D.d.C.; Silva, T.G.F.d.; Ferreira, S.O.; Grossi, J.A.S. Estimation of leaf water content in sunflower under drought conditions by means of spectral reflectance %J Engineering in Agriculture, Environment and Food. *Eng. Agric. Environ. Food* **2016**, *10*, 104–108. [CrossRef]
15. Rabanera, J.D.; Guzman, J.D.; Yaptenco, K.F. Rapid and Non-destructive measurement of moisture content of peanut (*Arachis hypogaea* L.) kernel using a near-infrared hyperspectral imaging technique. *J. Food Meas. Charact.* **2021**, *15*, 3069–3078. [CrossRef]
16. Sun, Z.; Zhou, J. L-1-PLS Based on Incremental Extreme Learning Machine. In Proceedings of the 9th IEEE Data Driven Control and Learning Systems Conference (DDCLS), Liuzhou, China, 20–22 November 2020; pp. 947–952. [CrossRef]
17. Hu, H.; He, Z.; Ling, Y.; Li, J.; Sun, L.; Li, B.; Liu, J.; Chen, W. A SOM-RBFnn-Based Calibration Algorithm of Modeled Significant Wave Height for Nearshore Areas. *J. Mar. Sci. Eng.* **2022**, *10*, 706. [CrossRef]
18. Yang, J.; Chen, Y. Tender Leaf Identification for Early-Spring Green Tea Based on Semi-Supervised Learning and Image Processing. *Agronomy* **2022**, *12*, 1958. [CrossRef]
19. Xie, C.; Zhu, H.Y.; Fei, Y.Q. Deep coordinate attention network for single image super-resolution. *IET Image Process.* **2022**, *16*, 273–284. [CrossRef]
20. Lian, X.-q.; Chen, Q.; Tang, S.-m.; Wu, J.-z.; Wu, Y.-l.; Gao, C. Quantitative Analysis Method of Key Nutrients in Lanzhou Lily Based on NIR and SOM-RBF. *Spectrosc. Spectr. Anal.* **2022**, *42*, 2025–2032. [CrossRef]
21. He, W.; Li, Y.; Wang, J.; Yao, Y.; Yu, L.; Gu, D.; Ni, L. Using Field Spectroradiometer to Estimate the Leaf N/P Ratio of Mixed Forest in a Karst Area of Southern China: A Combined Model to Overcome Overfitting. *Remote Sens.* **2021**, *13*, 3368. [CrossRef]
22. Wang, Y.; Wang, D.; Geng, N.; Wang, Y.; Yin, Y.; Jin, Y. Stacking-based ensemble learning of decision trees for interpretable prostate cancer detection. *Appl. Soft Comput.* **2019**, *77*, 188–204. [CrossRef]
23. Ni, C.; Wang, D.; Tao, Y. Variable weighted convolutional neural network for the nitrogen content quantization of Masson pine seedling leaves with near-infrared spectroscopy. *Spectrochim. Acta Part A-Mol. Biomol. Spectrosc.* **2019**, *209*, 32–39. [CrossRef] [PubMed]
24. Sun, J.; Cong, S.; Mao, H.; Wu, X.; Zhang, X.; Wang, P. CARS-ABC-SVR model for predicting leaf moisture of leaf-used lettuce based on hyperspectral. *Trans. Chin. Soc. Agric. Eng.* **2017**, *33*, 178–184.
25. Yu, L.; Liang, Y.; Zhang, Y.; Cao, J. Mechanical properties of wood materials using near-infrared spectroscopy based on correlation local embedding and partial least-squares. *J. For. Res.* **2020**, *31*, 1053–1060. [CrossRef]
26. Ren, G.; Zhang, X.; Wu, R.; Yin, L.; Hu, W.; Zhang, Z. Rapid Characterization of Black Tea Taste Quality Using Miniature NIR Spectroscopy and Electronic Tongue Sensors. *Biosensors* **2023**, *13*, 92. [CrossRef]
27. Ma, L.; Zhang, Y.; Zhang, Y.; Wang, J.; Li, J.; Gao, Y.; Wang, X.; Wu, L. Rapid Nondestructive Detection of Chlorophyll Content in Muskmelon Leaves under Different Light Quality Treatments. *Agronomy* **2022**, *12*, 3223. [CrossRef]
28. Zhu, R.; Jiang, D. Frequency modulation analysis of solar array using genetic algorithm. *Proc. Inst. Mech. Eng. Part G-J. Aerosp. Eng.* **2022**, *10*, 19. [CrossRef]
29. Wang, Z.; Zhang, Y.; Fan, S.; Jiang, Y.; Li, J. Determination of Moisture Content of Single Maize Seed by Using Long-Wave Near-Infrared Hyperspectral Imaging (LWNIR) Coupled with UVE-SPA Combination Variable Selection Method. *IEEE Access* **2020**, *8*, 195229–195239. [CrossRef]
30. Wang, Z.; Chen, J.; Zhang, J.; Tan, X.; Raza, M.A.; Ma, J.; Zhu, Y.; Yang, F.; Yang, W. Assessing canopy nitrogen and carbon content in maize by canopy spectral reflectance and uninformative variable elimination. *Crop. J.* **2022**, *10*, 1224–1238. [CrossRef]
31. Tabarangao, J.T.; Slepkov, A.D. Mimicking Multimodal Contrast with Vertex Component Analysis of Hyperspectral CARS Images. *J. Spectrosc.* **2015**, *2015*, 575807. [CrossRef]
32. Elrewainy, A.; Sherif, S.S. Kronecker least angle regression for unsupervised unmixing of hyperspectral imaging data. *Signal Image Video Process.* **2020**, *14*, 359–367. [CrossRef]
33. Cheng, J.; Sun, J.; Yao, K.; Xu, M.; Wang, S.; Fu, L. Hyperspectral technique combined with stacking and blending ensemble learning method for detection of cadmium content in oilseed rape leaves. *J. Sci. Food Agric.* **2022**, *103*, 2690–2699. [CrossRef]
34. Mantanus, J.; Ziemons, E.; Lebrun, P.; Rozet, E.; Klinkenberg, R.; Streel, B.; Evrard, B.; Hubert, P. Moisture content determination of pharmaceutical pellets by near infrared spectroscopy: Method development and validation. *Anal. Chim. Acta* **2009**, *642*, 186–192. [CrossRef] [PubMed]
35. Ishikawa, H.; Boukar, O.; Fatokun, C.; Shono, M.; Muranaka, S. Development of calibration model to predict nitrogen content in single seeds of cowpea (*Vigna unguiculata*) using near infrared spectroscopy. *J. Near Infrared Spectrosc.* **2017**, *25*, 211–214. [CrossRef]
36. Breiman, L. Stacked Regressions. *Mach. Learn.* **1996**, *24*, 49–64. [CrossRef]
37. Divina, F.; Gilson, A.; Gomez-Vela, F.; Torres, M.G.; Torres, J.E. Stacking Ensemble Learning for Short-Term Electricity Consumption Forecasting. *Energies* **2018**, *11*, 949. [CrossRef]
38. Frost, R.L.; Erickson, K.L. Near-infrared spectroscopic study of selected hydrated hydroxylated phosphates. *Spectrochim. Acta Part A-Mol. Biomol. Spectrosc.* **2005**, *61*, 45–50. [CrossRef] [PubMed]

Disclaimer/Publisher's Note: The statements, opinions and data contained in all publications are solely those of the individual author(s) and contributor(s) and not of MDPI and/or the editor(s). MDPI and/or the editor(s) disclaim responsibility for any injury to people or property resulting from any ideas, methods, instructions or products referred to in the content.

forests

MDPI

Article

Comparative Chloroplast Genome Analysis of Chinese Lacquer Tree (*Toxicodendron vernicifluum*, Anacardiaceae): East-West Divergence within Its Range in China

Lu Wang [1], Yao Li [1], Na He [2], Ye Peng [1], Yanming Fang [1,*], Xingwang Zhang [3,*] and Feilong Zhang [2]

[1] Co-Innovation Center for Sustainable Forestry in Southern China, Key Laboratory of State Forestry and Grassland Administration on Subtropical Forest Biodiversity Conservation, College of Biology and the Environment, Nanjing Forestry University, 159 Longpan Road, Nanjing 210037, China
[2] Xi'an Raw Lacquer Research Institute, 1 Tiantan Road, Xi'an 710061, China
[3] School of Life Sciences, Huaibei Normal University, 100 Dongshan Road, Huaibei 235000, China
* Correspondence: jwu4@njfu.edu.cn (Y.F.); zhangxingwang79@126.com (X.Z.)

Abstract: Chinese lacquer tree (*Toxicodendron vernicifluum*) is an important commercial arbor species known for the production of raw lacquer. Here, we investigated the intraspecific chloroplast (cp) genome variability of *T. vernicifluum* using two available and five newly sequenced cp genomes. We found that each of the seven cp genomes encoded 87 protein-coding genes, 37 tRNA genes, and eight rRNA genes. Phylogenetic analyses based on protein-coding genes indicated that the four individuals from western China formed a monophyletic group sister to the cluster containing the three individuals from eastern China. The cp genomes from western China exhibited a larger genome length and longer large single-copy (LSC), small single-copy (SSC), and inverted repeat (IR) regions than those from eastern China. A total of 466 single nucleotide polymorphisms (SNPs) and 141 insertion-deletion mutations were detected among the seven cp genomes, most of which were found between the eastern and western lineages. The two groups exhibited a similar number of microsatellites, long repeats, and tandem repeats. Notably, complementary repeat sequences were only found in the IRs of the individuals from eastern China, while reverse repeat sequences were only detected in the LSC of the individuals from western China. Eight intraspecific mutational hotspots were also identified, including six intergenic regions (*trnF-ndhJ*, *rpl32-trnL*, *ccsA-ndhD*, *trnH-psbA*, *psbC-trnS*, and *trnL-trnF*) and two gene regions (*rpl32* and *rps19*). The genomic resources presented in this study will be useful for further studies on evolutionary patterns and resource protection of *T. vernicifluum*.

Keywords: chloroplast; phylogeny; phylogeographic structure; SNPs; *Toxicodendron vernicifluum*

check for updates

Citation: Wang, L.; Li, Y.; He, N.; Peng, Y.; Fang, Y.; Zhang, X.; Zhang, F. Comparative Chloroplast Genome Analysis of Chinese Lacquer Tree (*Toxicodendron vernicifluum*, Anacardiaceae): East-West Divergence within Its Range in China. *Forests* **2023**, *14*, 818. https://doi.org/10.3390/f14040818

Academic Editor: David Lee

Received: 19 February 2023
Revised: 3 April 2023
Accepted: 12 April 2023
Published: 17 April 2023

Copyright: © 2023 by the authors. Licensee MDPI, Basel, Switzerland. This article is an open access article distributed under the terms and conditions of the Creative Commons Attribution (CC BY) license (https://creativecommons.org/licenses/by/4.0/).

1. Introduction

Toxicodendron vernicifluum (Stokes) F. A. Barkley, commonly known as the Chinese lacquer tree, is a deciduous and dioecious tree species in the sumac family Anacardiaceae. This species is famous for providing us with raw lacquer, an excellent binder, and painting material with various properties such as anti-corrosion, rust resistance, non-oxidation, acid resistance, alcohol resistance, and high-temperature resistance [1,2]. In addition, *T. vernicifluum* is an economic tree species that is sometimes used in Chinese medicine to treat internal parasites and to stop bleeding. Previous studies have also reported that the urushiols of this species may have anticancer activity against human cancer cells and that flavonoids extracted from its leaves have therapeutic potential as a multipotent agent to treat neurodegenerative diseases [3,4].

T. vernicifluum is naturally distributed in China and has been cultivated in Korea and Japan perhaps for thousands of years [2,5,6]. In western China, wild lacquer trees usually grow in mountainous areas with an altitude above 800 m (e.g., the Qinling Mountains,

the Daba Mountains, the Wuling Mountains, the Dalou Mountains, and the Wumeng Mountains). In eastern China, they are scattered in low-altitude areas (e.g., the Liaodong Peninsula, the Shandong Peninsula, and the Huangshan Mountains). By analyzing the sequence variation of two chloroplast (cp) DNA fragments (*trnL* and *trnL-F*), previous studies have shown that *T. vernicifluum* exhibited a clear east-west phylogeographic break that was associated with the stepped geomorphology of China [1,7]. The wild trees of the western lineage were mainly found in the "middle step" region that is characterized by high mountains and plateaus, while those of the eastern lineage were confined to the "low step" region that is made up of hills and plains. These findings suggested that *T. vernicifluum* may have undergone allopatric divergence between at least two glacial refugia [7].

Compared with a few sequence fragments, complete cp genomes contain a larger amount of phylogenetic information, often used for phylogenetic inference and species delimitation [8–10]. Cp genomes are more conserved than mitochondrial and nuclear genomes in terms of gene content, organization, and structure [11–13]. With the development of bioinformatics and high-throughput sequencing technologies, the value of cp genomes in understanding evolutionary biology and ecological applications has been widely recognized [14–16]. However, it should also be noted that interspecific cpDNA sharing is also frequently observed among co-occurring, closely related species (e.g., *Quercus*, *Populus*, and *Eucalyptus*) as a result of introgression (secondary contact) or shared geographic origin (ancestral sympatry) [17–19]. Thus, it is essential to use information from as many closely related species as possible to track the evolutionary history of cpDNA lineages.

The genus *Toxicodendron* included about 20 species, of which 16 are distributed in China [20]. In the last four years, cp genomes of several *Toxicodendron* species have been reported [21–23]. Comparative analyses of cp genomes were also reported for the genus *Toxicodendron* and other genera of Anacardiaceae, such as *Cotinus* [24], *Mangifera* [25], *Pistacia* [26,27], and *Rhus* [28]. For example, Barrett [29] exhibited an interesting finding that the gene rps19 was lost independently in the *Rhus integrifolia-ovata* complex and *R. chinensis*, with a further loss of the gene rps22 and a major contraction of the inverted repeat in two accessions of the latter. At the intraspecific level, Xu et al. [28] have detected obvious differences in cp genome length and the lengths of the large single-copy (LSC) and inverted repeat (IR) regions among four individuals of *R. chinensis*. The cp genomes of those individuals also varied in the numbers of protein-coding genes (126–132) and tRNA genes (36–37).

Recently, Zong et al. [30] compared the cp genomes of triploid *T. vernicifluum* and several cultivars of the species. They found that the size of those cp genomes varied but the structure and organization of genes were conservative. However, this study did not investigate the cp genome variation of natural populations of *T. vernicifluum*. Our present study particularly focused on the intraspecific cp genome variability of wild trees of *T. vernicifluum* sampled from its natural range in China. Given that previous studies using two cpDNA fragments have revealed an east-west phylogeographic split of *T. vernicifluum* associated with the stepped geomorphology of China [7], we hypothesized that there were significant differences between cp genomes of the species sampled from its western and eastern range in China. Here, we assembled and annotated the cp genomes of two *T. vernicifluum* trees from western China and three trees from eastern China and compared them with those previously reported (Figure 1). The observed patterns were also compared with the results based on nuclear ribosomal internal transcribed spacer (ITS) variation. We purposed to: (1) evaluate the genetic relationships of *T. vernicifluum* accessions using both cp genome and ITS variation; (2) investigate the intraspecific cp genome variability of *T. vernicifluum* between its eastern and western range in China; (3) explore potential variable regions useful for phylogeographic studies of *T. vernicifluum*.

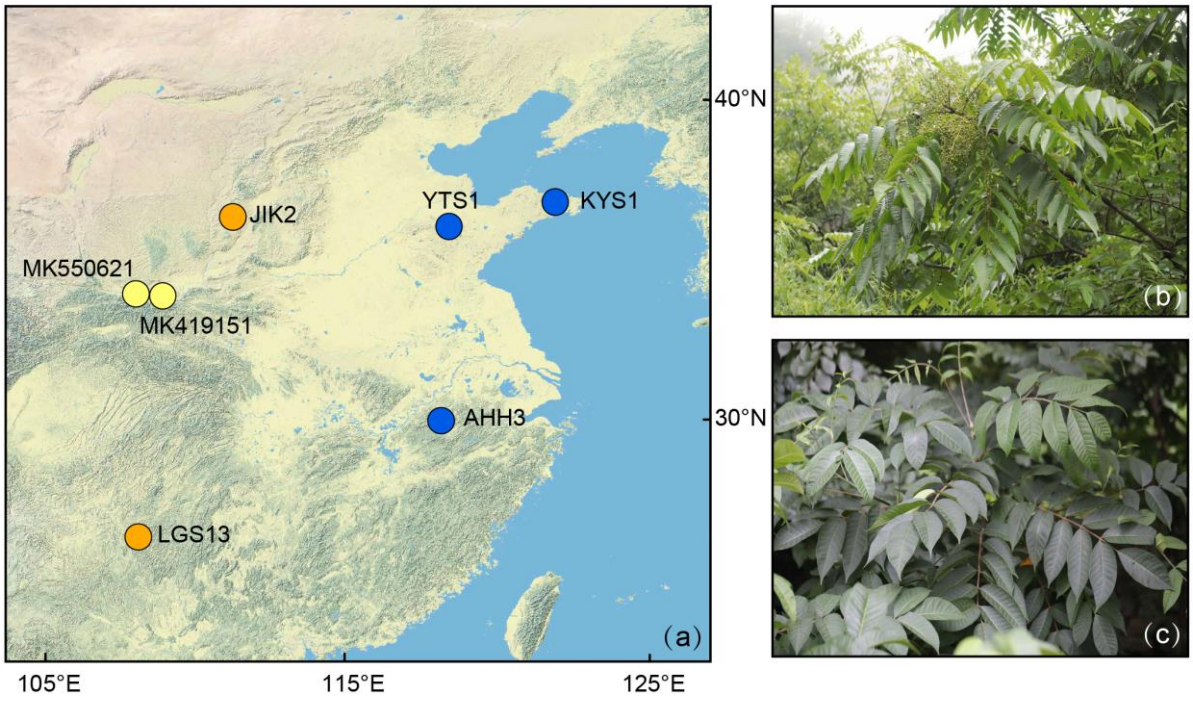


Figure 1. (**a**) Sampling sites of the seven *Toxicodendron vernicifluum* trees. The blue, orange, and yellow circles represent the three newly sequenced trees sampled from eastern China (voucher number: YTS1, KYS1, and AHH3), the two newly sequenced trees sampled from western China (voucher number: JIK2 and LGS13), and the two previously sequenced trees sampled from western China (GenBank accession number: MK419151 and MK550621), respectively. (**b**) Leaf photo of the individual sampled from western China (LGS13). (**c**) Leaf photo of the individual sampled from eastern China (KYS1). All photos were taken by Lu Wang.

2. Materials and Methods

2.1. Sampling, DNA Extraction, and Sequencing

Between July 2019 and August 2021, we sampled healthy and fresh leaves of five wild trees of *T. vernicifluum* from two sites in western China (voucher numbers: JIK2 and LGS13) and three sites in eastern China (voucher numbers: YTS1, KYS1, and AHH3) (Figure 1 and Table S1). Spatially explicit information was recorded for each tree using the 2bulu Outdoor Assistant app (https://www.2bulu.com/) (accessed on 25 June 2021). The voucher specimens of the five individuals were stored at the Herbarium of Nanjing Forestry University (NF) under voucher numbers shown in Table S1. Total genomic DNA was extracted from silica-gel dried leaves using the cetyltrimethylammonium bromide (CTAB) method [31]. The DNA integrity was evaluated with 1% agarose gel electrophoresis. The DNA concentration was measured by an ultra-micro ultraviolet-visible spectrophotometer (One Drop, Beijing, China). Qualified DNA samples were sent to Beijing Genomics Institute (BGI, Wuhan, China) for paired-end library preparation and whole-genome sequencing on a DNB-SEQ platform. Raw reads were filtered and trimmed using SOAPnuke 2.1.7 [32] with the following parameters: -n 0.01-l 20-q 0.3–adaMR 0.25–ada_trim–polyX 50–minReadLen 150.

2.2. Chloroplast Genome Assembly and Annotation

Paired-end clean reads were used for the de novo assembly of the five cp genomes with GetOrganelle 1.7.6.1 [33], which exploits SPAdes [34], Bowtie2 [35], BLAST+ [36], and Bandage [37] as dependencies. A wide range of k-mer lengths (-k 21, 45, 65, 85, 105) was used to benefit from the power of SPAdes. The maximum extension rounds (-R) were set to 15. The CpGAVAS2 pipeline [38] was applied to annotate protein-coding, rRNA, and tRNA genes using *T. vernicifluum* 'Dahongpao' (GenBank accession number:

MK550621) as the reference sequence. The Chloroplast Genome Viewer (CPGView) online tool (http://www.1kmpg.cn/cpgview) (accessed on 1 January 2023) [39] was used to visualize the cp genome structures.

2.3. Phylogenetic Analyses and Divergence Time Estimation Based on Chloroplast Genome Sequences

Twenty-three cp genomes were used to reconstruct the phylogeny of the tribe Rhoeae (Table 1). Those plastomes belonged to five species of the genus *Toxicodendron* (11 plastomes), six species of the genus *Rhus* (seven plastomes), one species of the genus *Cotinus* (one plastome), and three species of the genus *Pistacia* (three plastomes). *Mangifera indica* (GenBank accession number: KY635882) was selected as an outgroup following previous studies [40,41]. All the 23 cp genomes were annotated using the CpGAVAS2 pipeline [38], with *T. vernicifluum* 'Dahongpao' (GenBank accession number: MK550621) as the reference genome. Finally, nucleotide sequences of 77 common protein-coding genes were extracted, aligned, and concatenated using PhyloSuite 1.1.152 [42], resulting in an alignment of 67,432 bp in length.

Phylogenetic analyses were conducted using maximum likelihood (ML) and Bayesian Inference (BI) approaches for both un-partitioned sequence data and sequence data partitioned by genes. ModelFinder [43] was used to choose the optimal partitioning strategies and evolutionary models under the Bayesian Information Criterion (BIC). For the un-partitioned sequence data, TVM + F + R3 and GTR + F + I + G4 were selected as the best-fit substitution models for ML and BI analyses, respectively. For the sequence data partitioned by gene, the best-fit partition models were shown in Table S2. ML trees were reconstructed using IQ-tree 1.6.12 [44] with 10,000 ultrafast bootstrap (UFBS) replicates [45]. BI trees were built using MrBayes 3.2.6 [46]. Markov chain Monte Carlo (MCMC) runs were performed for 10 million generations, and trees were sampled every 1000 generations. The first 25% of the trees were discarded as burn-in to ensure that the chains were stationary. The remaining trees were used to generate a strict consensus tree and to calculate posterior probabilities for each node. All phylogenetic analyses mentioned above were conducted in Phylosuite 1.1.152 [42].

We used BEAST 2.6.7 [47] to estimate the divergence time among major cpDNA clades based on the concatenated sequences of 77 common protein-coding genes. The TVM + F + G4 model was selected as the best-fitting substitution model using ModelFinder [43] under the BIC. A combination of log-normal relaxed clock and Yule prior was used for node age estimation. Three calibration points were chosen according to previous phylogenetic studies of the genus *Toxicodendron* [48]. First, we used a secondary calibration point to set a normal prior with an offset of 74 million years ago (Ma), a mean of 0, and a sigma of 1.0 for the divergence between *Mangifera indica* and other members of the tribe Rhoeae (node I) [48]. Second, the reliable fossils of *Rhus* found in western North America in the middle Eocene [49] were used to set a log-normal prior with an offset of 44 Ma, a mean of 1.0, and a standard deviation of 0.85 for the stem age of *Rhus* (node II) [48]. Third, a leaf fossil of *Cotinus* found in North America in the early Oligocene/Late Eocene [50] was used to set a log-normal prior with an offset of 34 Ma, a mean of 1.0, and a standard deviation of 0.85 for the divergence between *Cotinus* and *Pistacia* (node III) [48]. Two independent MCMC runs were performed for 100 million generations and sampled every 10,000 generations. The generated log files were combined through LogCombiner 2.6.7 and then passed to Tracer 1.7.1 [51] for assessing convergence (effective sample size of all parameters > 200). TreeAnnotator 2.6.7 was used to construct a maximum clade credibility tree with a posterior probability limit of 0.5 and the first 25% of generations discarded as burn-in.

Table 1. Summary of the 22 complete chloroplast genomes of the tribe Rhoeae used by the phylogenetic analyses of this study. Those genomes belong to four genera, *Toxicodendron*, *Rhus*, *Cotinus*, and *Pistacia*. Newly generated sequences are marked by asterisks.

Species	Sources (Voucher Number)	GenBank acc. #	Length (bp)				GC (%)	Gene Number			
			Plastome	IRa/IRb	SSC	LSC		Full	PCG	tRNA	rRNA
T. vernicifluum	Qingzhou, Shandong, China (YTS1)	OQ168006 *	158,210	26,464	18,345	86,937	38.0	132	87	37	8
T. vernicifluum	Yantai, Shandong, China (KYS1)	OQ168008 *	158,209	26,464	18,344	86,937	38.0	132	87	37	8
T. vernicifluum	Huangshan, Anhui, China (AHH3)	OQ168009 *	158,223	26,464	18,345	86,950	38.0	132	87	37	8
T. vernicifluum	Jiaokou, Shanxi, China (JIK2)	OQ168007 *	159,593	26,512	19,070	87,499	37.9	132	87	37	8
T. vernicifluum	Leishan, Guizhou, China (LGS13)	OQ168010 *	159,565	26,513	19,071	87,468	38.0	132	87	37	8
T. vernicifluum	Xi'an, Shaanxi, China	MK419151	159,571	26,512	19,073	87,474	38.0	132	87	37	8
T. vernicifluum	Yangling, Shaanxi, China	MK550621	159,571	26,512	19,073	87,474	38.0	132	87	37	8
T. sylvestre	Lin'an, Zhejiang, China	MT211615	159,600	26,466	19,039	87,629	37.9	132	87	37	8
T. succedaneum	Chishui, Guizhou, China	MT211614	159,710	26,525	19,039	87,621	37.9	132	87	37	8
T. griffithii	Chenggan, Yunnan, China	MT269874	159,613	26,491	18,910	87,721	37.9	132	87	37	8
T. diversilobum	Washington Park, CA, USA	OP585546	159,543	26,526	18,796	87,695	38.0	132	87	37	8
R. chinensis	Shandong or Henan, China	MF351625	149,094	16,603	18,643	97,245	37.9	125	81	36	8
R. chinensis	Yanggu, Gangwon, South Korea	KX447140	149,011	16,742	18,646	96,881	37.8	125	81	36	8
R. hypoleuca	Unknown	MW238820	159,472	26,561	18,780	87,570	37.9	131	86	37	8
R. potaninii	Danfeng, Shaanxi, China	MT230556	159,620	26,476	18,947	87,721	37.9	132	87	37	8
R. punjabensis	Enshi, Hubei, China	MT230555	159,617	26,477	18,970	87,693	37.9	132	87	37	8
R. typhina	Mts. Lushan, Shandong, China	MT083895	160,204	26,549	19,318	87,788	37.8	132	87	37	8
R. wilsonii	Unknown	MW238821	159,814	26,528	18,842	87,916	37.8	132	87	37	8
C. coggygria	Mts. Jinyun, Chongqing, China	MT876478	158,843	26,830	18,063	87,120	38.0	131	85	38	8
P. weinmanniifolia	Unknown	MF630953	160,767	26,619	19,128	88,401	37.8	132	87	37	8
P. chinensis	Bazhong, Sichuan, China	MT157378	160,596	26,599	19,089	88,309	37.9	132	87	37	8
P. vera	Longnan, Gansu, China	MN551174	160,654	26,597	19,085	88,375	37.9	132	87	37	8

acc. #, accession number; GC, GC content; LSC, large single-copy; SSC, small single-copy; IR, inverted repeat; PCG, protein-coding gene.

2.4. Comparative Chloroplast Genome Analyses

The five newly sequenced and two previously published cp genomes of *T. vernicifluum* (GenBank accession number: MK419151 and MK550621) were aligned using MAFFT 7.3.13 [52] in the Phylosuite 1.1.152 platform [42]. The numbers of single nucleotide polymorphisms (SNPs) and insertion-deletion mutations (indels) in LSC, small single-copy (SSC) region, IRs, and protein-coding genes were counted by DnaSP 6.12.03 [53]. A TCS network was built with PopART 1.7 [54] based on the SNPs detected across the seven cp genomes.

To explore the highly variable regions across cp genomes of *T. vernicifluum* and its closely related species, shared genes, and intergenic regions were extracted by Phylosuite and aligned by MAFFT. The nucleotide diversity (π) values were calculated for 177 loci (114 genes and 63 intergenic spacers) across seven cp genomes of *T. vernicifluum*, for 176 loci (114 genes and 62 intergenic spacers) across 11 cp genomes of five *Toxicodendron* species, and for 167 loci (111 genes and 56 intergenic spacers) across 22 cp genomes of 15 species of the tribe Rhoeae (Table 1) using DnaSP 6.12.03 [53].

To investigate the genome variability of the seven cp genomes of *T. vernicifluum*, the mVISTA program was employed to plot the percentage of identity under the Shuffle-LAGAN mode, using the cp genome of *T. vernicifluum* YTS1 (GenBank accession number: OQ168006) as a reference [55]. Locally collinear blocks were identified by the Mauve module [56] in the Geneious 7.1.3 software [57] to detect the presence of large-scale evolutionary events such as rearrangements and inversions. The boundaries of LSC, SSC, and IR regions were visualized and compared among species using the IRscope software [58].

2.5. Repeat Sequence Identification

The REPuter online program [59] was used to identify large repetitive sequences, including forward, reverse, palindromic, and complementary repeats with the following parameters: minimum repeat size$\geq$30 bp, Hamming distance of 3, and maximum computed repeats of 50. Tandem Repeat Finder 4.09 [60] was used to identify tandem repeats, with the alignment weights for the match, mismatch, and indels set to 2, 7, and 7, respectively; matching probability (PM) and indel probability (PI) set to 80 and 10, respectively; minimum alignment score set to 50, and maximum period size set to 500. Simple sequence repeats (SSRs) were detected by the MISA-web tool [61,62] with the minimum repeat sizes for mono-, di-, tri-, tetra-, penta-, and hexanucleotides set to 10, 5, 4, 3, 3, and 3, respectively. The maximum sequence length between two SSRs for registration as a compound SSR was set to 100 bp.

2.6. Nuclear Ribosomal Internal Transcribed Spacer (ITS) Variation

We used the GetOrganelle 1.7.6.1 pipeline [33] to assemble the nuclear ribosomal DNA (rDNA) for the five newly sampled trees of *T. vernicifluum*. Assemblies were performed using the *k*-mer lengths of 35, 85, and 115 (i.e., -k 35, 85, 115). The maximum extension rounds (-R) were set to 10. The ITS sequences were extracted using the reference sequence of *T. succedaneum* (GenBank accession number: FJ945944). The obtained sequences were checked and aligned by BioEdit 7.2.5 [63]. ITS haplotypes were determined by DnaSP 6.12.03 [53]. A TCS network was constructed by PopART 1.7 [54].

3. Results and Discussion

3.1. Chloroplast Genome Assembly and Annotation

We assembled and annotated the complete cp genome sequences of five wild *T. vernicifluum* trees (Figure 1). After processing, a total of 60,743,870, 64,198,688, 64,056,786, 64,034,368, and 64,030,190 clean reads (150 bp in length) were obtained for samples YTS1, KYS1, AHH3, JIK2, and LGS13, respectively. The clean reads covered the entire assembled cp genome of the corresponding sample (100% coverage), representing an average depth of coverage of 3262.33×, 7762.28×, 8804.83×, 3986.53×, and 2658.80× for samples YTS1, KYS1, AHH3, JIK2, and LGS13, respectively. The newly generated plastomes were sub-

mitted to NCBI GenBank under accession numbers OQ168006–OQ168010. All five newly sequenced cp genomes encoded 132 genes, including 87 protein-coding genes, 37 tRNA genes, and eight rRNA genes (Figure 2). Among the 132 genes, 114 genes were unique, while 18 genes were duplicated, including seven protein-coding genes (*ndhB*, *rpl2*, *rpl23*, *rps12*, *rps7*, *ycf2*, and *ycf15*), seven tRNA genes (*trnA-UGC*, *trnI-CAU*, *trnI-GAU*, *trnL-CAA*, *trnN-GUU*, *trnR-ACG*, and *trnV-GAC*), and four rRNA genes (*rrn16*, *rrn23*, *rrn4.5*, and *rrn5*). These results were consistent with those of two previously reported accessions of *T. vernicifluum* (GenBank accession number: MK419151 and MK550621) [64,65] and with those of the other four species of *Toxicodendron* [21–23,66] (Table 1), suggesting that the cp genomes of *Toxicodendron* are highly conserved in gene content and order [67].

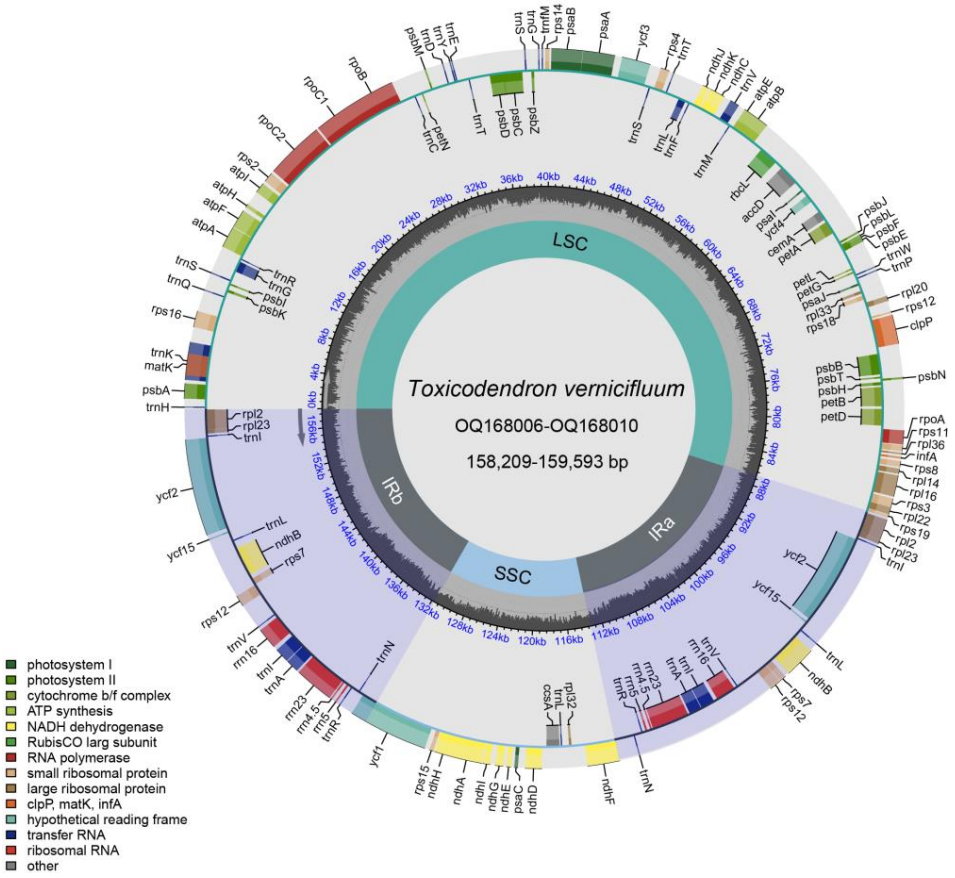


Figure 2. Gene circle map for the five newly sequenced chloroplast genomes of *Toxicodendron vernicifluum*. The genes were color-coded according to different functional groups. Genes on the inside and outside of the large circle are transcribed clockwise and counterclockwise, respectively. The darker gray columns in the inner circle correspond to the GC content. The circle map was generated by the CPGView online tool (http://www.1kmpg.cn/cpgview) (accessed on 1 January 2023).

3.2. Phylogenetic Analyses Based on Chloroplast Genome Sequences

We reconstructed the phylogenetic relationships of 22 accessions of the tribe Rhoeae (Table 1) and one outgroup based on 77 common protein-coding genes of cp genomes. The ML and BI analyses yielded similar tree topologies for both un-partitioned sequence data and sequence data partitioned by gene (Figures 3, S1 and S2). Our results supported the monophyly of *T. vernicifluum* [un-partitioned data: posterior probability (PP) = 1, bootstrap support value (BS) = 100; partitioned data: PP = 1, BS = 100]. These findings were consistent with previous studies showing that *T. vernicifluum* did not share any cpDNA haplotypes with closely related species such as *T. griffithii*, *T. radicans*, *T. succedaneum*, *T. sylvestre*, and *T. trichocarpum* [1,7], indicating that cpDNA markers could be effective in the delimitation of *T. vernicifluum* and its relatives. However, given that introgression and shared ancestral

polymorphism may result in interspecific cpDNA sharing, it is necessary to include more samples of closely related species with overlapping distributions in future work to better understand the cpDNA phylogeny of *T. vernicifluum* and its congeners [17–19].

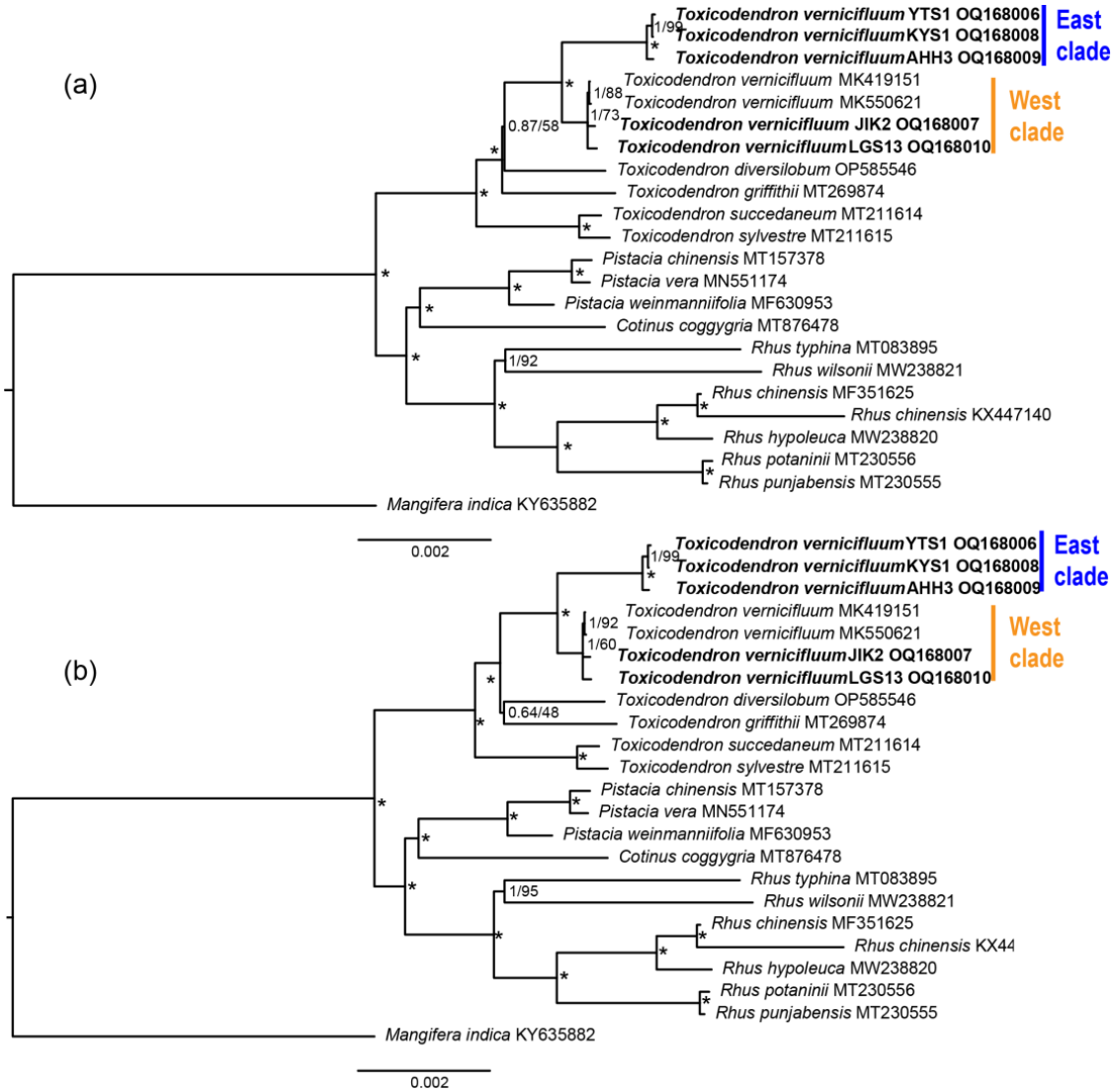


Figure 3. Phylogenetic trees inferred from maximum likelihood (ML) and Bayesian Inference (BI) approaches for (**a**) sequence data partitioned by genes and (**b**) un-partitioned sequence data. Numbers near the nodes are Bayesian posterior probabilities (PP, left of the slashes) and ML bootstrap support values (BS, right of the slashes). Nodes with PP of 1 and BS of 100 are marked by asterisks. Newly generated sequences in this study are indicated in bold.

Complete cp genomes contain more phylogenetic information that would be useful for evaluating intraspecific genetic relationships [68]. Our results showed the four *T. vernicifluum* individuals from western China (JIK2, LGS13, MK419151, and MK550621) formed a monophyletic group (un-partitioned data: PP = 1, BS = 100; partitioned data: PP = 1, BS = 100) sister to the cluster containing the three individuals from eastern China (YTS1, KYS1, and AHH3) (un-partitioned data: PP = 1, BS = 100; partitioned data: PP = 1, BS = 100). These results indicated that the cp genomes of *T. vernicifluum* split into two main clades: western China and eastern China lineages (Figure 3), supporting the conclusions of recent phylogeographic studies that an east-west phylogeographic split occurred in *T. vernicifluum* [1,7].

In western China, we found that the individual from southwestern China (LGS13, from the Guizhou Province) represented the basal branch, while the two individuals from northwestern China (MK419151 and MK550621, from the Shaanxi Province) formed a subclade (un-partitioned data: PP = 1, BS = 92; partitioned data: PP = 1, BS = 88) sister to that from northern China (JIK2, from the Shanxi Province). These results suggested that the *T. vernicifluum* trees may have undergone north-south divergence among the mountainous areas in western China. However, such patterns were not recovered by previous studies using only two cpDNA fragments [1,7].

In eastern China, we found that the two individuals from northeastern China (YTS1 and KYS1, from the Shandong Province) formed a subclade (un-partitioned data: PP = 1, BS = 99; partitioned data: PP = 1, BS = 99) sister to the individual from southeastern China (AHH3, from the Anhui Province). These findings supported that the *T. vernicifluum* trees may have also undergone north-south divergence in eastern China, congruent with previous results that two dominant chloroplast haplotypes were detected in the *T. vernicifluum* populations of northeastern and southeastern China [1,7].

Our results supported the monophyly of the genus *Toxicodendron* (un-partitioned data: PP = 1, BS = 100; partitioned data: PP = 1, BS = 100), which was found to be sister to the clade containing the remaining genera *Rhus*, *Cotinus*, and *Pistacia*. The topology of the tribe Rhoeae reported here was consistent with previous results obtained by nuclear and cpDNA fragments [48] or complete cp genome sequences [28]. However, the phylogenetic relationships of *Toxicodendron* species were not fully resolved (Figure 3). Using both nuclear and chloroplast DNA sequence data, previous studies have shown that *T. vernicifluum* was more closely related to *T. sylvestre* and *T. succedaneum* than to *T. griffithii* and *T. diversilobum*, implying the possibility of cyto-nuclear discordance in the phylogeny of *Toxicodendron* [69].

3.3. Divergence Time Estimation

The BEAST analyses grouped the seven *T. vernicifluum* individuals into eastern and western clades (Figure 4), which was consistent with the results of ML/BI analyses (Figure 3). The divergence time between the two clades was estimated to be 11.30 Ma (95% HPD: 4.18–22.47 Ma), suggesting that the two lineages may have diverged during the Late Miocene. This timing is comparable with the initial intraspecific divergence time of *Kerria japonica* (7.78 Ma; during the Late Miocene), a woody plant also presenting east-west phylogeographical breaks along the boundaries of the three-step landforms of China [70]. These findings implied that the geological and climatic events during the Late Miocene (e.g., Asian monsoon intensifications) may have been responsible for the onset of intraspecific diversification of *T. vernicifluum* [70]. The crown ages of the eastern and western clades of *T. vernicifluum* were estimated to be 1.80 Ma (95% HPD: 0.36–5.09 Ma) and 1.68 Ma (95% HPD: 0.39–4.51 Ma), respectively, suggesting that the Pleistocene climate fluctuations may have further driven the intraspecific cpDNA differentiation of *T. vernicifluum*.

3.4. Chloroplast Genome Comparison among the Accessions of T. vernicifluum, Toxicodendron, and the Tribe Rhoeae

All seven cp genomes of *T. vernicifluum* possessed a typical quadripartite structure, comprising one LSC region and one SSC region that were separated by two IRs (Figure 2). The seven cp genomes had similar GC contents (37.9–38.0%) but varied in genome length (Table 1). Compared with the three *T. vernicifluum* individuals from eastern China (average cp genome length: 158,214 bp), the four individuals from western China had larger cp genome length (average cp genome length: 159,575 bp) (Table 1). This was mainly attributed to that the SSC and LSC regions of the western China accessions were on average 727 and 537 bp longer than those of the eastern China accessions, respectively. Furthermore, the two IRs of the western China accessions were on average 96 bp longer than those of the eastern China accessions.

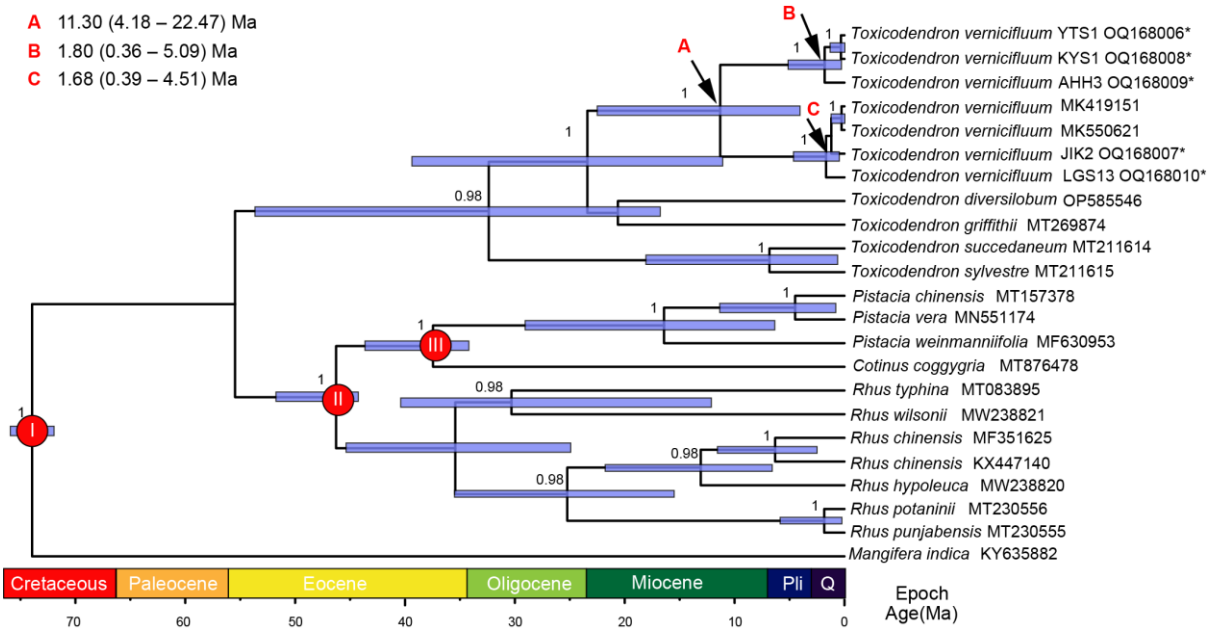


Figure 4. BEAST-derived chronogram for 22 individuals of the tribe Rhoeae, with *Mangifera indica* as an outgroup. Blue bars indicate the 95% highest posterior density (HPD) credibility intervals for node ages (million years ago, Ma). Posterior probabilities (>0.9) are labeled above nodes. Node I, II, and III are calibration points. Geological time abbreviations: Pli, Pliocene; Q, Quaternary.

The aligned cp genome sequences of the seven *T. vernicifluum* individuals were 159,932 bp in length. A total of 466 SNPs (0.29%) and 141 indels were detected (Table 2). The majority of the SNPs and indels were present in the LSC regions (331/109), followed by the SSC (111/20) and IR regions (24/12). The TCS network grouped the seven *T. vernicifluum* individuals into two clades: the eastern and western clades (Figure 5a). Those two clades were separated by 383 SNPs, indicating that most SNPs detected among the seven cp genomes existed between the eastern and western groups. Furthermore, SNPs and indels detected among the four *T. vernicifluum* individuals from western China were more than those found among the individuals from eastern China. No variations were found in the IR regions of the eastern China individuals.

Table 2. The numbers and distributions of single nucleotide polymorphisms (SNPs) and insertion-deletion mutations (indels) detected among the seven chloroplast genomes of *Toxicodendron vernicifluum*.

Index	Eastern Group	Western Group	All Samples
Number of samples	3	4	7
Aligned length (bp)	158,244	159,608	159,932
Total numbers of SNPs and indels	18/20	68/17	466/141
Numbers of SNPs and indels in LSC	11/17	50/13	331/109
Numbers of SNPs and indels in SSC	7/3	16/2	111/20
Numbers of SNPs and indels in IRs	0/0	2/2	24/12
Numbers of SNPs and indels in PCGs	14/0	19/0	150/39

LSC, large single-copy; SSC, small single-copy; IR, inverted repeat; PCG, protein-coding gene.

Chloroplast genomes of plants can provide highly variable regions that can be used as potential molecular markers for species identification and intra-/interspecific evolutionary studies [71,72]. We calculated the nucleotide diversity (π) values for common genes and intergenic regions across cp genomes to determine the hotspots of divergence at different taxonomic levels. The π values among the cp genomes of seven accessions of *T. vernicifluum*, 11 accessions of *Toxicodendron*, and 22 accessions of the tribe Rhoeae (Table 1) ranged from 0 to 0.126, from 0 to 0.129, from 0 to 0.036, respectively. Generally, intergenic spacers (average

π = 0.006, 0.009, 0.014 at the three taxonomic levels mentioned above) were found to be more variable than genes (average π = 0.001, 0.002, 0.005 at the three taxonomic levels mentioned above). Among the seven *T. vernicifluum* accessions, two gene regions (*rpl32* and *rps19*) and six intergenic regions (*trnF-ndhJ*, *rpl32-trnL*, *ccsA-ndhD*, *trnH-psbA*, *psbC-trnS*, and *trnL-trnF*) were identified as divergence hotspots based on the cutoff value of $\pi \geq 0.007$ (Figure 6). Among the 11 accessions of *Toxicodendron*, one gene region (rps19) and eight intergenic regions (*trnF-ndhJ*, *trnH-psbA*, *petD-rpoA*, *ccsA-ndhD*, *rpl32-trnL*, *atpF-atpH*, *trnL-trnF*, and *psbC-trnS*) were identified as divergence hotspots based on the cutoff value of $\pi \geq 0.013$ (Figure S3). Among the 22 accessions of the tribe Rhoeae, one gene region (psbM) and ten intergenic regions (*ccsA-ndhD*, *trnS-psbZ*, *petD-rpoA*, *ycf4-cemA*, *ndhG-ndhI*, *matK-rps16*, *trnD-trnY*, *trnL-trnF*, *ndhE-ndhG*, and *trnS-trnG*) were identified as divergence hotspots based on the cutoff value of $\pi \geq 0.002$ (Figure S4). Overall, the regions *trnF-ndhJ*, *rpl32-trnL*, *trnH-psbA*, *psbC-trnS*, and *rps19* were suitable for both phylogeographic studies of *T. vernicifluum* and phylogenetic studies of *Toxicodendron*, while the regions *ccsA-ndhD* and *trnL-trnF* were useful for evolutionary studies at all the three taxonomic levels. The mutational hotspots identified here also overlapped with those previously reported for six Anacardiaceae species [64], including *trnH-psbA*, *atpF-atpH*, *ccsA-ndhD*, *petD-rpoA*, and *trnL-trnF*. These hotspot regions could be utilized as potential molecular markers for reconstructing the phylogeny of *Toxicodendron* species and their relatives.

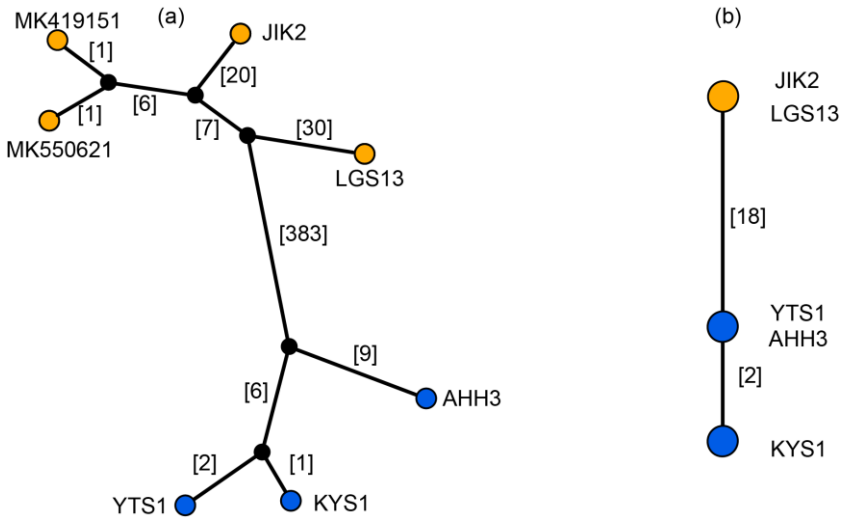


Figure 5. TCS network of the seven chloroplast (cp) genome sequences (**a**) and three nuclear ribosomal internal transcribed spacer (ITS) haplotypes (**b**) of *Toxicodendron vernicifluum*. The two networks were constructed by PopART 1.7. Numbers in brackets indicate the number of mutations between haplotypes. Samples from eastern and western China are marked in blue and orange, respectively. Note that two previously published cp genomes of *T. vernicifluum* (GenBank accession number: MK419151 and MK550621) are included in panel (**a**).

The hotspots of divergence identified above were also validated by the mVISTA analysis. We used the mVISTA program to plot the percentage of identity of seven *T. vernicifluum* individuals to investigate sequence divergence with YTS1 as a reference. As expected, a high similarity was found among the accessions of *T. vernicifluum*, with the IRs found to be more conserved than the LSC/SSC regions (Figure 7) [73,74]. The non-coding regions were significantly more variable than the coding regions. Consistent with the results of π value calculations, a high level of divergence was found for regions such as *ccsA-ndhD*, *trnH-psbA*, *rpl32-trnL*, and *trnF-ndhJ* between the individuals from eastern and western China. We also used the Mauve module to perform the synteny analysis. One local collinear block was detected and no rearrangement events and inversions were identified among the accessions of *T. vernicifluum* (Figure S5), *Toxicodendron* (Figure S6), and the tribe Rhoeae (Figure S7).

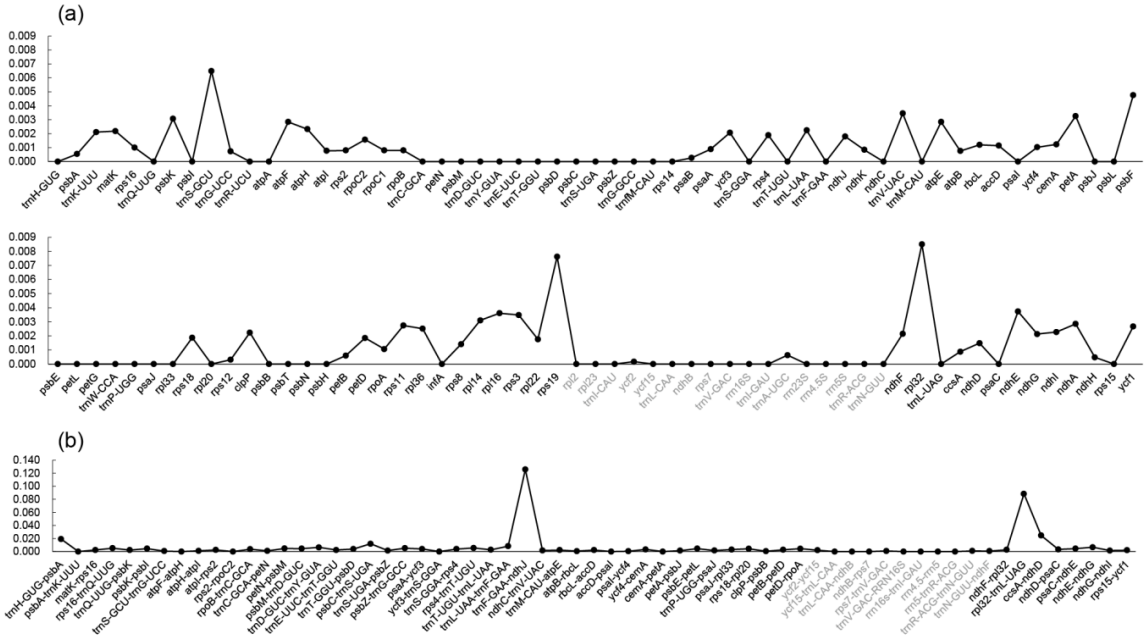


Figure 6. Nucleotide diversity (π) values estimated for 114 genes (**a**) and 63 intergenic regions (**b**) across the seven chloroplast genomes of *Toxicodendron vernicifluum* (GenBank accession number: OQ168006–OQ168010, MK419151, MK550621). Loci in the inverted repeats (IRs) are marked in gray. Note that the scales of the *y*-axis differ between (**a**,**b**).

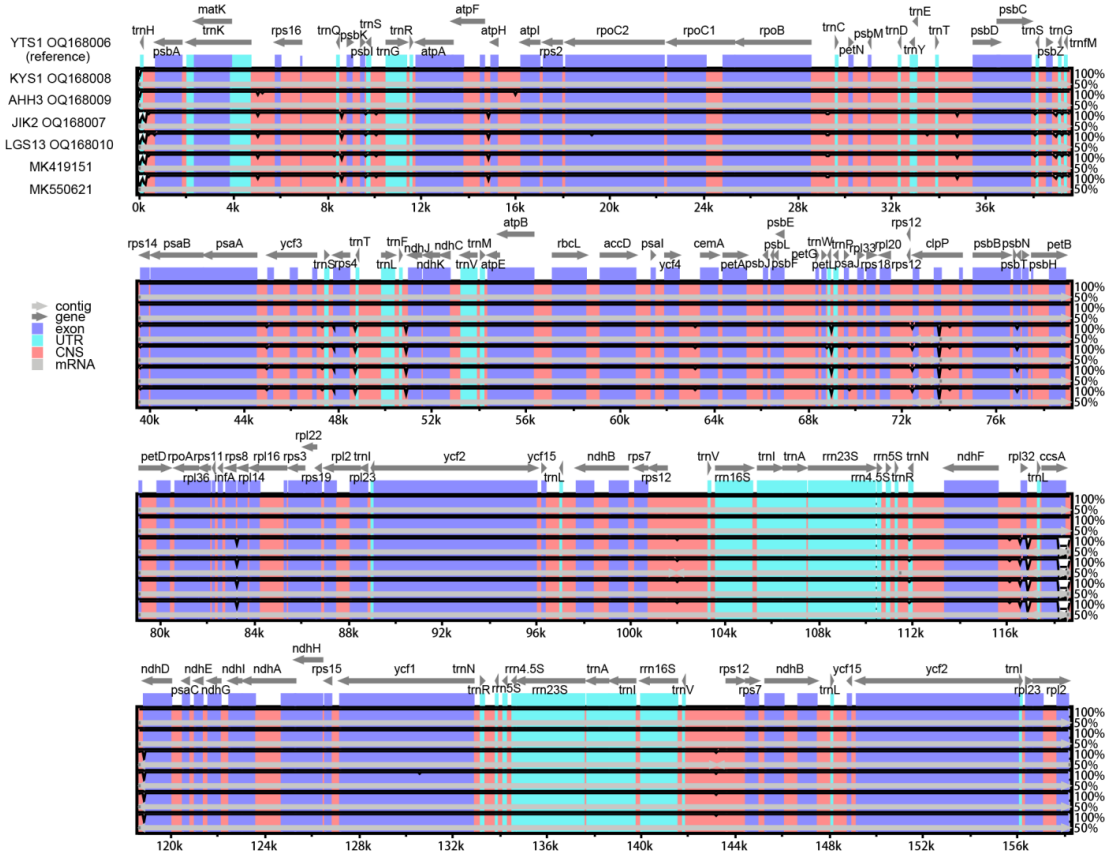


Figure 7. Sequence alignment of seven *Toxicodendron vernicifluum* chloroplast genomes using mVISTA with *T. vernicifluum* YTS1 as a reference. The vertical scale indicates the percent identity, ranging from 50% to 100%. The horizontal axis shows the location within the plastomes. Genome regions are color-coded as exon, intron, and untranslated regions (UTRs).

3.5. Expansion and Contraction of the IR Regions

The IR-SC border positions of the cp genomes of *T. vernicifluum* and the other four *Toxicodendron* species were highly conserved (Figure 8) [75]. The LSC/IRb junction was found between the genes *rps19* and *rpl2*. The IRb/SSC junction was found within the gene *ndhF*. The SSC/IRa junction was found within the gene *ycf1*. The IRa/LSC junction was found between the genes *rpl2* and *trnH*. Minor shifts of the IRa/LSC boundary were detected among *Toxicodendron* accessions. Specifically, the *trnH* gene was found to be 64 bp and 47 bp away from the IRa/LSC boundary for the *T. vernicifluum* individuals from eastern China and western China, respectively (Figure 8). Furthermore, the *trnH* gene was found to be 30–54 bp away from the IRa/LSC boundary for the other four *Toxicodendron* species (Figure 8).

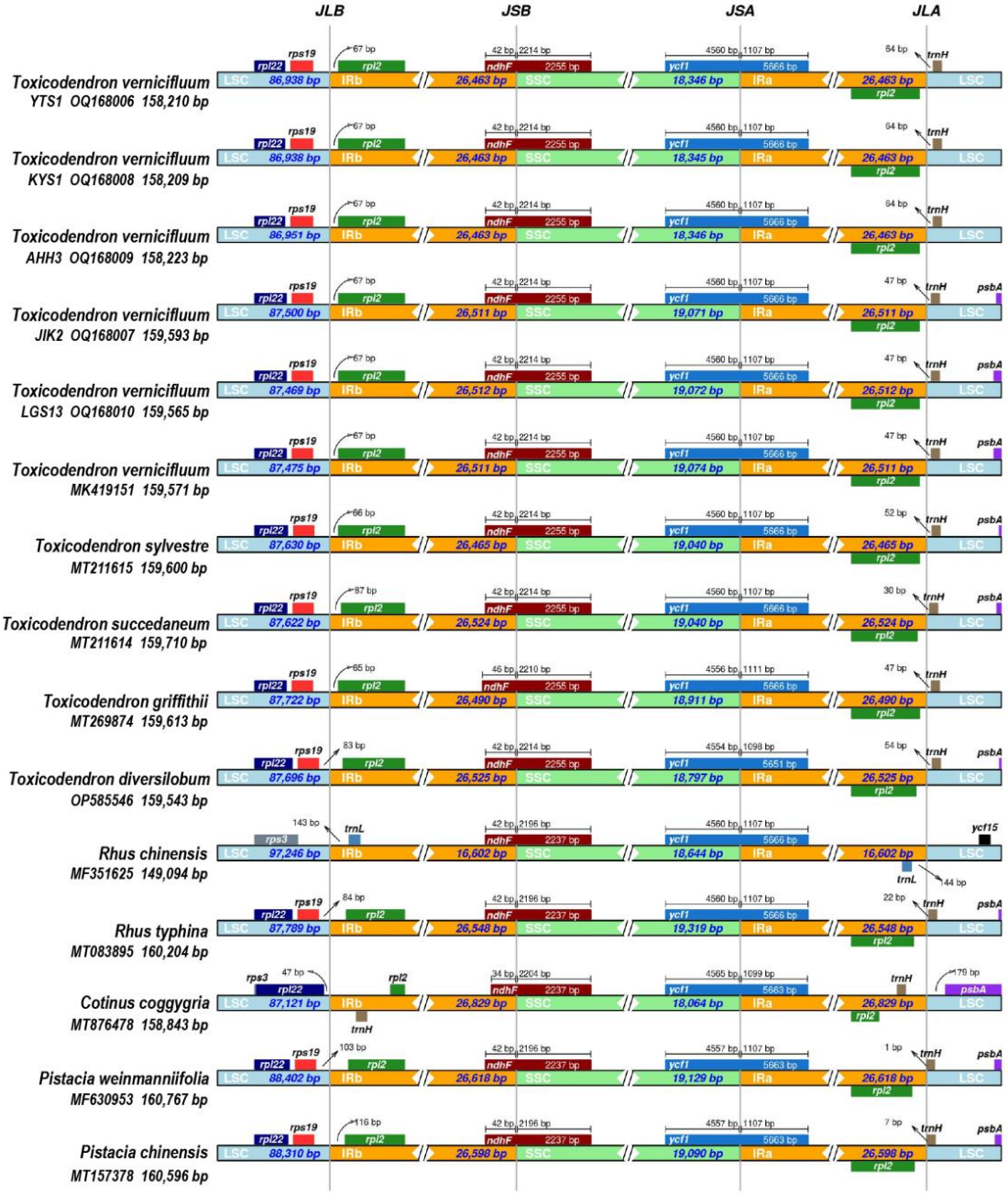


Figure 8. Comparison of inverted repeat (IR)-single-copy (SC) border positions among the chloroplast genomes of 15 accessions of the tribe Rhoeae. The sequence of *T. vernicifluum* MK550621 was not used because it differed from that of MK419151 by only two single nucleotide variants.

Compared to the species from other genera in the tribe Rhoeae, visible differences were detected regarding the lengths of IR regions (Table 1) and the SC/IR borders (Figure 8). Among those, *Rhus chinensis* presented the most significant difference from other species: its LSC/IRb border was located between the genes *rps3* and *trnL*, while its IRa/LSC border was located between the genes *trnL* and *ycf15*. This shift was mainly attributed to the loss of a long fragment (∼9800 bp in length) in the IR regions of *R. chinensis*, which contains genes such as *rpl2*, *rpl23*, *trnI-CAU*, and *ycf2* [29,64]. In addition, compared to other species, *rps19* was lost at the border of IRb/LSC and *trnH* was shifted from LSC to IRa in *Cotinus coggygria*.

3.6. Repeat Sequence Identification

For the *T. vernicifluum* individuals from eastern China, 68–69 SSRs were detected for each accession, including 43–44 mononucleotide SSRs, five dinucleotide SSRs, six trinucleotide SSRs, five tetranucleotide SSRs, one pentanucleotide SSR, and 7–9 compound SSRs (Table S3). For the *T. vernicifluum* individuals from western China, 66 SSRs were detected for each accession, including 45 mononucleotide SSRs, five dinucleotide SSRs, five trinucleotide SSRs, five tetranucleotide SSRs, one pentanucleotide SSR, and five compound SSRs. For the other four species of *Toxicodendron*, 71–82 SSRs were detected for each accession, including 46–56 mononucleotide SSRs, 4–5 dinucleotide SSRs, 4–5 trinucleotide SSRs, 4–5 tetranucleotide SSRs, one pentanucleotide SSR, and 10–13 compound SSRs. Overall, the two groups of *T. vernicifluum* had a similar number of SSRs, while the other four *Toxicodendron* species had more SSRs mainly because of their higher numbers of mononucleotide SSRs and compound SSRs.

Long-dispersed repeat sequences have been reported to play critical roles in genomic rearrangements and sequence variations of plastomes [76]. A total of 49 long dispersed repeats were detected for each accession of *T. vernicifluum* and the other four *Toxicodendron* species, with a length ranging from 30 to 78 bp (Table S4). Specifically, 20–21 forward repeats and 28 palindromic repeats were detected for each *T. vernicifluum* accession from eastern China; 22 forward repeats and 26 palindromic repeats were detected for each *T. vernicifluum* accession from western China; 21–22 forward repeats and 27–28 palindromic repeats were detected for each accession of the other four *Toxicodendron* species. Reverse repeats were only detected in the LSC region of *T. vernicifluum* accessions from western China, while complementary repeats were only detected in the IRs of *T. vernicifluum* accessions from eastern China. Furthermore, 46–47, 47, and 40–50 tandem repeats were detected for *T. vernicifluum* accession from eastern China, *T. vernicifluum* accession from western China, and accessions of the other four *Toxicodendron* species, respectively (Table S4).

3.7. Nuclear Ribosomal Internal Transcribed Spacer (ITS) Variation

A total of three ITS haplotypes were found for the five individuals of *T. vernicifluum*. The TCS network grouped them into eastern and western clades that were separated by 18 mutational steps (Figure 5b). Specifically, the two individuals from western China (JIK2 and LGS13) shared one ITS haplotype, while the other two individuals from eastern China (YTS1 and AHH3) shared another ITS haplotype that differed from the ITS haplotype of KYS1 by two mutational steps. The east-west divergence pattern recovered by ITS variation was consistent with the findings based on whole cp genome sequence variation (Figure 5a).

4. Conclusions

In this study, we sequenced five cp genomes of *T. vernicifluum* representing the wild individuals from eastern and western China. Our phylogenetic analyses based on protein-coding genes supported that the species split into two main clades: western China and eastern China lineages. Generally, chloroplast genomes of *T. vernicifluum* individuals from eastern and western China were highly conserved in terms of structure and gene content. However, obvious differences were still detected between them. The genome lengths of western China individuals were on average 1361 bp larger than that of eastern China individuals. The LSC, SSC, and two IR regions of western China individuals were also

found to be longer than those of eastern China individuals. Most of the SNPs and indels detected among the *T. vernicifluum* accessions occurred between the eastern and western lineages. Furthermore, complementary repeat sequences were only found in the individuals of eastern China while reverse repeats were only detected in the individuals from western China. Numerous mutational hotspots (e.g., *trnF-ndhJ*, *rpl32-trnL*, *ccsA-ndhD*, *trnH-psbA*, *psbC-trnS*, *trnL-trnF*, *rpl32*, and *rps19*) were also identified which can be used as potential molecular markers in phylogenetic analysis. The genomic resources presented in this study will be useful for further studies on evolutionary patterns and resource protection of *T. vernicifluum.*

Supplementary Materials: The following supporting information can be downloaded at: https://www.mdpi.com/article/10.3390/f14040818/s1, Figure S1: Phylogenetic trees inferred by the maximum likelihood (ML) approach for (a) sequence data partitioned by genes and (b) un-partitioned sequence data; Figure S2: Phylogenetic trees inferred by the Bayesian Inference (BI) approach for (a) sequence data partitioned by genes and (b) un-partitioned sequence data; Figure S3: Nucleotide diversity (π) among the complete chloroplast genome sequences of 11 accessions of *Toxicodendron*; Figure S4: Nucleotide diversity (π) among the complete chloroplast genome sequences of 22 accessions of the tribe Rhoeae; Figure S5: Gene map and MAUVE alignment of six chloroplast genomes of *Toxicodendron vernicifluum*; Figure S6: Gene map and MAUVE alignment of five chloroplast genomes of *Toxicodendron*; Figure S7: Gene map and MAUVE alignment of six chloroplast genomes of the tribe Rhoeae; Table S1: Geographic information of the five newly sequenced *Toxicodendron vernicifluum* samples in this study; Table S2: Optimal partitioning strategies and evolutionary models selected by ModelFinder using the Bayesian Information Criterion (BIC); Table S3: Numbers of simple sequence repeats (SSRs) of the 11 *Toxicodendron* plastomes; Table S4: Numbers of long dispersed repeats and tandem repeats in the 11 *Toxicodendron* plastomes.

Author Contributions: L.W., Y.F. and F.Z. conceived and designed this research. L.W., Y.L., Y.P. and F.Z. collected samples. L.W. performed experiments. L.W., N.H., Y.L. and X.Z. analyzed the data. L.W. wrote the original draft. X.Z., Y.L., Y.P. and Y.F. reviewed the draft. Y.F. and F.Z. supervised the project. All authors have read and agreed to the published version of the manuscript.

Funding: This research was supported by the Shaanxi Innovation Capability Support Plan "Fenxi Inspection and Testing Shared Experimental Base" (2023-CX-PT-08), Research and Development Program of Key Technologies for Conservation and Restoration of Two Wild Plant Species with Extremely Small Populations in the Mingxi County (22100210), the Natural Science Foundation from Education Commission of Anhui Province (2022AH050369), the National Natural Science Foundation of China (32201375), the China Postdoctoral Science Foundation (2020M681629), the Jiangsu Postdoctoral Research Foundation (2021K038A), and the Priority Academic Program Development of Jiangsu Higher Education Institutions (PAPD). L. W. was supported by the China Scholarship Council (202008320479).

Institutional Review Board Statement: Not applicable.

Informed Consent Statement: Not applicable.

Data Availability Statement: The newly generated chloroplast genome sequences of *Toxicodendron vernicifluum* were submitted to NCBI under GenBank accession numbers OQ168006–OQ168010. The nuclear ribosomal internal transcribed spacer (ITS) data were available from Zenodo: https://doi.org/10.5281/zenodo.7792326.

Acknowledgments: We thank numerous Chinese foresters and natural resource managers for their help in the sample collection.

Conflicts of Interest: The authors declare no conflict of interest.

References

1. Suzuki, M.; Noshiro, S.; Tanaka, T. Origin of urushi (*Toxicodendron vernicifluum*) in the neolithic Jomon period of Japan. *Bull. Nat. Mus. Jpn. Hist.* **2014**, *187*, 49–70.
2. Zhao, M.; Liu, C.; Zheng, G. Comparative studies of bark structure, lacquer yield and urushiol content of cultivated *Toxicodendron vernicifluum* varieties. *New. Zeal. J. Bot.* **2013**, *51*, 13. [CrossRef]

3. Hong, D.H.; Han, S.B.; Lee, C.W.; Park, S.H.; Jeon, Y.J.; Kim, M.J.; Kwak, S.S.; Kim, H.M. Cytotoxicity of urushiols isolated from sap of Korean lacquer tree (*Rhus vernicifera* Stokes). *Arch. Pharm. Res.* **1999**, *22*, 638–641. [CrossRef] [PubMed]
4. Cho, N.; Choi, J.H.; Yang, H. Neuroprotective and anti-inflammatory effects of flavonoids isolated from *Rhus verniciflua* in neuronal HT22 and microglial BV2 cell lines. *Food Chem. Toxicol.* **2012**, *50*, 1940–1945. [CrossRef]
5. Suzuki, M.; Yonekura, K.; Noshiro, S. Distribution and habitat of *Toxicodendron vernicifluum* (Stokes) F. A. Barkl. (*Anacardiaceae*) in China. *Jpn. J. Histor. Bot.* **2007**, *15*, 58–62.
6. Noshiro, S.; Suzuki, M. *Rhus verniciflua* Stokes grew in Japan since the Early Jomon Period. *Jpn. J. Histor. Bot.* **2004**, *12*, 3–11.
7. Wang, L.; Li, Y.; Noshiro, S.; Suzuki, M.; Arai, T.; Kobayashi, K.; Xie, L.; Zhang, M.Y.; He, N.; Fang, Y.M.; et al. Stepped geomorphology shaped the phylogeographic structure of a widespread tree species (*Toxicodendron vernicifluum*, *Anacardiaceae*) in East Asia. *Front. Plant Sci.* **2022**, *13*, 920054. [CrossRef]
8. Moore, M.J.; Soltis, P.S.; Bell, C.D.; Burleigh, J.G.; Soltis, D.E. Phylogenetic analysis of 83 plastid genes further resolves the early diversification of eudicots. *Proc. Natl. Acad. Sci. USA* **2010**, *107*, 4623–4628. [CrossRef]
9. Liu, L.; Wang, Y.; He, P.; Li, P.; Lee, J.; Soltis, D.E. Chloroplast genome analyses and genomic resource development for epilithic sister genera *Oresitrophe* and *Mukdenia* (*Saxifragaceae*), using genome skimming data. *BMC Genom.* **2018**, *19*, 235. [CrossRef]
10. Daniell, H.; Lin, C.S.; Yu, M.; Chang, W.J. Chloroplast genomes: Diversity, evolution, and applications in genetic engineering. *Genome Biol.* **2016**, *17*, 134. [CrossRef]
11. Meyer, C.P.; Paulay, G. DNA barcoding: Error rates based on comprehensive sampling. *PLoS Biol.* **2005**, *3*, e422. [CrossRef] [PubMed]
12. Birky, C.W. Uniparental inheritance of mitochondrial and chloroplast genes: Mechanisms and evolution. *Proc. Natl. Acad. Sci. USA* **1995**, *92*, 11331–11338. [CrossRef] [PubMed]
13. Dong, W.; Xu, C.; Cheng, T.; Lin, K.; Zhou, S. Sequencing angiosperm plastid genomes made easy: A complete set of universal primers and a case study on the phylogeny of Saxifragales. *Genome Biol. Evol.* **2013**, *5*, 989–997. [CrossRef] [PubMed]
14. Alkan, C.; Sajjadian, S.; Eichler, E.E. Limitations of next-generation genome sequence assembly. *Nat. Methods* **2011**, *8*, 61–65. [CrossRef] [PubMed]
15. Song, H.; Liu, F.; Li, Z.; Xu, Q.; Chen, Y.; Yu, Z.; Chen, N.S. Development of a high-resolution molecular marker for tracking *Phaeocystis globosa* genetic diversity through comparative analysis of chloroplast genomes. *Harmful Algae* **2020**, *99*, 101911. [CrossRef] [PubMed]
16. Xu, K.; Lin, C.; Lee, S.Y.; Mao, L.; Meng, K. Comparative analysis of complete *Ilex* (*Aquifoliaceae*) chloroplast genomes: Insights into evolutionary dynamics and phylogenetic relationships. *BMC Genom.* **2022**, *23*, 203. [CrossRef]
17. Huang, D.; Hefer, C.; Kolosova, N.; Douglas, C.; Cronk, Q. Whole plastome sequencing reveals deep plastid divergence and cytonuclear discordance between closely related balsam poplars, *Populus balsamifera* and *P. trichocarpa* (*Salicaceae*). *New Phytol.* **2014**, *204*, 693–703. [CrossRef]
18. Li, Y.; Wang, L.; Zhang, X.; Kang, H.; Liu, C.; Mao, L.; Fang, Y. Extensive sharing of chloroplast haplotypes among East Asian Cerris oaks: The imprints of shared ancestral polymorphism and introgression. *Ecol. Evol.* **2022**, *12*, e9142. [CrossRef]
19. Fahey, P.S.; Fowler, R.M.; Udovicic, F.; Cantrill, D.J.; Bayly, M.J. Use of plastid genome sequences in phylogeographic studies of tree species can be misleading without comprehensive sampling of co-occurring, related species. *Tree Genet. Genomes* **2021**, *17*, 43. [CrossRef]
20. Min, T.; Barfod, A. Anacardiaceae. In *Flora of China*; Wu, Z., Raven, P.H., Hong, D., Eds.; Science Press: Beijing, China; Missouri Botanical Garden Press: St. Louis, MA, USA, 2008; Volume 11, pp. 335–357.
21. Wang, L.; He, N.; Li, Y.; Fang, Y.; Zhang, F. The complete chloroplast genome sequence of *Toxicodendron succedaneum* (*Anacardiaceae*). *Mitochondrial DNA Part B* **2020**, *5*, 1956–1957. [CrossRef]
22. Li, Y.; Tang, Y.; Wu, T. The complete chloroplast genome of *Toxicodendron griffithii*. *Mitochondrial DNA Part B* **2020**, *5*, 2211–2212. [CrossRef]
23. Weisberg, A.J.; Kim, G.; Westwood, J.H.; Jelesko, J.G. Sequencing and de novo assembly of the *Toxicodendron radicans* (*poison ivy*) transcriptome. *Genes* **2017**, *8*, 317. [CrossRef] [PubMed]
24. Xu, L.; Zhou, N.; Zhao, S.; Li, J.; Pei, X.; Yu, J.; Guo, D. The complete plastid genome of *Cotinus coggygria* and phylogenetic analysis of the *Anacardiaceae*. *Genet. Mol. Biol.* **2021**, *44*, 3. [CrossRef] [PubMed]
25. Rossini, B.C.; de Moraes, M.L.T.; Marino, C.L. Complete chloroplast genome of *Myracrodruon urundeuva* and its phylogenetics relationships in *Anacardiaceae* family. *Physiol. Mol. Biol. Plants* **2021**, *27*, 801–814. [CrossRef] [PubMed]
26. Zarei, A.; Ebrahimi, A.; Mathur, S.; Lawson, S. The first complete chloroplast genome sequence and phylogenetic analysis of pistachio (*Pistacia vera*). *Diversity* **2022**, *14*, 577. [CrossRef]
27. Xu, Y.; Zhang, Y.; Ren, Z. Complete chloroplast genome of *Pistacia chinensis* Bunge (*Anacardiaceae*: Rhoideae), an important economical and ornamental plant. *Mitochondrial DNA Part B* **2020**, *5*, 1931–1932. [CrossRef]
28. Xu, Y.; Wen, J.; Su, X.; Ren, Z. Variation among the complete chloroplast genomes of the sumac species *Rhus chinensis*: Reannotation and comparative analysis. *Genes* **2022**, *13*, 1936. [CrossRef]
29. Barrett, C.F. Plastid genomes of the North American *Rhus integrifolia-ovata* complex and phylogenomic implications of inverted repeat structural evolution in *Rhus* L. *PeerJ* **2020**, *8*, e9315. [CrossRef]
30. Zong, D.; Qiao, Z.; Zhou, J.; Li, P.; Gan, P.; Ren, M.; He, C. Chloroplast genome sequence of triploid Toxicodendron vernicifluum and comparative analyses with other lacquer chloroplast genomes. *BMC Genom.* **2023**, *24*, 56. [CrossRef]

31. Doyle, J.J. A rapid DNA isolation procedure for small quantities of fresh leaf tissue. *Phytochem. Bull.* **1987**, *19*, 11–15.
32. Chen, Y.; Chen, Y.; Shi, C.; Huang, Z.; Zhang, Y.; Li, S.; Chen, Q. SOAPnuke: A MapReduce acceleration-supported software for integrated quality control and preprocessing of high-throughput sequencing data. *GigaScience* **2018**, *7*, gix120. [CrossRef] [PubMed]
33. Jin, J.J.; Yu, W.B.; Yang, J.B.; Song, Y.; de Pamphilis, W.C.; Yi, T.S.; Li, D.Z. GetOrganelle: A fast and versatile toolkit for accurate de novo assembly of organelle genomes. *Genome Biol.* **2020**, *21*, 241. [CrossRef] [PubMed]
34. Bankevich, A.; Nurk, S.; Antipov, D.; Gurevich, A.A.; Dvorkin, M.; Kulikov, A.S.; Lesin, V.M.; Nikolenko, S.I.; Pham, S.; Prjibelski, A.D.; et al. SPAdes: A new genome assembly algorithm and its applications to single-cell sequencing. *J. Comput. Biol.* **2012**, *19*, 455–477. [CrossRef] [PubMed]
35. Langmead, B.; Salzberg, S.L. Fast gapped-read alignment with Bowtie 2. *Nat. Methods* **2012**, *9*, 357–359. [CrossRef]
36. Camacho, C.; Coulouris, G.; Avagyan, V.; Ma, N.; Papadopoulos, J.; Bealer, K.; Madden, T.L. BLAST+: Architecture and applications. *BMC Bioinform.* **2009**, *10*, 421. [CrossRef]
37. Wick, R.R.; Schultz, M.B.; Zobel, J.; Holt, K.E. Bandage: Interactive visualization of de novo genome assemblies. *Bioinformatics* **2015**, *31*, 3350–3352. [CrossRef]
38. Liu, C.; Shi, L.; Zhu, Y.; Chen, H.; Zhang, J.; Lin, X.; Guan, X. CpGAVAS, an integrated web server for the annotation, visualization, analysis, and GenBank submission of completely sequenced chloroplast genome sequences. *BMC Genom.* **2012**, *13*, 715. [CrossRef]
39. Liu, S.; Ni, Y.; Li, J.; Zhang, X.; Yang, H.; Chen, H.; Liu, C. CPGView: A package for visualizing detailed chloroplast genome structures. *Mol. Ecol. Resour.* **2023**, *23*, 694–704. [CrossRef]
40. Nie, Z.L.; Sun, H.; Meng, Y.; Wen, J. Phylogenetic analysis of *Toxicodendron* (*Anacardiaceae*) and its biogeographic implications on the evolution of north temperate and tropical intercontinental disjunctions. *J. Syst Evol.* **2009**, *47*, 416–430. [CrossRef]
41. Angiosperm Phylogeny Group; Chase, M.W.; Christenhusz, M.J.; Fay, M.F.; Byng, J.W.; Judd, W.S.; Stevens, P.F. An update of the Angiosperm Phylogeny Group classification for the orders and families of flowering plants: APG IV. *Bot. J. Linn. Soc.* **2016**, *181*, 1–20. [CrossRef]
42. Zhang, D.; Gao, F.; Jakovlić, I.; Zou, H.; Zhang, J.; Li, W.X.; Wang, G.T. PhyloSuite: An integrated and scalable desktop platform for streamlined molecular sequence data management and evolutionary phylogenetic studies. *Mol. Ecol. Resour.* **2020**, *20*, 348–355. [CrossRef] [PubMed]
43. Kalyaanamoorthy, S.; Minh, B.Q.; Wong, T.K.F.; Haeseler, A.V.; Jermiin, L.S. ModelFinder: Fast model selection for accurate phylogenetic estimates. *Nat. Methods* **2017**, *14*, 587–589. [CrossRef] [PubMed]
44. Nguyen, L.T.; Schmidt, H.A.; von Haeseler, A.; Minh, B.Q. IQ-TREE: A fast and effective stochastic algorithm for estimating maximum-likelihood phylogenies. *Mol. Biol. Evol.* **2015**, *32*, 268–274. [CrossRef] [PubMed]
45. Minh, B.Q.; Nguyen, M.A.; von Haeseler, A. Ultrafast approximation for phylogenetic bootstrap. *Mol. Biol. Evol.* **2013**, *30*, 1188–1195. [CrossRef] [PubMed]
46. Ronquist, F.; Teslenko, M.; Van Der Mark, P.; Ayres, D.L.; Darling, A.; Höhna, S.; Larget, B.; Liu, L.; Suchard, M.; Huelsenbeck, J.P. MrBayes 3.2: Efficient Bayesian phylogenetic inference and model choice across a large model space. *Syst. Biol.* **2012**, *61*, 539–542. [CrossRef]
47. Bouckaert, R.; Vaughan, T.G.; Barido-Sottani, J.; Duchêne, S.; Fourment, M.; Gavryushkina, A.; Drummond, A.J. BEAST 2.5: An advanced software platform for Bayesian evolutionary analysis. *PLoS Comput. Biol.* **2019**, *15*, e1006650. [CrossRef]
48. Jiang, Y.; Gao, M.; Meng, Y.; Wen, J.; Ge, X.J.; Nie, Z.L. The importance of the North Atlantic land bridges and eastern Asia in the post-Boreotropical biogeography of the Northern Hemisphere as revealed from the poison ivy genus (*Toxicodendron*, *Anacardiaceae*). *Mol. Phylogenet. Evol.* **2019**, *139*, 106561. [CrossRef]
49. Manchester, S.R. Fruits and seeds of the middle Eocene Nut Beds flora, Clarno Formation, Oregon. *Palaeontogr. Am.* **1994**, *58*, 1–205.
50. MacGinitie, H.D. *Fossil Plants of the Florissant Beds*; Carnegie Institute: Washington, DC, USA, 1953.
51. Rambaut, A.; Drummond, A.J.; Xie, D.; Baele, G.; Suchard, M.A. Posterior summarisation in Bayesian phylogenetics using tracer 1.7. *Syst. Biol.* **2018**, *67*, 901–904. [CrossRef]
52. Katoh, K.; Standley, D.M. MAFFT multiple sequence alignment software version 7: Improvements in performance and usability. *Mol. Biol. Evol.* **2013**, *30*, 772–780. [CrossRef]
53. Rozas, J.; Ferrer-Mata, A.; Sánchez-DelBarrio, J.C.; Guirao-Rico, S.; Librado, P.; Ramos-Onsins, S.E.; Sánchez-Gracia, A. DnaSP 6: DNA sequence polymorphism analysis of large datasets. *Mol. Biol. Evol.* **2017**, *34*, 3299–3302. [CrossRef] [PubMed]
54. Leigh, J.W.; Bryant, D. POPART: Full-feature software for haplotype network construction. *Methods Ecol. Evol.* **2015**, *6*, 1110–1116. [CrossRef]
55. Frazer, K.A.; Pachter, L.; Poliakov, A.; Rubin, E.M.; Dubchak, I. VISTA: Computational tools for comparative genomics. *Nucleic Acids Res.* **2004**, *32*, 273–279. [CrossRef]
56. Darling, A.E.; Mau, B.; Perna, N.T. progressiveMauve: Multiple genome alignment with gene gain, loss and rearrangement. *PLoS ONE* **2010**, *5*, e11147. [CrossRef]
57. Kearse, M.; Moir, R.; Wilson, A.; Stones-Havas, S.; Cheung, M.; Sturrock, S.; Buxton, S.; Cooper, A.; Markowitz, S.; Duran, C.; et al. Geneious Basic: An integrated and extendable desktop software platform for the organization and analysis of sequence data. *Bioinformatics* **2012**, *28*, 1647–1649. [CrossRef]

58. Amiryousefi, A.; Hyvönen, J.; Poczai, P. IRscope: An online program to visualize the junction sites of chloroplast genomes. *Bioinformatics* **2018**, *34*, 3030–3031. [CrossRef] [PubMed]
59. Kurtz, S.; Choudhuri, J.V.; Ohlebusch, E.; Schleiermacher, C.; Stoye, J.; Giegerich, R. REPuter: The manifold applications of repeat analysis on a genomic scale. *Nucleic Acids Res.* **2001**, *29*, 4633–4642. [CrossRef]
60. Benson, G. Tandem repeats finder: A program to analyze DNA sequences. *Nucleic Acids Res.* **1999**, *27*, 573–580. [CrossRef]
61. Beier, S.; Thiel, T.; Münch, T.; Scholz, U.; Mascher, M. MISA-web: A web server for microsatellite prediction. *Bioinformatics* **2017**, *33*, 2583–2585. [CrossRef]
62. Thiel, T.; Michalek, W.; Varshney, R.; Graner, A. Exploiting EST databases for the development and characterization of gene-derived SSR-markers in barley (*Hordeum vulgare* L.). *Theor. Appl. Genet.* **2003**, *106*, 411–422. [CrossRef]
63. Hall, T.A. BioEdit: A user-friendly biological sequence alignment editor and analysis program for windows 95/98/NT. *Nucleic Acids Symp. Ser.* **1999**, *41*, 95–98.
64. Wang, L.; He, N.; Li, Y.; Fang, Y.M.; Zhang, F.L. Complete chloroplast genome sequence of Chinese lacquer tree (*Toxicodendron vernicifluum*, *Anacardiaceae*) and its phylogenetic significance. *BioMed Res. Int.* **2020**, *2020*, 9014873. [CrossRef] [PubMed]
65. Zhong, Y.; Zong, D.; Zhou, A.; He, X.F.; He, C.Z. The complete chloroplast genome of the *Toxicodendron vernicifluum* cv. Dahongpao, an elite natural triploid lacquer tree. *Mitochondrial DNA B* **2019**, *4*, 1227–1228. [CrossRef]
66. He, N.; Wang, L.; Li, Y.; Fang, Y.; Zhang, F. The complete chloroplast genome sequence of *Toxicodendron sylvestre* (*Anacardiaceae*). *Mitochondrial DNA Part B* **2020**, *5*, 2008–2009. [CrossRef]
67. Wicke, S.; Schneeweiss, G.M.; dePamphilis, C.W.; Müller, K.F.; Quandt, D. The evolution of the plastid chromosome in land plants: Gene content, gene order, gene function. *Plant Mol. Biol.* **2011**, *76*, 273–297. [CrossRef] [PubMed]
68. Hohmann, N.; Wolf, E.M.; Rigault, P.; Zhou, W.; Kiefer, M.; Zhao, Y.; Koch, M.A. *Ginkgo biloba*'s footprint of dynamic Pleistocene history dates back only 390,000 years ago. *BMC Genom.* **2018**, *9*, 299. [CrossRef]
69. Renoult, J.P.; Kjellberg, F.; Grout, C.; Santoni, S.; Khadari, B. Cyto-nuclear discordance in the phylogeny of *Ficus* section Galoglychia and host shifts in plant-pollinator associations. *BMC Evol. Biol.* **2009**, *9*, 248. [CrossRef]
70. Luo, D.; Xu, B.; Li, Z.M.; Sun, H. Biogeographical divides delineated by the three-step landforms of China and the East China Sea: Insights from the phylogeography of *Kerria japonica*. *J. Biogeogr.* **2021**, *48*, 372–385. [CrossRef]
71. Wang, W.; Chen, S.; Zhang, X. Whole-genome comparison reveals heterogeneous divergence and mutation hotspots in chloroplast genome of *Eucommia ulmoides* Oliver. *Int. J. Mol. Sci.* **2018**, *19*, 1037. [CrossRef]
72. Park, I.; Yang, S.; Kim, W. Sequencing and comparative analysis of the chloroplast genome of *Angelica polymorpha* and the development of a novel indel marker for species identification. *Molecules* **2019**, *24*, 1038. [CrossRef]
73. Huang, Y.; Wang, J.; Yang, Y. Phylogenomic analysis and dynamic evolution of chloroplast genomes in Salicaceae. *Front. Plant Sci.* **2017**, *8*, 1050. [CrossRef] [PubMed]
74. Liu, W.; Kong, H.; Zhou, J. Complete chloroplast genome of *Cercis chuniana* (*Fabaceae*) with structural and genetic comparison to six species in Caesalpinioideae. *Int. J. Mol. Sci.* **2018**, *19*, 1286. [CrossRef] [PubMed]
75. Zhu, A.; Guo, W.; Gupta, S. Evolutionary dynamics of the plastid inverted repeat: The effects of expansion, contraction, and loss on substitution rates. *New Phytol.* **2016**, *209*, 1747–1756. [CrossRef] [PubMed]
76. Weng, M.L.; Blazier, J.C.; Govindu, M.; Jansen, R.K. Reconstruction of the ancestral plastid genome in Geraniaceae reveals a correlation between genome rearrangements, repeats, and nucleotide substitution rates. *Mol. Biol. Evol.* **2014**, *31*, 645–659. [CrossRef] [PubMed]

Disclaimer/Publisher's Note: The statements, opinions and data contained in all publications are solely those of the individual author(s) and contributor(s) and not of MDPI and/or the editor(s). MDPI and/or the editor(s) disclaim responsibility for any injury to people or property resulting from any ideas, methods, instructions or products referred to in the content.

forests

MDPI

Article

Investigation of Water Distribution and Mobility Dynamics in Recalcitrant *Quercus acutissima* Seeds during Desiccation Using Magnetic Resonance Methods

Haiyan Chen and Yongbao Shen *

Collaborative Innovation Centre of Sustainable Forestry in Southern China, College of Forestry, Nanjing Forestry University, Nanjing 210037, China
* Correspondence: ybshen@njfu.edu.cn

Abstract: Recalcitrant seed vigor is closely related to seed moisture, so how do the water distribution and status change during seed drying? In this study, we investigated the association between water content (WC) and germination of *Quercus acutissima* seeds and used nuclear magnetic resonance (NMR) to monitor the water dynamics during seed drying. Results showed that freshly dispersed seeds had 38.8% WC, but drying to 14.8% WC resulted in a complete loss of vigor. Magnetic resonance images (MRI) reveal that the embryonic axis had the highest WC and the fastest rate of water loss, and seeds lost water from the embryonic axis to the apex and from the center to the end of cotyledons during desiccation. According to low-field NMR results, the proportion of free water in fresh seeds was the highest at 55%, followed by bound water at 10% and immobile water at 35%. During drying, the bound water and free water of seeds were lost simultaneously, and free water was lost most when the seeds died. Our results revealed that *Q. acutissima* seeds are highly sensitive to desiccation and that the water loss sites of the seeds were at the micropyle and scar. During desiccation, the bound water could not be retained, and the water balance in the seeds was broken, eventually leading to seed death.

Keywords: recalcitrant seeds; water loss site; water migration rule; MRI; NMR

check for updates

Citation: Chen, H.; Shen, Y. Investigation of Water Distribution and Mobility Dynamics in Recalcitrant *Quercus acutissima* Seeds during Desiccation Using Magnetic Resonance Methods. *Forests* **2023**, *14*, 738. https://doi.org/10.3390/f14040738

Academic Editor: Patrizia Trifilò

Received: 27 February 2023
Revised: 25 March 2023
Accepted: 2 April 2023
Published: 4 April 2023

Copyright: © 2023 by the authors. Licensee MDPI, Basel, Switzerland. This article is an open access article distributed under the terms and conditions of the Creative Commons Attribution (CC BY) license (https://creativecommons.org/licenses/by/4.0/).

1. Introduction

According to the water content of the seed when harvested and the response of seed vigor to desiccation, seeds can be categorized into orthodox, recalcitrant, and intermediate seeds [1,2]. The water content and water status of seeds are significant determinants of seed longevity and are closely related to the desiccation tolerance of the seeds [3]. Orthodox seeds can be dried to low WC (3%–7%) without loss of viability, and their longevity is prolonged with the decrease in WC and storage temperatures [4]. It has been reported that 8% of the world's seed plants produce desiccation-sensitive seeds [5]. Unlike orthodox seeds, recalcitrant seeds remain sensitive to desiccation both during development and after they are shed from the parent plant [6]. They do not undergo maturation drying, are typically shed at a relatively high WC (30%–65%), and suffer lethal damage when they lose only a small proportion of water [7]. Water is the mediator of seed physiological metabolism, and water status is essential for biological activity [8]. It is generally believed that seeds have two states of water: free water and bound water. In living organisms, bound and free water exist in different proportions yet maintain a dynamic balance. It has been shown that the survival and effectiveness of orthodox seeds depend on the ability of the cells to retain bound water [9]. In addition, it was speculated that desiccation-sensitive seeds might lack water tightly bound to macromolecules (or cannot be maintained after drying), but there was not enough evidence [10]. High sensitivity to water loss is a significant factor affecting the storage and long-term preservation of recalcitrant seeds, but

little is known at present regarding the changes in their water distribution and status in recalcitrant seeds during drying.

Recalcitrant seeds are typically characterized by larger size and thinner seed coats [11]. In addition, it was found that some specific structures of the seed coat of recalcitrant seeds can reduce the risk of seed death after dispersal. Xia [12] discovered that the morphological structure of the seed coat of *Quercus* species affects the pace of water entrance and exit, with a smaller scar drying more slowly. Depending on the environment in which the seeds are dispersed, *Aesculus chinensis* seeds may have a thick waxy layer covering the seed coat to minimize water loss [13]. However, in the classical sense, these characteristics help to avoid desiccation rather than tolerate desiccation [14]. Recalcitrant seeds are still at risk of water loss and death after prolonged drying. Therefore, it is ecologically vital to investigate the sites of seed water loss during drying.

MRI and LF-NMR provide a non-destructive, real-time visualization technology to monitor the water content, status, movement, and spatial distribution of seeds [15,16]. MRI is the most advanced imaging technique to investigate the internal anatomy of organisms [17]. However, only a few studies have been applied to the changing rules of water migration during seed drying. Ishida [18] used MRI to visualize the drying process of *Oryza sativa* seeds at different temperatures and investigated the water reduction in different parts of the seeds [18]. Song [19] explored the water migration of chestnut seeds during storage based on MRI and discovered that water was lost from the cotyledons faster than from the embryonic axis [19]. LF-NMR employs the spin relaxation properties of hydrogen nuclei in a magnetic field to explain, from a microscopic standpoint, the status and migration rule of water in a sample via the variation in relaxation time [20]. As a novel nondestructive testing technology, LF-NMR provides an excellent opportunity to visualize the changes in water status within the seed tissue during drying and has been widely used. Jiang [20] found differences in water status changes during the dehydration of orthodox and recalcitrant seeds using NMR [21]. Sun [21] found that there were three water statuses in Ginkgo biloba seeds, namely bound, immobile, and free water, and the change of free water during drying was more significant [22]. Jin [22] found that the drying treatment removed almost all of the free water and most of the immobile water during the drying of walnuts and had no significant effect on the content bound water and oil [23].

Quercus acutissima Carruth is a temperate deciduous broad-leaved forest tree native to East Asia, widespread in southeastern China. It is one of the most economically and ecologically valuable tree species in China [24,25]. Therefore, the protection, cultivation, and utilization of *Q. acutissima* are essential. *Q. acutissima* seeds are typical temperate recalcitrant seeds that are difficult to store for more than one year after they mature and disperse [26]. Presently, most research focuses on the physiological and biochemical changes of recalcitrant seeds during desiccation [27–29]. In order to reduce the risk of death from water loss once recalcitrant seeds mature and disperse, it is vital to figure out the sites of seed water loss and the relationship between changes in water status during drying and desiccation sensitivity.

In this study, we used nuclear magnetic resonance and scanning electron microscopy (SEM) to investigate the water loss of *Q. acutissima* seeds by drying. In this study, we used nuclear magnetic resonance and scanning electron microscopy (SEM) to study the water loss of *Q. acutissima* seeds by drying. The objectives were (1) to establish the relationship between WC and germination of *Q. acutissima* seeds; (2) to understand the water distribution and the water loss sites of *Q. acutissima* seeds by SEM of the seed coat and MRI; (3) to utilize LF-NMR to comprehend the changing rules of water status and content in the drying process of recalcitrant seeds, combined with the changes in seed germination rate, to study their relationship with the desiccation sensitivity of seeds.

2. Materials and Methods

2.1. Seed Collection and Conditioning

In mid-November 2021, *Quercus acutissima* seeds were harvested from the practice forest farm of Nanjing Forestry University (119°12′58″ E, 32°7′26″ N). Water selection was performed to remove insect-infested grain after the seeds were collected, and seeds without mechanical damage were chosen for testing.

2.2. Seed Drying

Three replicates of 100 similar-sized seeds (the longitudinal and transverse diameters were approximately 2.2 cm and 2.1 cm, respectively) were selected and placed in a sealed bag containing silica gel (seed to silica gel mass ratio of approximately 1:3, with all seeds buried in the silica gel). The silica gel was replaced when the color changed from dark blue to pink. During the first 24 h of drying, the seeds were weighed every 2 h; after drying for 24 h, the seeds were weighed every 12 h to monitor the change in seed water content in real-time. Samples were taken whenever seed WC dropped by 3%, using the initial WC as a control (CK); each sample was repeated three times.

2.2.1. Determination of Initial Water Content

The initial water content of the seeds was measured using the constant low-temperature oven drying method, following the regulations of the International Seed Testing Association [30]. We weighed the aluminium case with the lid ($M1$), then cut ten whole *Q. acutissima* seeds into 3–5 mm slices and evenly placed 5–8 g of these slices in a dried and weighed aluminium box with the lid ($M2$). After drying the sample for 17 h at 103 °C in a constant temperature oven, we removed it and placed it in a desiccator for 30 min to cool before weighing it with the box ($M3$). The seed WC was calculated using the following formula:

$$WC(\%) = (M2 - M3)/(M2 - M1) \times 100\%$$

2.2.2. Determination of Relative Water Content

According to the equation described by Feng [31], the current relative WC (R) of the seeds was calculated based on the initial WC (G), the weight of seed before ($W1$) and after ($W2$) desiccation:

$$R(\%) = (W2 - W1 \times (1 - G))/W2 \times 100\%$$

2.3. Germination Test

After desiccation, the seed germination was tested, and there were three replicates in each treatment, with 50 seeds in each replicate. The germination boxes (13 × 19 × 12 cm) were disinfected with 75% alcohol, after removing the seed coat [32], the de-coated seeds were placed on cotton beds, and subjected to germination tests in a constant temperature light box at 25 °C. Furthermore, we watered the seeds at 12:00 p.m. every day. The germination period was 28 days [33]. The germination rate was counted at the end of the experiment, and an embryonic axis protruding seed coat length of 2 mm was used as the criterion to determine whether the seed had germinated [34].

2.4. Observation of Seed Coat Structure

We used SEM (ThermoFisher Scientific, Waltham, MA, USA) to observe the microstructure of the seed coat. Five fresh seeds were randomly selected for assessment. The seed coat surface, apex, and scar sections of the seeds were prepared by cutting them longitudinally into 1 cm^2 pieces and mounting them on a sample table with double-sided tape. The samples were first fixed with formaldehyde–acetic acid–alcohol solution and then dried by critical-point drying. The samples were observed under SEM operated at 15 and 20 kV at 0.45–0.68 Torr.

2.5. Changes in Water Distribution and Water Status during Seed Drying

2.5.1. Changes in Water Distribution during Drying

A 7.0 T MRI scanner (Pharma Scan, BioSpin GmbH, Bruker Co., Billerica, MA, USA) was used to track the moisture spatial distribution during *Q. acutissima* seed desiccation. Three seeds were selected and dried with silica gel; the MRI scans were performed when the WC of the seeds was 38.8%, 35.8%, 32.8%, 29.8%, 26.8%, 23.8%, 20.8%, 17.8%, 14.8%. The direction of the MRI slice was parallel to the cross-section of the seed, and its thickness was 1 mm. The parameters set for MRI measurement were a TR of 2000 ms and a TE of 13 ms, with averages based on 20 repetitions. The spatial distribution of water in the seed was visualized using false colors (relative scales from zero (blue) to maximum (red)) [35].

2.5.2. Seed Measurement Region of Interest Signal-to-Noise Ratio Determination

The Measurement Region of Interest was delineated at the seed embryonic axis, cotyledon center, and cotyledon end (Figure 1c). The proton density-weighted images of seeds at each stage of water loss scanned by a high-field NMR instrument were used to obtain the image signal S of the region of interest and to determine the *image noise*. The signal-to-noise ratio (SNR) was calculated using the following formula:

$$signal - to - noise\ ratio = \frac{S}{image\ noise} \times 100\%$$

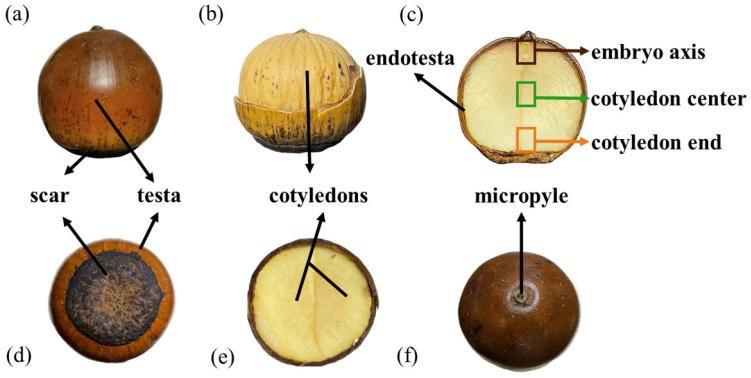


Figure 1. Morphological structure of *Quercus acutissima* seeds. (**a**) Front view of an intact seed; (**b**) seed with half of the seed coat removed; (**c**) transverse section of the seed; (**d**) scar at the bottom of seed; (**e**) longitudinal section of the seed; (**f**) micropyle of seed.

2.5.3. Changes in Water Status and Content during Seed Drying

The LF-NMR measurements were made using a 21 MHz NMR Analyzer (MesoMR23-060H-I, 0.5T; Suzhou Niumei Instrument Co., Ltd., Suzhou, China). Three replicates of 10 seeds were selected and dried with silica gel; the LF-NMR measurements were performed when the WC of the seeds was 38.8%, 35.8%, 32.8%, 29.8%, 26.8%, 23.8%, 20.8%, 17.8%, 14.8%. The samples were placed in an NMR tube with an outer diameter of 25 mm, and the temperature of the LF-NMR instrument was maintained at 32 °C during the transverse relaxation time measurements. The parameters for NMR measurement were set as follows: an echo time (TE) of 0.05 ms and a waiting time (TW) of 4000 ms, with data from 18,000 echoes acquired using eight repeated scans. The simultaneous iterative reconstruction technique (SIRT) was used to invert the CPMG data, which has the advantage of fast and straightforward iterative convergence and stable results [36].

2.5.4. Establishment of NMR Detection Method for Seed Water

The sum of the peak areas (total amplitude S) of the T_2 (transverse) relaxation curves is proportional to the number of hydrogen atoms in the sample which is mainly from water molecules. The WC of *Q. acutissima* seeds can be calculated using the sum of the areas

in the transverse relaxation curve of the NMR signal. The regression equation between the water quality in *Q. acutissima* seeds and the total amplitude *S* of NMR signals can be obtained using regression analysis based on the quality loss and the decrease in total signal amplitude at different drying stages.

2.6. Data Analysis

Excel (Version 2013; Microsoft Corp., Redmond, WA, USA) processed the experimental data. SPSS (Version 26.0; IBM Corp., Armonk, NY, USA) was used to conduct variance analysis on the measurement indicators. The MRI images were examined using Bruker ParaVision 5.1 software (Bruker, Germany). The Origin 2022 (OriginLab Corp, Northampton, MA, USA) and ImageJ (Rawak Software Inc., Stuttgart, Germany) were used to process the images. Statistical analysis was performed using a one-way analysis of variance (ANOVA) followed by Duncan's Multiple Range Test (DMRT). A correlation analysis was performed to estimate Pearson correlation coefficients. All reported values in this paper were mean ± SD for three replicates in each group. p-values < 0.05 were considered significant.

3. Results

3.1. Changes in Water Content and Germination Rate of Quercus acutissima Seeds during Desiccation

Q. acutissima is a dicotyledon; its seeds are nuts, the testa is thick and hard, the endotesta is thin film-like when fresh, and tightly faces the cotyledons (Figure 1). As desiccation time increased, Figure 2 shows a general declining trend in the WC and germination rate of *Q. acutissima* seeds. The initial WC of freshly harvested seeds was 38.8%, and the germination rate was 98.67%. The WC of the seeds decreased dramatically at the beginning of drying, but the rate of decrease slowed after 51 h. When the WC reduced from 38.8% to 35.8%, the germination rate declined from 98.67% to 94.67% without any significant difference. However, the germination rate dropped precipitously as dehydration intensified after 51 h of drying. With further desiccation to 26.8% WC (209 h), the germination rate was 52.0%, and nearly half of the seeds lost vigor. The seed germination rate dropped to 0 when the WC decreased to 14.8%. The Pearson correlation analysis (Table S2) revealed a highly significant positive correlation (p < 0.01, R = 0.982) between the germination rate and WC of *Q. acutissima* seeds, demonstrating that they were typical recalcitrant seeds that were extremely sensitive to water loss.

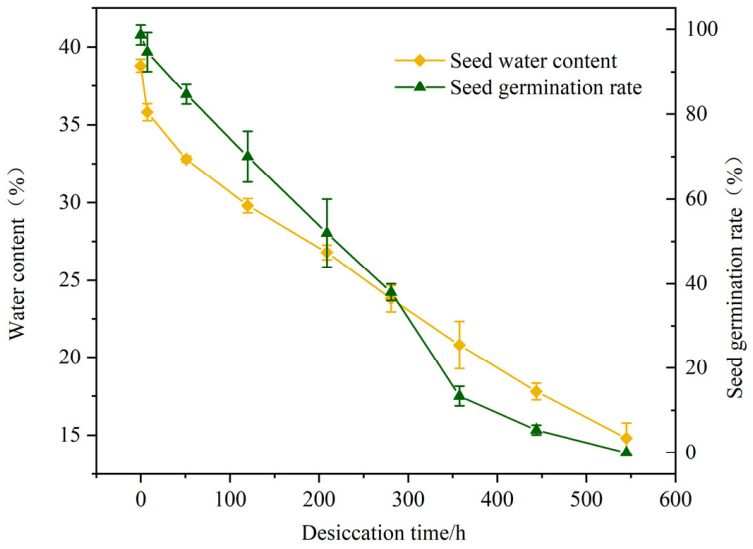


Figure 2. Changes in water content and germination rate of *Q. acutissima* seeds during desiccation.

3.2. Ultrastructure of the Seed Coat

Q. acutissima seed coat (Figure 3A) is composed mainly of the cuticle, palisade layer, and parenchyma, as revealed by the SEM image. There is a thick waxy deposit on the surface of the cuticle (Figure 3B). The palisade layer, which is tightly packed and consists of a monolayer of palisade cells without-gaps, is immediately adjacent to the cuticle. These two layers are the main structures that form a barrier to water flow (water uptake and water loss).

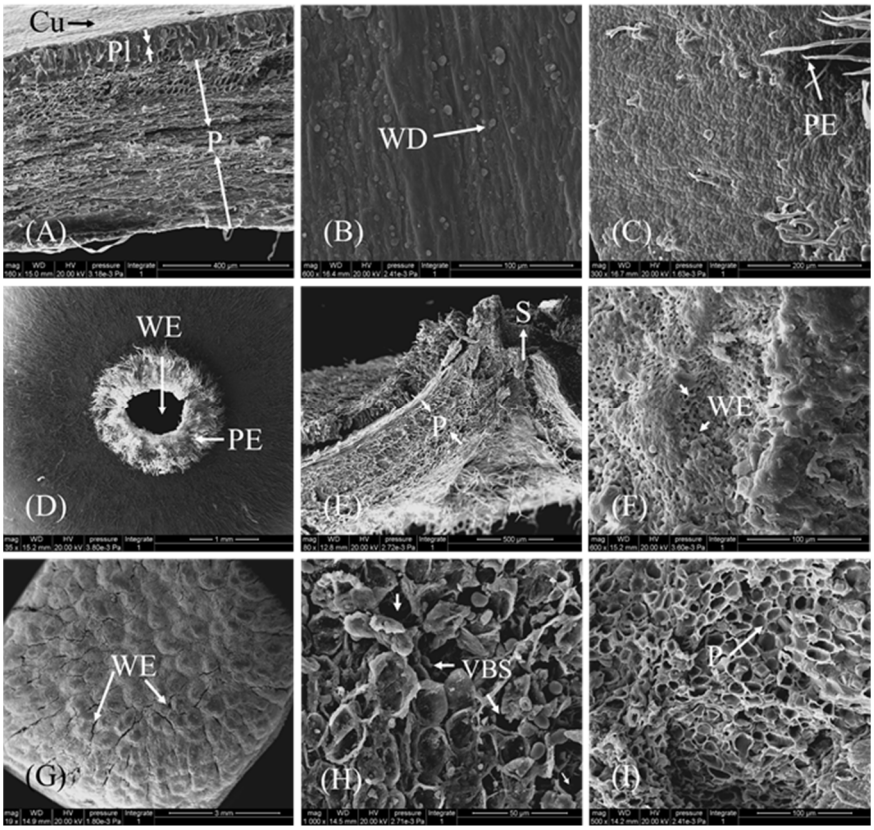


Figure 3. SEM images of the seed coat. (**A**) Testa cross-section (160×); (**B**) testa surface (600×); (**C**) perianth remains on the surface of the testa (300×); (**D**) micropyle (35×); (**E**) cross-section of the micropyle (80×); (**F**) endotesta in the middle of the micropyle (600×); (**G**) scar; (**H**) surface of scar (1000×); (**I**) cross-section of scar (500×). CU, cuticle; PI, palisade layer; P, parenchyma layer; WD, waxy deposits; VBS, vascular bundles; PE, perianth remains; S, stylar; WE, point of water entry.

However, we found two water gaps in the seed coat. The first one is located at the micropyle of the seed (Figure 3D,E), which is known from the cross-section of the micropyle (Figure 3E), and consists of parenchyma tissue with many tiny pores in the apex of the endotesta (Figure 3F). The rest of the micropyle is a closely arranged perianth remnant structure (Figure 3C). The scar (Figure 3G), in addition to the micropyle, is another water gap in the seed coat. There are many vascular bundles in the scar (Figure 3H), and its cross-section is loose parenchyma (Figure 3I), which is more efficient to transport water than the dense, waxy layer of the seed coat. It is inferred that the scar is the primary water entry and exit point for *Q. acutissima* seeds.

3.3. MRI Analysis during Seed Desiccation

Figure 4a demonstrates the MRI of a *Q. acutissima* seed cross-section during drying. We can observe that the fresh seed was full and had high WC, the red regions were the most distributed, and the testa, with a certain WC, was plainly visible from the MRI. Nevertheless, we can observe that water distribution in the seeds was uneven. The SNR

can digitize the results of MRI, and a higher SNR means a stronger ^{1}H signal intensity in the region, indicating a higher WC. Figure 4b reveals that the embryonic axis of fresh seeds had the highest SNR at 8.56, followed by the cotyledon center at 3.82 and the cotyledon end at 1.86, with the red water signal primarily localized in the embryonic axis and central cotyledon. It demonstrated that the embryonic axis and cotyledon centers have a high WC, and that there is a considerable difference between the WC of the embryonic axis and the cotyledon margins.

During seed dehydration, the SNR of the embryonic axis and the cotyledon center constantly declined as seed WC decreased. After 7 h of drying (the WC reduced from 38.8% to 35.8%), the water signal of the testa disappeared, and the SNR of the embryonic axis and the cotyledon fell to 8.13 and 3.8, which were both minor drops of 5% and 7%, respectively. At this time, the testa played a protective role; the seeds were not significantly injured by dehydration, and the germination rate remained high.

After drying for 120 h (the WC was reduced to 29.8%), the SNR of the embryonic axis and cotyledon center decreased significantly by 34% and 24%, respectively. The MRI images show that the red water signal began accumulating continuously at the end of the cotyledons, and the SNR of the cotyledon end increased to 2.53. This indicated that during drying, the embryonic axis and the center of the cotyledons, where the seeds had higher WC, lost water first after drying. Water was lost from the embryonic axis to the cotyledon periphery and the center to the end of the cotyledons.

After drying for 209–358 h (the WC reduced from 26.8% to 20.8%), the SNR of the embryonic axis showed a significant decrease and the area of the red water signal of the embryonic axis was reduced, indicating that the embryonic axis lost significant amounts of water and suffered dehydration injury. Simultaneously, the SNR of the end of the cotyledons kept increasing from 1.55 to 2.17, indicating that the seed water was progressively lost from the inside out. However, at this time, there was no significant difference in decreasing the cotyledon center's SNR, which indicated that with the increase in drying, the rate of water loss in the embryonic axis part was higher than in other parts.

Drying for 444–545 h (the WC lowered to 14.8%), the embryonic axis water signal eventually disappeared with the SNR decreased by 83% to 1.45, and the embryonic axis only had a little water at this time. The cotyledon water signal area was also reduced gradually, with SNR decreased by 52% to 1.85. In addition, the cotyledon periphery water signal faded away, and the seeds shrank (Table S1). When the seeds died, the SNR of the cotyledon center was the highest, and there was only a tiny amount of red water signal in the cotyledons of the seed.

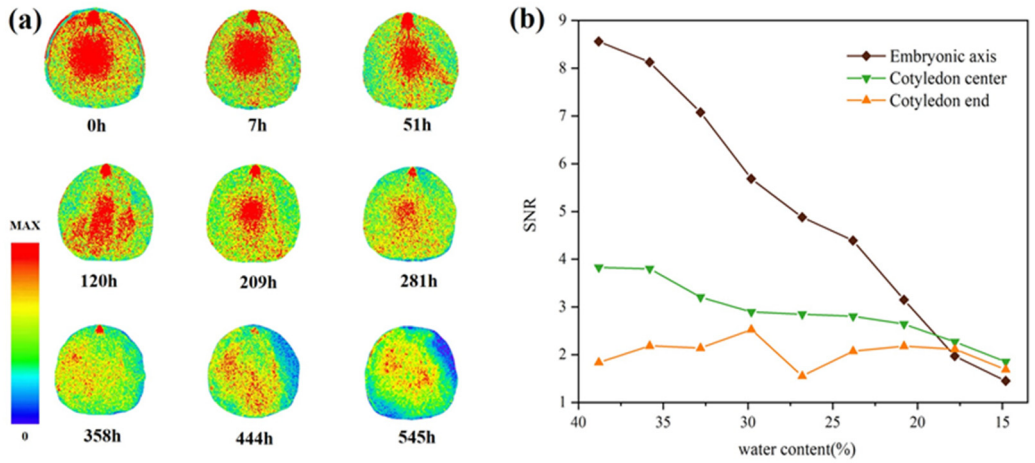


Figure 4. The changes in water signal (**a**) and SNR (**b**) of MR images during desiccation of *Q. acutissima* seeds. The spatial distribution of protons within the seed tissues is visualized by false colors (relative scales from zero (blue) to maximum (red)), red and blue represent hydrated, and water-free regions, respectively.

3.4. Division of T_2 Relaxation Time and Water Status during Desiccation

The duration of the transverse relaxation time reflects the water-binding forces and the degree of free hydrogen protons; therefore, the water status of a sample can be determined by comparing the peak positions of the poly-exponential simulation of CPMG relaxation curves. The shorter the relaxation time, the more tightly the hydrogen nucleus is attached to the substance, the more difficult it is to remove the hydrogen nucleus, and the lower is the water freedom [37]. Figure S1 demonstrates that the relaxation curve has three prominent peaks, and the T_2 relaxation times in the interval where each peak is placed can be identified as T_{21}, T_{22}, and T_{23}, respectively. The shortest relaxation time of T_{21} (0.1–1 ms) corresponds to bound water, primarily hydrogen-bonded to macromolecules in the cell, and has poor mobility [38]. The intermediate relaxation time of T_{22} (1–10 ms) is immobile water, mainly intercellular water with restricted but slightly higher mobile than bound water. T_{23}, with the longest relaxation time (10–1000 ms), is free water, which flows freely within the cells and is a good solvent that can participate in the material metabolism of the cells [39].

3.5. Changes in T_2 Inversion Spectrum during Dehydration of Q. acutissima Seeds

The relaxation range and peak time shifted due to the change in freedom degrees of the water during drying. Table 1 reveals that the bound water relaxation range remained relatively the same at first (39.8%–29.8%) and decreased from 0.34 ms to 0.17 ms when the WC dropped from 29.8% to 14.8% ($p < 0.05$). The change in the peak time of bound water was small, but it also showed a slow decreasing trend, and the peak point time decreased significantly from 0.13 ms to 0.10 ms when the seed WC dropped to 14.8%.

Table 1. LF-NMR parameters of *Q. acutissima* seeds during desiccation.

Water Content (%)	T21		T22		T23	
	Relaxation Range/ms	Peak Time/ms	Relaxation Range/ms	Peak Time/ms	Relaxation Range/ms	Peak Time/ms
38.8	0.34 ± 0.02 a	0.13 ± 0.02 a	6.15 ± 0.24 abc	1.91 ± 0.00 a	534.60 ± 0.48 a	29.33 ± 1.22 a
35.8	0.35 ± 0.00 a	0.12 ± 0.01 ab	5.58 ± 0.71 cd	1.91 ± 0.00 a	487.57 ± 20.36 b	28.02 ± 1.14 ab
32.8	0.35 ± 0.01 a	0.11 ± 0.01 bc	6.43 ± 0.27 ab	1.87 ± 0.08 a	475.34 ± 19.85 bc	29.38 ± 2.04 a
29.8	0.34 ± 0.00 a	0.11 ± 0.01 bc	6.78 ± 0.26 a	1.83 ± 0.00 a	444.10 ± 48.35 cd	28.02 ± 1.14 ab
26.8	0.30 ± 0.01 b	0.11 ± 0.01 bc	6.65 ± 0.50 ab	1.59 ± 0.11 b	412.61 ± 0.28 de	28.02 ± 1.14 ab
23.8	0.23 ± 0.00 c	0.11 ± 0.01 bc	6.41 ± 0.27 ab	1.48 ± 0.00 c	403.11 ± 0.28 e	26.75 ± 1.06 b
20.8	0.19 ± 0.00 d	0.11 ± 0.01 bc	6.00 ± 0.23 bcd	1.29 ± 0.00 d	376.07 ± 0.26 e	24.39 ± 0.99 c
17.8	0.19 ± 0.01 d	0.11 ± 0.01 bc	5.45 ± 0.22 d	1.10 ± 0.04 e	290.81 ± 11.79 f	18.47 ± 0.75 d
14.8	0.17 ± 0.02 d	0.10 ± 0.00 d	4.63 ± 0.31 e	0.78 ± 0.03 f	247.58 ± 17.18 g	18.04 ± 0.00 d

Note: Different lower-case letters after the values refer to a significant difference at the $p < 0.05$ level.

The free water relaxation time and peak time consistently decreased during dehydration. When the seed WC declined to 14.8%, the relaxation range decreased from 534.60 ms to 247.58 ms, a reduction of 53.68% relative to the initial value. The peak time was significantly reduced from 30.03 ms at the beginning to 26.75 ms when the WC dropped to 23.8%; in addition, when the WC reduced to 14.8%, the peak time further decreased to 18.04 ms, a reduction of 39.93%.

The relaxation range changes of the immobile water were more complex than that of the bound water and free water. When the seed WC dropped from 38.8% to 35.8%, the relaxation range reduced from 6.15 ms to 5.58 ms ($p < 0.05$). The immobile water relaxation range then increased significantly to 6.78 ms (35.8–29.8%). As the degree of desiccation intensified, with the WC decreased to 14.8%, the relaxation range decreased significantly to 4.6 ms, a fall of 24.7% from the initial. The peak time of immobile water had been decreasing during desiccation. In the early drying stages, the peak time decreased slowly from 1.91 ms to 1.83 ms (38.8%–29.8%) but fell drastically from 1.83 ms to 0.78 ms in the later stages (26.8%–14.8%). Overall, the relaxation ranges and peak time of the three water

states were significantly diminished during drying, indicating that the hydrogen proton degree of freedom gradually decreased, and the water binding capacity became stronger during drying.

3.6. Dynamic Changes of Peak Area and Its Proportion during Desiccation of Q. acutissima Seeds

We found that there is a significant linear relationship between *Q. acutissima* seed WC and peak area (Figure S2). Therefore, the peak areas S_{21}, S_{22}, and S_{23} can be used to quantify the relative contents of bound, immobile, and free water in the seeds of *Q. acutissima*. Figure 5 depicts the dynamic changes in the peak areas and proportion of the three water statuses during the desiccation of *Q. acutissima* seeds. Throughout the drying process, the total water content of *Q. acutissima* seeds declined consistently. In contrast, there was increase or decrease in the content of each water status; the changes in the trend of the proportion of water in each status also varied, indicating that the various water statuses in the seed cells were mutually transformed.

Bound, immobile, and free water accounted for 10%, 35%, and 55% of the total water in the fresh *Q. acutissima* seeds respectively, with the highest content of free water, which ensures vigorous metabolic activity and makes the seeds easier to germinate after they have dispersed. During desiccation, the peak area and proportion of free water declined with intensified drying due to partial conversion and drying loss. During the decrease of seed WC from 38.8% to 14.8%, the peak area decreased markedly from 21,087.02 to 4060.41, a decrease of 80.74%.

A different trend from free water, the peak area of immobile water showed a fluctuating trend. When the WC decreased from 35.8% to 32.8%, the peak area of immobile water increased markedly from 12,200.29 to 12,993.20. The increase in immobile water content may be because as the seed WC decreased, the cell structure began to contract, and some free water combined with the macromolecular groups to transform into immobile water. When the WC decreased from 32.8% to 14.8%, the peak area of the immobile water dropped to 9461.87, which was a 31.03% decrease, and the decline rate was slow. The change in the proportion of peaks of the immobile water shows a decreasing (38.8%–35.8%) and then an increasing (35.8%–14.8%) trend. As the seed WC decreased from 35.8% to 14.8%, the rate of free water loss within *Q. acutissima* seeds was higher than that of immobile water, causing the proportion of immobile water to continue to increase.

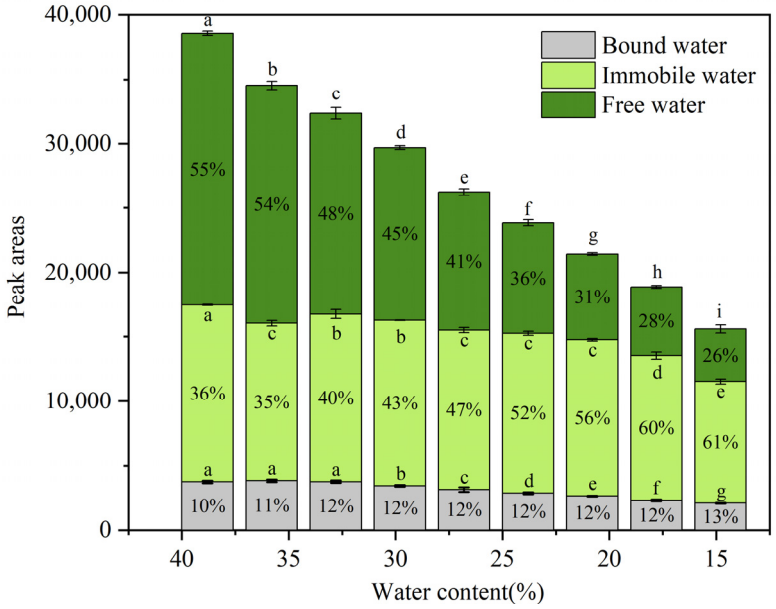


Figure 5. Changes in the peak area and proportion of free water, immobile water, and bound water during desiccation of *Q. acutissima* seeds. Different lower-case letters after the values refer to a significant difference at the $p < 0.05$ level.

During drying, the peak area of bound water showed a tendency to rise first and then fall, and the peak proportion showed a slowly increasing trend. As seed WC dropped from 38.8% to 32.8%, the peak area of bound water increased slightly from 3748.30 to 3833.09 with no significant difference change. The peak area of bound water gradually decreased when the WC dropped below 29.8%. When the water content decreased to 14.8%, the bound water peak area reduced to 2067.71, a drop of 44.83%. When seeds died, the proportion of immobile water was the maximum; during drying, the free water lost the most.

4. Discussion

4.1. Effect of Desiccation on Seed Germination of Q. acutissima

The desiccation sensitivity of the seeds of *Quercus* species is widespread, and their seeds do not undergo maturation drying, so they shed at relatively high-water content and metabolic activity [40,41]. Ganatsas [42] found that the viability of *Q. coccifera* and *Q. pubescens* acorns was highly dependent on WC and started to decline when the WC was lower than 28% and 26%, respectively. Leon-Lobos [43] also observed that the WC and germination rate of *Q.ilex* seeds and *Q.cerris* seeds decreased significantly with desiccation. In this study, freshly matured and shed *Q. acutissima* seeds were found to have high WC (38.9%) and germination rate (98.67%). Our study shows that the *Q. acutissima* seeds continuously lost germination upon moisture loss. The semi-lethal water content of *Q. acutissima* seeds was 26.8%; when the water content further decreased to 14.8% (545 h), *Q. acutissima* seeds completely lost their germination ability. The study results confirm the typical recalcitrant character of the seeds of *Q. acutissima* that are sensitive to desiccation. Therefore, the seeds must be maintained at a high moisture content during ex situ storage and transportation.

4.2. Water Loss Site of Q. acutissima Seed

MRI, as a non-destructive detection tool, can visualize the spatial distribution of seed water and water migration paths during water loss [44,45]. This study observed that the order of the water loss was first the embryonic axis and the cotyledons around the embryonic axis, then the center of the cotyledons, and finally, the end of the cotyledons. Sobrino-Vesperinas [46] discovered that the scar (the point of attachment of the pericarp to the parent plant), which contains vascular bundles, is the primary point of water uptake/loss in the *Q. suber* seed coat. In addition, an investigation of water absorption in *Quercus* revealed that the scar was the main route for water uptake in *Q. nuttallii* and *Q. palustris* [47]. In this study, we observed that the water loss paths were from the embryonic axis to the periphery of the cotyledons and from the center to the end of the cotyledons by MRI images during the desiccation of *Q. acutissima* seeds. Combined with the seed coat SEM observation, it was found that there are many tiny pores for water entry and loss in the endotesta at the micropyle, as well as water-transporting vascular bundles at the scar. These two water gaps are consistent with the water loss paths shown in MRI, so we inferred that the scar and the micropyle are the main sites of water loss in *Q. acutissima* seeds.

By dissecting the seed coat structure and measuring the water uptake rate of the seeds of *Quercus* species, Xia [12] discovered that both the micropyle and the scar had high water uptake rates, but the scar was thought to be the primary water loss site due to the area of the micropyle being small. Nevertheless, our study showed that the SNR of the embryonic axis declined at a significantly higher rate than that of the cotyledon center, indicating that the embryonic axis lost water more quickly. Combined with LF-NMR results, we deduced that the embryonic axis is composed primarily of free water, whereas the cotyledon center is composed of mainly bound and immobile water. This suggests that the cells of the embryonic axis were more vacuolated, which predisposed the cells to greater sensitivity to water loss. This also provides a plausible explanation for why in the MRI, the water signal of the embryonic axis disappeared, and only the water signal of the center of the cotyledons remained when the seed died. When seeds dry, the apex becomes the crucial point for water loss due to the high free water content and rapid loss of free water in the

embryonic axis. Correlation analysis showed that the embryonic axis SNR was highly significantly and positively correlated with seed germination, suggesting that water loss from the embryonic axis was an essential factor in seed vigor loss. This is congruent with the findings of Han [48] in the drying of chestnut seeds, where massive water loss and atrophy of the embryonic axis was the leading cause of seed death. The embryonic axis of *Q. acutissima* seed is located at the micropyle (the gap where water can pass easily), making it more vulnerable to desiccation injury. Therefore, the micropyle is as equally an important water loss site as the scar. Further research on effectively stopping water loss at the water loss site of *Q. acutissima* seeds will provide a reference for the transportation and preservation of recalcitrant seeds of the *Quercus* species.

4.3. The Changes in Water Status during Desiccation

During drying, we found that the relaxation range and peak time of all three water statuses decreased, indicating that water freedom was reduced. The reason may be because of the continual loss of water, the seeds underwent significant crumpling, the internal cell gaps became smaller, the internal cell structure more compact, the mobility of hydrogen protons decreased, and thus, the freedom of each water state decreased. Song [19] reported that the relaxation ranges of free, immobile, and bound water in chestnut seeds significantly reduced as storage duration increased. Sun [49] found, in a study of water changes during room temperature storage of *Ziziphus jujube*, that the mobility of bound water, immobile water, and free water inside the jujube increased as storage duration increased, and the peaks migrated to the right overall. The patterns of changes in the water status of the experimental materials during water loss were different, and we inferred that the differences in nutrients, storage conditions, and drying methods of various experimental materials made them respond differently to water loss.

4.4. Changes in the Water Content of Each Status during Drying

Water is vital for the survival of living organisms, and bound, and free water exist in various proportions yet maintain a dynamic balance [50]. When the seeds of *Q. acutissima* reached maturity and had been shed, free water content was highest and dropped greatest (80.74%) during the drying. Intracellular water was insufficient to sustain the active metabolism of recalcitrant seeds due to the extensive loss of free water. As a result, cellular activity declined, and seed vigor was lost. This result agrees with research on changes in the water status of olecranon peach during storage; the loss of excessive free water led the fruit to senescence [51].

Vertucci [10] speculated that desiccation-sensitive seeds might lack water tightly bound to macromolecules (or cannot be maintained after drying). Jiang [21] discovered that, after maturation and drying of orthodox seeds, free water can be lost entirely, whereas bound water is retained. On the contrary, it is worth pointing out that, in this study, bound water and free water loss occurred simultaneously while the drying of *Q. acutissima* seeds, and bound water decreased by 44.83%. Analysis of correlation revealed that the drop in seed germination rate had a highly significant positive correlation with both the massive loss of free water in the seed and the continual decline in bound water, demonstrating that *Q. acutissima* seed vigor is extremely sensitive to the loss of bound and free water. Bound water plays an important role in the stability of the cellular macromolecular structure and is directly related to the water retention capacity and degree of dehydration of the cell [52]. Due to the destruction of the internal structure and membrane of *Q. acutissima* seed tissues during drying and the degradation of other substances, the bound water became less restricted and was gradually lost [53]. Khan [54] suggested that the decrease in bound water may be attributed to the rupture of the cell membrane, hence the decrease in bound water would have a considerable impact on seed vigor. Using low-field NMR to identify the vigor of rice seeds, Song [55] similarly concluded that the bound water content of rice seeds with less vigor was lower. This implied that the loss of bound water causes the desiccation injury to the seeds to become eventually irreversible, resulting in the death of

the seeds. Notably, the content of bound water did not change significantly from 0 to 51 h of drying (38.8% to 32.8%), and the germination rate of the seeds remained high (>80%). Consequently, brief, sporadic desiccation events do not affect the survival of seeds, while continued desiccation leads to mortality [41]. Hence, to keep the seed vigor of *Q. acutissima* at a high level, it is vital to avoid drying the seeds for a long time and to keep the seed moisture content above 32.8% during storage and transport.

Kuroki [56] discovered that *Haberlea rhodopensis* could maintain a constant ratio of all water statuses during rapid drying. The finding implied that resurrection plants have a dynamic mechanism to maintain the water molecular structure in a constant status, which may be favorable for desiccation tolerance. Nevertheless, the equilibrium of the water status ratio was upset during *Q. acutissima* seed desiccation. In fresh *Q. acutissima* seeds, free water > immobile water > bound water; when the seeds died, immobile water > free water > bound water in the seeds. The proportion of the water status shifted significantly toward a sharp reduction in free water. It is challenging to keep the water status ratio of *Q. acutissima* in equilibrium during drying, which may be one of the reasons why recalcitrant seeds are sensitive to desiccation.

5. Conclusions

Our study shows that *Q. acutissima* seeds are extremely sensitive to water loss, with vigor being lost at a WC lowered to 14.8%. As a non-destructive, real-time visualization method, NMR provides new insights into water distribution and status changes during recalcitrant seed desiccation. Water in seeds can be divided into free water, immobile water, and bound water. As the seeds crumpled and hardened during drying, the free degree of all three statuses of water gradually decreased. We discovered that seed scar and micropyle were water loss sites during seed drying. The embryonic axis of *Q. acutissima* seeds has a higher WC than other parts of the seeds, and we inferred that most of the water in the embryonic axis is free water. Hence the water loss rate from the embryonic axis is faster. Fresh seeds have the highest proportion of free water which is lost the most during drying. Notably, bound water is also continuously lost during drying, and the seeds eventually die because the water balance is broken. Therefore, we recommend maintaining the seed moisture content above 32.8% to avoid the loss of bound water causing irreversible damage during seed storage. Further study on how to effectively prevent water flow from the water loss sites of *Q. acutissima* seeds is important for the maintenance of seed vigor.

Supplementary Materials: The following supporting information can be downloaded at: https://www.mdpi.com/article/10.3390/f14040738/s1, Figure S1: Transverse relaxation time (T_2) inversion spectrum of fresh *Q. acutissima* seed; Figure S2: Correlation of seed water and NMR signal amplitude in *Q. acutissima*; Table S1: Changes in the transverse and longitudinal diameter of seeds in MRI during drying; Table S2: Pearson correlation analysis of various indexes of *Q. acutissima* seeds during desiccation.

Author Contributions: Y.S. conceived the original research plans; H.C. designed and performed the experiments; H.C. analyzed the data; H.C. wrote the article with the contributions of all the authors. Y.S. modified the manuscript. All authors have read and agreed to the published version of the manuscript.

Funding: This work was supported by The Subject of Key R & D Plan of Innovation and Popularization of Forestry Technology in Jiangsu Province Project (LYKJ [2021]03) and Shandong Province (Major Scientific and Technological Innovation Project) (2021LZGC023).

Data Availability Statement: Not applicable.

Acknowledgments: We would like to thank the College of Forestry, Nanjing Forestry University, and Co-innovation Center for Sustainable Forestry in Southern China, Southern Tree Inspection Center National Forestry Administration.

Conflicts of Interest: The authors declare no conflict of interest. The funders had no role in the design of the study; in the collection, analyses, or interpretation of data; in the writing of the manuscript; or in the decision to publish the results.

References

1. Roberts, E.H. Predicting the storage life of seeds. *Seed Sci. Technol.* **1973**, *1*, 499–514.
2. Ellis, R.H.; Hong, T.D.; Roberts, E.H. An Intermediate Category of Seed Storage Behaviour? I. COFFEE. *J. Exp. Bot.* **1990**, *41*, 1167–1174. [CrossRef]
3. Krishnan, P.; Nagarajan, S.; Dadlani, M.; Dadlani, M.; Moharir, A.V. Characterization of wheat (*Triticum aestivum*) and soybean (*Glycine max*) seeds under accelerated ageing conditions by proton nuclear magnetic spectroscopy. *Seed Sci. Technol.* **2003**, *31*, 541–550. [CrossRef]
4. Pukacka, S.; Malec, M.; Ratajczak, E. ROS production and antioxidative system activity in embryonic axes of *Quercus robur* seeds under different desiccation rate conditions. *Acta Physiol. Plant.* **2011**, *33*, 2219–2227. [CrossRef]
5. Wyse, S.V.; Dickie, J.B. Predicting the global incidence of seed desiccation sensitivity. *J. Ecol.* **2017**, *105*, 1082–1093. [CrossRef]
6. Berjak, P.; Pammenter, N.W. From *Avicennia* to *Zizania*: Seed recalcitrance in perspective. *Ann. Bot.* **2008**, *101*, 213–228. [CrossRef] [PubMed]
7. Obroucheva, N.; Sinkevich, I.; Lityagina, S. Physiological aspects of seed recalcitrance: A case study on the tree *Aesculus hippocastanum*. *Tree Physiol.* **2016**, *36*, 1127–1150. [CrossRef] [PubMed]
8. Krishnan, P.; Singh, R.; Verma, A.P.S.; Joshi, D.K.; Singh, S. Changes in seed water status as characterized by NMR in developing soybean seed grown under moisture stress conditions. *Biochem. Biophys. Res. Commun.* **2014**, *444*, 485–490. [CrossRef] [PubMed]
9. Li, W.J.; Su, Y.J.; Su, X.T.; Pu, S.J. The effect of super-dry storage on seed physiology and its ultrastructure. *Shandong J. Anim. Sci. Vet. Med.* **2013**, *34*, 72–73.
10. Vertucci, C.W.; Leopold, A.C. The relationship between water binding and desiccation tolerance in tissues. *Plant Physiol.* **1987**, *85*, 232–238. [CrossRef]
11. Hamilton, K.N.; Offord, C.A.; Cuneo, P.; Deseo, M.A. A comparative study of seed morphology in relation to desiccation tolerance and other physiological responses in 71 Eastern Australian rainforest species. *Plant Species Biol.* **2013**, *28*, 51–62. [CrossRef]
12. Xia, K.; Daws, M.I.; Stuppy, W.; Zhou, Z.K.; Pritchard, H.W. Rates of Water Loss and Uptake in Recalcitrant Fruits of *Quercus* Species Are Determined by Pericarp Anatomy. *PLoS ONE* **2012**, *7*, e47368. [CrossRef] [PubMed]
13. Obroucheva, N.V.; Antipova, O.V. The role of water uptake in the transition of recalcitrant seeds from dormancy to germination. *Russ. J. Plant Physiol.* **2004**, *51*, 848–856. [CrossRef]
14. Levitt, J. *Responses of Plants to Environmental Stresses*; Academic Press: New York, NY, USA, 1980.
15. Hwang, S.S.; Cheng, Y.C.; Chang, C.; Lur, H.S.; Lin, T.T. Magnetic resonance imaging and analyses of tempering processes in rice kernels. *J. Cereal Sci.* **2009**, *50*, 36–42. [CrossRef]
16. Jia, C.; Wang, L.; Li, R.; Liu, C.P. Experimental study on drying characteristics of wheat by low-field nuclear magnetic resonance. *Dry. Technol.* **2016**, *35*, 1258–1265. [CrossRef]
17. da Silva, C.B.; Bianchini, V.D.M.; de Medeiros, A.D.; de Moraes, M.H.D.; Marassi, A.G.; Tannus, A. A novel approach for *Jatropha curcas* seed health analysis based on multispectral and resonance imaging techniques. *Ind. Crops Prod.* **2021**, *161*, 113186. [CrossRef]
18. Ishida, N.; Naito, S.; Kano, H. Loss of moisture from harvested rice seeds on MRI. *Magn. Reson. Imaging* **2004**, *22*, 871–875. [CrossRef]
19. Song, S.S.; Geng, Y.Y.; Feng, T.C.; Hu, B.K.; Liu, Y.N.; Wang, J.H.; He, J.L.; Liang, M.; Tan, H.M. Based on the analysis and imaging of low field nuclear magnetic resonance, explore the influence of chestnut moisture migration to the change of its texture in the storage process. *Sci. Technol. Food Ind.* **2020**, *41*, 44–49.
20. Li, Y.T.; Obadi, M.; Shi, J.C.; Sun, J.; Chen, Z.W.; Xu, B. Determination of moisture, total lipid, and bound lipid contents in oats using low-field nuclear magnetic resonance. *J. Food Compos. Anal.* **2020**, *87*, 103401. [CrossRef]
21. Jiang, X.C.; Yang, X.Q.; Fu, J.R.; He, J.X. Differences between the water status in orthodox seeds and that in recalcitrant seeds. *J. Nat. Sci. Hunan Norm. Univ.* **1996**, *3*, 54–58.
22. Sun, X.; Jiang, D.; Xu, L.; Hua, T.T.; Xuan, Y. Moisture distribution and migration of *Ginkgo biloba* seeds during air drying process. *J. Nanjing For. Univ.* **2019**, *43*, 188–192.
23. Jin, W.G.; Pei, J.J.; Wang, S.Q.; Chen, X.H.; Gao, R.C.; Tan, M.Q. Effect of continuous and intermittent drying on water mobility of fresh walnuts (*Juglans regia* L.): A LF-NMR study. *Dry. Technol.* **2022**, *40*, 254–264. [CrossRef]
24. Li, X.; Li, Y.F.; Zang, M.Y.; Li, M.Z.; Fang, Y.M. Complete Chloroplast Genome Sequence and Phylogenetic Analysis of *Quercus acutissima*. *Int. J. Mol. Sci.* **2018**, *19*, 2443. [CrossRef] [PubMed]
25. Zhang, X.W.; Li, Y.; Liu, C.Y.; Xia, T.; Zhang, Q.; Fang, Y.M. Phylogeography of the temperate tree species *Quercus acutissima* in China: Inferences from chloroplast DNA variations. *Biochem. Syst. Syst. Ecol.* **2015**, *63*, 190–197. [CrossRef]
26. Hu, Y.D.; Wu, J.; Jiang, J.B.; Wang, C. Contrast Tests of Different Storage Methods of Seeds of *Quercus acutissima*. *Prot. For. Sci. Technol.* **2009**, *2*, 40–41.
27. Gayatri, G.P.; Kumar, K.G.A.; Nair, P.S.; Deth, G.S.K.; Baiju, K.V. Dynamics of Water and Abscisic Acid During Embryogeny and Embryo Drying in the Recalcitrant Seeds of *Vateria indica* L. *J. Plant Growth Regul.* **2021**, *41*, 15–22. [CrossRef]
28. Chandra, J.; Keshavkant, S. Desiccation-induced ROS accumulation and lipid catabolism in recalcitrant *Madhuca latifolia* seeds. *Physiol. Mol. Biol. Plants* **2018**, *24*, 75–87. [CrossRef] [PubMed]
29. Francini, A.; Galleschi, L.; Saviozzi, F.; Pinzino, C.; Izzo, R.; Sgherri, C.; Navari-Izzo, F. Enzymatic and non-enzymatic protective mechanisms in recalcitrant seeds of *Araucaria bidwillii* subjected to desiccation. *Plant Physiol. Biochem.* **2006**, *44*, 556–563. [CrossRef] [PubMed]

30. International Seed Testing Association (ISTA). *International Rules for Seed Testing. Chapter 9: Determination of Moisture Content*; International Seed Testing Association (ISTA): Bassersdorf, Switzerland, 2004.
31. Feng, J.; Shen, Y.B.; Shi, F.H.; Li, C.Z. Changes in Seed Germination Ability, Lipid Peroxidation and Antioxidant Enzyme Activities of *Ginkgo biloba* Seed during Desiccation. *Forests* **2017**, *8*, 286. [CrossRef]
32. Liu, Y.; Li, Q.M.; Liu, G.Q.; Liu, Y.; Hou, L.Y.; Li, G.L. Inhibitory Mechanism of Seed Germination of *Quercus acutissima*. *Sci. Silvae Sin.* **2012**, *48*, 164–170.
33. Xia, K.; Daws, M.I.; Hay, F.R.; Zhou, Z.K.; Pritchard, H.W. A comparative study of desiccation responses of seeds of Asian Evergreen Oaks, *Quercus* subgenus *Cyclobalanopsis* and *Quercus* subgenus *Quercus*. *S. Afr. J. Bot.* **2012**, *78*, 47–54. [CrossRef]
34. Li, D.; Li, Y.; Qian, J.; Liu, X.; Xu, H.; Zhang, G.; Ren, J.; Wang, L.; Zhang, L.; Yu, H. Comparative Transcriptome Analysis Revealed Candidate Genes Potentially Related to Desiccation Sensitivity of Recalcitrant *Quercus variabilis* Seeds. *Front. Plant Sci.* **2021**, *12*, 717563. [CrossRef] [PubMed]
35. Wu, Y.; Shen, Y.B. The structural and chemical characteristics of the pericarp are important in *Tilia miqueliana* seed dormancy. *New For.* **2021**, *52*, 875–888. [CrossRef]
36. Zang, X.; Lin, Z.; Zhang, T.; Wang, H.; Cong, S.; Song, Y.; Li, Y.; Cheng, S.; Tan, M. Non-destructive measurement of water and fat contents, water dynamics during drying and adulteration detection of intact small yellow croaker by low field NMR. *J. Food Meas. Charact.* **2017**, *11*, 1550–1558. [CrossRef]
37. Williams, J.K.; Hong, M. Probing membrane protein structure using water polarization transfer solid-state NMR. *J. Magnetic. Reson.* **2014**, *247*, 118–127. [CrossRef] [PubMed]
38. Kamal, T.; Cheng, S.; Khan, I.A.; Nawab, K.; Zhang, T.; Song, Y.; Wang, S.; Nadeem, M.; Riaz, M.; Khan, M.A.U.; et al. Potential uses of LF-NMR and MRI in the study of water dynamics and quality measurement of fruits and vegetables. *J. Food Process. Preserv.* **2019**, *43*, e14202. [CrossRef]
39. Sun, Q.; Zhang, M.; Yang, P.Q. Combination of LF-NMR and BP-ANN to monitor water states of typical fruits and vegetables during microwave vacuum drying. *LWT-Food Sci. Technol.* **2019**, *116*, 108548. [CrossRef]
40. Goodman, R.C.; Jacobs, D.F.; Karrfalt, R.P. Evaluating desiccation sensitivity of *Quercus rubra* acorns using X-ray image analysis. *Can. J. For. Res.* **2005**, *35*, 2823–2831. [CrossRef]
41. Joet, T.; Ourcival, J.M.; Dussert, S. Ecological significance of seed desiccation sensitivity in *Quercus ilex*. *Ann. Bot.* **2013**, *111*, 693–701. [CrossRef]
42. Leon-Lobos, P.; Ellis, R.H. Comparison of seed desiccation sensitivity amongst *Castanea sativa*, *Quercus ilex* and *Q. cerris*. *Seed Sci. Technol.* **2018**, *46*, 233–237. [CrossRef]
43. Ganatsas, P.; Tsakaldimi, M. A comparative study of desiccation responses of seeds of three drought-resistant Mediterranean oaks. *For. Ecol. Manag.* **2013**, *305*, 189–194. [CrossRef]
44. Tuomainen, T.V.; Himanen, K.; Helenius, P.; Kettunen, M.I.; Nissi, M.J. Quantitative magnetic resonance imaging of Scots pine seeds and assessing germination potential. *Can. J. For. Res.* **2022**, *52*, 685–695. [CrossRef]
45. Terskikh, V.V.; Feurtado, J.A.; Ren, C.; Abrams, S.R.; Kermode, A.R. Water uptake and oil distribution during imbibition of seeds of western white pine (*Pinus monticola* Dougl. ex D. Don) monitored in vivo using magnetic resonance imaging. *Planta* **2005**, *221*, 17–27. [CrossRef]
46. Sobrino-Vesperinas, E.; Viviani, A.B. Pericarp micromorphology and dehydration characteristics of *Quercus suber* L. acorns. *Seed Sci. Res.* **2000**, *10*, 401–407. [CrossRef]
47. Bonner, F.T. Water Uptake and Germination of Red Oak Acorns. *Bot. Gaz.* **1968**, *129*, 83–85. [CrossRef]
48. Han, B.; Zhang, P.; Guo, S.J.; Dong, X.; Li, W.Q.; Jiao, J.M. Effects of Water Loss on Ultrastructure and Physiological changes and Germination of *Castanea mollissima*. *Seeds Genom. Appl. Biol.* **2020**, *40*, 2785–2792.
49. Sun, B.X.; Zhao, H.X.; Feng, X.Q. Changes in the water status of fresh jujubes during storage based on LF-NMR and MRI techniques. *J. Chin. Inst. Food Sci. Technol.* **2016**, *16*, 252–257.
50. Wa, H.T.; Dong, R.L. On the relationship between the ratio of free water and bound water in plant leaves and the drought resistance of plants. *Plant Physiol. J.* **1956**, *2*, 50–53.
51. Luo, J.Y.; Tang, M.; Qiu, Y.X.; Liu, J.L.; Wang, Q. Change of water status during olecranon peach storage by LF-NMR technique. *J. Zhongkai Univ. Agric. Eng.* **2019**, *32*, 23–27.
52. Ambastha, V.; Tiwari, B.S. Cellular Water and Anhydrobiosis in Plants. *J. Plant Growth Regul.* **2015**, *34*, 665–671. [CrossRef]
53. Zhu, K.; Li, Y.J.; Wang, Y.B.; Wang, J.S. Internal water phase changes and surface moisture loss kinetics of broad bean seeds during dehydration. *Sci. Technol. Food Ind.* **2020**, *41*, 51–57.
54. Khan, M.I.H.; Wellard, R.M.; Nagy, S.A.; Joardder, M.U.H.; Karim, M.A. Experimental investigation of bound and free water transport process during drying of hygroscopic food material. *Int. J. Therm. Sci.* **2017**, *117*, 266–273. [CrossRef]
55. Song, P.; Song, P.; Yang, H.W.; Yang, T.; Xu, J.; Wang, K.T. Detection of rice seed vigor by low-field nuclear magnetic resonance. *Int. J. Agric. Biol. Eng.* **2018**, *11*, 195–200. [CrossRef]
56. Kuroki, S.; Tsenkova, R.; Moyankova, D.; Muncan, J.; Morita, H.; Atanassova, S.; Djilianov, D. Water molecular structure underpins extreme desiccation tolerance of the resurrection plant *Haberlea rhodopensis*. *Sci. Rep.* **2019**, *9*, 12. [CrossRef] [PubMed]

Disclaimer/Publisher's Note: The statements, opinions and data contained in all publications are solely those of the individual author(s) and contributor(s) and not of MDPI and/or the editor(s). MDPI and/or the editor(s) disclaim responsibility for any injury to people or property resulting from any ideas, methods, instructions or products referred to in the content.

forests

MDPI

Article

Optimized Plant Diversity and Carbon Storage for Priority Protection Areas in China

Chaohe Tang, Yuran Dong and Lingfeng Mao *

Co-Innovation Center for Sustainable Forestry in Southern China, College of Biology and the Environment, Nanjing Forestry University, Nanjing 210037, China
* Correspondence: maolingfeng2008@163.com

Abstract: Biodiversity and carbon storage are two key ecosystem functions that are crucial to protect and maintain ecosystem balance. However, there is often little overlap between hotspots for these two different conservation purposes. Additionally, it is not well understood how these different spatial metrics affect these functions in protected ecosystems in China. Here, we explored the relationships between plant diversity metrics and carbon storage by using a large vascular plant distribution dataset, as well as soil fragile organic carbon and biomass carbon datasets in specific spatial areas across China. We also defined priority protection areas (PPAs) using a conservation prioritization method, where 30% of the study areas displayed the highest combined conservation value in carbon storage and plant species richness (SR), phylogenetic diversity (PD), phylogenetic endemism (PE) and evolutionary distinctness (ED). Our results indicated that the correlations between biodiversity metrics and carbon storage were very weak in spatial relationship. However, by including both of these functions in conservation targets, the PPAs could account for more than 95% of the species and evolutionary diversity (PD, ED), and stored large amounts of carbon. Additionally, we broadly divided the PPAs into win–win, high plant diversity, and high carbon areas based on the overlap of biodiversity and carbon storage hotspots. Altogether, our results highlight the importance of understanding and optimizing conservation efforts for different ecosystem functions in different PPAs. Ultimately, this work establishes an urgent need to expand protection in these areas to support mutual biodiversity and carbon storage beneficial solutions.

Keywords: biodiversity; ecosystem functions; hotspots; correlation; conservation

check for updates

Citation: Tang, C.; Dong, Y.; Mao, L. Optimized Plant Diversity and Carbon Storage for Priority Protection Areas in China. *Forests* **2023**, *14*, 621. https://doi.org/10.3390/f14030621

Academic Editor: Pablo Vergara

Received: 15 February 2023
Revised: 10 March 2023
Accepted: 17 March 2023
Published: 20 March 2023

Copyright: © 2023 by the authors. Licensee MDPI, Basel, Switzerland. This article is an open access article distributed under the terms and conditions of the Creative Commons Attribution (CC BY) license (https://creativecommons.org/licenses/by/4.0/).

1. Introduction

Climate change and biodiversity loss are two of the most urgent environmental challenges [1], human activities that cause climate change may further contribute to biodiversity loss [2]. For example, greenhouse gas emissions, including carbon dioxide, are a major component of climate change and exacerbate biodiversity loss [3]. In order to mitigate and reduce biodiversity loss due to climate change, we must increase holistic adaptation strategies based on different ecosystem approaches for varying priority protection areas (PPAs) [4].

Establishing protected areas (PAs) is an important measure to protect biodiversity, PAs can be established as biodiversity sites to reduce spatial effects on biodiversity [5,6]. However, climate change mitigation actions focus on the conservation and restoration of high-carbon stocks [7]. Under the context of changing climate, protecting these two functions is crucial and essential to keep ecosystems in balance. Still, it is not clear whether biodiversity and carbon can be protected simultaneously [8,9], since PPAs for biodiversity-based conservation do not adequately protect ecosystem services, such as carbon storage [10]. Similarly, PPAs that focus on carbon storage conservation do not effectively protect biodiversity [11–13]. In theory, defining PPA under two major ecosystem functions,

i.e., carbon storage of the ecosystem and biodiversity, could protect these ecosystem services in limited areas [10,14,15]. However, there are several inconsistencies in the spatial relationship between biodiversity and carbon storage that are not well understood [16,17].

When identifying PPAs, there are synergies and trade-offs between biodiversity and carbon storage that need to be considered [17,18]. In some areas, there are opportunities to achieve carbon conservation through direct biodiversity co-benefits [9,19]. However, in the regions where the co-benefits cannot be pursued, integrative conservation planning has to be based on the prioritization of carbon storage and their specific biodiversity issues, which will require separate conservation plans for each function [20] to avoid adverse consequences. Nonetheless, there is still a lack of research on the common benefits of PPA and other area-specific regional planning.

Previously, PPAs identification research on biodiversity and ecosystem services was often dominated by the terrestrial vertebrate richness and often relied on biodiversity metrics limited to species numbers, i.e., taxonomic diversity (TD), e.g., [21,22]. However, vertebrate richness-based priority areas differ from plant-based biodiversity hotspots [23]. Additionally, when only species richness (SR) is considered for prioritizing conservation areas, it could result in the loss of unique evolutionary information [24]. Thus, it is essential to combine multi-biodiversity metrics to protect evolutionary characteristics in a region.

Recently, some phylogenetic indexes were raised for different biodiversity evolutionary history dimensions, such as phylogenetic diversity (PD) [25], phylogenetic endemism (PE) [26] and evolutionary distinctness (ED) [27]. By considering the evolutionary information represented within each taxon, PD reveals the underlying evolutionary, ecological and biogeographic processes of biodiversity [28]. In these indices, regions with high PE also capture PD not found elsewhere, and ED can be used to infer regions inhabited by evolutionarily distinct taxa [29]. Furthermore, unique evolutionary histories can affect a species' susceptibility to extinction, since extinction risk is non-random [30,31]. Thus, to maximize biodiversity conservation values, multiple biodiversity dimensions should be considered in conservation planning [32].

Meanwhile, China played an important role in maintaining the global carbon balance [33]. However, due to human activities, land use types and land cover were constantly changing [34], and a large amount of terrestrial ecosystem carbon storage was released into the atmosphere [35]. There was, in recent times, uncertainty about the scale and spatial distribution of terrestrial ecosystem carbon sequestration in China [36,37]. The analysis of spatial patterns of carbon storage was important for developing effective sequestration strategies [38]. However, because of the uncertainty in the spatial relationship between biodiversity and carbon storage, it was still unclear whether setting conservation targets could capture the co-benefits of both.

In this work, we used China as an example to explore (i) the synergy of plant diversity and carbon storage in different spatial regions and (ii) the spatial layout optimization of PAs under PPAs, since China covers many biome types and large latitude spans [39]. Based on several carbon storage and plant diversity datasets, we identified specific areas of great conservation importance based on the relationship between biodiversity and carbon storage. We further zoned PPAs according to the overlap of high carbon and high biodiversity and also explored the coverage and protection vacancies of existing PAs. Together, our results provide recommendations for the spatial layout optimization of PAs in China but can be used to understand diversity and carbon storage relationships in unique spatial areas around the world that are currently affected by climate change.

2. Materials and Methods

2.1. Plant Spatial Distribution Data

We collected distribution data for all available terrestrial vascular plants from national and provincial flora, local flora, inventory and herbarium records in China based on the Chinese Vascular Plant Distribution Database and the Global Biodiversity Information Facility (GBIF; available at https://www.gbif.org/, accessed on 15 December 2021). We

divided the map of China into 50 km × 50 km grid cells and removed the grids with less than 50% of the boundary grid area, which resulted in 3805 grid cells. To reduce any effects of the area on diversity estimation, we transformed the county-level distribution data into gridded distribution data with a spatial resolution of 50 km× 50 km. Additionally, the coordinate data were converted into each covered grid, the county-level distribution data were matched to the grid cells, and duplicate data within each grid cell were removed to ensure that a species had only one record in each grid. We then standardized species names based on The Plant List system using the R program 'plantlist' package (https://github.com/helixcn/plantlist, accessed on 13 June 2022) and merged subspecies taxa into the corresponding species. In total, 2,945,870 distribution records with 33,519 terrestrial vascular plant species were kept for analysis.

2.2. Phylogenetic Tree

Based on a list of 33,519 terrestrial vascular plants, we used the V.PhyloMaker package [40] in R 4.1.2 (https://cran.r-project.org/src/base/R-4/, accessed on 15 June 2022), which is an interpreted language widely used in statistics for data exploration, statistical analysis and graphing, to generate phylogenetic trees. The backbone of the phylogenetic tree was implemented with a mega-tree derived primarily from Smith and Brown's [41] phylogeny for seed plants and Zanne et al.'s [42] phylogeny for pteridophytes. We utilized the Scenario 3 tree in V.PhyloMaker [40] to randomly insert each genus and species close to their relatives that were absent from the mega-phylogeny [40]. Of our total 33,519 taxa, 12,303 were matched at a species level, 18,973 at the level of genus and 2243 at the level of family.

2.3. Carbon Storage Data

In our analysis, carbon storage was the sum of the biomass carbon that included both above- and below-ground biomass carbon storage and vulnerable soil carbon storage. The biomass carbon dataset was from the publicly available global harmonized map of above- and below-ground biomass carbon density [43].

The vulnerable soil carbon was defined as the amount of carbon stock that may be lost due to land use in the next 30 years according to the Intergovernmental Panel on Climate Change (IPCC; https://www.ipcc.ch/, accessed on 2 December 2021) and Jung et al. [21]. Carbon in mineral and organic soil was considered vulnerable soil carbon and was found at a 30 cm and 200 cm depth, respectively [21]. Organic soils were defined as those soils with ≥5% probability of being histosols, according to the US Department of Agriculture soil order taxonomy. All other soils were considered to be mineral soils [21].

Based on this method, we estimated the probability of a soil sample to be mineral or organic for the soil organic carbon storage data (http://doi.org/10.5281/zenodo.2658183, accessed on 3 December 2021; https://doi.org/10.5281/zenodo.2536040, accessed on 2 December 2021). We then summed the vulnerable organic carbon and biomass carbon to obtain the total carbon and re-aggregated the 50 km^2 × 50 km^2 spatial resolution to match the biodiversity data.

2.4. Plant Diversity Metric Calculations

To measure the overall state of plant diversity for each grid, the TD, (i.e., SR), PD, PE and ED were used to present their current diversity and evolutionary history, respectively [29]. With these characteristics, PD was the sum of the lengths of branches that connect a set of species to the root of a phylogenetic tree [25], and the 'pd' function in the 'picante' package in the R program was used to determine this characteristic [44]. The 'pd' function is commonly used to calculate Faith's phylogenetic diversity. Additionally, PE is the sum of the branch length and/or evolutionary branch range for each branch on the spanning path of a set of taxa linked to the root of a tree [26], and we calculated PE in the function 'phylogenetic.endemism' in the 'phyloregion' package in the R program [45]. Additionally, ED represents the division of phylogenetic branch lengths by the total number

of species against them, and each species was weighted according to the number of unique evolutionary histories they represent [27,46], and was calculated using the 'evol.distinct' function also in the 'picante' package in the R program [44].

2.5. Statistical Analyses

To better understand the spatial relationship between biodiversity and carbon storage, we calculated Pearson's correlation coefficients and significance levels (p-values) for SR, PD, PE, ED and carbon storage for 3805 grids in China. Statistical analyses were performed in R 4.1.2 (https://cran.r-project.org/src/base/R-4/, accessed on 15 June 2022).

2.6. Synergy Priorities for Biodiversity and Carbon Storage

PPAs and hotspots were set at the highest value (30% of the area) to respond at the national level to the draft Global Biodiversity Framework to conserve at least 30% of the global land area [22]. We then generated a combined plant diversity (TD, PD, PE and ED) and carbon storage value prioritization map and extracted the top 30% of the area as the priority areas for conservation using the Zonation conservation prioritization software [47]. Here, the synergistic effect depends on the relative importance of conservation for biodiversity and carbon storage. In this analysis, we equally set these three metrics to balance the importance of TD, evolutionary history-related indexes (e.g., PD, PE and ED), and carbon storage. Meanwhile, the equal weight was also set for the three evolutionary history-related PD, PE and ED metrics for the synergistic effects. We then calculated the proportion of biodiversity and carbon storage for each PPA using these methods.

2.7. Overlap Analysis of Synergy Priorities and Hotspots

To explore the co-benefits of biodiversity and carbon in PPAs, we overlapped PPAs with biodiversity and carbon storage hotspots using ArcGIS 10.2, since not all high biodiversity and high carbon areas were fully overlapped. We divided biodiversity hotspots into two categories: taxonomic diversity hotspots (TDHs) and evolutionary diversity hotspots (EDHs), where the EDHs were related to evolutionary history indexes. Biodiversity hotspots and carbon storage hotspots (CSHs) were also generated using the Zonation conservation prioritization software [47].

2.8. Gap Analysis

To identify protection gaps in the PPAs for biodiversity and carbon storage, we used a gap analysis to assess the coverage of each PPA in the PAs in China. The protected areas boundary data in China was from the China Nature Reserve Specimen Resource Sharing Platform (available at http://bhq.papc.cn/, accessed on 15 August 2022) and the World Database on Protected Areas (https://www.protectedplanet.net/en, accessed on 10 June 2022). We overlapped the PPAs with the nature reserve coverage map and identified that the grids were not covered by the PAs for the protection gaps. This spatial analysis was also performed in ArcGIS 10.2.

3. Results

3.1. Relationships between Biodiversity Metrics and Carbon Storage

The PD, SR, PE and ED biodiversity-related indexes were highly and significantly correlated based on their Pearson's correlations (Statistical test, $p < 0.001$, $n = 3805$), and the coefficients ranged from 0.70 to 0.99 (Table 1). However, the correlations between carbon storage and PD, SR, PE and ED were very weak, and the coefficients were only 0.18, 0.19, 0.08 and 0.17, respectively.

Table 1. Pearson's correlation coefficient matrix between species richness (SR), phylogenetic diversity (PD), phylogenetic endemism (PE), evolutionary distinctness (ED) and carbon storage (n = 3805). p-values are represented as *** $p < 0.001$.

	SR	PD	PE	ED	Carbon Storage
PD	0.970 ***				
PE	0.711 ***	0.704 ***			
ED	0.988 ***	0.981 ***	0.767 ***		
Carbon storage	0.190 ***	0.186 ***	0.082 ***	0.170 ***	

3.2. Priority Protection Areas

To locate the major PPAs in China, we used conservation priority values from the integrated plant diversity and carbon storage datasets and mapped these characteristics, which are illustrated in Figure 1a,b. We found that biodiversity and carbon synthesis priority hotspots were mainly distributed in southwest, south and northeast China (Figure 1a). In Figure 1b, the synergy priorities covered 96.7% of the species, 97.4% of the PD, 97.0% of the ED and 53% of the carbon storage. Because the PE calculations were related to the geographic extent of each branch, these results were based on equivalent spatial units that can be compared directly between regions but cannot be used to calculate the proportion of PE that was protected.

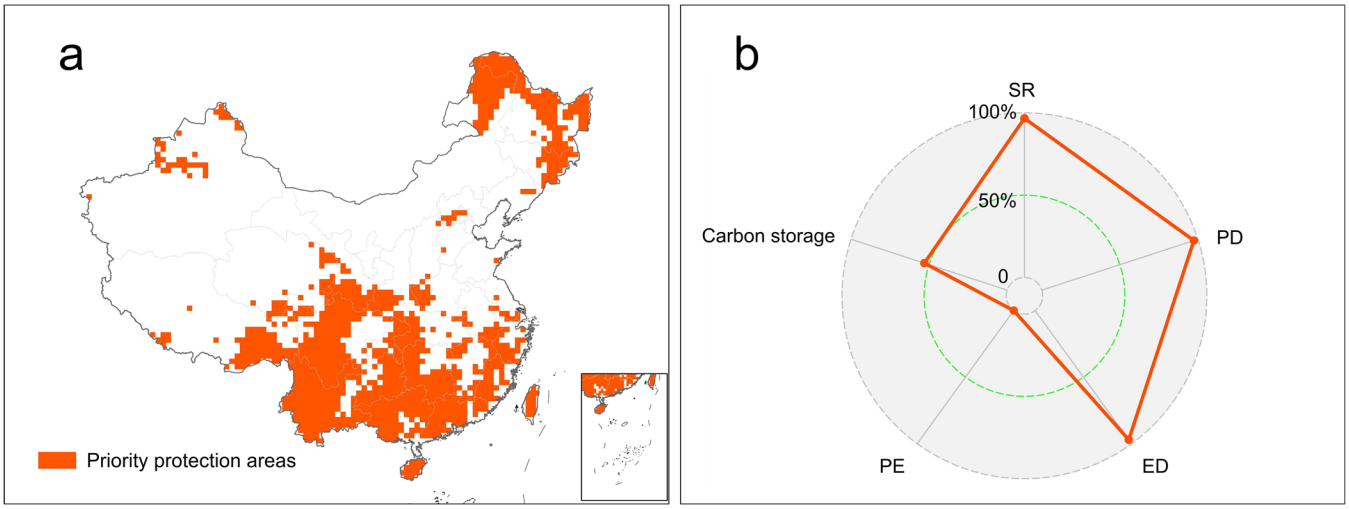


Figure 1. (**a**) Map of priority protection areas (PPAs) for plant diversity and carbon storage. PPAs were set as the 30% of land area with the highest combined value of taxonomic diversity (TD; i.e., species richness; SR), evolutionary history-related indices (e.g., phylogenetic diversity; PD, phylogenetic endemism; PE and evolutionary distinctiveness; ED), and carbon storage. The weights of taxonomic diversity, evolutionary history-related indices and carbon storage were equal. PD, PE and ED were also set the same weight, (**b**) Proportion of SR, PD, ED and carbon storage covered in the PPAs. The dotted circles show the proportion range of 0–100%. The orange line shows the extent to which the PPAs contribute to the protection of SR, PD, ED and carbon storage. Because the calculation of PE was related to the geographical extent of each branch, the percentage of PE coverage cannot be calculated.

3.3. Overlap of Priority Protection Areas with Independent Hotspots for Biodiversity and Carbon Storage

To understand the overlap between biodiversity and carbon storage hotspots in China, we mapped taxonomic diversity, evolutionary history and carbon hotspots in Figure 2a–e to understand how these characteristics extend across the mainland. We found the plant diversity hotspots were mainly concentrated in the southern regions (Figure 2a,b). However, the highest areas for carbon storage were concentrated in the northeast and southwest (Figure 2c). By overlapping synergy priorities with biodiversity and carbon storage hotspots (Figure 2d),

we found that PPAs overlapped with 79.7% of TDHs, 78.1% of EDHs and 59.0% of CSHs. Additionally, 36.4% of the synergy priorities overlapped with TDHs, EDHs and CSHs, and 40.0% of the PPAs overlapped with TDHs and EDHs, while 18.0% of priorities overlapped only with CSHs. We also found a very small number of PPAs overlapped only with EDHs, TDHs and CSHs, or EDHs and CSHs, or with no hotspots at all (Figure 2e).

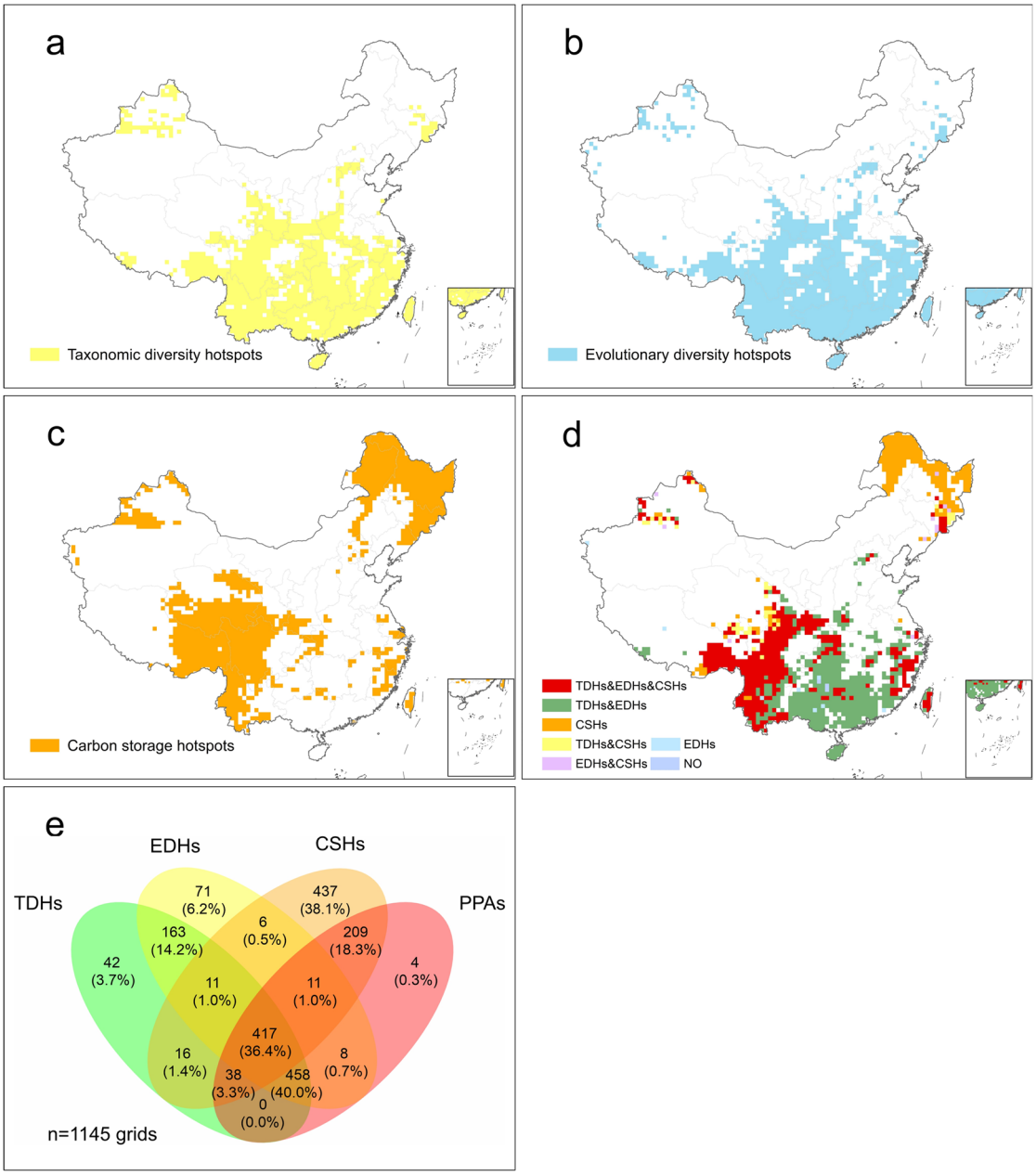


Figure 2. Hotspots map of taxonomic diversity (**a**), evolutionary diversity (i.e., evolutionary history-related indices) (**b**) and carbon storage (**c**). Hotspots were set as the highest value 30% of the area, (**d**) Overlapping map of taxonomic diversity hotspots (TDHs), evolutionary diversity hotspots (EDHs) and carbon storage hotspots (CSHs) in PPAs. For instance, TDHs & EDHs & CSHs means PPAs overlapped with TDHs, EDHs and CSHs, NO means PPAs did not overlap with any hotspot, (**e**) the number and percentage of grids where PPAs overlapped with TDHs, EDHs and CSHs (n = 1145 grids).

Based on the results of the overlap analysis, the synergy priorities can be broadly classified into three types: (1) win–win areas for biodiversity and carbon storage, (2) high biodiversity areas and (3) high carbon areas. Win–win areas for biodiversity and carbon

storage were mainly in the southwestern and southeastern coast of China, and accounted for 36.4% of the priority protection areas and 11.0% of the national area. High carbon areas were mainly in northeastern China, and accounted for 18.3% of the priority protection areas and 5.5% of the national area. Additionally, high biodiversity areas were mainly in southern China, and accounted for 40.0% of the priority protection areas and 12.0% of the national area. (Figure 2d). The win–win areas for biodiversity and carbon storage showed that they can achieve a win–win situation to pursue mutual benefits, while the remaining high biodiversity/low carbon and high carbon/low biodiversity areas will still require careful planning to avoid adverse consequences based on biodiversity and carbon storage priorities.

3.4. Protection Gaps in Priority Protection Areas

After exploring the overlap of different hotspot types, we also investigated protection gaps for different biodiversity and carbon storage hotspots in PPAs. Figure 3a illustrates the number of different overlapping types of grids for biodiversity and carbon storage hotspots and their relative abundance in PAs. The overlap of PPAs and PAs in the coverage map showed that 54.9% (629 out of 1145) of the grid was covered by PAs. Among the three main types of synergy priorities, biodiversity and carbon storage win–win areas had a maximum coverage of 60.7% of the PAs, while high biodiversity areas accounted for 54.8% of the PAs and high carbon areas accounted for the lowest coverage of PAs at 48.8% (Figure 3a). We present the map of protection gaps in PPAs in Figure 3b, and it can provide a theoretical basis for the spatial layout optimization of PAs in China.

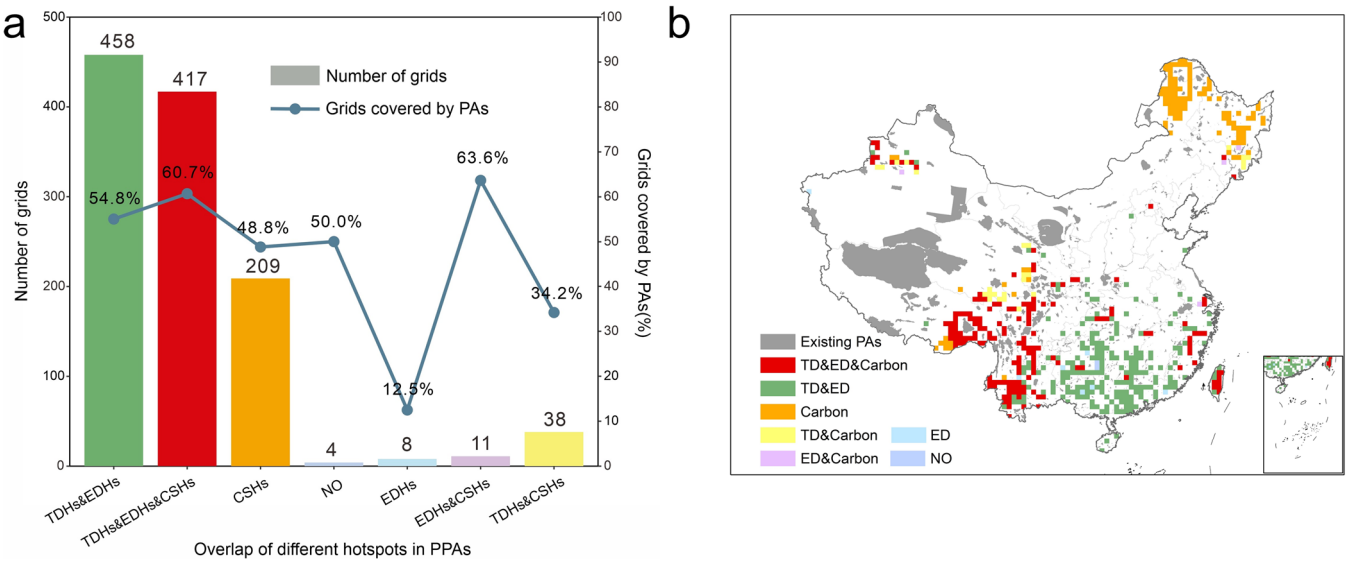


Figure 3. (**a**) The number of different overlapping types of grids for taxonomic diversity hotspots (TDHs), evolutionary diversity hotspots (EDHs) and carbon storage hotspots (CSHs) in priority protection areas (PPAs) and the proportion covered by the protected areas (PAs). The horizontal coordinate indicated the type of overlap between PPAs and TDHs, EDHs, CSHs, the bar chart indicated the number of grids in PPAs and the line chart indicated the proportion of the grids covered by PAs, (**b**) protection gap map of different biodiversity and carbon storage hotspots in PPAs in China. Areas in gray were existing protected areas.

4. Discussion

By using an integrated prioritization approach, we incorporated taxonomic and evolutionary dimensions of biodiversity with carbon storage into conservation objectives. This allowed us to explore the correlations between biodiversity and carbon storage at the national level and further divided the priorities into three potential conservation scenarios based on the relationship between high biodiversity and high carbon storage in PPAs.

From our data, we identified areas that contribute significantly to biodiversity conservation and climate stabilization and analyzed the win–win and trade-offs for both scenarios in PPAs. Together, our findings will contribute to the spatial optimization of PAs and provide recommendations to achieve biodiversity and climate goals.

4.1. Priority Protection Areas of Biodiversity and Carbon Storage

In previous research, there were many debates over how to maximize the co-benefits of carbon storage and biodiversity because of their different correlations at varied scales [9]. Several previous studies found a positive correlation between biodiversity and carbon storage in terrestrial ecosystems [18,48,49]. However, others also found limited or even negative correlations between biodiversity and carbon [50–52]. Our results indicated that even though plant diversity-related metrics were highly correlated (statistical test, $p < 0.001$, $n = 3805$), the relationships between carbon storage and these metrics were still very weak (Table 1) and showed little overlap in spatial hotspots in China. Therefore, setting conservation targets based on biodiversity or carbon storage alone will not provide effective protection for both.

To maximize the conservation of biodiversity and carbon, we need to use an integrated ranking approach to prioritize all biodiversity components and carbon storage [10]. PPAs were defined as the top 30% of the most conserved plants for diversity and carbon storage. These areas contain more than 95% of plant species numbers, 97.4% of the PD, 97.0% of the ED, which indicates their high efficiency and importance for diversity conservation. However, using limited priorities to protect carbon sequestration is not entirely effective. Still, they can protect more than 50% of carbon storage, which is higher than the mean function for all areas. A possible reason why carbon storage is in a smaller proportion compared to biodiversity may be because local species concentrate in small areas that sequester land surface use, which allows for carbon to be more evenly distributed [11]. These results imply that PPAs identification for these two ecosystem functions is generally worth using relatively small areas to protect maximum biodiversity and carbon storage to reduce the effects of climate change and human activities.

4.2. Synergies and Trade-Offs between Biodiversity and Carbon Storage

Although we identified important areas for biodiversity and carbon storage using an integrated ranking approach, synergies and trade-offs between them still exist in these PPAs. Many previous studies showed that high carbon and high biodiversity areas are limited because they do not geographically overlap, e.g., [17,51]. Specifically, areas where high carbon and high plant diversity do not overlap are more widespread than potential win–win areas [53]. Our results suggested that 36.4% of PPAs overlapped with plant diversity and carbon storage hotspots, which were labeled as win–win areas. These regions were not uniformly distributed and were mainly in the southwestern and southeastern coast of China. However, in other PPAs, high biodiversity and high carbon storage did not overlap.

Because of the limited spatial overlap of high biodiversity and high carbon storage areas, their spatial distribution needs to be considered when developing conservation strategies. For example, reducing emissions was an effective measure to mitigate climate change from deforestation and forest degradation (REDD+) [54–56]. This reduction in emissions from deforestation and forest degradation was seen as a win–win solution for carbon storage and biodiversity conservation [57,58]. However, since high biodiversity and high carbon storage areas do not always overlap, some areas with high biodiversity will not benefit from carbon-focused conservation [18]. Particularly, some studies found that focusing on large-scale carbon sequestration plantations may have a negative impact on biodiversity [59]. If the spatial distribution of biodiversity and carbon storage were not simultaneously considered when setting conservation targets, they could cause a shift in deforestation activities from areas with high carbon to areas with low carbon storage, and would also critically affect biodiversity conservation [60,61]. Our results showed that

co-benefits can be achieved between biodiversity and carbon storage in win–win regions within certain PPAs. These results imply that specific policies that maintain carbon storage usually provide additional benefits to biodiversity conservation and those that conserve biodiversity would contribute to maintaining carbon storage. In other areas, however, the prioritization of biodiversity and carbon storage needs to be taken into account to develop separate conservation mechanisms [53].

In addition to the win–win areas, our results divided the PPAs into two other categories: (1) high biodiversity areas and (2) high carbon areas. High carbon areas are mainly located in the forested areas of northeastern China and possess high forest cover that acts as important carbon sinks. In the absence of accelerated natural disturbances, climate variability and land use change, forests are likely to continue to sequester carbon in the future [62]. In particular, high-carbon areas maintain carbon stocks to ensure that natural forests are not damaged further, while also maintaining long-term ecological integrity and taking advantage of opportunities to ensure a net positive impact on biodiversity [60].

In contrast, high biodiversity areas were mainly located in southern China. From our results, high biodiversity areas may represent opportunities for carbon storage policies to focus on ecosystem restoration and improve connectivity. Together, this approach would help to maintain high levels of biodiversity and improve carbon sequestration and storage potential in this area [53]. Ultimately, we suggest that the spatial relationship between biodiversity and carbon storage should be revisited when new conservation strategies are developed, and that different conservation measures need to be created based on examining high biodiversity and high carbon storage overlap patterns.

4.3. Conservation Implication

In this study, we identified areas that were important for biodiversity conservation and carbon storage maintenance. These PPAs may provide more protection for biodiversity and carbon storage with less land use. Our results showed that the existing PAs did not provide comprehensive protection for both biodiversity and carbon storage. Only 54.80% of the PPAs were covered by PAs, and among them, high carbon areas received even less attention. From our data, we recommended optimizing the spatial layout of current PAs based on our protection gaps map and the establishment of new PAs from the theoretical basis we created.

Although more research is needed in the future, the terrestrial, vascular plant data we used helps to start taxonomic diversity research in PAs in China. Ideally, future analyses should consider as many taxa as possible (e.g., vertebrates, invertebrates, etc.) to ensure data completeness, and we need to enhance the collection of data for other taxa in the future. Additionally, data on other ecosystem services (e.g., food, water, etc.) should also be integrated to provide other possible benefits in a limited area. However, with the continuous improvement of data monitoring methods, we expect to improve conservation planning by combining land use types at a higher resolution. Ultimately, with regard to evolving conservation planning due to climate change, new approaches to protect biodiversity and ecosystem services must be improved to ensure the well-being of future generations.

5. Conclusions

Using China as an example, we found that the correlations between biodiversity metrics and carbon storage were very weak in terms of large spatial relationships, but that PPAs could maintain significant carbon storage while conserving most plant diversity (e.g., SR, PD, ED). By examining the spatial distribution of high plant diversity and high carbon storage areas in the PPAs and their current coverage by PAs, it is concluded that the inclusion of plant diversity and carbon storage in conservation objectives can be effective in protecting the benefits of both. Even though there was limited overlap between high plant diversity and high carbon storage areas in the PPAs, conservation strategies need to be developed based on their spatial relationships.

Author Contributions: L.M. contributed to the study's conception and design; material preparation, data collection, and analysis were performed by C.T., Y.D. and L.M.; the first draft of the manuscript was written by C.T. and L.M. All authors have read and agreed to the published version of the manuscript.

Funding: Jiangsu Social Development Project (BE2022792), the Strategic Priority Research Program of the Chinese Academy of Sciences (XDB31000000), National Natural Science Foundation of China (31870506).

Institutional Review Board Statement: Not applicable.

Informed Consent Statement: Not applicable.

Data Availability Statement: The datasets generated during and/or analyzed during the current study are available from the references cited in the paper.

Acknowledgments: We thank Yuheng Chen, Xudong Lu, Xiuping Wu, Xiao Li from Nanjing Forestry University for their assistance on data processing, as well as anonymous reviewers for their helpful suggestions. We would like to thank Kelly Dunham for editing the manuscript.

Conflicts of Interest: The authors declare no conflict of interest.

References

1. Shin, Y.; Midgley, G.F.; Archer, E.R.M.; Arneth, A.; Barnes, D.K.A.; Chan, L.; Hashimoto, S.; Hoegh-Guldberg, O.; Insarov, G.; Leadley, P.; et al. Actions to halt biodiversity loss generally benefit the climate. *Glob. Chang. Biol.* **2022**, *28*, 2846–2874. [CrossRef] [PubMed]
2. De Vos, J.M.; Joppa, L.N.; Gittleman, J.L.; Stephens, P.R.; Pimm, S.L. Estimating the normal background rate of species extinction. *Conserv. Biol.* **2015**, *29*, 452–462. [CrossRef] [PubMed]
3. Urban, M.C. Accelerating extinction risk from climate change. *Science* **2015**, *348*, 571–573. [CrossRef]
4. Visconti, P.; Butchart, S.H.M.; Brooks, T.M.; Langhammer, P.F.; Marnewick, D.; Vergara, S.; Yanosky, A.; Watson, J.E.M. Protected area targets post-2020. *Science* **2019**, *364*, 239–241. [CrossRef]
5. Rodrigues, A.S.; Akcakaya, H.R.; Andelman, S.J.; Bakarr, M.I.; Boitani, L.; Brooks, T.M.; Chanson, J.S.; Fishpool, L.D.; Da Fonseca, G.A.; Gaston, K.J.; et al. Global gap analysis: Priority regions for expanding the global protected-area network. *BioScience* **2004**, *54*, 1092–1100. [CrossRef]
6. Watson, J.E.M.; Dudley, N.; Segan, D.B.; Hockings, M. The performance and potential of protected areas. *Nature* **2014**, *515*, 67–73. [CrossRef]
7. Venter, O.; Koh, L.P. Reducing emissions from deforestation and forest degradation (REDD+): Game changer or just another quick fix? *Ann. N. Y. Acad. Sci.* **2012**, *1249*, 137–150. [CrossRef] [PubMed]
8. Midgley, G.F.; Bond, W.J.; Kapos, V.; Ravilious, C.; Scharlemann, J.P.; Woodward, F.I. Terrestrial carbon stocks and biodiversity: Key knowledge gaps and some policy implications. *Curr. Opin. Environ. Sustain.* **2010**, *2*, 264–270. [CrossRef]
9. Di Marco, M.; Watson, J.E.M.; Currie, D.J.; Possingham, H.P.; Venteret, O. The extent and predictability of the biodiversity-carbon correlation. *Ecol. Lett.* **2018**, *21*, 365–375. [CrossRef] [PubMed]
10. Girardello, M.; Santangeli, A.; Mori, E.; Chapman, A.; Fattorini, S.; Naidoo, R.; Bertolino, S.; Svenning, J.C. Global synergies and trade-offs between multiple dimensions of biodiversity and ecosystem services. *Sci. Rep.* **2019**, *9*, 5636. [CrossRef]
11. Thomas, C.D.; Anderson, B.J.; Moilanen, A.; Eigenbrod, F.; Heinemeyer, A.; Quaife, T.; Roy, D.B.; Gillings, S.; Armsworth, P.R.; Gaston, K.J. Reconciling biodiversity and carbon conservation. *Ecol. Lett.* **2013**, *16*, 39–47. [CrossRef] [PubMed]
12. Reside, A.E.; VanDerWal, J.; Moran, C. Trade-offs in carbon storage and biodiversity conservation under climate change reveal risk to endemic species. *Biol. Conserv.* **2017**, *207*, 9–16. [CrossRef]
13. Ferreira, J.; Lennox, G.D.; Gardner, T.A.; Thomson, J.R.; Berenguer, E.; Lees, A.C.; Mac Nally, R.; Aragão, L.E.O.C.; Ferraz, S.F.B.; Louzada, J.; et al. Carbon-focused conservation may fail to protect the most biodiverse tropical forests. *Nat. Clim. Chang.* **2018**, *8*, 744–749. [CrossRef]
14. Carwardine, J.; Hawkins, C.; Polglase, P.; Possingham, H.P.; Reeson, A.; Renwick, A.R.; Watts, M.; Martin, T.G. Spatial priorities for restoring biodiverse carbon forests. *BioScience* **2015**, *65*, 372–382. [CrossRef]
15. Bryan, B.A.; Runting, R.K.; Capon, T.; Perring, M.P.; Cunningham, S.C.; Kragt, M.E.; Nolan, M.; Law, E.A.; Renwick, A.R.; Eber, S.; et al. Designer policy for carbon and biodiversity co-benefits under global change. *Nat. Clim. Chang.* **2016**, *6*, 301–305. [CrossRef]
16. Sabatini, F.M.; de Andrade, R.B.; Paillet, Y.; Ódor, P.; Bouget, C.; Campagnaro, T.; Gosselin, F.; Janssen, P.; Mattioli, W.; Nascimbene, J.; et al. Trade-offs between carbon stocks and biodiversity in European temperate forests. *Glob. Chang. Biol.* **2019**, *25*, 536–548. [CrossRef]
17. Soto-Navarro, C.; Ravilious, C.; Arnell, A.; De Lamo, X.; Harfoot, M.; Hill, S.L.L.; Wearn, O.R.; Santoro, M.; Bouvet, A.; Mermoz, S.; et al. Mapping co-benefits for carbon storage and biodiversity to inform conservation policy and action. *Philos. Trans. R. Soc. B* **2020**, *375*, 20190128. [CrossRef]

18. Strassburg, B.B.; Kelly, A.; Balmford, A.; Davies, R.G.; Gibbs, H.K.; Lovett, A.; Miles, L.; Orme, C.D.L.; Price, J.; Turner, R.K.; et al. Global congruence of carbon storage and biodiversity in terrestrial ecosystems. *Conserv. Lett.* **2010**, *3*, 98–105. [CrossRef]
19. Rahman, M.M.; Zimmer, M.; Ahmed, I.; Donato, D.; Kanzaki, M.; Xu, M. Co-benefits of protecting mangroves for biodiversity conservation and carbon storage. *Nat. Commun.* **2021**, *12*, 3875. [CrossRef]
20. Luintel, H.; Scheller, R.M.; Bluffstone, R.A. Assessments of biodiversity, carbon, and their relationships in Nepalese forest commons: Implications for global climate initiatives. *For. Sci.* **2018**, *64*, 418–428. [CrossRef]
21. Jung, M.; Arnell, A.; de Lamo, X.; García-Rangel, S.; Lewis, M.; Mark, J.; Merow, C.; Miles, L.; Ondo, I.; Pironon, S.; et al. Areas of global importance for conserving terrestrial biodiversity, carbon and water. *Nat. Ecol. Evol.* **2021**, *5*, 1499–1509. [CrossRef] [PubMed]
22. Zhu, L.; Hughes, A.C.; Zhao, X.-Q.; Zhou, L.-J.; Ma, K.-P.; Shen, X.-L.; Li, S.; Liu, M.-Z.; Xu, W.-B.; Watson, J.E.M. Regional scalable priorities for national biodiversity and carbon conservation planning in Asia. *Sci. Adv.* **2021**, *7*, eabe4261. [CrossRef]
23. Jenkins, C.N.; Pimm, S.L.; Joppa, L.N. Global patterns of terrestrial vertebrate diversity and conservation. *Proc. Natl. Acad. Sci. USA* **2013**, *110*, E2602–E2610. [CrossRef]
24. Mazel, F.; Guilhaumon, F.; Mouquet, N.; Devictor, V.; Gravel, D.; Renaud, J.; Cianciaruso, M.V.; Loyola, R.; Diniz-Filho, J.A.F.; Mouillot, D.; et al. Multifaceted diversity-area relationships reveal global hotspots of mammalian species, trait and lineage diversity. *Glob. Ecol. Biogeogr.* **2014**, *23*, 836–847. [CrossRef]
25. Faith, D.P. Conservation evaluation and phylogenetic diversity. *Biol. Conserv.* **1992**, *61*, 1–10. [CrossRef]
26. Rosauer, D.; Laffan, S.W.; Crisp, M.D.; Donnellan, S.C.; Cook, L.G. Phylogenetic endemism: A new approach for identifying geographical concentrations of evolutionary history. *Mol. Ecol.* **2009**, *18*, 4061–4072. [CrossRef]
27. Isaac, N.J.; Turvey, S.T.; Collen, B.; Waterman, C.; Baillie, J.E. Mammals on the EDGE: Conservation priorities based on threat and phylogeny. *PLoS ONE* **2007**, *2*, e296. [CrossRef] [PubMed]
28. Faith, D.P. Topics in Biodiversity and Conservation. In *Biodiversity Conservation and Phylogenetic Systematics*; Hawksworth, D.L., Chaurasia, A., Eds.; Springer: Berlin, Germany, 2016; Volume 14, pp. 39–56.
29. Daru, B.H.; le Roux, P.; Gopalraj, J.; Park, D.S.; Holt, B.G.; Greve, M. Spatial overlaps between the global protected areas network and terrestrial hotspots of evolutionary diversity. *Glob. Ecol. Biogeogr.* **2019**, *28*, 757–766. [CrossRef]
30. Fritz, S.A.; Purvis, A. Selectivity in mammalian extinction risk and threat types: A new measure of phylogenetic signal strength in binary traits. *Conserv. Biol.* **2010**, *24*, 1042–1051. [CrossRef]
31. Davies, T.J.; Yessoufou, K. Revisiting the impacts of non-random extinction on the tree-of-life. *Biol. Lett.* **2013**, *9*, 20130343. [CrossRef]
32. Brum, F.T.; Graham, C.H.; Costa, G.C.; Hedges, S.B.; Penone, C.; Radeloff, V.C.; Rondinini, C.; Loyola, R.; Davidson, A.D. Global priorities for conservation across multiple dimensions of mammalian diversity. *Proc. Natl. Acad. Sci. USA* **2017**, *114*, 7641–7646. [CrossRef]
33. Levine, M.D.; Aden, N.T. Global carbon emissions in the coming decades: The case of China. *Annu. Rev. Environ. Resour.* **2008**, *33*, 19–38. [CrossRef]
34. Li, J.; Guo, X.; Chuai, X.; Xie, F.; Yang, F.; Gao, R.; Ji, X. Reexamine China's terrestrial ecosystem carbon balance under land use-type and climate change. *Land. Use Policy* **2021**, *102*, 105275. [CrossRef]
35. Chuai, X.; Huang, X.; Lu, Q.; Zhang, M.; Zhao, R.; Lu, J. Spatiotemporal changes of built-up land expansion and carbon emissions caused by the Chinese construction industry. *Environ. Sci. Technol.* **2015**, *49*, 13021–13030. [CrossRef]
36. Wang, L.; Gao, J.; Shen, W.; Shi, Y.; Zhang, H. Carbon storage in vegetation and soil in Chinese ecosystems estimated by carbon transfer rate method. *Ecosphere* **2021**, *12*, e03341. [CrossRef]
37. Yang, Y.; Shi, Y.; Sun, W.; Chang, J.; Zhu, J.; Chen, L.; Wang, X.; Guo, Y.; Zhang, H.; Yu, L.; et al. Terrestrial carbon sinks in China and around the world and their contribution to carbon neutrality. *Sci. China Life Sci.* **2022**, *65*, 860–895. [CrossRef]
38. Xu, L.; Yu, G.; He, N.; Wang, Q.; Gao, Y.; Wen, D.; Li, S.; Niu, S.; Ge, J. Carbon storage in China's terrestrial ecosystems: A synthesis. *Sci. Rep.* **2018**, *8*, 2806. [CrossRef] [PubMed]
39. Lu, L.-M.; Mao, L.-F.; Yang, T.; Ye, J.-F.; Liu, B.; Li, H.-L.; Sun, M.; Miller, J.T.; Mathews, S.; Hu, H.-H.; et al. Evolutionary history of the angiosperm flora of China. *Nature* **2018**, *554*, 234–238. [CrossRef]
40. Jin, Y.; Qian, H.V. PhyloMaker: An R package that can generate very large phylogenies for vascular plants. *Ecography* **2019**, *42*, 1353–1359. [CrossRef]
41. Smith, S.A.; Brown, J.W. Constructing a broadly inclusive seed plant phylogeny. *Am. J. Bot.* **2018**, *105*, 302–314. [CrossRef] [PubMed]
42. Zanne, A.E.; Tank, D.C.; Cornwell, W.K.; Eastman, J.M.; Smith, S.A.; FitzJohn, R.G.; McGlinn, D.J.; O'Meara, B.C.; Moles, A.T.; Reich, P.B.; et al. Three keys to the radiation of angiosperms into freezing environments. *Nature* **2014**, *506*, 89–92. [CrossRef]
43. Spawn, S.A.; Sullivan, C.C.; Lark, T.J.; Gibbs, H.K. Harmonized global maps of above and belowground biomass carbon density in the year 2010. *Sci. Data* **2020**, *7*, 112. [CrossRef]
44. Kembel, S.W.; Cowan, P.D.; Helmus, M.R.; Cornwell, W.K.; Morlon, H.; Ackerly, D.D.; Blomberg, S.P.; Webb, C.O. Picante: R tools for integrating phylogenies and ecology. *Bioinformatics* **2010**, *26*, 1463–1464. [CrossRef]
45. Guerin, G.R.; Lowe, A.J. Mapping phylogenetic endemism in R using georeferenced branch extents. *SoftwareX* **2015**, *3*, 22–26. [CrossRef]

46. Cadotte, M.W.; Davies, T.J. Rarest of the rare: Advances in combining evolutionary distinctiveness and scarcity to inform conservation at biogeographical scales. *Divers. Distrib.* **2010**, *16*, 376–385. [CrossRef]
47. Lehtomäki, J.; Moilanen, A. Methods and workflow for spatial conservation prioritization using Zonation. *Environ. Modell. Softw.* **2013**, *47*, 128–137. [CrossRef]
48. Buchanan, G.M.; Donald, P.F.; Butchart, S.H.M. Identifying priority areas for conservation: A global assessment for forest-dependent birds. *PLoS ONE* **2011**, *6*, e29080. [CrossRef] [PubMed]
49. Siikamäki, J.; Newbold, S.C. Potential biodiversity benefits from international programs to reduce carbon emissions from deforestation. *Ambio* **2012**, *41*, 78–89. [CrossRef] [PubMed]
50. Paoli, G.D.; Wells, P.L.; Meijaard, E.; Struebig, M.J.; Marshall, A.J.; Obidzinski, K.; Tan, A.; Rafiastanto, A.; Yaap, B.; Ferry Slik, J.W.; et al. Biodiversity conservation in the REDD. *Carbon Balance Manag.* **2010**, *5*, 7. [CrossRef] [PubMed]
51. Murray, J.P.; Grenyer, R.; Wunder, S.; Raes, N.; Jones, J.P.G. Spatial patterns of carbon, biodiversity, deforestation threat, and REDD+ projects in Indonesia. *Conserv. Biol.* **2015**, *29*, 1434–1445. [CrossRef]
52. Beaudrot, L.; Kroetz, K.; Alvarez-Loayza, P.; Amaral, I.; Breuer, T.; Fletcher, C.; Jansen, P.A.; Kenfack, D.; Lima, M.G.M.; Marshall, A.R.; et al. Limited carbon and biodiversity co-benefits for tropical forest mammals and birds. *Ecol. Appl.* **2016**, *26*, 1098–1111. [CrossRef]
53. Armenteras, D.; Rodríguez, N.; Retana, J. National and regional relationships of carbon storage and tropical biodiversity. *Biol. Conserv.* **2015**, *192*, 378–386. [CrossRef]
54. Agrawal, A.; Nepstad, D.; Chhatre, A. Reducing emissions from deforestation and forest degradation. *Annu. Rev. Environ. Resour.* **2011**, *36*, 373–396. [CrossRef]
55. Berenguer, E.; Ferreira, J.; Gardner, T.A.; Aragão, L.E.O.C.; De Camargo, P.B.; Cerri, C.E.; Durigan, M.; De Oliveira, R.C.; Vieira, I.C.G.; Barlow, J. A large-scale field assessment of carbon stocks in human-modified tropical forests. *Glob. Chang. Biol.* **2014**, *20*, 3713–3726. [CrossRef]
56. Guizar-Coutiño, A.; Jones, J.P.G.; Balmford, A.; Carmenta, R.; Coomes, D.A. A global evaluation of the effectiveness of voluntary REDD+ projects at reducing deforestation and degradation in the moist tropics. *Conserv. Biol.* **2022**, *36*, e13970. [CrossRef]
57. Harvey, C.A.; Dickson, B.; Kormos, C. Opportunities for achieving biodiversity conservation through REDD. *Conserv. Lett.* **2010**, *3*, 53–61. [CrossRef]
58. Phelps, J.; Webb, E.L.; Adams, W.M. Biodiversity co-benefits of policies to reduce forest-carbon emissions. *Nat. Clim. Chang.* **2012**, *2*, 497–503. [CrossRef]
59. Lindenmayer, D.B.; Hulvey, K.B.; Hobbs, R.J.; Colyvan, M.; Felton, A.; Possingham, H.; Steffen, W.; Wilson, K.; Youngentob, K.; Gibbons, P. Avoiding bio-perversity from carbon sequestration solutions. *Conserv. Lett.* **2012**, *5*, 28–36. [CrossRef]
60. Gardner, T.A.; Burgess, N.D.; Aguilar-Amuchastegui, N.; Barlow, J.; Berenguer, E.; Clements, T.; Danielsen, F.; Ferreira, J.; Foden, W.; Kapos, V.; et al. A framework for integrating biodiversity concerns into national REDD+ programmes. *Biol. Conserv.* **2012**, *154*, 61–71. [CrossRef]
61. Jones, K.B.; Zurlini, G.; Kienast, F.; Petrosillo, I.; Edwards, T.; Wade, T.G.; Li, B.-L.; Zaccarelli, N. Informing landscape planning and design for sustaining ecosystem services from existing spatial patterns and knowledge. *Landsc. Ecol.* **2013**, *28*, 1175–1192. [CrossRef]
62. Pan, Y.; Birdsey, R.A.; Fang, J.; Houghton, R.; Kauppi, P.E.; Kurz, W.A.; Phillips, O.L.; Shvidenko, A.; Lewis, S.L.; Canadell, J.G.; et al. A large and persistent carbon sink in the world's forests. *Science* **2011**, *333*, 988–993. [CrossRef] [PubMed]

Disclaimer/Publisher's Note: The statements, opinions and data contained in all publications are solely those of the individual author(s) and contributor(s) and not of MDPI and/or the editor(s). MDPI and/or the editor(s) disclaim responsibility for any injury to people or property resulting from any ideas, methods, instructions or products referred to in the content.

forests

MDPI

Article

Ilex danxiaensis (Aquifoliaceae), a Distinct New Tree Species Endemic to Danxia Mountain in Guangdong Province, China, Based on Molecular and Morphological Evidence

Chenxue Lin [1], Wanyi Zhao [2], Zaixiong Chen [3], Qiang Fan [2,*] and Kewang Xu [1,*]

[1] Key Laboratory of National Forestry and Grassland Administration on Subtropical Forest Biodiversity Conservation, Co-Innovation Center for Sustainable Forestry in Southern China, College of Biology and the Environment, Nanjing Forestry University, Nanjing 210037, China
[2] State Key Laboratory of Biocontrol and Guangdong Provincial Key Laboratory of Plant Resources, School of Life Sciences, Sun Yat-Sen University, Guangzhou 510275, China
[3] Administrative Commission of Danxiashan National Park, Shaoguan 512300, China
* Correspondence: fanqiang@mail.sysu.edu.cn (Q.F.); xukw10@njfu.edu.cn (K.X.)

Abstract: Many holly species are dominant species in evergreen broad-leaved forests, and they play an important role in the formation and maintenance of forest ecosystems in tropical and subtropical regions. Here, a new holly species (*Ilex danxiaensis* K. W. Xu & Q. Fan) of Aquifoliaceae was discovered from Guangdong, China, when conducting biodiversity investigations in the Danxia landform. We inferred the phylogenetic position of the new species based on sequences from three nuclear markers, namely internal transcribed spacer (ITS), external transcribed spacer (ETS), and chloroplast glutamine synthetase gene (*nepGS*). The results demonstrated a close relationship among the new species and members of *I.* sect. *Lioprinos*. The inferred phylogenetic position of the new species is also supported by morphological evidence that all of these species are characterized by having axillary cymes inflorescences and abaxially 1-sulcate pyrenes. However, the new species can be distinguished from others by having puberulent branchlets, petioles, peduncles, and pedicel; (1–)2–3-flowered cymes of male inflorescences; 1-flowered cymes of female inflorescences; ciliate sepals, 4-merous flowers, pink or white female flowers; and 4 pyrenes.

Keywords: biodiversity conservation; *Ilex*; Danxia Mountain; molecular phylogeny; new species

check for updates

Citation: Lin, C.; Zhao, W.; Chen, Z.; Fan, Q.; Xu, K. *Ilex danxiaensis* (Aquifoliaceae), a Distinct New Tree Species Endemic to Danxia Mountain in Guangdong Province, China, Based on Molecular and Morphological Evidence. *Forests* **2023**, *14*, 583. https://doi.org/10.3390/f14030583

Academic Editor: Carol A. Loopstra

Received: 17 February 2023
Revised: 8 March 2023
Accepted: 13 March 2023
Published: 15 March 2023

Copyright: © 2023 by the authors. Licensee MDPI, Basel, Switzerland. This article is an open access article distributed under the terms and conditions of the Creative Commons Attribution (CC BY) license (https://creativecommons.org/licenses/by/4.0/).

1. Introduction

As the only genus of Aquifoliaceae, *Ilex* is characterized by unisexual flowers, axillary cymose inflorescences (sometimes reduced to one flower), and fruits containing 1–6(–23) pyrenes [1]. It comprises more than 400 species in the tropical to temperate regions of the world, with its biodiversity center in South America and Asia [2]. The total species number in the genus is still ill-defined due to insufficient taxonomic revision of the genus worldwide [3]. A total of 204 species have been recorded, and additional new species have been discovered and added to the checklist of *Ilex* in China [4–11]. The majority of these *Ilex* species are distributed in montane forests in southern areas of the Yangtze River [4]. The *Ilex* species are evergreen or deciduous trees and shrubs, and plants of the genus are dioecious [1]. Many species of the holly genus are dominant species in evergreen broad-leaved forests, and they play an important role in the formation and maintenance of forest ecosystems in tropical and subtropical areas [12,13]. Therefore, determining the phylogeny and taxonomy of genus *Ilex* has important implications for the study of forest biodiversity and the role of pivotal species in forest ecosystems.

Phylogenetically, *Ilex* (Aquifoliaceae) are well placed within the order Aquifoliales, at the base of the Campanulids [14]. However, the infrageneric relationships and taxonomy of the genus remain poorly understood [15–18]. Recently, Yang et al. [19] proposed a

comprehensive classification of the genus based on a combination of morphological traits, distribution patterns, and phylogeny that was reconstructed using the three nuclear genes of internal transcribed spacer (ITS), external transcribed spacer (ETS), and chloroplast glutamine synthetase gene (*nepGS*). They made a major revision of the previous classification because the nonmonophyly taxa (subgenera, sections, and series) in the previous classification were based only on morphology data. A total of 14 sections of the genus were recognized in their study: *I.* sect. *Cassinoides* Loes.; *I.* sect. *Glabra* Yi Yang & H. Peng; *I.* sect. *Lioprinos* (Loes.) S. Y. Hu; *I.* sect. *Ilex*; *I.* sect. *Indico-Malaicae* Loes.; *I.* sect. *Micrococca* (Loes.) S. Y. Hu; *I.* sect. *Microdontae* Loes.; *I.* sect. *Paltoria* (Ruiz & Pav.); *I.* sect. *Prinoides* (DC.) A. Gray; *I.* sect. *Prinos* (L.) A. Gray; *I.* sect. *Prinifoliae* Loes.; *I.* sect. *Pseudoprinos* S. Y. Hu; *I.* sect. *Pseudoaquifolium* S. Y. Hu; and *I.* sect. *Repandae* (Loes.) Yi Yang & H. Peng. However, interspecific hybridization and introgression events make this lineage very complex in terms of phylogeny and taxonomy [16,20]. There are still some clades/taxa that have not been well resolved due to the low resolution of the phylogeny. In addition, the macromorphology (e.g., leaf shape and leaf size) of the *Ilex* species often shows great variability at the intraspecific level, resulting in difficulties in discriminating between different species [2].

Recently, we conducted a comprehensive botanical expedition in the Danxia Mountain National Nature Reserve, Renhua County, Guangdong Province, China (Figure 1). During this expedition, we encountered an unusual species of *Ilex*. In general, this species belongs to members of *I.* sect. *Lioprinus*, and, morphologically, it is most similar to *I. hirsuta* C. J. Tseng ex S. K. Chen et Y. X. Feng in having branchlets, petioles, peduncles, and pedicel puberulent; leaf margin sparsely serrate; inflorescences cymes; and pyrenes broadly one-sulcate abaxially. However, this species has male inflorescences monochasium, flowers four-merous, female flowers pink or white, and pyrenes four, while *I. hirsuta* has male inflorescences monochasium or dichasium, flowers five-merous, and four or five pyrenes. After carefully examining herbarium specimens and the relevant literature, we confirmed that it represents an undescribed new species [21–23]. Here, we describe it as *I. danxiaensis* K. W. Xu & Q. Fan with a report on its phylogenetic position based on three nuclear genes.

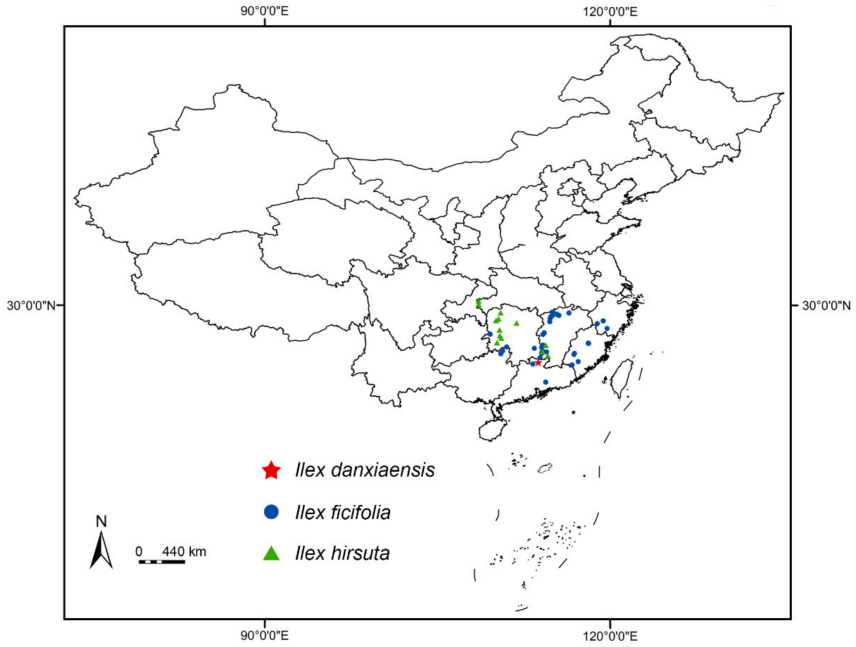


Figure 1. Distribution map of the three morphological similar species *Ilex danxiaensis*, *I. ficifolia*, and *I. hirsuta* in China, on the basis of the specimens examined in this study and flora of China.

2. Material and Methods

2.1. Morphological Study

The investigations were carried out on pollen samples from two different origins (Agongyan and Huangshakeng of Danxia Mountain) obtained from living specimens in wild populations. Mature and well-developed pollen grains were selected for investigation. Measurements of stomate morphology were conducted using mature and intact leaves obtained from living specimens. Morphology of pollen grains and stomates was observed using an ESEM-Quanta 200 (FEI, Hillsboro, OR, USA) after being sputter-coated with gold. To determine pyrene morphology, we collected the mature red fruits and rinsed each fruit sarcocarp using clean water. We counted the pyrene number of each fruit. Then, the clean pyrene features of the new species were obtained using an Olympus SZX10 dissecting microscope (Olympus Corp., Tokyo, Japan). Quantitative values of each morphological character were measured using ImageJ software (Version 1.54b, Bethesda, MD, USA, Rasband 1997–2017) [24]. All digital images of specimens examined in this study were provided by the National Specimen Information Infrastructure (available at http://www.nsii.org.cn/ accessed 5 August 2022), Global Biodiversity Information Facility (available at https://www.gbif.org/ accessed 6 August 2022), and JSTOR (available at https://plants.jstor.org/ accessed 5 August 2022). Voucher specimens were deposited in the Herbarium of Sun Yat-Sen University (SYS) and Nanjing Forestry University (NF).

2.2. Phylogenetic Study

To identify the new species, genomic DNA was extracted from silica-gel-dried leaves using the modified 2 × CTAB procedure according to Doyle et al. [25] and used as the template for polymerase chain reaction (PCR). Two nuclear markers were selected for amplification. The primers ITSF and ITSR were used for ITS amplification [18], and the primers GScp687f and GScp994r were used for *nepGS* amplification [26]. Each amplification was carried out in 50 μL of a reaction mixture containing 30 μL 2 × PCR Master Mixture (containing 2 × Taq DNA polymerase, 2 × polymerase chain reaction buffer, 2 × dNTP, and Mg^{2+}, Tiangen), 14 μL of ddH_20, 1 μL of each primer, and 4 μL of DNA template. Polymerase chain reaction thermocycling conditions for ITS and *nepGS* involved an initial denaturation step of 95 °C for 4 min, followed by 35 cycles of 95 °C for 45 s, 58 °C for 1 min, 72 °C for 2 min, and a final extension of 72 °C for 10 min. PCR products were purified and sequenced by TSINGKE Biological Technology (Guangzhou, China).

To test the precise phylogenetic position of the new species *Ilex danxiaensis*, we reconducted phylogenetic analyses using a combined matrix of three nuclear (ITS including ITS1, 5.8S, ITS2, ETS, and *nepGS*) sequences according to results of Yang et al. [19]. We preliminarily speculated that the new species belongs to *I.* sect. *Lioprinos* (Loes.) S. Y. Hu according to its morphological characteristics in our field work. Therefore, the sampling strategy of this study tried to include as many members of *I.* sect. *Lioprinos* as possible, and representative species of each section proposed by Yang et al. [19]. Finally, our data matrix totally contained 91 accessions representing 89 species, including 3 accessions of the new species, 85 accessions of other *Ilex* species, and 3 accessions of outgroup species (Supplemental Data S1). The ITS and *nepGS* of the new species were newly sequenced in this study, and the rest were downloaded from GenBank.

The newly generated raw sequences were assembled and edited using Sequencher (Version 4.14, Ann Arbor, MI, USA). All sequences of ITS, ETS, and *nepGS* were initially aligned using MAFFT (Version 7.480, Tokyo, Japan) [27] and manually adjusted using BioEdit (Version 7.5.5, Wooster, OH, USA) [28]. For each nuclear marker, the maximum-likelihood (ML) tree searches and bootstrapping (BS) were conducted using RAxML-HPC2 on XSEDE (Version 8.2.10, San Diego, CA, US) on the CIPRES web server with 1000 bootstrap replicates [29], with 5000 rapid bootstrap analyses followed by a search for the best-scoring tree in a single run [30,31]. Comparisons of tree topologies from the ML analyses of each individual marker did not identify any well-supported conflicts. Thus, the three nuclear genes were concatenated and analyzed in unison. Bayesian inference (BI) was

conducted using MrBayes (Version 3.2.7a, Stockholm, Sweden) [32] on the CIPRES web server [29] with the temperature parameter set to 0.2, and other priors set to their default values. Two independent runs, each with four simultaneous chains (one cold and three heated), were conducted, each beginning with a random tree and sampling one tree every 1000 generations of 10,000,000 generations. After the first 25% of trees were discarded as burn-in, the remaining trees were used to construct a majority-rule consensus tree with Bayesian posterior probabilities (PPs). ModelFinder [33] was used to select the best-fitting model for ML and BI analyses. The Akaike information criterion (AIC) [34] was used to select among models instead of the hierarchical likelihood ratio test.

3. Results

3.1. Morphological Characteristics of the New Species

Our morphological study showed that the new species has puberulent branchlets, petioles, peduncles, and pedicel; (1–)2–3-flowered cymes of male inflorescences; 1-flowered cymes of female inflorescences; ciliate sepals; 4-merous flowers; pink or white female flowers; and 4 pyrenes, longitudinally 1-sulcate abaxially (Figures 2 and 3). The pollen of the new species is tricolporate, isopolar, and clavate. The polar axis (P) is ca. 45.13 μm; the equatorial axils (E) are ca. 30.98 μm. The exine is ornamented with conspicuous gemmae and clavae of variable size (Figure 4A–C). The stoma (Figure 4D,E) of this new species is amphicyclocytic. The average density of stomata is ca. 275/μm^2 (Figure 4D). The average size of the normal stomata is 37.3 × 33.3 μm. The leaf blades are sparsely puberulent (Figure 4F).

3.2. Phylogenetic Position of the New Species

In this study, a total of six new sequences of the two nuclear genes ITS and *nepGS* were newly generated for the new species (Supplemental Data S1), while other sequences of three nuclear genes (ITS, ETS, and *nepGS*) were downloaded from GenBank. Our final data matrix totally contained 91 accessions representing 89 species, including 3 accessions of the new species, 85 accessions of other *Ilex* species, and 3 accessions of outgroup species (Supplemental Data S1). The alignment length of the nuclear data matrix was 2417 bp, of which 1654 sites were identical, 486 characters were parsimony-informative, and 277 variable characters were parsimony-uninformative. The best-fit nucleotide substitution models GTR+F+I+G4 for ML and BI analyses were selected using ModelFinder [33] based on the Akaike information criterion. The tree topologies by the ML and BI analyses were generally concordant when using the concatenated dataset. The ML phylogeny of genus *Ilex* and outgroups based on the concatenated data is presented in Figure 5.

Our phylogenetic tree inferred from the three nuclear genes resolved our 88 accessions of *Ilex* into 16 strongly or moderately supported clades (Figure 5), of which the moderately supported (MLBS: 66%; BIPP: 1) clade *I.* sect. *Lioprinos* contains the most species (including 24 species) compared with the other strongly or moderately supported clades. Each section proposed by Yang et al. [19] was also resolved as a monophyletic clade with a high or moderate support value in our analyses. In addition to the 14 sections, the strongly supported (MLBS: 83%; BIPP: 0.9) clade containing 2 species (*I. mucronate* (L.) M. Powell, Savol., & S. Andrews and *I. amelanchier* M. A. Curtis ex Chapm.) and the clade only containing 1 species (*I. canariensis* Poir) were also resolved as monophyletic clades (Figure 5). The phylogenetic relationships within each clade were well resolved in the previous study, while the backbone relationships of genus *Ilex* were not well resolved with many weakly supported nodes using the current three nuclear dataset (Figure 5).

Just as we predicted based on morphology evidence, the new species was resolved as a member of *I.* sect. *Lioprinos* in our phylogenetic tree. Together with *I. chinensis* Sims and *I. purpurea* Hassk., they formed a moderately supported clade (MLBS: 65%; BIPP: 1) that was resolved as sister to a clade containing *I. ficifolia* C. J. Tseng ex S. K. Chen & Y. X. Feng, *I. hirsuta*, *I. melanophylla* H. T. Chang, and *I. tainingensis* G. S. He. Although the new

species is most similar to *I. ficifolia* and *I. hirsuta* in morphology, our phylogenetic analyses demonstrate that they are not very closely related.

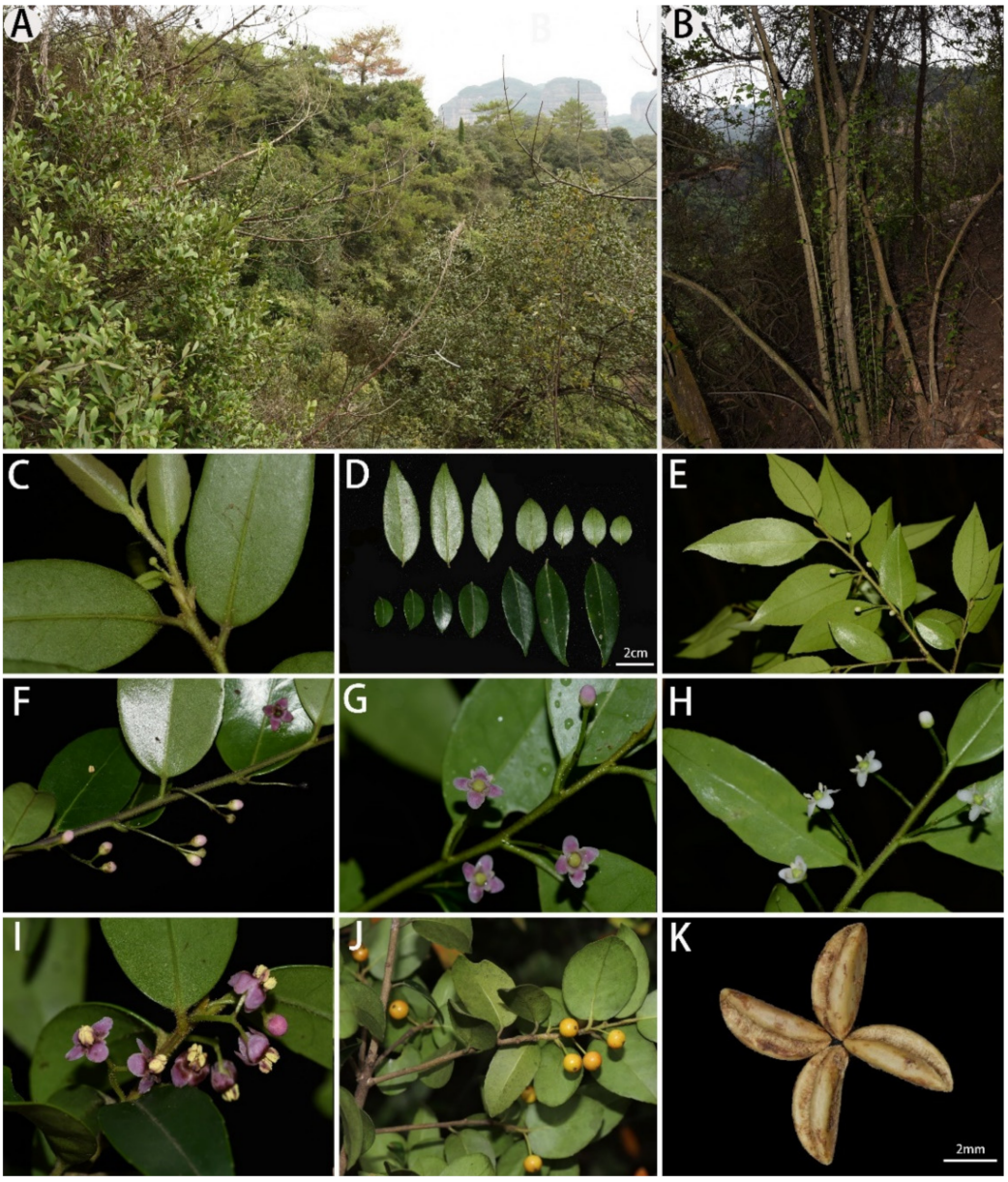


Figure 2. *Ilex danxiaensis* K. W. Xu & Q. Fan, sp. nov. (**A**) Habitat; (**B**) tree trunk; (**C**) annual branches; (**D**) morphological variation of leaf blades; (**E**) female flower buds; (**F**) male flower buds; (**G**) female inflorescence with pink flowers; (**H**) female inflorescence with white flowers; (**I**) male inflorescence and flowers; (**J**) infructescences and fruit; (**K**) pyrenes.

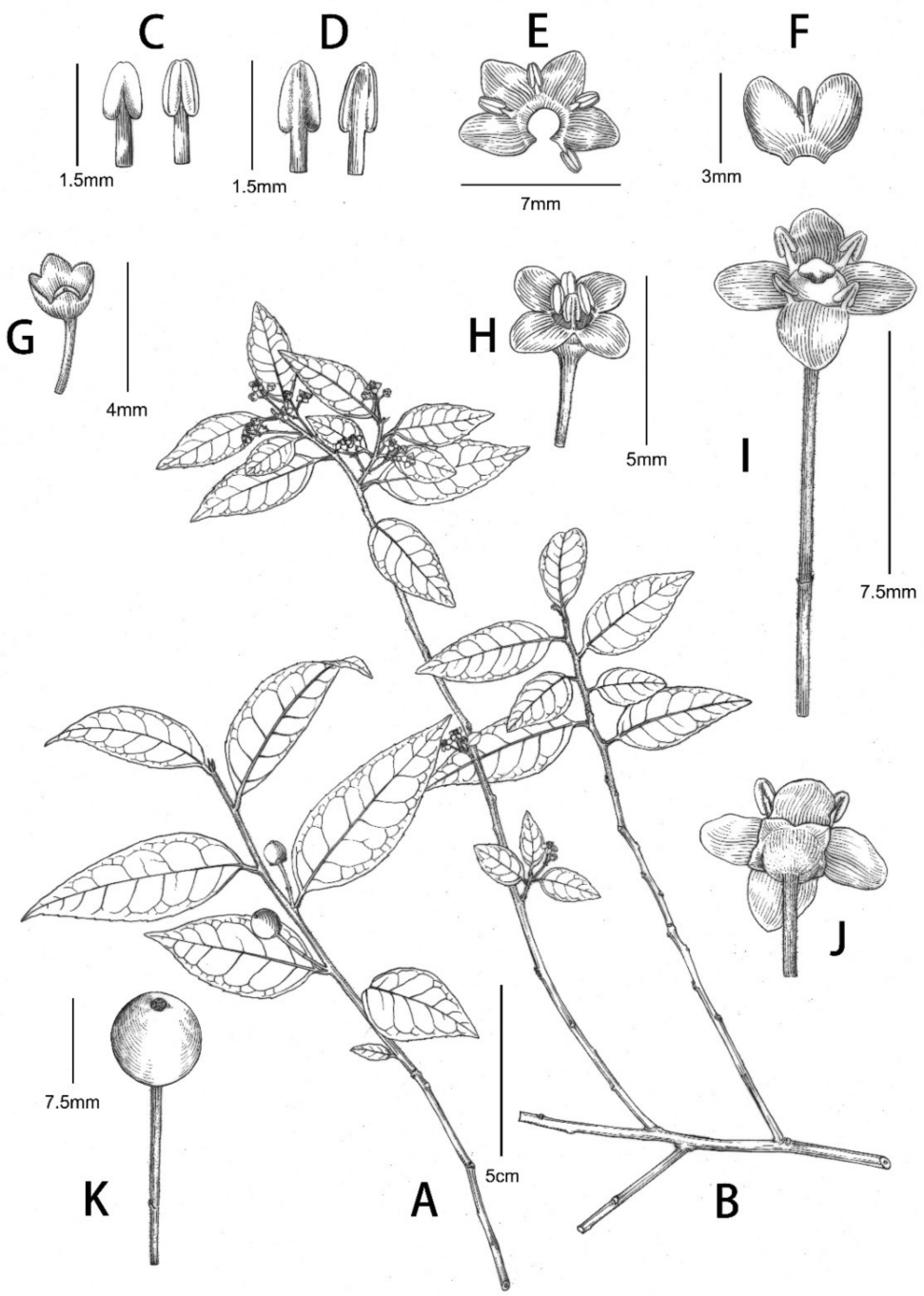


Figure 3. *Ilex danxiaensis* K. W. Xu & Q. Fan, sp. nov. (**A**) Fruiting branches; (**B**) female flowering branches; (**C**) fertile stamen; (**D**) staminodes; (**E**) petals and stamens of male flowers; (**F**) petals and staminodes of female flowers; (**G**) ciliate sepal; (**H**) male flower; (**I**) female flower; (**J**) dorsal view of male flower; (**K**) fruit. Drawn by Yun-Xiao Liu.

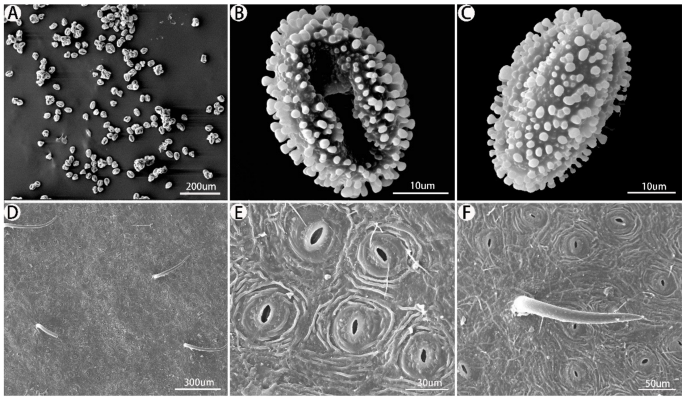


Figure 4. SEM photomicrographs of pollen grains and stomata of *Ilex danxiaensis* sp. nov. (**A**–**C**) Pollen grains; (**D**–**F**) stomata.

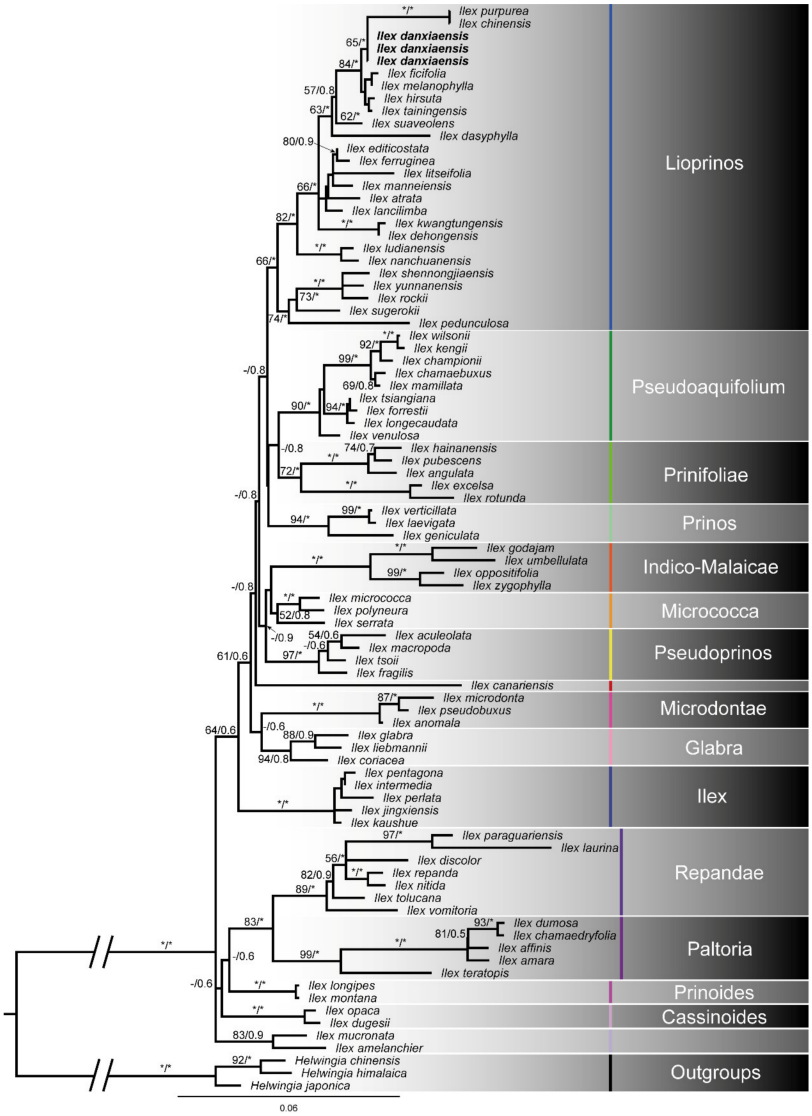


Figure 5. Maximum likelihood (ML) tree of genus *Ilex* from phylogenetic analysis of combined ITS, ETS, and *nepGS* sequence data. Numbers near each branch are maximum-likelihood bootstrap support (MLBS) and Bayesian inference posterior probability (BIPP). Dash means that MLBS $\leq$ 50% or BIPP $\leq$ 0.5. "*" means that MLBS =100% or BIPP=1.0. The new species *Ilex* danxiaensis is indicated in bold in the ML tree.

4. Discussion

4.1. Morphological Comparison

Ilex danxiaensis is morphologically most similar to *I. hirsuta* in having branchlets, petioles, peduncles, and pedicel puberulent; leaf margin sparsely serrate; inflorescences cymes; and pyrenes broadly one-sulcate abaxially. However, the new species can be easily distinguished from *I. hirsuta* by having male inflorescences monochasium, flowers four-merous, female flowers pink or white, and four pyrenes (Figures 2 and 3). In addition, the new species is morphologically similar to *I. ficifolia* in having leaf margin serrulate, inflorescences cymes, peduncles and midvein pubescent, sepals ciliate, and pyrenes broadly one-sulcate abaxially. Nevertheless, the new species has flowers 4-merous, (1–)2–3-flowered cymes of male inflorescences, calyx shallowly 4-lobed, 4 stamens, 1-flowered cymes of female inflorescences, 1-fruited infructescences, and fruit pedicels pubescent (Figures 2 and 3). In contrast, *I. ficifolia* has flowers 4–5-merous, 7-flowered cymes of male inflorescences, calyx shallowly 5-lobed, stamens 5, 3-flowered cymes of female inflorescences, 1–3-fruited infructescences, and fruit pedicels glabrescent [4]. The species can be easily distinguished from each other by the morphological characters listed in Table 1. The pollen size of *Ilex* species is between 17 and 47 mm × 18 and 48 mm [1], which is also supported by that of the new species (average size ca. 45.13 × 30.98 μm). The stoma of this new species is amphicyclocytic, which is similar to the members of *I.* sect. *Lioprinus* (e.g., *I. editicostata* Hu et Tang, *I. ficifolia*, *I. hirsuta*, *I. lancilimba* Merr., etc.) [35].

Table 1. Morphological comparisons among *Ilex danxiaensis* and its morphologically similar species.

Characteristic	*Ilex danxiaensis*	*I. ficifolia*	*I. hirsuta*
Annual branch	densely puberulent	glabrescent	densely puberulent
Petiole	2–5 mm	5–10 mm	ca. 15 mm
Leaf blade	(1.5–)6–8 × (1.2–)2.5–3.5 cm; sparsely puberulent	4–7 × 1.5–3 cm; glabrous	6–7 × 2.5–4 cm; densely hirsute
Male inflorescence	cymes, (1–)2–3-flowered	cymes, 7-flowered	cymes, 1-3-flowered
Male flower	flowers 4-merous; calyx shallowly 4-lobed	flowers 4- or 5-merous; calyx shallowly 5-lobed	flowers 5-merous; calyx shallowly 5-lobed
Female inflorescence	cymes, 1-flowered	cymes, 3-flowered	unknown
Female flower	flowers 4-merous	flowers 4- or 5-merous	unknown
Infructescences	1-fruited	1–3-fruited	1–3-fruited;
Peduncles	ca. 5 mm	0.7–15 mm	ca. 15 mm
Pyrene number per fruit	4	5	4 or 5

4.2. Phylogenetic Analyses

To further determine the phylogenetic position of the new species, we conducted ML and BI analyses for the genus *Ilex* using the sequence data of ITS, ETS, and *nepGS*. With the genus *Helwingia* as the outgroup, the phylogram showed that the genus *Ilex* is well supported as monophyly (Figure 5), which was also supported by the previous phylogenetic studies of the family Aquifoliaceae [16–19]. By using a similar data matrix when conducting our phylogenetic analyses, we generated shallow phylogenetic relationships of the genus *Ilex* similar to those reported by Yang et al. [19]. All the accessions of genus *Ilex* sampled in this study were divided into 16 major clades based on a combination of morphological and distributional characteristics in our phylogenetic tree (Figure 5). Comparisons of our tree topologies with those of Yang et al. [19] did not identify any well-supported conflicts. However, the deep relationships of the genus were somewhat discrepant between the two analyses largely due to the low resolution of the phylogenetic tree reconstructed using the three nuclear genes. For example, in the present study, *I.* sect. *Lioprinos* was weakly resolved as sister to a clade containing three sections (*I.* sect. *Prinifoliae*, *I.* sect. *Prinos*, and *I.* sect. *Pseudoaquifolium*), while in the analyses of Yang et al. [19], *I.* sect. *Lioprinos* was weakly resolved as sister to a clade containing four sections (*I.* sect. *Microdontae*, *I.* sect. *Prinifoliae*, *I.* sect. *Prinos*, and *I.* sect. *Pseudoaquifolium*). Another example, *I.* sect. *pal-*

toria, was resolved as sister to *I.* sect. *repandae* in our phylogeny, while in the analyses of Yang et al. [19], *I.* sect. *paltoria* was resolved as sister to all other members of genus *Ilex*. These phylogenetic inconsistencies demonstrated that the current backbone phylogenetic relationships of the genus *Ilex* are unstable based on the data matrix of three nuclear genes. Future phylogenetic studies using more comprehensive datasets are urgently needed for the troublesome genus *Ilex* (Figure 5).

Though the deep relationships within the genus were not well resolved in the current analyses, three accessions of *I. danxiaensis* were well resolved to cluster together in our phylogenetic tree. Together with *I. chinensis* and *I. purpurea*, they formed a moderately supported clade, which revealed that they might be closely related to each other (Figure 5). In fact, *I. chinensis* and *I. purpurea* were initially assigned to *I.* sect. *Lioprinos* based on morphological evidence [4]. Members of this section are characterized by having leaf margin serrulate, inflorescences cymes, and pyrenes broadly one-sulcate abaxially [4]. Recently, Yang et al. [19] also confirmed that they belong to members of *I.* sect. *Lioprinos* based on their phylogenetic analyses. Therefore, the new species is unarguably a member of *I.* sect. *Lioprinos* based on our phylogenetic analyses (Figure 5). Morphologically, the new species is characterized by having branchlets, petioles, peduncles, and pedicel puberulent, leaf margin sparsely serrate, inflorescences cymes, flowers white or pink, fruit red, four pyrenes each fruit, and pyrenes broadly one-sulcate abaxially. These features also support the conclusion that this species is a member of *I.* sect. *Lioprinos* based on molecular phylogeny. Thus, the status of the new species was confirmed, and the relationships among the new species and its closely related species in *I.* sect. *Lioprinus* were supported by both morphology and molecular data.

4.3. Distribution Ranges of Ilex danxiaensis and the Two Morphologically Similar Species

Ilex danxiaensis is currently known only from two populations on Danxia Mountain in Renhua County, Guangdong Province of China. It might be restricted to the Danxia landform of South China (Figure 1). However, its morphologically similar species *I. hirsuta* is sporadically distributed in regions of central and east China and *I. ficifolia* is widely distributed in regions of central, east, and south China (Figure 1). The latter two species *I. hirsuta* and *I. ficifolia* mainly occur in acidic soils, rarely in the areas of the Danxia landform.

4.4. Conservation Significance

The conservation status of the new species *I. danxiaensis* caught our attention. The new species is suggested as an endangered species and listed as CR, which is attributed to its extremely small populations with less than 50 mature individuals. In addition, its typical locality, Danxia Mountain, is a well-known national scenic area. The activities of tourists might be a potential threat for regional biodiversity in Danxia Mountain.

Danxia Mountain, located in the northern part of Guangdong province, is one of the famous examples of Danxia landform characterized by red-colored sandstones and conglomerates of largely Cretaceous age [36]. Danxia Mountain harbors many endemic species and is a mountain with very rich endemic elements owing to its unique geological and geomorphic structure [36]. Local governments have made great efforts to protect biodiversity in the mountain and carried out numerous biodiversity surveys in recent years. Consequently, a lot of new and endemic species have been found there, e.g., *Lespedeza danxiaensis* Q. Fan, W. Y. Zhao & K. W. Jiang [37] and *Asplenium danxiaense* K. W. Xu [38]. The discovery of these species serves to reveal the formation and maintenance mechanism of regional biodiversity on Danxia Mountain. As a result, the biological conservation of primary vegetation and endangered species of this biodiversity hot spot is quite important, and conservation action is necessary.

4.5. Taxonomic Treatment

Ilex danxiaensis K. W. Xu & Q. Fan, sp. nov. (Figures 2 and 3).

Type. China. Guangdong: Shaoguan City, Danxia Mountain, Agongyan, elev. 210 m, 25°01′39.08″ N, 113°45′15.13″ E, 11 October 2020, *Q. Fan 18438* (holotype SYS!; isotype NF!).

Diagnosis. The new species morphologically resembles *I. hirsuta* in having branchlets, petioles, peduncles, and pedicel puberulent; leaf margin sparsely serrate; inflorescences cymes; and pyrenes broadly one-sulcate abaxially. It differs in having male inflorescences monochasium (vs. male inflorescences monochasium or dichasium), flowers four-merous (vs. flowers five-merous), and four pyrenes (vs. four or five pyrenes).

Description. Shrubs or trees, evergreen, up to 8 m tall. Annual branches subterete, green to greyish-green, densely puberulent, hairs yellowish-brown; perennial branches grayish white, glabrescent; lenticels sparse, indistinct. Petiole 2–5 mm, adaxially longitudinally sulcate, densely puberulent when young; leaf blade abaxially greenish, adaxially dark green, narrow elliptic or ovate-lanceolate, (1.5–)6–8 × (1.2–)2.5–3.5 cm, leathery, midvein raised and pubescent abaxially when mature, flat, or impressed and glabrescent adaxially, lateral veins 4–6(–8) pairs, slightly raised on both surfaces, anastomosing near margin, reticulate veins obvious abaxially, obscure adaxially, base cuneate or obtuse, basal margin near entire, upper serrulate, slightly recurved, apex acuminate. Inflorescences: cymes, solitary, axillary. Male inflorescences: cymes, (1–)2–3-flowered; peduncles (3–)5–12 mm, brown-yellow pilose; bracteoles 1, basal, subulate, ca. 1 mm; flowers pink, 4-merous; pedicel 3–5 mm; calyx shallowly 4-lobed, lobes obtuse, ciliate; petal rotate, ovate, ca. 1.5 × 3 mm, basally slightly connate; stamens 4, ca. 1/2 as long as petals, anthers oblong. Female inflorescences: one-flowered cymes; peduncles ca. 4 mm, brown-yellow pilose; bracteoles 2, subulate, ca. 1 mm; pedicels ca. 1 cm; calyx four-lobed, lobes ciliate; four petals, ovate, ca. 1.5 × 3 mm; staminodes ca. 1.5 mm, sterile anthers ovoid; ovary broadly globose, ca. 2 mm in diam., persistent stigma discoid. Infructescences: 1-fruited cymes; peduncles ca. 5 mm, brown-yellow pilose; fruit pedicels 9–10 mm, pubescent; bracteoles 2, subulate. Fruit yellowish-brown, shiny, subglobose, 5–7 mm in diam.; persistent calyx patelliform, explanate, ciliate, four-lobed; stigma persistent; four pyrenes, ellipsoidal, ca. 4.8 mm long, abaxially broadly and deeply one-sulcate. Fl. May, Fr. Oct–Dec.

Phenology. It starts to flower in May and bears fruits from October to December.

Distribution and habitat. *Ilex danxiaensis* is currently known only from the type of locality, Danxia Mountain National Nature Reserve (Agongyan and Huangshakeng), Guangdong, China (Figure 1). It usually occurs in subtropical evergreen broad-leaved forest at ca. 200 m elevation of mountains with Danxia landform.

Conservation assessment. *Ilex danxiaensis* is endemic to Danxia Mountain National Nature Reserve of Shaoguan City. Currently, only two large populations with no more than 50 mature individuals have been found. According to IUCN Red List criteria D [39], this species should be listed as critically endangered (CR). More extensive fieldwork in nearby mountains with Danxia landform will be needed to accurately assess its conservation status.

Etymology. Based on the mountain name, Danxia, in northern Guangdong, China, and the Latin suffix, -ensis, of origin, referring to the type of locality of the species.

Vernacular name. We propose a Chinese name, Dānxiáshān dōngqīng (丹霞山冬青) to reflect the type locality of the new species.

Additional specimens examined (paratypes). China. Guangdong: Shaoguan City, Danxia Mountain, Agongyan, elev. ca. 210 m, 25°01′39.08″ N, 113°45′15.13″ E, 17 April 2021, *Q. Fan 18960* (SYS!, NF!); China. Guangdong: Shaoguan City, Danxia Mountain, Huangshakeng, elev. 211 m, 25°00′52.23″ N, 113°44′22.33″ E, 18 April 2021, *Q. Fan 18966* (SYS!, NF!).

5. Conclusions

We described a new species of the holly genus *Ilex* (Aquifoliaceae) from Guangdong Province in China, and provided evidence for its phylogenetic position based on the sequence data of ITS, ETS, and *nepGS*. *Ilex danxiaensis* K. W. Xu & Q. Fan, sp. Nov. was only known from a narrow range of the Danxia Mountain in the northern part of Guangdong Province in China, and occurred on the hillside near mountaintop. In our fieldwork, only two populations of the new species were found, and further more detailed investigations on the species are urgently needed to ascertain its distributional range and population status. With our description, we contribute to a better knowledge of the diversity of the genus *Ilex* in southern China, and suggested that more comprehensive phylogenetic and taxonomic studies would highlight the evolution patterns of this group.

Supplementary Materials: The following supporting information can be downloaded at: https://www.mdpi.com/article/10.3390/f14030583/s1, Supplemental Data S1. List of taxa sampled, GenBank accession numbers, and voucher information (/indicates accessions with missing data).

Author Contributions: Field observation and collection, W.Z., Z.C., and Q.F.; data analysis and morphological study, K.X.; experiment and photo typesetting, C.L.; writing—original draft preparation, C.L.; writing—review and editing, K.X. and Q.F. All authors have read and agreed to the published version of the manuscript.

Funding: This work was supported by the Guangdong Provincial Special Research Grant for the Creation of National Parks (2021GJGY034), the Natural Science Foundation of Jiangsu Province (#BK20210612), the National Natural Science Foundation of China (#32100167), and the Nanjing Forestry University project funding (#163108093).

Conflicts of Interest: The authors declare no conflict of interest.

References

1. Loizeau, P.A.; Savolainen, V.; Andrews, S.; Spichiger, R. Aquifoliaceae. The families and genera of vascular plants. In *Flowering Plants. Eudicots*; Kubitzki, K., Ed.; Springer: Berlin/Heidelberg, Germany, 2016; pp. 31–36.
2. Loizeau, P.A.; Barriea, G.; Manen, J.F.; Broennimann, O. Towards an understanding of the distribution of *Ilex*, L. (Aquifoliaceae) on a world-wide scale. *Biol. Skr.* **2005**, *55*, 501–520.
3. Powell, M.; Savolainen, V.; Cuénoud, P.; Manen, J.F.; Andrews, S. The mountain holly (*Nemopanthus mucronatus*: Aquifoliaceae) revisited with molecular data. *Kew Bull.* **2000**, *55*, 341–347. [CrossRef]
4. Chen, S.K.; Ma, H.Y.; Feng, Y.X. Aquifoliaceae. In *Flora of China 19*; Wu, Z.Y., Raven, P.H., Hong, D.Y., Eds.; Science Press: Beijing, China; Missouri Botanical Garden Press: St. Louis, MO, USA, 2008; pp. 449–461.
5. Huang, Y.-F.; Zhuang, Q.-W.; Lai, M.-X. *Ilex jingxiensis* sp. nov. (Aquifoliaceae) from a limestone area along the Sino-Vietnamese border region of China. *Nord. J. Bot.* **2014**, *32*, 848–851. [CrossRef]
6. Jiang, L.; Xu, K.-W.; Fan, Q.; Peng, H. A new species of *Ilex* (Aquifoliaceae) from Jiangxi Province, China, based on morphological and molecular data. *Phytotaxa* **2017**, *298*, 147–157. [CrossRef]
7. Jiang, L.; Wu, L.-F.; Huang, G.-B.; Yu, J.-R.; He, B.-S.; Xu, K.-W. A new species of *Ilex* sect. *Ilex (Aquifoliaceae*) from Guangdong, China. *Phytotaxa* **2020**, *428*, 153–158. [CrossRef]
8. Lin, Q.W.; Zheng, S.Q.; Lin, M.M.; Wu, J.P.; Qiu, Y.X.; Wang, X. A new species of *Ilex* from Fujian province. *Bull. Bot. Res.* **2013**, *33*, 257–259.
9. Shang, C.B.; Tang, K.S. A new species of *Ilex* from Hunan Province. *Bull. Bot. Res.* **2010**, *30*, 645–647.
10. Shi, S.; Chen, S.-F.; Zhong, F.-H.; Wu, G.-X.; Liao, W.-B.; Fan, Q. *Ilex sanqingshanensis* sp. nov. (Aquifoliaceae) from Jiangxi Province, China. *Nord. J. Bot.* **2015**, *33*, 662–667. [CrossRef]
11. Xu, K.W.; Shi, X.; Fan, Q.; Xu, W.B.; Liao, W.B. *Ilex calcicola* (Aquifoliaceae), a new species from a limestone area of Guangxi, China. *Phytotaxa* **2017**, *326*, 245–251. [CrossRef]
12. Barbosa, J.Z.; Motta, A.C.V.; dos Reis, A.R.; Corrêa, R.S.; Prior, S.A. Spatial distribution of structural elements in leaves of *Ilex paraguariensis*: Physiological and ecological implications. *Trees* **2020**, *34*, 101–110. [CrossRef]
13. López-Rojo, N.; Pozo, J.; Pérez, J.; Basaguren, A.; Martínez, A.; Tonin, A.M.; Correa-Araneda, F.; Boyero, L. Plant diversity loss affects stream ecosystem multifunctionality. *Ecology* **2019**, *100*, e02847. [CrossRef]
14. Angiosperm Phylogeny Group. An update of the Angiosperm Phylogeny Group classification for the orders and families of flowering plants: APG IV. *Bot. J. Linn. Soc.* **2016**, *181*, 1–20. [CrossRef]
15. Cuénoud, P.; Martinez, M.; Loizeau, P.A.; Spichiger, R.; Andrews, S.; Manen, J.F. Molecular phylogeny and biogeography of the genus *Ilex*, L. (Aquifoliaceae). *Ann. Bot.* **2000**, *85*, 111–122. [CrossRef]

16. Manen, J.F.; Barriera, G.; Loizeau, P.A.; Naciri, Y. The history of extant *Ilex* species (Aquifoliaceae): Evidence of hybridization within a Miocene radiation. *Molec. Phylogen. Evol.* **2010**, *57*, 961–977. [CrossRef]
17. Manen, J.F.; Boulter, M.C.; Naciri-Graven, Y. The complex history of the genus *Ilex*, L. (Aquifoliaceae): Evidence from the comparison of plastid and nuclear DNA sequences and from fossil data. *Pl. Syst. Evol.* **2022**, *235*, 79–98. [CrossRef]
18. Yao, X.; Song, Y.; Yang, J.B.; Tan, Y.H.; Corlett, R.T. Phylogeny and biogeography of the hollies (*Ilex*, L., Aquifoliaceae). *J. Syst. Evol.* **2021**, *59*, 73–82. [CrossRef]
19. Yang, Y.; Jiang, L.; Liu, E.D.; Liu, W.L.; Chen, L.; Kou, Y.X.; Fan, D.M.; Cheng, S.M.; Zhang, Z.Y.; Peng, H. Time to update the sectional classification of *Ilex* (Aquifoliaceae): New insights from *Ilex* phylogeny, morphology, and distribution. *J. Syst. Evol.* **2022**, 1–11. [CrossRef]
20. Shi, L.; Li, N.W.; Wang, S.Q.; Zhou, Y.B.; Huang, W.J.; Yang, Y.C.; Ma, Y.P.; Zhou, R.C. Molecular evidence for the hybrid origin of *Ilex dabieshanensis* (Aquifoliaceae). *PLoS ONE* **2016**, *11*, e0147825. [CrossRef]
21. Chen, S.K.; Feng, Y.X. Validation of some Chinese species of *Ilex*, L. (Aquifoliaceae). *J. Syst. Evol.* **1999**, *37*, 143.
22. Chen, S.K.; Ma, H.; Feng, Y.; Barriera, G.; Loizeau, P.A. Aquifoliaceae. In *Flora of China*; Wu, Z.Y., Raven, P.H., Hong, D.Y., Eds.; Science Press: Beijing, China; Missouri Botanical Garden Press: St. Louis, MO, USA, 2008; Volume 11, pp. 359–438.
23. Zhu, H.L.; Liu, J.G.; Fischer, G.A.; Zhang, J.L. Ten newly recorded taxa to the flora of Hong Kong, China. *Guihaia Addit.* **2018**, *38*, 1221–1228.
24. Collins, T.J. ImageJ for microscopy. *Biotechniques* **2007**, *43* (Suppl. S1), S25–S30. [CrossRef] [PubMed]
25. Doyle, J.J.; Doyle, J.L. A rapid DNA isolation procedure for small quantities of fresh leaf tissue. *Phytochem. Bull.* **1987**, *19*, 15.
26. Emshwiller, E.; Doyle, J.J. Chloroplast-expressed glutamine synthetase (ncpGS): Potential utility for phylogenetic studies with an example from *Oxalis* (Oxalidaceae). *Molec. Phylogen. Evol.* **1999**, *12*, 310–319. [CrossRef] [PubMed]
27. Katoh, K.; Standley, D.M. MAFFT multiple sequence alignment software version 7: Improvements in performance and usability. *Molec. Biol. Evol.* **2013**, *30*, 772–780. [CrossRef] [PubMed]
28. Hall, T.A. *BioEdit: A User-Friendly Biological Sequence Alignment Editor and Analysis Program for Windows 95/98/NT*; Nucleic Acids Symposium Series; Information Retrieval Ltd.: London, UK, 1999; Volume 41, pp. 95–98.
29. Miller, M.A.; Pfeiffer, W.; Schwartz, T. Creating the CIPRES Science Gateway for Inference of Large Phylogenetic Trees. In Proceedings of the Gateway Computing Environments Workshop, New Orleans, LA, USA, 14 November 2010; pp. 1–8.
30. Stamatakis, A. RAxML-VI-HPC: Maximum likelihood-based phylogenetic analyses with thousands of taxa and mixed models. *Bioinformatics* **2006**, *22*, 2688–2690. [CrossRef]
31. Stamatakis, A.; Hoover, P.; Rougemont, J. A rapid bootstrap algorithm for the RAxML Web servers. *Syst. Biol.* **2008**, *57*, 758–771. [CrossRef]
32. Ronquist, F.; Huelsenbeck, J.P. MrBayes 3: Bayesian phylogenetic inference under mixed models. *Bioinformatics* **2003**, *19*, 1572–1574. [CrossRef]
33. Kalyaanamoorthy, S.; Minh, B.Q.; Wong, T.K.F.; Von Haeseler, A.; Jermiin, L.S. ModelFinder: Fast model selection for accurate phylogenetic estimates. *Nat. Methods* **2017**, *14*, 587–589. [CrossRef]
34. Posada, D.; Buckley, T.R. Model selection and model averaging in phylogenetics: Advantages of akaike information criterion and bayesian approaches over likelihood ratio tests. *Syst. Biol.* **2004**, *53*, 793–808. [CrossRef]
35. Li, X.C.; Sun, B.N.; Lin, Z.C.; Ding, S.T.; Xiao, L.; Wu, J.Y. Epidermal anatomy of the genus *Ilex* and its taxonomic significance. *J. Lanzhou Univ. Nat. Sci.* **2010**, *46*, 13–29.
36. Peng, H. The concept, research history and existing problems of Danxia. In Proceedings of the First international symposium on Danxia landform, Guangdong, China, 26–28 May 2009.
37. Zhao, W.Y.; Jiang, K.W.; Chen, Z.X.; Tian, B.; Fan, Q. *Lespedeza danxiaensis* (Fabaceae), a new species from Guangdong, China, based on molecular and morphological data. *PhytoKeys* **2021**, *185*, 43. [CrossRef]
38. Xu, K.W.; Lin, C.X.; Guo, J.Q.; Zhou, X.X.; Liao, W.B.; Mao, L.F. *Asplenium danxiaense* sp. nov. (Aspleniaceae, Aspleniineae), a new tetraploid fern species from Guangdong, China, based on morphological and molecular data. *Eur. J. Taxon.* **2022**, *798*, 162–173. [CrossRef]
39. Guidelines for Using the IUCN Red List Categories and Criteria. Version 15. Available online: https://www.iucnredlist.org/resources/redlistguidelines (accessed on 10 January 2023).

Disclaimer/Publisher's Note: The statements, opinions and data contained in all publications are solely those of the individual author(s) and contributor(s) and not of MDPI and/or the editor(s). MDPI and/or the editor(s) disclaim responsibility for any injury to people or property resulting from any ideas, methods, instructions or products referred to in the content.

forests

MDPI

Article

Hydraulic and Economical Traits in Short- and Long-Shoot Leaves of *Ginkgo biloba* Males and Females

Huihui Liu [1,2,†], Cheng Zhang [1,†], Yanqiong Meng [1], Fengyu Zhang [1], Nuo Huang [1], Jianan Wang [1,3] and Yiyong Li [1,3,*]

[1] School of Forestry and Landscape Architecture, Anhui Agricultural University, Changjiang West Road 130, Shushan District, Hefei 230036, China
[2] College of Biology and the Environment, Nanjing Forestry University, Longpan Road 159, Xuanwu District, Nanjing 210037, China
[3] Hefei Urban Ecosystem Research Station, National Forestry and Grassland Administration, Changjiang West Road 130, Shushan District, Hefei 230036, China
* Correspondence: yiyonglee@ahau.edu.cn
† These authors contributed equally to this work.

Abstract: *Ginkgo biloba* is a dioecious heterophyllous tree species with two leaf types. Short shoots always bear many leaves, which are undivided or slightly bilobed, but long-shoot leaves are smaller and are deeply divided into two or more lobes. To clarify the functional difference between the two leaf types, we investigated the morphology, anatomy, gas exchange, and hydraulic traits of the two leaf types in male and female trees. Our results showed that long-shoot leaves possessed a lower specific leaf area (*SLA*), higher leaf thickness, gas exchange rates, and average tracheid number than short-shoot leaves. When compared to short-shoot leaves, long-shoot leaves in male trees had higher leaf hydraulic conductance (K_{leaf}) and leaf water potential of 50% loss in K_{leaf} (leaf *P50*), while female trees exhibited relatively higher K_{leaf}. When comparing sexual differences, male trees possessed higher leaf thickness, leaf dissection index, vein density (*VD*), and predawn leaf water potential and lower *SLA*, tracheid number, and midday leaf water potential, while no significant difference in leaf *P50* was observed between the two sexes. Male trees exhibited greater leaf gas exchange rates, which were tightly associated with other functional traits, such as *VD* and K_{leaf}. We found strong shoot-based and sex-related heterogeneities in the leaf hydrology, anatomy, and economy of *Ginkgo biloba*. Moreover, male ginkgoes may perform better due to their greater leaf hydraulic efficiency and gas exchange rates.

Keywords: dioecious; heterophylly; leaf anatomy; hydraulic efficiency; leaf gas exchange

check for updates

Citation: Liu, H.; Zhang, C.; Meng, Y.; Zhang, F.; Huang, N.; Wang, J.; Li, Y. Hydraulic and Economical Traits in Short- and Long-Shoot Leaves of *Ginkgo biloba* Males and Females. *Forests* **2023**, *14*, 535. https://doi.org/10.3390/f14030535

Academic Editor: Rosana López Rodríguez

Received: 4 February 2023
Revised: 3 March 2023
Accepted: 7 March 2023
Published: 8 March 2023

Copyright: © 2023 by the authors. Licensee MDPI, Basel, Switzerland. This article is an open access article distributed under the terms and conditions of the Creative Commons Attribution (CC BY) license (https://creativecommons.org/licenses/by/4.0/).

1. Introduction

Many plant species have different leaf forms within a single plant, which is termed heterophylly. In some cases, heterophylly has been recognized as an adaptive mechanism that allows plants to respond optimally to micro-environmental heterogeneity [1]. The development of heteromorphic leaves may reflect an ecological adaptation of plants. For example, the floating and aerial leaves of *Nuphar lutea* (L.) Smith. should be considered sun-adapted, while submerged near-base leaves should be considered shade-adapted. This phenomenon can be an adaptive strategy for plants to ensure photosynthetic efficiency under different light intensities [2]. Another form of heterophylly is that some plants have distinct leaf forms developed from different shoot types, such as short shoots and long shoots. Short shoots are linked with reproductive organs, whereas long shoots are contributed to the rapid extension of branches and perform photosynthesis at high rates [3,4]. Although many heterophylly has been studied in angiosperm species [2,5], further research is needed on gymnosperms [4,6].

A notable gymnosperm with shoot-based heterophylly is *Gingko biloba* L. (Ginkgoaceae), which has two leaf types that differ in their morphology. The short-shoot varieties bear many leaves, which are undivided or slightly bilobed and appear in early spring from overwintering buds, while the leaves of long-shoot varieties are smaller and are deeply divided into two or more lobes [4,7]. Previous studies suggested that the morphological differences between sun and shade leaves (a form of heterophylly) might be mainly controlled through restricted hydraulic supply during cell expansion, which results in deeper lobes, higher vein density, and stomatal density in sun leaves [8,9]. Notably, short-shoot leaves in ginkgoes absorb water exclusively through mature stems, whereas long-shoot leaves rely on water provided by the xylem that is not yet fully developed [4]. In addition, Little et al. [10] found that the short shoots of *G. biloba* produce more radial tracheids per single ring than long shoots. Thus, the differences in developmental and morphological traits between long-shoot leaves and short-shoot leaves suggest that long-shoot leaves might have a greater hydraulic threshold, and consequently, the leaves developed from these two shoot types may differ in their carbon economy (e.g., gas exchange, specific leaf area, and leaf thickness) and hydrology.

The leaves are the bottleneck of the plant hydraulic system, and their venation network must be sufficient to provide enough water for a given stomatal pore area and gas exchange rate [11,12]. Previous studies have found strong positional variations in leaf anatomy, which proved that the structure could be heterogeneous even in a given leaf [12–15]. Leigh et al. [4] further confirmed this result by finding that the leaf vein density, stomatal density, and tracheid numbers in *G. biloba* were highly heterogeneous among positions. Unfortunately, many studies on the leaf anatomy of *G. biloba* still focus on a single region [16–18]. Notably, *G. biloba* has distinctive fan-shaped leaves with an open dichotomous venation pattern. By understanding the differences in the anatomical traits of fan-shaped leaves, we may be able to explore the adaptation mechanisms of these two leaf types when they are under abiotic stress.

Dioecy was found in almost 65% (8 of the 12 families) of contemporary gymnosperms [19], and dioecious plant species play an essential role in terrestrial ecosystems [20,21]. In nature, both structure and physiology could markedly differ between individual dioecious plants. According to a recent review of *Populus*, Melnikova et al. [22] concluded that the growth and photosynthesis of females were more susceptible to inhibition by drought stress than males. Olano et al. [23] found that the xylem anatomy traits of male *Juniperus thurifera* (L.) Spach, a dioecious conifer species, showed a more conservative strategy, while females sacrificed hydraulic safety for higher hydraulic conductivity. Such phenomena indicated sex-specific variation in the ability to resist environmental stress, and male individuals may perform better than female ones under abiotic or biotic stresses [24–26]. The morphological, proteomic, and/or physiological research of single-sex ginkgo responses to drought or salt stress has been undertaken [27,28]. However, the differences in adaptation to environmental conditions between sexes remain unclear.

Urban trees were often exposed to more severe dry heat stress due to the urban heat island (UHI) effect. Increased UHI will lead to increased evapotranspiration of trees; thus, drought stress in urban trees may be more severe in the future [29]. *Ginkgo biloba* has been widely planted in China for centuries and has become a popular roadside tree due to its high economic and landscape values and drought-resistance ability [18,30]. Thus, the aims of this study were to (1) determine the differences in hydraulic, anatomical, and economic traits between long- and short-shoot leaves, and (2) test the drought resistance of male and female ginkgoes. We hypothesized that (1) long-shoot leaves tend to have higher hydraulic efficiency due to their initial hydraulic constraints, and (2) male plants exhibit superior drought resistance than females due to their greater leaf hydraulic efficiency.

2. Material and Methods

2.1. Study Site and Plant Material

The study site (31°86′19″ N, 117°25′70″ E) was located at Anhui Agricultural University Campus, Hefei, Central Anhui Province, China. It has a humid subtropical monsoon climate with an average temperature of 15.7 °C, and an average rainfall of 1000 mm. From July to September 2021, eight mature trees (four of each sex) growing in an exposed area were selected for the study. The diameter at breast height ranged between 30.0 and 32.6 cm and showed no significant difference between the two sexes. We used a 6 m long averruncator to collect the fully extended branches (height about 3 m) facing south. The sampled tree individuals in this study were transplanted from a nursery in Hefei city around 2010. The scheme of experimental design and the climate of the study area are shown in Figures 1 and S1, respectively.

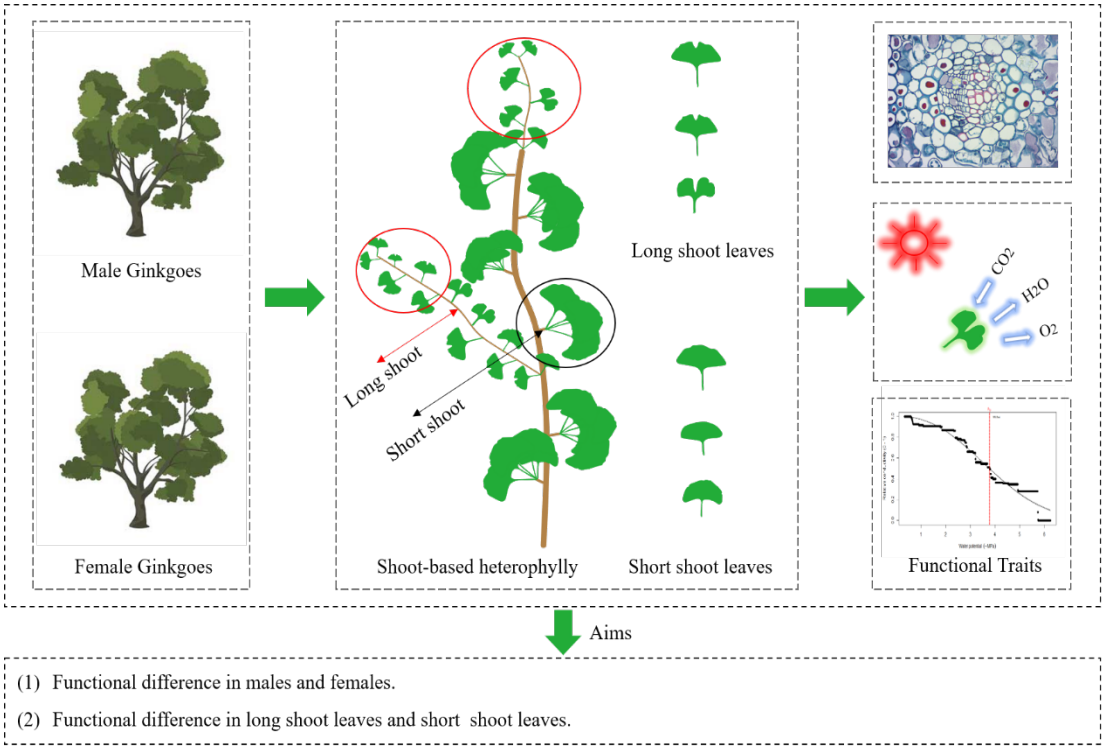


Figure 1. The scheme of experimental design.

2.2. Leaf Water Potential

The leaf water potentials were measured using two Scholander-type pressure chambers (PMS 1505D, PMS Instruments Co., Albany, OR, USA). On consecutive sunny days in July 2021, we collected three fully extended branches from each tree individual and six leaves (three leaves in each shoot type) from each branch. The measurements were performed between 05:30 and 07:00 for the predawn leaf water potential (Ψ_{pd}; MPa) and between 13:00 and 15:00 for the midday leaf water potential (Ψ_{md}; MPa).

2.3. Leaf Gas Exchange and Hydraulic Conductance

In August 2021, a total of 12 fully extended branches with expanded healthy leaves 2–3 m above the ground from 4 individuals per sex were collected. Three fresh and healthy leaves from each shoot type were randomly chosen for gas exchange measurements using a portable photosynthesis system (Li-6800, Li-Cor Inc., Lincoln, NE, USA) between 09:00 and 11:30 on sunny days. Depending on the weather condition of measurement, the chamber's CO_2 concentration was 400 μmol mol^{-1}, the light intensity was 800 μmol m^{-2} s^{-1}, the relative humidity was 60%, and the leaf temperature was 25 °C. During measurements, the

branches were put into a large bucket full of water to avoid water loss. Leaf gas exchange parameters were monitored to ensure reaching a stable state before data were recorded. The instantaneous water use efficiency (WUE_i; mmol mol^{-1}) was calculated as the net photosynthesis rate (A; μmol m^{-2} s^{-1}) divided by the transpiration rate (Tr; mmol m^{-2} s^{-1}).

The leaf hydraulic conductance (K_{leaf}; mmol m^{-2} s^{-1} MPa^{-1}) was measured using the gas exchange method [31]. Briefly, a total of nine leaves in each shoot type were measured from each tree individual. The leaves were wrapped in black plastic bags and aluminum foil on the night before the measurement, and thus, the wrapped leaf water potential (Ψ_w; MPa) was assumed to be equivalent to the stem water potential. On the next day, the adjacent leaves of the wrapped leaves were selected for gas exchange measurements. When the leaf gas exchange was finished, the water potentials of the leaves used for gas exchange (Ψ_{gas}; MPa) and Ψ_w were immediately measured using two Scholander-type pressure chambers, respectively.

$$K_{leaf} = \frac{Tr}{\Psi_w - \Psi_{gas}}$$

2.4. Leaf Vulnerability Curves

Before the leaf vulnerability curve was plotted, considering the fact that long-shoot leaves are relatively less common than short-shoot leaves, we collected three branches (about 60 cm long) from each sex and immediately recut them (about 5 cm long) underwater. In the lab, the cut branches were covered overnight with a black plastic bag until the leaf water potential was >-0.10 MPa.

The branches were removed from the water and covered with black plastic bags so that the leaf water potential of the whole branch was balanced between the upper (long shoot) and the lower (short shoot) values. The branches were dehydrated naturally for 72 h, and the leaf water potentials for long shoots and short shoots were measured every 1 h to ensure that there was no significant difference between the two leaf types. Therefore, unless otherwise stated, when measuring the values for the vulnerability curve of long-shoot leaves, the water potential of short-shoot leaves was used instead when the number of long-shoot leaves was insufficient.

A total of 48 leaves (24 leaves of each shoot type) from 8 individuals were selected to plot the leaf vulnerability curve, which was evaluated using the optical technique [32]. When the leaf water potential of the cut branches was close to 0 MPa, we began to dehydrate them for 72 h in a black plastic bag while imaging the healthy and fully expanded leaf. We cleaned the leaf surface with deionized water and clamped the leaf firmly in the middle with two transparent glass plates (the leaf was still attached to the shoot). This limited the leaf movement and shrinking during dehydration. The leaf was imaged every 5 min using a custom-built imaging clamp (http://www.opensourceov.org, accessed on 3 February 2023). The imaged area near the center of the leaf was at least 500 mm^2. The leaf water potential was measured every 1 to 2 h via a Scholander-type pressure chamber. Image sequences were analyzed as described in http://www.opensourceov.org/process/ (accessed on 3 February 2023) to measure the embolized area for each image and generate the vulnerability curve, expressed as a percentage of embolized pixels vs. leaf water potential; also, the leaf water potential of 50% loss in K_{leaf} (leaf $P50$) was calculated using the R package 'fitplc' [33].

2.5. Leaf Morphology and Anatomy

After the K_{leaf} measurement, the leaves were collected and cleaned with deionized and then scanned using a scanner. Leaf area and perimeter were measured using ImageJ (National Institute of Health, Bethesda, MD, USA). After leaf-area measurement, the leaf samples were oven-dried at 60 °C for 72 h to estimate their dry mass. The leaf dissection index (LDI) and specific leaf area (SLA; cm^2 g^{-1}) were calculated as follows:

$$LDI = \text{Leaf perimeter} / \sqrt[2]{\text{Leaf area}}$$

$$SLA = \text{Leaf dry mass}/\text{Leaf area}$$

A total of 80 leaves (40 leaves of each shoot type) from 4 individuals per sex were selected to measure the vein density (*VD*; mm mm^{-2}) at 3 locations on each leaf (at the apex, middle, and base). The pre-experiment found that the leaf veins of *G. biloba* could be clearly observed under the microscope even if the leaves were not treated. Thus, the leaf samples were saved in FAA (37% formalin + 70% alcohol + 100% acetic acid) fixative solution to consume most of the leaf pigments, making it possible that all the vein networks could be seen without further clearing or staining. The samples were then imaged using a light microscope, and the total vein length was analyzed using ImageJ. The *VD* was defined as the total vein length per unit of leaf area. The stomatal density (*SD*; no mm^{-2}) of the abaxial leaf surface was determined for the apex, middle, and base with clear nail varnish and measured under 10× magnification using a light microscope (DM2500, Leica Microsystems Ltd., Wetzlar, Germany). Leaf thickness and the parameters of tracheid measurements were performed on 18 leaves (9 leaves of each shoot type) in each tree. Leaf cross-sections at the three locations (at the apex, middle, and base) were obtained via a rotary microtome (RM2255, Leica Microsystems Ltd., Germany). The leaf thickness and the number of every tracheid lumen in a vein cross-section were photographed with a light microscope (DM2500, Leica Microsystems Ltd., Germany) at 10× magnification and 40× magnification, respectively, and then measured using ImageJ. At the same time, the tracheid was assumed to be oval. Thus, the average tracheid diameter was calculated by multiplying the length of the two axes together and taking the square root of the product.

2.6. Statistical Analysis

Two-way nested ANOVA was used to estimate the effects of leaf type and position, as well as of leaf type and sex. An independent-sample *t*-test was conducted to identify the anatomical differences between the two sexes. Multiple comparisons were performed using Ducan's test to evaluate the differences in variables between leaf types using SPSS 20.0 (SPSS, Inc., Chicago, IL, USA). A p value of less than 0.05 was considered statistically significant. Leaf vulnerability curve fitting, principal component analyses (PCA), and correlation analysis were conducted using R 4.1.2 (The R Foundation for Statistical Computing, Austria).

3. Results

3.1. Leaf Morphoanatomical Traits of Long Shoot and Short Shoot

Long-shoot leaves exhibited remarkably lower specific leaf area (*SLA*) and greater leaf dissection index (*LDI*) than short-shoot leaves in both sex individuals (Figure 2). Meanwhile, males showed significantly higher *LDI* and lower *SLA* than females (Figure 2). The nested ANOVA found that the leaf thickness and average tracheid number were significantly affected by position ($p < 0.001$) and leaf type (Figure 3), and these two traits in long-shoot leaves were almost higher than in short-shoot leaves in both sex individuals. Meanwhile, the tracheid of long-shoot leaves' basal region was narrower and relatively abundant than that of short-shoot leaves in male and female *G. biloba* (Figure 3c–f). However, the leaf tracheid diameter, stomatal density (*SD*), and vein density (*VD*) in male *G. biloba* were unaffected by leaf type, while the *SD* and *VD* in female *G. biloba* were affected by leaf type (Figures 3e,f and 4). The leaf thickness and *VD* were decreased from the base to the apex in both two leaf types (Figures 3a,b and 4c,d). Regardless of the leaf type and position effects, males possessed a lower average tracheid number but higher *VD* and thicker leaves than females (Table S2).

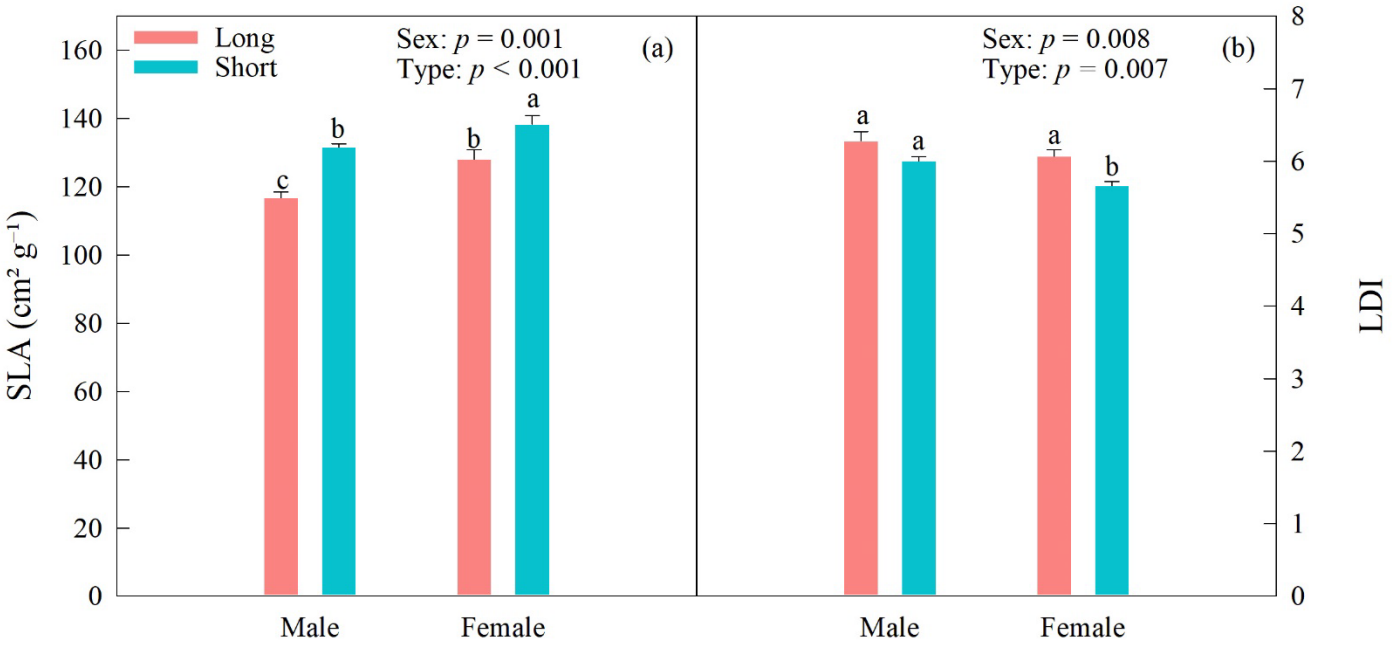


Figure 2. Specific leaf area (**a**) and leaf dissection index (**b**) differences between long- and short-shoot leaves in males and females *Ginkgo biloba*. Values are mean ± SE (n = 4). Lowercase letters indicate significant differences between long- and short-shoot leaves of males and females at the $p < 0.05$ level.

3.2. Leaf Gas Exchange of Long Shoot and Short Shoot

Long-shoot leaves exhibited significantly higher net photosynthesis rate and transpiration rate (*Tr*) than short-shoot leaves in both sexes (Figure 5a,c). The *Tr* of male long-shoot leaves was significantly higher than that of short-shoot leaves (p = 0.02). The net photosynthesis rate, *Tr*, and stomatal conductance (g_s) in both leaf types had similar trends. Moreover, the WUE_i of male long-shoot leaves and g_s of female long-shoot leaves were significantly higher than those of short-shoot leaves (Figure 5b,d). Without considering leaf-type effects, males exhibited markedly higher net photosynthesis rate, *Tr*, g_s, and a higher instantaneous water use efficiency (WUE_i) than females.

3.3. Leaf Hydraulics of Long Shoot and Short Shoot

In females, the predawn leaf water potential (Ψ_{pd}) of short-shoot leaves was more negative than that of long-shoot leaves (Figure 6a). Additionally, a significant difference in the midday leaf water potential (Ψ_{md}) between the two leaf types in male and female *G. biloba* was observed, with the water potential of short-shoot leaves being more negative (Figure 6b). Male long-shoot leaves exhibited remarkably greater leaf hydraulic conductance (K_{leaf}) and the water potential of 50% loss in leaf hydraulic conductance (leaf *P50*) compared with short-shoot leaves, whereas female long-shoot leaves displayed slightly higher K_{leaf} (Figure 6c,d). No significant difference was observed in leaf *P50* between males and females without considering the effects of leaf types. Females had a more negative Ψ_{pd}, while males had a more negative Ψ_{md} and higher K_{leaf} (Figure 6).

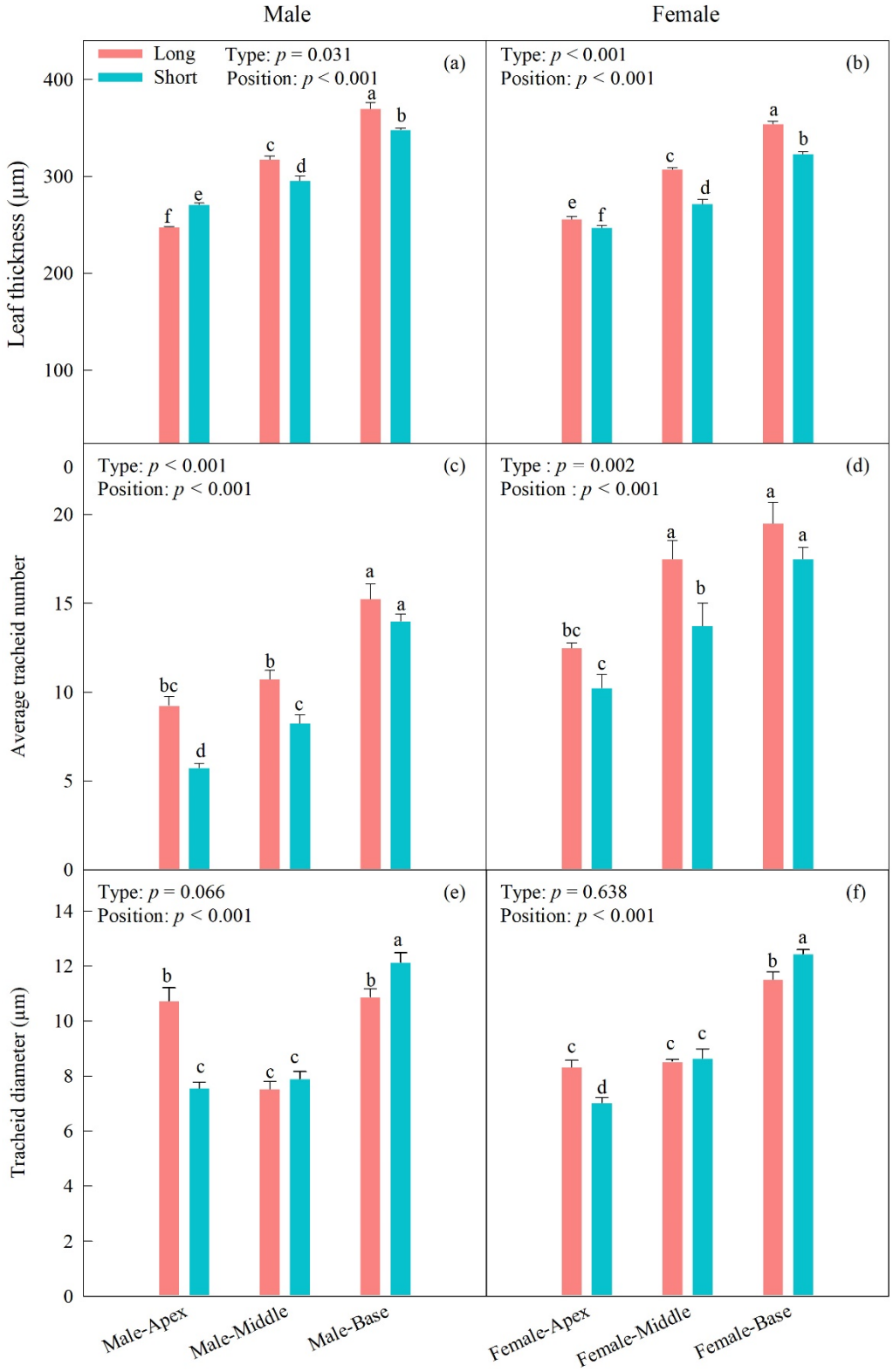


Figure 3. Leaf thickness (**a**,**b**), tracheid number (**c**,**d**), and tracheid diameter (**e**,**f**) variations at different positions between long- and short-shoot leaves in *Ginkgo biloba* males (left panels) and females (right panels). Values are mean ± SE (n = 4). Lowercase letters in each sex indicate significant differences between long- and short-shoot leaves at the $p < 0.05$ level.

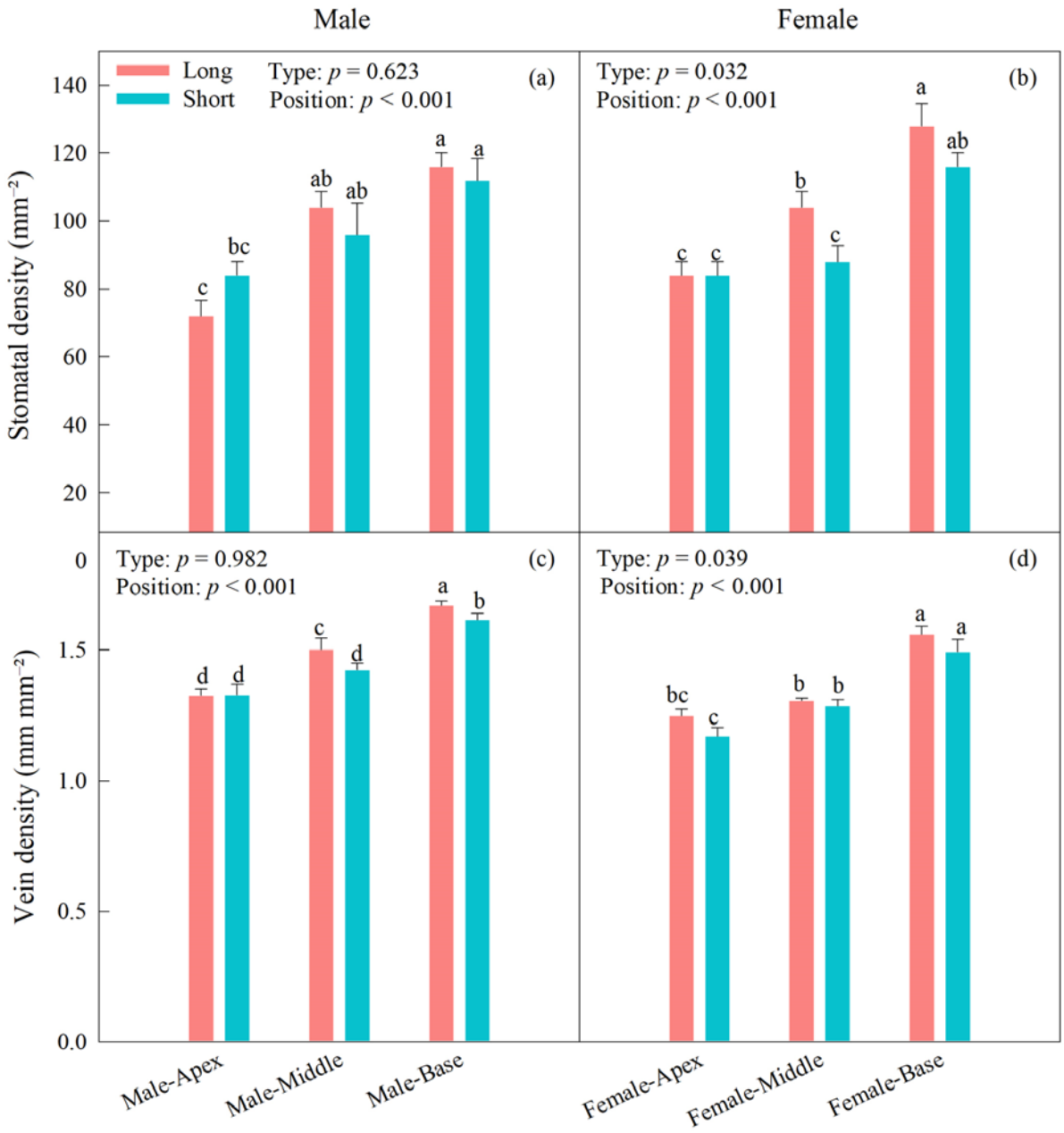


Figure 4. Leaf stomatal density (**a**,**b**) and vein density (**c**,**d**) variations at different locations on the leaf between long- and short-shoot leaves in *Ginkgo biloba* males (left panels) and females (right panels). Values are mean ± SE (n = 4). Lowercase letters in each sex indicate significant differences between long- and short-shoot leaves at the $p < 0.05$ level.

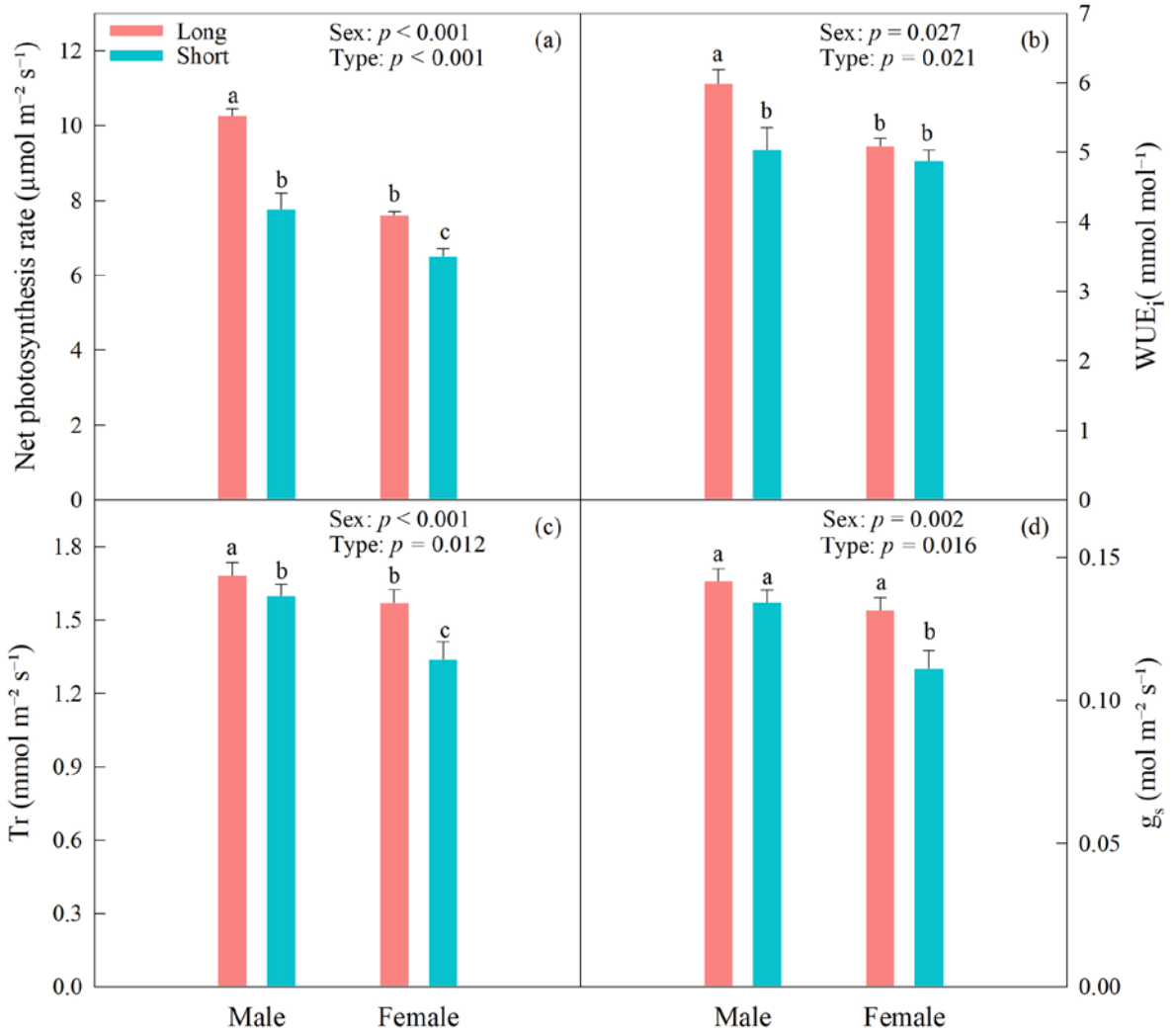


Figure 5. Leaf net photosynthesis rate (**a**), instantaneous water use efficiency (**b**), transpiration rate (**c**), and stomatal conductance (**d**) differences between long- and short-shoot leaves in male and female *Ginkgo biloba*. Values are mean ± SE (n = 4). Lowercase letters indicate significant differences between long- and short-shoot leaves of males and females at the $p < 0.05$ level.

3.4. Trait Coordination

We found that *VD* was greatly correlated with the leaf thickness and negatively correlated with *SLA* and tracheid number. In addition, the leaf net photosynthesis rate was positively correlated with *LDI*, leaf thickness, *VD*, *Tr*, g_s, and WUE_i, while it was negatively correlated with *SLA*. K_{leaf} was strongly related to Ψ_{pd}, the net photosynthesis rate, *Tr*, g_s, *LDI*, *SLA*, *VD*, and leaf thickness, while it was independent of tracheid number and the traits associated with leaf *P50* (Figure 7).

Overall, leaf types and sexes significantly affected the morphoanatomical and physiological responses for *Gingko biloba* (Figure S2). *LDI*, the net photosynthesis rate, g_s, WUE_i, *VD*, K_{leaf}, and Ψ_{pd} were located at the positive end, whereas *SLA* was located at the negative end on the PC1 axis. The PC2 axis was mostly influenced by Ψ_{md}, tracheid number (*TN*), *SD*, and the leaf drought tolerance trait (leaf *P50*) on the positive side.

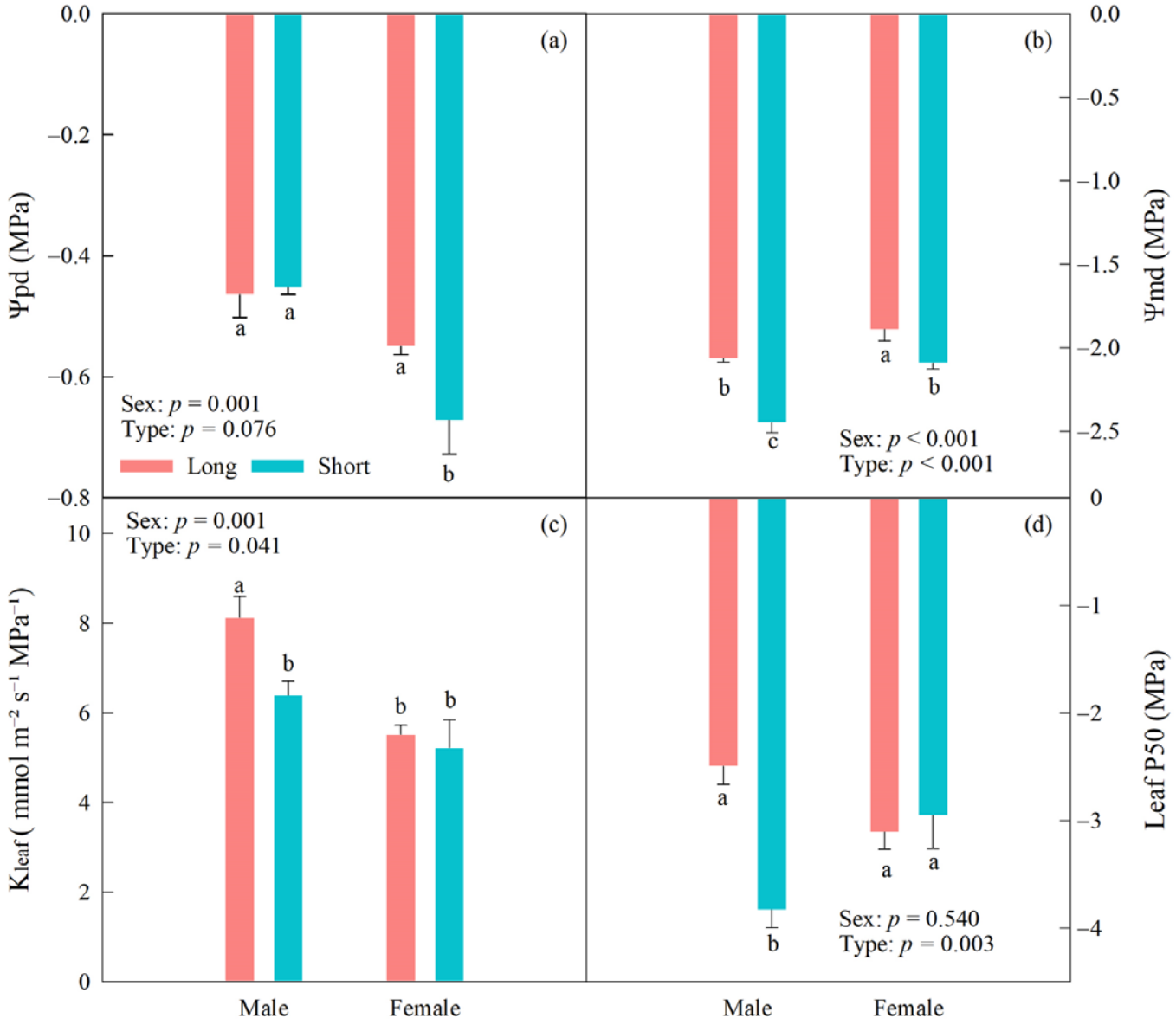


Figure 6. Predawn leaf water potential (**a**), midday leaf water potential (**b**), leaf hydraulic conductance (**c**), and water potential of 50% loss in leaf hydraulic conductance (**d**) differences between long- and short-shoot leaves in male and female *Ginkgo biloba*. Values are mean ± SE (n = 4). Lowercase letters indicate significant differences between long- and short-shoot leaves of males and females at the $p < 0.05$ level.



Figure 7. Correlation analysis among leaf morphology and hydraulic and gas exchange traits. *SD*: stomatal density; *LT*: leaf thickness; *VD*: vein density; WUE_i: instantaneous water use efficiency; g_s: stomatal conductance; *A*: net photosynthesis rate; *Tr*: transpiration rate; *SLA*: specific leaf area; *LDI*: leaf dissection index; K_{leaf}: leaf hydraulic conductance; Ψ_{md}: midday leaf water potential; Ψ_{pd}: predawn leaf water potential; *P50*: water potential of 50% loss in leaf hydraulic conductance; *TN*: average tracheid number; *TD*: average tracheid diameter.

4. Discussion

4.1. Variation in Leaf Functional Traits between Long- and Short-Shoot Leaves

In the present study, we found a strong heterogeneity in leaf functional traits between the two leaf types in *Ginkgo biloba*. We found that the net photosynthesis rate, vein density (*VD*), and leaf hydraulic conductance (K_{leaf}) were higher in long-shoot leaves than in short-shoot leaves. Similar to the long shoots of other species, which extended their canopy by taking advantage of elevated radiation conditions, long-shoot leaves might achieve rapid growth through higher gas exchange rates and an adequate leaf water supply [4]. The positive relationships among *VD*, K_{leaf}, and net photosynthesis rate further support the findings of Leigh et al. [4].

When improving the water conductivity or maintaining a high photosynthesis rate, air bubbles may invade the vascular system and subsequently increase the risk of cavitation [4,34]. As an important hydraulic trait, the water potential of 50% loss in leaf hydraulic conductance (leaf *P50*) was closely associated with plant drought tolerance [35,36]. The long-shoot varieties showed higher leaf *P50* than their short-shoot counterpart, indicating a lower resistance to embolism (lower hydraulic safety). However, long-shoot leaves might reduce the risk of embolism through coordination between economical traits and other hydraulic traits. Specifically, long-shoot leaves possessed higher *VD* and leaf thickness and lower specific leaf area (*SLA*) than short-shoot leaves under the same external conditions, and these three traits were tightly related. The higher *VD* implied that when leaves were at risk of embolism, long-shoot leaves could transport water through non-embolized veins, achieving a more flexible water transport strategy [37]. Moreover, it has been suggested that selection stress in drought conditions favors plants with low *SLA* due to their higher leaf dry matter content [38,39], and a previous study reported that *G. biloba* could enhance the water retention ability by keeping higher leaf thickness when facing drought and/or heat stress [40]. Hence, the coordination between leaf functional traits might help long-shoot leaves acclimate to future drought conditions.

In addition to the above discussion, the leaf thickness, tracheid number, stomatal density (*SD*), and *VD* were higher in long-shoot leaves than in short-shoot leaves, and these traits in these two leaf types decreased from basal to apical regions (Figures 3 and 4), indicating that there was a strong variation in leaf structural traits. The trade-off between the tracheid size and number (more abundant and narrower tracheids) of long-shoot leaves might also represent an adaptation for increased safety during periods of high evaporative demand in summer. Moreover, we also found that long-shoot leaves could achieve the trade-off between hydraulic efficiency (higher K_{leaf}) and hydraulic safety.

4.2. Variation in Leaf Functional Traits between Males and Females

Inconsistent with our initial hypothesis, our analysis demonstrated that the difference in leaf *P50* between males and females was not significant (Figure 6). The low variation exhibited by leaf *P50* between sexes was in agreement with the results reported for gymnosperms and reinforced the conservative nature of this trait [23,41]. Another reasonable explanation was that the differences in sexes might be obscured by the differences in leaves within single-sex species. Thus, leaf *P50* might not be the main factor affecting the difference in drought-resistance capacity between males and females under natural conditions. Interestingly, the Ψ_{pd} and *Tr* of female short-shoot leaves were lower than those of the other leaves. Such phenomena might be attributed to the finding that the water transport efficiency of female short-shoot leaves was lower than those of other leaves. Compared with male long- and short-shoot leaves, the female short-shoot leaves also showed lower leaf thickness, *VD*, WUE_i, and K_{leaf}.

We found that males had higher *VD*, K_{leaf}, and leaf thickness than females. The correlation analysis emphasized the fact that the coordination between these anatomical and hydraulic traits might play an important role in water transport (Figure 7). The higher *VD* might be a major factor in increasing K_{leaf} by improving the water exchange area between the xylem and the surrounding mesophyll cells and reducing the distance of water passing through the mesophyll space [42,43]. Furthermore, we observed that males sustained higher gas exchange rates in summer by maintaining higher *VD*, K_{leaf}, and instantaneous water use efficiency (WUE_i). A previous study suggested that the change in K_{leaf} is usually linked with stomatal closure and, accordingly, affects the photosynthesis of plants [44], because CO_2 and water exchange between leaves and air share a common route through stomatal pores. When the ability of CO_2 assimilation is reduced, this, in turn, limits the development of leaf veins, indicating that there is a trade-off between the investment and return of leaf structure [34]. Hence, it was not surprising that males tended to show greater net photosynthesis rate, K_{leaf}, and *VD* than females. These results indicate that males might achieve an ecological advantage in summer due to their higher gas exchange

rates and hydraulic efficiency. Many previous studies have demonstrated sex-specific differences in resistance to environmental stress, nutrient uptake, and utilization strategies, and consequently, male individuals perform better than female individuals [20,45,46]. We suspected that the sex-specific differences in the hydraulic traits and resource utilization of ginkgoes might result in a situation where females are more prone than males to future urban drought conditions, thus ultimately leading to a population decline. Our study revealed that the net photosynthesis rate differed between males and females. Similar results were also reported by Correia and Barradas [47], who found that the net photosynthesis rate and stomatal conductance (g_s) of *Pistacia lentiscus* L. (Anacardiaceae) under natural environments in summer were higher in males than that in females. However, the pattern of leaf photosynthesis in dioecious trees might be complex. Jin et al. [48] reported that the leaf net photosynthesis of female Ginkgoes was higher than that of males in April, whereas Shi et al. [49] found that the leaf net photosynthesis of male ginkgoes was higher in August. Such phenomena suggest that sex-related differences in photosynthetic patterns are probably related to the measurement time due to the different reproductive costs of dioecious trees. Therefore, the dynamic changes in leaf gas exchange between male and female ginkgoes, and the hydraulic and economic traits of other dioecious trees need further research.

5. Conclusions

Our results showed that long-shoot leaves were thicker, with lower *SLA* and higher average tracheid number, Ψ_{md}, net photosynthesis rate, and *Tr* than short-shoot leaves in male and female *Ginkgo biloba*. In addition, due to its unique fan-shaped leaves, there was also considerable heterogeneity in the anatomical traits of different positions of the leaves. The two leaf types of males could achieve the trade-off between hydraulic efficiency and safety in that lower K_{leaf} was accompanied by more negative leaf *P50*. Although no significant difference in leaf *P50* was observed, males may perform better in summer via higher leaf hydraulic efficiency and gas exchange rates than females. We found discrepancies in hydraulic and carbon economic traits between the two leaf types in males and females *G. biloba*. It should be noted that this study had a small sample size and was conducted on only one site. Future studies are necessary to explore the hydraulic and economic traits of dioecious plants over a large-scale environmental gradient.

Supplementary Materials: The following supporting information can be downloaded at: https://www.mdpi.com/article/10.3390/f14030535/s1. Figure S1: The climate conditions of study area in 2020 (a) and 2021 (b), respectively; Figure S2: Principal component analyses on long shoot and short shoot leaves physiological and anatomical traits of males and females *Ginkgo biloba*. *SD*: stomatal density; *VD*: vein density; g_s: stomatal conductance; *A*: net photosynthesis rate; WUE_i: instantaneous water use efficiency; *SLA*: specific leaf area; *LDI*: leaf dissection index; K_{leaf}: leaf hydraulic conductance; Ψ_{md}: midday leaf water potential; Ψ_{pd}: predawn leaf water potential; *P50*: water potential of 50% loss in leaf hydraulic conductance; *TN*: average tracheid number; *TD*: average tracheid diameter; Table S1: An overview table of all measurements including the name, the unit, total number of measured leaves from each tree, and the number of final replicates; Table S2: Results from independent-samples t-test for the difference between males and females *Ginkgo biloba* on leaf anatomical traits; Table S3: Information about the statistical output from two-way nested ANOVA.

Author Contributions: Y.L. conceived this study. H.L. and C.Z. conducted the experiment. H.L. wrote the main manuscript. Y.M., F.Z., N.H. and J.W. edited the manuscript. All authors have read and agreed to the published version of the manuscript.

Funding: This research was funded by the National Natural Science Foundation of China (31800511) and the Scientific Research Project of Anhui Higher Education Institutions (2022AH050916).

Institutional Review Board Statement: The presented research did not involve human subjects or animals and therefore did not require ethics approval. All methods were carried out in compliance with local and national regulations. The first author (Huihui Liu) identified and deposited

voucher specimens in the herbarium of the School of Forestry and Landscape Architecture, Anhui Agricultural University.

Informed Consent Statement: Not applicable.

Data Availability Statement: Datasets are available from the corresponding author upon reasonable request.

Conflicts of Interest: The authors declare that the research was conducted in the absence of any commercial or financial relationships that could be construed as a potential conflict of interest.

Abbreviations

SD	stomatal density
LT	leaf thickness
VD	vein density
WUE_i	instantaneous water use efficiency
g_s	stomatal conductance
A	net photosynthesis rate
Tr	transpiration rate
SLA	specific leaf area
LDI	leaf dissection index
K_{leaf}	leaf hydraulic conductance
Ψ_{md}	midday leaf water potential
Ψ_{pd}	predawn leaf water potential
P50	water potential of 50% loss in leaf hydraulic conductance
TN	average tracheid number
TD	average tracheid diameter

References

1. Nakayama, H.; Sinha, N.R.; Kimura, S. How do plants and phytohormones accomplish heterophylly, leaf phenotypic plasticity, in response to environmental cues. *Front. Plant Sci.* **2017**, *8*, 1717. [CrossRef] [PubMed]
2. Kordyum, E.; Klimenko, E. Chloroplast ultrastructure and chlorophyll performance in the leaves of heterophyllous *Nuphar lutea* (L.) Smith. plants. *Aquat. Bot.* **2013**, *110*, 84–91. [CrossRef]
3. Miyazawa, Y.; Kikuzawa, K. Phenology and photosynthetic traits of short shoots and long shoots in *Betula grossa*. *Tree Physiol.* **2004**, *24*, 631–637. [CrossRef] [PubMed]
4. Leigh, A.; Zwieniecki, M.A.; Rockwell, F.E.; Boyce, C.K.; Nicotra, A.B.; Holbrook, N.M. Structural and hydraulic correlates of heterophylly in *Ginkgo biloba*. *New Phytol.* **2011**, *189*, 459–470. [CrossRef] [PubMed]
5. Zhang, C.X.; Tanabe, K.; Tamura, F.; Itai, A. Spur characteristics, fruit growth, and carbon partitioning in two late-maturing Japanese pear (*Pyrus pyrifolia* Nakai) cultivars with contrasting fruit size. *J. Am. Soc. Hortic. Sci.* **2005**, *130*, 252–260. [CrossRef]
6. Meyen, S.V. Basic features of gymnosperm systematics and phylogeny as evidenced by the fossil record. *Bot. Rev.* **1984**, *50*, 1–111. [CrossRef]
7. Critchfield, W. Shoot growth and heterophylly in *Ginkgo biloba*. *Bot. Gaz.* **1970**, *131*, 150–162. [CrossRef]
8. Zwieniecki, M.A.; Boyce, C.K.; Holbrook, N.M. Hydraulic limitations imposed by crown placement determine final size and shape of *Quercus rubra* L. leaves. *Plant Cell Environ.* **2004**, *27*, 357–365. [CrossRef]
9. Boyce, C.K. Seeing the forest with the leaves—Clues to canopy placement from leaf fossil size and venation characteristics. *Geobiology* **2009**, *7*, 192–199. [CrossRef]
10. Little, S.A.; Jacobs, B.; McKechnie, S.J.; Cooper, R.L.; Christianson, M.L.; Jernstedt, J.A. Branch architecture in *Ginkgo biloba*: Wood anatomy and long shoot-short shoot interactions. *Am. J. Bot.* **2013**, *100*, 1923–1935. [CrossRef]
11. Sack, L.; Streeter, C.M.; Holbrook, N.M. Hydraulic analysis of water flow through leaves of sugar maple and red oak. *Plant Physiol.* **2004**, *134*, 1824–1833. [CrossRef]
12. Li, S.; Zhang, Y.J.; Sack, L.; Scoffoni, C.; Ishida, A.; Chen, Y.J.; Cao, K.F. The heterogeneity and spatial patterning of structure and physiology across the leaf surface in giant leaves of *Alocasia macrorrhiza*. *PLoS ONE* **2013**, *8*, e66016. [CrossRef] [PubMed]
13. Martre, P.; Durand, J.L. Quantitative analysis of vasculature in the leaves of *Festuca arundinacea* (Poaceae): Implications for axial water transport. *Int. J. Plant Sci.* **2001**, *162*, 755–766. [CrossRef]
14. Nardini, A.; Gortan, E.; Ramani, M.; Salleo, S. Heterogeneity of gas exchange rates over the leaf surface in tobacco: An effect of hydraulic architecture? *Plant Cell Environ.* **2008**, *31*, 804–812. [CrossRef]
15. Li, S.; Cao, K. Heterogeneity of anatomical structure in giant leaves of *Musa balbisiana*. *Chin. Sci. Bull.* **2014**, *59*, 522–528. [CrossRef]
16. Pandey, S.; Kumar, S.; Nagar, P.K. Photosynthetic performance of *Ginkgo biloba* L. grown under high and low irradiance. *Photosynthetica* **2003**, *41*, 505–511. [CrossRef]

17. Kiyomizu, T.; Yamagishi, S.; Kume, A.; Hanba, Y.T. Contrasting photosynthetic responses to ambient air pollution between the urban shrub Rhododendronxpulchrum and urban tall tree *Ginkgo biloba* in Kyoto city: Stomatal and leaf mesophyll morpho-anatomies are key traits. *Trees Struct. Funct.* **2019**, *33*, 63–77. [CrossRef]
18. Wang, S.; Wang, W.; Wang, S.; Yang, L.; Gu, J. Intraspecific variations of anatomical, morphological and chemical traits in leaves and absorptive roots along climate and soil gradients: A case study with *Ginkgo biloba* and *Eucommia ulmoides*. *Plant Soil* **2021**, *469*, 73–88. [CrossRef]
19. Walas, L.; Mandryk, W.; Thomas, P.A.; Tyrala-Wierucka, Z.; Iszkulo, G. Sexual systems in gymnosperms: A review. *Basic Appl. Ecol.* **2018**, *31*, 1–9. [CrossRef]
20. Chen, J.; Liu, Q.; Yu, L.; Korpelainen, H.; Niinemets, U.; Li, C.Y. Elevated temperature and CO_2 interactively modulate sexual competition and ecophysiological responses of dioecious *Populus cathayana*. *For. Ecol. Manag.* **2021**, *481*, 118747. [CrossRef]
21. Liu, J.Y.; Zhang, R.; Xu, X.; Fowler, J.C.; Miller, T.E.X.; Dong, T.F. Effect of summer warming on growth, photosynthesis and water status in female and male *Populus cathayana*: Implications for sex-specific drought and heat tolerances. *Tree Physiol.* **2020**, *40*, 1178–1191. [CrossRef] [PubMed]
22. Melnikova, N.V.; Borkhert, E.V.; Snezhkina, A.V.; Kudryavtseva, A.V.; Dmitriev, A.A. Sex-specific response to stress in *Populus*. *Front. Plant Sci.* **2017**, *8*, 1827. [CrossRef] [PubMed]
23. Olano, J.M.; Gonzalez-Munoz, N.; Arzac, A.; Rozas, V.; von Arx, G.; Delzon, S.; Garcia-Cervigon, A.I. Sex determines xylem anatomy in a dioecious conifer: Hydraulic consequences in a drier world. *Tree Physiol.* **2017**, *37*, 1493–1502. [CrossRef]
24. Zhao, H.X.; Li, Y.P.; Zhang, X.L.; Korpelainen, H.; Li, C.Y. Sex-related and stage-dependent source-to-sink transition in *Populus cathayana* grown at elevated CO_2 and elevated temperature. *Tree Physiol.* **2012**, *32*, 1325–1338. [CrossRef]
25. Chen, F.G.; Shen, J.; Min, D.; Ke, L.X.; Tian, X.; Korpelainen, H.; Li, C.Y. Male *Populus cathayana* than female shows higher photosynthesis and less cellular injury through ABA-induced manganese transporting inhibition under high manganese condition. *Trees Struct. Funct.* **2018**, *32*, 255–263. [CrossRef]
26. Li, Z.; Wu, N.; Liu, T.; Tang, M.; Chen, H. Gender-related responses of dioecious plant *Populus cathayana* to AMF, drought and planting pattern. *Sci. Rep.* **2020**, *10*, 11530. [CrossRef]
27. Zhao, H.Y.; Liang, H.Y.; Chu, Y.B.; Sun, C.C.; Wei, N.; Yang, M.N.; Zheng, C.X. Effects of salt stress on chlorophyll fluorescence and the antioxidant system in *Ginkgo biloba* L. Seedlings. *Hortscience* **2019**, *54*, 2125–2133. [CrossRef]
28. Chang, B.; Ma, K.B.; Lu, Z.G.; Lu, J.K.; Cui, J.W.; Wang, L.; Jin, B. Physiological, transcriptomic, and metabolic responses of *Ginkgo biloba* L. to drought, salt, and heat stresses. *Biomolecules* **2020**, *10*, 1653. [CrossRef]
29. Wang, X.M.; Wang, X.K.; Su, Y.B.; Zhang, H.X. Land pavement depresses photosynthesis in urban trees especially under drought stress. *Sci. Total Environ.* **2019**, *653*, 120–130. [CrossRef]
30. He, M.; Shi, D.; Wei, X.; Hu, Y.; Wang, T.; Xie, Y. Gender-related differences in adaptability to drought stress in the dioecious tree *Ginkgo biloba*. *Acta Physiol. Plant.* **2016**, *38*, 124. [CrossRef]
31. Wang, X.; Du, T.; Huang, J.; Peng, S.; Xiong, D. Leaf hydraulic vulnerability triggers the decline in stomatal and mesophyll conductance during drought in rice. *J. Exp. Bot.* **2018**, *69*, 4033–4045. [CrossRef] [PubMed]
32. Brodribb, T.J.; Skelton, R.P.; McAdam, S.A.M.; Bienaime, D.; Lucani, C.J.; Marmottant, P. Visual quantification of embolism reveals leaf vulnerability to hydraulic failure. *New Phytol.* **2016**, *209*, 1403–1409. [CrossRef] [PubMed]
33. Duursma, R.; Choat, B. Fitplc—An R package to fit hydraulic vulnerability curves. *J. Plant Hydraul.* **2017**, *4*, 002. [CrossRef]
34. Li, S.; Hamani, A.K.M.; Zhang, Y.Y.; Liang, Y.P.; Gao, Y.; Duan, A.W. Coordination of leaf hydraulic, anatomical, and economical traits in tomato seedlings acclimation to long-term drought. *BMC Plant Biol.* **2021**, *21*, 536. [CrossRef]
35. Brodribb, T.J.; Cochard, H. Hydraulic failure defines the recovery and point of death in water-stressed conifers. *Plant Physiol.* **2009**, *149*, 575–584. [CrossRef] [PubMed]
36. Blackman, C.J.; Brodribb, T.J.; Jordan, G.J. Leaf hydraulic vulnerability is related to conduit dimensions and drought resistance across a diverse range of woody angiosperms. *New Phytol.* **2010**, *188*, 1113–1123. [CrossRef]
37. Sack, L.; Scoffoni, C. Leaf venation: Structure, function, development, evolution, ecology and applications in the past, present and future. *New Phytol.* **2013**, *198*, 983–1000. [CrossRef]
38. Fonseca, C.R.; Overton, J.M.; Collins, B.; Westoby, M. Shifts in trait-combinations along rainfall and phosphorus gradients. *J. Ecol.* **2000**, *88*, 964–977. [CrossRef]
39. Shipley, B.; Vu, T.T. Dry matter content as a measure of dry matter concentration in plants and their parts. *New Phytol.* **2002**, *153*, 359–364. [CrossRef]
40. Zheng, Y.; Wang, A.; Su, L.; Guo, J.; Duan, C.; Ying, X.; Gong, X.; Hao, G. Hydraulics and non-structural carbohydrate contents of *Ginkgo biloba* under different environmental conditions in Shenyang City, China. *Chin. J. Appl. Ecol.* **2022**, *33*, 711–719. [CrossRef]
41. Anderegg, W.R.L. Spatial and temporal variation in plant hydraulic traits and their relevance for climate change impacts on vegetation. *New Phytol.* **2015**, *205*, 1008–1014. [CrossRef] [PubMed]
42. Nardini, A.; Salleo, S. Water stress-induced modifications of leaf hydraulic architecture in sunflower: Co-ordination with gas exchange. *J. Exp. Bot.* **2005**, *56*, 3093–3101. [CrossRef]
43. Sack, L.; Frole, K. Leaf structural diversity is related to hydraulic capacity in tropical rain forest trees. *Ecology* **2006**, *87*, 483–491. [CrossRef]
44. Xiong, D.; Yu, T.; Zhang, T.; Li, Y.; Peng, S.; Huang, J. Leaf hydraulic conductance is coordinated with leaf morpho-anatomical traits and nitrogen status in the genus *Oryza*. *J. Exp. Bot.* **2015**, *66*, 741–748. [CrossRef] [PubMed]

45. Xia, Z.C.; He, Y.; Zhou, B.; Korpelainen, H.; Li, C.Y. Sex-related responses in rhizosphere processes of dioecious *Populus cathayana* exposed to drought and low phosphorus stress. *Environ. Exp. Bot.* **2020**, *175*, 104049. [CrossRef]
46. Yu, L.; Huang, Z.D.; Tang, S.L.; Korpelainen, H.; Li, C.Y. *Populus euphratica* males exhibit stronger drought and salt stress resistance than females. *Environ. Exp. Bot.* **2023**, *205*, 105114. [CrossRef]
47. Correia, O.; Barradas, M.C.D. Ecophysiological differences between male and female plants of *Pistacia lentiscus* L. *Plant Ecol.* **2000**, *149*, 131–142. [CrossRef]
48. Jin, J.; Jiang, H.; Yu, S.; Zhou, G. Sex-linked photosynthetic physiologic research and the evolutionary ecological analysis in relict plant, *Ginkgo biloba* L. *Acta Ecol. Sin.* **2008**, *28*, 1128–1136.
49. Shi, D.W.; Wei, X.D.; Chen, G.X.; Xu, Y.L. Changes in Changes in photosynthetic characteristics and antioxidative protection in male and female Ginkgo during natural senescence. *J. Am. Soc. Hortic. Sci.* **2012**, *137*, 349–360. [CrossRef]

Disclaimer/Publisher's Note: The statements, opinions and data contained in all publications are solely those of the individual author(s) and contributor(s) and not of MDPI and/or the editor(s). MDPI and/or the editor(s) disclaim responsibility for any injury to people or property resulting from any ideas, methods, instructions or products referred to in the content.

forests

MDPI

Article

Effects of Pruning on Vegetation Growth and Soil Properties in Poplar Plantations

Kaidong Huang [1], Cheng Xu [1], Zhuangzhuang Qian [2], Kang Zhang [1] and Luozhong Tang [1,*]

[1] Co-Innovation Center for Sustainable Forestry in Southern China, College of Forestry, Nanjing Forestry University, Nanjing 210037, China
[2] School of Forestry and Landscape Architecture, Anhui Agricultural University, Hefei 230036, China
* Correspondence: nanlintang@njfu.edu.cn

Abstract: Artificial pruning is an important silvicultural practice that can produce clear wood in poplar plantations. This study focused on the growth of poplar, understory vegetation diversity and soil properties in response to different pruning intensities in poplar plantations. We implemented three different pruning treatments based on the height-to-crown base (HCB) to tree height (H) ratio in *Populus deltoides* 'Nanlin 3804' plantations: CK (no pruning), a 1/3 pruning treatment and a 1/2 pruning treatment. The poplar growth conditions, understory vegetation biodiversity and soil properties were investigated for one year after pruning. Compared with CK, the 1/2 pruning treatment significantly decreased the increment of diameter at breast height (DBHi) and stem volume increment (Vi) by 16.4% and 12.8%, respectively. Meanwhile, pruning significantly promoted understory vegetation biomass and increased the Shannon–Weiner diversity index of understory vegetation, and these variables were positively correlated with pruning intensity. The 1/2 pruning treatment significantly reduced the contents of soil nitrate nitrogen (NO_3-N), total inorganic nitrogen (IN) and microbial biomass nitrogen (MBN) by 21.9%, 13.9% and 22.4%, respectively. However, the 1/3 pruning treatment had no significant influence. Pruning mainlyaffectedthe soil enzyme activity in the surface (0–10 cm) layer. The 1/3 and 1/2 pruning treatments significantly decreased soil urease activity by 20.1% and 15.0%, respectively. Furthermore, nonmetric multidimensional scaling analysis showed that the seasonal variation in soil properties was significant, and significant differences among pruning treatments were mainly observed in July and October. Redundancy analysis showed that the growth of aboveground vegetation was significantly correlated with soil properties, particularly soil IN content and urease activity. Therefore, the results highlighted that pruning could promote the growth of understory vegetation and accelerate the transformation of soil nutrients. The 1/2 pruning treatment significantly inhibited the growth of poplar in terms of DBH and V, while the 1/3 pruning treatment promoted the growth of poplar in the short term. Overall, we think that the 1/3 pruning intensity is more suitable for pruning practice.

Keywords: pruning; poplar plantation; understory vegetation; soil properties

check for updates

Citation: Huang, K.; Xu, C.; Qian, Z.; Zhang, K.; Tang, L. Effects of Pruning on Vegetation Growth and Soil Properties in Poplar Plantations. *Forests* **2023**, *14*, 501. https://doi.org/10.3390/f14030501

Academic Editor: Phillip G. Comeau

Received: 16 February 2023
Revised: 24 February 2023
Accepted: 28 February 2023
Published: 3 March 2023

Copyright: © 2023 by the authors. Licensee MDPI, Basel, Switzerland. This article is an open access article distributed under the terms and conditions of the Creative Commons Attribution (CC BY) license (https://creativecommons.org/licenses/by/4.0/).

1. Introduction

Poplar is an important economic and ecological tree species in China because of its fast growth, abundant biomass and strong regeneration capacity [1]. Due to the rapid urbanization and economic development in China, the demand for wood is growing [2]. Establishing fast-growing poplar plantations is regarded as the main tool for producing more wood under reduced land area [3]. As a basic management measure in plantations, pruning plays an important role in improving trunk shape, but it is often overlooked in practice. Due to the lack of timely and correct pruning, the side branches of poplar have a greater inhibitory effect on the trunk with increasing tree height, which seriously reduces the timber quality of poplar [4].

Branches are regarded as the main components of the crown, and their growth and distribution affect the structure and functions of the crown [5]. Artificial pruning is recognized as a basic silvicultural practice that can effectively promote wood quality [6–8]. However, there are still contradictory conclusions about the effect of pruning on tree growth. Some researchershave reported that canopy loss could lead to a reduction in the leaf area of trees and a reduction in photosynthetic capacity, thereby inhibiting the growth of trees [3,9]. Other researchers reported that although pruning reduced leaf area, itcould improve the light andwateruse efficiency per unit area of leaves; the photosynthetic efficiency per unit area of leaves was improved, which could help trees maintain normal growth [1,10–12]. Trees can produce compensatory physiological responses to pruning, such as increased water use efficiency and leaf nutrient contents. These changes are dependent on species and are generally thought to be closely related to pruning intensity [13]. In plantation ecosystems, pruning can change the forest microclimate, understory vegetation and surface microenvironment, and in turn lead to changes in soil characteristics, such as changes in the soil organic matter mineralization rate and soil enzyme activities [14,15]. Tetemke et al. [16] found that pruning could change the competition between understory vegetation for light, water and other resources. On the other hand, changes in understory vegetation structure and diversity have a strong potential to alter soil nutrients and thus the growth of upper trees. Therefore, there is a tradeoff between tree growth and understory competition under different pruning intensities.

Most previous studies have mainly focused on the effects of pruning on the growth and quality of poplar [17]. However, there is little information regarding the change in soil properties after pruning and the relationship between the growth of understory vegetation and soil properties in poplar plantations. In addition, considering the complex effects of pruning on the growth of understory vegetation and soil properties, there are many contradictory conclusions from previous studies. Therefore, we focused on the growth of poplar, understory vegetation diversity and soil properties in response to different pruning intensities in poplar plantations. We hypothesized that (1) 1/3 pruning intensity would promote the growth of poplars by removing the lower branches of tree crowns that receive less light, while the 1/2 pruning treatment would inhibit the growth of poplars, and (2) 1/2 pruning intensity would promote the growth of understory vegetation by providing more resources needed for survival, accelerating soil nutrient consumption and reducing soil nutrient content. The findings could improve the comprehensive understanding of the effect of pruning intensities on the vegetation growth and soil properties, and could also provide a scientific basis for the successful management of poplar plantations.

2. Materials and Methods

2.1. StudyArea

This study was conducted at Linchaichang Forestry Farm (118°32′48′′ E, 33°39′15′′ N), which is located in Suqian City, Jiangsu Province, China. This area is located in a plain area and belongs to the warm temperate monsoon climate zone, with an average annual air temperature of 14.2 °C, an average annual precipitation of 910 mm, and a total annual sunshine duration of 2291 h. The soil is developed fromlacustrine sediments, and the mineral soil of this area is with a clay texture (pH 7.8–8.5). We selected *Populus deltoides* 'Nanlin 3804′ as the research material, which is a male clone and was certified as a national genetically improved tree variety in 2010. The poplar (*Populus deltoides* 'Nanlin 3804′) plantation was established in the spring of 2014 by using 1-year-old seedlings with 6 m × 8 m row spacing (6 m plant spacing in the south–north direction and 8 m row spacing in the east–west direction). More than 95% of the trees were conserved before the experimental design. In the first year (2014) and second year (2015) after afforestation, wheat was interplanted in this field. Thereafter, no management was applied in the plantation, supporting its transition to a natural state.

2.2. Experimental Design

In this study, three different pruning treatments (CK, no pruning; 1/3 pruning treatment; 1/2 pruning treatment) were implemented in poplar plantations based on the height-to-crown base (HCB) to tree height (H) ratio after pruning. A completely randomized design with three replicates was applied in the field experiment, resulting in a total of 9 plots. The area of each plot was 2500 m^2 (50 m × 50 m), with 8 m buffer zones between adjacent plots to avoid edge effects, and the number of trees was more than 50 in each plot. We used a pole pruning saw to apply the pruning treatment in March 2018. Before pruning, the mean H was 16.90 m, the mean DBH was 21.20 cm, the mean crown diameter (CD) was 4.85 m, the mean HCB was 2.49 m and the canopy closure was 0.5.

2.3. Field Investigation

2.3.1. Growth Characteristic Investigation

In March 2018 and January 2019, H, DBH, CD and HCB were measured for each tree in each plot. Nine standard plots were set to investigate the growth characteristics of understory vegetation in October 2018. In each of the standard plots, two 1 m × 1 m subplots were set at 2 m, 4 m and 6 m on the west side of the tree row, for a total of 54 subplots. The species, quantity and coverage of understory vegetation were investigated in each subplot and used to calculate the Shannon–Weiner diversity index (*H′*), Menhinick's richness index (*Dm*) and Pielou's evenness index (*Jsw*). After the understory vegetation diversity survey, all aboveground parts of the understory vegetation were harvested and weighed in each subplot. The fresh plant samples were sealed and brought back to the laboratory, dried in an oven at 105 °C for 30 min and baked to a constant weight at 65 °C, and then the dry–fresh ratio of the understory vegetation was calculated. The biomass of understory vegetation under different treatments was calculated according to the dry–fresh ratio.

Descriptions of the investigated site are provided in Tables 1 and 2.

Table 1. Main stand characteristics (mean ± standard error) of the poplar plantation before pruning.

T	DBH (cm)	H (m)	HCB (m)	CD (m)	
				EW	NS
CK	20.89 ± 0.75a	17.08 ± 0.39a	2.35 ± 0.16a	4.94 ± 0.18a	4.73 ± 0.18a
1/3	21.52 ± 0.68a	16.83 ± 0.48a	2.58 ± 0.17a	5.06 ± 0.36a	4.87 ± 0.17a
1/2	21.20 ± 0.48a	16.79 ± 0.26a	2.50 ± 0.17a	4.74 ± 0.19a	4.73 ± 0.21a
Mean	21.20 ± 0.25	16.90 ± 0.13	2.49 ± 0.10	4.91 ± 0.13	4.78 ± 0.06

Note: T represents the pruning treatment; DBH represents diameter at breast height; H represents tree height; HCB represents height-to-crown base; CD represents crown diameter; EW represents east–west direction; NS represents north–south direction.

Table 2. Soil physicochemical properties (mean ± standard error) of the poplar plantation before pruning.

T	D	BD ($g \cdot cm^{-3}$)	P (%)	TN ($g \cdot kg^{-1}$)	TP ($g \cdot kg^{-1}$)	TK ($g \cdot kg^{-1}$)	OM ($g \cdot kg^{-1}$)
CK	0–10 cm	1.23 ± 0.08Aa	54.50 ± 1.73Aa	0.90 ± 0.14Aa	0.88 ± 0.05Aa	16.24 ± 0.79Aa	28.61 ± 2.09Aa
	10–20 cm	1.31 ± 0.01Aa	49.88 ± 2.64Aa	0.55 ± 0.06Ba	0.74 ± 0.03Ba	15.69 ± 0.35Aa	19.89 ± 0.99Ba
	20–50 cm	-	-	0.22 ± 0.02Ca	0.59 ± 0.02Ca	13.22 ± 0.39Ba	7.00 ± 0.64Ca
1/3	0–10 cm	1.13 ± 0.08Aa	57.15 ± 1.75Aa	0.81 ± 0.19Aa	0.87 ± 0.11Aa	16.63 ± 0.29Aa	29.04 ± 1.52Aa
	10–20 cm	1.29 ± 0.06Aa	51.59 ± 5.77Aa	0.50 ± 0.10Aa	0.72 ± 0.04Aa	16.56 ± 0.53Aa	18.71 ± 1.41Ba
	20–50 cm	-	-	0.24 ± 0.06Ba	0.55 ± 0.03Ba	13.49 ± 0.69Ba	10.02 ± 1.60Ca
1/2	0–10 cm	1.18 ± 0.12Aa	55.39 ± 2.31Aa	0.92 ± 0.15Aa	0.91 ± 0.03Aa	15.86 ± 0.45Aa	31.27 ± 1.41Aa
	10–20 cm	1.30 ± 0.07Aa	50.94 ± 1.94Aa	0.64 ± 0.04Ba	0.77 ± 0.05Ba	15.71 ± 0.54ABa	20.72 ± 2.15Ba
	20–50 cm	–	–	0.28 ± 0.06Ca	0.57 ± 0.02Ca	14.14 ± 1.03Ba	6.68 ± 1.24Ca

Note: T represents the pruning treatment; D represents soil depth; BD represents soil bulk density; P represents soil porosity; TN represents total nitrogen content; TP represents total phosphorus content; TK represents total potassium content; OM represents organic matter content. Different lowercase letters indicate significant differences between different pruning treatmentsat the same soil depth ($p < 0.05$); different capital letters indicate significant differences between different soil depths in the same treatment ($p < 0.05$). The error bars are the standard errors.

2.3.2. Soil Sampling and Laboratory Analysis

In March 2018 (spring), July 2018 (summer), October 2018 (autumn) and January 2019 (winter), soil samples were obtained from the 0–10 cm, 10–20 cm and 20–50 cm soil layers at 10 points in an "S" shape in each standard plot by using a soil auger (with a diameter of 5 cm). Soil samples at each depth from each plot were mixed to create a composite sample. A total of 108 composite samples were collected. After removing the plant residues, these soil samples were transported to the laboratory for soil property analysis. Each sample was divided into two portions: one portion of the fresh samples was sieved through a 2 mm mesh for the determination of microbial biomass and inorganic nitrogen content; the second portion was air-dried and sieved through a 0.25 mm mesh for the determination of soil enzyme activities.

Soil water content (SWC) was assessed by oven drying to constant mass at 105 °C. Soil ammonium nitrogen (NH_4-N) and nitrate nitrogen (NO_3-N) contents were determined in 2 mol/L KCl extracts (1:10 soil to solution ratio) using a continuous flow analyzer (Bran Luebbe Inc., AA3, Norderstedt, Germany). The soil total inorganic nitrogen (IN) content was the sum of the ammonium nitrogen (NH_4-N) content and nitrate nitrogen (NO_3-N) content. The soil microbial biomass in fresh soil samples was fumigated by chloroform and extracted by 0.5 mol/L K_2SO_4 (1:4 soil to solution ratio) [18]. The microbial biomass carbon (MBC) content in the solution was measured using a carbon analyzer (Shimadzu Inc., TOC-VCPN, Kyoto, Japan). The microbial biomass nitrogen (MBN) content was determined using a continuous flow analyzer (Bran Luebbe Inc., AA3, Norderstedt, Germany).

Soil catalase activity was expressed as the volume of 0.02 mol/L $KMnO_4$ consumed by 1 g of soil within 20 min. Soil urease activity was expressed as the mass of ammonium nitrogen produced by consuming urea in 1 g of soil over 1 h. Soil saccharase activity was expressed as the mass of glucose produced by 1 g of soil within 24 h [19,20].

2.4. Data Calculations and Statistical Analysis

2.4.1. Data Calculations

Stem volume was calculated from the following equation [21]:

$$V = 0.0000267 \times (H + 3) \times DBH^2$$

where V is the stem volume of the tree (m^3), DBH is the diameter at breast height of the tree (cm) and H is the tree height (m).

The annual growth of trees (Hi, $DBHi$, CDi and Vi) was the difference between the growth indicators (H, DBH, CD and V) investigated in March 2018 and January 2019.

Understory vegetation diversity was calculated by the following equation [22]:

$$\text{The Shannon–Weiner diversity index } (H') : H' = -\sum_{i=1}^{S} P_i \ln P_i$$
$$\text{Menhinick's richness index } (D_m) : D_m = S/\sqrt{N}$$
$$\text{Pielou's evenness index } (J_{sw}) : J_{sw} = H'/\ln S$$

where P_i is the proportion of species i in each subplot, S is the total number of species in each subplot and N is the total number of vegetation species i in each subplot.

2.4.2. Statistical Analysis

In this study, one-way ANOVA (SPSS 22, IBM-SPSS Inc., Chicago, IL, USA) was used to analyze the differences in poplar growth indexes and understory vegetation biodiversity indexes among different pruning treatments, and Duncan's method was used to test for significance of the differences. A repeated measures ANOVA was conducted to analyze the interaction effects of pruning treatment, sampling season and soil depth on the soil properties. Nonmetric multidimensional scaling (NMDS) plots from the software CANOCO 5.0 (Microcomputer Power, Ithaca, NY, USA) were used to show clusters based on soil properties and enzyme activities under different pruning treatments during four seasons.

Pearson correlation coefficients (Pearson's R) and linear fit analysis were used to reveal the relationships between soil properties and soil enzyme activities using SPSS 22.0 software. Moreover, redundancy analysis (RDA) was used to identify the relationships among the poplar growth index, understory vegetation diversity and soil properties using CANOCO 5.0 software.

3. Results

3.1. Growth of Poplar and Understory Vegetation Diversity

As shown in Figure 1, the Hi and CDi of poplar showed no significant responses to pruning treatments ($p > 0.05$). Compared with those in the CK treatment, the Hi and CDi of poplar in the 1/3 pruning treatment increased by 9.5% and 9.4%, respectively, but these differences were not significant ($p > 0.05$). The Hi and CDi of poplar in the 1/2 pruning treatment were almost the same as those in CK. In contrast, there were significant differences in the DBHi of poplar among pruning treatments. Compared with CK, the 1/2 pruning treatment significantly reduced the DBHi of poplar by 16.4% ($p < 0.05$). The DBHi of poplar in the 1/3 pruning treatment was lower than that in CK by 9.1%, but the difference was not significant ($p > 0.05$). The 1/2 pruning treatment significantly reduced the Vi of poplar by 12.8% ($p < 0.05$) compared with that in CK. However, the 1/3 pruning treatment increased the Vi of poplar by 3.2%, which was not a significant change ($p > 0.05$).

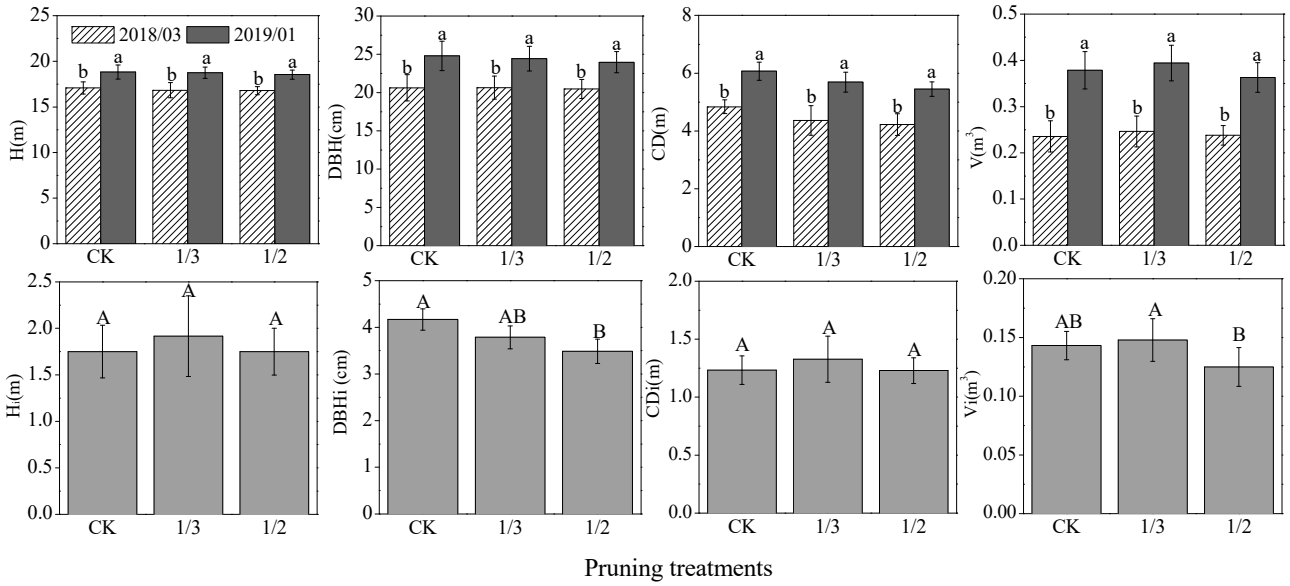


Figure 1. Growth characteristics of poplar after pruning treatments. Note: H represents tree height, Hi represents the tree height increment; DBH represents diameter at breast height, DBHi represents the increment of diameter at breast height; CD represents crown diameter, CDi represents the increment of crown diameter; V represents stem volume, Vi represents the stem volume increment. Different lowercase letters indicate significant differences between different sampling times in the same treatment ($p < 0.05$); different capital letters indicate significant differences between different pruning treatments during the same period ($p < 0.05$). The error bars are the standard errors.

In addition, the pruning treatments significantly increased the understory vegetation biomass (Figure 2). Compared with CK, the 1/3 and 1/2 pruning treatments increased the understory vegetation biomass by 35.7% and 63.0%, respectively ($p < 0.01$). In contrast, pruning had weaker effects on understory vegetation diversity within one year after pruning, and only the Shannon–Weiner diversity index (H') was significantly increased after pruning ($p < 0.01$). The effect of the 1/2 pruning treatment was greater than that of the 1/3 pruning treatment ($p < 0.05$). There were no significant differences in Menhinick's richness indexes (Dm) or Pielou's evenness indexes (Jsw) among the different pruning treatments.

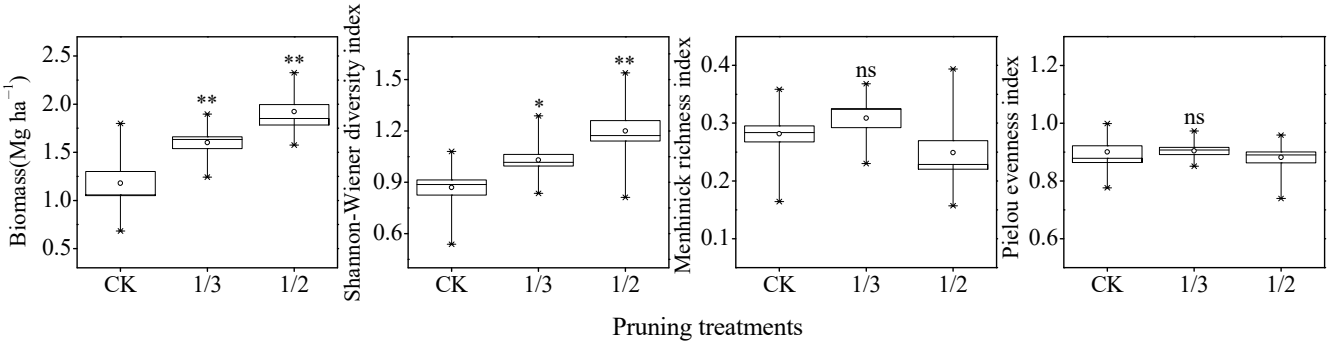


Figure 2. Effects of pruning on understory vegetation biomass, the Shannon–Weiner diversity index (*H'*), Menhinick's richness index (*Dm*) and Pielou's evenness index (*Jsw*) in October 2018. Note: The box represents ± SE, the whiskers show the minimum and maximum, the small circle is the mean, and the horizontal line is the median. Statistically significant differences between pruning treatments and CK are indicated by symbols: ** $p < 0.01$, * $p < 0.05$ and ns—no significant difference.

3.2. Soil Properties

3.2.1. Soil Water and Inorganic Nitrogen Contents

The SWC and NH_4-N contents showed obvious seasonal changes ($p < 0.05$), but there were no significant differences among the different pruning treatments (Figure 3). The contents of NO_3-N and IN in the 1/3 pruning treatment and 1/2 pruning treatment were lower than those in CK, especially in July and October 2018. Compared with CK, the two pruning treatments significantly reduced the contents of NO_3-N and IN in the topsoil layer (0–10 cm). The contents of NO_3-N and IN under the 1/2 pruning treatment were lower by 21.9% and 13.9%, respectively ($p < 0.01$), than those in CK. However, the NO_3-N and IN contents of the 10–20 cm soil layer under the two pruning treatments were significantly lower than those in CK in July 2018 ($p < 0.01$). The repeated measures ANOVA showed significant effects of the interaction between pruning treatments and sampling seasons onNH_4-N, NO_3-N and IN (Table 3).

Table 3. F and *p* values for the effects of pruning treatments (T), sampling seasons (S) and soil depths (D) on the soil properties from repeated measures ANOVA.

Source	F(*p*) Value SWC	NH_4-N	NO_3-N	IN	MBC	MBN	Catalase	Saccharase	Urease
T	0.629 (0.536)	4.665 (0.012)	9.247 (<0.001)	8.053 (0.001)	5.805 (0.005)	6.730 (0.003)	17.002 (<0.001)	10.822 (<0.001)	9.382 (<0.001)
S	248.398 (<0.001)	307.926 (<0.001)	41.898 (<0.001)	19.866 (<0.001)	4.702 (0.005)	65.714 (<0.001)	2414.374 (<0.001)	429.663 (<0.001)	242.015 (<0.001)
D	51.448 (<0.001)	14.178 (<0.001)	130.396 (<0.001)	127.363 (<0.001)	78.109 (<0.001)	236.031 (<0.001)	90.699 (<0.001)	2193.513 (<0.001)	1152.01 (<0.001)
T × S	0.939 (0.473)	8.245 (<0.001)	2.307 (0.043)	4.382 (0.001)	0.744 (0.616)	1.499 (0.191)	2.504 (0.029)	1.895 (0.094)	3.14 (0.009)
T × D	0.224 (0.924)	1.256 (0.295)	1.444 (0.228)	1.32 (0.271)	3.21 (0.018)	0.478 (0.752)	1.606 (0.182)	6.98 (<0.001)	2.069 (0.094)
S × D	5.762 (<0.001)	3.313 (0.006)	16.377 (<0.001)	16.278 (<0.001)	1.293 (0.271)	25.984 (<0.001)	4.975 (<0.001)	83.914 (<0.001)	40.196 (<0.001)
T × S × D	0.389 (0.963)	1.235 (0.277)	1.321 (0.226)	1.656 (0.095)	0.623 (0.815)	0.722 (0.725)	0.244 (0.955)	3.288 (<0.001)	2.364 (0.013)

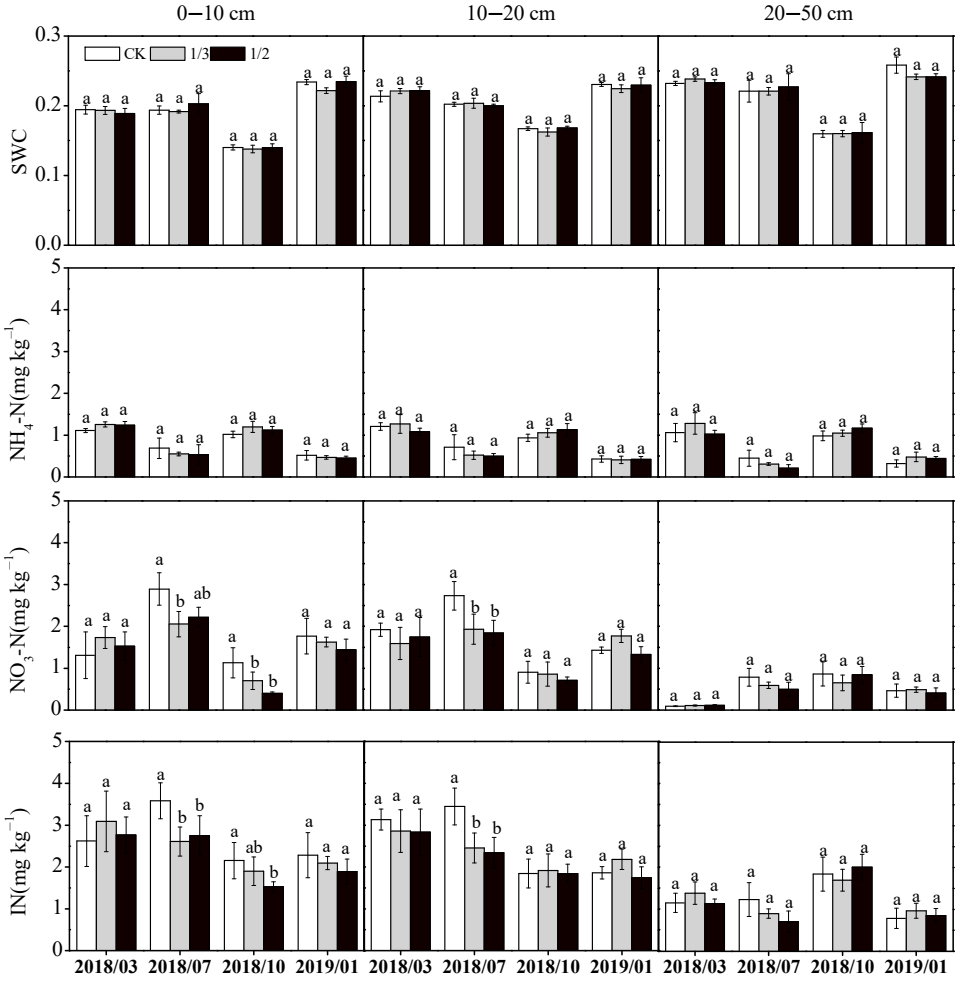


Figure 3. Dynamic changes in soil water and inorganic nitrogen contents in the poplar plantation after pruning treatments. Note: The same lowercase letter over two columns indicates no significant difference between pruning treatments at the same time point ($p > 0.05$), while different lowercase letters indicate significant differences between pruning treatments at the same time point ($p < 0.05$). Soil properties include soil water content (SWC), soil ammonium nitrogen (NH_4-N), soil nitrate nitrogen (NO_3-N) and soil total inorganic nitrogen (IN); 2018/03, 2018/07, 2018/10 and 2019/01 represent the sampling time year/month; 0–10 cm, 10–20 cm and 20–50 cm represent different soil sampling depths. This is the same below.

3.2.2. Soil Microbial Biomass

As shown in Figure 4, the pruning treatment significantly affected the MBC content ($p < 0.05$). In the 0–10 cm soil layer, the MBC content under the 1/3 pruning treatment was significantly lower than that under the CK and 1/2 pruning treatments ($p < 0.01$). However, there was no significant difference in the MBC content among the three treatments in the 10–20 cm and 20–50 cm soil layers. In the 0–10 cm soil layer, the two pruning treatments showed significantly lower MBN contents than CK in July 2018, while the content of MBN in the 1/3 pruning treatment was significantly lower than that in CK only in October 2018, with a change of 15.8%–29.1% ($p < 0.05$). In the 10–20 cm soil layer, compared with CK, the 1/2 pruning treatment significantly reduced the MBN content ($p < 0.05$). However, there was no significant difference in the MBN content among the three pruning treatments in the 20–50 cm soil layer ($p > 0.05$). The interaction effects of pruning treatment and sampling season on MBC and MBN were not significant (Table 3).

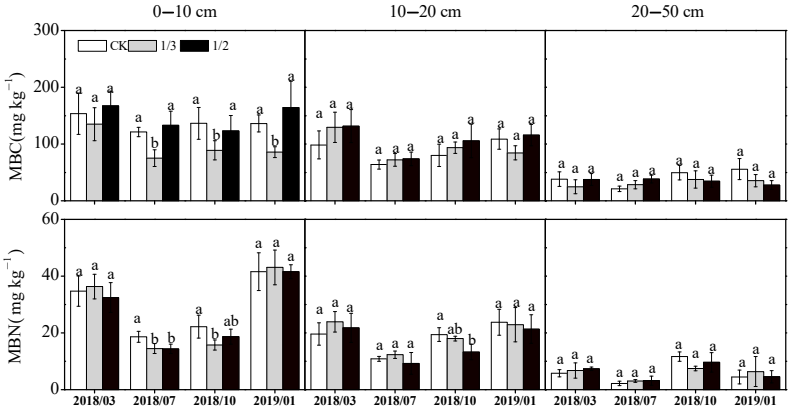


Figure 4. Dynamic changes in soil microbial biomass carbon (MBC) and nitrogen (MBN) in the poplar after pruning treatments. Note: The same lowercase letter over two columns indicates no significant difference between pruning treatments at the same time point ($p > 0.05$), while different lowercase letters indicate significant differences between pruning treatments at the same time point ($p < 0.05$).

3.2.3. Soil Enzyme Activities

As shown in Figure 5, the activities of three soil enzymes responded differently to the changes in pruning treatment, of which soil urease activity had the most significant response to pruning intensity. In July 2018 and October 2018, compared with CK, pruning significantly decreased the average soil urease activity, and the soil urease activities in the 0–10 cm soil layer under the 1/3 and 1/2 pruning treatments decreased by 20.1% and 15.0%, respectively ($p < 0.05$). The responses of soil saccharase activity to pruning were mainly concentrated in the 0–10 cm soillayer, and the average activity of the 1/3 pruning treatment during the four seasons decreased by 13.3% compared with that in CK. After July 2018, there were no significant differences in soil saccharase activities among the three treatments. In addition, no significant impact was observed for soil catalase activities among the different treatments. The pruning treatments and sampling seasons showed significant interaction effects on various soil enzyme activities, except for saccharase activities (Table 3).

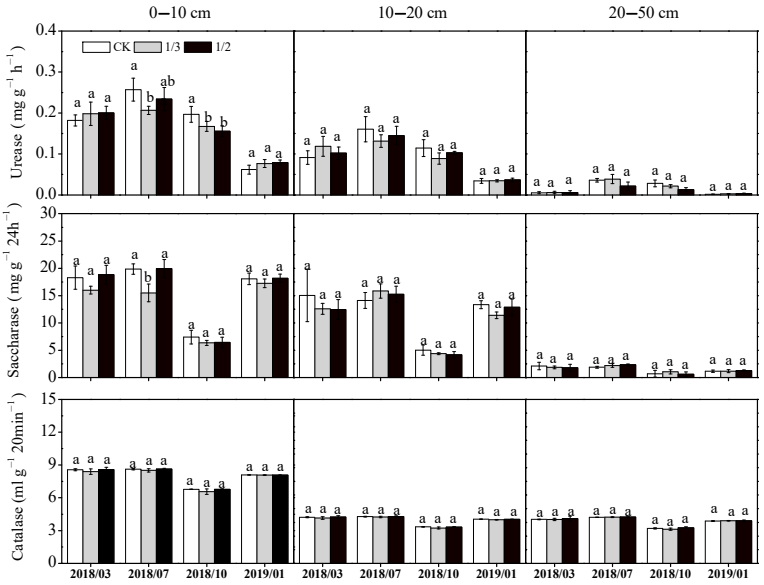


Figure 5. Dynamic change in soil enzyme activities in the poplar plantation after pruning treatments. Note: The same lowercase letter over two columns indicates no significant difference between pruning treatments at the same time point ($p > 0.05$), while different lowercase letters indicate significant differences between pruning treatments at the same time point ($p < 0.05$).

3.2.4. Nonmetric Multidimensional Scaling Analysis of Soil Properties and Enzyme Activities

Nonmetric multidimensional scaling (NMDS) analysis was used to show the response of soil properties and enzyme activities in the 0–50 cm soil layer to the three pruning treatments during four seasons. As the dispersion of different points shows in Figure 6, soil properties and enzyme activities clustered more strongly on the basis of temporal variation than on the basis of pruning treatment. However, the cluster of sample points for CK was distant from those for the 1/3 and 1/2 pruning treatments in October 2018.

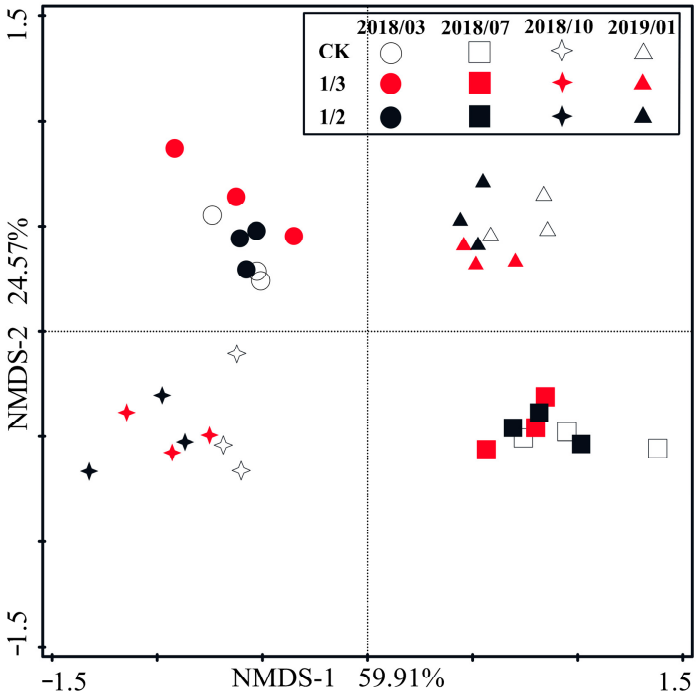


Figure 6. Nonmetric multidimensional scaling analysis (NMDS) of soil properties and enzyme activities under different pruning treatments during four periods.

3.3. Relationship between Soil Properties and Soil Enzyme Activities

The linear fitting and Pearson correlation coefficient (Pearson's R) results revealed an overall significant correlation between soil properties and soil enzyme activities in the poplar plantation after pruning treatments. As shown in Figure 7, the linear relationships between SWC ($p < 0.05$) and IN ($p < 0.01$) and catalase activities were significant and positive, and the other enzyme activities (saccharase and urease) were significantly correlated with soil properties ($p < 0.01$), except for saccharase and SWC. Additionally, the Pearson correlation coefficients between SWC and IN and the three soil enzyme activities were higher than those between the MBC and MBN contents and soil enzyme activities, which implied that the three enzymes were more sensitive to changes in SWC and IN.

3.4. Relationships among Poplar Growth, Understory Vegetation Characteristics and Soil Properties

The RDA results in Figure 8 indicated that Hi, CDi and DBHi were significantly affected by soil properties. CDi had a negative correlation with MBN ($p < 0.05$); in contrast, CDi had a positive correlation with IN ($p < 0.05$). There was a positive correlation between DBHi and soil properties, particularly for IN ($p < 0.05$). Moreover, urease activities had the greatest influence on the growth of poplar, followed by catalase, among the three soil enzyme activities ($p < 0.05$). Among the soil available nutrients, MBN and IN had a large influence on the growth of poplar.

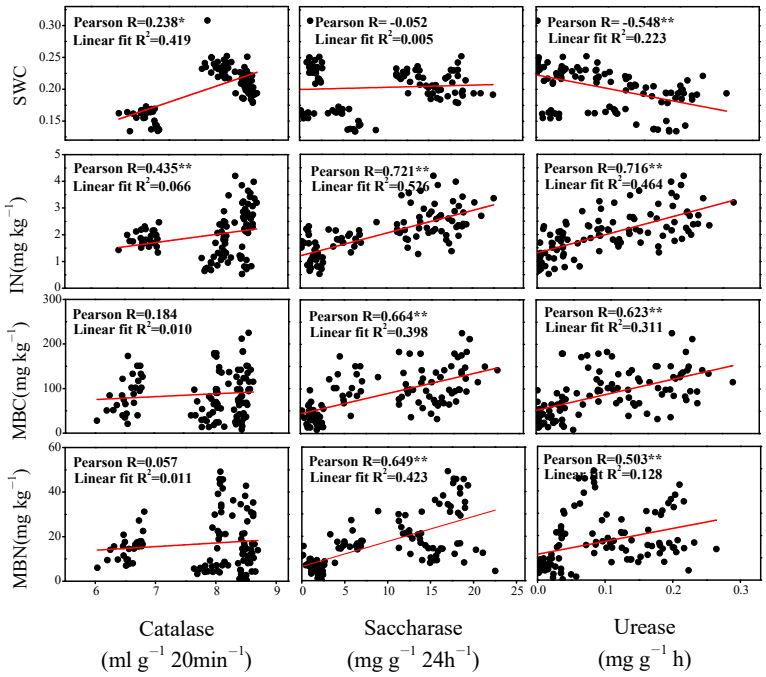


Figure 7. Linear fitting and Pearson correlation coefficients (Pearson's R) between soil properties and soil enzyme activities in the poplar plantation after pruning treatments. Note: Statistically significant values are indicated by symbols: ** $p < 0.01$; * $p < 0.05$.

3.5. Relationships among Poplar Growth, Understory Vegetation Characteristics and Soil Properties

The RDA results in Figure 8 indicated that Hi, CDi and DBHi were significantly affected by soil properties. CDi had a negative correlation with MBN ($p < 0.05$); in contrast, CDi had a positive correlation with IN ($p < 0.05$). There was a positive correlation between DBHi and soil properties, particularly for IN ($p < 0.05$). Moreover, urease activities had the greatest influence on the growth of poplar, followed by catalase, among the three soil enzyme activities ($p < 0.05$). Among the soil available nutrients, MBN and IN had a large influence on the growth of poplar.

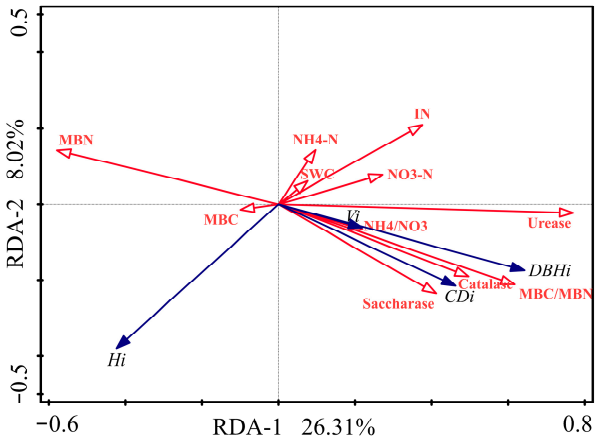


Figure 8. RDA between the poplar growth characteristics (blue arrows) and soil properties (red arrows) under different pruning treatments during four periods. Note: the results of RDA are used to identify the relationships between the poplar growth and soil properties; n (36) = three pruning treatments × four periods × three replications. The percentages on the *x*-axis and *y*-axis reflect the response rate of the soil properties to the changes in poplar growth characteristics in different dimensions. NH_4/NO_3 represents the ratio of soil ammonium nitrogen (NH_4-N) to nitrate nitrogen (NO_3-N); the same applies below.

Figure 9 shows that there was a significant negative correlation between understory vegetation biomass and soil available nutrients such as NH_4-N, NO_3-N and IN ($p < 0.01$). On the basis of soil enzyme activities, catalase was the only soil enzyme that had a significant positive correlation with understory vegetation biomass ($p < 0.05$). The Shannon–Weiner diversity index and Menhinick's richness index of understory vegetation had a significant negative correlation with NH_4-N, NO_3-N, IN and catalase ($p < 0.05$), and the Shannon–Weiner diversity index had a significant positive correlation with catalase ($p < 0.05$). Pielou's evenness index was positively correlated with catalase ($p < 0.01$) but significantly negatively correlated with NH_4-N, IN and NH_4/NO_3 ($p < 0.05$). Generally, SWC, MBN, saccharase and urease were not significantly correlated with understory vegetation.

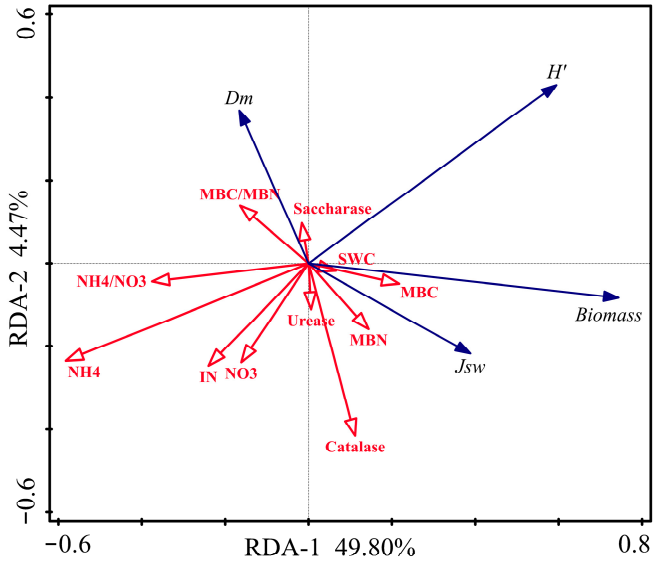


Figure 9. RDA between the understory vegetation characteristics (blue arrows) and soil properties (red arrows) under different pruning treatments. Note: the results of RDA are used to identify the relationships between the understory vegetation characteristics and soil properties; n (27) = three pruning treatments× nine replications. The percentages on the *x*-axis and *y*-axis reflect the response rate of the soil properties to the changes in understory vegetation characteristics in different dimensions.

4. Discussion

4.1. Effects of Pruning Intensity on Poplar Growthand Understory Vegetation

Tree growth mainly relies on leaf photosynthesis to produce and accumulate carbohydrates, and pruning is recognized as a basic silvicultural practice that plays an important role in improving stem shape and timber quality [23]. Previous studies have suggested that pruning reduces the height and diameter growth of trees [24–28]. However, we found that the 1/3 pruning treatment had a certain negative effect on the DBHi of poplar and had a positive influence on the height increment (Hi), crown diameter (CDi) and volume (Vi) growth of poplar. The 1/2 pruning treatment significantly reduced the DBHi and Vi of poplar (Figure 1). These results are consistent with those of some previous studies [9,29,30]. It is likely that pruning reduced the leaf area and transpiration of trees, but the light use efficiency, water use efficiency and CO_2 assimilation rate of leaves per unit area might be improved correspondingly [31–33], further maintaining the growth of trees at a normal level [10,12,13]. Maurin and DesRochers [3] found that pruning increased the N content of leaves and improved the net photosynthesis of the remaining leaves in hybrid poplar. In our study, the intensity of the 1/3 pruning treatment was relatively low, mainly with the pruning of the lower branches of the tree crown. These branches might have a poor net photosynthetic rate due to weak light [34]. Therefore, the Hi, CDi and Vi of poplar after the 1/3 pruning treatment were higher than those of the CK. However, apart from pruning the branches with a negative net photosynthetic rate, the 1/2 treatment with a

relatively high pruning intensity also included pruning the other branches that had a high net photosynthetic rate, resulting in a reduction in the total photosynthetic products in leaves and seriously affecting the DBHi and Vi of poplar [13].

Pruning changes the understory microclimate, such as light, temperature and humidity, by changing the canopy structure and increasing understory environmental heterogeneity, resulting in differences in the quantity and composition of understory vegetation and thus further affecting understory vegetation species diversity [35–38]. We found that the understory vegetation biomass increased with increasing pruning intensity within one year after pruning. This may have been caused by the accumulation of photosynthetic products, with canopy pruning improving understory light intensity and photosynthetically active radiation [39,40]. There were weaker effects of pruning on the understory vegetation diversity within one year after pruning, and only the Shannon–Weiner diversity index increased with increasing pruning intensity. It is possible that pruning greatly impacts native shade-tolerant plants, while invasive light-loving plants are not fully established in a short period, which implies a time hysteresis effect in the response of understory vegetation diversity to changes in the understory environment [41,42]. It also indicated that the Shannon–Weiner diversity index is sensitive to changes in the understory environment.

4.2. Effects of Pruning Intensity on Soil Properties in Poplar Plantations

Soil properties were greatly affected by the aboveground plants and the understory microenvironment. Our results showed significant differences in soil properties between different pruning treatments (Figure 6). These were also reported in previous experiments [43,44]. On the one hand, canopy pruning could change the understory microclimate, promote the growth of understory vegetation and increase water consumption (Figure 2). On the other hand, branch and leaf loss could decrease water consumption by leaf transpiration and thus decrease the water requirement of trees [45]. The difference in SWC between pruning intensities was also reduced, coupled with the buffering effect of understory vegetation cover. As shown in our results, there was no significant difference in SWC between the different pruning treatments (Figure 3). The content of soil inorganic nitrogen basically depends on the balance among soil nitrogen mineralization, absorption and fixation by plant roots and soil microorganisms [46]. In our study, from July 2018 to the period after pruning, the contents of soil nitrate nitrogen (NO_3-N) and total inorganic nitrogen (IN) under the pruning treatments were significantly lower than those in CK (no pruning). It is likely that pruning promoted the growth of understory vegetation (Figure 2) and led to a corresponding increase in the consumption of soil inorganic nitrogen. However, other researchers reported that pruning could reduce the input of litter and thus reduce soil fertility [47]. Overall, canopy pruning significantly decreased the soil NO_3-N and IN contents in the poplar plantation, but no significant difference in NH_4-N content was found between pruning treatments, thus indicating that NO_3-N was sensitive to environmental changes.

Understory vegetation changes affect the distribution and utilization of soil water and nutrients, thus affecting soil biological activities such as soil enzyme activities and microbial biomass [48]. Pruning improved the understory microenvironment, promoted the growth of understory vegetation and resulted in a corresponding increase in the nutrient absorption of understory vegetation from soil. In turn, this led to a decrease in soil microbial biomass and enzyme activity by decreasing soil nutrients [49]. In our study, we found that low pruning intensity (1/3 pruning treatment) significantly reduced the MBC content in the 0–10 cm soil layer, while high pruning intensity (1/2 pruning treatment) had no significant effect on the MBC content. From another perspective, high pruning intensity can be regarded as a stress to plants. Pramanik et al. [50] found that pruning stress could promote an increase in root exudates and increase the content of MBC in rhizosphere soil. However, the total consumption of MBC by tree and understory vegetation also greatly increased, causing nonsignificant changes in soil MBC. In addition, other researchers indicated that low IN content could inhibit the production of MBN in soil [51]. Our study revealed that pruning significantly decreased the soil MBN content compared with that in

CK (no pruning) during the growing season (Jul 2018–Oct 2018). A possible reason for this observation is that MBN could be transformed with soil IN; therefore, soil MBN contents decreased with the high consumption of soil IN in the growing season [52].

The activities of the three soil enzymes (catalase, urease and saccharase) showed a significant change with seasonal variation and responded differently to pruning treatments (Figure 5). Starting in July 2018, soil urease activities were significantly decreased by pruning in poplar plantations compared with CK, as were the variation trends of soil IN and MBN (Figures 6 and 7). This is consistent with the findings of Deng et al. [53] and Li et al. [54]—that a decrease in the soil available N pool reduced soil urease activities. Soil catalase activities showed significant seasonal changes and were positively correlated with SWC (Figure 7). However, soil catalase activities were not significantly affected by pruning and microbial biomass, which could be because of the higher pH (7.8–8.5) in our study area [55].

4.3. Relationships between Soil Properties and the Growth of Poplar Trees and Understory Vegetation

Soil nutrients are closely related to the growth of aboveground vegetation. Most of the water and nutrients required for tree growth are absorbed from the soil and dispersed through tree transpiration [56–58]. Numerous studies have confirmed that the biomass and diversity of understory vegetation can reflect soil nutrient quality [59,60]. We found that pruning increased the understory vegetation biomass and diversity index in poplar plantations (Figure 2). Our previous study suggested that pruning increased the understory light intensity, promoted the photosynthesis of understory vegetation and increased the absorption of soil nutrients and water by plants [61]. At the same time, the growth of aboveground vegetation also promoted the decomposition of litter and root exudates to feed back to the soil, thereby affecting soil microorganism and enzyme activities. In addition, RDA revealed that DBHi and Hi were significantly correlated with soil properties, especially soil urease and IN. Understory vegetation biomass was negatively correlated with soil NO_3-N and NH_4-N. The Shannon–Weiner diversity index and Menhinick's richness index of understory vegetation were negatively correlated with soil NO_3-N, NH_4-N and catalase activities. The results of RDA combined with previous conclusions [62–64] further confirm our conclusions.

In conclusion, our short-term study demonstrates that pruning can affect the growth of aboveground vegetation and thus change soil properties in a poplar plantation. IN is the most sensitive to changes in aboveground vegetation, and the activity of soil urease displays significantly stronger responses to aboveground vegetation than other enzymes. Further research is needed to verify the long-term effects of pruning intensity on vegetation growth and soil properties.

5. Conclusions

This study concluded that low pruning intensity (1/3 pruning treatment) could promote the growth of poplar, while high pruning intensity (1/2 pruning treatment) could reduce the DBH and V growth of poplar. Pruning could improve understory vegetation biomass and the Shannon–Weiner diversity. At the same time, high pruning intensity (1/2 pruning treatment) reduced the contents of soil nitrate nitrogen (NO_3-N), total inorganic nitrogen (IN) and microbial biomass nitrogen (MBN). In addition, pruning decreased soil urease activities, while there were no significant changes in soil saccharase and catalase activities after pruning. In conclusion, pruning could promote the growth of understory vegetation and change the soil inorganic nitrogen content and enzyme activity in the short term. Low pruning intensity can promote the height and volume growth of poplar, while high pruning intensity could inhibit the DBH and volume growth of poplar. The results of this study have practical significance for plantation management and provide an effective theoretical basis for the scientific management of plantations.

Author Contributions: K.H.: Methodology, Investigation, Data curation, Formal analysis, Visualization, Writing—Original draft. C.X., Z.Q. and K.Z.: Formal analysis, Methodology, Investigation,

Writing—Review and editing. L.T.: Conceptualization, Funding acquisition, Methodology, Project administration, Supervision, Writing—Review and editing. All authors have read and agreed to the published version of the manuscript.

Funding: This work was funded by The National Key Research and Development Program of China (grant number 2021YFD2201202).

Data Availability Statement: Not applicable.

Conflicts of Interest: The authors declare no conflict of interest.

References

1. Zhang, J.; Liu, L.Q. Effects of pruning intensity on nonstructural carbohydrates of *Populus alba* × *P. talassica* in the arid desert region of Northwest China. *J. For. Res.* **2021**, *32*, 823–830. [CrossRef]
2. Arnold, R.J.; Xie, Y.J.; Luo, J.Z.; Wang, H.R.; Midgley, S.J. A tale of two genera: Exotic *Eucalyptus* and *Acacia* species in China. 2. Plantation resource development. *Int. Forest. Rev.* **2020**, *22*, 153–168. [CrossRef]
3. Maurin, V.; DesRochers, A. Physiological and growth responses to pruning season and intensity of hybrid poplar. *For. Ecol. Manag.* **2013**, *304*, 399–406. [CrossRef]
4. Desrochers, A.; Maurin, V.; Tarroux, E. Production and role of epicormic shoots in pruned hybrid poplar: Effects of clone, pruning season and intensity. *Ann. For. Sci.* **2015**, *72*, 425–434. [CrossRef]
5. Ishii, H.; Clement, J.P.; Shaw, D.C. Branch growth and crown form in old coastal Douglas-fir. *For. Ecol. Manag.* **2000**, *131*, 81–91. [CrossRef]
6. Dănescu, A.; Ehring, A.; Bauhus, J.; Albrecht, A.; Hein, S. Modelling discoloration and duration of branch occlusion following green pruning in *Acer pseudoplatanus* and *Fraxinus excelsior*. *For. Ecol. Manag.* **2015**, *335*, 87–98. [CrossRef]
7. Wang, C.S.; Hein, S.; Zhao, Z.G.; Guo, J.J.; Zeng, J. Branch occlusion and discoloration of *Betula alnoides* under artificial and natural pruning. *For. Ecol. Manag.* **2016**, *375*, 200–210. [CrossRef]
8. York, R.A. Long-term taper and growth reductions following pruning intensity treatments in giant sequoia (*Sequoiadendron giganteum*). *Can. J. For. Res.* **2019**, *49*, 1189–1197. [CrossRef]
9. Li, R.S.; Han, J.M.; Guan, X.; Chi, Y.G.; Zhang, W.D.; Chen, L.C.; Wang, Q.K.; Xu, M.; Yang, Q.P.; Wang, S.L. Crown pruning and understory removal did not change the tree growth rate in a Chinese fir (*Cunninghamia lanceolata*) plantation. *For. Ecol. Manag.* **2020**, *464*, 118056. [CrossRef]
10. Binkley, D.; Laclau, J.P.; Sterba, H. Why one tree grows faster than another: Patterns of light use and light use efficiency at the scale of individual trees and stands. *For. Ecol. Manag.* **2013**, *288*, 1–4. [CrossRef]
11. Chen, D.Y.; Wang, Y.K.; Wang, X.; Nie, Z.Y.; Gao, Z.Y.; Zhang, L.L. Effects of branch removal on water use of rain-fed jujube (*Ziziphus jujuba* Mill.) plantations in Chinese semiarid Loess Plateau region. *Agric. Water Manag.* **2016**, *178*, 258–270. [CrossRef]
12. Ortega-Vargas, E.; Burgueño-Ferreira, J.A.; Ávila-Reséndiz, C.; Campbell, W.B.; Jarillo-Rodríguez, J.; López-Ortiz, S. Morphological and physiological responses of *Guazuma ulmifolia* Lam. to different pruning dates. *Agroforest. Syst.* **2019**, *93*, 461–470. [CrossRef]
13. Alcorn, P.J.; Bauhus, J.; Thomas, D.S.; James, R.N.; Smith, R.G.B.; Nicotra, A.B. Photosynthetic response to green crown pruning in young plantation-grown *Eucalyptus pilularis* and *E. cloeziana*. *For. Ecol. Manag.* **2008**, *255*, 3827–3838. [CrossRef]
14. Ge, X.M.; Tian, Y.; Tang, L.Z. Nutrient distribution indicated whole-tree harvesting as a possible factor restricting the sustainable productivity of a poplar plantation system in China. *PLoS ONE* **2015**, *10*, e0125303. [CrossRef] [PubMed]
15. Zhao, Y.; Li, M.; Deng, J.Y.; Wang, B.T. Afforestation affects soil seed banks by altering soil properties and understory plants on the eastern Loess Plateau, China. *Ecol. Indic.* **2021**, *126*, 107670. [CrossRef]
16. Tetemke, B.A.; Birhane, E.; Rannestad, M.M.; Eid, T. Species diversity and stand structural diversity of woody plants predominantly determine aboveground carbon stock of a dry Afromontane forest in Northern Ethiopia. *For. Ecol. Manag.* **2021**, *500*, 119634. [CrossRef]
17. Danilović, M.; Sarić, R.; Cirović, V.; Pudja, V. The impact of pruning on tree development in poplar *Populus* × *canadensis* "I-214" plantations. *iForest* **2022**, *15*, 33–37. [CrossRef]
18. Brookes, P.C.; Landman, A.; Pruden, G.; Jenkinson, D.S. Chloroform fumigation and the release of soil nitrogen: A rapid direct extraction method to measure microbial biomass nitrogen in soil. *Soil Biol. Biochem.* **1985**, *17*, 837–842. [CrossRef]
19. Singh, D.K.; Kumar, S. Nitrate reductase, arginine deaminase, urease and dehydrogenase activities in natural soil (ridges with forest) and in cotton soil after acetamiprid treatments. *Chemosphere* **2008**, *71*, 412–418. [CrossRef] [PubMed]
20. Zhang, C.; Liu, G.B.; Xue, S.; Song, Z.L. Rhizosphere soil microbial activity under different vegetation types on the Loess Plateau, China. *Geoderma* **2011**, *161*, 115–125. [CrossRef]
21. Tang, L.Z.; Wu, L.; Ge, X.M.; Tian, Y.; Dun, X.J.; Liu, D.; Fang, S.Z. Comparative studies on the growth of different poplar clones on beach land of Yangtse River. *For. Res.* **2013**, *26*, 123–128. [CrossRef]
22. Shaheen, H.; Ullah, Z.; Khan, S.M.; Harper, D.M. Species composition and community structure of western Himalayan moist temperate forests in Kashmir. *For. Ecol. Manag.* **2012**, *278*, 138–145. [CrossRef]

23. Ares, A.; Brauer, D. Aboveground biomass partitioning in loblolly pine silvopastoral stands: Spatial configuration and pruning effects. *For. Ecol. Manag.* **2005**, *219*, 176–184. [CrossRef]
24. Neilsen, W.A.; Pinkard, E.A. Effects of green pruning on growth of *Pinus radiata*. *Can. J. For. Res.* **2003**, *33*, 2067–2073. [CrossRef]
25. Pinkard, E.A. Effects of pattern and severity of pruning on growth and branch development of pre-canopy closure *Eucalyptus nitens*. *For. Ecol. Manag.* **2002**, *157*, 217–230. [CrossRef]
26. Pinkard, E.A. Physiological and growth responses related to pattern and severity of green pruning in young *Eucalyptus globulus*. *For. Ecol. Manag.* **2003**, *182*, 231–245. [CrossRef]
27. Víquez, E.; Pérez, D. Effect of pruning on tree growth, yield, and wood properties of *Tectona grandis* plantations in Costa Rica. *Silva Fenn.* **2005**, *39*, 381–390. [CrossRef]
28. Zeng, B. Aboveground biomass partitioning and leaf development of Chinese subtropical trees following pruning. *For. Ecol. Manag.* **2003**, *173*, 135–144. [CrossRef]
29. Hevia, A.; Álvarez-González, J.G.; Majada, J. Comparison of pruning effects on tree growth, productivity and dominance of two major timber conifer species. *For. Ecol. Manag.* **2016**, *374*, 82–92. [CrossRef]
30. Springmann, S.; Rogers, R.; Spiecker, H. Impact of artificial pruning on growth and secondary shoot development of wild cherry (*Prunus avium* L.). *For. Ecol. Manag.* **2011**, *261*, 764–769. [CrossRef]
31. Forrester, D.I.; Collopy, J.J.; Beadle, C.L.; Warren, C.R.; Baker, T.G. Effect of thinning, pruning and nitrogen fertiliser application on transpiration, photosynthesis and water-use efficiency in a young *Eucalyptus nitens* plantation. *For. Ecol. Manag.* **2012**, *266*, 286–300. [CrossRef]
32. Forrester, D.I.; Collopy, J.J.; Beadle, C.L.; Baker, T.G. Effect of thinning, pruning and nitrogen fertiliser application on light interception and light-use efficiency in a young *Eucalyptus nitens* plantation. *For. Ecol. Manag.* **2013**, *288*, 21–30. [CrossRef]
33. Lisboa, M.; Acuña, E.; Cancino, J.; Chao, F.; Muñoz, F.; Rodríguez, R.; Volker, P. Physiological response to pruning severity in *Eucalyptus regnans* plantations. *New Forests* **2014**, *45*, 753–764. [CrossRef]
34. Beadle, C.; Barry, K.; Hardiyanto, E.; Irianto, R.; Junarto; Mohammed, C.; Rimbawanto, A. Effect of pruning *Acacia mangium* on growth, form and heart rot. *For. Ecol. Manag.* **2007**, *238*, 261–267. [CrossRef]
35. Berrill, J.P.; Dagley, C.M.; Coppeto, S.A.; Gross, S.E. Curtailing succession: Removing conifers enhances understory light and growth of young aspen in mixed stands around Lake Tahoe, California and Nevada, USA. *For. Ecol. Manag.* **2017**, *400*, 511–522. [CrossRef]
36. Schmidt, T.L.; Wardle, T.D. Impact of pruning eastern redcedar (*Juniperus virginiana*). *West. J Appl. For.* **2002**, *17*, 189–193. [CrossRef]
37. Torras, O.; Saura, S. Effects of silvicultural treatments on forest biodiversity indicators in the Mediterranean. *For. Ecol. Manag.* **2008**, *255*, 3322–3330. [CrossRef]
38. Zhao, N.X.; Xu, Y.J.; Chen, L.P.; Jiang, M.; Dong, K.; Wang, J.L.; Gao, Y.B. Species identities impact the responses of intensity and importance of competition to the soil fertility changes. *Glob. Ecol. Conserv.* **2021**, *27*, e01519. [CrossRef]
39. Ares, A.; Louis, D.S.; Brauer, D. Trends in tree growth and understory yield in silvopastoral practices with southern pines. *Agroforest. Syst.* **2003**, *59*, 27–33. [CrossRef]
40. Brockerhoff, E.G.; Ecroyd, C.E.; Leckie, A.C.; Kimberley, M.O. Diversity and succession of adventive and indigenous vascular understorey plants in *Pinus radiata* plantation forests in New Zealand. *For. Ecol. Manag.* **2003**, *185*, 307–326. [CrossRef]
41. Halpern, C.B.; Halaj, J.; Evans, S.A.; Dovčiak, M. Level and pattern of overstory retention interact to shape long-term responses of understories to timber harvest. *Ecol. Appl.* **2012**, *22*, 2049–2064. [CrossRef]
42. Roberts, M.W.; D'Amato, A.W.; Kern, C.C.; Palik, B.J. Long-term impacts of variable retention harvesting on ground-layer plant communities in *Pinus resinosa* forests. *J. Appl. Ecol.* **2016**, *53*, 1106–1116. [CrossRef]
43. Lull, C.; Bautista, I.; Lidón, A.; del Campo, A.D.; González-Sanchis, M.; García-Prats, A. Temporal effects of thinning on soil organic carbon pools, basal respiration and enzyme activities in a Mediterranean Holm oak forest. *For. Ecol. Manag.* **2020**, *464*, 118088. [CrossRef]
44. Ren, C.J.; Kang, D.; Wu, J.P.; Zhao, F.Z.; Yang, G.H.; Han, X.H.; Feng, Y.Z.; Ren, G.X. Temporal variation in soil enzyme activities after afforestation in the Loess Plateau, China. *Geoderma* **2016**, *282*, 103–111. [CrossRef]
45. Jin, S.S.; Wang, Y.K.; Wang, X.; Bai, Y.H.; Shi, L.G. Effect of pruning intensity on soil moisture and water use efficiency in jujube (*Ziziphus jujube* Mill.) plantations in the hilly Loess Plateau Region, China. *J. Arid Land.* **2019**, *11*, 446–460. [CrossRef]
46. Gallardo, A. Effect of tree canopy on the spatial distribution of soil nutrients in a Mediterranean Dehesa. *Pedobiologia* **2003**, *47*, 117–125. [CrossRef]
47. Andivia, E.; Vázquez-Piqué, J.; Fernández, M.; Alejano, R. Litter production in holm oak trees subjected to different pruning intensities in Mediterranean dehesas. *Agroforest. Syst.* **2013**, *87*, 657–666. [CrossRef]
48. Ou, Z.Y.; Pang, S.L.; He, Q.F.; Peng, Y.H.; Huang, X.R.; Shen, W.H. Effects of vegetation restoration and environmental factors on understory vascular plants in a typical karst ecosystem in southern China. *Sci. Rep.* **2020**, *10*, 12011. [CrossRef]
49. Jennings, T.N.; Smith, J.E.; Cromack, K.; Sulzman, E.W.; McKay, D.; Caldwell, B.A.; Beldin, S.I. Impact of postfire logging on soil bacterial and fungal communities and soil biogeochemistry in a mixed-conifer forest in central Oregon. *Plant Soil.* **2012**, *350*, 393–411. [CrossRef]
50. Pramanik, P.; Phukan, M.; Ghosh, S.; Goswami, A.J. Pruned tea bushes secrete more root exudates to influence microbiological properties in soil. *Arch. Agron. Soil Sci.* **2018**, *64*, 1172–1180. [CrossRef]

51. Yang, Y.; Zhang, X.Y.; Zhang, C.; Wang, H.M.; Fu, X.L.; Chen, F.S.; Wan, S.Z.; Sun, X.M.; Wen, X.F.; Wang, J.F. Understory vegetation plays the key role in sustaining soil microbial biomass and extracellular enzyme activities. *Biogeosciences* **2018**, *15*, 4481–4494. [CrossRef]
52. Chen, X.L.; Wang, D.; Chen, X.; Wang, J.; Diao, J.J.; Zhang, J.Y.; Guan, Q.W. Soil microbial functional diversity and biomass as affected by different thinning intensities in a Chinese fir plantation. *Appl. Soil Ecol.* **2015**, *92*, 35–44. [CrossRef]
53. Deng, J.; Chong, Y.J.; Zhang, D.; Ren, C.J.; Zhao, F.Z.; Zhang, X.X.; Han, X.H.; Yang, G.H. Temporal variations in soil enzyme activities and responses to land use change in the Loess Plateau, China. *Appl. Sci.* **2019**, *9*, 3129. [CrossRef]
54. Li, X.F.; Zhang, Y.; Ding, C.X.; Liu, Y.; Wu, K.X.; Jiang, F.Z.; Su, D.R. Water addition promotes vegetation recovery of degraded alpine meadows by regulating soil enzyme activity and nutrients in the Qinghai–Tibetan Plateau. *Ecol. Eng.* **2020**, *158*, 106047. [CrossRef]
55. Li, J.; Zhao, B.Q.; Li, X.Y.; Jiang, R.B.; So, H.B. Effects of long-term combined application of organic and mineral fertilizers on microbial biomass, soil enzyme activities and soil fertility. *Agric. Sci. China* **2008**, *7*, 336–343. [CrossRef]
56. Rivaie, A.A. The effects of understory vegetation on P availability in *Pinus radiata* forest stands: A review. *J. For. Res.* **2014**, *25*, 489–500. [CrossRef]
57. Su, X.P.; Wang, M.H.; Huang, Z.Q.; Fu, S.L.; Chen, H.Y.H. Forest understorey vegetation: Colonization and the availability and heterogeneity of resources. *Forests* **2019**, *10*, 944. [CrossRef]
58. Yu, J.T.; Zhang, X.N.; Xu, C.Y.; Hao, M.H.; Choe, C.; He, H.J. Thinning can increase shrub diversity and decrease herb diversity by regulating light and soil environments. *Front. Plant Sci.* **2022**, *13*, 948648. [CrossRef] [PubMed]
59. Pohl, M.; Alig, D.; Körner, C.; Rixen, C. Higher plant diversity enhances soil stability in disturbed alpine ecosystems. *Plant Soil.* **2009**, *324*, 91–102. [CrossRef]
60. Siefert, A.; Ravenscroft, C.; Althoff, D.; Alvarez-Yépiz, J.C.; Carter, B.E.; Glennon, K.L.; Heberling, J.M.; Jo, I.S.; Pontes, A.; Sauer, A.; et al. Scale dependence of vegetation–environment relationships: A meta-analysis of multivariate data. *J. Veg. Sci.* **2012**, *23*, 942–951. [CrossRef]
61. Zhang, K.; Huang, K.D.; Zhao, X.J.; She, J.W.; Zheng, X.; Tang, L.Z. Effects of pruning on microclimate and understory vegetation in a poplar plantation. *Ecol. Environ. Sci.* **2019**, *28*, 1548–1556. [CrossRef]
62. Choe, C.H.; Kim, J.H.; Xu, C.Y.; Choe, J.S.; Man, H.S.; Jo, S.M. Effect of soil nutrient spatial heterogeneity by cutting disturbance on understory plant diversity in broadleaved-Korean pine forest in Changbai Mountain, China. *Eur. J. For. Res.* **2021**, *140*, 603–613. [CrossRef]
63. Chytrý, M.; Tichý, L.; Roleček, J. Local and regional patterns of species richness in Central European vegetation types along the pH/calcium gradient. *Folia Geobot.* **2003**, *38*, 429–442. [CrossRef]
64. Weiher, E.; Forbes, S.; Schauwecker, T.; Grace, J.B. Multivariate control of plant species richness and community biomass in blackland prairie. *Oikos* **2004**, *106*, 151–157. [CrossRef]

Disclaimer/Publisher's Note: The statements, opinions and data contained in all publications are solely those of the individual author(s) and contributor(s) and not of MDPI and/or the editor(s). MDPI and/or the editor(s) disclaim responsibility for any injury to people or property resulting from any ideas, methods, instructions or products referred to in the content.

forests

MDPI

Article

Plastome Phylogeny and Taxonomy of *Cinnamomum guizhouense* (Lauraceae)

Zhi Yang [1,2], David Kay Ferguson [3] and Yong Yang [1,2,*]

[1] Co-Innovation Center for Sustainable Forestry in Southern China, Nanjing Forestry University, 159 Longpan Rd., Nanjing 210037, China
[2] College of Biology and the Environment, Nanjing Forestry University, Nanjing 210037, China
[3] Department of Paleontology, University of Vienna, 1090 Vienna, Austria
* Correspondence: yangyong@njfu.edu.cn

Abstract: Taxonomy of the genus *Cinnamomum* Schaeff. (Lauraceae) is difficult because of parallel evolution of morphology. Recent phylogenomic and taxonomic studies have clarified the problem and subdivided the Asian *Cinnamomum* into two genera, i.e., *Camphora* Fabr. and *Cinnamomum* sensu stricto. Here we sequenced and characterized the plastome of a recently described species *Cinnamomum guizhouense* C.Y. Deng, Zhi Yang et Y. Yang, performed a phylogenomic analysis, and also conducted a comparative analysis. The plastome of *Cinnamomum guizhouense* is 152,739 bp long and quadri-parted with a pair of inverted repeat regions (IR: 20,132 bp) divided by a small single copy region (SSC: 18,852 bp) and a large single copy region (LSC: 93,623 bp). The plastome possesses a total of 128 genes including 82 protein-coding genes, 36 tRNA genes, and eight rRNA genes, which is similar to most published plastomes of the core Lauraceae group. The plastome of *Cinnamomum guizhouense* displays higher similarity to *Camphora* than *Cinnamomum*. Our phylogenomic result suggests that *Cinnamomum guizhouense* belongs to the *Camphora* clade. As a result, we propose a new combination, i.e. *Camphora guizhouensis* (C.Y. Deng, Zhi Yang et Y. Yang) Zhi Yang et Y.Yang, comb. nov.

Keywords: *Cinnamomum guizhouense*; Lauraceae; phylogenomics; plastome; taxonomy

check for updates

Citation: Yang, Z.; Ferguson, D.K.; Yang, Y. Plastome Phylogeny and Taxonomy of *Cinnamomum guizhouense* (Lauraceae). *Forests* **2023**, *14*, 310. https://doi.org/10.3390/f14020310

Academic Editor: Tadeusz Malewski

Received: 9 November 2022
Revised: 24 January 2023
Accepted: 1 February 2023
Published: 4 February 2023

Copyright: © 2023 by the authors. Licensee MDPI, Basel, Switzerland. This article is an open access article distributed under the terms and conditions of the Creative Commons Attribution (CC BY) license (https://creativecommons.org/licenses/by/4.0/).

1. Introduction

The family Lauraceae, a mostly woody family of primitive angiosperms, contains over 3000 species and has a wide distribution range in the tropics with Tropical America and Tropical Asia as the diversity centers [1]. Taxonomy of the family has been notorious for its difficulty because of paucity of characters and parallel evolution of morphology [2–4]. Recent plastome phylogeny has provided high resolution for nine major clades in the family including Hypodaphnideae, Cryptocaryeae, Cassytheae, Neocinnamomeae, Caryodaphnopsideae, the *Mesilaurus* clade, Perseae, Cinnamomeae, and Laureae [5,6]. However, many generic complexes exist within these clades, e.g. the *Beilschmiedia* group in the Cryptocaryeae [7], the *Alseodaphne* group in the Perseae [8–10], the *Cinnamomum* group in the Cinnamomeae [4,11], and the *Litsea* group and the *Ocotea* group in the Laureae [12–15], how to identify the generic clades and classify them in combination with morphological characters remain problematic. Recent taxonomic studies have proposed new classifications of some of the above-mentioned generic complexes based on phylogenetic studies [4,9,11,14,15]. Taxonomic problems remain due to inadequate species sampling. One way to resolve these taxonomic problems is to include species in new phylogenetic trees and re-consider their taxonomy within a phylogenetic context.

Cinnamomum Schaeff. belongs to the *Cinnamomum-Ocotea* clade or the tribe Cinnamomeae [5,6]. Plants of the genus are economically important and have been used for a long time because of their timber, cinnamon and camphor [16]. However, the taxonomy of the genus has been ambiguous for a long time.

Traditional classification based on morphology treated the genus *Cinnamomum* in its broad sense. Meissner [17] restricted the genus *Cinnamomum* to tropical and subtropical Asia, and subdivided the genus into two sections, i.e., sect. *Malabathrum* (≡sect. *Cinnamomum*) possessing non-perulate buds, opposite and tripliveined leaves lacking domatia in the axils of lateral veins, and sect. *Camphora* Meisn. having perulate buds, alternate and pinnately-veined leaves, and domatia in the axils of lateral veins. Kostermans [16] included American species formerly treated as *Phoebe* Nees in the genus *Cinnamomum* s.l.; but he accepted Meissner's idea and classified the genus into two sections. Rohwer [1] and van der Werff [18] followed the treatment of Kostermans; Rohwer [1] estimated that the genus had up to 350 species including 60 American species.

Molecular phylogenetic studies revealed that the genus *Cinnamomum* s.l. is polyphyletic and should be reclassified. Based on nrITS and a few plastid markers, Chanderbali et al. [19] conducted a phylogeny of the Lauraceae and suggested that the genus *Cinnamomum* is polyphyletic though they sampled only eight species. This result was confirmed and corroborated by Huang et al. [20] with a better species sampling strategy. Rhode et al. [11] excluded the American species from *Cinnamomum* and transferred them to *Aiouea* Aubl.. Zeng et al. [21] found that the upper leaf epidermal cells of *Cinnamomum* include two types: leaf epidermal cells regular and periclinal walls non-reticulate (sect. *Camphora*), leaf epidermal cells irregular and periclinal walls reticulate (sect. *Cinnamomum*) with a few exceptions in the clade of sect. *Cinnamomum*. Using a combination of morphology, anatomy and molecular phylogeny, Yang et al. [22] finally separated the Asian *Cinnamomum* into two genera, i.e. *Camphora* Fabr. and *Cinnamomum* s.s.

Cinnamomum guizhouense C.Y. Deng, Zhi Yang et Y. Yang is a recently described endangered species only represented by two mature trees in Guizhou, southwestern China [22], established before the taxonomic treatment of *Cinnamomum* [4]. The species possesses pinnately veined and alternate leaves and perulate buds [22]. Considering parallel evolution of morphological characters [4,22], it remains unclear whether *Cinnamomum guizhouense* belongs to the genus *Cinnamomum* or not. Molecular phylogeny is an effective approach to determine the systematic position of species [23], and plastomes have been widely used to solve the phylogenetic and taxonomic problems of Lauraceae [10,13,24,25]. Here, we sequenced the plastome of *Cinnamomum guizhouense*, conducted a phylogenomic study, and made a taxonomic treatment of the species in combination with morphology and phylogeny.

2. Materials and Methods

2.1. Plant Materials and Plastome Sequencing

Chloroplast genomes of two samples (C.Y. Deng et Q.M. Ban 2021001 and 2021002) were newly sequenced from silica-gel dried leaf materials (Table 1); one of the samples C.Y. Deng et Q.M. Ban 2021001 belongs to the type collection of *Cinnamomum guizhouense*. To determine the systematic position of *Cinnamomum guizhouense*, plastomes of Cinnamomeae and Laureae were chosen as ingroups, four plastomes of Perseeae were selected as the outgroup. Totally, 31 plastomes were downloaded from NCBI (https://www.ncbi.nlm.nih.gov/, accessed on 9 October 2022) with details listed in Table 2.

Total genomic DNA was extracted from the leaf using a DNA extraction kit (D115-100, Gene Better, Beijing, China). Whole genome sequencing was conducted by Illumina Novo Seq6000 (Novogene, Beijing, China). A total of ~2 Gb of 150 bp paired-end reads were obtained from each sample.

Table 1. Vouchers of species used in this study.

Taxon	Collection	Locality	Latitude	Longitude	Collection Date	Herbarium
Cinnamomum guizhouense C.Y. Deng et al.	C.Y. Deng and Q.M. Ban 2021001	Guizhou: Wangmo	25°21′8″	106°17′44″	20210220	NF
Cinnamomum guizhouense C.Y. Deng et al.	C.Y. Deng and Q.M. Ban 2021002	Guizhou: Wangmo	25°21′8″	106°17′44″	20210220	NF

Table 2. Sequences obtained from GenBank.

Taxon	Accession
Cinnamomeae	
Camphora bodinieri (H. Lév.) Y. Yang et al.	MH394418
Camphora glandulifera (Wall.) Nees	OL943973
Camphora officinarum Nees	MF421523
Camphora parthenoxylon (Jack) Nees	MT621587
Cinnamomum aromaticum Nees	NC_046019
Cinnamomum burmanni (Nees et T.Nees) Blume	MT621613
Cinnamomum guizhouense C.Y. Deng et al. S2021001	OP818854
Cinnamomum guizhouense C.Y. Deng et al. S2021002	OP818855
Cinnamomum chekiangense Nakai	MT621639
Cinnamomum pittosporoides Hand.-Mazz.	NC_048978
Cinnamomum verum J. Presl	NC_046019
Ocotea aciphylla (Nees et Mart.) Mez	OM135246
Ocotea daphnifolia (Meisn.) Mez	OM135247
Ocotea foetens (Aiton) Baill.	OM135248
Sassafras tzumu (Hemsl.) Hemsl.	NC_045268
Laureae	
Actinodaphne obovata (Nees) Blume	NC_50360
Actinodaphne trichocarpa C.K. Allen	MF939342
Laurus azorica (Seub.) Franco	MK041220
Lindera aggregata (Sims) Kosterm.	NC_045252
Lindera communis Hemsl.	NC_045255
Lindera glauca (Siebold et Zucc.) Blume	NC_035953
Lindera robusta (C.K. Allen) H.B. Cui	MH220738
Litsea coreana H. Lév.	NC_045251
Litsea elongata (Nees) Hook. f.	NC_050364
Litsea pungens Hemsl.	NC_050368
Nectandra angustifolia (Schrad.) Nees et Mart.	MF939340
Neolitsea pallens (D. Don) Momiy. et H. Hara	NC_050370
Neolitsea sericea (Blume) Koidz.	MF939341
Parasassafras confertiflorum (Meisn.) D.G. Long	NC_042696
outgroup	
Alseodaphne semecarpifolia Nees	NC_37491
Machilus thunbergii Siebold et Zucc.	NC_038204
Persea americana Mill.	NC_031198
Phoebe sheareri (Hemsl.) Gamble	NC_031191

2.2. Plastome Assembly and Annotation

Circle plastomes were assembled with GetOrganelle (Version 1.7.5.0, Kunming, China) [26] using de novo strategy. Annotation was conducted with GeSeq (https://chlorobox.mpimp-golm.mpg.de/geseq.html, accessed on 29 October 2022, Munich, Germany) [27], then adjusted manually in Geneious Prime (Version 2020.0.5, Auckland, New Zealand). All sequences downloaded from NCBI were re-annotated to avoid potential annotation errors, and ambiguous genes were double-checked by CpGAVAS2 (http://47.96.249.172:16019/analyzer/home, accessed on 29 October 2022, Beijing, China) [28]. The gene map of the plastome was generated by CHLOROPLOT software (https://irscope.shinyapps.io/Chloroplot/, accessed on 30 October 2022, Helsinki, Finland) [29].

2.3. Repeats Analysis

We conducted repeat sequence analyses of the two plastomes with CpGAVAS2. Long repeats (including direct and palindromic repeats) were detected by Vmatch (Version 2.2.1, http://www.vmatch.de/, accessed on 29 October 2022, Hamburg, Germany). Totally, hamming distance of three and repeats no less than 30 bp were searched. Long tandem repeats (LTR, size of repeat unit $\geq$ 7) were identified with the Tandem Repeats Finder (TRF, Version 3.01, https://tandem.bu.edu/trf/trf.html, accessed on 29 October 2022, Boston, MA, USA) [30]. The weights for match, mismatch, indels were set at 2, 7and 7, respectively. The detection parameters of match and indel was set at 80 and 10, respectively. The minimum alignment score was set at 50. The maximum period size was limited to 500 bp. We identified simple sequence repeats (SSRs) with MIcroSAtellite identification (MISA, Version 2.1, https://webblast.ipk-gatersleben.de/misa/, accessed on 29 October 2022, Seeland, Germany) [31] with a set of minimum repeat times of mononucleotides, dinucleotides, trinucleotides, tetranucleotides, pentanucleotides and hexanucleotides set at 10, 6, 5, 5, 5, and 5, respectively.

2.4. Phylogenetic Analysis

Complete chloroplast sequences were used to infer the phylogenetic position of *Cinnamomum guizhouense*. Sequences were aligned with MAFFT (Version 7.480, Tokyo, Japan) [32], followed by a manual check using BioEdit (Version 7.5.5, Wooster, OH, USA) [33]. Gap sites of sequences were removed with Gblocks (Version 0.91b, Barcelona, Spain) [34].

For phylogeny, both Maximum likelihood (ML) and Bayesian inference (BI) were conducted. ModelFinder [35] was used to determine the best-fit model according to the best Bayesian Information Criterion (BIC) score. ML phylogeny was inferred by IQ-TREE (Version 2.1.2, Vienna, Austria) [36] with 5,000 ultrafast bootstraps [37] under K3Pu+F+I+G4 model. BI phylogeny was conducted using MrBayes (Version 3.2.6, Stockholm, Sweden) [38] with the following designations: GTR+F+I+G4 model, number of generations 1,000,000, sampling frequency 1,000; the initial 25% of sampled data were discarded as burn-in. Phylogenetic trees were browsed and adjusted with iTOL (Version 6.6, https://itol.embl.de/, accessed on 30 October 2022, Heidelberg, Germany) [39].

2.5. Comparative Genome Analysis

The pairwise sequence similarity between *Cinnamomum guizhouense* and query sequences of *Cinnamomum* (*Cinnamomum aromaticum*, *Cinnamomum burmanni*, *Cinnamomum chekiangense*, *Cinnamomum pittosporoides* and *Cinnamomum verum*) and *Camphora* (*Camphora bodinieri*, *Camphora glandulifera*, *Camphora parthenoxylon* and *Camphora officinarum*) were computed in R using the "simplot" function of "ggmsa" package [40]. The sequence differences between *Cinnamomum guizhouense* and sampled species of *Camphora* were detected using "seqdiff" function. The sliding window and step size were set at 200 bp and 20 bp, respectively. The similarity and sequence difference plots were illustrated by the "ggplot2" package [41]. IR expansion and contraction plot of plastomes were drawn manually in Adobe Illustrator (Version 2020, San Jose, California, CA, USA).

3. Results

3.1. General Characters of the Plastome

4,247,464 and 4,439,324 pair-end reads were used for de novo assembly of the two plastomes of *Cinnamomum guizhouense* and the mean sequencing coverage of them was 320× and 142×, respectively. The two plastomes of *Cinnamomum guizhouense* were largely congruent, showing no differences in length, gene organization, structure and repeats, and possessing eight variable nucleotide sites. The plastome of *Cinnamomum guizhouense* consists of a total of 128 genes including 82 protein-coding genes, 36 tRNA genes, and eight rRNA genes (Figure 1). The plastome was 152,739 bp in length and consisted of a pair of inverted repeat regions (IR: 20,132 bp), which were divided by a small single copy region (SSC: 18,852 bp) and a large single copy region (LSC: 93,623 bp). The guanine-cytosine

(G-C) content was differentiated in the complete plastome, LSC, SSC, and IRs, which were 39.1%, 37.9%, 33.8% and 44.4%, respectively.

Direct, palindromic and tandem repeats with lengths ranging from 9 bp to 72 bp were detected in the plastome (Figure 2a). Totally, 74 repeats were found, which included 25 direct repeats, 23 palindromic repeats and 26 tandem repeats. Tandem repeats were shorter than other two repeats with lengths almost less than 30 bp. The longest repeat with a length of 72 bp belonged to a direct repeat and was distributed in LSC.

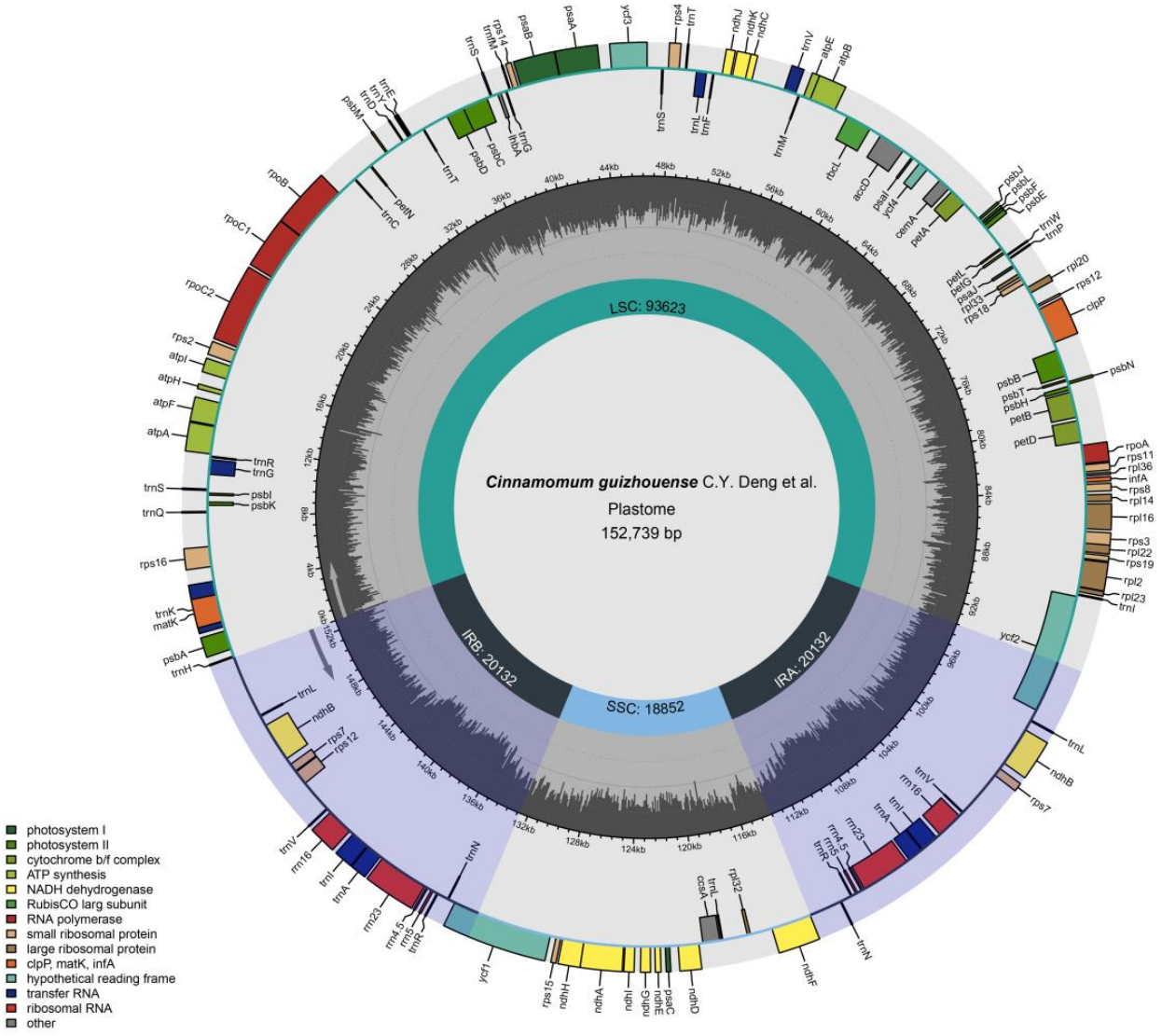


Figure 1. Gene map of *Cinnamomum guizhouense* C.Y. Deng et al.

A total of 73 SSRs was detected in the plastome, 78.1% of which were found in LSC (Figure 2b). Among SSRs, only mononucleotide and dinucleotide units were found. The mononucleotide repeat was the most common SSR representing 93.2%, all of which belonged to A or T monomers. Two AG/CT repeats were found in LSC, while two of three AT/AT were found in LSC and one in SSC, separately.

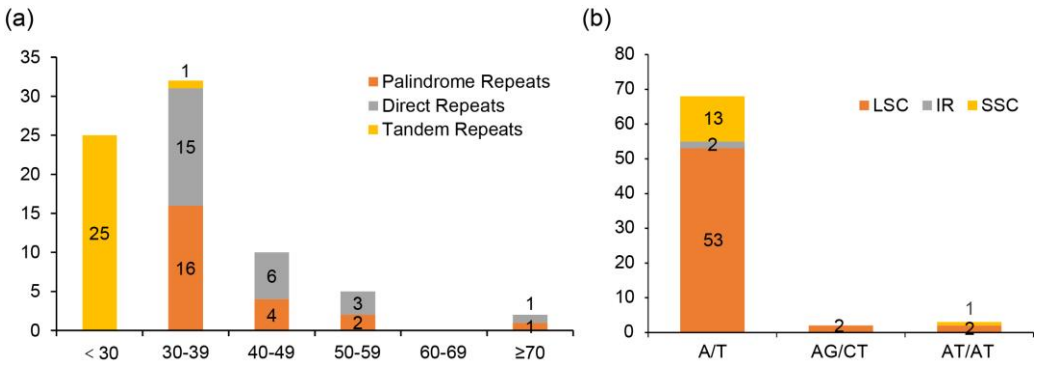


Figure 2. Repeats analysis of the plastome of *Cinnamomum guizhouense* C.Y. Deng et al. (**a**) Number and length of repeats; (**b**) Number and distribution of SSRs.

3.2. Phylogenetic Position of Cinnamomum guizhouense

The topologies using ML and BI methods based on plastomes were congruent and highly supported (Figure 3a). *Camphora* was sister to *Sassafras* (ML: 100%, BI: 1.00). The genus *Cinnamomum* s.s. was sister to a clade including *Camphora* and *Sassafras* (ML: 100%, BI: 1.00). Two samples of *Cinnamomum guizhouense* belonged to the *Camphora* clade. *Cinnamomum guizhouense* was sister to *Camphora bodinieri* (ML: 71%, BI: 1.00), they formed a small clade sister to *Camphora officinarum* (ML: 63%, BI: 0.99). *Camphora glandulifera* is sister to *Camphora parthenoxylon*, they together formed a small clade (ML: 100%, BI: 1.00) which was sister to the small clade including other sampled *Camphora* species (ML: 100%, BI: 1.00).

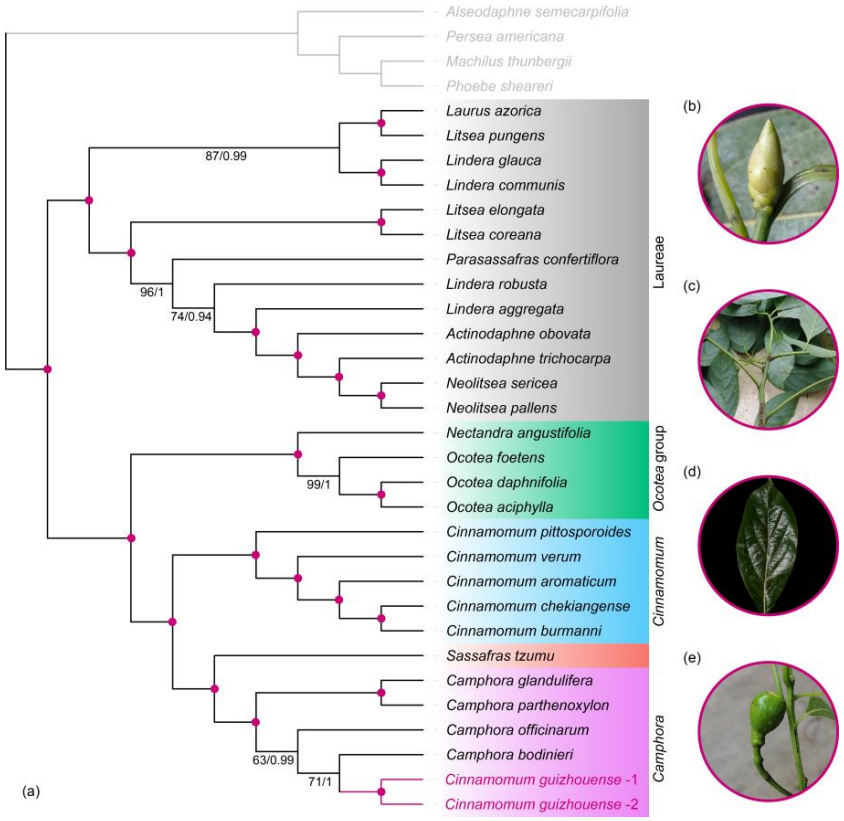


Figure 3. Phylogenetic tree displaying the phylogenetic position of *Cinnamomum guizhouense* C.Y. Deng et al. (**a**) Phylogenetic tree inferred from Bayesian inference and maximum likelihood analysis based on complete plastomes. Ultrafast bootstrap support values (<100%) and Bayesian posterior probabilities (<1) are shown below the branches; (**b**–**e**) Morphology of *Cinnamomum guizhouense*; (**b**) Large perulate terminal buds; (**c**) Alternate leaves; (**d**) Pinnately-veined leaf; (**e**) Deep fruit cupule.

3.3. Comparative Analysis of the Plastomes

Plastome differences between *Cinnamomum guizhouense* and the four species of *Camphora* and the five species of *Cinnamomum* included in this study were displayed in Figure 4. Generally, the plastome of *Cinnamomum guizhouense* showed a higher similarity to those of *Camphora* than to those of *Cinnamomum*. Hotspot regions were discovered near IR boundaries. IRs were more conserved than LSC and SSC, and non-coding regions were more variable than coding regions. In a comparison between *Cinnamomum guizhouense* and sampled species of *Cinnamomum*, nine highly variable regions with a similarity lower than 90% were detected (Figure 4a), included seven non-coding regions (*rps16_trnQ-UUG*, *psbM_trnD-GUC*, *trnF-GAA_ndhJ*, *atpB_rbcL*, *petA_psbJ*, *trnN-GUU_ndhF*, *ndhF_rpl32*) and two coding genes (*ndhF* and *ycf1*). Only five highly variable regions with a similarity lower than 90% were identified between *Cinnamomum guizhouense* and sampled species of *Camphora* (Figures 4b and S1), included *trnN-GUU_ndhF*, *ycf1* and *ycf2* × 3. At the locus *ycf2* in the IR regions, *Cinnamomum guizhouense* showed no difference from *Camphora* species excepting *Camphora bodinieri* (Figure S1).

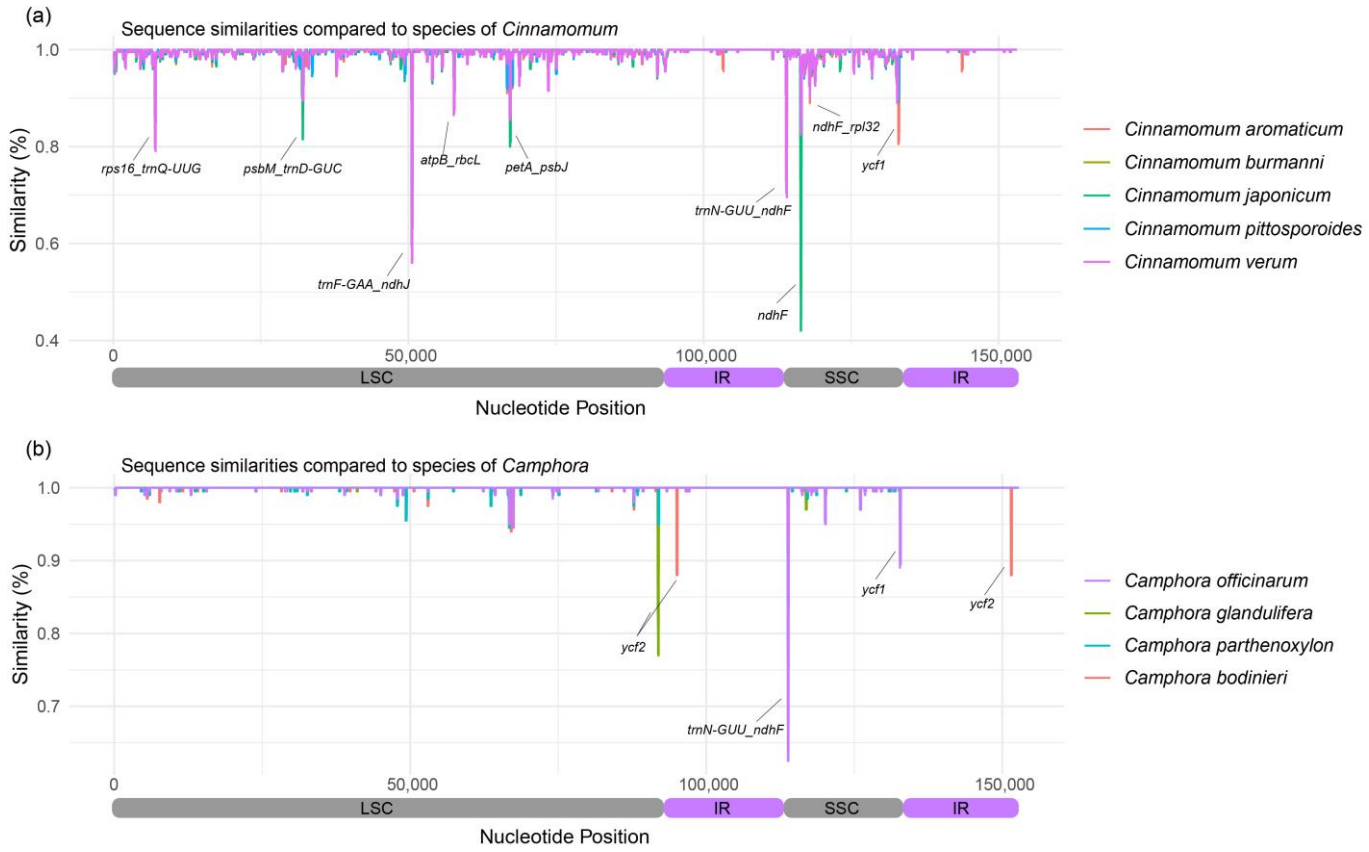


Figure 4. Similarity analysis of the plastome of *Cinnamomum guizhouense* C.Y. Deng et al. (**a**) The similarity plot of the plastome of *Cinnamomum guizhouense* in comparison with the sampled species of *Cinnamomum* Schaeff. (**b**) The similarity plot of the plastome of *Cinnamomum guizhouense* in comparison with the sampled species of *Camphora* Fabr. Regions with similarity lower than 90% are indicated.

The plastome of *Cinnamomum guizhouense* showed no obvious contraction and expansion of IRs in comparison with the four sampled plastomes of *Camphora*, only one nucleotide less between *ycf2* and *trnL-CAA* (Figure 5). *Camphora officinarum* was distinct from other sampled *Camphora* species in missing 21 nucleotides between *ycf1* and *ndhF* and gaining eight nucleotides between *ycf2* and *trnH-GUG*.

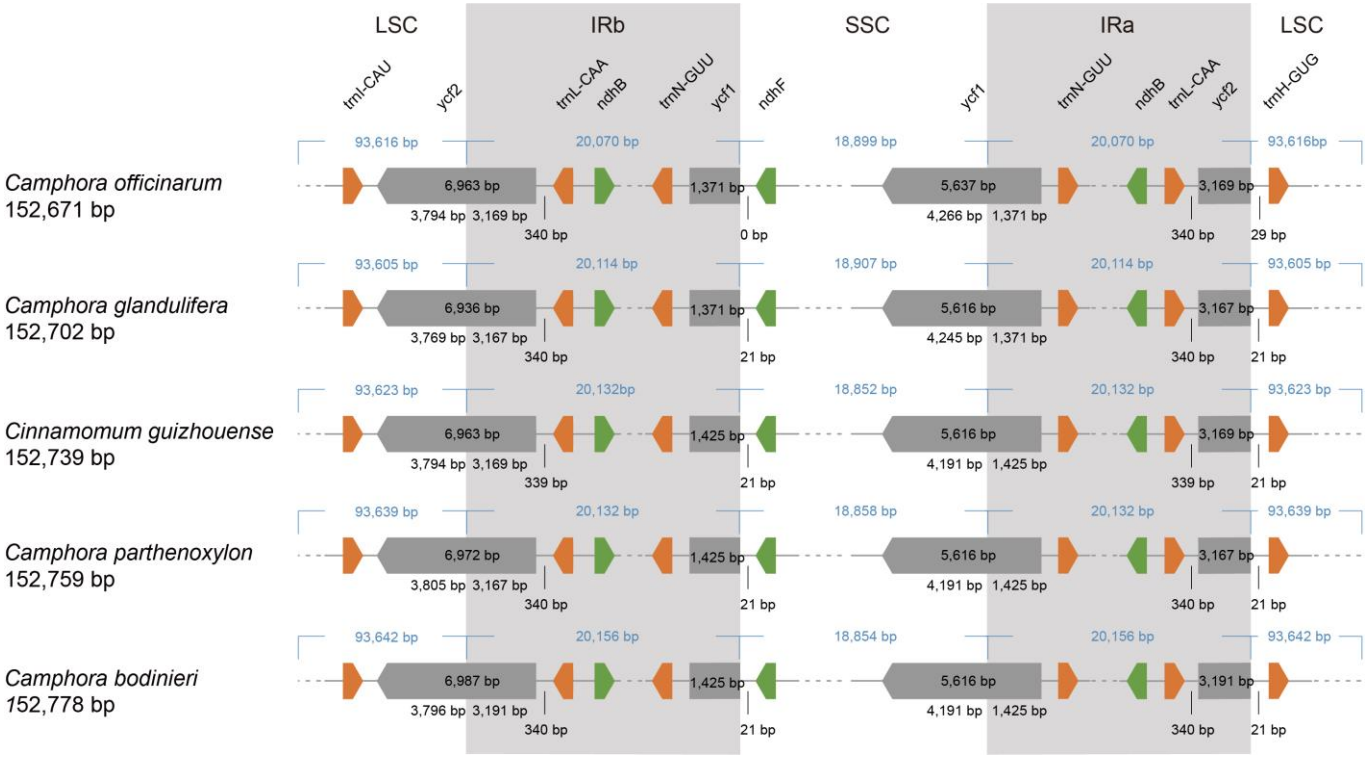


Figure 5. Contraction and expansion of IRs in the plastome of *Cinnamomum guizhouense* C.Y. Deng et al. compared with four plastomes of *Camphora* Fabr.. Genes and their relative positions were not drawn to scale.

4. Discussion

4.1. Phylogenomics and Its Systematic Significance

Yang et al. [4] divided the Asian *Cinnamomum* into two genera, i.e. *Camphora* and *Cinnamomum* according to multi-disciplinary evidence including morphology, anatomy and molecular phylogeny. *Camphora* and *Cinnamomum* were monophyletic in both nuclear and plastome phylogenies. The genus *Cinnamomum* possesses irregular cell shape, sinuous anticlinal walls, and reticulate periclinal walls of upper leaf epidermis, inconspicuous, non-perulate, terminal buds and usually tripliveined leaves; there are exceptions in this clade, *Cinnamomum chago* B.S. Sun & H.L. Zhao, *Cinnamomum saxatile* H.W. Li and *Cinnamomum longipetiolatum* H.W. Li have pinnately-veined leaves. The genus *Camphora* possesses regular cell shape, straight anticlinal walls, and non-reticulate periclinal walls of upper leaf epidermis, prominent perulate terminal buds and pinnately-veined leaves [22].

In this study, both ML and BI trees based on plastomes show congruent topologies with previous studies that *Cinnamomum* is sister to a clade consisting of *Camphora* and *Sassafras* (Figure 3a) [5,10,22]. The two samples of *Cinnamomum guizhouense* constitute a monophyletic group which falls within the *Camphora* clade with robust support and shows a close relationship to *Camphora bodinieri* (Figure 3a). This result is also corroborated by the macromorphology of the species. *Cinnamomum guizhouense* possesses large perulate buds, pinnately-veined and alternate leaves and is similar to *Camphora* but markedly different from *Cinnamomum* (Figure 1b–e) [22]. Considering both morphology and molecular phylogeny, we transfer *Cinnamommum guizhouense* to *Camphora*.

4.2. Plastome Evolution

Plastome organization of *Cinnamomum guizhouense* shows similarity to the sampled plastomes of the core Lauraceae group in lacking re-arrangement, gain and loss of genes (Figure 2). *Cinnamomum guizhouense* shows higher plastome sequence similarity to *Camphora* than to *Cinnamomum* (Figure 4), which supports the taxonomic transfer of *Cinnamomum*

guizhouense to *Camphora*. The five sampled plastomes of *Camphora* showed rather low variability and contained only 31 parsimony-informative characters among the entire plastomes. The low divergence among the *Camphora* plastomes may have been caused by recent diversification of the genus as suggested in the study of Xiao and Ge [10]. Further studies with extensive species sampling of the genus are necessary to verify this hypothesis.

4.3. Taxonomic Treatment

Camphora guizhouensis (C.Y. Deng, Zhi Yang et Y. Yang) Zhi Yang et Y. Yang, comb. nov.

Basionym. *Cinnamomum guizhouense* C.Y. Deng, Zhi Yang et Y. Yang, PhytoKeys 202: 37, figs. 1-3 (2022).

Holotype: CHINA. Guizhou, Wangmo Co., 25°21′8"N, 106°17′44"E, elev. 1081 m, 20 Feb 2021, C.Y. Deng & Q.M. Ban 2021001 (holotype: NF; isotypes: NF, NAS, XIN).

5. Conclusions

Here we sequenced and characterized the plastome of a recently reported species of Lauraceae: *Cinnamomum guizhouense*. The plastome is similar to the plastomes of the core Lauraceae group in gene number and organization, four-parted with a total of 128 genes including 82 protein-coding genes, 36 tRNA genes, and eight rRNA genes. Our phylogenomic result suggests that *Cinnamomum guizhouense* belongs to the *Camphora* clade, as the plastome of the species has a greater similarity to *Camphora* than *Cinnamomum*. A new combination is proposed: *Camphora guizhouense* (C.Y. Deng, Zhi Yang et Y. Yang) Zhi Yang et Y. Yang, comb. nov.

Supplementary Materials: The following supporting information can be downloaded at: https://www.mdpi.com/article/10.3390/f14020310/s1, Figure S1: The sequence differences of the plastome of *Cinnamomum guizhouense* C.Y. Deng et al. compared with four plastomes of *Camphora* Fabr., e.g. (**a**) *Camphora officinarum*, (**b**) *Camphora glandulifera*, (**c**) *Camphora parthenoxylon*, (**d**) *Camphora bodinieri*. The top panels are bar charts showing the number of variants over the whole sequence. The bottom panel shows the gene organization of *Cinnamomum guizhouense*.

Author Contributions: Conceptualization, Y.Y.; methodology, Z.Y.; software, Z.Y.; formal analysis, Z.Y.; data curation, Z.Y.; writing—original draft preparation, Y.Y. and Z.Y.; writing—review and editing, Y.Y., Z.Y. and D.K.F.; visualization, Z.Y.; funding acquisition, Y.Y. All authors have read and agreed to the published version of the manuscript.

Funding: This work was supported by the National Natural Science Foundation, China (31970205) and the *Metasequoia* funding of the Nanjing Forestry University.

Data Availability Statement: Not applicable.

Acknowledgments: We thank C. Y. Deng for his kind help with the photos.

Conflicts of Interest: The authors declare no conflict of interest.

References

1. Rohwer, J.G. Lauraceae. In *Flowering Plants: Dicotyledons Magnoliid, Hamamelid and Caryophyllid Families*; Kubitzki, K., Rohwer, J.G., Bittrich, V., Eds.; Springer: Berlin, Germany, 1993; Volume 2, pp. 366–390.
2. van der Werff, H. An annotated key to the genera of Lauraceae in the Flora Malesiana region. *Blumea* **2001**, *46*, 125–140.
3. Nishida, S.; van der Werff, H. Are cuticular characters useful in solving generic relationships of problematic species of Lauraceae? *Taxon* **2007**, *56*, 1229–1237. [CrossRef]
4. Yang, Z.; Liu, B.; Yang, Y.; Ferguson, D.K. Phylogeny and taxonomy of Cinnamomum (Lauraceae). *Ecol. Evol.* **2022**, *12*, e9378. [CrossRef] [PubMed]
5. Song, Y.; Yu, W.B.; Tan, Y.H.; Jin, J.J.; Wang, B.; Yang, J.B.; Liu, B.; Corlett, R.T. Plastid phylogenomics improve phylogenetic resolution in the Lauraceae. *J. Syst. Evol.* **2020**, *58*, 423–439. [CrossRef]
6. Liu, Z.F.; Ma, H.; Ci, X.Q.; Li, L.; Song, Y.; Liu, B.; Li, H.W.; Wang, S.L.; Qu, X.J.; Hu, J.L.; et al. Can plastid genome sequencing be used for species identification in Lauraceae? *Bot. J. Linn. Soc.* **2021**, *197*, 1–14. [CrossRef]
7. Rohwer, J.G.; de Moraes, P.L.R.; Rudolph, B.; van der Werff, H. A phylogenetic analysis of the *Cryptocarya* group (Lauraceae), and relationships of *Dahlgrenodendron*, *Sinopora*, *Triadodaphne*, and *Yasunia*. *Phytotaxa* **2014**, *158*, 111–132. [CrossRef]

8. Rohwer, J.G.; Li, J.; Rudolph, B.; Schmidt, A.S.; van der Werff, H.; Li, H. Is *Persea* (Lauraceae) monophyletic? Evidence from nuclear ribosomal ITS sequences. *Taxon* **2009**, *58*, 1153–1167. [CrossRef]
9. Mo, Y.Q.; Li, L.; Li, J.W.; Rohwer, J.G.; Li, H.W.; Li, J. *Alseodaphnopsis*: A new genus of Lauraceae based on molecular and morphological evidence. *PLoS ONE* **2017**, *12*, e0186545. [CrossRef]
10. Xiao, T.W.; Ge, X.J. Plastome structure, phylogenomics, and divergence times of tribe Cinnamomeae (Lauraceae). *BMC Genom.* **2022**, *23*, 642. [CrossRef]
11. Rohde, R.; Rudolph, B.; Ruthe, K.; Lorea-Hernandez, F.G.; de Moraes, P.L.R.; Rohwer, J.G. Neither *Phoebe* nor *Cinnamomum* the tetrasporangiate species of *Aiouea* (Lauraceae). *Taxon* **2017**, *66*, 1085–1111. [CrossRef]
12. Xiao, T.W.; Xu, Y.; Jin, L.; Liu, T.J.; Yan, H.F.; Ge, X.J. Conflicting phylogenetic signals in plastomes of the tribe Laureae (Lauraceae). *PeerJ* **2020**, *8*, e10155. [CrossRef] [PubMed]
13. Trofimov, D.; Cadar, D.; Schmidt-Chanasit, J.; Rodrigues de Moraes, P.L.; Rohwer, J.G. A comparative analysis of complete chloroplast genomes of seven *Ocotea* species (Lauraceae) confirms low sequence divergence within the *Ocotea* complex. *Sci. Rep.* **2022**, *12*, 1120. [CrossRef] [PubMed]
14. Trofimov, D.; de Moraes, P.L.R.; Rohwer, J.G. Towards a phylogenetic classification of the *Ocotea* complex (Lauraceae): Classification principles and reinstatement of *Mespilodaphne*. *Bot. J. Linn. Soc.* **2019**, *190*, 25–50. [CrossRef]
15. Trofimov, D.; Rohwer, J.G. Towards a phylogenetic classification of the *Ocotea* complex (Lauraceae): An analysis with emphasis on the Old World taxa and description of the new genus *Kuloa*. *Bot. J. Linn. Soc.* **2020**, *192*, 510–535. [CrossRef]
16. Kostermans, A.J.G.H. A monograph of the genus *Cinnamomum* Schaeff. (Lauraceae). Part I. *Gingkoana* **1986**, *6*, 1–171.
17. Meissner, C. Lauraceae. In *Prodromus Systematis Naturalis Regni Vegetablis*; de Candolle, A.P., Ed.; Masson and Fils: Paris, France, 1864; Volume 15, pp. 1–260.
18. van der Werff, H.; Richter, H.G. Toward an improved classification of Lauraceae. *Ann. MO. Bot. Gard.* **1996**, *83*, 409–418. [CrossRef]
19. Chanderbali, A.S.; van der Werff, H.; Renner, S.S. Phylogeny and historical biogeography of Lauraceae: Evidence from the chloroplast and nuclear genomes. *Ann. MO. Bot. Gard.* **2001**, *88*, 104–134. [CrossRef]
20. Huang, J.F.; Li, L.; van der Werff, H.; Li, H.W.; Rohwer, J.G.; Crayn, D.M.; Meng, H.H.; van der Merwe, M.; Conran, J.G.; Li, J. Origins and evolution of cinnamon and camphor: A phylogenetic and historical biogeographical analysis of the *Cinnamomum* group (Lauraceae). *Mol. Phylogenet. Evol.* **2016**, *96*, 33–44. [CrossRef]
21. Zeng, G.; Liu, B.; Rohwer, J.G.; Ferguson, D.K.; Yang, Y. Leaf epidermal micromorphology defining the clades in *Cinnamomum* (Lauraceae). *PhytoKeys* **2021**, *182*, 125–148. [CrossRef]
22. Yang, Z.; Deng, C.Y.; Wang, L.L.; Ban, Q.; Yang, Y. A new species of *Cinnamomum* (Lauraceae) from southwestern China. *PhytoKeys* **2022**, *202*, 35–44. [CrossRef]
23. Guo, C.; Luo, Y.; Gao, L.M.; Yi, T.S.; Li, H.T.; Yang, J.B.; Li, D.Z. Phylogenomics and the flowering plant tree of life. J. *Integr. Plant Biol.* **2022**, accepted. [CrossRef] [PubMed]
24. Zhang, Y.; Tian, Y.; Tng, D.Y.; Zhou, J.; Zhang, Y.; Wang, Z.; Li, P.; Wang, Z. Comparative chloroplast genomics of *Litsea* Lam. (Lauraceae) and its phylogenetic implications. *Forests* **2021**, *12*, 744. [CrossRef]
25. Song, W.; Chen, Z.; Shi, W.; Han, W.; Feng, Q.; Shi, C.; Engel, M.S.; Wang, S. Comparative analysis of complete chloroplast genomes of nine species of *Litsea* (Lauraceae): Hypervariable regions, positive selection, and phylogenetic relationships. *Genes* **2022**, *13*, 1550. [CrossRef] [PubMed]
26. Jin, J.J.; Yu, W.B.; Yang, J.B.; Song, Y.; dePamphilis, C.W.; Yi, T.S.; Li, D.Z. GetOrganelle: A fast and versatile toolkit for accu-rate de novo assembly of organelle genomes. *Genome Biol.* **2020**, *21*, 241. [CrossRef] [PubMed]
27. Tillich, M.; Lehwark, P.; Pellizzer, T.; Ulbricht-Jones, E.S.; Fischer, A.; Bock, R.; Greiner, S. GeSeq—Versatile and accurate annotation of organelle genomes. *Nucleic Acids Res.* **2017**, *45*, W6–W11. [CrossRef]
28. Shi, L.; Chen, H.; Jiang, M.; Wang, L.; Wu, X.; Huang, L.; Liu, C. CPGAVAS2, an integrated plastome sequence annotator and analyzer. *Nucleic Acids Res.* **2019**, *47*, W65–W73. [CrossRef]
29. Zhang, S.; Poczai, P.; Hyvönen, J.; Tang, J.; Amiryousefi, A. Chloroplot: An online program for the versatile plotting of or-ganelle genomes. *Front. Genet.* **2020**, *11*, 576124. [CrossRef]
30. Benson, G. Tandem repeats finder: A program to analyze DNA sequences. *Nucleic Acids Res.* **1999**, *27*, 573–580. [CrossRef]
31. Beier, S.; Thiel, T.; Münch, T.; Scholz, U.; Mascher, M. MISA-web: A web server for microsatellite prediction. *Bioinformatics* **2017**, *33*, 2583–2585. [CrossRef]
32. Katoh, K.; Standley, D.M. MAFFT multiple sequence alignment software version 7: Improvements in performance and usa-bility. *Mol. Biol. Evol.* **2013**, *30*, 772–780. [CrossRef]
33. Hall, T.A. BioEdit: A user-friendly biological sequence alignment editor and analysis program for Windows 95/98/NT. *Nucleic Acids Symp.* **1999**, *41*, 95–98. [CrossRef]
34. Talavera, G.; Castresana, J. Improvement of phylogenies after removing divergent and ambiguously aligned blocks from protein sequence alignments. *Syst. Biol.* **2007**, *56*, 564–577. [CrossRef] [PubMed]
35. Kalyaanamoorthy, S.; Minh, B.Q.; Wong, T.K.F.; von Haeseler, A.; Jermiin, L.S. ModelFinder: Fast model selection for accurate phylogenetic estimates. *Nat. Methods* **2017**, *14*, 587–589. [CrossRef]
36. Nguyen, L.T.; Schmidt, H.A.; von Haeseler, A.; Minh, B.Q. IQ–TREE: A fast and effective stochastic algorithm for estimating maximum–likelihood phylogenies. *Mol. Biol. Evol.* **2015**, *32*, 268–274. [CrossRef]

37. Minh, B.Q.; Nguyen, M.A.T.; von Haeseler, A. Ultrafast approximation for phylogenetic bootstrap. *Mol. Biol. Evol.* **2013**, *30*, 1188–1195. [CrossRef]
38. Ronquist, F.; Teslenko, M.; van der Mark, P.; Ayres, D.L.; Darling, A.; Höhna, S.; Larget, B.; Liu, L.; Suchard, M.A.; Huelsenbeck, J.P. MrBayes 3.2: Efficient Bayesian phylogenetic inference and model choice across a large model space. *Syst. Biol.* **2012**, *61*, 539–542. [CrossRef]
39. Letunic, I.; Bork, P. Interactive tree of life (iTOL) v5: An online tool for phylogenetic tree display and annotation. *Nucleic Acids Res.* **2021**, *49*, W293–W296. [CrossRef] [PubMed]
40. Zhou, L.; Feng, T.; Xu, S.; Gao, F.; Lam, T.T.; Wang, Q.; Wu, T.; Huang, H.; Zhan, L.; Li, L.; et al. ggmsa: A visual exploration tool for multiple sequence alignment and associated data. *Brief Bioinform.* **2022**, *23*, bbac222. [CrossRef] [PubMed]
41. Wickham, H. *ggplot2: Elegant Graphics for Data Analysis*, 2nd ed.; Springer: Cham, Switzerland, 2016; pp. 1–260.

Disclaimer/Publisher's Note: The statements, opinions and data contained in all publications are solely those of the individual author(s) and contributor(s) and not of MDPI and/or the editor(s). MDPI and/or the editor(s) disclaim responsibility for any injury to people or property resulting from any ideas, methods, instructions or products referred to in the content.

forests

MDPI

Article

Seed Distribution and Phenotypic Variation in Different Layers of a Cunninghamia Lanceolata Seed Orchard

Yu Duan [1], Tengyun Ye [1], Daiquan Ye [2] and Jian Zhou [1,*]

[1] Co-Innovation Center for Sustainable Forestry in Southern China, College of Biology and the Environment, Nanjing Forestry University, Nanjing 210037, China
[2] Yangkou State Forest Farm, Nanping 353211, China
* Correspondence: zhiwu@njfu.edu.cn; Tel.: +86-13951875093

Abstract: The phenotypic characteristics of forest seeds are the basis of germplasm innovation, genetic improvement, and biological research, and they also are the reference for the development of seed orchards. In this study, we analyzed seed quantity characteristics, phenotypic differentiation, and variation patterns in three seed-bearing clones from different crown layers of the Chinese fir (*Cunninghamia lanceolata* (Lamb.) Hook) orchard located in Fujian Province, China. We divided the clones into six layers according to crown height and the sunny and shady sides, 14 phenotypic characteristics, and five quality indexes, and we measured the germination rate of seeds. The rate of seeds filled with tannin-like substance in the upper sunny layer was low, but it was high in the lower shady layer. The germination rate was highest in the upper sunny layer and lower in the middle and lower shady sides. Values of most of the 14 phenotypic traits tested differed significantly among clones and layers. The average value of the phenotypic differentiation coefficient was 81.16%, indicating that variation among clones explained most of the total phenotypic variation. The repeatability of the 14 phenotypic traits was high (R > 0.80), indicating that these traits are highly heritable. The phenotypic characteristics of cones and seeds varied from 6.86% to 129.51%. The 14 phenotypic traits exhibited different degrees of correlation, and seed weight, seed circumference, seed width, and seed area can be used to predict other seed traits. However, the correlations between cone traits were not strong. Our results show that when establishing a dwarfing Chinese fir seed orchard, the distribution and variation of seeds in different crown layers of clones should be considered, and clones with more cones in the lower crown layer should be selected as parents.

Keywords: *Cunninghamia lanceolata* (Lamb.) Hook; seed orchard; seed type; germination percentage; phenotypic traits; phenotypic differentiation

check for updates

Citation: Duan, Y.; Ye, T.; Ye, D.; Zhou, J. Seed Distribution and Phenotypic Variation in Different Layers of a Cunninghamia Lanceolata Seed Orchard. *Forests* **2023**, *14*, 240. https://doi.org/10.3390/f14020240

Academic Editor: Cate Macinnis-Ng

Received: 25 November 2022
Revised: 15 January 2023
Accepted: 23 January 2023
Published: 28 January 2023

Copyright: © 2023 by the authors. Licensee MDPI, Basel, Switzerland. This article is an open access article distributed under the terms and conditions of the Creative Commons Attribution (CC BY) license (https://creativecommons.org/licenses/by/4.0/).

1. Introduction

The Chinese fir, *Cunninghamia lanceolata* (Lamb.) Hook, is the main afforestation tree species in China, and it has good wood properties, high yield, and abundant germplasm resources [1]. The seed types of Cunninghamia lanceolata can be divided into three types: good seed, seeds filled with tannin-like substance, and empty seed. The seeds filled with tannin-like substance mainly occurs in the middle and late stage of embryo abortion, accompanied by the filling of tannin substances, which may be related to many factors such as clonal heredity, self-pollination infertility, bad climatic conditions, etc. [2]. High quality of cones and seeds in Chinese fir seed orchards ensures good seeds, strong seedlings, and high yield. Therefore, improving the utilization rate of germplasm and promoting good seed generation is essential for improving the afforestation process. The number of cones and seeds of Chinese firs determines the seed yield of the seed orchard [3]. The seed yield is also related to the cone and seed phenotype, so the number, germination characteristics, and phenotypic characteristics of Chinese fir cones and seeds are important indicators for studying their quality and phenotypic variation [4].

Plant phenotypic diversity is an important component of genetic diversity and is the result of the interaction of genes and the environment [5]. Of the tools commonly used for genetic diversity research, such as phenotyping, cytology, biochemistry, and molecular markers, phenotyping is the most feasible and direct method [6]. Assessing the degree of phenotypic variation is research content to reveal the adaptation of organisms to different environments [7]. The phenotypic variation of seed and fruit traits determines the diffusion ability and population distribution pattern of a species, and it is an economically important trait for the breeding of improved forest varieties [8]. Studies of phenotypic variation of the genera *Cunninghamia* R. Br. [9] and *Pinus* Linn [10] have laid a foundation for resource protection and genetic improvement of related tree species [11].

The main goals of seed production in seed orchards are to improve the genetic quality of seeds and to facilitate seed harvesting. The ninth national inventory of forest resources showed that the area of Chinese fir plantations reached 148 million mu, and the stock volume reached 755 million m3, accounting for 1/4 and 1/3 of the total area and stock volume of the country's artificial arbor forests, both ranking first [12]. The cone is the basic unit of seed production of Chinese fir and other coniferous trees [13]. Ayari and Khouja reported that the cone yield of *Pinus* is not uniform and often varies among crown heights [14]. In a study of pine trees, Debain et al. found that the number of cones produced in the upper layer of the crown was higher [15]. Seeds from different layers differ not only in seedling growth potential but also in seed morphology and quality. For example, Shen and Gao studied the seed quality from different crown heights of Chinese fir and found that the proportion of good seeds in the upper layer was high, followed by the middle and lower parts [16]. Therefore, it is very important to study the phenotypic variation of cone number and seed quality of Chinese fir in different layers of crown [17]. Additionally, in a study of seed phenotype, Frank and Robert found that the seed size of forest trees is one of the most stable phenotypic characteristics [18].

At present, a large number of Chinese fir seed orchards have been established in China, and they provide high-quality seeds for large-scale afforestation. However, at present, seed orchards are all non-dwarfed seed orchards. With the gradual increase in the tree body, the seed-bearing layer moves upward, and the operation of seed collection and pollination becomes increasingly difficult. Therefore, the "dwarfing" of seed orchards is the management direction of improved seed bases, and the dwarfing experiments and technical schemes for Chinese fir mother plants are gradually developing. One of the common "dwarfing" schemes of Chinese fir seed orchard refers to the operation of cutting off the upper trunk and pruning the side branches [19]. At home and abroad, tree seed orchards such as Douglas fir (*Pseudotsuga menziesii* (Mirb.) Franco) [20], Black pine (*Pinus thunbergii* Parl.) [21], Japanese larch (*Larix kaempferi* (Lamb.) Carr.) [22], Masson pine (*Pina massoniana* Lamb.) [23], and other tree species have been cut off the upper trunk and pruned the side branches in order to decline the seed-bearing layer of trees and improve seed yield. It is crucial that we understand the layering characteristics of the Chinese fir cone setting so that seed setting and/or quality are not reduced after the mother plant is dwarfed. Zheng et al. reported that dwarfing *Pina massoniana* clones with different seed setting characteristics increased the amount of female cones of middle- and high-yield clones by more than 20%, but did not significantly improve the low-yield clones. Differences were found for studied cone and seed characters among orchards and crown positions. Variation among grafts within clone was higher than among clones for most characters for any individual characters. The coefficient of variation within clones was often higher than among clones [24]. This result illustrates that dwarfing clones with different seed setting abilities has quite different effects.

To date, little is known about the effect of seed setting characteristics from different crown layers on the seed yield after tree dwarfing and pruning. In this study, we evaluated seed yield and seed quality of Chinese fir from different layers of the crown using modern phenotypic analysis methods. We selected three Chinese fir clones with different seed setting characteristics to study seed quality, germination rate, and phenotypic characteristics at different crown layers. Our results provide a reference for the selection of clones from dwarf Chinese fir seed orchards as well as a theoretical basis and technical reference for the construction and management of a new generation of seed orchards.

2. Materials and Methods

2.1. Study Area

The experimental area is located in Yangkou in a state-owned forest farm near Daoping Village, in Fujian Province (longitude 117.902773°; latitude 26.823542°). It is the central production area of Chinese fir. The farm was founded in 1956 and has a total operating area of 4133 hm^2 and a total forest stock of 590,000 m^3. The seed garden is located in the low mountains and hills of the Wuyi Mountains. The area is dominated by fertile and deep red soil and has a subtropical climate. The annual average temperature is 18.5 °C, the annual average precipitation is 1880 mm, and the frost-free period can reach 305 days. The climate is mild, the rainfall is abundant, and the plant growth period is long, making it a suitable locale for the growth of fir, pine, and other timber species.

2.2. Study Materials

In 2011, 670 clones were collected, and they were grafted onto two-year rootstocks in March 2013. We adopted artificial belt land preparation, with a bandwidth of 1.2 m, excavation specification of 60 cm × 40 cm × 40 cm, and plant row spacing of 3 m × 3 m, to generate the third Chinese fir germplasm gene bank. We selected the following three representative Chinese fir clones from the 670 clones according to their characteristics in the lower crown: (1) more seed bearing in the lower layer (jiang26), (2) medium seed bearing in the lower layer (jiang18), and (3) no seed bearing in the lower layer (jiangA13). We evaluated three clones from each group (Table 1).

Table 1. Basic information about the three Chinese fir clones assessed in the study.

Clone Number	Test Strain Number	Number of Cones on the Upper Sunny Side	Number of Cones on the Upper Shady Side	Number of Cones on the Middle Sunny Side	Number of Cones on the Middle Shade Side	Number of Cones on the Lower Sunny Side	Number of Cones on the Lower Shady Side	Clonal Seed Setting Characteristics
jiang26	jiang26-1	328	194	247	95	354	118	more seed bearing in the lower layer
jiang26	jiang26-2	205	233	286	103	295	84	
jiang26	jiang26-3	170	181	185	76	265	89	
jiang18	jiang18-1	175	183	242	107	138	69	medium seed bearing in the lower layer
jiang18	jiang18-2	151	135	108	70	114	37	
jiang18	jiang18-3	334	110	31	178	174	131	
jiangA13	jiangA13-1	220	118	113	55	0	0	no seed bearing in the lower layer
jiangA13	jiangA13-2	203	121	132	50	0	0	
jiangA13	jiangA13-3	184.	108	122	76	0	0	

2.3. Study Method

In late November 2020, we measured three growth indexes (tree height, diameter at breast height, and crown width) of clones jiang26, jiang18, and jiangA13. We divided the three experimental plants of jiang26 and jiang18 into six layers (upper sunny side, upper shady side, middle sunny side, middle shady side, lower sunny side, and lower shady side) and randomly collected six cones from each layer, for a total of 216 cones. Because the lower crown layer of clone jiangA13 does not bear fruit, we divided it into four layers (upper sunny side, upper shady side, middle sunny side, and middle shady side) and randomly collected six cones from each layer, for a total of 72. In total, we tested 288 cones.

For each experimental plant and layer, we randomly chose three cones, measured their fresh weight (CW, g), and took photos. We then removed the bract scales and seeds from the base of each selected cone [25], took photos, recorded the one seed weight (OSW, g). The quality of a seed is to weigh all the seeds in a cone one by one, and then obtain the average. We then dissected the seeds and recorded the number of empty seeds, seeds filled with tannin-like substance, and good seeds. The phenotypic characteristics of cones, bract scales, and seeds were determined using ImageJ software [26]. These traits included longitudinal diameter of cones (CL, cm), transverse diameter of cones (CD, cm), bract scale area (WPA, cm), bract scale perimeter (WPP, cm), bract scale length (WPL, cm), bract scale width (WPW, cm), bract scale length-width ratio (WPL/WPW), seed area (SA, cm), seed perimeter (SP, cm), seed length (SL, cm), seed width (SW, cm), and seed length-width ratio (SL/SW).

The other three cones from each clone/layer were dried to make the seeds fall off naturally. The seeds were collected from each cone, washed three times with ultrapure water, placed in a Petri dish with filter paper, and placed in an artificial climate room with a temperature of 25 °C and a humidity of 75% for 21 days. We recorded the number of germinated seeds every day to calculate the seed germination rate [27].

2.4. Data Analysis

We analyzed all data using R (4.1.1 is Version of R). We applied single factor analysis of variance (F-test) and multiple comparisons to study the good seed rate, seeds filled with tannin-like substance rate, empty seed rate, total seed number, and seed germination rate. The nested linear model [28] was used to analyze the variance of phenotypic variation among and within the Chinese fir clones. The linear model is as follows:

$$y_{ijk} = \mu + p_j + bi_{(j)} + e_{ijk} \quad (1)$$

where μ is the overall average value; p_j is the family effect; $bi_{(j)}$ is the repetitive effect; and e_{ijk} is a random error. Multiple comparison selection Newman-Keuls.

We used Pearson correlation to analyze the bivariate correlation, and we conducted cluster analysis according to the Euclidean distance of each trait among clones.

The mean value (x), standard deviation (SD), and phenotypic variation coefficient (CV) of each phenotypic trait of cones, bract scales, and seeds of different Chinese fir clones in each crown layer were calculated as follows:

$$\mathrm{CV} = \frac{\mathrm{SD}}{\mathrm{X}} \times 100\% \quad (2)$$

We calculated the phenotypic variation coefficient $v_{(st)}$ as:

$$v_{(ST)} = \frac{\delta^2_{t/s}}{\left(\delta^2_{t/s} + \delta^2_s\right)} \quad (3)$$

where $\delta^2_{t/s}$, δ^2_s are the difference between clones and within clones.

The clonal repeatability (R) of each characteristic was estimated using the following formula [29]:

$$\mathrm{R} = 1 - \frac{1}{\mathrm{F}} \quad (4)$$

where F is the F value in the analysis of variance.

We used the following formula to calculate the seed germination rate (GP%) [30]:

$$GP\% = \frac{N_n}{N} \times 100\% \quad (5)$$

where N_n is the number of germinating seeds and N is the total number of seeds.

3. Results

3.1. Distribution Characteristics of Seed Types in Different Crown Layers

The number of seeds, good seed rate, seeds filled with tannin-like substance rate, and empty seed rate in a single cone differed among the three clones and among different layers of the crown (Table 2). The number of seeds in a single cone of clone jiang26 ranged from 74.33 to 104.67, and the number of seeds differed significantly between the upper sunny side and lower shade side. For clone jiang18, the number of seeds in a single cone ranged from 99.89 to 112.89, and for clone jiangA13 the range was 100.22 to 115. The number of seeds in a single cone of the three clones did not differ among the upper sunny side, upper shady side, central sunny side, and central shady side. However, in the lower sunny side and lower shady side of the crown, the number of seeds in a single cone of clone jiang26 was significantly lower than that of clone jiang18.

The percentage of good seeds in a single cone of clone jiang26 ranged from 12.56% to 44.22%, and the percentage of good seeds in the upper sunny side was significantly higher than that in the central shady side, lower sunny side, and lower shady side. For clone jiang18, the percentage of good seeds in single cone ranged from 11.1% to 22.12%, and the range was 18.24% to 23.96% for clone jiangA13. In the upper sunny side, the good seed rate of jiang26 was extremely significantly higher than that of jiang18 and jiangA13.

The rate of seeds filled with tannin-like substance of a single cone of clone jiang26 ranged from 34.19% to 65.88%. The rate for the upper sunny side was the lowest, and that of the lower shady side was the highest. For clone jiang18, the percentage of seeds filled with tannin-like substance in single cone was 23.97% to 34.88%, and that for clone jiangA13 was 15.67% to 29.90%. The rate for the upper shady side of clone jiang26 was significantly higher than that of clone jiangA13, and the rate for the central shady side of jiang26 was significantly higher than that of clones jiang18 and jiangA13. Additionally, the rates for the lower sunny side and lower shady side of clone jiang26 were significantly higher than those of clone jiang18.

The percentage of empty seeds in a single cone of clone jiang26 was 21.56% to 34.02%, the range for clone jiang18 was 53.11% to 62.49%, and that for clone jiangA13 was 53.70% to 60.38%. The empty seed rate for the upper sunny side, upper shady side, and central sunny side was significantly lower for clone jiang26 than for clones jiang18 and jiangA13, and the empty particle ratio of the central shady side was extremely significantly lower than that of clones jiang18 and jiangA13. The empty seed rates for the lower sunny side and lower shady side of clone jiang26 were significantly lower than those of clone jiang18.

For clone jiang26, the rate of seeds filled with tannin-like substance was significantly higher than the good seed rate and the empty seed rate. For clone jiang18, the good seed rate was significantly lower than that of seeds filled with tannin-like substance and the empty seed rate, and the rate of seeds filled with tannin-like substance was significantly lower than the empty seed rate. The empty seed rate of clone jiangA13 was significantly higher than that of seeds filled with tannin-like substance and the good seed rate.

In general, the two indexes of good seed rate and seeds filled with tannin-like substance rate of the high seed-bearing clones in the lower layer (jiang26) were significantly higher than those of the other two types of clones ($p < 0.001$), and the empty seed rate was significantly lower than those of the other two types of clones ($p < 0.001$). When we compared the high seed-bearing clones (jiang26) and the medium seed-bearing clones (jiang18), there was no significant difference in the number of single cone seeds and the good seed rate in the lower crown layer. The rate of seeds filled with tannin-like substance of the higher seed-bearing clones was significantly higher than that of the clones with medium seed bearing in the lower layer ($p < 0.001$), while the empty seed rate was significantly lower than that of the medium seed bearing clones in the lower layer ($p < 0.001$).

Table 2. Distribution of different quality and types of seeds in different crown layers in the three Chinese fir clones.

Clone Number	Position	Number of Seeds per Cone	Good Seed Rate (%)	Seeds Filled with Tannin-Like Substance Rate (%)	Empty Seed Rate (%)
jiang26	Upper sunny side	104.67 ± 21.20 a	44.22 ± 17.89 a A	34.19 ± 5.29 cd AB	21.59 ± 15.62 c B
jiang26	Upper shady side	95.56 ± 16.12 ab	27.18 ± 16.31 b A	38.80 ± 6.50 bcd A	34.02 ± 17.36 abc A
jiang26	Central sunny side	94.22 ± 20.04 ab	26.48 ± 14.27 b A	41.49 ± 13.74 bc A	32.03 ± 20.22 bc A
jiang26	Central shady side	97.56 ± 9.98 ab	16.72 ± 6.58 b B	55.97 ± 11.02 ab A	27.32 ± 14.81 c B
jiang26	Lower sunny side	92.00 ± 14.32 ab	17.06 ± 9.92 b B	56.62 ± 10.22 ab A	26.32 ± 16.19 c B
jiang26	Lower shady side	74.33 ± 20.63 b	12.56 ± 9.83 b B	65.88 ± 16.83 a A	21.56 ± 21.67 c B
jiang18	Upper sunny side	112.89 ± 18.03 a	22.12 ± 11.42 b B	24.77 ± 11.89 cd B	53.11 ± 13.97 ab A
jiang18	Upper shady side	100.44 ± 16.18 a	15.48 ± 13.18 b B	26.98 ± 21.90 cd B	57.54 ± 22.30 ab A
jiang18	Central sunny side	105.22 ± 23.71 a	12.01 ± 13.44 b B	25.50 ± 14.54 cd B	62.49 ± 24.44 a A
jiang18	Central shady side	101.11 ± 15.46 a	12.19 ± 8.41 b C	29.14 ± 13.46 cd B	58.66 ± 19.40 ab A
jiang18	Lower sunny side	104.11 ± 6.13 a	15.66 ± 10.18 b B	23.97 ± 9.22 cd B	60.36 ± 17.03 ab A
jiang18	Lower shady side	99.89 ± 14.56 a	11.10 ± 9.40 b C	34.88 ± 19.97 cd B	54.02 ± 20.67 ab A
jiangA13	Upper sunny side	115.00 ± 31.92 a	18.31 ± 12.80 b B	22.97 ± 22.44 cd B	58.72 ± 21.11 ab A
jiangA13	Upper shady side	102.56 ± 11.94 a	23.96 ± 16.77 b B	15.67 ± 8.96 d B	60.38 ± 14.06 ab A
jiangA13	Central sunny side	100.22 ± 18.34 a	12.04 ± 9.27 b C	29.90 ± 22.27 cd B	58.06 ± 18.60 ab A
jiangA13	Central shady side	101.67 ± 11.91 a	18.24 ± 13.42 b B	28.05 ± 15.07 cd B	53.70 ± 14.68 ab A

Significant differences among values in the same row are indicated by capital letters: the same letter indicates no significant difference, and different letters indicate significant difference ($p < 0.05$). Significant differences among values in the same column are indicated by lowercase letters: the same letter indicates no significant difference, and different letters indicate significant difference ($p < 0.05$). The same is true in the following tables.

3.2. Variation of Seed Germination Ability in Different Crown Layers

We detected extremely significant differences in seed germination rates in different layers of the canopies of the three Chinese fir clones (Figure 1). The highest germination rate of clone jiang26 occurred on the upper sunny side (51.50%) and the lowest rate on the lower shady side (20.29%). For clone jiangA13, the highest and lowest germination rates were on the upper sunny side (48.33%) and middle sunny side (23.61%), respectively. The average germination rate of clone jiang18 was relatively low. When comparing the same crown layer among clones, we found that the germination rate of clone jiang26 was 1.91 times greater than that of jiangA13 on the central sunny side, and the rates of clones jiang26 and jiangA13 were 1.80 times greater than that of clone jiang18 on the central shady side8. Therefore, among the three clones tested, in the middle layer, the germination rate of the high seed-bearing clone (jiang26) was significantly higher than that of the other two clones ($p < 0.001$). However, the germination rates of the two clones that bore seeds in the lower crown layer (jiang26 and jiang18) did not differ significantly.

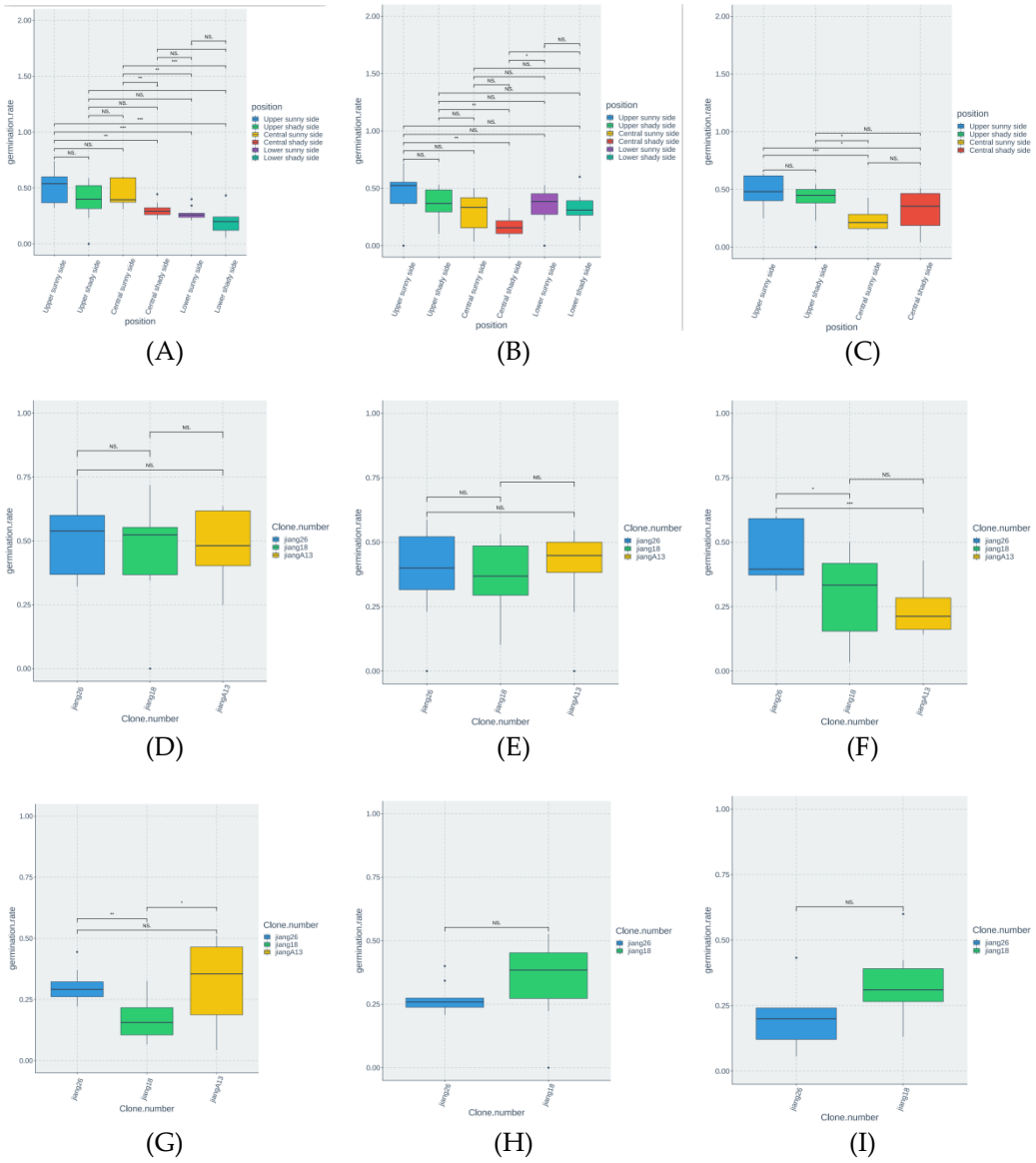


Figure 1. (**A**) Germination rate of Chinese fir clone jiang26 in different crown layers, (**B**) germination rate of clone jiang18 in different crown layers, (**C**) germination rate of clones jiangA13 in different crown layers, (**D**) germination rate of Chinese fir clones from the upper sunny side, (**E**) germination rate of clones from the upper shady side, (**F**) germination rate of clones from the central sunny side, (**G**) germination rate of clones from the central shady side, (**H**) germination rate of clones of different from the lower sunny side, (I) germination rate of clones from the lower shaded side. Significance levels: NS, $p > 0.05$; *, $p < 0.05$; ***, $p < 0.001$.

3.3. Phenotypic Variation of Cone and Seed Traits and Differentiation of Phenotypic Traits

Table 3 shows the results of nested variance analysis, variance components, and $v_{(st)}$ of the three clones from the upper sunny side, upper shady side, central sunny side, and central shady side. With the exception of CW, CD, and CL of cones for the within clone comparison, the phenotypic characteristics of cones and seeds were very significantly different within and among the clones. The percentage of variance components among the 14 phenotypic traits varied from 2.42% to 55.46%, with an average of 19.34%. The percentage of variance components in the total variation was 0.00% to 3.20%, with an average of 1.75%. The variance component percentage of random error was 44.54% to 96.46%, with an average of 78.91%. The variance components among clones were greater than those within clones, indicating that the variation among clones was the main explanation of the total phenotypic

variation of Chinese fir. At the same time, the variation range of the $v_{(st)}$ of cone and seed traits ranged from 50.00% to 100%, and the average $v_{(st)}$ of the 14 phenotypic traits was 87.97%. This result indicates that the phenotypic variation of the Chinese fir seed orchard population accounted for 87.97% of the variation among clones and 12.03% of that within clones. The diversity among clones also was greater than that within clones. Among the 14 traits, the trait with the largest $v_{(st)}$ was CD (100%), followed by the WPW (99.17%), and SW had the smallest $v_{(st)}$ (50.00%). The $v_{(st)}$ of the 14 phenotypic traits in clones was lower than 50%. These results show that the phenotypic variation in the upper and middle crown layers for the three clones with different seed-bearing characteristics mainly existed among the clones.

Table 4 shows the variance components and $v_{(st)}$ for the two clones that bore seeds in the lower crown layer (jiang26 and jiang18) for the lower sunny side and lower shady side. Thirteen phenotypic traits were significantly different between jiang26 and jiang18, but WPP was not. We found significant differences within clones for 11 phenotypic traits, but not for CL, WPW, or OSW. The percentage of variance components among the 14 phenotypic traits varied from 0 to 65.16%, with an average of 21.03%. The percentage of variance components in the total variation was 0 to 14.95%, with an average of 3.58%, and that of random error was 19.89% to 98.37%, with an average of 75.39%. The variance components among clones were greater than those within clones, indicating that the variation among clones was the main explanation of the total phenotypic variation of Chinese fir. The variation range of $v_{(st)}$ of the 14 cone and seed traits ranged from 0.00% to 100%, with an average of 74.34%. Thus, the phenotypic variation of the Chinese fir seed orchard population accounted for 74.34% of the variation among clones and 25.66% of that within clones. Additionally, the diversity among clones was greater than that within clones. WPW had the largest $v_{(st)}$ (100.00%), followed by OSW (99.46%), but the $v_{(st)}$ was 0.00% for WPL and WPP. The $v_{(st)}$ of all phenotypic traits except WPP, WPL, and WPL/WPW was less than 50% within clones, indicating that the phenotypic variation of the two clones in the lower crown layer mainly existed among the clones.

The repeatability of all phenotypic traits for the three clones in the upper sunny side, upper shady side, central sunny side, and central shady side of the crown ranged from 89.44% to 99.94% (Table 3), and all 14 phenotypic traits had high repeatability (R > 0.80). Except for CL (R = 89.44%), the other 13 phenotypic traits were highly heritable (R $\geq$ 90%). The repeatability of all phenotypic traits for the jiang26 and jiang18 clones in the lower sunny side and lower shady side of the crown ranged from 55.63% to 99.85% (Table 4). Except for WPP (R = 55.63%), which had mid and high repeatability, the other 13 phenotypic traits had high repeatability (R > 0.80) and strong heritability (R $\geq$ 90%). These results show that the yield and quality of cones and seeds from the three clones were stable, thus these characteristics can be stably inherited in the offspring and are less affected by the environment.

Table 3. Variance component, phenotypic differentiation coefficient, and repeatability of phenotypic characters of cones and seeds of Chinese fir clones in the upper and middle crown layers.

Phenotypic Traits	Variance Component			Variance Component Percentage			V(st) (%)	F		R(%)
	Between Clones	Within Clones	Random Error	Between Clones	Within Clones	Random Error		Between Clones	Within Clones	
CW	4.2880	0.3570	10.2320	28.8200	2.4000	68.7800	92.31	16.4010 ***	1.3140	93.90
CD	12.3010	0.0000	9.8790	55.4600	0.0000	44.5400	100.00	45.2420 ***	0.4130	97.79
CL	5.7630	1.0180	25.5850	17.8000	3.1400	79.0500	84.99	9.4660 ***	1.3580	89.44
WPA	0.0300	0.0030	0.2190	12.0100	1.2400	86.7600	90.91	341.6000 ***	9.5400 ***	99.71
WPP	0.0310	0.0120	1.1800	2.5700	0.9700	96.4600	72.09	70.9680 ***	7.0320 ***	98.59
WPL	0.0100	0.0010	0.1200	7.7700	1.0900	91.1400	90.91	212.6750 ***	8.1920 ***	99.53
WPW	0.0060	0.0001	0.0580	9.1100	0.7300	90.1600	99.17	248.2920 ***	5.8620 ***	99.60
WPL/WPW	0.0390	0.0020	0.2370	13.9300	0.8700	85.2000	95.12	399.2850 ***	7.1350 ***	99.75
OSW	0.0044	0.0002	0.0237	15.6200	0.7700	83.5900	95.65	698.0020 ***	9.5670 ***	99.86
SA	0.0020	0.0002	0.0050	24.0800	3.2000	72.7300	90.91	1260.8600 ***	41.4400 ***	99.92
SP	0.0500	0.0030	0.1130	30.0300	1.9600	68.0100	94.34	1653.4700 ***	27.5400 ***	99.94
SL	0.0060	0.0010	0.0150	27.3700	2.6500	69.9800	85.71	1476.0000 ***	35.8700 ***	99.93
SW	0.0010	0.0010	0.0210	2.4200	2.6700	94.9100	50.00	120.8800 ***	26.8500 ***	99.17
SL/SW	0.7610	0.0900	2.3530	23.7500	2.8000	73.4500	89.42	1227.1100 ***	36.0400 ***	99.92

Significance level: ***, $p < 0.001$. CW is one cone fresh weight; CD is transverse diameter of cones; CL is longitudinal diameter of cones; WPA is bract scale area; WPP is bract scale perimeter; WPL is bract scale length; WPW is bract scale width; WPL/WPW is bract scale length-width ratio; OSW is one seed weight; SA is seed area; SP is seed perimeter; SL is seed length; SW is seed width; SL/SW is seed length-width ratio.

Table 4. Variance component, phenotypic differentiation coefficient, and repeatability of phenotypic characters of cones and seeds of Chinese fir clones in the lower crown layer.

Phenotypic Traits	Variance Component			Variance cOmponent Percentage			V(st)(%)	F		R(%)
	Between Clones	Within Clones	Random Error	Between Clones	Within Clones	Random Error		Between Clones	Within Clones	
CW	3.0630	1.2810	4.9710	32.8800	13.7500	53.3700	70.51	14.4090 ***	3.3190 *	93.06
CD	26.4690	6.0720	8.0790	65.1600	14.9500	19.8900	81.34	66.7370 ***	7.7640 **	98.50
CL	35.2230	5.3520	13.9060	64.6500	9.8200	25.5300	86.81	50.0560 ***	4.464	98.00
WPA	0.0290	0.0030	0.2230	11.2800	1.3300	87.3900	90.63	161.5900 ***	10.0100 ***	99.38
WPP	0.0000	0.0220	1.3530	0.0000	1.6300	98.3700	0.00	2.254	10.8180 ***	55.63
WPL	0.0000	0.0030	0.1420	0.0000	1.9100	98.0900	0.00	12.2100 ***	12.5300 ***	91.81
WPW	0.0020	0.0000	0.0560	4.0700	0.0000	95.9300	100.00	50.1920 ***	0.355	98.01
WPL/WPW	0.0040	0.0050	0.2920	1.4000	1.7500	96.8500	44.44	28.5700 ***	11.7100 ***	96.50
OSW	0.0551	0.0003	0.0232	19.1800	0.1000	80.7200	99.46	394.0820 ***	2.054	99.75
SA	0.0015	0.0000	0.0036	28.7200	0.3800	70.9000	98.72	673.5760 ***	5.4270 **	99.85
SP	0.0300	0.0010	0.0840	26.2800	0.4700	73.2500	96.77	598.1890 ***	6.3760 **	99.83
SL	0.0026	0.0002	0.0114	18.2100	1.1600	80.6300	94.14	385.5400 ***	12.9100 ***	99.74
SW	0.0024	0.0003	0.0140	14.1900	1.8500	83.9600	88.89	298.1800 ***	19.2700 ***	99.66
SL/SW	0.1140	0.0140	1.2390	8.3300	1.0400	90.6300	89.06	162.1600 ***	10.5100 ***	99.38

Significance levels: *, $p < 0.05$; **, $p < 0.01$; ***, $p < 0.001$.

3.4. Variation Characteristics of Phenotypic Characters of Chinese Fir Cones and Seeds

Tables 5 and 6 show that the 14 phenotypic traits of Chinese fir varied extensively among clones and crown different layers. The order of the phenotypic CV of the high seed bearing clone in the lower crown layer (jiang26) was as follows: OSW > WPA > WPL/WPW > WPW > CW > WPP > SA > WPL > SW > SL/SW > SP > SL > CD > CL, and that of the medium seed bearing clone in the lower crown layer (jiang18) was OSW > WPA > WPL/WPW > WPW > SA > WPP > WPL > SW > CW > SL > SP > SL/SW > CL > CD. The phenotypic CV of the no seed bearing in the lower crown layer clone (jiangA13) was ordered as follows: OSW > SA > WPL/WPW > WPA > WPW > SW > CW > SL > SP > WPP > SL/SW > WPL > CL > CD. For all three clones, the phenotypic character with the largest CV was OSW. The OSW of the jiang26 clone varied from 0.0075 g to 0.0095 g, that of the jiang18 clone varied from 0.0052 g to 0.0067 g, and that of the jiangA13 clone varied from 0.0038 g to 0.0040 g. The phenotypic traits with the smallest variation range were CL and CD. Our data show that the phenotypic characteristics of the cones and seeds of all three clones provide abundant resources for the breeding of improved Chinese fir varieties.

The variation of the phenotypic characteristics of cones and seeds also differed among the different crown layers. The phenotypic CV in the upper sunny side was in the order of OSW > WPA > WPL/WPW > WPW > SA > CW > WPP > SW > WPL > SL > SP > SL/SW > CL > CD. For the upper shade side, the order was OSW > SA > WPA > WPL/WPW > WPW > SW > CW > SP > SL > WPP > WPL > SL/SW > CL > CD. The order for the central sunny side was OSW > WPA > WPL/WPW > WPW > SA > CW > SW > WPP > SL > SP > WPL > SL/SW > CL > CD. The phenotypic CV for the middle shade side was as follows: OSW > WPA > WPL/WPW > WPW > SA > SW > WPP > CW > WPL > SP > SL > SL/SW > CL > CD. For the lower sunny side, the order was OSW > WPA > WPL/WPW > WPW > SA > WPP > WPL > SW > CW > SL > SP > SL/SW > CD > CL. The order for the lower shade side was OSW > WPA > WPL/WPW > WPW > SA > WPP > CW > WPL > SW > SL > SP > SL/SW > CL > CD.

In the different crown layers, OSW had the largest CV, and CL and CD had the smallest CVs. In the upper sunny side, the phenotypic CV of OSW was 72.73%–83.00% and that of CD was 7.70%–14.24%. In the upper shade side, the phenotypic CV of OSW was 76.28%–129.51%, and that of CD was 7.19%–15.86%. In the middle sunny side, the phenotypic CV of OSW was 51.53%–95.72%, and that of CD was 11.01%–12.48%. In the middle shade side, the phenotypic CV of OSW was 47.19%–80.78%, and that of CD was 5.33%–7.74%. In the lower sunny side, the phenotypic CV of OSW was 59.49%–84.34%, and that of CL was 7.72%–9.23%. In the lower shade side, the phenotypic CV of OSW was 47.51%–74.09%, and that of cone diameter was 9.27%–10.93%. These results show that there were significant differences in cone and seed traits among different layers of Chinese fir. OSW was the most unstable characteristic, and CD and CL were the most stable.

Table 5. Average values of phenotypic characters of bract scales and seeds from different crown layers of the three Chinese fir clones.

Clone Number	Position	CW (g)	CD (cm)	CL (cm)	WPA (cm^2)	WPP (cm)	WPL (cm)	WPW (cm)	WPL/WPW	OSW (g)	SA (cm^2)	SP (cm)	SL (cm)	SD (cm)	SL/SW
jiang26	Upper sunny side	11.79 ± 3.92	29.81 ± 4.25	37.18 ± 5.19	1.19 ± 0.55	4.57 ± 1.13	1.66 ± 0.36	0.63 ± 0.25	3.05 ± 1.28	0.0089 ± 0.0064	0.23 ± 0.06	1.82 ± 0.28	0.65 ± 0.10	0.26 ± 0.05	2.60 ± 0.39
jiang26	Upper shady side	14.28 ± 4.08	30.80 ± 2.33	37.81 ± 3.53	1.15 ± 0.58	4.55 ± 1.25	1.65 ± 0.39	0.62 ± 0.27	3.10 ± 1.27	0.0081 ± 0.0062	0.22 ± 0.06	1.81 ± 0.29	0.64 ± 0.09	0.27 ± 0.07	2.46 ± 0.40
jiang26	Central sunny side	10.98 ± 3.58	30.42 ± 3.56	37.24 ± 4.60	1.22 ± 0.63	4.58 ± 1.22	1.63 ± 0.38	0.66 ± 0.27	2.86 ± 1.23	0.0084 ± 0.0043	0.23 ± 0.06	1.81 ± 0.28	0.64 ± 0.10	0.26 ± 0.05	2.49 ± 0.42
jiang26	Central shady side	10.92 ± 2.43	30.47 ± 5.40	41.05 ± 4.36	1.07 ± 0.53	4.42 ± 1.16	1.60 ± 0.36	0.61 ± 0.26	3.11 ± 1.44	0.0075 ± 0.0035	0.21 ± 0.05	1.78 ± 0.25	0.63 ± 0.09	0.25 ± 0.06	2.56 ± 0.43
jiang26	Lower sunny side	12.44 ± 2.62	32.88 ± 4.06	43.17 ± 3.99	1.15 ± 0.59	4.46 ± 1.21	1.61 ± 0.38	0.62 ± 0.26	3.09 ± 1.61	0.0090 ± 0.0053	0.23 ± 0.06	1.84 ± 0.30	0.65 ± 0.10	0.27 ± 0.06	2.46 ± 0.39
jiang26	Lower shady side	9.77 ± 2.87	27.70 ± 3.03	39.39 ± 2.85	1.02 ± 0.56	4.32 ± 1.27	1.56 ± 0.40	0.60 ± 0.27	3.10 ± 1.40	0.0095 ± 0.0045	0.23 ± 0.06	1.86 ± 0.26	0.66 ± 0.10	0.27 ± 0.05	2.54 ± 0.42
jiang18	Upper sunny side	9.54 ± 2.68	23.89 ± 1.84	35.87 ± 4.93	0.87 ± 0.37	4.27 ± 1.08	1.47 ± 0.35	0.66 ± 0.24	2.46 ± 0.90	0.0067 ± 0.0052	0.19 ± 0.06	1.68 ± 0.28	0.61 ± 0.10	0.23 ± 0.05	2.73 ± 0.38
jiang18	Upper shady side	6.62 ± 1.46	21.99 ± 1.58	29.98 ± 4.07	0.78 ± 0.33	4.04 ± 0.95	1.39 ± 0.31	0.62 ± 0.22	2.48 ± 1.01	0.0056 ± 0.0073	0.16 ± 0.06	1.52 ± 0.33	0.55 ± 0.12	0.21 ± 0.06	2.62 ± 0.47
jiang18	Central sunny side	7.71 ± 1.85	23.82 ± 2.62	33.65 ± 2.53	0.78 ± 0.34	4.09 ± 1.08	1.43 ± 0.34	0.61 ± 0.25	2.69 ± 1.20	0.0052 ± 0.0050	0.16 ± 0.07	1.50 ± 0.37	0.55 ± 0.13	0.21 ± 0.06	2.72 ± 0.49
jiang18	Central shady side	8.41 ± 2.01	23.64 ± 1.26	34.40 ± 4.47	0.84 ± 0.38	4.28 ± 1.09	1.50 ± 0.35	0.64 ± 0.25	2.64 ± 1.02	0.0060 ± 0.0048	0.18 ± 0.06	1.60 ± 0.28	0.58 ± 0.10	0.22 ± 0.05	2.70 ± 0.37
jiang18	Lower sunny side	8.51 ± 1.27	23.05 ± 1.58	34.31 ± 2.65	0.84 ± 0.38	4.18 ± 1.06	1.48 ± 0.36	0.60 ± 0.23	2.75 ± 1.01	0.0059 ± 0.0050	0.17 ± 0.06	1.58 ± 0.29	0.57 ± 0.11	0.22 ± 0.05	2.69 ± 0.40
jiang18	Lower shady side	8.05 ± 1.76	22.05 ± 2.04	30.67 ± 4.95	0.84 ± 0.36	4.45 ± 1.12	1.58 ± 0.37	0.65 ± 0.24	2.74 ± 1.03	0.0059 ± 0.0043	0.18 ± 0.06	1.62 ± 0.31	0.59 ± 0.12	0.22 ± 0.05	2.76 ± 0.38
jiangA13	Upper sunny side	11.04 ± 3.34	26.46 ± 2.48	33.40 ± 4.93	1.14 ± 0.52	4.55 ± 1.14	1.66 ± 0.36	0.62 ± 0.25	3.13 ± 1.47	0.0040 ± 0.0033	0.13 ± 0.06	1.34 ± 0.35	0.48 ± 0.13	0.19 ± 0.06	2.68 ± 0.56
jiangA13	Upper shady side	11.19 ± 4.59	26.19 ± 4.15	33.40 ± 7.15	1.02 ± 0.44	4.30 ± 0.99	1.59 ± 0.20	0.56 ± 0.38	3.22 ± 0.42	0.0041 ± 0.0037	0.16 ± 0.15	1.42 ± 0.54	0.52 ± 0.39	0.19 ± 0.40	2.85 ± 0.26
jiangA13	Central sunny side	11.53 ± 3.55	26.29 ± 3.28	34.06 ± 5.86	1.02 ± 0.42	4.32 ± 0.97	1.58 ± 0.31	0.59 ± 0.22	3.10 ± 1.41	0.0038 ± 0.0034	0.12 ± 0.06	1.28 ± 0.35	0.46 ± 0.13	0.18 ± 0.06	2.58 ± 0.50
jiangA13	Central shady side	12.60 ± 3.23	27.52 ± 2.18	36.32 ± 7.10	1.12 ± 0.43	4.56 ± 0.93	1.66 ± 0.31	0.62 ± 0.21	3.02 ± 1.33	0.0040 ± 0.0032	0.13 ± 0.06	1.37 ± 0.34	0.49 ± 0.12	0.19 ± 0.06	2.56 ± 0.40

Table 6. Variation coefficients of phenotypic characters of bract scales and seeds from different crown layers of the three Chinese fir clones.

Clone Number	Position	CW (g) (%)	CD (cm) (%)	CL (cm) (%)	WPA (cm^2) (%)	WPP (cm) (%)	WPL (cm) (%)	WPW (cm) (%)	WPL/WPW (%)	OSW (g) (%)	SA (cm^2) (%)	SP (cm) (%)	SL (cm) (%)	SD (cm) (%)	SL/SW (%)
jiang26	Upper sunny side	33.23	14.24	13.96	46.77	24.70	21.72	39.67	42.07	72.73	25.83	15.12	14.92	21.13	14.97
jiang26	Upper shady side	28.58	7.56	9.34	50.01	27.45	23.72	43.96	40.92	76.28	25.18	15.80	14.50	26.15	16.12
jiang26	Central sunny side	32.60	11.69	12.34	51.45	26.67	23.28	41.28	43.10	51.53	27.41	15.46	15.38	20.10	16.67
jiang26	Central shady side	22.28	17.74	10.62	49.74	26.19	22.54	43.23	46.38	47.19	23.94	13.97	13.58	21.97	16.66
jiang26	Lower sunny side	21.11	12.34	9.24	51.02	27.16	23.83	41.95	52.04	59.49	27.73	16.15	15.80	22.04	15.90
jiang26	Lower shady side	29.43	10.93	7.24	54.74	29.37	25.44	45.26	45.38	47.51	24.39	13.96	14.81	17.02	16.46
jiang18	Upper sunny side	28.08	7.70	13.75	42.76	25.41	23.96	36.53	36.38	78.10	30.25	16.73	17.07	22.03	14.12
jiang18	Upper shady side	22.14	7.19	13.59	42.63	23.58	22.16	35.77	40.49	129.51	37.80	21.60	21.75	27.49	17.92
jiang18	Central sunny side	23.96	11.01	7.51	44.24	26.39	23.86	41.19	44.50	95.72	42.21	24.48	24.61	27.23	17.89
jiang18	Central shady side	23.91	5.33	12.98	44.74	25.43	23.18	38.94	38.59	80.78	32.62	17.79	17.99	21.12	13.84
jiang18	Lower sunny side	14.98	6.86	7.72	44.82	25.43	23.99	38.00	36.92	84.34	33.14	18.11	18.55	21.19	15.06
jiang18	Lower shady side	21.90	9.27	16.16	42.53	25.27	23.45	37.35	37.66	74.09	34.57	19.23	19.71	21.05	13.75
jiangA13	Upper sunny side	30.28	9.36	14.77	45.52	25.08	21.58	40.64	46.81	83.00	46.50	25.86	25.95	31.33	21.04
jiangA13	Upper shady side	41.04	15.86	21.40	43.58	22.98	20.43	37.80	42.18	90.27	92.47	38.14	38.85	39.77	25.55
jiangA13	Central sunny side	30.81	12.48	17.20	41.44	22.53	19.91	37.08	45.34	90.07	49.57	27.56	27.88	31.45	19.21
jiangA13	Central shady side	25.60	7.91	19.56	38.38	20.40	18.51	33.76	44.06	79.58	43.92	24.68	24.50	29.04	15.71

3.5. Correlation between Phenotypic Characters of Chinese Fir Cones and Seeds

Figure 2 shows that there were different degrees of correlation between the phenotypic characters of Chinese fir cones and seeds. OSW was positively correlated with SL ($p < 0.01$, r = 0.92), SA ($p < 0.01$, r = 0.95); and SP ($p < 0.01$, r = 0.92). SL was positively correlated with SA ($p < 0.01$, r = 0.97) and SP ($p < 0.01$, r = 0.99) and negatively correlated with SL/SW ($p < 0.01$, r = –0.95). SA was positively correlated with SP ($p < 0.01$, r = 0.98) and negatively correlated with SL/SW ($p < 0.01$, r = -0.89). SP was negatively correlated with SL/SW ($p < 0.01$, r = –0.93). WPL was positively correlated with WPA ($p < 0.01$, r = 0.80) and WPP ($p < 0.01$, r = 0.92) and negatively correlated with WPL/WPW ($p < 0.01$, r = - 0.96). WPA was positively correlated with WPP ($p < 0.01$, r = 0.94). The correlations between WPA and SP ($p < 0.01$, r = 0.71), SA ($p < 0.01$, r = 0.66), and SL ($p < 0.01$, r = 0.69) were low, as was the correlation between the WPP and SA ($p < 0.01$, r = 0.61). The correlations between CD and CW ($p < 0.01$, r = 0.68) and between CW and CL ($p < 0.05$, r = 0.60) were also low. Overall, the correlation of cone phenotype, bract scale phenotype, and seed phenotype was low. WPP was positively correlated WPA and WPW, and SW was positively correlated with SA, SP, and SW but not with SL.

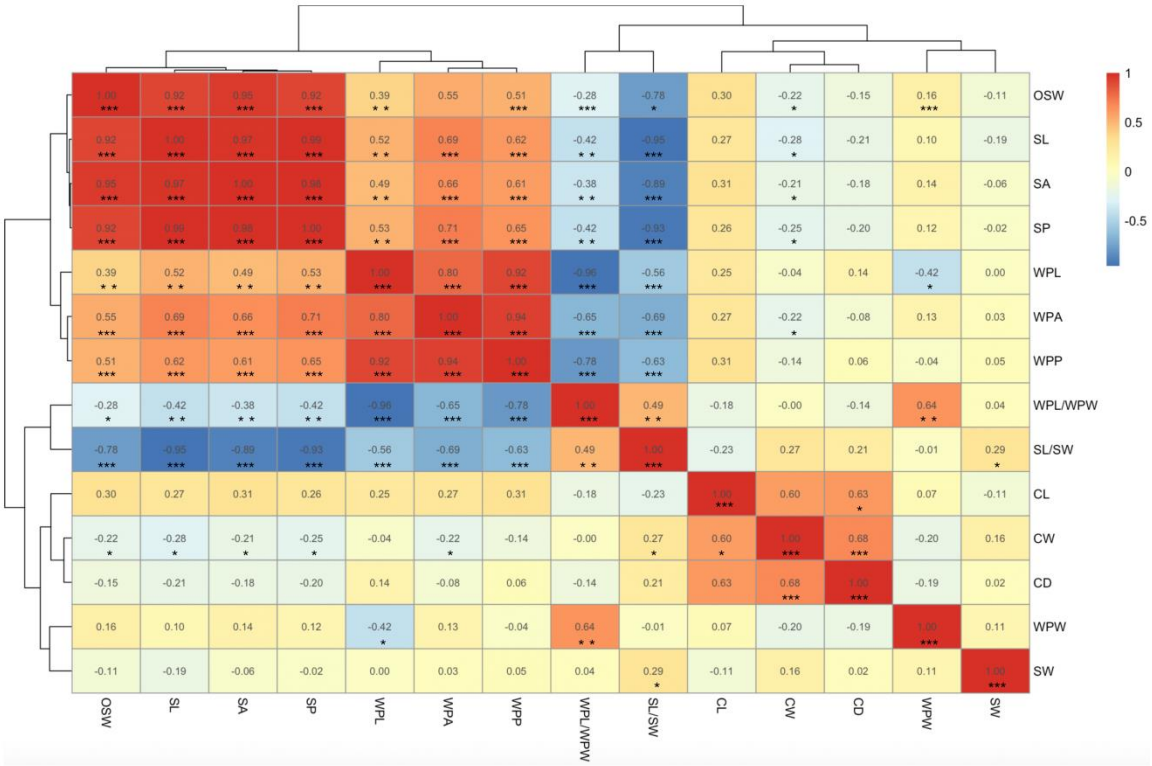


Figure 2. Results of correlation analysis and significant difference tests between Chinese fir cone and seed phenotypic characteristics.

4. Discussion

4.1. Effect of Different Clones and Layers on Seed Types

We found that the parent tree of Chinese fir with different fruit types in the Chinese fir seed orchard affected the total number of seeds produced by cones, the rate of good seeds, and the rate of seeds filled with tannin-like substance, but it did not affect the formation of empty seeds. In the jiang26 clone, the total number of seeds produced by cones decreased significantly with decreasing height of the crown layer; that is, the total number of seeds produced by cones in the upper layer of the crown was significantly higher than that in the lower layer of the crown. However, no significant difference in the total number of seeds produced by cones among the different crown layers was detected in the mother plants of the jiang18 and jiangA13 clones. This result indicates that for Chinese fir clones, the effect of seed setting (i.e., crown layer) is mainly due to the amount of fruit set by the mother plant, which depends on the nutrient supply. Yu et al. reported similar results for Chinese fir [31]. Additionally, Peter et al. reported that when the number of cone seeds of Spreading pine (*Pinus patula* Schltdl. et Cham.) in the upper part of the crown was large, resulting in nutrient deficiency, the number of seeds in the lower cones was small [32]. The percentage of seeds filled with tannin-like substance was significantly high for clone jiang26, and the percentage of empty seeds was significantly high level for clones jiang18 and jiangA13. The genetic difference among clones is an important factor that affects these two values. This scenario was also observed in Japanese larch (*Larix kaempferi* Lamb. Carr) [33]. In another study of three clones with different seed setting ability in the lower crown layer, Weng et al. showed that a higher number of clones resulted in a higher number of seeds filled with tannin-like substance [34]. During the development of Chinese fir seeds, the competition for nutrients among various seeds in the cones is extremely fierce. Gao et al. found that the proportion of seeds filled with tannin-like substance among total seeds collected from fruiting branches with five cones was >70%, whereas the value was only 40% for fruiting branches with only one cone [35].

The effect of crown layer on rate of seeds filled with tannin-like substance and rate of empty seed is different. In our Chinese fir seed orchard, we detected a high rate of good seeds and a low rate of seeds filled with tannin-like substance on the sunny side of the upper crown and a low rate of good seeds and a high rate of seeds filled with tannin-like substance on the shady side of the lower crown. In clone jiang26, the good seed rates on the upper sunny side and lower shady side were 44.22% and 12.56%, respectively, and the rates of seeds filled with tannin-like substance in these settings were 34.19% and 65.88%, respectively. In clone jiang18, the good seed rates on the upper sunny side and lower shady side were 22.12% and 11.10%, and the rates of seeds filled with tannin-like substance were 24.77% and 34.88%, respectively. Yu et al. [36] and Guan et al. [37] reported similar findings. The sunny side of the upper layer of the Chinese fir crown has good light environment conditions, strong photosynthesis, and rich nutrition, which are conducive to the normal development of Chinese fir embryos. In contrast, the shady side of the lower layer of the crown has weak light and poor nutrition conditions, resulting in abnormal development of embryos and endosperm. Aborted seeds are filled with tannins, resulting in the formation of a large number of seeds filled with tannin-like substance [38]. Our results show that the formation of empty seeds has little relationship with the crown layer of the mother tree of Chinese fir, which is consistent with results reported by Ye et al. [39]. This phenomenon is related to the widespread use of artificial pollination in Yangkou Forest. Artificial pollination can effectively eliminate the difference of pollination in different crown layers and different orientations. Determining how to eliminate the self-incompatibility caused by the affinity between artificial pollination and pollinated mother plants requires further research.

4.2. Effect of Different Clones and Different Layers on Seed Quality

The seed germination rate reflects the quality of seed and is also related to the early growth of seedlings [40]. Some researchers believe that excellent seed sources can be selected using the germination ability of seeds as a reference [41]. In our study, the germination rate of Chinese fir seeds was 32.28%. The germination rate of seeds from different parts of different clones also differed significantly, the high seed bearing clone in the lower crown layer have higher germination rate in the upper sun side, and the germination rate of seeds from the sunny side was higher than that of the shady side. The amount of sunlight on the sunny side is greater than that on the shady side, and therefore photosynthesis is stronger, and the endosperm has more nutrients, both of which are conducive to seed germination. We found that the seed germination rate of different Chinese fir clones was significantly related to seed size, with heavy seeds having a higher germination rate. This finding was similar to that reported by Bu et al. [42] but inconsistent with the research results of Chen et al. [43]. Therefore, to evaluate the quality of Chinese fir seeds in the future, we should not only pay attention to the seed germination rate, but also the seed size and weight. These biological characteristics will affect the quality of seedlings and the composition of seed orchard population [44,45].

4.3. Phenotypic Variation of Cones and Seeds

The diversity of phenotypic is generated by the combined action of genetic information and internal and external factors. It is an important representation of the genetic information of a population of organisms [46], and it is also the product of long-term adaptation and evolution [47]. In this study, we evaluated the cones and seeds of three Chinese fir clones that differed in the seed-bearing characteristics of cones in the lower part of the crown. To understand the level of genetic diversity of the population, we used nested variance to analyze the variation of phenotypic traits [48], including the variation of phenotypic traits between and within clones, the phenotypic differentiation coefficient, and repeatability. Most of the 14 phenotypic traits of the cones and seeds studied differed significantly among and within clones, indicating abundant genetic variation of Chinese fir cones. This result laid a foundation for the selection of excellent clones for use in seed orchards. The variation between clones was greater than that within clones, which indicates that Chinese

fir has wide adaptability to the environment [49]. Similar results were reported for Phoebe bournei (*Phoebe bournei* (Hemsl.) Yang) [50], Korean pine(*Pinus koraiensis* Sieb. et Zucc.) [51], and Pinus yunnanensis (*Pinus yunnanensis* Franch) [52]. Therefore, inter-clonal variation is not only affected by genetic diversity, but also affected by long-term restricted gene exchange and changes in geographical environmental factors. Its phenotypic differentiation is adaptive evolution in long-term selection [53].

In our study, the average $v_{(st)}$ of the three Chinese fir clones was 81.15%, which is higher than that of Picea crassifolia(*Picea crassifolia* Kom.) by 74.20% [25], and it is higher than that of Sawtooth oak(*Quercus acutissima* Carruth.) by 78.84% [54], as well as lower than that of Sinocalycanthus chinensis(*Calycanthus chinensis* Cheng et S. Y. Chang) by 89.30% [55]. Our results show that the phenotypic differentiation of cones and seeds of the three Chinese fir clones was in the middle of the range and that the differentiation among clones was higher than that within clones. We also found that the repeatability of 14 phenotypic traits was >89.00%, which is similar to that of Korean pine(*Pinus koraiensis* Sieb. Et Zucc.) [56]. They are also significantly higher than 77.67% of the phenotypic traits of Picea crassifolia [57] and 61.00% of Pinus radiata(*Pinus radiata* D. Don) [58]. Therefore, our results indicate that the yield and quality of Chinese fir cones and seeds are stable and that these traits can be stably inherited by their offspring and are less affected by the environment [59].

Phenotypic variation is the most direct manifestation of biological genetic variation, and therefore it is a major focus of phenotypic diversity research [60]. Among the 14 phenotypic traits of Chinese fir that we studied, the CV of OSW was the largest (77.51%), indicating that the number of seed types of different clones differs significantly. The CVs of CL and CD were the smallest, indicating that the cone phenotype was more stable. The CV of SL was small, which is basically consistent with reports of Conjugated oak(*Quercus franchetii* (Skan)) and Quercus mongolica(*Quercus mongolica* Fisch. ex Ledeb) [61,62]. Therefore, the plasticity of different indicators of phenotypic traits among the three Chinese fir clones and different layers of each clone in this study has great differences, and the plasticity of a class of traits (such as cone size, etc.) with strong correlation with fitness is generally low because it is less affected by the environment and relatively stable. The plasticity of a type of character (such as the weight of a single seed) with weak correlation with fitness is generally higher because it is greatly affected by the environment and changes greatly [63]. Our correlation analysis showed that the WPP was highly significantly positively correlated with WPA and WPWE, and OSW was highly significantly positively correlated with SA, SP, and SW, but not with SL. Similar findings were reported for Chinese fir [64–66], European red pine (*Pinus sylvestris* L.) [67], and European spruce (*Picea abies* (L.) Karst.) [68]. Therefore, SW can be used as an index to predict other seed traits in production.

5. Conclusions

In summary, we found that the clones with different seed-bearing characteristics in the lower crown layer had a great impact on the yield and quality of the Chinese fir seed orchard. When establishing a dwarfing Chinese fir seed orchard, the cone situation of different crown layers of different clones must be considered. Clones with more cones in the lower layer should be selected, and indicators such as seed yield, number of good seeds, number of seeds filled with tannin-like substance, and empty seeds as well as high seed weight and seed width should be used in the selection process. When building seed orchards, a good ecological environment with suitable sunshine and fertile soil is needed. Managers should pay attention to the development of each clone, regulate its vegetative and reproductive growth, and conduct artificial pollination to reduce the formation of empty seeds. If necessary, tree thinning, fruit thinning, fertilizer application, hormone application, and other measures should be taken to ensure that cones and seeds have sufficient nutritional conditions, which will improve the yield and quality of seeds.

Author Contributions: J.Z. conceived the project. Y.D. and D.Y. conducted on-site investigation and data collection. Y.D. and T.Y. conducted the statistical analysis. Y.D. wrote the first draft. J.Z.

contributed to improving the quality of the manuscript. All authors have read and agreed to the published version of the manuscript.

Funding: This work was supported by the National Natural Science Foundation of China (grant number 32171818) and Fujian Province Science and Technology Research Funding (grant number 2022FKJ05).

Data Availability Statement: Not applicable.

Acknowledgments: We thank the Yangkou State Forest Farm of Fujian Province for its careful management of the experimental site and the field staff who assisted in the investigation.

Conflicts of Interest: The authors declare that they have no competing interests.

References

1. Zhao, Q.; Yao, C.; Xie, H.; Lin, H.; Li, J.; Su, J.; Hong, T. Effects of endophytic fungi of Cunninghamia lanceolata on host physiological characteristics under mixed stress allelochemicals. *Chin. J. Appl. Env. Biol.* **2021**, *27*, 749–759. [CrossRef]
2. Kang, G.L. Comprehensive Analysis on the Causes of the Hollow and Astringent Seeds of Chinese Fir. *J. Zhejiang For. Coll.* **1997**, *14*, 88–93.
3. Fang, Y.; Yang, H.; Wu, H.; Lei, X.; Zhang, X.; Yang, C.; Huang, Z.; Chen, L.; Peng, Z. Genetic diversity analysis of Cunninghamia lanceolata in the 2nd and 2.5th Generation Seed Orchard. *J. Sichuan Agric. Univ.* **2022**, *40*, 371–378. [CrossRef]
4. Cheng, L.; Dai, J.; He, J.; Xie, L.; Liang, J.; Dong, L.; Lan, X.; Huang, K.; Bai, T.; Huang, H. Genetic diversity analysis and comprehensive evaluation of cone and seed quality of Cunninghamia lanceolata. *J. South. Agric.* **2021**, *52*, 2805–2813. [CrossRef]
5. Zhu, R.; Yang, Q.; Li, S.; Yang, C.; Cheng, X. Advances at Phenotypic Plasticity in Plant Responses to Environmental Factors. *J. Southwest For. Univ.* **2021**, *41*, 183–187. [CrossRef]
6. Chen, H.; Tao, Y.; Luo, Y.; Hu, Y.; Lan, Z. Analysis of Phenotypic Diversity of 10 Tea Plants in Southwest China. *Mol. Plant Breed.* **2022**, *2*, 1–17.
7. Xie, Y.; Yu, H.; Pang, Z.; Zhang, M.; Yu, H.; Zhang, S.; Zhao, X. Phenotypic diversity analysis and superior family selection of seed traits in six Acer species in northeast China. *Plant Sci. J.* **2021**, *39*, 610–619. [CrossRef]
8. Wahyuni, S.; Susilowati, M.; Bakri, A.; Bermawie, N. Fruit and seed variation of wild nutmeg (Myristica schefferi Warb.) in South Aceh, Indonesia. *IOP Conf. Ser. Earth Environ. Sci.* **2022**, *974*, 012067. [CrossRef]
9. Hongjing, D.; Sen, C.; Huiquan, Z.; Dehuo, H.; Jun, L.; Huazhong, L.; Hu, R.; Sun, Y.; Li, Y. Variation in the Growth Traits and Wood Properties of Chinese Fir from Six Provinces of Southern China. *Forests* **2016**, *7*, 192. [CrossRef]
10. Li, X.; Cai, K.; Zhao, Q.; Li, H.; Wang, X.; Tigabu, M.; Sederoff, R.; Ma, W.; Zhao, X. Morphological and comparative transcriptome analysis of three species of five-needle Pines: Insights Into phenotypic evolution and phylogeny. *Front. Plant Sci.* **2022**, *13*, 795631. [CrossRef]
11. Zhan, H.; Du, C.; Liu, X.; Pei, X.; Li, R.; Zhang, Y.; Zhang, S. Phenotypic and molecular analysis of three wild Scutellaria species in Shanxi Province. *Acta Agric. Boreali-Occident. Sin.* **2022**, *31*, 1–8. [CrossRef]
12. Wang, Y.; Song, C.; He, Z.; Zheng, M. Species Structure of Cunninghamia Lanceolata and Growth Retention Density of Large Diameter Wood and Site Effect. *J. Beihua Univ.* **2022**, *23*, 246–252. [CrossRef]
13. Verónica, L.; Mónica, B.; Claudia, D.; Rodrigo, D.R.; Andrea, Á. Inter-annual variability of Pinus pinea L. cone productivity in a non-native habitat. *New For.* **2020**, *51*, 1055–1068. [CrossRef]
14. Ayari, A.; Khouja, M.L. Ecophysiological variables influencing Aleppo pine seed and cone production: A review. *Tree Physiol.* **2014**, *34*, 426–437. [CrossRef]
15. Debain, S.; Curt, T.; Lepart, J.; Prevosto, B. Reproductive variability in Pinus sylvestris in southern France: Implications for invasion. *J. Veg. Sci.* **2003**, *14*, 509–516. [CrossRef]
16. Shen, Y.; Gao, H. Study on seed quality of different clones and crown height in Chinese Fir Seed Orchard. *J. Nanjing For. Univ.* **1997**, *1*, 85–88.
17. Hauke, K.M.; Borowiak, E.; Barzdajn, W.; Kowalkowski, W.; Korzeniewicz, R.; Wawro, T. Cone and Seeds Variability in Seed Orchards and Seed Stands of Pinus sylvestris. *Balt. For.* **2019**, *25*, 187–192. [CrossRef]
18. Frank, C.S.; Robert, K.C. Effect of seed weight on height growth of Douglas-fir (Pseudotsugamenziesii (Mirb.) Franco var. menziesii) seedlings in a nursery. *Can. J. Forest. Res.* **1985**, *15*, 1109–1115. [CrossRef]
19. Shen, X.H. "Dwarfing" of Seed Orchards is the Management Direction of Improved Seed Bases—Experience From Investigating Seed Orchards in Guangdong and Other Provinces (Regions). *For. Sci. Technol.* **2017**, *11*, 29. [CrossRef]
20. Scott, E.K.; Jim, S.; Michael, J.A.T.; Jeff, D.; Sara, L.; Marilyn, L.C.; Glenn, T.H. High-density Miniaturized Seed Orchards of Douglas-fir. *New For.* **2015**, *46*, 121–140. [CrossRef]
21. Michael, S.; Clint, H.; Joe, W.; Clare, H.; Steve, R. Effects of Crown-Pruning on Seed and Pollen Cone Production in Two Lodgepole Pine Seed Orchards in British Columbia. *New For.* **1995**, *10*, 133–143. [CrossRef]
22. Matsushita, M.; Nishikawa, H.; Tamura, A. Effects of Girdling Intensity, Pruning Season and Thinning on Tree Growth, Crown Vigor and Wound Recovery in Japanese Larch. *Forests* **2022**, *13*, 449. [CrossRef]

23. Zheng, Y.; Zhang, H.; Zhang, Z.; Zhou, Z.; Tong, J.; Huang, H. Effect of dwarfing on occurrence of female dtrobilus of Pinus massoniana and its effect on branch growth. *J. Northeast For. Univ.* **2021**, *49*, 1–5. [CrossRef]
24. Bilir, N.; Prescher, F.; Lindgren, D.; Kroon, J. Variation in Cone and Seed Characters in Clonal Seed Orchards of Pinus Sylvestris. *New For.* **2008**, *36*, 187–199. [CrossRef]
25. Lin, P.; Zhang, Z.; Guan, S.; Wang, N. Cone types and seed distribution characteristics of Cunninghamia lanceolata primary seed orchard in Mu Mountain Forest Farm. *J. Zhejiang A F Univ.* **1990**, *4*, 69–72.
26. Zhao, H.; Lu, D.; Liu, X.; Zhang, H.; Zhao, X.; Zhao, M.; Zhao, G.; Chen, G.; Xu, Y.Z. Phenotypic diversity of Picea crassifolia clones based on cones and seeds. *J. Cent. South Univ. For. Technol.* **2020**, *40*, 39–46. [CrossRef]
27. *GB 2772-1999*; Rules for Germination Inspection of Forest Seeds. State Quality and Technical Supervision: Beijing, China, 1999.
28. Qi, M.; He, G.; Li, G.; Chen, Y.; Zhi, J. Estimation of genetic parameters and selection of parents for high generation breeding of Cunninghamia lanceolata at different levels. *J. Northeast For. Univ.* **2011**, *39*, 4–8. [CrossRef]
29. Ling, J.; Xiao, Y.; Yang, G.; Ma, J.; Zhao, Q.; Yuan, H.; Wang, J.; Ma, W. Variation and selection of growth and shape and quality traits of clones of Sorbus bungeana. *For. Res.* **2019**, *32*, 149–156. [CrossRef]
30. Wang, W.; Cai, M.; Wan, J. Effects of different hormones on Seed Germination and seedling growth of Luan Huang. *For. Sci. Technol.* **2021**, *46*, 9–11. [CrossRef]
31. Yu, F.; Xiao, S.; Yu, R.; Huang, T.; Zheng, B.; Wang, Y.; Wu, Y. Prediction of seed yield and quality of Cunninghamia lanceolata by cone cutting method. *Seed* **1992**, *4*, 19–21. [CrossRef]
32. Peter, M.A.; Alice, A.O.; Jesse, O.O. Morphometrics of Pinus patula crown and its effect on cone characteristics and seed yield in Kenya. *J. Hortic. For.* **2020**, *12*, 94–100. [CrossRef]
33. Sui, J.; Zhang, Z.; Li, S.; Hou, Y.; Yang, N. Studies on the gamete production and seeds distribution in a cone among clones of Larix kaempferi (Lamb.) Carr. *J. Fujian Agric. For. Univ. Nat. Sci. Ed.* **2011**, *40*, 145–150. [CrossRef]
34. Weng, C.; Qi, M.; Hua, C.; Li, Z.; Bao, X.; Luo, X. Genetic analysis on seed sowing quality traits of Chinese-fir and causes study for their hollow, kernel and woody seeds. *J. Fujian For. Sci. Technol.* **2016**, *43*, 160–165. [CrossRef]
35. Gao, Z.; Shi, Z.; Xu, Y.; Zhu, Z.; Shen, R. Studies on the developmental physiology of Chinese Fir Seeds, the causes of astringent seeds and the measures to reduce abortion. *For. Res.* **2000**, *13*, 659–666. [CrossRef]
36. Yu, X.; Li, P.; He, F.; Lin, X.; Li, Y. Study on aborted seeds of Cunninghamia lanceolata and their astringent substances. *Acta Bot. Boreal. Occident. Sin.* **1989**, *9*, 252–256.
37. Guan, K.; Huang, J.; He, F. Seed yield and full grain rate of cones in Chinese Fir Seed Orchard. *J. Zhejiang For. Coll.* **1997**, *02*, 19–25.
38. Zhang, Y.; Zuo, D.; Chen, Y.; Xiong, S.; Wang, Z.; Lin, S. Anatomical observation of ovule of Cunninghamia lanceolata. *J. For. Environ.* **2017**, *37*, 142–147. [CrossRef]
39. Ye, P.; Chen, Y.; Jiang, S.; Guo, M.; Liu, D. Study on variation of seed viability of Cunninghamia lanceolata. *J. Nanjing For. Univ.* **1981**, *3*, 22–32.
40. Li, Y.; Liu, S.; Peng, G.; Qi, Q.; Liu, B.; Qi, L.; Gai, Y.; Jiang, X. Transition point from heterotrophic to autotrophic in germination and seedling growth of Masson pine. *J. Beijing For. Univ.* **2014**, *36*, 9–16. [CrossRef]
41. Zhang, L.; Wei, X.; Li, Z.; Lu, J. Comparison of morphology, germination characteristics and contents of Trachycarpus fortunei seeds from different geographical provenace. *Seed* **2016**, *35*, 36–40. [CrossRef]
42. Bu, H.; Du, G.; Chen, X.; Xu, X.; Liu, K.; Wen, S. Community-Wide Germination Strategies in an Alpine Meadow on the Eastern Qinghai-Tibet Plateau: Phylogenetic and Life-History Correlates. *Plant Ecol.* **2008**, *195*, 87–98. [CrossRef]
43. Chen, N.; Wang, P.; Wu, P.; Jia, Y.; Ma, X. Differences in seed biological characteristics of different half-sib Chinese fir. *J. For. Environ.* **2015**, *35*, 230–235. [CrossRef]
44. Cerabolini, B.; Ceriani, R.; Caccianiga, M.; Andreis, R.; Raimondi, B. Seed Size, Shape and Persistence in Soil: A Test on Italian Flora from Alps to Mediterranean Coasts. *Seed Sci. Res.* **2003**, *13*, 75–85. [CrossRef]
45. Arne, S.; Anne, C.; Lucy, C.; Lydia, K.; Guja, B.J.; Jimenez-Alfaro, B.; Larson, J.; Nicotra, A.; Poschlod, P.; Silveira, F.A.O.; et al. A Research Agenda for Seed-Trait Functional Ecology. *New Phytol.* **2019**, *221*, 1764–1775. [CrossRef]
46. Kortessis, N. Digest: The complex interplay of phenotypic variation and diversifying selection. *Evol. Int. J. Org. Evol.* **2021**, *75*, 2994–2995. [CrossRef] [PubMed]
47. Guo, W.; Li, Y.; Zhao, F.; Tie, J.; Liao, F.; Zhong, S.; Lin, C.; Ye, W. Phenotypic genetic diversity of Pinus elliottii × P. caribaea Morelet var.hondurensis clones. *Bull. Bot. Res.* **2019**, *39*, 259–266. [CrossRef]
48. Qiao, Q.; Feng, Z.; Ren, H.; An, K.; Zhang, L.; Sun, Z. Phenotypic diversity of wing fruites and seeds in natural populatuons of Acer truncatum Bunge in China. *Chin. J. Ecol.* **2017**, *36*, 2707–2715. [CrossRef]
49. Ou, Y.; Zheng, R.; Xiao, H.; Su, S.; Fang, L. Phenotypic genetic diversity of open-pollinated progenies of first generation Chinese fir seed orchard. *J. Cent. South Univ. For. Technol.* **2015**, *35*, 22–26. [CrossRef]
50. Yingang, L.; Xinhong, L.; Junwei, M.; Xiaomian, Z.; Li-an, X. Phenotypic variation in Phoebe bournei populations preserved in the primary distribution area. *J. For. Res.* **2018**, *29*, 35–44. [CrossRef]
51. David, K.K.; Qinhui, Z.; Xinxin, Z.; Luping, J.; Jinpeng, Z.; Jingyuan, W.; Khasa, D.P.; You, X.; Zhao, X. Phenotypic variability and genetic diversity in a Pinus koraiensis clonal trial in northeastern China. *Genes* **2020**, *11*, 673. [CrossRef]
52. Liu, Z.; Gao, C.; Li, J.; Miao, Y.; Cui, K. Phenotypic diversity analysis and superior family selection of industrial raw material forest species-Pinus yunnanensis Franch. *Forests* **2022**, *13*, 618. [CrossRef]

53. Gao, F.; Wen, S.; Wei, S.; Ou, H.B.; Wang, Z.H. Variation Analysis of Seed and Leaf Phenotypic Traits of Albizia Odoratissima from Different Provenances. *J. Cent. South Univ. For. Technol.* **2023**, *2*, 1–10. [CrossRef]
54. Lu, F.; Jie, X.; Han, B.; Qiao, J.; Dong, X.; Wu, D.; Lu, L.; Li, W. Analysis of phenotypic variation of Quercus acutissima natural population seeds. *For. Res.* **2021**, *34*, 174–179. [CrossRef]
55. Li, S.; Gan, X.; Han, H.; Xu, N.; Hou, Z.; Chen, Y.; Deng, X. Leaf Phenotypic Traits of tetracentron sinense, an endangered plant species. *For. Res.* **2016**, *29*, 687–697.
56. David, K.K.; Yuxi, L.; Dawei, Z.; Hongtao, L.; Zuoyi, F.; Jingyuan, W.; Wang, L.; Wang, Q.; Wang, D.; Chiang, V.L.; et al. Clonal variations in cone, seed and nut traits in a Pinus koraiensis seed orchard in Northeast China. *J. For. Res.* **2021**, *32*, 171–179. [CrossRef]
57. Lu, D.; Zhang, H.; Li, B.; Zhao, H. Phenotypic traits of half sibs-seeds and their offspring seddlings on Picea crassifolia superior individual trees. *Bull. Bot. Res.* **2018**, *38*, 377–383. [CrossRef]
58. Wu, H.X.; Ker, R.; Chen, Z.; Ivkovic, M. Balancing Breeding for Growth and Fecundity in Radiata Pine (Pinus radiata D. Don) Breeding Programme. *Evol. Appl.* **2020**, *14*, 834–846. [CrossRef] [PubMed]
59. Wei, J.; Chen, S.; Lu, X.; Zhang, F.; Pan, Z.; Liu, Y. Evaluation and selection of excellent provenances of Pinus koraiensis based on growth and wood properties. *J. Beijing For. Univ.* **2022**, *44*, 12–23. [CrossRef]
60. Huang, J.; Yuan, F.; Zhou, M.; Huang, T.; Zhang, Y.; Liang, Q. Phenotype correlation analysis and excellent germplasm screening of herb Bletilla Rchb. f. based on comprehensive evaluation from thirty-three geographic populations. *BMC Plant. Biol.* **2022**, *22*, 154. [CrossRef]
61. Chang, E.; Xiao, G.; Li, P.; Li, Y.; Zhang, Q.; Ding, Y.; Huang, C. Seed morphological characteristics and variation of Quercus franchetii. *J. West China For. Sci.* **2019**, *48*, 159–164. [CrossRef]
62. Liang, D.; Jiang, L.; Zhang, Q.; Zhao, X.; Zheng, Y.; Yu, S.; Feng, J. Variation of seed characters in 11 provenances and families of Quercus mongolica in Liaoning Province. *J. Northeast For. Univ.* **2019**, *47*, 1–5. [CrossRef]
63. Yang, X.; Xu, Y.; Gong, B.C. Diversity of Phenotypic Characters of Two Persimmon Resources in Dabie Mountains. *For. Res.* **2022**, *4*, 188–196. [CrossRef]
64. Cheng, L.; Chen, Q.; Chen, S.; Dai, J.; Dong, L.; Chen, X.; Tan, W.; Chen, D.; Huang, K.; Li, K.P.; et al. Study on cone and seed qualities among different Cunninghamia lanceolata clones. *Guangxi For. Sci.* **2021**, *50*, 1–7. [CrossRef]
65. Cheng, L.; Chen, X.; Tan, W.; Lan, X.; Chen, Q.; Chen, D.; Dai, J.; Huang, K.; Liang, Q.; Jia, S.; et al. Analysis on seed yield and quality in the second-generation seed orchard of Cunninghamia lanceolata. *Hubei Agric. Sci.* **2021**, *60*, 97–100. [CrossRef]
66. Cheng, L.; Li, K.; Dong, L.; Chen, D.; Tan, W.; Chen, Q.; Lan, X.; Dai, J.; Huang, K.; Yuan, Y.; et al. Seed quality analysis and comprehensive evaluation of different clones of Cunninghamia lanceolata. *Seed* **2021**, *40*, 98–103. [CrossRef]
67. Sevik, H.; Topacoglu, O. Variation and inheritance pattern in cone and seed characteristics of Scots pine (Pinus sylvestris L.) for evaluation of genetic diversity. *J. Environ. Biol.* **2015**, *36*, 1125–1130.
68. Trujillo-Moya, C.; George, J.; Fluch, S.; Geburek, T.; Grabner, M.; Karanitsch-Ackerl, S.; Konrad, H.; Mayer, K.; Sehr, E.M.; Wischnitzki, E.; et al. Drought Sensitivity of Norway Spruce at the Species' Warmest Fringe: Quantitative and Molecular Analysis Reveals High Genetic Variation Among and Within Provenances. *G3 Genes Genomes Genet.* **2018**, *8*, 1225–1245. [CrossRef]

Disclaimer/Publisher's Note: The statements, opinions and data contained in all publications are solely those of the individual author(s) and contributor(s) and not of MDPI and/or the editor(s). MDPI and/or the editor(s) disclaim responsibility for any injury to people or property resulting from any ideas, methods, instructions or products referred to in the content.

forests

MDPI

Article

Research on 3D Phenotypic Reconstruction and Micro-Defect Detection of Green Plum Based on Multi-View Images

Xiao Zhang [1,2], Lintao Huo [1], Ying Liu [1,*], Zilong Zhuang [1], Yutu Yang [1] and Binli Gou [1]

[1] Jiangsu Co-Innovation Center of Efficient Processing and Utilization of Forest Resources, College of Mechanical and Electronic Engineering, Nanjing Forestry University, Nanjing 210037, China
[2] Nanjing Institute of Agricultural Mechanization, Ministry of Agriculture and Rural Affairs, Nanjing 210014, China
* Correspondence: liuying@njfu.edu.cn

Abstract: Rain spots on green plum are superficial micro-defects. Defect detection based on a two-dimensional image is easily influenced by factors such as placement position and light and is prone to misjudgment and omission, which are the main problems affecting the accuracy of defect screening of green plum. In this paper, using computer vision technology, an improved structure from motion (SFM) and patch-based multi-view stereo (PMVS) algorithm based on similar graph clustering and graph matching is proposed to perform three-dimensional sparse and dense reconstruction of green plums. The results show that, compared with the traditional algorithm, the running time of this algorithm is lower, at only 26.55 s, and the mean values of camera optical center error and pose error are 0.019 and 0.631, respectively. This method obtains a higher reconstruction accuracy to meet the subsequent plum micro-defect detection requirements. Aiming at the dense point cloud model of green plums, through point cloud preprocessing, the improved adaptive segmentation algorithm based on the Lab color space realizes the effective segmentation of the point cloud of green plum micro-defects. The experimental results show that the average running time of the improved adaptive segmentation algorithm is 2.56 s, showing a faster segmentation speed and better effect than the traditional K-means and K-means++ algorithms. After clustering the micro-defect point cloud, the micro-defect information of green plums was extracted on the basis of random sample consensus (RANSAC) plane fitting, which provides a theoretical model for further improving the accuracy of sorting the appearance quality of green plums.

Keywords: green plum; SFM; 3D point cloud; point cloud segmentation; micro-defect detection

check for updates

Citation: Zhang, X.; Huo, L.; Liu, Y.; Zhuang, Z.; Yang, Y.; Gou, B. Research on 3D Phenotypic Reconstruction and Micro-Defect Detection of Green Plum Based on Multi-View Images. *Forests* **2023**, *14*, 218. https://doi.org/10.3390/f14020218

Academic Editor: Eric Casella

Received: 1 December 2022
Revised: 5 January 2023
Accepted: 22 January 2023
Published: 23 January 2023

Copyright: © 2023 by the authors. Licensee MDPI, Basel, Switzerland. This article is an open access article distributed under the terms and conditions of the Creative Commons Attribution (CC BY) license (https://creativecommons.org/licenses/by/4.0/).

1. Introduction

Detecting the surface defects of small-sized fruits such as green plums, jujubes, and nectarines on the basis of two-dimensional images is easily influenced by factors such as image acquisition angle, light change, and lens distortion at present. It is sometimes difficult to distinguish superficial micro-defects (rain spots, scars, pits, etc.), resulting in misjudgment and omission when sorting fruit appearance quality, which is the main problem affecting the accuracy of fruit defect screening. Janos et al. [1] took apples as the research object, applied the particle filter algorithm for post-image processing, and constructed a pixel-based PLS-DA model. The experimental results showed that the intact recognition rate of apples was 100%, and the damage recognition rate was 98%. LÜ Q, Wang J [2,3], and other scholars have carried out nondestructive testing based on two-dimensional images for insect eyes and fine damage to kiwifruit and jujube. The experimental results showed that the recognition rate of intact jujube samples was 98%, while that of pest samples was only 94%. The recognition error of fine scratches on kiwifruit was 14.5%, and the recognition rate of defective samples was much lower than that of intact samples. The three-dimensional reconstruction technology can display the three-dimensional structure of

small fruit in detail. For example, Wang et al. [4] used RGB-D technology based on Lab color information to segment mango using the Otsu segmentation method, and estimated mango size through depth information. Nguyen et al. [5] used RGB-D to collect 3D point cloud data of apples, segmented them using the Euclidean clustering method, and transformed them into two-dimensional images to realize the recognition of overlapping fruits. Wu [6] used a 3D laser scanner to collect the point cloud information of four sides of jujube. After preprocessing, such as point cloud filtering and outlier elimination, the point cloud model of jujube was established. The volume and surface area of jujube were calculated using the convex hull method, triangular grid method, and projection slice method. When using the rich information contained in the three-dimensional dense point cloud to detect the micro-defects on the surface of small fruit, the errors caused by the 2D image acquisition angle, light change, and lens distortion can be avoided as far as possible, the three-dimensional information of small fruit can be displayed in detail, and the detailed information of the fruit surface can be extracted through point cloud segmentation. However, there is little research on the detection of micro-defects on small fruit surfaces based on the 3D point cloud reconstruction model at present. We tried to propose a feasible theoretical method to build a 3D model and extract micro-defect information of a single green plum based on multi-angle images, which provided a research basis for further improving the accuracy of small fruit appearance quality sorting.

At present, 3D reconstruction technology has been widely used in the fields of dynamic face verification, urban scene classification, forest environment detection, 3D measurement of objects, etc. [7–10]. The SFM (structure from motion) algorithm is a three-dimensional reconstruction algorithm that determines the spatial and geometric relationship of the target by the movement of the camera shooting position. It is a very important algorithm in the field of 3D reconstruction [11–13]. Gomez Monoso F et al. [14] used SFM technology to accomplish 3D reconstruction, which overcame the overlapping errors under 2D image recognition and achieved the highest classification accuracy of 98% for actual pedestrians, billboards, printed advertisements, and posts. Gobbi B et al. [15] used SFM technology to model forests in three dimensions and derive ecological indicators describing forest conditions. Li S et al. [16] proposed a fast and integrated 3D reconstruction method for small static objects using the laser scanning and SFM algorithm. Experimental results showed that this method improves the speed, accuracy, completeness, and visual effect of 3D reconstruction of small objects. Yang Z et al. [17] obtained the key features of crop area using the algorithm based on vegetation index and scale-invariant feature transform (SIFT) matching. The comparison between the obtained phenotypic parameters and the manual measurement results showed that the root-mean-square error (RMSE) values of the plant height, leaf number, leaf length, and leaf angle were 1.82, 1.57, 2.43, and 4.7, respectively. The measurement accuracy of each index was greater than 80%. This study provides a convenient and fast method for extracting three-dimensional phenotypic parameters of crops. At present, institutions and scholars have carried out relevant research on 3D defect feature extraction, segmentation, and detection [18]. For example, Borsu V et al. [19] used feature extraction and classification techniques to accurately locate the position and deformation type of defects in the three-dimensional grid of the car body surface and marked the deformation position. Experiments showed that the reliable marking of the deformation area had sufficient accuracy. Tang P et al. [20] proposed three surface flatness defect detection algorithms and applied the algorithms to two different scanners based on the time of flight (TOF) and amplitude modulation continuous wave (AMCW) principles. The results showed that the scanning distance and angular resolution greatly affect the defect detection accuracy. Marani R et al. [21] proposed a three-dimensional reconstruction system for high-precision surface defect detection, which identified surface defects of small objects such as coins and drills, and solved the problem of occlusion. Experiments showed that the system has high detection accuracy and can reach a resolution of 15 μm. The above studies show that the detection method is accurate and effective, but there are few studies on fruit surface micro-defect detection based on a 3D point cloud reconstruction model.

The above research shows that the detection method is accurate and effective, but the research on micro-defect detection of small fruit surfaces based on the 3D point cloud reconstruction model is less. To solve the misjudgment and omission of micro-defect detection on the surface of small-sized fruits, such as green plums, caused by two-dimensional image acquisition angle, light change, and lens distortion, the accuracy of sorting the appearance quality of green plums was improved. In this paper, based on the multi-view two-dimensional image sequence of green plums, an improved SFM and PMVS algorithm based on similar graph clustering and graph matching is proposed to reconstruct the three-dimensional sparse and dense reconstruction of fresh green plums. High reconstruction accuracy is obtained to meet the requirements of subsequent green plum micro-defect (rain spot) detection. On the basis of a dense point cloud model of green plum, an improved adaptive segmentation algorithm based on Lab space is proposed to achieve the effective segmentation of micro-defects on green plum. This method greatly reduces the running time of the algorithm and obtains good segmentation results. Based on random sample consensus (RANSAC), the rain spot defect information of greengage is extracted, which provides a theoretical model for further improving the accuracy of the appearance quality sorting of green plum.

2. Materials and Methods

2.1. Test Sample

In May 2022, 100 samples of green plums were purchased online from Yunnan Province, China. The surface defects of green plums were diverse. According to the severity, green plums were divided into five categories: rot (the highest severity), crack, scar, rain spot, and intact. Among them, rot, crack, and scar were the most obvious, and the rain spot defects had the characteristics of being dispersed, shallow, and small, as shown in Figure 1. A typical rain spot defect of green plums was selected for multi-view image sequence acquisition, which made the experimental samples representative.



(**a**) (**b**) (**c**) (**d**) (**e**)

Figure 1. Classification of green plums samples: (**a**) decay; (**b**) scar; (**c**) crack; (**d**) spot; (**e**) intact.

2.2. Experimental Platform

The research adopted a self-built green plum image acquisition device platform, as shown in Figure 2; the test device consisted of an industrial camera, rotary table, light source, black box, etc. The camera was an MV-EM510 C industrial camera with a 4.0 mm focal length lens. The pixel size of the camera was 3.45 μm × 2.2 μm, the frame rate was 15 frames per second, and the exposure time was 30–5,000,000 μs. The camera was fixed to the dark box frame through a clamp, horizontally facing the center of the rotary table, and it was about 150 mm away from the measured object. The light source used two LED lights. The rotary table speed was 60 s per circle, and the rotation angle was 360°. In the center of the rotary table, a steel needle, painted white, with a length of 50 mm, was fixed. The system was connected to a computer via Ethernet.

2.3. Imaging

Zhang Zhengyou's calibration method [22] was used to calibrate the camera. This method has the characteristics of simple operation and high precision. When collecting images, uniform illumination and sufficient light should be ensured. Through the preliminary test, it was found that when collecting the information on a single green plum, due to the monochromatic and limited shape features of the green plums, the number of

feature points detected was scarce, and the effect of the SFM algorithm reconstruction in the later period was extremely poor with potential for failure. By adding a feature-rich calibration plate, the reconstruction effect was the best. Operation involved the use of a soft trigger, along with timer control, which was placed in the black box whiteboard to reduce the interference of complex environments. The distance between the lens and the green plums was 150 mm, and the height of the main optical axis was 200 mm. During the image acquisition, the fruit pedicle of the green plum sample was first inserted into the steel needle tip, the rotation was started, the light source and the focal length were adjusted, and when the sample was clearly displayed in front of the camera, it was started to work. The acquisition interval angle was set to 10°, the angle range was 0–360°, and the speed of rotary table was 30 s/r. The external MCU was used to send a pulse signal with a frequency of 1.2 Hz to trigger the camera to collect images, and the current frame data was saved in the camera buffer. Figure 3 shows a set of 36 rain spot green plum images taken from multiple angles. Each image was 3840 × 2160 pixels, and the image storage format was JPG.

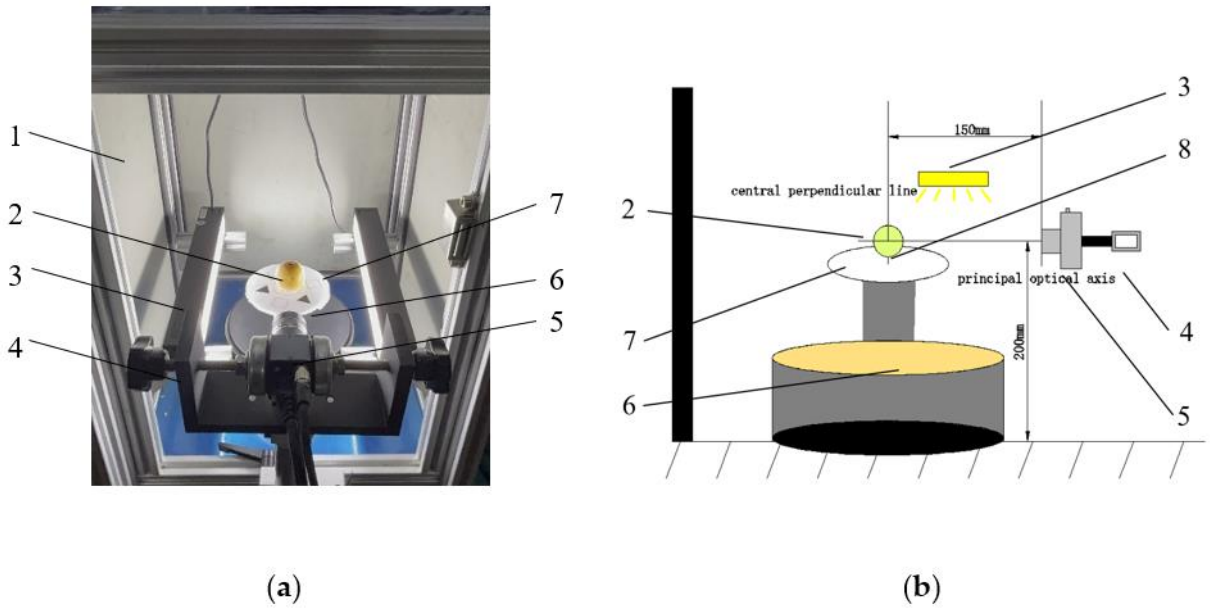


Figure 2. Classification of green plum samples: (**a**) experimental device; (**b**) experimental principle. 1. Dark box; 2. plum sample; 3. light source; 4. camera light source bracket; 5. camera; 6. rotary table; 7. calibration board; 8. steel needle.

2.4. Computing Environment

The hardware used was as follows: Win10 64 bit, i7 8750H 2.20 GHz CPU, 32 GB memory, NVIDIA GTX1070 GPU, and 8 G graphics. The software used was as follows: the OpenMVG platform was used to build the SFM framework, Ncut was used to realize the clustering of similar images, and Ceres Slover library was used to optimize the bundle adjustment. The point cloud processing and segmentation were completed by the large cross-platform open-source C++ point cloud library (PCL) under Microsoft Visual Studio and Robot Operating System. The effects were manually visualized with MeshLab and Cloud compare software.

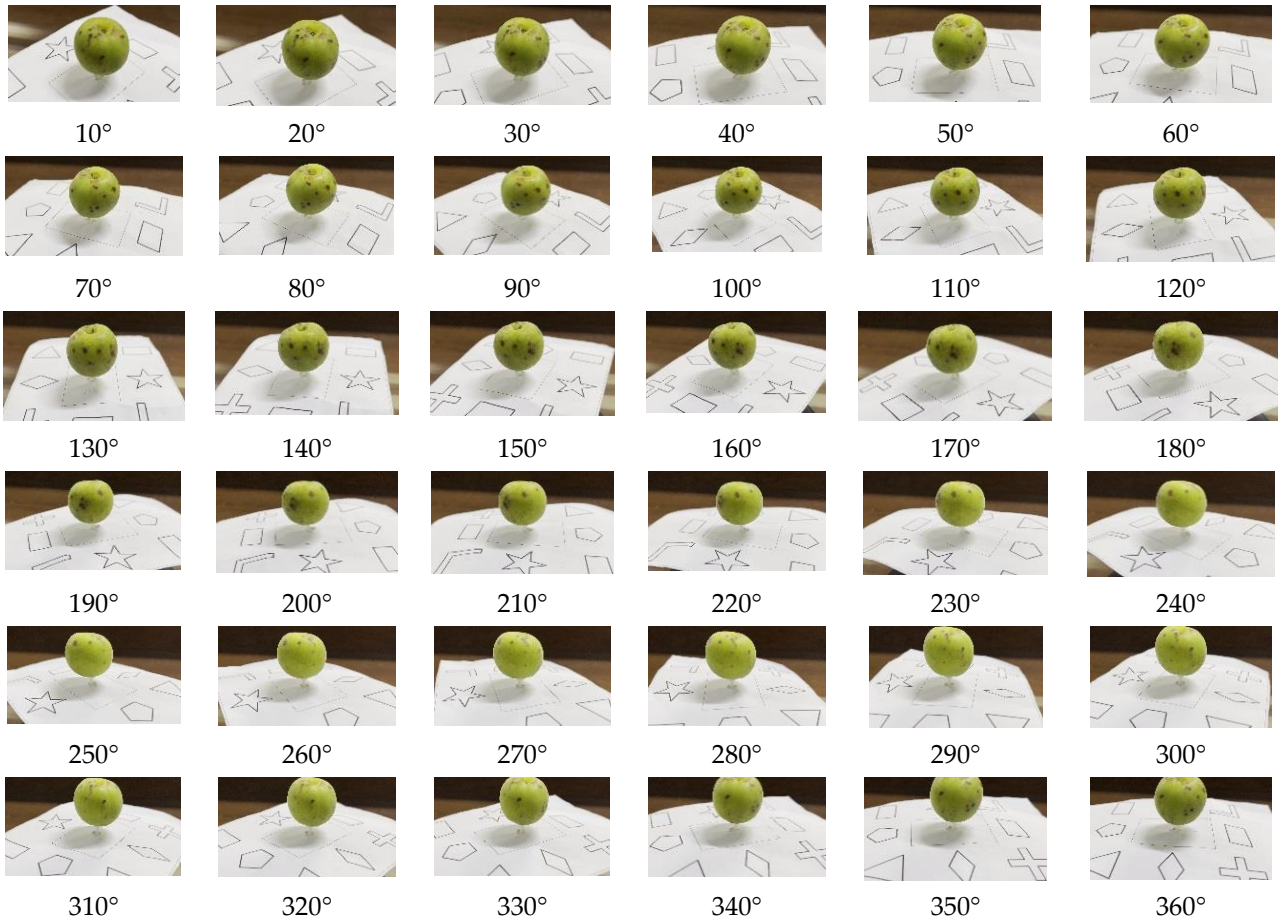


Figure 3. Set of 36 multi-angle rain spot plum images.

3. The 3D Point Cloud Information Construction of Plum

The multi-view images of green plum cause an inconspicuous disparity between images and high information repeatability because of the small scene. The coarse matching of features in traditional SFM reconstruction can cause a large number of repeated matches. It is necessary to eliminate and optimize the mismatching points, resulting in a long running time. Aiming at the low-parallax characteristics of the image dataset, this paper conducted similar graph clustering using the Fisher vector, as well as reduced some repetitive and unnecessary matching processes via parallel computing of intraclass matching and interclass fusion. On this basis, the dense reconstruction method was used to obtain the three-dimensional point cloud model of green plum. In this paper, the traditional incremental SFM 3D point cloud reconstruction framework was improved, and the improved 3D reconstruction algorithm framework is shown in Figure 4.

After the feature points were detected using the SIFT operator, similarity graph clustering and graph matching were used. Firstly, the similarity was determined by Fisher vector coding to classify the images; then, the matching graph was generated in each image class, and the image sequence trajectory was constructed. According to the matching graph results, the appropriate initialization image pairs were selected, and the global optimal camera pose parameters were found under the iterative optimization of distributed bundle adjustment. Then, the feature points were triangulated to obtain the sparse model of the three-dimensional point cloud, and the PMVS [23–25] algorithm was used for dense reconstruction, thereby improving the efficiency of the three-dimensional reconstruction process of plum from coarse to fine, as well as reducing the running time of the algorithm and the memory occupied by the computer during operation.

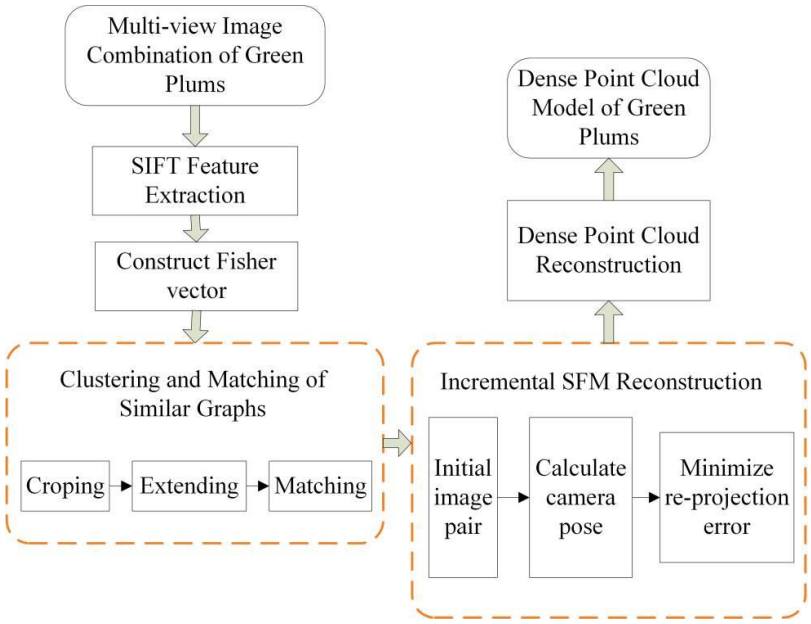


Figure 4. Block schematic of improved plum 3D reconstruction algorithm.

3.1. The 3D Reconstruction of Plum Based on Similarity Graph Clustering

3.1.1. Transformer Module

Using computer vision technology to reconstruct the three-dimensional reconstruction of green plums, it is necessary to obtain green plum images with different angles and continuous sequences. The key points on each image are called feature points. Image feature point detection is one of the cores of image processing. In this paper, SIFT was used to detect the feature points of the image. One green plum image was represented as a 128-dimensional feature vector set by the SIFT algorithm. The feature description algorithm mainly includes scale space pole detection, key point precise positioning, key point direction determination, and feature vector generation.

After using the SIFT operator to detect feature points and calculate feature descriptions, this paper used similarity judgment to divide the atlas before constructing matching. Using the distance between Fisher vectors to judge similarity can obtain higher efficiency and better results [26]. The set of SIFT features $X = \{x_1, x_2 \cdots, x_T\}$ was extracted from the image, the number of feature points extracted from different pictures was not the same, and the length of the feature vectors was different. It is necessary to raise the dimensions to form a 128-dimensional SIFT feature vector and eliminate the impact of light changes through normalization. Therefore, the similarity judgment measure of key points in two images can be carried out in a unified form. Since the feature points are independent of each other and obey the Gaussian distribution, the likelihood function can be defined by Equations (1)–(3).

$$L(X|\lambda) = \log P(X|\lambda) = \sum_{t=1}^{T} \log P(x_t|\lambda) \quad (1)$$

Here, $P(x_t|\lambda)$ is a weighted mixture of K Gaussian distributions.

$$P(x_t|\lambda) = \sum_{i=1}^{K} w_i P_i(x_t|\lambda) \quad (2)$$

The partial derivative of the likelihood function is calculated as a function of the weight w_i, mean μ_i, and variance σ_i, and then normalized to the Fisher vector.

$$\Phi_X = \left[f_{w_i}^{-1/2} \frac{\partial L(X|\lambda)}{\partial w_i}, f_{\mu_i^d}^{-1/2} \frac{\partial L(X|\lambda)}{\partial \mu_i^d}, f_{\sigma_i^d}^{-1/2} \frac{\partial L(X|\lambda)}{\partial \sigma_i^d} \right] \tag{3}$$

A smaller Fisher distance results in a higher similarity of the two images. Accordingly, a similarity graph $C_i = (v_i, \varepsilon_i)$ is constructed, where ε_i represents the weight of the connection edge between the image pairs, which is obtained by the difference between the global extremum of Fisher distance and the distance of the image pair v_i, so as to obtain the positive correlation between the weight size and the similarity size [27]. By using the multi-cluster image clustering method to construct similar image clustering [28], the bad matching pairs can be detected by loop consistency to avoid the cumulative error caused by the wrong matching hidden in the long path [29].

$$\{C_k | C_k = (v_k, \varepsilon_k)\} \tag{4}$$

When constructing an image cluster using Equation (4), two constraints need to be satisfied:

(a) The number of images $|v_i|$ in each image cluster must not be higher than the upper bound $\Delta_{up} = 12$;
(b) Associated images between image clusters must have an overlap rate $\varepsilon_k \geq 0.7$.

3.1.2. Incremental SFM Sparse Reconstruction

The incremental motion recovery structure was obtained for each image class and its matching map based on similarity, which mainly included (1) calculating the fundamental matrix, (2) merging tracks, (3) finding the initial image pair, (4) calculating the camera pose and triangulating the coordinates, and (5) minimizing the reprojection error. The computation was repeated using distributed beam method parity to obtain more 3D points and globally better camera poses t, R. The loop was iterated to achieve an incremental motion recovery structure until all images in the trajectory were processed. The minimum spanning tree was used to fuse t and R corresponding to different image classes so as to obtain the global sparse reconstruction results of green plum.

3.1.3. Dense Point Cloud Reconstruction

In order to meet the subsequent analysis of the bruise point cloud data and the requirements of segmenting defects, the information needs to be thickened; the 3D thickened point cloud model was obtained using the face slice-based PMVS algorithm. Each feature point in the sparse point cloud was projected onto the source image, and then the geometric information of that feature point was diffused to the surrounding area; the points that were repeatedly diffused were screened out by consistency comparison.

3.2. Green Plum Point Cloud Reconstruction Results and Analysis

3.2.1. Comparison of Feature Point Matching Results with Different Thresholds

SIFT was selected for feature point detection. The feature points were matched according to the Euclidean distance of the descriptor between the two feature points. The matching point pairs with the shortest distance and the ratio of the nearest distance to the second nearest distance less than the set threshold H were selected. The number of matches should be moderate. A large number of matches would result in a longer computation time and larger reconstruction error, while a small number would result in poor model accuracy. The error rate of matching should be as small as possible so that the error rate of matching pairs with different threshold values H can be compared and the best threshold value H can be selected. By comparison, it was found from Table 1 that a threshold value of 0.7 gave the best results for all indicators combined.

Table 1. Feature point matching results for different thresholds.

Thresholds	Time (s)	Points	Error Points	Error Rate
0.5	9.52	88	1	1.14
0.6	9.88	106	5	4.72
0.7	10.06	159	8	5.03
0.8	12.92	272	25	9.19
0.9	18.67	506	70	13.83

3.2.2. Comparison of the Results of Different SFM Reconstruction Algorithms

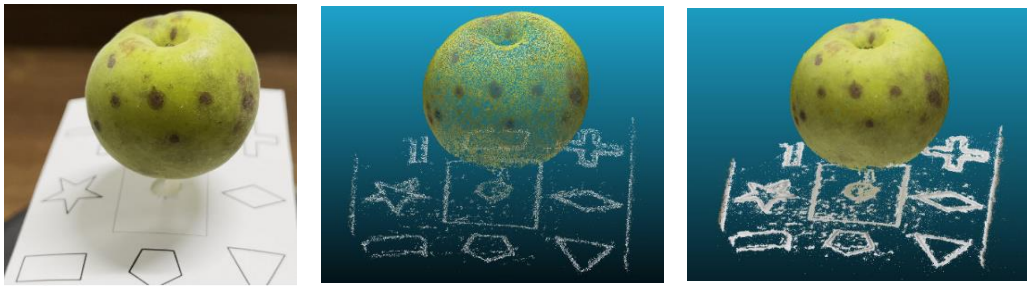
In order to verify the improved algorithm proposed in this paper, the green plum image sequences (36 images) acquired above were input into Bundler [30], Visual SFM [31,32], and the improved algorithm proposed in this paper, and the total running time T_{total} of the algorithm, the mean value of camera range error $\overline{RE}$, and the mean value of camera pose error $\overline{PE}$ were taken as the experimental indices for the evaluation of efficiency and accuracy. According to Section 3.1.1, $\Delta_{up} = 12$, $\varepsilon_k \geq 0.7$, the experimental results are shown in Table 2. From the experimental results, it can be seen that the algorithm proposed in this paper had the lowest running time and the best results in terms of $\overline{PE}$ and $\overline{RE}$.

Table 2. Experimental results of different SFM reconstruction algorithms.

Algorithm	Images	T_{total}	Range Error $\overline{RE}$	Pose Error $\overline{PE}$
Bundler	36	76.32	0.035	0.973
Visual SFM	36	38.93	0.021	0.692
Baseline Version of OpenMVG	36	35.37	0.022	0.675
Proposed Approach	36	26.55	0.019	0.631

3.2.3. Comparison of the Results of Different SFM Reconstruction Algorithms

Using the modified SFM sparse reconstruction, the reconstruction result was obtained, as shown in Figure 5b. Using the PMVS algorithm, the results of the dense reconstruction were as shown in Figure 5c. A featurerich calibration plate was added to make sure that the reconstruction effect was the best. Comparison of sparse and dense reconstructed models of the green plum point cloud is shown in Table 3.



(**a**) (**b**) (**c**)

Figure 5. Comparison of sparse and dense point cloud reconstructions of green plum. (**a**) Rain spot green plum image. (**b**) Improved SFM sparse reconstruction. (**c**) Dense reconstruction.

Table 3. Comparison of sparse and dense reconstructed models of the green plum point cloud.

Model	Time (s)	Data Size (MB)	Points
Sparse point cloud reconstruction	37	8.32	221,405
Dense point cloud reconstruction	125	70.51	2,000,692

4. Adaptive Segmentation of Green Plum Micro-Defect (Rain Spot) Detection Based on Dense Point Cloud

In this paper, the point cloud was preprocessed to remove the background and other interference areas, an improved adaptive segmentation method based on the Lab color space was used to achieve effective segmentation and clustering of the green plum rain spot point cloud, and the defect information of the green plum rain spot was extracted on the basis of RANSAC plane fitting. The details are shown in Figure 6.

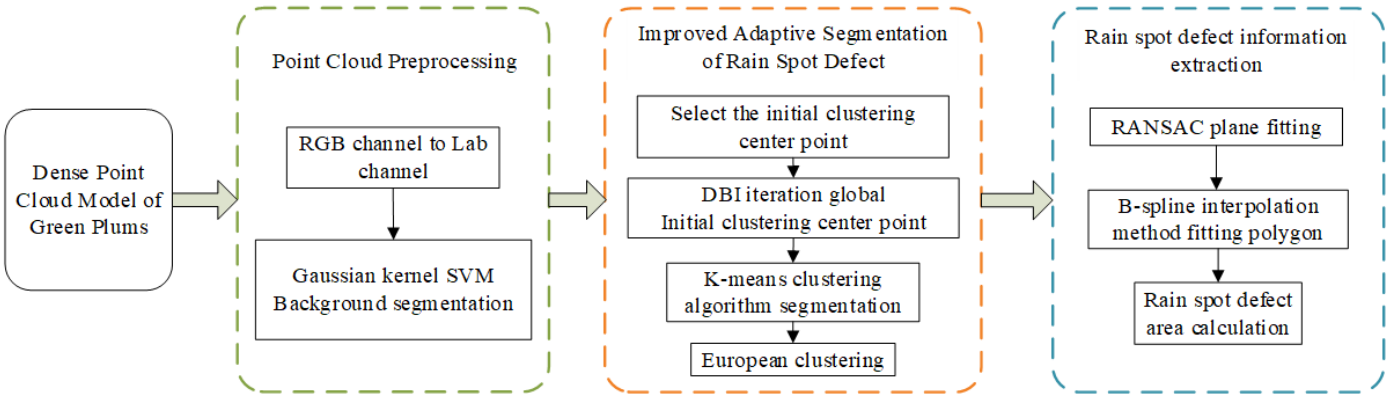
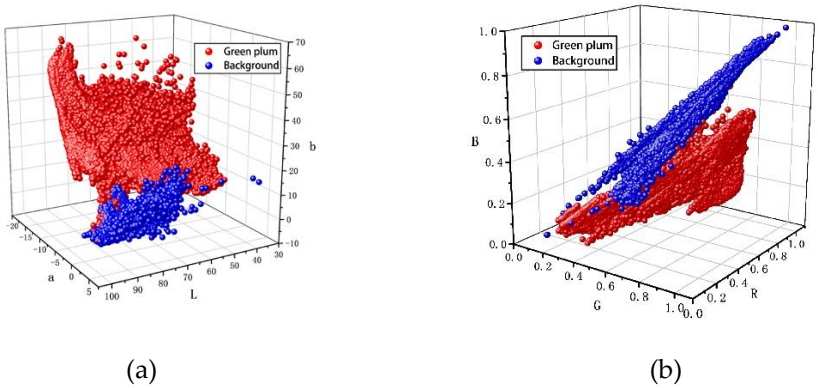


Figure 6. Block schematic of the detection of micro defects in green plums.

4.1. Point Cloud Preprocessing

In order to extract the green plum point cloud, the point cloud was first converted from the RGB color space to the Lab color space, which is more in line with the human visual senses. Due to the influence of the experimental light environment, the color intensity value of the reconstructed point cloud fluctuated greatly. The distributions of the background point cloud and the green plum point cloud in RGB color space is shown in Figure 7a. The distributions of the background point cloud and the green plum point cloud in Lab color space is shown in Figure 7b. There was a large overlap area between the two. It was impossible to accurately distinguish the two using threshold segmentation based on color features alone.



(a) (b)

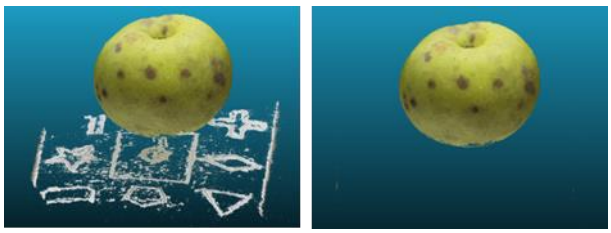
Figure 7. Distribution of plum and background point cloud in different color space. (**a**) The distributions of the background point cloud and the green plum point cloud in RGB color space. (**b**) The distributions of the background point cloud and the green plum point cloud in Lab color space.

The support vector machine (SVM) was used as the binary classifier, and the RBF radial basis function was selected as the kernel function to deal with the nonlinear situation, which has appropriate hyperplane parameters that can be adjusted more simply and quickly than the polynomial kernel function. The normalized data matrix was used as the input data of the SVM model, and the point categories were used as the output data of the SVM model. The training and test results are shown in Table 4.

Table 4. Comparison of point cloud data classification results.

Color Space	Training Set			Test Set		
	Accuracy	Background Error	Green Plums Error	Accuracy	Background Error	Green Plums Error
Lab	98.7%	0.01%	2.4%	99.4%	0.0%	1.3%
RGB	99.7%	0.1%	0.7%	98.6%	0.0%	2.9%

In the training set, the classification accuracy of SVM in the RGB color space was 99.7%, while the classification accuracy in the Lab color space was 98.7%; better results were obtained in the RGB color space. However, in the test set, the classification accuracy in the RGB space was 99.16%, and the classification accuracy in the Lab color space was 99.4%. The results show that the conversion of RGB to Lab color space could obtain a wider color gamut and more color performance. From the test results, it can be seen that the misclassification points mainly focused on the misclassification of green plum points into background points. In view of the rich color changes on the surface of green plum, the Lab color space had a higher generalization ability than RGB. The results before and after background segmentation are shown in Figure 8 a,b.



(a) (b)

Figure 8. Before and after green plum background segmentation. (**a**) The results before background segmentation. (**b**) The results after background segmentation.

4.2. Rain Spot Defect Information Extraction

An improved adaptive segmentation algorithm based on the Lab color space is proposed to effectively segment the point clouds of rain spot defects of green plum. In order to avoid the initial clustering center randomly selected by the K-means algorithm being too close, this paper iteratively obtained the global initial clustering center by improving the maximum and minimum distance method. Firstly, two initial data points with the farthest distance were selected; however, the traditional maximum and minimum distance method needed to traverse the Euclidean distance between each point in the dataset $X(n)$, and then the two points with the largest distance were selected as the initial clustering center points [33,34]. In this paper, two methods with time complexity $O(N^2)$ were used to determine the largest initial point.

Through the global initial clustering center determined by the Davies–Bouldin index (DBI), the pixels on the surface of the green plum were classified to realize the segmentation of the rain spot defect. The DBI uses interclass distance and intraclass dispersion, i.e., the ratio of the sum of intra-cluster distance to the sum of inter-cluster distance [35,36].

(1) Plane fitting based on RANSAC

RANSAC was used to perform plane fitting on each cluster class clustered by defects of rain spots, and the number of iterations k and error tolerance range dis_{error} were set. The number of iterations is responsible for ensuring that the RANSAC algorithm can perform enough epochs to find the best model estimation, and the error tolerance range indicates that the points are allowed to be distributed within the range of distances from the prediction model [37–40].

Two parameters, iteration number k and error tolerance range dis_{error}, are determined by control variables. According to the comprehensive analysis of segmentation accuracy, completeness, and segmentation quality, the optimal error tolerance threshold of the model was 0.007. Under the condition of a threshold of 0.007, the iteration rounds were compressed, and it was determined that the parameters stabilized when the iteration rounds reached eight times. After iterative optimization, RANSAC was applied to perform plane fitting on each cluster of rain spots, as shown in Figure 9a,b and the point clouds corresponding to the cluster were projected onto the plane along the normal direction, as shown in Figure 9c,d.

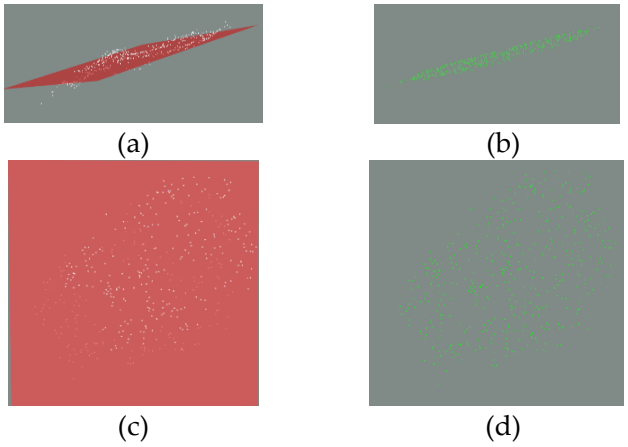


Figure 9. Plane fitting based on RANSAC. (**a**,**b**) Plane fitting on each cluster of two different rain spots. (**c**,**d**) The cluster were projected onto the plane along the normal direction.

The point clouds were decentered and rotated to the XOY plane, as shown in Figure 10a,b. The experimental results show that the average error of the Z-axis coordinate of the point cloud rotated to the XOY plane was 0.0152, which meets the actual needs.

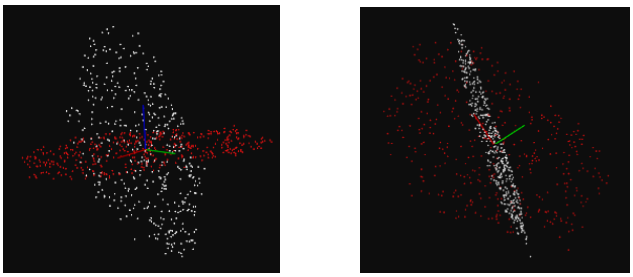


Figure 10. Point clouds translation to the XOY plane by decentralization and rotation. (**a**,**b**) The different point clouds were decentered and rotated to the XOY plane.

(2) Green Plum Rain Spot Defect Roundness and Area

The shape of rain spot defects was usually a small circular patch, while cracks and damage defects were irregular. In order to prevent other types of defects from being extracted, screening is needed. In this paper, the B-spline interpolation method was used to fit the polygon. According to the definition of "roundness", a positive circle is 1; the closer the contour value is to 1, the closer the contour is to the circle. The curve contour was transformed into a sampling point, the sampling density was set, and the distance between the sampling points was calculated to approximate the length of the curve. The triangular area of all sampling points was calculated using the Helen formula and combined to obtain the total curve contour area.

4.3. Extraction Results and Analysis of Plum Rain Spot Defect Information

(1) Adaptive segmentation results and analysis of plum rain spots

The improved adaptive segmentation algorithm was compared with the traditional K−means and K−means++ [41,42] algorithms. The average running time of the improved adaptive segmentation algorithm was 2.56 s, while the average running time of the traditional K−means and K−means++ algorithm was 6.91 s and 4.06 s. The segmentation comparison result is shown in Figure 11, where the red area denotes the segmented rain spot defect. The algorithm effectively improved the adaptability of segmentation, reduced the number of subsequent iterations of the K−means algorithm, and greatly reduced the computational complexity of the algorithm. Therefore, the improved adaptive segmentation algorithm showed faster segmentation speed and better results. The clustering of rain spot defect point clouds by Euclidean clustering provided a basis for extracting the information of rain spot defects. Different colors represented different color channels, and the red box area was the part of defect segmentation error. The clustering result is shown in Figure 12.

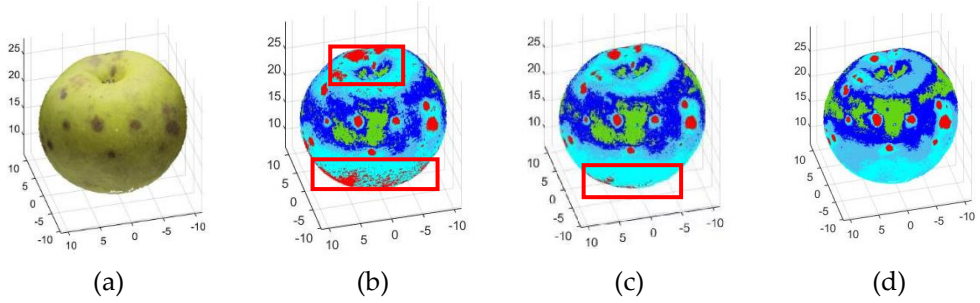


Figure 11. Comparison of different algorithms for plum rain spot segmentation: (**a**) 3D point cloud; (**b**) traditional K—means algorithm; (**c**) K—means++ algorithm; (**d**) proposed method.

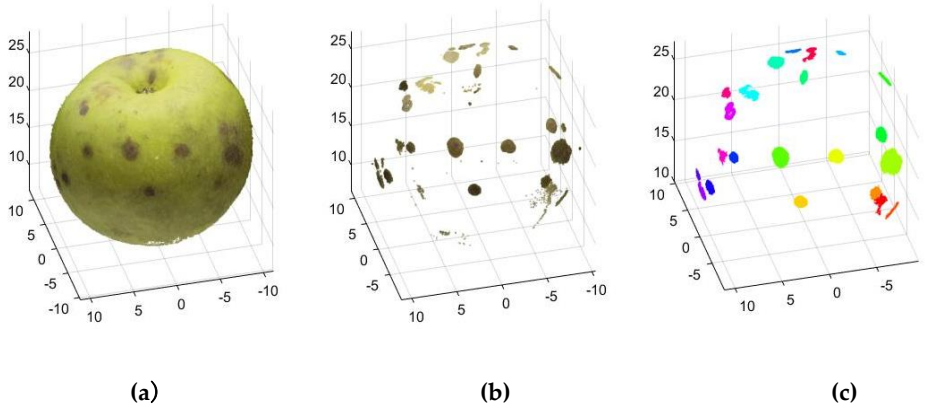


Figure 12. Plum rain spot clustering result. (**a**) 3D point cloud; (**b**) Primitive european clustering (**c**) European clustering through different color channels.

(2) Comparison of different bar curve fitting results

The point cloud contour points were extracted, and the polygon was fitted using the B-spline interpolation method. The micro-defect fitting results of different curve control points and curve orders were compared, as shown in Figure 13. It can be seen that when the number of curve control points was 10 and the order of the spline curve was 3, the fitted curve was best.

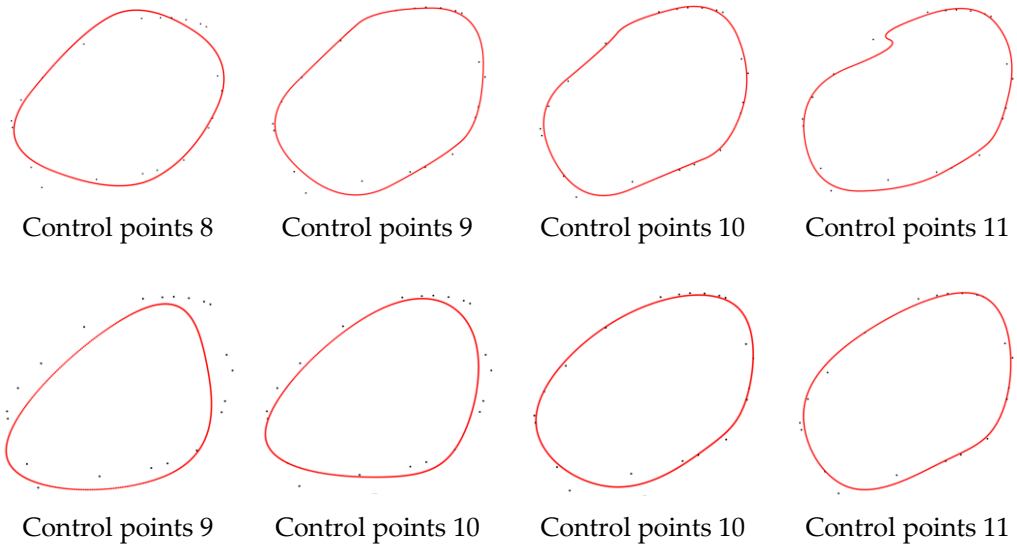


Figure 13. Fitting results of micro-defects with different curve control points and orders. (**a**) The fitting of different control points when the curve order was 3. (**b**) The fitting of different control points when the curve order was 4.

(3) Comparison of green plum rain spot defect area calculation results

After segmentation, extraction, and fitting of three-dimensional rain spot defects, the triangular area of all sampling points was calculated in turn, and the total curve contour area was obtained by merging. During the experiment, the same sample parameter values were measured three times; the mean value was taken as the final manual measurement result of the sample and compared with the surface area obtained by the three-dimensional rain spot defect segmentation and extraction calculation. The experimental results show that with the increase in sampling point density, the relative error gradually decreased. When the sampling density was 80, it reached the optimal value, and the relative error did not change with the subsequent increase in sampling density. The results are shown in Table 5.

Table 5. Comparison of green plum rain spot defect area calculation results.

Sampling Density	Circumference (mm)	Area (mm^2)	Roundness	Actual Area (mm^2)	Relative Error
1	8.5585	5.2399	0.8989	6.0137	0.1289
5	8.9922	5.9295	0.9215		0.0143
10	9.0122	5.9664	0.9231		0.0081
20	9.0160	5.9735	0.9234		0.0069
40	9.0169	5.9750	0.9235		0.0067
80	9.0170	5.9754	0.9235		0.0066
100	9.0171	5.9754	0.9235		0.0066
120	9.0171	5.9755	0.9235		0.0066

5. Conclusions

(1) Aiming at the point cloud reconstruction of green plums, a multi-view two-dimensional image sequence of green plums was obtained using the established image acquisition device platform. An improved in-motion recovery SFM and PMVS algorithm based on similar graph clustering and graph matching was proposed to reconstruct the three-dimensional sparse and dense reconstruction of the green plums. Compared with the traditional algorithm, the running time of the algorithm was lower, at only 26.55 s, and the camera optical center error mean and pose error mean were also the smallest, at 0.019 and

0.631, respectively. A high reconstruction accuracy was obtained to meet the subsequent green plum micro-defect (rain spot) detection requirements.

(2) For the detection of green plum micro-defects (rain spots), an improved adaptive segmentation algorithm based on the Lab color space was proposed for the dense point cloud model of green plums to realize the effective segmentation of green plum micro-defects (rain spots). The experimental results show that the average running time of the improved adaptive segmentation algorithm was 2.56 s, while the average running time of the traditional K-means and K-means++ algorithm was 6.91 s and 4.06 s. It represented a faster segmentation speed and better effect than the traditional K-means and K-means++ algorithms. After the segmentation and clustering of the micro-defect point cloud, the micro-defect (rain spot) information of green plums was extracted on the basis of random sampling consistency plane fitting, thus providing a theoretical model for further improving the accuracy of appearance quality sorting of green plums.

(3) Shortcomings: misjudgment of micro-defect detection on the surface of small fruits such as green plum caused by 2D image acquisition angle, light change, lens distortion, etc. In view of the above problems, we tried to propose a feasible theoretical method to build a 3D model and extract micro-defect information of a single green plum based on multi-angle images, and the model performance basically met the requirements, but it took a long time. Based on the above research foundation, the reconstruction algorithm, image processing, and other aspects will be optimized to further reduce the time under the condition of meeting the requirements of detection accuracy. It is also possible to carry out 3D reconstruction and micro-defect detection of the green plum sample group so as to further improve the detection efficiency and provide reference for the actual sampling application.

Author Contributions: Conceptualization, X.Z. and Y.L.; data curation, X.Z.; formal analysis, Z.Z.; funding acquisition, Y.L.; investigation, Y.L. and B.G.; methodology, X.Z.; project administration, Y.L.; resources, Y.L.; software, X.Z., L.H. and Z.Z.; supervision, L.H.; validation, L.H.; visualization, X.Z.; writing—original draft, X.Z.; writing—review & editing, Y.L. and Y.Y. All authors have read and agreed to the published version of the manuscript.

Funding: This research was funded by the Jiangsu agricultural science and technology innovation fund project (Project#: CX(18)3071). LIU YING. Research on key technologies of intelligent sorting for green plum; 2020 Jiangsu graduate research and innovation plan (Project#: KYCX20_0882): Research on green plum defect sorting system based on artificial intelligence. LIU YANG.

Data Availability Statement: Not applicable.

Acknowledgments: The authors would like to extend their sincere gratitude for the technical support from the Nanjing Institute of Agricultural Mechanization, Ministry of Agriculture and Rural Affairs.

Conflicts of Interest: The authors declare no conflict of interest.

References

1. Keresztes, J.C.; Goodarzi, M.; Saeys, W. Real-time pixel based early apple bruise detection using short wave infrared hyperspectral imaging in combination with calibration and glare correction techniques. *Food Control* **2016**, *66*, 215–226. [CrossRef]
2. Lü, Q.; Tang, M. Detection of hidden bruise on kiwi fruit using hyperspectral imaging and parallelepiped classification. *Procedia Environ. Sci.* **2012**, *11*, 1172–1179. [CrossRef]
3. Wang, J.; Nakano, K.; Ohashi, S. Detection of external insect infestations in jujube fruit using hyperspectral reflectance imaging. *Biosyst. Eng.* **2011**, *108*, 345–351. [CrossRef]
4. Weilin, W.; Changying, L. Size Estimation of Sweet Onions Using Consumer-grade RGB-depth Sensor. *J. Food Eng.* **2014**, *142*, 231–234.
5. Nguyen, T.T.; Vandevoorde, K.; Wouters, N.; Kayacan, E.; De Baerdemaeker, J.G.; Saeys, W. Detection of Red and Bicoloured Apples on Tree with an RGB-D Camera. *Biosyst. Eng.* **2016**, *146*, 156–159. [CrossRef]
6. Wu, M.; Luo, H.; Li, C.; Yi, X.; Yousaf, K.; Soomro, S.A.; Ji, F.; Chen, K. Automatic measurement method of volume and surface area of jujube based on laser point cloud. *Int. Agric. Eng.* **2019**, *28*, 261–268.
7. Li, J.B.; Hu, Z.W.; Xu, Z.D.; Guo, Y.Q. Three-dimensional dynamic analysis of ancient buildings with novel high damping isolation trenches. *J. Vib. Control.* **2022**, *28*, 2409–2420. [CrossRef]

8. Li, Q.; Yuan, P.; Lin, Y.; Tong, Y.; Liu, X. *Pointwise Classification of Mobile Laser Scanning Point Clouds of Urban Scenes Using Raw Data*; Nanjing Forestry University, College of Mechanical and Electronic Engineering: Nanjing, China, 2021; p. 024523.
9. Li, Z.; Zou, H.; Sun, X.; Zhu, T.; Ni, C. 3D Expression-Invariant Face Verification Based on Transfer Learning and Siamese Network for Small Sample Size. *Electronics* **2021**, *10*, 2128. [CrossRef]
10. Che, J.; Sun, Y.; Jin, X.; Chen, Y. 3D Measurement of Discontinuous Objects with Optimized Dual-frequency Grating Profilometry. *Meas. Sci. Rev.* **2021**, *21*, 197–204. [CrossRef]
11. Jing, R.; Gong, Z.; Zhao, W.; Pu, R.; Deng, L. Above-bottom biomass retrieval of aquatic plants with regression models and SfM data acquired by a UAV platform-a case study in Wild Duck Lake Wetland, Beijing, China. *ISPRS J. Photogramm. Remote Sens.* **2017**, *134*, 122–134. [CrossRef]
12. Jordi, G.; Ricardo, S.; Joan, R.; Alexandre, E.; Eduard, G. Fuji-SfM dataset: A collection of annotated images and point clouds for Fuji apple detection and location using structure-from-motion photogrammetry. *Data Brief* **2020**, *30*, 105591.
13. Schonberger, J.L.; Frahm, J.M. Structure-from-Motion Revisited. In Proceedings of the IEEE Conference on Computer Vision and Pattern Recognition, Las Vegas, NV, USA, 27–30 June 2016; pp. 4104–4113.
14. Gomez-Donoso, F.; Castano-Amoros, J.; Escalona, F.; Cazorla, M. Three-dimensional reconstruction using SFM for actual pedestrian classification. *Expert Syst. Appl.* **2023**, *213*, 119006. [CrossRef]
15. Gobbi, B.; Van, R.A.; Gasparri, N.I.; Vanacker, V. Forest degradation in the Dry Chaco: A detection based on 3D canopy reconstruction from UAV-SfM techniques. *For. Ecol. Manag.* **2022**, *526*, 120554. [CrossRef]
16. Li, S.; He, Y.; Li, Q.; Chen, M. Using Laser Measuring and SFM Algorithm for Fast 3D Reconstruction of Objects. *J. Russ. Laser Res.* **2018**, *39*, 591–599. [CrossRef]
17. Yang, Z.; Han, Y. A Low-Cost 3D Phenotype Measurement Method of Leafy Vegetables Using Video Recordings from Smartphones. *Sensors* **2020**, *20*, 6068. [CrossRef]
18. Zhou, Y.; Tuzel, O. Voxelnet: End-to-end learning for point cloud based 3d object detection. In Proceedings of the IEEE Conference on Computer Vision and Pattern Recognition, Salt Lake City, UT, USA, 18–23 June 2018; pp. 4490–4499.
19. Borsu, V.; Yogeswaran, A.; Payeur, P. Automated surface deformations detection and marking on automotive body panels. In Proceedings of the 2010 IEEE International Conference on Automation Science and Engineering, Toronto, ON, Canada, 21–24 August 2010; pp. 551–556.
20. Tang, P.; Akinci, B.; Huber, D. Characterization of three algorithms for detecting surface flatness defects from dense point clouds [C]//Three-Dimensional Imaging Metrology. *Int. Soc. Opt. Photonics* **2009**, *7239*, 197–208.
21. Marani, R.; Roselli, G.; Nitti, M.; Cicirelli, G.; D'Orazio, T.; Stella, E. A 3D vision system for high resolution surface reconstruction. In Proceedings of the 2013 Seventh International Conference on Sensing Technology (ICST), Wellington, New Zealand, 3–5 December 2013; pp. 157–162.
22. Zhang, Z. A Flexible New Technique for Camera Calibration. *IEEE Trans. Pattern Anal. Mach. Intell.* **2000**, *22*, 1330–1334. [CrossRef]
23. Furukawa, Y.; Ponce, J. Accurate, Dense, and Robust Multi-View Stereopsis. In Proceedings of the IEEE Computer Society Conference on Computer Vision and Pattern Recognition, San Francisco, CA, USA, 13–18 June 2010; 32, pp. 1362–1376.
24. Saravan, N.; Siddabattuni, V.N.S.K.; Ramachandran, K.I. A comparative study on classification of features by SVM and PMVS extracted using Morlet wavelet for fault diagnosis of spur bevel gear box. *Expert Syst. Appl.* **2008**, *35*, 1351–1366. [CrossRef]
25. Wang, A.; An, N.; Zhao, Y.; Iwahori, Y.; Kang, R. 3D Reconstruction of Remote Sensing Image Using Region Growing Combining with CMVS-PMVS. *Int. J. Multimed. Ubiquitous Eng.* **2016**, *11*, 29–36. [CrossRef]
26. Scharstein, D.; Szeliski, R. A Taxonomy and Evaluation of Dense Two-Frame Stereo Correspondence Algorithms. *Int. J. Comput. Vis.* **2002**, *47*, 7–42. [CrossRef]
27. Florent, P.; Jorge, S.; Thomas, M. Improving the Fisher Kernel for Large-Scale Image Classification. In Proceedings of the European Conference on Computer Vision, Heraklion, Greece, 5–11 September 2010.
28. Zhu, S.; Shen, T.; Zhou, L.; Zhang, R.; Wang, J.; Fang, T.; Quan, L. Parallel Structure from Motion from Local Increment to Global Averaging. In Proceedings of the ECCV, Tel Aviv, Israel, 23–27 October 2017.
29. Shen, T.; Zhu, S.; Fang, T.; Zhang, R.; Quan, L. Graph-based consistent matching for structure-from-motion. In Proceedings of the ECCV 2016, Amsterdam, The Netherlands, 11–14 October 2016.
30. Snavely, N.; Seitzs, M.; Szeliski, R. *Modeling Worldfrom Internet Photo Collections*; Kluwer Academic Publishers: Dordrecht, Netherlands, 2008.
31. Johannes, L.S.; Enliang, Z.; Jan-Michael, F.; Pollefeys, M. Pixelwise view selection for unstructured multi-view stereo. In Proceedings of the ECCV 2016, Amsterdam, The Netherlands, 11–14 October 2016; pp. 501–518.
32. Moulon, P.; Monasse, P.; Marlet, R. Adaptive Structure from Motion witha Contrario Model Estimation. In Proceedings of the Asian Conference on Computer Vision; Springer: Berlin/Heidelberg, Germany, 2012; pp. 257–270.
33. Wang, F.F.; Li, Q.; Zhang, M.J. Research on improvement of k-means clustering Algorithm. *Gansu Sci. Technol.* **2017**, *46*, 68–70.
34. Pham, T.; Nguyenthihong, D.; Vovan, T. Improving the ANFIS Forecating Model for Time Series Based on the Fuzzy Cluster Analysis Algorithm. *Int. J. Fuzzy Syst. Appl. IJFSA* **2022**, *11*, 1–20. [CrossRef]
35. Wang, Q.L.; Qiao, F.; Jiang, Y.H. Improved K-means algorithm based on aggregation distance parameter. *Comput. Appl.* **2019**, *39*, 2586–2590.

36. Kumar, A.; Kumar, S. Color image segmentation via improved K-means algorithm. *Int. J. Adv. Comput. Sci. Appl.* **2016**, *7*, 46–53. [CrossRef]
37. Zhang, H.X.; Zhang, Y.E. K-means clustering color image segmentation method based on Lab space. *J. Gannan Norm. Univ.* **2019**, *40*, 44–48.
38. Kumar, R.; Srivastava, R.; Srivastava, S. Image segmentation using hybrid color K-means approach. *Int. J. Comput. Vis. Image Process. (IJCVIP)* **2017**, *7*, 79–90. [CrossRef]
39. Su, Y.L.; Ping, X.L.; Li, N. A planar extraction algorithm based on RANSAC 3D point cloud. *Laser&Infrared* **2019**, *49*, 780–784.
40. Arslan, A.; Erteneinan, M. A comparative study for obtaining effective Leaf Area Index from single Terrestrial Laser Scans by removal of wood material. *Measurement* **2021**, *178*, 109262. [CrossRef]
41. Yu, M.; Wenjuan, C. Optimization and Parallelization of Fuzzy Clustering Algorithm Based on the Improved Kmeans++ Clustering. *IOP Conf. Ser. Mater. Sci. Eng.* **2020**, *768*, 072106.
42. Du, W.; Zhu, Y.; Li, S.; Liu, P. Spikelets detection of table grape before thinning based on improved YOLOV5s and Kmeans under the complex environment. *Comput. Electron. Agric.* **2022**, *203*, 385–392. [CrossRef]

Disclaimer/Publisher's Note: The statements, opinions and data contained in all publications are solely those of the individual author(s) and contributor(s) and not of MDPI and/or the editor(s). MDPI and/or the editor(s) disclaim responsibility for any injury to people or property resulting from any ideas, methods, instructions or products referred to in the content.

forests

MDPI

Article

The Species Richness-Environment Relationship for Cherries (*Prunus* subgenus *Cerasus*) across the Northern Hemisphere

Chen-Long Fu [1], Chun-Ping Xie [2], Muhammad Idrees [3], Xian-Gui Yi [1], Xian-Rong Wang [1] and Meng Li [1,*]

[1] Co-Innovation Center for Sustainable Forestry in Southern China, College of Biology and the Environment, Nanjing Forestry University, Nanjing 210037, China
[2] Biology Department, Qiongtai Normal University, Haikou 571127, China
[3] College of Life Science, Neijiang Normal University, Neijiang 641112, China
* Correspondence: limeng@njfu.edu.cn

Abstract: Understanding large-scale patterns of biodiversity and their drivers remains significant in biogeography. Cherries species (*Prunus* subgenus *Cerasus*, Rosaceae) are economically and ecologically important in ecosystems and human agricultural activities. However, the mechanisms underlying the patterns of the species richness–environment relationship in *Cerasus* remain poorly understood. We collected and filtered worldwide specimen data to map the species richness of *Cerasus* at the global scale. The map of *Cerasus* species richness was created using 21,043 reliable recorded specimens. The center of *Cerasus* diversity was determined using spatial cluster analysis. Stepwise regression analysis was carried out using five groups of 21 environmental variables and an integrated model was included to assess the impact of the overall environment. We calibrated each of the four integrated models and used them to predict the global *Cerasus* species richness and that of the other continents. Our results revealed that *Cerasus* species have two centers of diversity (the southwest of China and Honshu Island in Japan) with differing environmental variables influencing the distribution patterns of these two centers. In the southwest of China, hygrothermal conditions are the main driving factor while in Japan, habitat heterogeneity is the main driving factor. The relationship between the abundance of *Cerasus* and the various groups of factors generally supports both the productivity and the habitat heterogeneity hypotheses. However, these hypotheses do not fully explain the *Cerasus* species richness pattern, indicating that other factors such as historical environment, topography, and human activities likely played a role in pattern formation. The high level of habitat heterogeneity and better hygrothermal conditions may have played an important role in the establishment of its globally consistent richness–climate relationship. Our results can provide valuable information for the classification and conservation of *Cerasus* natural resources as well as contribute to furthering our understanding of biogeography at a global scale.

Keywords: *Cerasus*; global geographical patterns; environmental variables; hypothesis; species richness

check for updates

Citation: Fu, C.-L.; Xie, C.-P.; Idrees, M.; Yi, X.-G.; Wang, X.-R.; Li, M. The Species Richness-Environment Relationship for Cherries (*Prunus* subgenus *Cerasus*) across the Northern Hemisphere. *Forests* **2023**, *14*, 193. https://doi.org/10.3390/f14020193

Academic Editor: Maciej Pach

Received: 5 December 2022
Revised: 16 January 2023
Accepted: 18 January 2023
Published: 19 January 2023

Copyright: © 2023 by the authors. Licensee MDPI, Basel, Switzerland. This article is an open access article distributed under the terms and conditions of the Creative Commons Attribution (CC BY) license (https://creativecommons.org/licenses/by/4.0/).

1. Introduction

Species richness is a fundamental measure of species diversity and the basis for biodiversity conservation strategies [1,2]. Geographical patterns of species richness provide essential information for the planning of conservation districts and the management of biodiversity [3], especially under global climate changes [4].

To further understand the mechanisms underlying the species richness patterns, many hypotheses have been proposed and tested [5–9]. The contemporary environment, mainly including climate (temperature, precipitation, and climate seasonality) and habitat heterogeneity, is typically expected to be the primary driver of species richness at a global scale [8,10]. As a result, two types of hypotheses, the energy hypothesis and the habitat heterogeneity hypothesis, have gained widespread attention. According to the energy

hypothesis, energy is the main driver of species richness in an area, with higher energy areas having higher species richness [11]. The energy hypothesis can be divided into the productivity hypothesis, the cold tolerance hypothesis, the water-energy dynamics hypothesis, and so on, depending on the effect of different forms of energy on species diversity [5,7,12,13]. According to the habitat heterogeneity hypothesis, regions with more complex ecosystems and higher spatial heterogeneity provide more ecological niches, thus accommodating more species and increasing species richness [8]. However, species richness is influenced by several factors and processes [14–16]. Furthermore, a growing number of studies has shown that mechanisms underlying species richness are complex and cannot be explained by one hypothesis [15,17]. Therefore, the species richness distribution patterns and their formation mechanisms are still worth discussing. Recent studies are gradually exploring the distribution patterns of species richness and their formation mechanisms at the genera level [18–20].

Prunus species are commercially important fruit (plums, apricots, peaches, and cherries) and ornamental trees. The genus is thought to have originated in East Asia and is widely distributed both in the temperate zone of the Northern Hemisphere and in the subtropical and tropical forests of Asia, Africa, South America, and Australia. As the genus *Prunus* contains several subgenera, most of which have economically important tree species within each subgenus, researchers have mostly focused on a particular subgenus [21]. The subgenus *Cerasus*, as known as cherry, is widely distributed in the temperate regions of the Northern Hemisphere. Cherries are economically and ecologically important trees with great commercial value [22,23]. Fruits are accepted as nutrient-dense foods with relatively low caloric content. They have significant amounts of bioactive components including polyphenols, fiber, vitamin C, carotenoids, and potassium [24]. The flowering cherry is one of the most popular ornamental trees in the world. Some species could be used for vegetation restoration due to their adaptability [25]. The cherry also provides food for birds and mammals in the forest, allowing its seed to spread [26]. In recent years, research on *Cerasus* has focused on the exploitation of specific species, physiological and biochemical aspects, genetic variation, and phylogeny [23,27–30]. The relationship between species richness and environmental variables in *Cerasus* has not been adequately explored. Exploring the distribution pattern of species richness and its relationship with environmental variables will facilitate resource conservation of *Cerasus* as well as systematic and evolutionary research of the genus.

In this study, we combined *Cerasus* species distribution data and environmental variables to (i) assess the relative importance of contemporary climate and habitat heterogeneity on the species richness patterns of subgenus *Cerasus*; and (ii) assess the difference in higher *Cerasus* species richness regions caused by energy or/and spatial heterogeneity.

2. Materials and Methods

2.1. Species Distribution Data

The geographical distribution data of subgenus *Cerasus* were obtained from herbarium specimens recorded by the Global Biodiversity Information Facility (GBIF, https://www.gbif.org/ (accessed on 6 May 2022)) and Chinese Virtual Herbarium (CVH, https://www.cvh.ac.cn/ (accessed on 6 May 2022)). All species names were standardized according to Catalogue of Life (COL, 2019 Annual Checklist, http://www.catalogueoflife.org/annual-checklist/2019/ (accessed on 15 August 2022)). The following steps have been implemented to improve species records: (1) All records were double-checked to ensure the accuracy of the coordinates and specimen records that lacked coordinates were replaced by selecting the coordinates of a point on the map based on the recorded location; (2) all cultivars were not considered in this study; (3) for some species like *Prunus avium*, only wild records were kept; (4) *P. yedoensis* is believed to have originated in a nursery in Tokyo, and then spread throughout Japan [31]. Therefore, a point was placed in Tokyo to replace its distribution. The final list included 79 species and infraspecific units (Supplementary Table S1).

The global administrative area vector map was downloaded from the GADM database (https://gadm.org/data.html (accessed on 15 August 2022)). To minimize the effects of the area on species richness, by overlapping the distribution maps with the 300 × 300 km grid cells in ArcGIS 10.2, the global administrative area vector map was converted to gridded distributions with a 300 × 300 km spatial resolution. The area of the grid cells was not significantly correlated with species richness at the global scales ($p > 0.05$). The total number of species in each grid cell was used to calculate the species richness.

2.2. Environmental Data

To estimate the effects of environmental variables on large-scale patterns of *Cerasus* species richness, we chose 21 variables to analyze the association between species richness and environmental variables. The environmental variables were grouped into five types: environmental energy availability, water availability, climate seasonality, habitat heterogeneity, and soil properties (Table 1).

Table 1. Environment variables and their abbreviations used in the analyses.

Groups	Abbreviations	Environmental Variables
Environmental energy availability	MAT	Mean annual temperature (°C)
	MTWQ	Mean temperature of the coldest quarter (°C)
	MTCQ	Mean temperature of the warmest quarter (°C)
	PET	Potential evapotranspiration (mm)
	PETmin	Minimum monthly potential evapotranspiration (mm)
Water availability	MAP	Mean annual precipitation (mm)
	AET	Actual evapotranspiration (mm)
	WD	Water deficit (mm)
	PWQ	Precipitation of warmest quarter (mm)
	PCQ	Precipitation of coldest quarter (mm)
Climate seasonality	ART	Annual range of temperature (°C)
	TSN	Temperature seasonality (standard deviation of monthly mean temperatures × 100)
	PSN	Precipitation seasonality (standard deviation of monthly precipitation)
Habitat heterogeneity	RELE	Range of elevation (m) within each grid cell
	RMAT	Range of mean annual temperature (°C) within each grid cell
	RMAP	Range of mean annual precipitation (mm) within each grid cell
Soil properties	AWC	Available water storage capacity
	RBD	Reference bulk density (kg/dm^3)
	USDA	The relative proportion of different grain sizes of mineral particles in soil
	OC	Organic carbon (% weight)
	CEC	Cation exchange capacity (cmol/kg)
	TEB	Total exchange bases (cmol/kg)
	pH	Hydrogen ion concentration
	ECE	Electrical conductivity (dS/m)

Energy availability variables included the mean annual temperature (MAT, °C), mean temperature of the warmest quarter (MTWQ, °C), mean temperature of the coldest quarter (MTCQ, °C), potential evapotranspiration (PET, mm), and minimum monthly potential evapotranspiration (PETmin, mm). Water availability variables included the mean annual precipitation (MAP, mm), actual evapotranspiration (AET, mm), water deficit (WD, mm), precipitation of warmest quarter (PWQ, mm), and precipitation of coldest quarter (PCQ, mm). Due to the results of the precipitation models being consistent with the rainfall models

developed by Xu et al., MAP was used to represent rainfall [20]. Climate seasonality variables included an annual range of temperature (ART, °C), temperature seasonality (TSN), and precipitation seasonality (PSN). Habitat heterogeneity included the range of elevation (RELE, m), range of mean annual temperature (RMAT, °C), and range of mean precipitation (RMAP, mm) within each grid cell. Soil properties measured included the available water storage capacity (AWC), reference bulk density (RBD, kg/dm^3), USDA (used to describe the relative proportion of different grain sizes of mineral particles in a soil), organic carbon (OC, % weight), cation exchange capacity (CEC, cmol/kg), total exchange bases (TEB, cmol/kg), pH, and electrical conductivity (ECE, dS/m).

MAT, MTWQ, MTCQ, MAP, PWQ, PCQ, elevation, and climate seasonality data with a spatial resolution of 30 arc seconds were downloaded from the WorldClim database (https://www.worldclim.org/ (accessed on 15 August 2022)). PET and AET were obtained from the Consortium of International Agricultural Research Centers (https://cgiarcsi.community/category/data/ (accessed on 15 August 2022)) at a spatial resolution of 30 arc seconds. PETmin was calculated as the monthly minimum PET of a year, and WD was calculated as the difference between PET and AET. Using the ArcGIS zonal statistic tool, RELE, RMAT, and RMAP were calculated as the range of elevation, mean annual temperature, and mean annual precipitation within each grid cell. Soil variables were obtained from the Harmonized World Soil Database v1.2 (https://www.fao.org/soils-portal/soil-survey/soil-maps-and-databases/harmonized-world-soil-database-v12/en/ (accessed on 15 August 2022)).

2.3. Statistical Analysis

Global patterns of *Cerasus* species richness were drawn first. The Jenks function in ArcGIS 10.2 was used to categorize the species richness into five groupings. The environmental variables in the grids corresponding to the maximum grading intervals were retrieved as suitable ranges for the growth conditions of *Cerasus*. Moran's I was calculated to examine whether species richness within each grid cell was spatially autocorrelated. A clustering diagram was created to further investigate the global patterns of *Cerasus* species richness. According to Tobler's First Law [32], everything is related to everything else, but near things are more related to each other. The regions of cluster can be considered as the main distribution regions of the subgenus *Cerasus*. High–high cluster indicates high species richness in the area, which may also be the center of its differentiation; low–low cluster indicates that the area meets the environmental conditions for the growth of certain species.

To assess the effects of each set of variables, stepwise regression analyses were conducted for the species richness and environmental variables. Meanwhile, an integrated model was added. The adjusted R^2 was used to determine the degree of influence of each model. Higher adjusted R^2 indicates a better model fit and more reliable results.

We calibrated each of the four integrated models and used them to predict the global species richness and that of the other continents to test for consistency in the richness–environment relationship. We then calculated the root mean squared error (RMSE) for each prediction to assess the predictive power of the models. Lower RMSEs indicate higher predictive power and consistency in the richness–environment relationship between the predicted continent and the geographical distribution data used to construct the model. All statistical analyses were performed in R v4.0.3 using package "leaps" and function "glm".

3. Results

3.1. Global Patterns of Cerasus Species Richness

The *Cerasus* showed different distributions and species richness patterns in eastern Asia, Europe, and North America (Figure 1). They were widely distributed in Europe and North America, although species richness within each grid cell did not exceed three. Of the 79 cherry plant species, three species were found in Europe, four in North America, and 73 species in Asia. Most species were only found on one continent, with the exception of *P. mahaleb*, which was found in both Europe and Asia. Over 90% of the species in

the subgenus *Cerasus* occurred in eastern Asia, but about 20 of them had fewer than 10 specimen records.

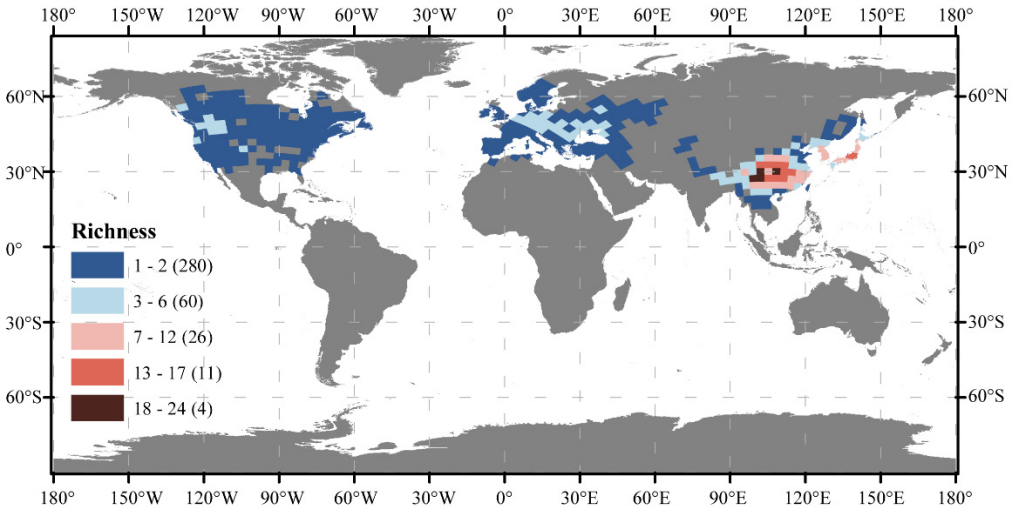


Figure 1. The map of species richness of subgenus *Cerasus* included 381 grid cells covering an area of 2.88×10^7 km^2. Numbers in brackets indicate how many grid cell there are under that richness class.

At the global scale, the Moran's I was 0.761 (Figure 2), indicating a high degree of spatial autocorrelation in species richness. Spatial cluster analysis at the global scale was performed (Figure 3a). The results showed that the high–high clusters were concentrated in eastern Asia, while low–low clusters were found in northeastern North America, southwestern California, the southern part of the Scandinavia Peninsula, and near the middle reaches of the Volga River. A high–low outlier existed only in Moscow. This result showed that eastern Asia is the center of biodiversity for *Cerasus*. Therefore, further geographic clustering analysis was carried out in eastern Asia. The results (Figure 3b) suggested that the high–high clusters were concentrated in southwestern China and on Honshu Island in Japan. We speculated that these two regions were the biodiversity centers of *Cerasus*.

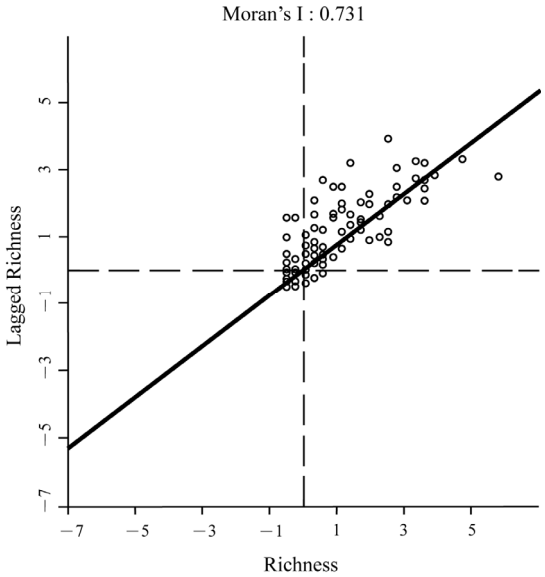


Figure 2. The Moran's I of subgenus *Cerasus*. The closer the Moran's I is to 1, the more pronounced the aggregation effect is in the spatial distribution.

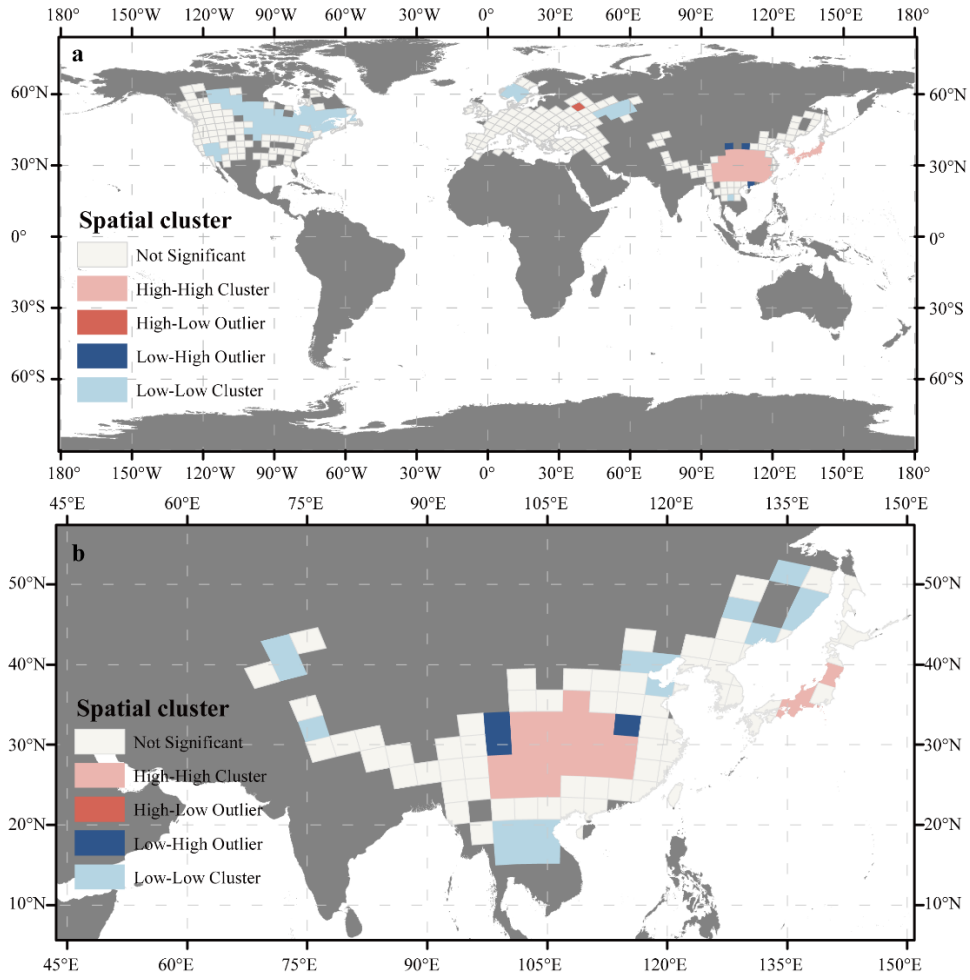


Figure 3. (**a**) Clustering the geographical distribution of species richness at the global scale. (**b**) Clustering the geographical distribution of the species richness of eastern Asia. High–high cluster means a high value for itself and a correspondingly high value for the adjacent areas; high–low outlier means a high value for itself and a low value for the adjacent areas; low–high outlier means a low value for itself and a high value for the adjacent areas; low–low cluster means a low value for itself and a correspondingly low value for the adjacent areas.

The climate variables for each grid cell were estimated by averaging within that grid, and the climatic environmental range at the highest level of species richness was considered as the optimal distribution range for *Cerasus*. The environmental data extracted according to the grid cell division was shown in Table 2. Although the maximum species richness was 24, the average species richness within each grid cell was 2.82, coupled with a median of 1. On one hand, it indicated that the *Cerasus* species richness was low in most distribution regions. On the other hand, only a few regions were highly diverse. The values of MAP and PWQ were higher than the averages, while the AET and PCQ values were lower than the averages. This indicates that regions with abundant precipitation and rain–heat synchronization are suitable for *Cerasus* growth. The optimal range of climate seasonality was relatively narrow, while the optimal range of ecological heterogeneity was relatively wider. These results indicate that regions with stable seasonal climate variation and a high degree of habitat heterogeneity are suitable for *Cerasus* growth.

Table 2. Descriptive statistics of species richness and environmental factors in the subgenus *Cerasus*.

	Min	Max	Mean	Median	SD	Optimal Range	
						Lower Limit	Upper Limit
Richness	1	24	2.82	1	3.61		
MAT/°C	−7.06	26.30	8.58	8.35	6.82	6.13	15.14
MTWQ/°C	6.81	33.16	19.14	18.87	4.91	13.47	24.41
MTCQ/°C	−33.82	15.78	−8.56	−7.44	10.55	−9.85	1.17
PET/mm	0.89	2722.32	1148.62	1106.17	400.82	950.81	1211.56
PETmin/mm	0.01	8.35	34.30	26.89	27.21	38.73	74.71
MAP/mm	167.47	2540.83	848.70	698.83	456.25	869.59	1307.80
AET/mm	250.55	3649.93	934.94	792.18	524.55	634.04	811.49
PWQ/mm	0.49	1435.15	285.58	240.03	210.53	483.20	571.81
PCQ/mm	5.85	987.23	149.85	116.88	124.45	23.09	72.85
ART/°C	15.95	57.69	34.63	34.29	8.67	24.13	28.64
TSN	202.56	1658.14	881.07	851.74	287.92	511.73	771.02
PSN	11.83	127.63	50.22	46.02	26.48	62.79	91.69
RELE/m	86.00	8614.00	1982.30	1737.00	1562.75	2630.00	6691.00
RMAT/°C	1.75	44.98	11.22	9.88	7.92	12.99	32.08
RMAP/mm	99.00	8490.00	881.63	566.00	954.36	434.00	3093.00

3.2. Richness–Environment Relationships

The species richness of *Cerasus* was used as the dependent variable and each group variable as the independent variable in a stepwise regression analysis (Table 3). The model produced similar results at all three regional and global scales. At the global scale, the adjusted R^2 of the water availability model (adj. R^2 = 0.1807) was the highest among every single group of variables. The adjusted R^2 of the soil properties model (adj. R^2 = 0.0951) was the lowest. However, water availability was not the most essential variable in the three continents. Environmental energy availability was considered as the most important driving factor in these regions. Environmental energy availability was the most explicable single group variable in both eastern Asia (adj. R^2 = 0.2066) and Europe (adj. R^2 = 0.172). In North America, the environmental energy availability of 33.44% of model interpretation was second only to habitat heterogeneity (adj. R^2 = 0.3495). The variable with the lowest explanatory degree varied from continent to continent: water availability in eastern Asia, habitat heterogeneity in Europe, and soil properties in North America, which was consistent with the global scale. The model had low explanatory power and poor fit results when only one group of variables was used to measure the relationship between richness and environment, while the integrated model using just three groups of variables had at least 40% of the explanatory power (adj. $R^2 \geq 0.4157$).

Table 3. Stepwise regression models for each group of variables and the integrated model for the globe and three continents.

	Globe			Eastern Asia			Europe			North America		
Group	Variables	Coefficients	adj. R^2/%	Variables	Coefficients	adj. R^2/%	Variables	Coefficients	adj. R^2/%	Variables	Coefficients	adj. R^2/%
Energy Availability	PET PETmin	−0.5501 *** 0.6606 ***	15.06	MTCQ PET	0.5791 *** −0.647 ***	20.66	MAT PETmin	0.9606 *** −0.9306 ***	17.2	MAT MTCQ	−1.561 *** 1.739 ***	33.44
Water Availability	PWQ PCQ	0.4176 *** −0.06357	18.07	PCQ	0.2055 *	3.33	MAP PCQ	0.4799 ** −0.5705 ***	8.303	PWQ PCQ	−0.3228 *** 0.3884 ***	19.31
Climate Seasonality	ART PSN	−0.2589 *** 0.2524 ***	12.6	PSN	−0.3501 ***	11.44	TSN PSN	−0.1827 * −0.3031 ***	11.53	TSN	−0.4314 ***	18.04
Habitat heterogeneity	RELE RMAP	0.3942 *** −0.106	11.82	RELE RMAP	0.3432 ** −0.2756 **	13.82	RMAT	0.02042	2.422	RELE RMAP	0.3614 *** 0.3051 ***	34.95
Soil Properties	AWC RBD	−0.2775 *** −0.3013 ***	9.51	AWC ECE	−0.4068 *** −0.3796 ***	17.2	ECE pH	−0.2647 ** 0.2899 **	10.56	CEC OC TEB	1.43 ** −1.226 *** −0.5197 *	8.575
Integrated Model	MAT PET PWQ RELE RMAP	0.4973 *** −0.4985 *** 0.3547 *** 0.6054 *** −0.4847 ***	41.92	PSN RELE RMAP AWC	−0.4908 *** 0.5464 *** −0.2916 *** −0.435 ***	49.09	MAT PETmin PCQ PWQ	0.9697 *** −0.3074 −0.4467 *** 0.6929 ***	41.57	TSN RELE $PETmin^2$ ECE	−0.3282 *** 0.5731 *** −0.3609 *** −0.2127 ***	46.74

Note: *** p-value < 0.001; ** p-value < 0.01; * p-value < 0.05.

We calibrated the four integrated models with continental and global data and tested them with other data. The results of all four models were similar by calculating and comparing the RMSE. RMSE was used to evaluate the difference between model prediction and the real value at first, but regardless of whether the model was based on eastern Asia or tested with eastern Asian data, the RMSE was higher than the others (Figure 4). The RMSE of the models calibrated with eastern Asia using European or North American data testing was also at least twice as high as those calibrated with other regions. This phenomenon reflects the anomalies in the eastern Asian data. In this situation, we believe that eastern Asia should be divided into two sections for further discussion: northeast of eastern Asia and southwest of eastern Asia. Similarly, stepwise regression analysis was also performed on the five groups of variables and the integrated model. The adjusted R^2 of these two regions was higher than that in eastern Asia (Table 4), but the main single group of variables affecting the two regions was different. The main influencing factor of northeastern Asia was habitat heterogeneity. In addition, the model interpretation of environmental energy availability, water availability, and soil properties could exceed 50%. In the southwest of eastern Asia, the main influencing factor was environmental energy availability, followed by water availability.

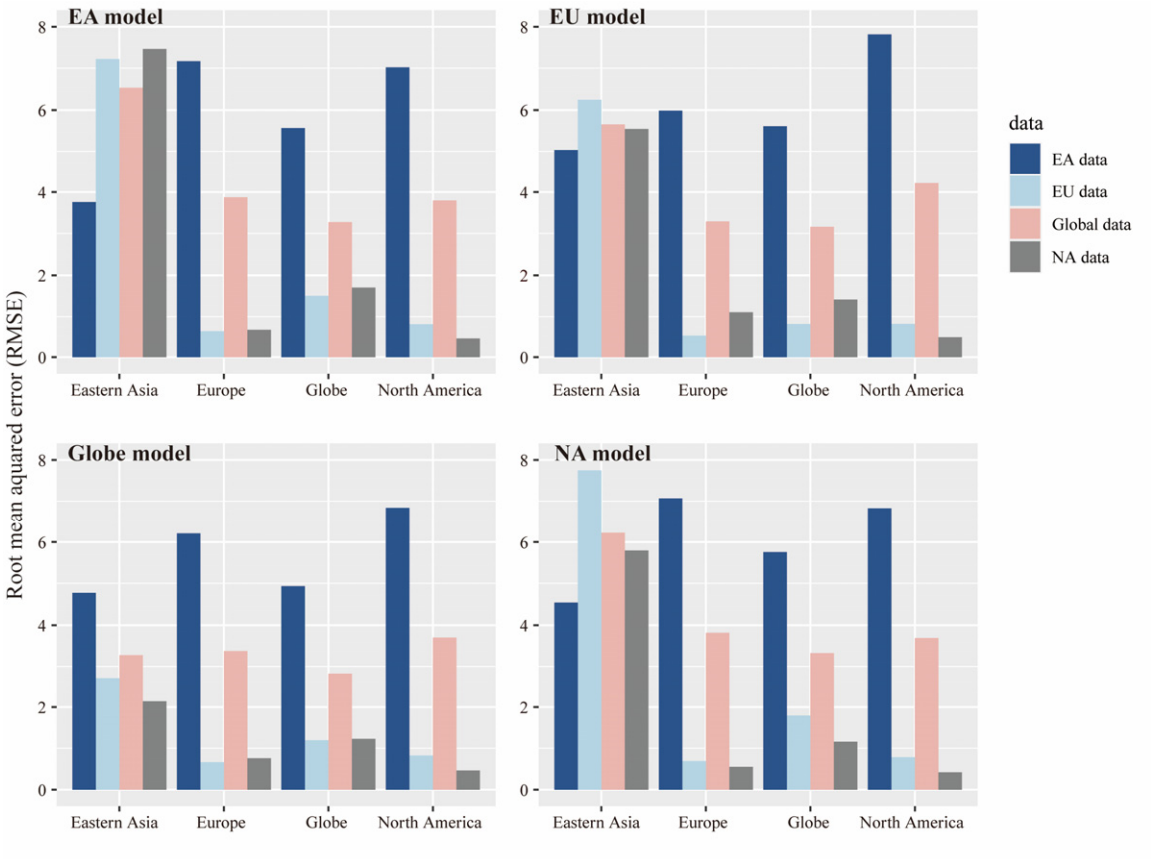


Figure 4. Root mean squared errors of the four integrated models were assessed when they were used to predict the subgenus *Cerasus* species richness at the global scale and in eastern Asia (EA), North America (NA), and Europe (EU) (color bars). Each of the four models was calibrated separately using eastern Asian data, European data, North American data, and Global data (*x*-axis).

Table 4. Stepwise regression models for each group of variables and integrated model for two regions in eastern Asia.

	Northeast of Eastern Asia			Southwest of Eastern Asia		
Group	**Variables**	**Coefficients**	**adj. R^2/%**	**Variables**	**Coefficients**	**adj. R^2/%**
Energy Availability	MTCQ	0.7711 ***	58.11	MAT PET	0.4706 *** −0.933 ***	45.75
Water Availability	AET PCQ	0.5359 *** 0.3455 *	61.23	AET WD	−1.393 *** −1.211 ***	41.94
Climate Seasonality	TSN	−0.7013 ***	47.48	PSN	−0.4478 ***	18.98
Habitat heterogeneity	RELE RMAP	0.2682 * 0.6717 ***	66.93	RELE RMAT	1.727 *** −1.621 ***	19.06
Soil Properties	AWC TEB	−0.5726 *** −0.8255 ***	50.26	CEC USDA	0.7867 *** −0.7061 ***	20.99
Integrated Model	RELE MAT PCQ	0.4514 *** 0.6081 *** 0.2175 *	84.33	AET PSN RELE RMAP	−0.5839 *** −0.6329 *** 0.5193 *** −0.2326 **	62.81

Note: *** p-value < 0.001; ** p-value < 0.01; * p-value < 0.05.

4. Discussion

4.1. Supporting Hypothesis

As the distribution of the subgenus *Cerasus* in Europe and North America has been widely influenced by human activity, we focused on species distributed in Asia to explore the relationship between species richness patterns and environmental variables. We also conducted stepwise regression analysis for each group of variables to find the best model. Integrated models were also constructed using these five groups of variables. These results showed that the richness distribution pattern of *Cerasus* was influenced by a combination of environmental variables such as energy availability, water availability, and habitat heterogeneity, and that no single environmental factor or hypothesis could explain the richness pattern of the species adequately. Meanwhile, the *Cerasus* richness patterns supported different kinds of environmental hypotheses. AET represented the actual amount of water transported from the surface to the atmosphere, which could be representative of both solar and moisture influences [33]. Therefore, AET was considered to be the best univariate climate indicator to represent the productivity hypothesis. The species richness of the *Cerasus* increased with AET. This phenomenon is consistent with the predictions of the productivity hypothesis. In the southwest of eastern Asia, the adjusted R^2 for the single group of variables for energy availability or water availability was higher than the other single group, suggesting that the distribution of the subgenus *Cerasus* also supports the water-energy dynamics hypothesis. The suitable distribution regions of the *Cerasus* in northeastern Asia were mostly islands or mountains that were isolated from each other. These regions may have distinct habitats from each other, thus facilitating the coexistence of species. Species differentiation processes were facilitated in mutually isolated habitats due to mechanisms such as the founder effect and genetic drift [8]. Therefore, species richness was high where habitat heterogeneity was high. The habitat heterogeneity hypothesis has been validated. In conclusion, the distribution pattern of *Cerasus* in China supports the productivity hypothesis, while the distribution pattern in Japan supported the habitat heterogeneity hypothesis.

4.2. Geographical Pattern of Cerasus in Eastern Asia

The adjusted R^2 of integrated models for three continents and the globe were not high (adj. $R^2 \leq 0.4909$), and the RMSE of the model that was tested or calibrated with eastern Asian data was higher than that of the others. Combined with cluster analysis, we

proposed that Honshu Island in Japan and southwest China were the centers of biodiversity of *Cerasus*. As a result, the eastern Asia dataset could be thought of as two different datasets for groups. The main factors influencing the species richness patterns of these two groups were likely to be different. These two datasets may interfere with each other, resulting in a poor model fit. Our regression analysis of the data from these two biodiversity centers concluded that the main environmental variables affecting the two areas were different, because the environments for these two biodiversity centers differed significantly, and therefore the distribution pattern of the two regions cannot be adequately explained by a single model.

To determine whether it is a complex dataset, we attempted to explain using phylogenetics. According to the evolutionary tree constructed by Li et al. [34], *Cerasus* could be divided into four clades. A clade containing most cherry species occurred in eastern Asia [34]. These species were also grouped according to their distribution. Our hypothesis was partly supported by the results of the article. This phenomenon is also found in other genera. *Quercus* originated in the temperate zone of North America and diversified southward in parallel as temperatures dropped in the higher latitudes. Now, *Quercus* has two centers of distribution, the eastern United States and Mexico [35]. However, the available evidence suggests that the differentiation of the *Cerasus* species was most likely a reticulated process rather than a simple linear process. Therefore, the evolution and dispersal routes of *Cerasus* species as well as the differentiation of species in eastern Asia still need to be noted in future conservation research.

4.3. Geographical Pattern of Cerasus in Europe and North America

Cherries are important economic and ornamental trees. Despite the exclusion of artificially cultivated specimens during the preliminary data processing, the distribution of the subgenus *Cerasus* has been influenced to some extent by human activity, especially in Europe and North America. *P. avium* and *P. mahaleb* are the principal rootstocks used for sweet and sour cherries worldwide [36]. *P. mahaleb* is also used in urban greenery [37]. *P. pensylvanica* is regarded as a wild fruit species with commercial potential and it has been cultivated in regions like Saskatchewan in Canada [38,39]. Therefore, the subgenus *Cerasus* in Europe and North America is not a good example for exploring the relationship between species richness and environment, as this distribution has been dispersed by the human race.

Peaches, for example, are thought to have originated in China, later being introduced to Persia and then rapidly spreading across Europe [40]. Cultivated trees spread their seeds by birds or other natural forces. The seeds germinated naturally in the wild and were therefore considered wild. This phenomenon has the potential to cause species to break through their original topographical barriers and become intermittently distributed in different regions. The adjusted R^2 was lower in both Europe and North America, indicating that these models did not adequately explain the local species richness patterns as well. In summary, we believe that these human activities have influenced the distribution patterns of the *Cerasus* species to some extent, and played an important role in the pattern formation.

4.4. Differences in Species Richness between North America and East Asia

East Asia and North America share similar environments with comparable latitudes, landforms, and areas, except that of North America having a coastline in the west [41]. Both regions have similar flora origins and are geologically and historically part of the Laurasia. The number of species in the subgenus *Cerasus* differs considerably between the two continents. The subgenus *Cerasus* is thought to have originated in East Asia and migrated to North America though the North Atlantic Land Bridge and the Bering Land Bridge [21]. The high species richness of East Asia is often attributed to the unique climate, geomorphological features, and geological history of East Asia [42–45]. The uplift of the Qinghai–Tibet Plateau has resulted in a complex topography and high ecological heterogeneity in southwestern China [46,47]. At the same time, the unique East Asia

monsoon climate and complex topography provide refuge for organisms that have survived dramatic climatic fluctuations since the mid-Cenozoic [47,48]. Therefore, China has a higher angiosperm phylogenetic diversity than America [49]. At the Last Glacial Maximum (LGM), extensive ice sheets in North America may also have had a lasting impact on the relationship between species richness and climate. During this period, *Pinus* and *Quercus* migrated south and accelerated their divergence, and after the glacial period, they expanded rapidly northward to form the current centers of diversity [35,50,51]. The genus *Prunus* originated in East Asia. The Bering Land Bridge is an important migration corridor for the *Prunus* in eastern Asian and eastern North America. Global cooling event could have resulted in vicariance between the two populations and subsequently brought about the diversification of the North American and eastern Asian lineages [21]. The environment may have driven different patterns of diversification and evolution between East Asia and North America. As a result, we believe that the high species richness of the *Cerasus* in East Asia is due to the fact that for *Cerasus*, the environment in East Asia is more conducive to diversification than in North America.

5. Conclusions

This study used data from the global distribution and environmental variables to analyze the distribution patterns of the subgenus *Cerasus* species richness and the variables that influenced them. (1) Our results indicate that Honshu Island in Japan and southwest China are the biodiversity hotspots of the extant *Cerasus*. (2) The drivers were different for the two different *Cerasus* species biodiversity centers: hygrothermal conditions are the main driving factor in the southwest of China, while habitat heterogeneity is the main driving factor in Honshu Island of Japan. (3) The high level of habitat heterogeneity and better hygrothermal conditions may have played an important role in the establishment of the cherries' globally consistent richness–climate relationship.

Supplementary Materials: The following supporting information can be downloaded at: https://www.mdpi.com/article/10.3390/f14020193/s1, Table S1: List of *Cerasus* species and distribution.

Author Contributions: Conceptualization, C.-L.F., M.I. and M.L.; Data curation, C.-L.F., C.-P.X., M.I. and X.-G.Y.; Formal analysis, C.-L.F., C.-P.X., X.-G.Y., X.-R.W. and M.L.; Funding acquisition, X.-R.W.; Methodology, C.-L.F., C.-P.X., M.I., X.-R.W. and M.L.; Project administration, M.L.; Software, C.-L.F. and M.L.; Writing—original draft, C.-L.F. and M.L.; Writing—review & editing, C.-L.F. and M.L. All authors have read and agreed to the published version of the manuscript.

Funding: This research was funded by grants from the Key Modern Agriculture Project of Science and Technology Department of Jiangsu Province, China (Grant No. BE2020343).

Data Availability Statement: Not applicable.

Conflicts of Interest: The authors declare no conflict of interest.

References

1. D'Antraccoli, M.; Roma-Marzio, F.; Carta, A.; Landi, S.; Bedini, G.; Chiarucci, A.; Peruzzi, L. Drivers of floristic richness in the Mediterranean: A case study from Tuscany. *Biodivers. Conserv.* **2019**, *28*, 1411–1429. [CrossRef]
2. Gotelli, N.J.; Colwell, R.K. Quantifying biodiversity: Procedures and pitfalls in the measurement and comparison of species richness. *Ecol. Lett.* **2001**, *4*, 379–391. [CrossRef]
3. Grytnes, J.A.; Vetaas, O.R. Species richness and altitude: A comparison between null models and interpolated plant species richness along the Himalayan altitudinal gradient, Nepal. *Am. Nat.* **2002**, *159*, 294–304. [CrossRef]
4. Krogsgaard Svendsen, I. The Effects that the Current Climate Crisis have on the Biogeography and Environment, Needed Adaptations and Conservation. *Am. J. BioScience* **2020**, *8*, 20–27. [CrossRef]
5. Currie, D.J.; Mittelbach, G.G.; Cornell, H.V.; Field, R.; Guegan, J.F.; Hawkins, B.A.; Kaufman, D.M.; Kerr, J.T.; Oberdorff, T.; O'Brien, E.; et al. Predictions and tests of climate-based hypotheses of broad-scale variation in taxonomic richness. *Ecol. Lett.* **2004**, *7*, 1121–1134. [CrossRef]
6. Field, R.; O'Brien, E.M.; Whittaker, R.J. Global models for.predicting woody plant richness from climate: Development and evaluation. *Ecology* **2005**, *86*, 2263–2277. [CrossRef]

7. O'Brien, E.M.; Field, R.; Whittaker, R.J. Climatic gradients in woody plant (tree and shrub) diversity: Water-energy dynamics, residual variation, and topography. *Oikos* **2000**, *89*, 588–600. [CrossRef]
8. Tews, J.; Brose, U.; Grimm, V.; Tielborger, K.; Wichmann, M.C.; Schwager, M.; Jeltsch, F. Animal species diversity driven by habitat heterogeneity/diversity: The importance of keystone structures. *J. Biogeogr.* **2004**, *31*, 79–92. [CrossRef]
9. Wang, Z.H.; Fang, J.Y.; Tang, Z.Y.; Lin, X. Patterns, determinants and models of woody plant diversity in China. *Proc. R. Soc. B-Biol. Sci.* **2011**, *278*, 2122–2132. [CrossRef]
10. Hawkins, B.A.; Rodriguez, M.A.; Weller, S.G. Global angiosperm family richness revisited: Linking ecology and evolution to climate. *J. Biogeogr.* **2011**, *38*, 1253–1266. [CrossRef]
11. Hawkins, B.A.; Field, R.; Cornell, H.V.; Currie, D.J.; Guegan, J.F.; Kaufman, D.M.; Kerr, J.T.; Mittelbach, G.G.; Oberdorff, T.; O'Brien, E.M.; et al. Energy, water, and broad-scale geographic patterns of species richness. *Ecology* **2003**, *84*, 3105–3117. [CrossRef]
12. Wang, Z.H.; Tang, Z.Y.; Fang, J.Y. The species-energy hypothesis as a mechanism for species richness pattern. *Biodivers. Sci.* **2009**, *17*, 613–624. [CrossRef]
13. Wright, D.H. Species-Energy Theory: An Extension of Species-Area Theory. *Oikos* **1983**, *41*, 496–506. [CrossRef]
14. Jetz, W.; Rahbek, C. Geographic range size and determinants of avian species richness. *Science* **2002**, *297*, 1548–1551. [CrossRef]
15. Kreft, H.; Jetz, W. Global patterns and determinants of vascular plant diversity. *Proc. Natl. Acad. Sci. USA* **2007**, *104*, 5925–5930. [CrossRef] [PubMed]
16. Whittaker, R.J.; Willis, K.J.; Field, R. Scale and species richness: Towards a general, hierarchical theory of species diversity. *J. Biogeogr.* **2001**, *28*, 453–470. [CrossRef]
17. Suissa, J.S.; Sundue, M.A.; Testo, W.L. Mountains, climate and niche heterogeneity explain global patterns of fern diversity. *J. Biogeogr.* **2021**, *48*, 1296–1308. [CrossRef]
18. Fang, W.J.; Cai, Q.; Zhao, Q.; Ji, C.J.; Zhu, J.L.; Tang, Z.Y.; Fang, J.Y. Species richness patterns and the determinants of larch forests in China. *Plant Divers.* **2022**, *44*, 436–444. [CrossRef]
19. Rao, M.D.; Manuel, J.S.; Xiang, X.; Zhang, M.; Mi, X.; Zhang, J.; Ma, K.; Jens-Christian, S. Environmental and evolutionary drivers of diversity patterns in the tea family (Theaceae s.s.) across China. *Ecol. Evol.* **2018**, *8*, 11663–11676. [CrossRef]
20. Xu, X.T.; Dimitrov, D.; Shrestha, N.; Rahbek, C.; Wang, Z.H. A consistent species richness-climate relationship for oaks across the Northern Hemisphere. *Glob. Ecol. Biogeogr.* **2019**, *28*, 1051–1066. [CrossRef]
21. Chin, S.W.; Shaw, J.; Haberle, R.; Wen, J.; Potter, D. Diversification of almonds, peaches, plums and cherries–Molecular systematics and biogeographic history of *Prunus* (Rosaceae). *Mol. Phylogenetics Evol.* **2014**, *76*, 34–48. [CrossRef]
22. McCune, L.M.; Kubota, C.; Stendell-Hollis, N.R.; Thomson, C.A. Cherries and Health: A Review. *Crit. Rev. Food Sci. Nutr.* **2010**, *51*, 1–12. [CrossRef] [PubMed]
23. Wang, Y.; Hu, G.P.; Liu, Z.S.; Zhang, J.; Ma, L.; Tian, T.; Wang, H.; Chen, T.; Chen, Q.; He, W.; et al. Phenotyping in flower and main fruit traits of Chinese cherry *Cerasus pseudocerasus* (Lindl.) G.Don. *Sci. Hortic.* **2022**, *296*, 110920. [CrossRef]
24. Karaat, F.E.; Gunduz, K.; Saracoglu, O.; Yildirim, H. Pomological and phytochemical evaluation of different cherry species: Mahaleb (*Prunus mahaleb* L.), wild sweet cherry (*Prunus avium* L.) and wild sour cherry (*Prunus cerasus* L.), sweet and sour cherry cultivars. *Acta Sci. Pol.-Hortorum Cultus* **2019**, *18*, 181–191. [CrossRef]
25. Wang, Y.C.; Bao, W.K.; Wu, N. Shrub island effects on a high-altitude forest cutover in the eastern Tibetan Plateau. *Ann. For. Sci.* **2011**, *68*, 1127–1141. [CrossRef]
26. Hernandez, A. Cherry removal by seed-dispersing mammals: Mutualism through commensal association with frugivorous birds. *Pol. J. Ecol.* **2008**, *56*, 127–138.
27. Ding, L.; Xu, L.J.; Chu, X.; Yang, L.; Zhu, H.L.; Huang, J.X. Dissimilarity analysis of microbial communities in the rhizosphere and tissues of diseased and healthy cherry trees (*Cerasus pseudocerasus*). *Can. J. Plant Pathol.* **2021**, *43*, 612–621. [CrossRef]
28. Eken, B.U.; Kirdok, E.; Velioglu, E.; Ciftci, Y.O. Assessment of genetic variation of natural populations of wild cherry (*Prunus avium* L.) via SSR markers. *Turk. J. Bot.* **2022**, *46*, 14–25. [CrossRef]
29. Hou, Q.D.; Li, S.; Shang, C.Q.; Wen, Z.; Cai, X.W.; Hong, Y.; Qiao, G. Genome-wide characterization of chalcone synthase genes in sweet cherry and functional characterization of CpCHS1 under drought stress. *Front. Plant Sci.* **2022**, *13*, 3054. [CrossRef]
30. Shirasawa, K.; Esumi, T.; Itai, A.; Isobe, S. Cherry Blossom Forecast Based on Transcriptome of Floral Organs Approaching Blooming in the Flowering Cherry (*Cerasus* x *yedoensis*) Cultivar 'Somei-Yoshino'. *Front. Plant Sci.* **2022**, *13*, 802203. [CrossRef]
31. Shirasawa, K.; Esumi, T.; Hirakawa, H.; Tanaka, H.; Itai, A.; Ghelfi, A.; Nagasaki, H.; Isobe, S. Phased genome sequence of an interspecific hybrid flowering cherry, 'Somei-Yoshino' (*Cerasus* x *yedoensis*). *DNA Res.* **2019**, *26*, 379–389. [CrossRef] [PubMed]
32. Tobler, W. A Computer Movie Simulating Urban Growth in the Detroit Region. *Econ. Geogr.* **1970**, *46*, 234–240. [CrossRef]
33. Clarke, A.; Gaston, K.J. Climate, energy and diversity. *Proc. R. Soc. B-Biol. Sci.* **2006**, *273*, 2257–2266. [CrossRef]
34. Li, M.; Song, Y.F.; Sylvester, S.P.; Wang, X.R. Comparative analysis of the complete plastid genomes in *Prunus* subgenus *Cerasus* (Rosaceae): Molecular structures and phylogenetic relationships. *PLoS ONE* **2022**, *17*, e0266535. [CrossRef]
35. Hipp, A.L.; Manos, P.S.; González-Rodríguez, A.; Hahn, M.; Kaproth, M.; McVay, J.D.; Avalos, S.V.; Cavender-Bares, J. Sympatric parallel diversification of major oak clades in the Americas and the origins of Mexican species diversity. *New Phytol.* **2018**, *217*, 439–452. [CrossRef] [PubMed]
36. Moghadam, E.G.; Khalighi, A. Relationship between vigor of Iranian *Prunus mahaleb* L. selected dwarf rootstocks and some morphological characters. *Sci. Hortic.* **2007**, *111*, 209–212. [CrossRef]

37. Bujdosó, G.; Hrotkó, K. *Cherries: Botany, Production and Uses*; Quero-Garcia, J., Iezzoni, A., Pulawska, J., Lang, G., Eds.; Cherry production; CABI International: Wallingford, UK, 2017; pp. 1–13.
38. Shiell, K.J.; St-Pierre, R.G.; Zatylny, A.M. Timing, magnitude and causes of flower and immature fruit loss in pin cherry and choke cherry. *Can. J. Plant Sci.* **2002**, *82*, 157–164. [CrossRef]
39. St-Pierre, R.G.; Zatylny, A.M.; Tulloch, H.P. Evaluation of growth, yield, and fruit size of chokecherry, pincherry, highbush cranberry, and black currant cultivars in Saskatchewan. *Can. J. Plant Sci.* **2005**, *85*, 659–664. [CrossRef]
40. Lurie, S.; Crisosto, C.H. Chilling injury in peach and nectarine. *Postharvest Biol. Technol.* **2005**, *37*, 195–208. [CrossRef]
41. Qian, H. A comparison of the taxonomic richness of temperate plants in East Asia and North America. *Am. J. Bot.* **2002**, *89*, 1818–1825. [CrossRef]
42. Qian, H. A comparison of generic endemism of vascular plants between East Asia and North America. *Int. J. Plant Sci.* **2001**, *162*, 191–199. [CrossRef]
43. Qian, H.; Jin, Y.; Ricklefs, R.E. Phylogenetic diversity anomaly in angiosperms between eastern Asia and eastern North America. *Proc. Natl. Acad. Sci. USA* **2017**, *114*, 11452–11457. [CrossRef] [PubMed]
44. Yin, X.; Qian, H.; Sui, X.H.; Zhang, M.H.; Mao, L.F.; Svenning, J.C.; Ricklefs, R.E.; He, F.L.; Hurlbert, A. Effects of climate and topography on the diversity anomaly of plants disjunctly distributed in eastern Asia and eastern North America. *Glob. Ecol. Biogeogr.* **2021**, *30*, 2029–2042. [CrossRef]
45. Zuo, Y.J.; Wen, J.; Zhou, S.L. Intercontinental and intracontinental biogeography of the eastern Asian-Eastern North American disjunct *Panax* (the ginseng genus, Araliaceae), emphasizing its diversification processes in eastern Asia. *Mol. Phylogenetics Evol.* **2017**, *117*, 60–74. [CrossRef]
46. Molnar, P.; Boos, W.R.; Battisti, D.S. Orographic Controls on Climate and Paleoclimate of Asia: Thermal and Mechanical Roles for the Tibetan Plateau. *Annu. Rev. Earth Planet. Sci.* **2010**, *38*, 77–102. [CrossRef]
47. Xing, Y.W.; Ree, R.H. Uplift-driven diversification in the Hengduan Mountains, a temperate biodiversity hotspot. *Proc. Natl. Acad. Sci. USA* **2017**, *114*, E3444–E3451. [CrossRef] [PubMed]
48. Wen, J.; Zhang, J.Q.; Nie, Z.L.; Zhong, Y.; Sun, H. Evolutionary diversificatons of plants on the Qinghai-Tibetan Plateau. *Front. Genet.* **2014**, *5*, 4. [CrossRef]
49. Hu, H.H.; Ye, J.F.; Liu, B.; Mao, L.F.; Smith, S.A.; Barrett, R.L.; Soltis, P.S.; Soltis, D.E.; Chen, Z.D.; Lu, L.M. Temporal and spatial comparisons of angiosperm diversity between eastern Asia and North America. *Natl. Sci. Rev.* **2022**, *9*, nwab199. [CrossRef] [PubMed]
50. Norris, J.R.; Betancourt, J.L.; Jackson, S.T. Late Holocene expansion of ponderosa pine (*Pinus ponderosa*) in the Central Rocky Mountains, USA. *J. Biogeogr.* **2016**, *43*, 778–790. [CrossRef]
51. Zinck, J.W.; Rajora, O.P. Post-glacial phylogeography and evolution of a wide-ranging highly-exploited keystone forest tree, eastern white pine (*Pinus strobus*) in North America: Single refugium, multiple routes. *BMC Evol. Biol.* **2016**, *16*, 56. [CrossRef]

Disclaimer/Publisher's Note: The statements, opinions and data contained in all publications are solely those of the individual author(s) and contributor(s) and not of MDPI and/or the editor(s). MDPI and/or the editor(s) disclaim responsibility for any injury to people or property resulting from any ideas, methods, instructions or products referred to in the content.

forests

MDPI

Article

Quantification of Root Systems and Soil Macropore Networks Association to Soil Saturated Hydraulic Conductivity in Forested Wetland Soils

Yinghu Zhang [1,2,3], Lu Wang [1,2,3], Wenqi Zhang [1,2,3], Zhenming Zhang [4] and Mingxiang Zhang [4,*]

[1] Co-Innovation Center for Sustainable Forestry in Southern China, Nanjing Forestry University, Nanjing 210037, China
[2] Jiangsu Provincial Key Laboratory of Soil Erosion and Ecological Restoration, Nanjing Forestry University, Nanjing 210037, China
[3] Priority Academic Program Development of Jiangsu High Education Institutions (PAPD), Nanjing Forestry University, Nanjing 210037, China
[4] School of Ecology and Nature Conservation, Beijing Forestry University, Qinghua East Road 35, Beijing 100083, China
* Correspondence: zhangmingxiang@bjfu.edu.cn

Abstract: Understanding the relationship between root systems, soil macropore networks, and soil hydraulic properties is important to better assess ecosystem health. In this study, treatments were performed in forested wetland soils with different vegetation densities, i.e., large (LWa) and small communities (LWb) of reed (*Phragmites australis* (Cav.) Trin. ex Steud.). At each plot, three undisturbed PVC cylinders (10 cm in diameter and 50 cm in height) were obtained, and X-ray microtomography (μCT) scanning was used to determine the root and macropore architectures. Results showed that the values of total root length and total root volume at LWa were significantly larger than those at LWb ($p < 0.05$). Imaged macroporosity, macropore volume, macropore length density, macropore node density, macropore branch density, mean macropore surface area, mean macropore diameter, and mean macropore volume at LWa were significantly larger than those at LWb ($p < 0.05$), whereas mean macropore length, mean macropore branch length, and mean macropore tortuosity at LWb were larger than those at LWa. Total root length and total root volume were positively correlated with soil saturated hydraulic conductivity. Imaged macroporosity, macropore volume, macropore length density, macropore node density, macropore branch density, mean macropore surface area, mean macropore diameter, and mean macropore volume were positively correlated with soil saturated hydraulic conductivity, whereas mean macropore length, mean macropore branch length, and mean macropore tortuosity were negatively correlated with soil saturated hydraulic conductivity. In conclusion, root systems and soil macropore networks constitute a complex synthesis inside soil environments, and together affect soil hydrological responses.

Keywords: root systems; soil macropores; soil saturated hydraulic conductivity; Yellow River Delta

check for updates

Citation: Zhang, Y.; Wang, L.; Zhang, W.; Zhang, Z.; Zhang, M. Quantification of Root Systems and Soil Macropore Networks Association to Soil Saturated Hydraulic Conductivity in Forested Wetland Soils. *Forests* **2023**, *14*, 132. https://doi.org/10.3390/f14010132

Academic Editor: Thomas H. DeLuca

Received: 16 November 2022
Revised: 7 January 2023
Accepted: 10 January 2023
Published: 11 January 2023

Copyright: © 2023 by the authors. Licensee MDPI, Basel, Switzerland. This article is an open access article distributed under the terms and conditions of the Creative Commons Attribution (CC BY) license (https://creativecommons.org/licenses/by/4.0/).

1. Introduction

The Yellow River Delta is one of the most active deltas in China [1]. Forested wetland is an important component in this area, which shows positive influences on soil and water conservation, ecological functions, and vegetation interactions with soil erodibility [2,3]. However, during the last several decades, the delta has experienced environmental changes, such as agricultural exploration, expansion of the urban residential area, vegetation degradation, and petroleum refining, which result in deterioration of the structure and function of the wetland ecosystems [4]. For example, the overexploitation of petroleum in the delta can cause a series of environmental problems. The petroleum that is retained in the soils cannot be removed by the power of nature. Further, it can be transported efficiently through soil macropores to the groundwater levels. In particular, more soil fissures could be developed

due to the serious degradation of forested wetland. Therefore, it is vital to develop a common method to restore the degraded wetland. Reed is one of the most widely distributed dominant species in the Yellow River Delta. Reed community is widely distributed in coastal marshes with shallow groundwater depth. It can withstand and present different ecological characteristics with different water and salt habitat conditions. Reed plays an important role in forested wetland ecosystems [5] due to its purification of wastewater and its accumulation of nutrients. Reed is used in the restoration and reconstruction of wetland ecosystems. Root systems of reed are the interface between aboveground vegetation and belowground soils. They can not only support vegetation growth by absorbing water, minerals, and nutrients from the soils, but they also form more root channels during their decomposition. However, in different stages of wetland restoration, how the root systems of reed community interact with the surrounding soils (i.e., soil macropores) is still unclear.

Soil macropores formed by root systems are a major factor influencing water flow and solute transport [1]. The interaction between root systems and soil macropores is increasingly studied [4,6–8]. Most studies quantifying the interaction between root systems and soil macropores have shown that root systems can promote the formation of soil macropores and increase soil microporosity [7]. For example, Bodner et al. [9] concluded that coarse root systems increased macroporosity (larger than 37.5 μm in diameter) by 30%, and root biomass increased soil macropore area and length. Hu et al. [7] found that a large number of soil macropores in soils can be attributed to the greater development of root systems. Root systems affect soil macropore architecture through mechanical intercalation and by squeezing the surrounding soils during the intercalation processes [10]. Therefore, understanding the interaction between root systems, soil macropores, and soil hydrology could provide more information for the development of degraded wetlands. Root systems and soil macropore networks play crucial roles in soil hydrological responses, such as soil hydraulic conductivity [11]. Soil hydraulic conductivity, which determines the ability of soil to conduct water, is an important soil hydraulic property influencing water flow and solute transport [12]. Soil hydraulic conductivity is of ecological and hydrological significance. Soil hydraulic conductivity is strongly dependent on root systems and soil macropores [13]. Previous studies have been designed to confirm soil hydraulic conductivity by characterizing the geometry of soil macropore spaces including macropore distribution, macropore tortuosity, and other macropore attributes [13]. For example, the impact of soil macropores on soil hydraulic conductivity depends on their arrangement and 3D characteristics including macropore length, volume, surface area, and mean tortuosity [14,15]. Despite there being some research available about soil hydraulic conductivity development under different land uses, such as grassland, cultivated lands, shrub areas, and forest-covered soils [13,16–18], there are very limited data about the development of soil hydraulic conductivity in degraded soils. There exists a large body of evidence that wetland degradation can promote soil fissure development. Soil fissures such as soil macropores can impact hydrological responses. Particularly, pollutants and other contaminants carried by water can be transported from the soil surface to groundwater levels via those soil fissures, which further threaten soil ecology and hydrology [19]. We hypothesize that the density of root systems can lead to different attributes of soil macropores, and they can together impact soil hydrological responses. However, less explored is the relationship between root systems and soil macropores, and their joint effects on soil hydraulic conductivity in degraded soils. In this study, we mainly evaluated (1) the visualization of the three-dimensional structure of root systems and soil macropore networks, (2) the correlation between root systems and soil macropore parameters (imaged macroporosity, macropore volume, macropore length density, macropore node density, macropore branch density, mean macropore surface area, mean macropore diameter, mean macropore volume, mean macropore length, mean macropore branch length, and mean macropore tortuosity), and (3) the effects of root systems and soil macropores on soil saturated hydraulic conductivity.

2. Materials and Methods

2.1. Study Area

The study area is located in the Yellow River Delta National Natural Reserve (118°32.981′–119°20.450′ E, 37°34.768′–38°12.310′ N) in northeastern Shandong Province, China (Figure 1). The Yellow River Delta National Natural Reserve covers an area of 153 km^2. The main landform types in the study area comprise a land zone, tidal flat zone, and subtidal zone. The climate is warm-temperate continental with a mean annual precipitation of 576.7 mm, mean annual potential evapotranspiration of 1962 mm, and mean annual temperature of 12.1 °C. The frost-free period is 196 d [20]. The study area's main soil texture is determined by soil particle size classification developed by the U.S. Department of Agriculture (USDA). Based on the USDA system, soil particle sizes in the study area are divided into three groups: sand, silt, and clay. Soil texture in the area is sandy silt, and soil types are fluvo-aquic and saline soils formed by the Yellow River's alluvial deposits (Table 1). The three main vegetation types are deciduous broad-leaved forests, marsh vegetation, and salt-bearing vegetation. The dominant vegetation is locust (*Robinia pseudoacacia* L.) in the deciduous broad-leaved forest communities, reed in marsh vegetation communities, and tamarisk (*Tamarix chinensis*) and seepweed (*Suaeda glauca*) in the salt-bearing vegetation communities [20].

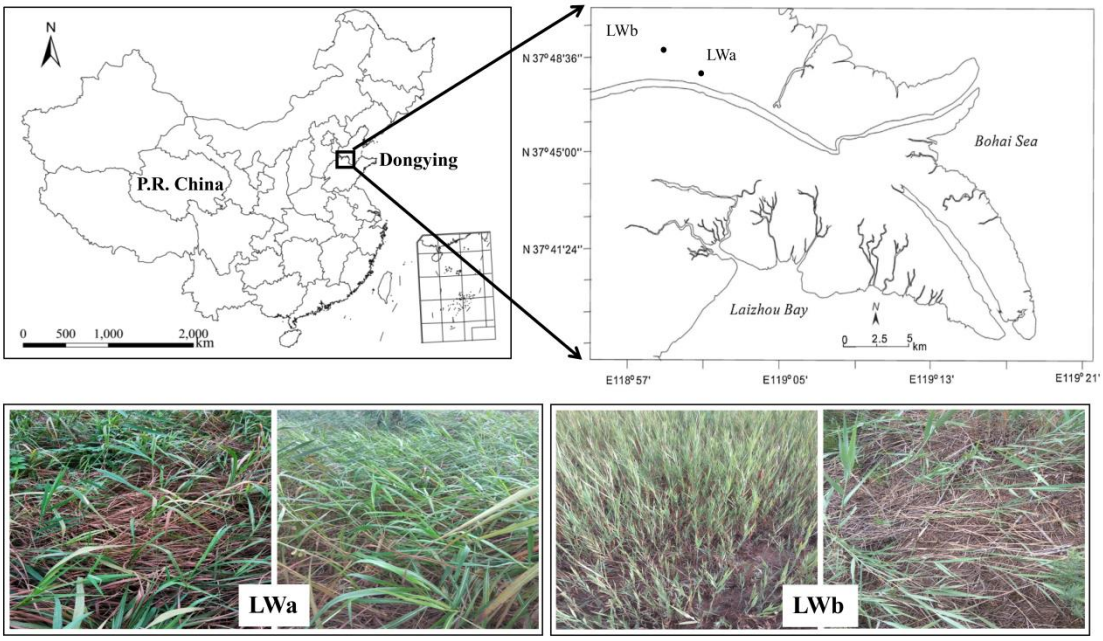


Figure 1. Location of the study area.

Table 1. Soil properties at each soil depth at LWa and LWb.

Plots	Soil Depth (cm)	Total Soil Porosity (%)	Soil Capillary Porosity (%)	Soil Non-Capillary Porosity (%)	Sand	Silt	Clay	Soil Bulk Density (g/cm^3)	Soil Organic Matter (g/kg)	Soil Total Nitrogen (g/kg)	Soil Total Phosphorus (g/kg)	Soil Available Phosphorus (mg/kg)
LWa	0–10	0.563 ± 0.024	0.520 ± 0.049	0.043 ± 0.037	0.211 ± 0.082	0.563 ± 0.115	0.226 ± 0.044	0.912 ± 0.094	21.039 ± 9.265	1.345 ± 0.631	0.614 ± 0.033	3.927 ± 1.933
	10–20	0.483 ± 0.011	0.468 ± 0.010	0.014 ± 0.008	0.170 ± 0.041	0.623 ± 0.123	0.207 ± 0.135	1.304 ± 0.052	5.050 ± 0.503	0.358 ± 0.043	0.569 ± 0.055	2.398 ± 1.031
	20–40	0.479 ± 0.016	0.471 ± 0.012	0.009 ± 0.005	0.327 ± 0.120	0.561 ± 0.122	0.112 ± 0.032	1.384 ± 0.002	3.857 ± 1.257	0.270 ± 0.094	0.538 ± 0.045	1.792 ± 0.111
	40–60	0.464 ± 0.029	0.454 ± 0.021	0.011 ± 0.015	0.521 ± 0.130	0.413 ± 0.127	0.067 ± 0.006	1.427 ± 0.177	2.692 ± 0.709	0.183 ± 0.039	0.518 ± 0.038	1.655 ± 0.231

Table 1. *Cont.*

Plots	Soil Depth (cm)	Total Soil Porosity (%)	Soil Capillary Porosity (%)	Soil Non-Capillary Porosity (%)	Sand	Silt	Clay	Soil Bulk Density (g/cm^3)	Soil Organic Matter (g/kg)	Soil Total Nitrogen (g/kg)	Soil Total Phosphorus (g/kg)	Soil Available Phosphorus (mg/kg)
LWb	0–10	0.478 ± 0.016	0.472 ± 0.015	0.006 ± 0.002	0.202 ± 0.053	0.669 ± 0.069	0.129 ± 0.019	1.406 ± 0.061	11.244 ± 2.839	0.694 ± 0.038	0.694 ± 0.073	3.576 ± 0.279
	10–20	0.468 ± 0.017	0.463 ± 0.016	0.004 ± 0.001	0.193 ± 0.071	0.688 ± 0.077	0.113 ± 0.007	1.388 ± 0.021	2.781 ± 0.693	0.200 ± 0.033	0.582 ± 0.003	1.749 ± 0.181
	20–40	0.468 ± 0.013	0.461 ± 0.018	0.007 ± 0.005	0.387 ± 0.067	0.542 ± 0.060	0.071 ± 0.010	1.418 ± 0.039	2.535 ± 1.072	0.159 ± 0.073	0.584 ± 0.021	2.552 ± 0.746
	40–60	0.491 ± 0.006	0.490 ± 0.005	0.001 ± 0.001	0.243 ± 0.172	0.656 ± 0.145	0.101 ± 0.036	1.467 ± 0.058	2.126 ± 1.340	0.188 ± 0.052	0.576 ± 0.027	2.781 ± 0.292

2.2. Soil Sampling

In the wet season of July 2017, the reed treatment was conducted at the sampling plots. In addition, all the plots for the LWa (large) and LWb (small) communities of reed treatments were located at the same plot and had similar soil properties. Due to alluvial deposits from the upstream of the Yellow River, there is no soil spatial variability in the sampling plots, and we therefore excavated a total of 6 PVC samples across plots. In our study, LWa represents areas with high vegetation cover (98%) and height (2.0 m), whereas LWb represents areas with low vegetation cover (30%) and height (0.6 m). Soil sampling locations were randomly selected at each treatment due to few spatial variabilities in soil properties. Undisturbed soil columns using PVC cylinders (4 mm wall thickness, 10 cm in diameter, and 50 cm in height) with three replicates were extracted vertically from the soil profiles at the depths of 0–50 cm at each sampling plot. We moistened the soils with water before sampling [7]. The excavation procedure of those undisturbed soil columns, using PVC cylinders to avoid damage to the soil structure during soil sampling, was as follows: (1) the aboveground reeds were carefully clipped and the litter was completely removed carefully with minimal disturbance; (2) a large pit was dug in the experimental plots using a pick; (3) the soil clod was carved carefully with small shovels and hand tools, and the roots were cut with pliers; (4) four vertical lateral sides were excavated, and then cylindrical-shaped soil sides were excavated with small shovels; (5) the top surfaces of the PVC cylinders were prepared carefully with a knife and cleaned with a brush to remove loose soil particles resulting from digging; (6) the soil column was trimmed at the bottom, and the bottom was sealed with plastic film and cloth; and (7) the soil column excavated by the PVC cylinders was tightened with iron wire and then transported carefully [21]. The cylinders were placed into a box and wrapped with sponge to prevent crushing. Six soil columns were collected in this study and transported from the field to the laboratory for X-ray CT scanning. Soil water content of the undisturbed soil columns can influence the threshold values used for the image segmentation. The soil columns from different experimental plots were taken at different times with different initial soil water content. Therefore, each soil column must be wetted before X-ray CT scanning to minimize the variability of initial soil water content. By ponding water at the top surface of each soil column and draining with the bottom of the column open to the atmosphere for 3 days, we made the initial soil water content more consistent [22].

2.3. CT Scanning and Macropore Data Acquisition

The industrial CT has a higher resolution compared with the medical CT. The undisturbed soil columns were scanned with an industrial X-ray CT. The scanning parameters were as follows: resolution of 0.05 mm, voltage of 150 kV, and current of 480 μA. The CT scanning mode was sequential, the scanning spacing between projections was 0.1 mm, and 4200 slices were obtained from each soil column (Figure 2). VGStudio MAX (software VGStudio MAX 2.2, Volume Graphics company, Germany) was utilized to reconstruct the

scanned images. All images were transformed from 16-bit images to 8-bit images for later processing. The region of interest was selected to exclude the voids near the soil column walls and to minimize the effects of beam hardening [22].

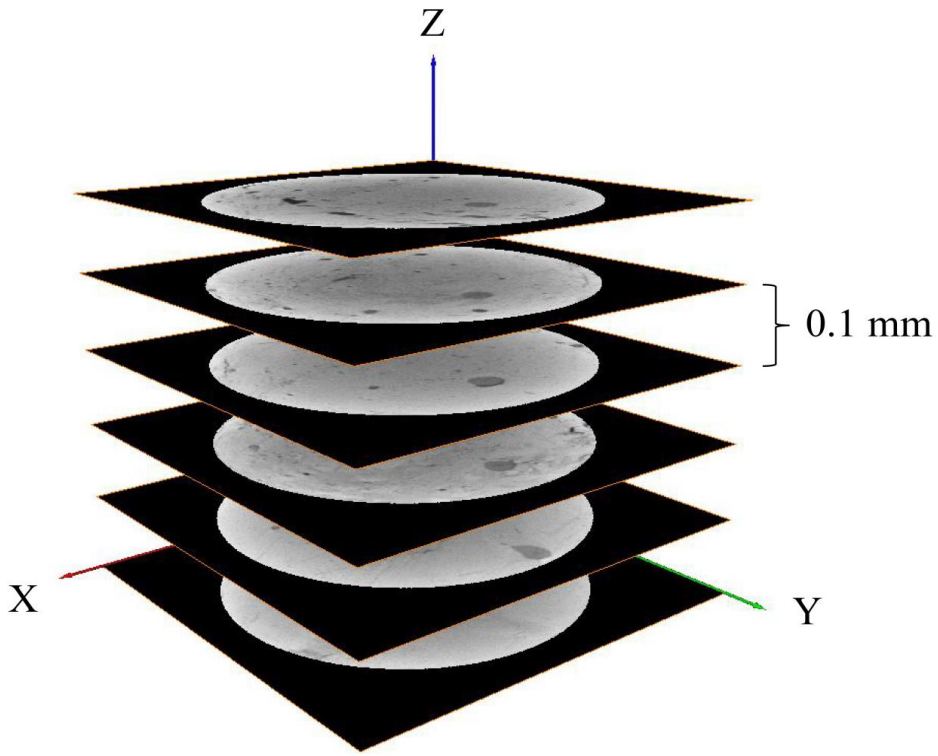


Figure 2. Slices obtained from whole soil columns.

To reduce the negative influences of noise and brightness variation before image segmentation, the normalize and the 3D median filter plugins were activated in the ImageJ software. The normalize plugins recalculate the grey levels of images to make the brightness of the grey images consistent. The 3D median filter can reduce the noise of the grey images [23]. Afterwards, all CT images were resampled using Avizo (software Avizo 9.0, the Victor Smorgon Group company, Australia). We determined the threshold values of the soil macropores to a depth of 50 cm in the sampling sites to acquire some binary images using a manually created macropore [7]. The threshold values of soil macropores (larger than 0.05 mm in diameter) were obtained following Hu et al. [7] (Figure 3). A manually created macropore (Plexiglas cylinder) with a known diameter measured by a digital caliper was inserted into an undisturbed soil column and then removed from the column. The column was then scanned by X-ray CT. We selected the upper, middle, and lower parts of the Plexiglas cylinder, respectively. First, we assumed a threshold value for the thresholding sample, and then calculated the soil macropore size based on the image analysis [7]. Then, we compared the calculated size of the soil macropore with the actual macropore size determined by a digital caliper. If the difference was >1%, the threshold value was reset until the calculated and actual size of the soil macropore were the same [7]. If the difference between the calculated and actual diameters of the soil macropores was within 1%, it was regarded as the threshold value. Using the threshold value, the images were translated into binary images. In the binary images, the black areas are soil macropores, and the white areas are the soil matrix [7].

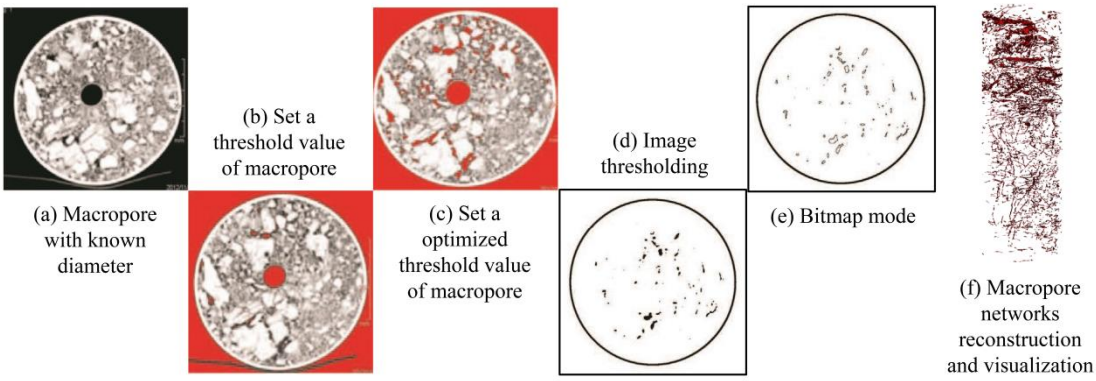


Figure 3. The process of reconstruction and visualization of soil macropores [22].

After segmentation, three-dimensional architectures of soil macropores were reconstructed by Avizo 9.0 software [7]. Soil macroporosity, mean diameter, mean surface area, network density, length density, node density, branch density, mean length, and mean branch length were determined using the Avizo 9.0 software module 'Label Analysis'. The mean tortuosity was evaluated using the Avizo 9.0 software module 'Centroid Path Tortuosity'. The volume (V_p) was evaluated using the Avizo 9.0 software module 'Volume Fraction' [24]. Since soil macropores are three-dimensional, the skeletonization of soil macropores was considered to determine the topology and length of the soil macropores and to reconstruct the soil macropore networks. A network of one soil macropore may include several branches of connected soil macropores or just one individual soil macropore [25]. The specific procedures used in this study for characterization of soil macropore networks are referenced to Luo et al. [25] and Hu et al. [7].

$$P = \frac{V_p}{V_t} \tag{1}$$

where P(%) is soil macroporosity, V_p is the soil macropore volume of the region of interest (mm^3), and V_t is the total sample volume of the region of interest (mm^3).

$$\rho_d = \frac{N_d}{V_t} \tag{2}$$

where ρ_d is the soil macropore network density (number, mm^{-3}), and N_d is the number of soil macropore networks.

$$\rho_n = \frac{N_n}{V_t} \tag{3}$$

where ρ_n is the soil macropore node density (number, mm^{-3}), and N_n is the number of soil macropore nodes.

$$\rho_t = \frac{L_t}{V_t} \tag{4}$$

where ρ_t is the soil macropore length density (mm, mm^{-3}), and L_t is the total actual length of soil macropores (mm).

$$L_t = \frac{V_p}{S} \tag{5}$$

where S is the soil macropore surface area (mm^2).

$$\tau = \frac{L_t}{L_l} \tag{6}$$

where τ is the soil macropore tortuosity, and L_l is the total straight-line distance of all the soil macropores in the total sample (mm).

$$\overline{\tau} = \frac{\sum_{i=1}^{n} L_{ti}}{\sum_{i=1}^{n} L_{li}} \quad (7)$$

where $\overline{\tau}$ is the mean soil macropore tortuosity, i is the index of a soil macropore branch, and n is the total number of soil macropore branches [25].

2.4. Root Systems Data Acquisition

The threshold values were considered to distinguish among soil macropores, root systems, and solid phases. In order to avoid selecting most of the impurities (i.e., soil mineral particles, soil organic matter, and microorganisms), we took advantage of the magic wand tool in the Avizo 9.0 software to select roots in the two-dimensional images (Figure 4). The tool was also applied to all slices. Meanwhile, the visualization of root systems was shown in the visual window [13]. If the selected root space did not match the measured root volume and surface, we enlarged the selected area to make it match better. If the enlarged root area of a two-dimensional slice included unnecessary parts at the edge of the root systems, all slice voxels were shrunk until the selected area reached a reasonable area [13]. If a root was not continuous in a single soil column sample, another root spot was selected in the two-dimensional slice until all root systems were traced. After segmentation and binarization, the visualization of root systems was obtained. Since root systems are 3D, skeletonization of root systems is necessary to effectively visualize the root networks in 3D [26] and accurately calculate the root system parameters (i.e., total root length and total root volume) [7]. Skeletonization of 3D root networks can improve the quantification of length-based root system parameters [25] and show the connectivity among root systems [27]. Many root systems in large soil columns may have dead ends; therefore, the skeletons of root systems with dead ends could be accurately calculated. The skeleton of a root is its central line, from which the distance is the closest to more than one boundary point [25].

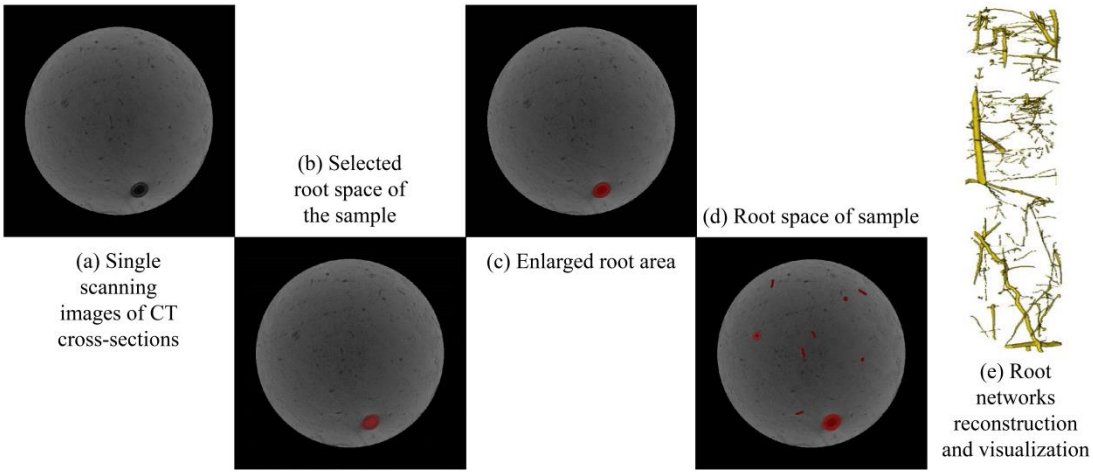


Figure 4. The process of reconstruction and visualization of root systems [13].

2.5. Determination of Soil Saturated Hydraulic Conductivity (Ks)

Using a ring knife at different soil depths (0–10, 10–20, 20–40, and 40–60 cm), undisturbed soil columns were excavated from the soil profiles and placed in water for 24 h. During soaking, the water surface was kept level with the upper mouth of the ring knife, and water was not allowed to flood the soil surface of the upper mouth of the ring knife. The ring knife was removed at a predetermined time, an empty ring knife put on, and the ring knife placed on the funnel, which was covered with a beaker. Water was added

to the empty ring knife above, so the water surface was 1 mm lower than the ring knife edge, and 2 cm below the water layer. After adding water, a stopwatch was used to time the first drop of water from the funnel. The beaker under the funnel was replaced every 1, 2, 3, 5, and 10 min. The interval time depended on the speed of water infiltration. A measuring cylinder was used to measure the amount of water seepage. The test lasted until the amount of water outflow was equal in unit time.

Darcy's law was used to determine K_s, as below [28].

$$Q = K_s \times i \times A \tag{8}$$

where Q is the flow rate at steady conditions in ml/min, K_s is the soil saturated hydraulic conductivity in cm/min, A is the cross-sectional area of the soil column in cm^2 (equal to 38.5 cm^2 for a soil column of 7 cm diameter), and i is the hydraulic gradient as follows:

$$i = \frac{\Delta H}{L} \tag{9}$$

where ΔH is the difference between the soil hydraulic head on the soil surface and bottom of the soil column in cm, and L is the length of the soil column in cm. In this study, the value of L was 10 cm. The flow rate was the effluent volume divided by time. Finally, soil saturated hydraulic conductivity was calculated as follows:

$$K_S = \frac{\Delta V}{\Delta T \times i \times A} \tag{10}$$

where ΔV is the volume of the outflow, and ΔT is the time step.

2.6. Statistical Analysis

All statistical analyses were conducted using SPSS 22.0 software. Differences among the measured root and soil macropore parameters between the different sampling sites were analyzed using the least significant difference (LSD) test. Statistical significance was determined at $p < 0.05$ level to quantify the relationship between root systems, soil macropores, and soil saturated hydraulic conductivity.

3. Results

3.1. Characterization between Root Systems and Soil Macropores

The 3D visualizations of root and macropore networks in sampling sites are shown in Figure 5. The total root length and volume in the region of interest at the depths of 0–50 cm were 15,100 ± 3125 mm and 78,100 ± 2136 mm^3 at LWa and 8900 ± 921 mm and 12,800 ± 3162 mm^3 at LWb. The correlations between the estimated total root length and total root volume determined by X-ray CT and those determined by the standard root systems washing method are shown in Figure 6. The results showed that X-ray CT is a suitable method for root system characterization. Root system density in LWa non-compacted soils was distinctly richer than that in LWb compacted soils ($p < 0.05$) (Figure 7).

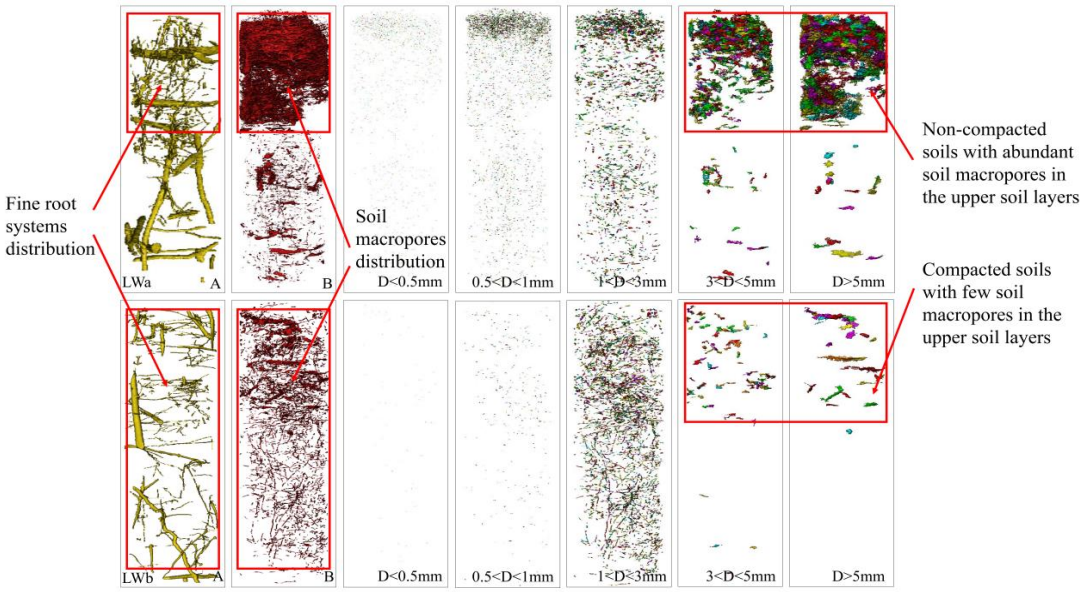
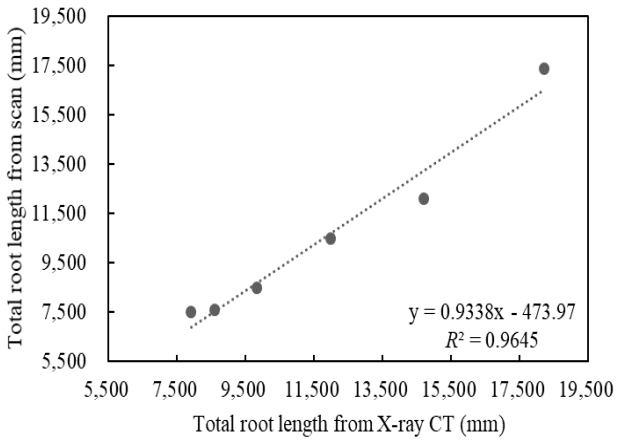


Figure 5. Three-dimensional structure of the root and macropore networks at LWa and LWb (A represents the 3D structure of root systems, B represents the 3D structure of soil macropores, and D represents equivalent diameter).



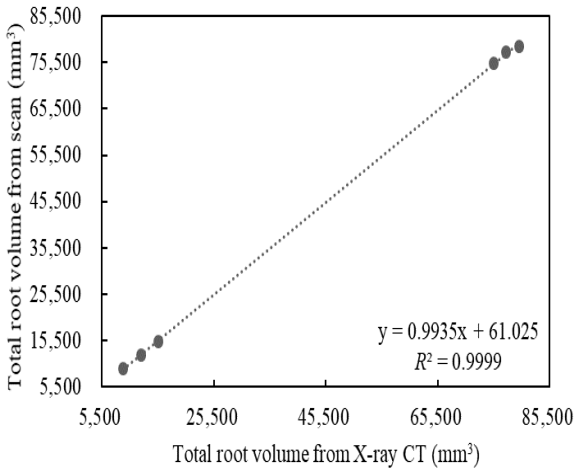


Figure 6. Comparisons between total root length and total root volume determined by X-ray CT and root system scanning after water washing.

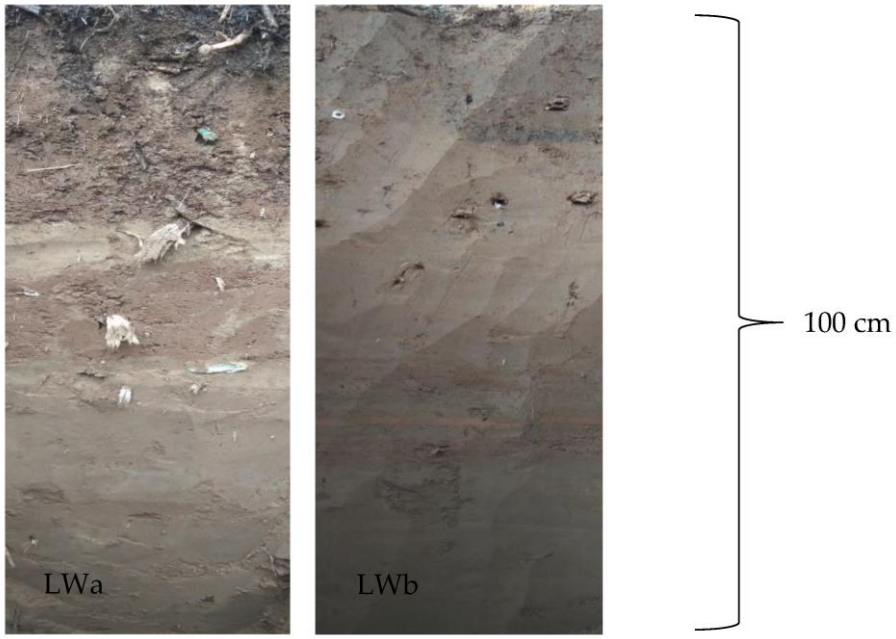


Figure 7. Photographs of sampling site soil profiles.

The number of soil macropores was considerably higher at LWa than at LWb (Table 2). The LWa in the region of interest at the depths of 0–50 cm had a comparatively higher imaged macroporosity (larger than 0.05 mm in diameter) (0.021 ± 0.007 mm^3 mm^{-3}), macropore total volume ($10.3 \times 10^4 \pm 6132$ mm^3), length density ($45.5 \times 10^4 \pm 11{,}026$ mm m^{-3}), node density ($11.3 \times 10^4 \pm 4031$ number m^{-3}), branch density ($10.2 \times 10^4 \pm 5121$ number m^{-3}), mean surface area (32.1 ± 10.2 mm^2), mean diameter (2.9 ± 0.8 mm), and mean volume (5.6 ± 1.3 mm^3) than LWb (0.005 ± 0.002 mm^3 mm^{-3}, $1.5 \times 10^4 \pm 3021$ mm^3, $1.8 \times 10^4 \pm 2957$ mm m^{-3}, $0.7 \times 10^4 \pm 1275$ mm m^{-3}, $0.08 \times 10^4 \pm 215$ number m^{-3}, 14.7 ± 3.6 mm^2, 1.5 ± 0.6 mm, and 3.6 ± 1.1 mm^3). In contrast, the LWa in the region of interest at the depths of 0–50 cm had a comparatively lower macropore mean length (180.3 ± 36.2 mm), branch length (205.2 ± 70.2 mm), and tortuosity (1.1 ± 0.5) than LWb (416.9 ± 120.1 mm, 444.5 ± 90.5 mm, and 1.2 ± 0.5).

Table 2. Number of soil macropores in entire soil columns at LWa and LWb.

Plots	Equivalent Diameter (mm)	Number of Soil Macropores
LWa	0.05 < D < 0.5	7072 ± 562 ^{aA}
	0.5 < D < 1	6502 ± 783 ^{aA}
	1 < D < 3	2837 ± 612 ^{aB}
	3 < D < 5	772 ± 122 ^{aC}
	D > 5	505 ± 101 ^{aC}
LWb	0.05 < D < 0.5	280 ± 92 ^{bC}
	0.5 < D < 1	454 ± 68 ^{bB}
	1 < D < 3	3383 ± 534 ^{aA}
	3 < D < 5	84 ± 10 ^{bD}
	D > 5	22 ± 12 ^{bE}

Lowercase letters represent the significant difference in number of soil macropores with the same diameter between LWa and LWb; capital letters represent the significant difference in number of soil macropores between different diameters at the same site.

The results of the correlation analyses between root systems and soil macropores are shown in Figure 8. Total root length and total root volume were positively correlated with imaged macroporosity, macropore volume, length density, node density, branch density, mean macropore surface area, mean macropore diameter, and mean macropore volume,

whereas they were negatively correlated with mean macropore length, mean macropore branch length, and mean macropore tortuosity.

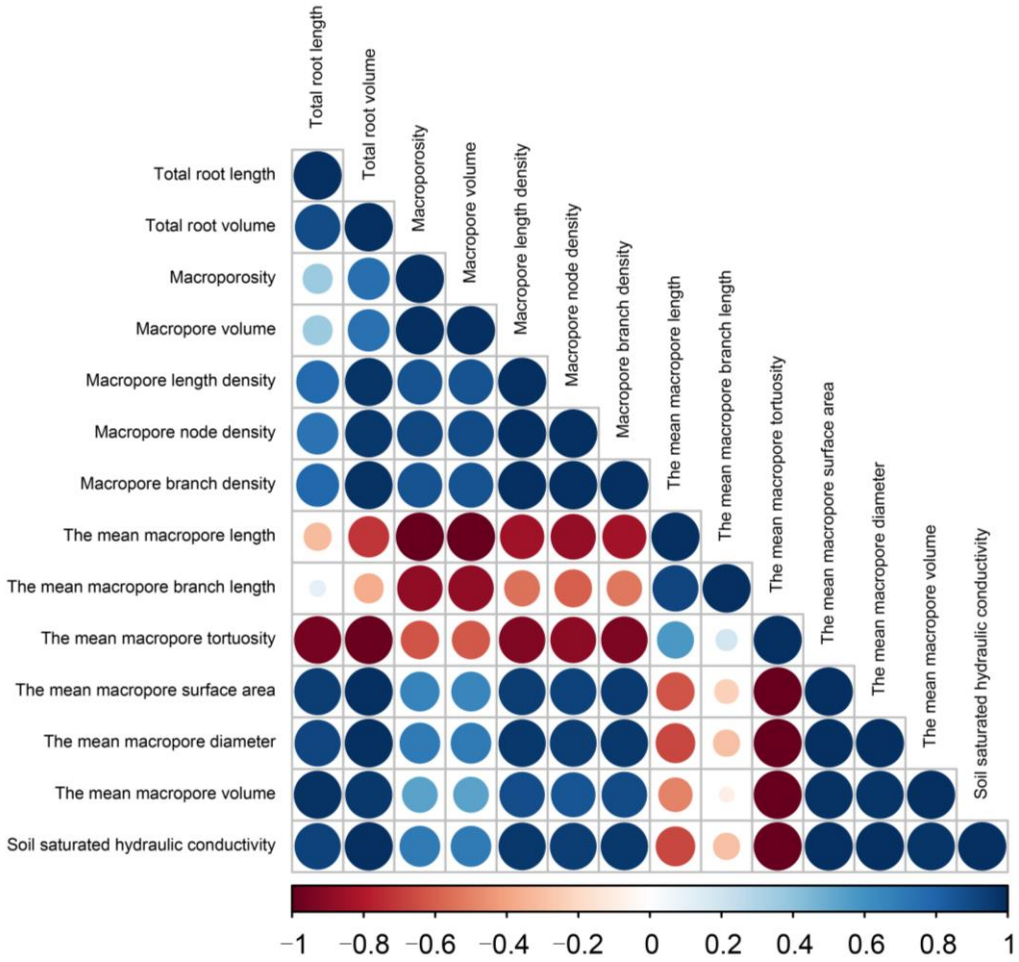


Figure 8. The correlation analyses between root systems, soil macropores, and soil saturated hydraulic conductivity.

3.2. Quantification between Root Systems, Soil Macropores, and Soil Saturated Hydraulic Conductivity

Of all the soil columns studied, soil saturated hydraulic conductivity at each soil depth was significantly greater at LWa (7.38 ± 2.28 cm/h at 0–10 cm, 0.72 ± 0.60 cm/h at 10–20 cm, 0.54 ± 0.48 cm/h at 20–40 cm, and 0.42 ± 0.36 cm/h at 40–60 cm) than that at LWb (0.29 ± 0.35 cm/h at 0–10 cm, 0.60 ± 0.46 cm/h at 10–20 cm, 1.20 ± 0.67 mL/min at 20–40 cm, 0.26 ± 0.40 cm/h at 40–60 cm).

Figure 8 depicts the relationship between root systems, soil macropores, and soil saturated hydraulic conductivity. The correlation analysis results shown in Figure 8 indicate that total root length and total root volume are positively correlated with soil saturated hydraulic conductivity. The correlation analysis results indicated in Figure 8 show that imaged macroporosity, macropore volume, macropore length density, macropore node density, macropore branch density, mean macropore surface area, mean macropore diameter, and mean macropore volume are positively correlated with soil saturated hydraulic conductivity, whereas mean macropore length, mean macropore branch length, and mean macropore tortuosity are negatively correlated with soil saturated hydraulic conductivity.

4. Discussion

4.1. Effects of Forested Wetland Conditions on Root Systems Distribution

More roots were located at LWa than at LWb. This is in contrast to research suggesting that increased soil bulk density in compacted soils can increase total root length due to the increased production of fine root systems to facilitate the acquisition of soil resources [29]. However, some studies indicated that soil compaction can generally have a negative effect on total root length and elongation [30,31]. Compacted soils at the LWb site may increase root systems penetration resistance [32] and affect their clustering [33]. Root length decreased in compacted soils [32–34]. This is because root system growth can be restricted by the penetration resistance of soils [35]. Furthermore, low soil nutrients at LWb also restrict root development [36,37]. For LWa with non-compacted soils, the root systems were thicker and more fibrous (Figure 5), which is consistent with the results of Kristoffersen and Riley [38]. This is because non-compacted soils at LWa have a large number of coarse soil macropores (Figure 5). Those walls of soil macropores are richer in soil nutrients than the surrounding soil matrix. Root systems can grow into those soil macropores or along the walls of soil macropores without any resistance [39]. However, this is in contrast to the study by Wang et al. [40]. They confirmed that soil compaction increased the average diameter of root systems, indicating that soil compaction made root systems thicker. In our study, a better soil physical-chemical condition at LWa can provide a suitable environment for the balance and development of forested wetland ecosystems. It can be regarded as a sink of soil nutrients and water resources, which can be beneficial for the root systems.

4.2. Effects of Forested Wetland Conditions on Soil Macropores

Values of most attributes of soil macropores were richer at LWa than at LWb. The findings could be explained by the fact that the presence of abundant root systems at LWa improved soil macropore structure and increased macropore density [7,11,27]. In contrast, the few root systems at LWb would not protect soil macropore structure, which results in higher macropore tortuosity at LWb [7] and decreased macroporosity and number of soil macropores [27]. Higher soil bulk density at LWb leads to the loss of soil macropores [41]. There is a complex relationship between root systems and soil macropores. These results are consistent with those of Hu et al. [13]. In their study, they confirmed that root density was significantly and positively correlated with imaged macroporosity, macropore surface area density, length density, node density, and branch density [13]. In another study, Kochiieru et al. [1] also confirmed that root volume is significantly correlated with the volume of fine and very fine soil macropores, but they concluded that root length density is positively correlated with the volume of very fine soil macropores. A positive correlation between root system parameters and most attributes of macropores was revealed in our study, which indicates that root systems have a significant effect on soil macropore development [42]. Root systems with high total length and volume have a high degree of lignification [43]. The surface of root systems may have been sufficiently rough, which can result in the formation of soil macropores between the rough root surface and surrounding soils. The rough convexity of root systems' surface increased the disturbance to the surrounding soils during the stretching and thickening processes of root systems [43]. It is possible that root systems with high total length and volume may generate large air gaps between the root and surrounding soils [9]. Root systems with high stiffness induce strong movement of soil particles, which can increase the interaggregate void space [43]. In addition, the disruption of macroaggregates due to the shifting of root systems may also form new pores inside the aggregate, which can increase the number and volume of soil macropores as well as other attributes of soil macropores. Root systems can modify soil macropore networks by different mechanisms, such as translocating soil aggregates, increasing soil aggregation through root exudates and related biological activities, and root decomposition [42]. However, there remains many soil macropores that do not contain root systems in our experimental data (Figure 5). It is possible that soil macropores are not continuously connected to the soil surface or that root system architecture in the soil surface cannot facilitate soil macropore

location [42,44]. Therefore, a healthy forested wetland ecosystem can make the soils more ventilated. The favorable environments in the forested wetland can facilitate the turnover process of soil nutrients and cycling of other organisms in the ecosystems. The beneficial environments can also increase the connectivity of soils so as to make soil pores more effective in soil functions.

4.3. Effects of Forested Wetland Conditions on Soil Saturated Hydraulic Conductivity

In the LWb soil depth 20–40 cm, the sandy loam layer is characterized by higher soil saturated hydraulic conductivity compared with other soil layers, which is consistent with the results of Jiang et al. [45]. In the LWb soil depth 20–40 cm, the sand content dramatically increases, and the silt content reduces compared with other soil layers. With an increase in sand content, the number of soil macropores will increase, which results in increased soil saturated hydraulic conductivity [16].

In our study, total root length and volume are positively correlated with soil saturated hydraulic conductivity. These results are consistent with Shi et al. [46] and Zhu et al. [47]. Soil hydraulic conductivity is altered particularly within soils where root systems are concentrated. Specifically, root length and median root radius are the best predictors for soil hydraulic conductivity changes [48]. A close positive relationship between total root length and soil hydraulic conductivity was observed, indicating that higher soil hydraulic conductivity could be attributed to larger total root length [49]. The positive correlation between root volume and soil hydraulic conductivity suggests that root volume is also important in increasing soil hydraulic conductivity [16]. Coarse root systems are likely to increase soil saturated hydraulic conductivity via the formation and development of soil macropores through the amalgamation of soil particles into soil aggregates and root channels during their decomposition [47,50]. Furthermore, the expansion of coarse root systems is likely to cause compression of soil particles [50], which also promotes the formation of soil macropores and increased soil saturated hydraulic conductivity [47]. However, fine root systems at low density can clog soil pores during their growth, whereas fine root systems at high density tend to eliminate soil macropore volume, so both fine root systems can lead to reduced soil saturated hydraulic conductivity [50]. For example, Archer et al. [16] confirmed that coarse root systems can promote soil hydraulic conductivity. This is because coarse root systems are older than fine root systems, and they will shrink and expand their root branching with time [51]. Such physical movement can create conduits for preferential water flow and solute transport [48]. The presence of such conduits could increase soil hydraulic conductivity [52]. During the establishment of root systems, soil hydraulic conductivity can decrease as root systems fill the soil macropores. Over time, soil hydraulic conductivity can increase as root systems begin to die back. Finally, an equilibrium point is reached when root systems fill those old root channels, which results in higher soil hydraulic conductivity [16]. However, some studies confirmed that root systems within a specific range of diameters from 0.5 mm to 2 mm played an important role in soil hydraulic conductivity, whereas root systems with notably smaller or larger diameters may have less effect on soil hydraulic conductivity [46]. Furthermore, the enhancement of soil saturated hydraulic conductivity because of root systems can be expected in fine-textured soils [50]. Overall, the positive correlation between total root length, total root volume, and soil saturated hydraulic conductivity may be attributed to two aspects. Firstly, due to root system growth and decomposition, well-connected large soil macropores or root channels were formed, which can directly increase soil saturated hydraulic conductivity [53,54]. Secondly, root systems can increase total soil porosity via binding and bonding soil particles [55], and can also improve soil structure by releasing soil exudates and increasing soil organic matter content by root systems decomposition [54], thereby indirectly increasing soil saturated hydraulic conductivity [47].

In our study, most of the attributes of soil macropores can positively influence soil hydraulic conductivity. This is because soil macropores can cause water to flow mainly through those macropores [56]. Previous studies confirmed that the most important prop-

erties of soil macropores explaining soil hydraulic conductivity are (1) the volume of percolating macropores, (2) the diameter of macropores, and (3) the number of macropores [57]. Hu et al. [13] and Borges et al. [58] revealed that soil macropore length density was significantly and positively correlated with soil hydraulic conductivity. Furthermore, soil hydraulic conductivity was also directly influenced by soil microporosity [13]. Decreased soil macroporosity and increased macropore tortuosity can cause decreased soil hydraulic conductivity [41]. High macropore volume confirmed that more water can flow through those macropores without any resistance—this is because soil macropores with high macropore volume can effectively discharge the air in soils and reduce the inhibition of air pressure on soil infiltration [59]. Meanwhile, soil macropores also increase lateral permeability and vertical infiltration, thus affecting soil hydraulic conductivity [59].

5. Conclusions

The values of total root length and total root volume were significantly larger at the large communities of reed than those at the small communities of reed ($p < 0.05$). Imaged macroporosity, macropore volume, macropore length density, macropore node density, macropore branch density, mean macropore surface area, mean macropore diameter, and mean macropore volume at the large communities of reed were significantly larger than those at the small communities of reed ($p < 0.05$), whereas mean macropore length, mean macropore branch length, and mean macropore tortuosity were the opposite. Total root length and total root volume were positively correlated with soil saturated hydraulic conductivity. Imaged macroporosity, macropore volume, macropore length density, macropore node density, macropore branch density, mean macropore surface area, mean macropore diameter, and mean macropore volume were positively correlated with soil saturated hydraulic conductivity, whereas mean macropore length, mean macropore branch length, and mean macropore tortuosity were negatively correlated with soil saturated hydraulic conductivity. This study was conducted using a small sample size, so future studies should be carried out on a larger-scale area and sample size both in space and time. Further, different soil types should also be considered in a future study.

Author Contributions: Conceptualization, Y.Z.; methodology, Y.Z.; software, Y.Z., W.Z. and L.W.; formal analysis, Y.Z., W.Z. and L.W.; investigation, Y.Z., W.Z. and L.W.; writing—original draft preparation, Y.Z.; writing—review and editing, Z.Z. and M.Z.; funding acquisition, M.Z. All authors have read and agreed to the published version of the manuscript.

Funding: This research was supported by the National Natural Science Foundation of China (41907007), Jiangsu Province Natural Science Foundation for Youth (BK20190747), and the National Natural Science Foundation of China (41771547).

Acknowledgments: The authors are grateful to the National Natural Science Foundation of China and Jiangsu Province Natural Science Foundation for Youth for financial support. We are highly thankful to the anonymous reviewers and editors for their careful reading and insightful comments and suggestions on our manuscript.

Conflicts of Interest: The authors of this manuscript declare that they have no competing interests or involvement in any organization or entity with any financial or nonfinancial interest in the subject matter or materials discussed in this manuscript.

References

1. Kochiieru, M.; Lamorski, K.; Feiza, V.; Feiziene, D.; Volungevicius, J. Quantification of the relationship between root parameters and soil macropore parameters under different land use systems in Retisol. *Int. Agrophysics* **2020**, *34*, 301–308. [CrossRef]
2. Chirol, C.; Spencer, K.L.; Carr, S.J.; Möller, I.; Evans, B.; Lynch, J.; Brooks, H.; Royse, K.R. Effect of vegetation cover and sediment type on 3D subsurface structure and shear strength in saltmarshes. *Earth Surf. Process. Landf.* **2021**, *46*, 2279–2297. [CrossRef]
3. Evans, B.; Brooks, H.; Chirol, C.; Kirkham, M.; Möller, I.; Royse, K.; Spencer, K.; Spencer, T. Vegetation interactions with geotechnical properties and erodibility of salt marsh sediments. *Estuar. Coast. Shelf Sci.* **2022**, *265*, 107713. [CrossRef]
4. Zhang, Y.H.; Chen, J.H.; Zhang, J.C.; Zhang, Z.; Zhang, M. Novel indicator for assessing wetland degradation based on the index of hydrological connectivity and its correlation with the root-soil interface. *Ecol. Indic.* **2021**, *133*, 108392. [CrossRef]

5. Engloner, A.I. Structure, growth dynamics and biomass of reed (Phragmites australis)–A review. *Flora-Morphol. Distrib. Funct. Ecol. Plants* **2009**, *204*, 331–346. [CrossRef]
6. Ghestem, M.; Sidle, R.C.; Stokes, A. The influence of plant root systems on subsurface flow: Implications for slope stability. *Bioscience* **2011**, *61*, 869–879. [CrossRef]
7. Hu, X.; Li, X.Y.; Wang, P.; Liu, Y.; Wu, X.C.; Li, Z.C.; Zhao, Y.D.; Cheng, Y.Q.; Guo, L.L.; Lyu, Y.L. Influence of exclosure on CT-measured soil macropores and root architecture in a shrub-encroached grassland in northern China. *Soil Tillage Res.* **2019**, *187*, 21–30. [CrossRef]
8. Chirol, C.; Carr, S.J.; Spencer, K.L.; Moeller, I. Pore, live root and necromass quantification in complex heterogeneous wetland soils using X-ray computed tomography. *Geoderma* **2021**, *387*, 114898. [CrossRef]
9. Bodner, G.; Leitner, D.; Kaul, H.-P. Coarse and fine root plants affect pore size distributions differently. *Plant Soil* **2014**, *380*, 133–151. [CrossRef]
10. Qiao, J.; Liu, X.; Zhu, Y.; Jia, X. Three-dimensional quantification of soil pore structure in wind-deposited loess under different vegetation types using industrial X-ray computed tomography. *Catena* **2021**, *199*, 105098. [CrossRef]
11. Wang, J.; Qin, Q.; Bai, Z. Characterizing the effects of opencast coal-mining and land reclamation on soil macropore distribution characteristics using 3D CT scanning. *Catena* **2018**, *171*, 212–221. [CrossRef]
12. Ben-Hur, M.; Yolcu, G.; Uysal, H.; Lado, M.; Paz, A. Soil structure changes: Aggregate size and soil texture effects on hydraulic conductivity under different saline and sodic conditions. *Soil Res.* **2009**, *47*, 688–696. [CrossRef]
13. Hu, X.; Li, X.Y.; Li, Z.C.; Gao, Z.; Wu, X.C.; Wang, P.; Lyu, Y.L.; Liu, L.Y. Linking 3-D soil macropores and root architecture to near saturated hydraulic conductivity of typical meadow soil types in the Qinghai Lake Watershed, northeastern Qinghai–Tibet Plateau. *Catena* **2020**, *185*, 104287. [CrossRef]
14. Pierret, A.; Capowiez, Y.; Belzunces, L.; Moran, C. 3D reconstruction and quantification of macropores using X-ray computed tomography and image analysis. *Geoderma* **2002**, *106*, 247–271. [CrossRef]
15. Luo, L.; Lin, H.; Halleck, P. Quantifying soil structure and preferential flow in intact soil using X-ray computed tomography. *Soil Sci. Soc. Am. J.* **2008**, *72*, 1058–1069. [CrossRef]
16. Archer, N.; Quinton, J.N.; Hess, T. Below-ground relationships of soil texture, roots and hydraulic conductivity in two-phase mosaic vegetation in South-east Spain. *J. Arid Environ.* **2002**, *52*, 535–553. [CrossRef]
17. Bodhinayake, W.; Cheng Si, B. Near-saturated surface soil hydraulic properties under different land uses in the St Denis National Wildlife Area, Saskatchewan, Canada. *Hydrol. Process.* **2004**, *18*, 2835–2850. [CrossRef]
18. Julich, S.; Kreiselmeier, J.; Scheibler, S.; Petzold, R.; Schwärzel, K.; Feger, K.-H. Hydraulic Properties of Forest Soils with Stagnic Conditions. *Forests* **2021**, *12*, 1113. [CrossRef]
19. Zhang, Y.; Huang, C.; Zhang, W.; Chen, J.; Wang, L. The concept, approach, and future research of hydrological connectivity and its assessment at multiscales. *Environ. Sci. Pollut. Res.* **2021**, *28*, 52724–52743. [CrossRef]
20. Bai, J.; Yu, Z.; Yu, L.; Wang, D.; Guan, Y.; Liu, X.; Gu, C.; Cui, B. In-situ organic phosphorus mineralization in sediments in coastal wetlands with different flooding periods in the Yellow River Delta, China. *Sci. Total Environ.* **2019**, *682*, 417–425. [CrossRef]
21. Zhang, J.M.; Xu, Z.M.; Li, F.; Hou, R.J.; Ren, Z. Quantification of 3D macropore networks in forest soils in Touzhai valley (Yunnan, China) using X-ray computed tomography and image analysis. *J. Mt. Sci.* **2017**, *14*, 474–491. [CrossRef]
22. Hu, X.; Li, Z.C.; Li, X.Y.; Liu, Y. Influence of shrub encroachment on CT-measured soil macropore characteristics in the Inner Mongolia grassland of northern China. *Soil Tillage Res.* **2015**, *150*, 1–9. [CrossRef]
23. Liu, B.; Fan, H.; Han, W.; Zhu, L.; Zhao, X.; Zhang, Y.; Ma, R. Linking soil water retention capacity to pore structure characteristics based on X-ray computed tomography: Chinese Mollisol under freeze-thaw effect. *Geoderma* **2021**, *401*, 115170. [CrossRef]
24. Ferreira, T.R.; Pires, L.F.; Wildenschild, D.; Heck, R.J.; Antonino, A.C. X-ray microtomography analysis of lime application effects on soil porous system. *Geoderma* **2018**, *324*, 119–130. [CrossRef]
25. Luo, L.; Lin, H.; Li, S. Quantification of 3-D soil macropore networks in different soil types and land uses using computed tomography. *J. Hydrol.* **2010**, *393*, 53–64. [CrossRef]
26. Peth, S.; Horn, R.; Beckmann, F.; Donath, T.; Fischer, J.; Smucker, A. Three-dimensional quantification of intra-aggregate pore-space features using synchrotron-radiation-based microtomography. *Soil Sci. Soc. Am. J.* **2008**, *72*, 897–907. [CrossRef]
27. Feng, Y.; Wang, J.; Bai, Z.; Reading, L.; Jing, Z. Three-dimensional quantification of macropore networks of different compacted soils from opencast coal mine area using X-ray computed tomography. *Soil Tillage Res.* **2020**, *198*, 104567. [CrossRef]
28. Gholizadeh-Sarabi, S.; Sepaskhah, A.R. Effect of zeolite and saline water application on saturated hydraulic conductivity and infiltration in different soil textures. *Arch. Agron. Soil Sci.* **2013**, *59*, 753–764. [CrossRef]
29. Ola, A.; Schmidt, S.; Lovelock, C.E. The effect of heterogeneous soil bulk density on root growth of field-grown mangrove species. *Plant Soil* **2018**, *432*, 91–105. [CrossRef]
30. Smith, K.D.; May, P.B.; Moore, G.M. The influence of compaction and soil strength on the establishment of four Australian landscape trees. *J. Arboric.* **2001**, *27*, 1–7. [CrossRef]
31. Cambi, M.; Hoshika, Y.; Mariotti, B.; Paoletti, E.; Picchio, R.; Venanzi, R.; Marchi, E. Compaction by a forest machine affects soil quality and Quercus robur L. seedling performance in an experimental field. *For. Ecol. Manag.* **2017**, *384*, 406–414. [CrossRef]
32. Yue, L.K.; Wang, Y.; Wang, L.; Yao, S.; Cong, C.; Ren, L.; Zhang, B. Impacts of soil compaction and historical soybean variety growth on soil macropore structure. *Soil Tillage Res.* **2021**, *214*, 105166. [CrossRef]

33. Colombi, T.; Torres, L.C.; Walter, A.; Keller, T. Feedbacks between soil penetration resistance, root architecture and water uptake limit water accessibility and crop growth—A vicious circle. *Sci. Total Environ.* **2018**, *626*, 1026–1035. [CrossRef]
34. Lipiec, J.; Horn, R.; Pietrusiewicz, J.; Siczek, A. Effects of soil compaction on root elongation and anatomy of different cereal plant species. *Soil Tillage Res.* **2012**, *121*, 74–81. [CrossRef]
35. Stewart, J.; Moran, C.; Wood, J. Macropore sheath: Quantification of plant root and soil macropore association. *Plant Soil* **1999**, *211*, 59–67. [CrossRef]
36. López-Bucio, J.; Cruz-Ramırez, A.; Herrera-Estrella, L. The role of nutrient availability in regulating root architecture. *Curr. Opin. Plant Biol.* **2003**, *6*, 280–287. [CrossRef]
37. Martínez, M.M.; Ortega, R.; Janssens, M.; Fincheira, P. Use of organic amendments in table grape: Effect on plant root system and soil quality indicators. *J. Soil Sci. Plant Nutr.* **2018**, *18*, 100–112. [CrossRef]
38. Kristoffersen, A.Ø.; Riley, H. Effects of soil compaction and moisture regime on the root and shoot growth and phosphorus uptake of barley plants growing on soils with varying phosphorus status. *Nutr. Cycl. Agroecosystems* **2005**, *72*, 135–146. [CrossRef]
39. Landl, M.; Huber, K.; Schnepf, A.; Vanderborght, J.; Javaux, M.; Glyn Bengough, A.; Vereecken, H. A new model for root growth in soil with macropores. *Plant Soil* **2017**, *415*, 99–116. [CrossRef]
40. Wang, M.; He, D.; Shen, F.; Huang, J.; Zhang, R.; Liu, W.; Zhu, M.; Zhou, L.; Wang, L.; Zhou, Q. Effects of soil compaction on plant growth, nutrient absorption, and root respiration in soybean seedlings. *Environ. Sci. Pollut. Res.* **2019**, *26*, 22835–22845. [CrossRef]
41. Colombi, T.; Braun, S.; Keller, T.; Walter, A. Artificial macropores attract crop roots and enhance plant productivity on compacted soils. *Sci. Total Environ.* **2017**, *574*, 1283–1293. [CrossRef]
42. Zhou, H.; Whalley, W.R.; Hawkesford, M.J.; Ashton, R.W.; Atkinson, B.; Atkinson, J.A.; Sturrock, C.J.; Bennett, M.J.; Mooney, S.J. The interaction between wheat roots and soil pores in structured field soil. *J. Exp. Bot.* **2021**, *72*, 747–756. [CrossRef]
43. Zhang, Y.H.; Jiang, J.; Zhang, J.C.; Zhang, Z.; Zhang, M. Effects of roots systems on hydrological connectivity below the soil surface in the Yellow River Delta wetland. *Ecohydrology* **2022**, *15*, e2393. [CrossRef]
44. Granse, D.; Titschack, J.; Ainouche, M.; Jensen, K.; Koop-Jakobsen, K. Subsurface aeration of tidal wetland soils: Root-system structure and aerenchyma connectivity in Spartina (Poaceae). *Sci. Total Environ.* **2022**, *802*, 149771. [CrossRef]
45. Jiang, X.J.; Liu, W.; Chen, C.; Liu, J.; Yuan, Z.-Q.; Jin, B.; Yu, X. Effects of three morphometric features of roots on soil water flow behavior in three sites in China. *Geoderma* **2018**, *320*, 161–171. [CrossRef]
46. Shi, X.; Qin, T.; Yan, D.; Tian, F.; Wang, H. A meta-analysis on effects of root development on soil hydraulic properties. *Geoderma* **2021**, *403*, 115363. [CrossRef]
47. Zhu, P.; Zhang, G.; Zhang, B. Soil saturated hydraulic conductivity of typical revegetated plants on steep gully slopes of Chinese Loess Plateau. *Geoderma* **2022**, *412*, 115717. [CrossRef]
48. Yu, Y.; Loiskandl, W.; Kaul, H.P.; Himmelbauer, M.; Wei, W.; Chen, L.; Bodner, G. Estimation of runoff mitigation by morphologically different cover crop root systems. *J. Hydrol.* **2016**, *538*, 667–676. [CrossRef]
49. Deguchi, T.; Iwama, K.; Matsumoto, M.; Tanigawa, J. Effect of varietal difference in root system on hydraulic conductance in potatoes under different soil water conditions and planting dates. *Potato Res.* **2015**, *58*, 103–119. [CrossRef]
50. Lu, J.; Zhang, Q.; Werner, A.D.; Li, Y.; Jiang, S.; Tan, Z. Root-induced changes of soil hydraulic properties–A review. *J. Hydrol.* **2020**, *589*, 125203. [CrossRef]
51. Nuttall, J.G.; Davies, S.; Armstrong, R.; Peoples, M. Testing the primer-plant concept: Wheat yields can be increased on alkaline sodic soils when an effective primer phase is used. *Aust. J. Agric. Res.* **2008**, *59*, 331–338. [CrossRef]
52. Gile, L.; Gibbens, R.; Lenz, J. Soils and sediments associated with remarkable, deeply-penetrating roots of crucifixion thorn (koeberlinia spinosazucc.). *J. Arid Environ.* **1995**, *31*, 137–151. [CrossRef]
53. Hao, H.X.; Wei, Y.J.; Cao, D.N.; Guo, Z.L.; Shi, Z.H. Vegetation restoration and fine roots promote soil infiltrability in heavy-textured soils. *Soil Tillage Res.* **2020**, *198*, 104542. [CrossRef]
54. Zhu, P.; Zhang, G.; Wang, H.; Xing, S. Soil infiltration properties affected by typical plant communities on steep gully slopes on the Loess Plateau of China. *J. Hydrol.* **2020**, *590*, 125535. [CrossRef]
55. De Baets, S.; Poesen, J.; Knapen, A.; Barberá, G.G.; Navarro, J. Root characteristics of representative Mediterranean plant species and their erosion-reducing potential during concentrated runoff. *Plant Soil* **2007**, *294*, 169–183. [CrossRef]
56. Ilek, A.; Kucza, J.; Witek, W. Using undisturbed soil samples to study how rock fragments and soil macropores affect the hydraulic conductivity of forest stony soils: Some methodological aspects. *J. Hydrol.* **2019**, *570*, 132–140. [CrossRef]
57. Cheik, S.; Bottinelli, N.; Minh, T.T.; Doan, T.T.; Jouquet, P. Quantification of three dimensional characteristics of macrofauna macropores and their effects on soil hydraulic conductivity in northern Vietnam. *Front. Environ. Sci.* **2019**, *7*, 31. [CrossRef]
58. Borges, J.A.; Pires, L.F.; Cássaro, F.A.; Auler, A.C.; Rosa, J.A.; Heck, R.J.; Roque, W.L. X-ray computed tomography for assessing the effect of tillage systems on topsoil morphological attributes. *Soil Tillage Res.* **2019**, *189*, 25–35. [CrossRef]
59. Beven, K.; Germann, P. Macropores and water flow in soils. *Water Resour. Res.* **1982**, *18*, 1311–1325. [CrossRef]

Disclaimer/Publisher's Note: The statements, opinions and data contained in all publications are solely those of the individual author(s) and contributor(s) and not of MDPI and/or the editor(s). MDPI and/or the editor(s) disclaim responsibility for any injury to people or property resulting from any ideas, methods, instructions or products referred to in the content.

forests

MDPI

Article

Effects of Soil Warming on Soil Microbial Metabolism Limitation in a *Quercus acutissima* Forest in North Subtropical China

Jinlong Wang †, Meijia Zhou †, Haibo Hu, Jie Kuai, Xia Wang and Lei Chu *

Co-Innovation Center for Sustainable Forestry in Southern China, Key Laboratory of Soil and Water Conservation and Ecological Restoration in Jiangsu Province, Nanjing Forestry University, Nanjing 210037, China
* Correspondence: chuleinjfu@njfu.edu.cn; Tel.: +86-18751890035
† These authors contributed equally to this work.

Abstract: In order to explore the influence of climate warming on soil microbial metabolism in the ecosystem and reveal the relationship between soil microbial metabolism limitation and environmental factors, in this study, the effects of warming on soil enzyme activities and nutrient availability were investigated by setting underground heating cables at 2 °C and 4 °C soil warming in a typical *Quercus acutissima* forest in the northern subtropics, and enzyme stoichiometric models were used to evaluate the limits of soil microbial metabolism. The results showed that soil warming significantly increased the activities of β-1,4-glucosidase (BG) and L-leucine aminopeptidase (LAP), and significantly increased the contents of nitrate nitrogen (NO_3^--N) and available phosphorus (AP) in soil. The soil warming increased soil microbial C limitation and alleviated soil microbial P limitation. Our study showed that the change of soil microbial C and P limitation caused by warming may cause a large amount of SOM decomposition in a short period, leading to a large fluctuation of soil carbon turnover, which is not conducive to the stability of the soil C pool. This study provides important insights linking microbial metabolism to soil warming and improves our understanding of C cycling in forest systems.

Keywords: soil warming; soil enzyme activities; nutrient availability; microbial C; P limitation; microbial metabolism

check for updates

Citation: Wang, J.; Zhou, M.; Hu, H.; Kuai, J.; Wang, X.; Chu, L. Effects of Soil Warming on Soil Microbial Metabolism Limitation in a *Quercus acutissima* Forest in North Subtropical China. *Forests* **2023**, *14*, 19. https://doi.org/10.3390/f14010019

Academic Editor: Choonsig Kim

Received: 23 October 2022
Revised: 28 November 2022
Accepted: 13 December 2022
Published: 22 December 2022

Copyright: © 2022 by the authors. Licensee MDPI, Basel, Switzerland. This article is an open access article distributed under the terms and conditions of the Creative Commons Attribution (CC BY) license (https://creativecommons.org/licenses/by/4.0/).

1. Introduction

Global climate change is one of the global issues that society is concerned about, and its most direct manifestation is global climate warming. Over the last century of observations, the average global temperature has risen by 1.07 °C [1]. According to the simulation results of the CMIP 5 model, by the end of the 21st century, the global average surface soil temperature may rise as high as 2.6~4.8 °C compared with the period from 1986 to 2005, which is most serious environmental problem facing mankind at present. As key biological factors in the terrestrial ecosystem, soil microorganisms play an important role in regulating soil nutrient cycling and are sensitive to soil temperature [2]. Soil microorganisms influence nutrient cycling by producing various enzymes that regulate the decomposition and mineralization of soil organic matter [3,4], which in turn provide energy and available nutrients for soil microbial metabolic activities [5,6]. Therefore, soil enzymes are key participants in microbial metabolism and soil organic matter decomposition, and soil enzymatic stoichiometry can be used as an important index to evaluate soil nutrient availability and soil microbial metabolism [7]. The carbon-metabolizing enzyme β-1,4-glucosidase (BG), nitrogen-metabolizing enzymes β-1,4-*N*-acetylglucosidase (NAG) and L-leucine aminopeptidase (LAP), and phosphorous-metabolizing enzyme acid phosphatase (ACP) are usually the main research objects [8]. Because these four enzymes can catalyze the generation of bioavailable terminal monomers [9], this process is closely related to

nutrient cycling in the ecosystem. At present, there is no uniform conclusion on the response of soil enzyme activities to soil temperature change. Melillo et al. [10] showed that increasing soil temperature would enhance the activities of microorganisms and enzymes, accelerate the decomposition of soil organic matter, enhance soil respiration, and positively affect global change. Liu et al. [11] found that changes such as the decrease of soil water caused by the increase in soil temperature would reduce the availability of soil water and affect the metabolic activities and enzyme activities of soil microorganisms by limiting the diffusion loss of reaction substrates. Many studies showed that the soil enzyme activity was significantly affected by many temperature-related factors, including temperature increase amplitude, soil moisture content, and temperature increase duration [12–14].

Given that temperature is an important driver of ecosystem processes [15], climate warming is bound to affect soil enzyme activities and change ecosystem C, N, and P cycles, which in turn change the nutrient limitation of soil microorganisms [16]. Zheng et al. [17] found short-term soil warming decreased microbial C limitation and increased microbial P limitation by affecting soil available nutrients and soil water content. Therefore, with the background of global warming, it is of great significance to elucidate the variation characteristics of soil enzyme activities for studying soil nutrient availability, microbial nutrient metabolism, and soil C pool stability in specific regions. Moreover, Moorhead et al. [16,18] proposed quantifying soil microorganisms' relative C limitation by vector length and the relative N and P limitation of soil microorganisms by vector angle, which can directly reflect the relative nutrient requirements of soil microorganisms. This method can help us intuitively understand the soil microbial metabolism in the ecosystem with the background of global warming [19] and reveal the relationship between soil microbial metabolism limitation and environmental factors [4]. It is helpful to elucidate the mechanism of soil C, N, and P cycling and thus improve our ability to predict soil C stocks under climate warming [20].

The existing soil warming experiments focus on temperate and tropical ecosystems, and few studies have been conducted in the northern subtropical region, which is particularly sensitive to climate change. To comprehensively assess the effects of climate warming on soil enzyme activities, soil nutrient availability, and soil microbial metabolism characteristics in the north subtropical forest ecosystem, this study took a *Quercus acutissima* forest in the Northern subtropical region as the research subject, and soil climate warming to increase soil temperature (warming by 2 °C, 4 °C) by burying heating cables. Therefore, we hypothesized that: (1) soil warming would have a positive effect on soil enzyme activities; (2) soil warming would decrease microbial C limitation and increase microbial P limitation; and (3) soil water content would be the key factor affecting microbial metabolism limitation.

2. Materials and Methods

2.1. Study Site

The study area is located in Zhenjiang, Jiangsu Province, which belongs to the north subtropical monsoon climate zone with four distinct seasons and sufficient light. The annual average temperature is 15.2 °C, the highest temperature is 39.6 °C, and the lowest temperature is −16.7 °C. The average annual precipitation is 1055.6 mm, with a great inter-annual variation. The average annual relative humidity is 79%. The study area is located in the hilly region of Jianghuai, and the terrain is mostly hilly and gentle. The soil layer thickness is generally 40~60 cm, and the soil pH is 4.5~5.0. The forest vegetation belongs to the east of the north subtropical region of China, and the zonal vegetation is a deciduous broad-leaved mixed forest with evergreen components. The test site is based on the *Quercus acutissima* forest. Shrubs mainly include *Rosa multiflora*, *Fortunearia Sinensis*, *Callicarpa cathayana*, *Ilex cornuta*, *Symplocos paniculata*, etc. Herbaceous plants mainly include *Parthenocissus tricuspidata* and *Adiantum capillus-veneris* [21].

2.2. Experimental Treatments

The study plots were set in Jurong City, Jiangsu Province, and three sample plots were arranged in a *Q. acutissima* forest with relatively uniform topography and slope, with a distance of more than 10 m from each other. Four 3 × 3 m subplots were set in each sample plot, a total of 12 subplots, with a spacing of more than 3 m between the subplots. Four treatments (soil temperature increase of 2 °C, soil temperature increase of 4 °C, disturbed control, and blank control) were randomly applied to four subplots in each sample plot. In December 2019, the same heating cables were laid in parallel in each plot. The heating power per unit area of the soil was calculated according to the plot area, which was arranged in parallel with a depth of 10 cm and a spacing of 20 cm and surrounded in the outermost circle to ensure the uniformity of warming in the plot. The temperature sensor buried at 10 cm was used to collect and compare the soil temperature data of the control field and the warming sample field. The temperature controller scanned every 10 min, and the relay switch was controlled by the temperature controller to warm the soil. The cables were arranged in the same way as before but without heating. Three months after the cable was laid out, it was powered on for warming (March 2020) to reduce the impact of soil disturbance.

2.3. Soil Sample Collection

In March 2021 (1 year of warming), soil samples ranging from 0 to 10 cm were collected in each subplot after removing surface litter according to the 5-point sampling method. Soil samples from 5 points in each plot were evenly mixed to collect a total of 12 bags of soil samples. The samples were quickly frozen with dry ice and brought back to the laboratory. Gravel and plant roots were picked out and divided into two parts after a 2 mm sieve. One part was stored in a −20 °C refrigerator for long-term determination of soil enzyme activities and available nutrients, and the other part was dried naturally for determination of soil physical and chemical properties.

2.4. Determination of Soil Physical and Chemical Properties and Enzyme Activities

Soil TN and SOC contents were determined by an elemental analyzer (Vario EL iii, Elementar, Frankfurt, Germany). Soil TP content was prepared by H_2SO_4-H_2O_2 de-boiling solution and measured by molybdenum-antimony anticolorimetric method. Soil water content was determined after oven-drying 10 g of fresh soil at 105 °C for 48 h. Soil pH was measured by a pH meter (soil and water ratio 2.5:1, Sartorius Gmb H: Gottingen, Germany). Soil DOC concentration was extracted with 0.5 M K_2SO_4 and shaken for 60 min at 200 rpm on a reciprocal shaker. The extracts were filtered through a Millipore 0.45-μm filter and then measured using a TOC analyzer (Shimadzu TOC-L, Kyoto, Japan). Soil NO_3^--N concentration was quantified by spectrophotometry, and soil NH_4^+-N was determined by (indophenol blue) colorimetric method [22]. The activities of BG, NAG, LAP, and ACP in soil were tested with the kit produced by Keming Biology (http://www.cominbio.com/index.html, accessed on 28 March 2022).

2.5. Analysis Methods

Based on the vector theory of enzyme chemistry proposed by Moorhead et al. [18,23], vector length (vector L) and vector angle (vector A) calculated by enzyme stoichiometric ratio were used in this study. Soil microbial nutrient limitation was analyzed by calculating vector length (vector L) and vector angle (vector A) of all data:

$$X = (BG)/(BG + AP)$$

$$Y = (BG)/(BG + NAG + LAP)$$

$$\text{Vector L} = \text{SQRT}(X^2 + Y^2)$$

$$\text{Vector A} = \text{DEGREES}[\text{ATAN2}(X,Y)]$$

where X represents the relative activity of C and P metabolic enzymes and Y represents the relative activity of C and N metabolic enzymes. Vector L is the straight-line distance from the origin to the point (x,y), representing the degree of soil microbial C limitation. Vector A is the arctangent function of the extension line from origin to point (x,y), representing the limitation degree of soil microorganisms N and P. Vector angles greater than 45° indicate microbial P-limit, while vector angles less than 45° indicate N-limit.

SPSS 21.0 (SPSS Inc., Chicago, IL, USA) and Canoco 5.0 were used for data analysis. One-way analysis of variance was used to analyze the differences in soil physical and chemical properties, soil enzyme activities, and enzyme stoichiometric ratios, and Pearson correlation analysis and redundancy analysis were performed. GraphPad Prism 9 was used for plotting.

3. Results

3.1. Effects of Soil Warming on Soil Physical and Chemical Properties

Table 1 showed that compared with T0 treatment, T2 and T4 treatments significantly reduced SOC content by 19.3% and 17.9% (both $p < 0.05$), respectively, and decreased SWC by 14.84% and 20.01%, respectively (both $p < 0.05$). Compared with the T0 treatment, T4 treatment significantly increased the contents of soil NO_3^--N and AP by 18.82% and 98.58% (both $p < 0.05$). Soil N/P under T2 and T4 treatments significantly decreased compared with T0 treatment ($p < 0.05$). Moreover, soil TN, TP, NH_4^+-N, DOC, pH, and C/N had no significant response to soil warming ($p > 0.05$).

Table 1. Soil physical and chemical properties contents under different treatments.

Treatments	T0	T2	T4
pH	4.60 ± 0.21 a	4.45 ± 0.09 a	4.46 ± 0.20 a
SWC (%)	21.05 ± 1.08 a	18.18 ± 0.61 b	17.54 ± 0.64 b
SOC ($g \cdot kg^{-1}$)	22.70 ± 3.99 b	18.33 ± 3.13 a	18.63 ± 2.42 a
TN ($g \cdot kg^{-1}$)	1.53 ± 0.35 a	1.13 ± 0.31 a	1.30 ± 0.17 a
TP ($g \cdot kg^{-1}$)	0.34 ± 0.09 a	0.32 ± 0.08 a	0.35 ± 0.05 a
NH_4^+-N ($mg \cdot kg^{-1}$)	17.75 ± 0.43 a	19.45 ± 4.64 a	16.17 ± 1.86 a
NO_3^--N ($mg \cdot kg^{-1}$)	21.95 ± 4.32 b	24.21 ± 5.17 ab	26.08 ± 5.14 a
AP ($mg \cdot kg^{-1}$)	1.41 ± 0.39 b	2.21 ± 0.57 ab	2.80 ± 0.50 a
DOC ($mg \cdot kg^{-1}$)	141.19 ±16.88 a	153.41 ± 19.20 a	150.82 ± 23.97 a
C/N	14.73 ± 0.56 ab	15.97 ± 1.17 a	14.34 ± 0.37 b
C/P	65.99 ±1.01 a	55.87 ± 6.69 a	53.72 ± 6.09 a
N/P	4.48 ± 0.19 a	3.49 ± 0.51 b	3.74 ± 0.34 b

All results were mean ± standard error. Lowercase letters represent significant differences in soil nutrient contents under different treatments ($p < 0.05$). SWC: soil water content; SOC: soil organic carbon; TN: total nitrogen; TP: total phosphorus; NO_3^--N: nitrate nitrogen; NH_4^+-N: ammonium nitrogen; AP: available phosphorus; DOC: dissolved organic carbon; C/N: SOC/TN; C/P: SOC/TP; N/P: TN/TP. T0: control without warming; T2: 2 °C warming treatment; T4: 4 °C warming treatment.

3.2. Changes in Soil Enzyme Activities and Soil Enzymatic Stoichiometry

In general, soil warming changed soil enzyme activities, but it depended on the type of enzyme. Specifically, compared with the T0 treatment, the activity of BG significantly increased under T2 and T4 treatments by 125.74% and 80.55% ($p < 0.05$, Figure 1a), while the activity of LAP only significantly increased under T4 treatment ($p < 0.05$, Figure 1b). Moreover, NAG and ACP activities did not respond to soil warming ($p > 0.05$, Figure 1c,d).

Soil enzymatic stoichiometry reflects the relative requirements of soil microorganisms for C, N, and P acquisition. In this study, BG: (NAG+LAP), BG: AP, and (NAG+LAP): AP increased with soil warming. Specifically, BG: (NAG+LAP) under T2 treatment was significantly higher than that under T0 treatment ($p < 0.05$, Figure 2a). Compared with the T0 treatment, soil warming significantly increased BG: AP ($p < 0.05$), but had no significant effect on (NAG+LAP): AP (Figure 2b,c).

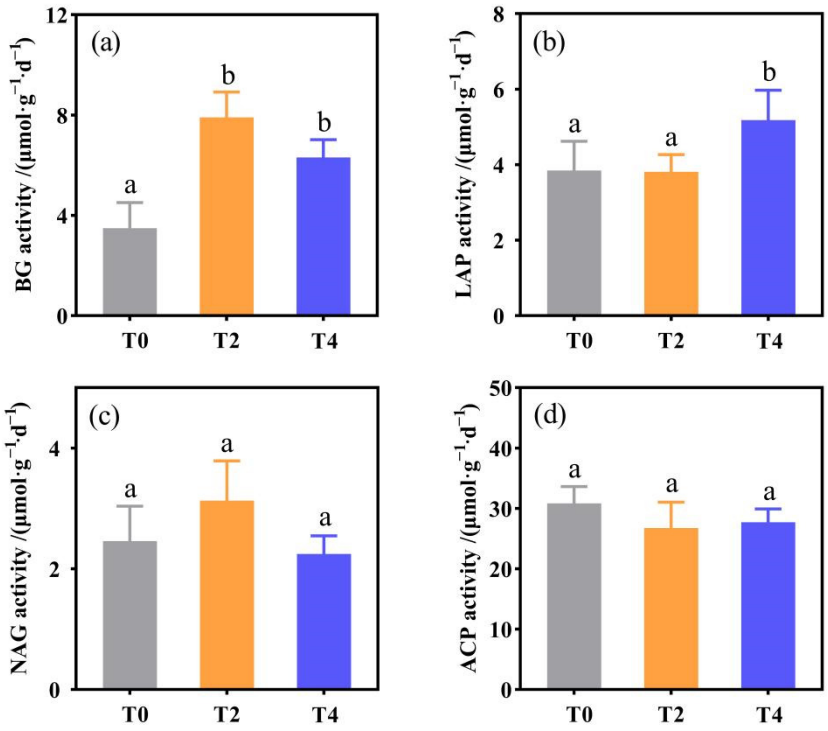


Figure 1. Changes in soil enzyme activities under different treatments: (**a**) the activity of BG (β-1,4-glucosidase); (**b**) the activity of NAG (β-1,4-*N*-acetylglucosidase); (**c**) the activity of LAP (L-leucine aminopeptidase); (**d**) the activity of ACP (acid phosphatase). T0: control without warming; T2: 2 °C warming treatment; T4: 4 °C warming treatment. Lowercase letters represent significant differences in soil enzyme activity under different treatments ($p < 0.05$).

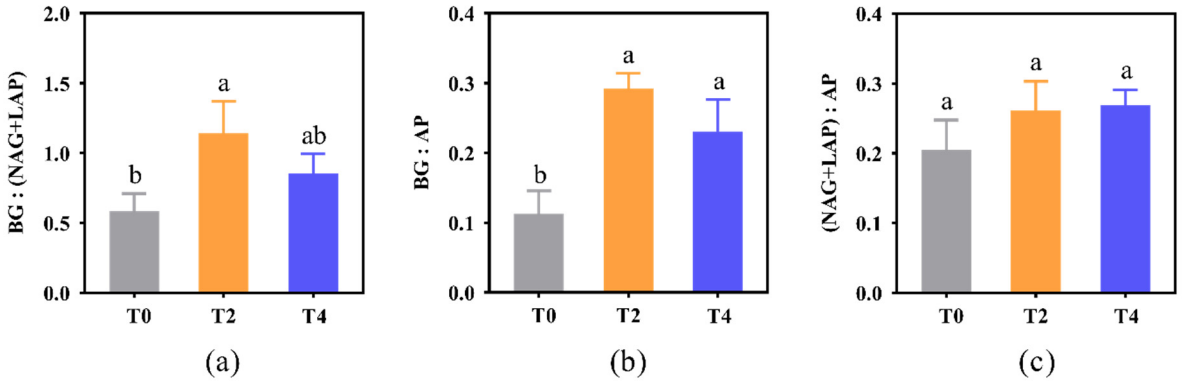


Figure 2. Changes in soil enzymatic stoichiometry under different treatments. (**a**) ratio of C metabolizing enzyme to N metabolizing enzymes; (**b**) ratio of C metabolizing enzyme to P metabolizing enzyme; (**c**) ratio of N metabolizing enzymes to P metabolizing enzyme. BG: β-1,4-glucosidase; NAG: β-1,4-*N*-acetylglucosidase; LAP: L-leucine aminopeptidase; ACP: acid phosphatase. T0: control without warming; T2: 2 °C warming treatment; T4: 4 °C warming treatment. Lowercase letters represent significant differences in soil enzyme activity under different treatments ($p < 0.05$).

3.3. Associations of Microbial C and P Limitation with other Factors

The results of correlation analysis further showed that SOC, SWC, and microbial P limitation were significantly negatively correlated with microbial C limitation ($p < 0.05$, Figure 3a,b,d). AP was positively correlated with microbial C limitation ($p < 0.05$, Figure 3c). Furthermore, AP and NO_3^--N were significantly negatively correlated with microbial P limitation ($p < 0.05$, Figure 3e,f).

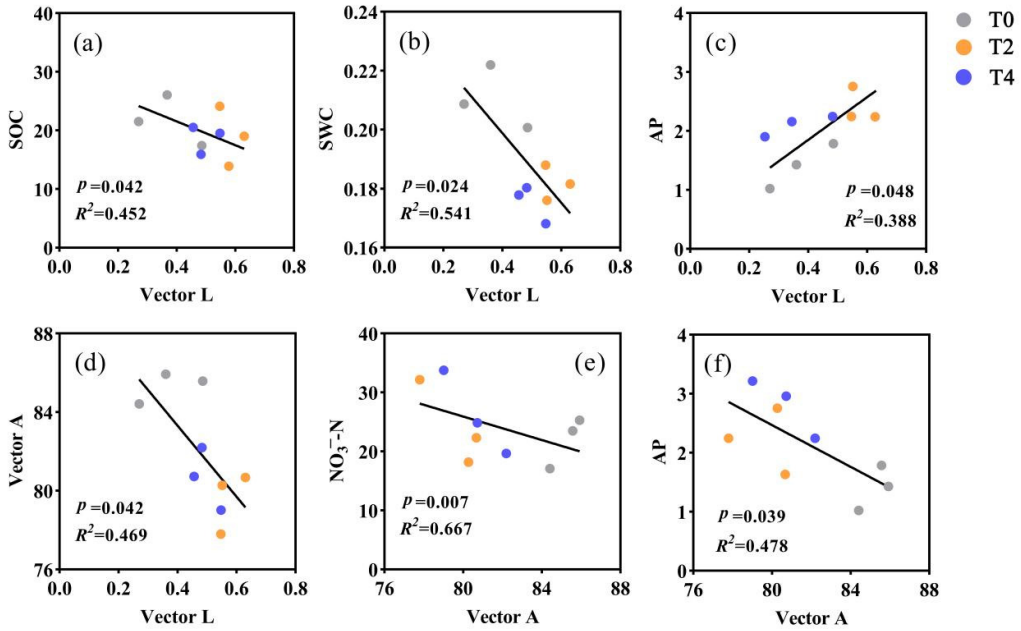
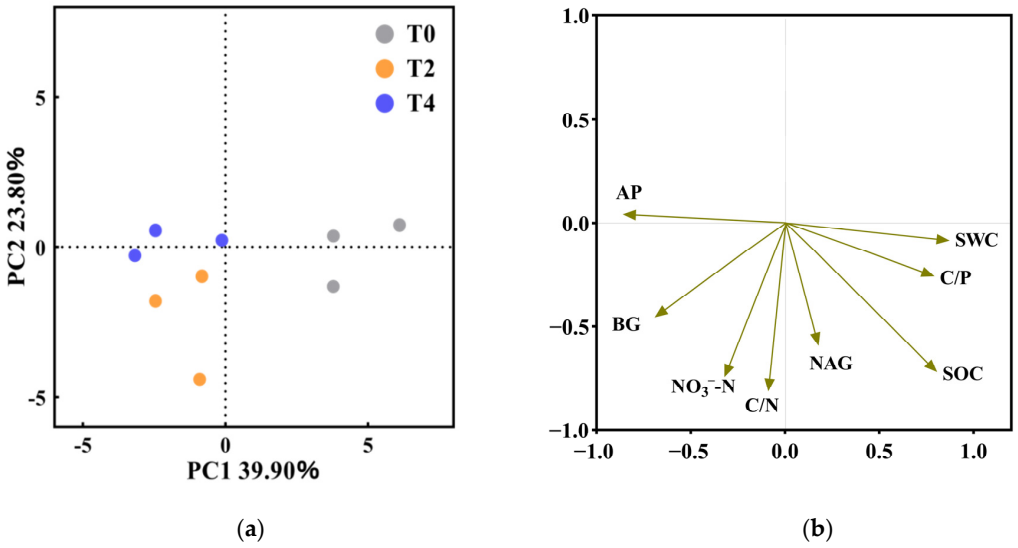


Figure 3. Relationships between microbial C limitation with SOC (**a**), SWC (**b**), AP (**c**), and microbial P limitation (**d**). Relationships between microbial P limitation with NO_3^--N (**e**), AP (**f**). T0: control without warming; T2: 2 °C warming treatment; T4: 4 °C warming treatment.

3.4. Response of Soil Enzyme Activity and Microbial C, P Limitation to Environmental Factors

Dimensionality reduction of the factors involved in this study was carried out by principal components, and the results (Figure 4a) showed that the first two axes of principal components explained 63.70% of the total variance contribution rate. There was a significant difference in PC1 between the T0 treatment and the two warming treatments. SWC, AP, and BG were the main difference factors, but there was no significant difference between T2 and T4 treatment. Among them, SWC, C/P, SOC, C/N, AP, NO_3^--N, NAG, and BG have the highest contribution to the two principal components (Figure 4b).



(**a**) (**b**)

Figure 4. Principal component analysis (PCA) of soil and enzyme activity factors under different treatments. T0: control without warming; T2: 2 °C warming treatment; T4: 4 °C warming treatment. (**a**) Different colors represent different treatments, the farther the distance between points represents the greater the sample difference; (**b**) According to the quality of variables in principal component analysis, eight variables with greater contribution were selected.

RDA analysis was conducted with soil enzyme activity and microbial C, P limitation as response variables, and soil physical and chemical properties as explanatory variables, respectively (Figure 5). The explanation rate of the first two ranking axes reached 77.76%, the first axis explained 57.79% of the variables, and the second axis explained 19.97% of the variables. SWC (p = 0.008) was the significant factor affecting soil, with explanatory rates of 44.6%.

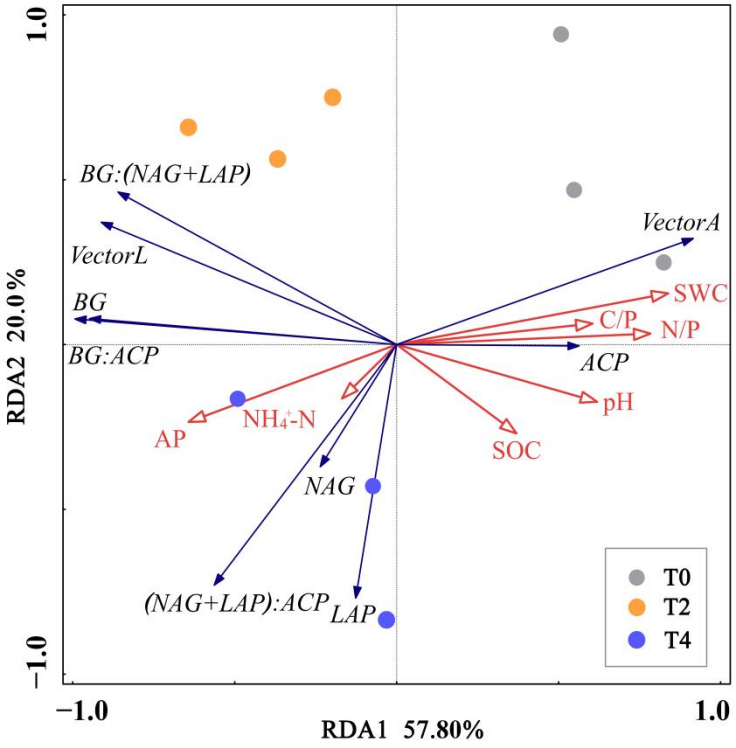


Figure 5. Redundancy analysis (RDA) of soil properties, soil enzyme activities, and microbial C, P limitation. T0: control without warming; T2: 2 °C warming treatment; T4: 4 °C warming treatment. SWC: soil water content; SOC: soil organic carbon; $NH4^+$-N: ammonium nitrogen; AP: available phosphorus; C/P: SOC/TP; N/P: TN/TP; BG: β-1,4-glucosidase; NAG: β-1,4-N-acetylglucosidase; LAP: L-leucine aminopeptidase; ACP: acid phosphatase.

4. Discussion

4.1. Effects of Soil Warming on Soil Enzyme Activities

Soil enzymes are mainly derived from soil microorganisms, plant root exudates, soil animal exudates, and their residues. As reported, soil enzymes are affected by soil temperature [24], soil water content [25], and nutrient availability [26]. The C-metabolizing enzyme BG is associated with a relatively unstable carbon pool and is a major component of cellulase, mainly involved in the hydrolysis of glycosidic bonds between atomic groups in cellulose [27]. In our study, soil warming increased the activity of BG, which is consistent with the results of Caitlin et al. [28]. Moreover, we found that BG activity was significantly negatively correlated with SOC and SWC (Table A1), indicating that the SOC decomposition rate and SWC level may be the main factors affecting its activity under warming conditions [29]. Previous studies have shown that increasing temperature and decreasing SWC will accelerate the cycling rate of unstable carbon and promote the decomposition of SOC [15,30,31]. Qi et al. [32,33] found that temperature change could significantly change soil enzyme activities by affecting the soil water-driven SOC decomposition rate, which was similar to our findings.

The response of soil enzyme activities to different temperature gradients was also different. Specifically, LAP activity increased significantly only under T4 treatment, while NAG and ACP activities did not change significantly. On the one hand, some hydrolases were not sensitive to small temperature increases [33]. On the other hand, since the

samples of this experiment were collected in March, the temperature was relatively low, which would lead to the passivation of some soil enzymes, and the seasonal variation of temperature had a significant impact on enzymes [19,34]. However, these results are in contrast to a recent meta-analysis. Chen et al. [35] studied the effects of soil warming on soil enzymes and found that soil warming only significantly affected oxidase but did not have a consistent and significant effect on hydrolase. One of the author's explanations was that soil hydrolases mainly degrade unstable reaction substrates, and soil warming leads to the decrease of substrate availability, which will gradually inhibit soil enzyme activities [36]. Although warming can directly increase enzyme activity by increasing enzyme kinetics [37], the effects of these two directions cancel each other, resulting in an insignificant response to warming.

Soil pH is also an important factor affecting soil enzyme activities and their stoichiometric ratios [38]. In this study, pH was significantly negatively correlated with BG activity and BG/AP (Table A1), which is consistent with the results of Sinsabaugh et al. [39] on enzyme activities at a global ecological scale. This may be because pH regulates soil enzyme activities by influencing the soil microbial community structure, the binding state between enzymes and soil particles, soil nutrients, and soil functions [40]. In addition, the warming time of this experiment is relatively short, and long-term warming experiments usually exceed 10 years [35,41,42]. In the future, we will focus on exploring the coupling relationship between soil enzyme activities and seasonal dynamic changes in temperature and duration of warming.

4.2. Effects of Soil Warming on Soil Nutrient Availability

The results of this study revealed that the T2 and T4 treatments increased the contents of AP and NO_3^--N in soil and improved soil N and P availability in the *Q. acutissima* forest in the north subtropical region [14,43]. Many studies found that the availability of soil N increased with the increase of soil temperature, because the increasing temperature increases the activities of soil N metabolizing enzymes and related microorganisms, accelerates the mineralization rate of soil N, and promotes the accumulation of soil available N [44,45], which is consistent with the results of our study. However, during the whole experimental period, the response of AP to soil warming was different from the results of previous studies. In contrast to soil N, P supply in soil is controlled by a combination of biotic and abiotic (adsorption/desorption and dissolution) processes [46]. Usually, soil warming promotes the uptake of phosphorus by surface plants, increases the content of litter phosphorus, and reduces soil available phosphorus [41,47]. However, as the *Q. acutissima* forest in the experimental area of this study belongs to an overmature forest, short-term warming of 1 year may not affect its growth.

The correlation results (Table A2) showed that AP and SWC were significantly negatively correlated, indicating that there was some coupling relationship between them. The decrease of SWC may be caused by warming, which is not conducive to the migration and diffusion of P components in the soil [48] and can reduce the leaching loss of slow-available P in the surface soil [49,50], which provides a possibility for the increase of soil AP.

4.3. Effects of Soil Warming on Soil Microbial Nutrient Limitation

Soil microbes can regulate soil nutrient availability, and the change in soil temperature will affect the soil microbial community and activity, thereby affecting the process of nutrient absorption and release [41]. Therefore, there is a close relationship between soil microbial nutrient limitation and soil nutrient availability. However, the limiting factors of soil microbial nutrients under warming conditions in different regions are still unclear. In this study, the lnBG: ln(NAG+LAP): lnACP of soil in the north subtropical *Q. acutissima* forest was about 1:1.57:2.89, which was different from the global average of 1:1:1 [39,41], indicating that N and P elements available to soil microorganisms in the study area were relatively lacking. A serious north subtropical soil microbial P limit has been confirmed, because the soil P element mainly comes from rock weathering, and the rainfall erosion and

soil erosion soil P element loss [51], and in the north subtropical acid soil metal ion binding ability is strong, and availability P element is easily incorporated into the stability of the closed state storage P. The utilization rate of the P element is reduced [50,51]. The soil lnBG: ln(NAG+LAP): lnACP after warming treatment was about 1:1.02:1.71, which gradually tended to be balanced compared with T0 treatment, indicating that warming alleviated the relative N and P limitations of microorganisms in the north subtropical forest system. The analysis showed that BG: ACP was significantly negatively correlated with TN/TP and soil pH (Table A1), which was consistent with Guan's findings [52]. The decreasing trend of TN/TP was induced by soil warming, which further proved that warming alleviated phosphorus limitation in the study area, However, soil P limitation still exists in the study area (Figure 6).

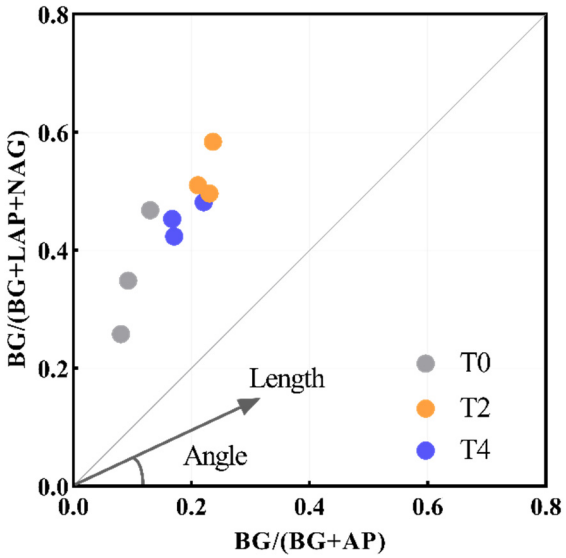


Figure 6. The variation of vector length and angle. T0: control without warming; T2: 2 °C warming treatment; T4: 4 °C warming treatment.

Soil enzymatic stoichiometry can reflect soil microbial nutrient acquisition ability, nutrient resource utilization, and microbial nutrient limitation [5], and sometimes can be used as a biological index to measure soil fertility [53]. Our results revealed that BG: ACP and BG:(NAG+LAP) were significantly increased compared with the T0 treatment. According to the principle of resource allocation, the relative input of soil microorganisms to C metabolic enzymes was greater than that of N and P metabolic enzymes due to warming [54]. In addition, the significant increase of vector L due to warming also indicates the transition of soil microorganisms to the C-limit (Figure 6). Linear regression analysis showed that SOC and SWC were significantly correlated with vector L. The relative increase of soil microbial C limitation may be related to the significant decomposition of SOC caused by warming [32,55]. The results of PCA and RDA showed that SWC is the most important factor affecting soil enzyme activity and soil microbial nutrient limitation among soil physical and chemical properties, and it is also the main factor distinguishing significant differences in soil enzyme activity and soil microbial nutrient limitation under different temperature changes. Therefore, warming may change the decomposition of SOC driven by SWC, thereby indirectly changing soil enzyme activities and microbial metabolic limitation [30,33]. Linear regression analysis showed that AP and NO_3^--N was significantly negatively correlated with vector A, and AP was significantly positively correlated with vector L($p < 0.05$, Figure 3c,e,f), indicating that the limitation of soil microorganisms C and P was strongly affected by the available nutrients of the soil, which was similar to Cui's results [56].

In this study, there were significant changes in soil microbial C and P limitations, and there was a significant negative correlation between them ($p < 0.05$, Figure 3d), reflecting

the coupling relationship between soil microbial C and P limitations under warming conditions, which jointly play an important role in soil nutrient cycling [6]. It is generally believed that soil microbial C and P limitations will accelerate the decomposition of SOM to produce more available nutrients [56], which will stimulate the decomposition of SOC. In this study, soil microbial C limitation was significantly correlated with SOC ($p < 0.05$, Figure 3a), indicating that the limitation of soil microorganisms C may be detrimental to SOC assimilation by soil microorganisms [57–59]. In addition, changes in soil microbial C and P limitations caused by soil warming may cause a large amount of SOM decomposition in a short period and affect soil C sequestration. Under the current global warming, it will be more difficult to accurately estimate global soil carbon storage in the short term.

5. Conclusions

Based on a 1-year field warming experiment, we found that soil warming significantly altered enzyme activity, but it depended on the type of enzyme. Warming significantly increased the activities of BG and LAP, and the changes of these enzymes were directly mediated by warming temperature, seasonal temperature, and SWC. Warming significantly reduced SOC content and soil SWC but significantly increased AP and NO_3^--N contents, and increased soil available N and P. After one year of short-term warming, soil microbial N and P limitations were alleviated due to the improvement of soil available nutrients, but soil microbial P limitation still existed in the north subtropical *Quercus acutissima* forest. The enhancement of soil microbial C limitation was mainly attributed to the decomposition and loss of SOC driven by SWC changes caused by warming, which indirectly changed soil microbial C limitation. In addition, the change of soil microbial C and P limitations caused by soil warming will cause a large amount of SOM decomposition in a short period, which is not conducive to soil C sequestration. Under the current climate warming, accurate estimation of global soil carbon storage will become more difficult.

Author Contributions: Conceptualization, J.W. and M.Z.; methodology, J.W.; software, J.W. and M.Z.; validation, J.W. and M.Z.; formal analysis, J.W.; investigation, J.W., X.W. and J.K.; resources, J.W.; data curation, J.W.; writing—original draft preparation, J.W.; writing—review and editing, L.C., H.H. and M.Z.; visualization, J.K.; supervision, L.C. and H.H.; project administration, L.C. and H.H.; funding acquisition, H.H. All authors have read and agreed to the published version of the manuscript.

Funding: This research was funded by the positioning research project of forest ecological system in Yangtze River delta of National Forestry and Grassland Administration, grant number 2021132068; Special fund project for technology innovation on Carbon Peak Carbon-neutral in 2021, Jiangsu Province, grant number BE2022305, and Technical support and collaboration project from Wuxi Water Conservancy Bureau, grant number 2107116.

Institutional Review Board Statement: Not applicable.

Informed Consent Statement: Not applicable.

Data Availability Statement: The data that support the findings of this study are available from the authors upon reasonable request.

Conflicts of Interest: The authors declare no conflict of interest.

Appendix A

Table A1. Correlation analysis of soil enzyme activities and environmental factors.

	SOC	TN	TP	SWC	PH	NO_3^--N	NH_4^+-N	AP	DOC	C/N	C/P	N/P
BG	−0.84 *	−0.398	−0.021	−0.642 *	−0.717 *	0.436	0.279	0.442	0.046	0.353	−0.356	−0.56
LAP	0.043	0.157	0.148	−0.093	−0.424	0.202	−0.188	0.405	−0.047	−0.506	−0.126	0.116
NAG	0.372	0.158	0.368	0.102	0.143	0.2	0.856 **	−0.249	0.048	0.572	0.001	−0.22
ACP	0.539	0.562	0.101	0.252	0.652	−0.155	0.306	−0.733 *	−0.798 *	0.236	0.903 **	0.881 **
CEs/NEs	−0.439	−0.57	−0.259	−0.61	−0.662	0.256	0.068	0.384	0.053	0.333	−0.332	−0.543
CEs/PEs	−0.365	−0.51	−0.036	−0.642	−0.814 **	0.44	0.15	0.607	0.302	0.241	−0.587	−0.760 *
NEs/PEs	−0.062	−0.121	0.274	−0.183	−0.595	0.379	0.188	0.579	0.474	−0.145	−0.618	−0.572

** and * indicate significant difference at $p < 0.01$ and $p < 0.05$. CEs/NEs: BG/(NAG+LAP); CEs/PEs: BG/ACP; NEs/PEs: (NAG+LAP): ACP.

Table A2. Correlation analysis between environmental factors.

	SOC	TN	TP	pH	SWC	NO_3^--N	NH_4^+-N	AP	DOC	C/N	C/P	N/P
SOC	1	0.961 **	0.844 **	−0.157	0.651	0.431	0.383	−0.408	−0.119	0.394	0.625	0.442
TN		1	0.807 **	−0.085	0.660	0.3736	0.154	−0.387	−0.087	0.124	0.619	0.553
TP			1	−0.405	0.261	0.721 *	0.234	0.050	0.300	0.334	0.122	−0.031
pH				1	0.428	−0.825 **	−0.023	−0.590	−0.141	−0.286	0.231	0.372
SWC					1	−0.240	0.240	−0.832 **	−0.314	0.123	0.763 *	0.705 *
NO_3^--N						1	0.233	0.464	0.221	0.308	−0.146	−0.282
NH_4^+-N							1	−0.322	−0.407	0.861 **	0.376	0.012
AP								1	0.422	−0.187	−0.797 *	−0.710 *
DOC									1	−0.140	−0.692 *	−0.628
C/N										1	0.206	−0.234
C/P											1	0.902 **
N/P												1

** and * indicate significant difference at $p < 0.01$ and $p < 0.05$.

References

1. Pörtner, H.; Roberts, D.C.; Adams, H.; Adler, C.; Aldunce, P.; Ali, E.; Begum, R.A.; Betts, R.; Kerr, R.B.; Biesbroek, R. *Climate Change 2022: Impacts, Adaptation and Vulnerability*; IPCC Sixth Assessment Report; Intergovernmental Panel on Climate: Geneva, Switzerland, 2022.
2. Zhang, Y.; Dong, S.; Gao, Q.; Liu, S.; Zhou, H.; Ganjurjav, H.; Wang, X. Climate change and human activities altered the diversity and composition of soil microbial community in alpine grasslands of the Qinghai-Tibetan Plateau. *Sci. Total Environ.* **2016**, *562*, 353–363. [CrossRef] [PubMed]
3. Rosinger, C.; Rousk, J.; Sandén, H. Can enzymatic stoichiometry be used to determine growth-limiting nutrients for microorganisms?-A critical assessment in two subtropical soils. *Soil Biol. Biochem.* **2019**, *128*, 115–126. [CrossRef]
4. Li, Y.; Zhou, H.; Chen, W.; Wu, Y.; Qiao, L.; Yan, Z.; Liu, G.; Xue, S. Long-term warming does not affect soil ecoenzyme activity and original microbial nutrient limitation on the Qinghai—Tibet Plateau. *Soil Ecol. Lett.* **2022**, *4*, 383–398. [CrossRef]
5. Yang, Y.; Liang, C.; Wang, Y.; Cheng, H.; An, S.; Chang, S.X. Soil extracellular enzyme stoichiometry reflects the shift from P-to N-limitation of microorganisms with grassland restoration. *Soil Biol. Biochem.* **2020**, *149*, 107928. [CrossRef]
6. Cui, Y.; Fang, L.; Guo, X.; Wang, X.; Zhang, Y.; Li, P.; Zhang, X. Ecoenzymatic stoichiometry and microbial nutrient limitation in rhizosphere soil in the arid area of the northern Loess Plateau, China. *Soil Biol. Biochem.* **2018**, *116*, 11–21. [CrossRef]
7. Hill, B.H.; Elonen, C.M.; Jicha, T.M.; Cotter, A.M.; Trebitz, A.S.; Danz, N.P. Sediment microbial enzyme activity as an indicator of nutrient limitation in Great Lakes coastal wetlands. *Freshw. Biol.* **2006**, *51*, 1670–1683. [CrossRef]
8. Sinsabaugh, R.L.; Lauber, C.L.; Weintraub, M.N.; Ahmed, B.; Allison, S.D.; Crenshaw, C.; Contosta, A.R.; Cusack, D.; Frey, S.; Gallo, M.E. Stoichiometry of soil enzyme activity at global scale. *Ecol. Lett.* **2008**, *11*, 1252–1264. [CrossRef]
9. Deng, L.; Peng, C.; Huang, C.; Wang, K.; Liu, Q.; Liu, Y.; Hai, X.; Shangguan, Z. Drivers of soil microbial metabolic limitation changes along a vegetation restoration gradient on the Loess Plateau, China. *Geoderma* **2019**, *353*, 188–200. [CrossRef]
10. Melillo, J.M.; Steudler, P.A.; Aber, J.D.; Newkirk, K.; Lux, H.; Bowles, F.P.; Catricala, C.; Magill, A.; Ahrens, T.; Morrisseau, S. Soil warming and carbon-cycle feedbacks to the climate system. *Science* **2002**, *298*, 2173–2176. [CrossRef]
11. Liu, W.; Zhang, Z.; Wan, S. Predominant role of water in regulating soil and microbial respiration and their responses to climate change in a semiarid grassland. *Glob. Change Biol.* **2009**, *15*, 184–195. [CrossRef]
12. Zuccarini, P.; Asensio, D.; Ogaya, R.; Sardans, J.; Peñuelas, J. Effects of seasonal and decadal warming on soil enzymatic activity in a P-deficient Mediterranean shrubland. *Glob. Change Biol.* **2020**, *26*, 3698–3714. [CrossRef] [PubMed]
13. Brockett, B.F.; Prescott, C.E.; Grayston, S.J. Soil moisture is the major factor influencing microbial community structure and enzyme activities across seven biogeoclimatic zones in western Canada. *Soil Biol. Biochem.* **2012**, *44*, 9–20. [CrossRef]
14. Xu, Z.; Hu, R.; Xiong, P.; Wan, C.; Cao, G.; Liu, Q. Initial soil responses to experimental warming in two contrasting forest ecosystems, Eastern Tibetan Plateau, China: Nutrient availabilities, microbial properties and enzyme activities. *Appl. Soil Ecol.* **2010**, *46*, 291–299. [CrossRef]
15. Zhou, X.; Chen, C.; Wang, Y.; Xu, Z.; Han, H.; Li, L.; Wan, S. Warming and increased precipitation have differential effects on soil extracellular enzyme activities in a temperate grassland. *Sci. Total Environ.* **2013**, *444*, 552–558. [CrossRef]
16. Allison, S.D.; Treseder, K.K. Warming and drying suppress microbial activity and carbon cycling in boreal forest soils. *Glob. Change Biol.* **2008**, *14*, 2898–2909. [CrossRef]
17. Zheng, H.; Liu, Y.; Chen, Y.; Zhang, J.; Li, H.; Wang, L.; Chen, Q. Short-term warming shifts microbial nutrient limitation without changing the bacterial community structure in an alpine timberline of the eastern Tibetan Plateau. *Geoderma* **2020**, *360*, 113985. [CrossRef]
18. Moorhead, D.L.; Sinsabaugh, R.L.; Hill, B.H.; Weintraub, M.N. Vector analysis of ecoenzyme activities reveal constraints on coupled C, N and P dynamics. *Soil Biol. Biochem.* **2016**, *93*, 1–7. [CrossRef]
19. Sistla, S.A.; Schimel, J.P. Seasonal patterns of microbial extracellular enzyme activities in an arctic tundra soil: Identifying direct and indirect effects of long-term summer warming. *Soil Biol. Biochem.* **2013**, *66*, 119–129. [CrossRef]
20. Conant, R.T.; Ryan, M.G.; Ågren, G.I.; Birge, H.E.; Davidson, E.A.; Eliasson, P.E.; Evans, S.E.; Frey, S.D.; Giardina, C.P.; Hopkins, F.M. Temperature and soil organic matter decomposition rates–synthesis of current knowledge and a way forward. *Glob. Change Biol.* **2011**, *17*, 3392–3404. [CrossRef]
21. Zhou, M.; Hu, H.; Wang, J.; Wang, X.; Tian, Z.; Deng, W.; Wu, C.; Zhu, L.; Lu, Q.; Feng, Y. Effects of nitric acid rain stress on soil nitrogen fractions and fungal communities in a northern subtropical forest, China. *Sci. Total Environ.* **2023**, *856*, 158904. [CrossRef]
22. Zhou, M.; Hu, H.; Wang, J.; Zhu, Z.; Feng, Y. Nitric Acid Rain Increased Bacterial Community Diversity in North Subtropical Forest Soil. *Forests* **2022**, *13*, 1349. [CrossRef]
23. Moorhead, D.L.; Rinkes, Z.L.; Sinsabaugh, R.L.; Weintraub, M.N. Dynamic relationships between microbial biomass, respiration, inorganic nutrients and enzyme activities: Informing enzyme-based decomposition models. *Front. Microbiol.* **2013**, *4*, 223. [CrossRef] [PubMed]
24. Sardans, J.; Peñuelas, J.; Estiarte, M. Changes in soil enzymes related to C and N cycle and in soil C and N content under prolonged warming and drought in a Mediterranean shrubland. *Appl. Soil Ecol.* **2008**, *39*, 223–235. [CrossRef]
25. Menichetti, L.; Reyes Ortigoza, A.L.; García, N.; Giagnoni, L.; Nannipieri, P.; Renella, G. Thermal sensitivity of enzyme activity in tropical soils assessed by the Q10 and equilibrium model. *Biol. Fertil. Soils* **2015**, *51*, 299–310. [CrossRef]
26. Fang, X.; Zhou, G.; Li, Y.; Liu, S.; Chu, G.; Xu, Z.; Liu, J. Warming effects on biomass and composition of microbial communities and enzyme activities within soil aggregates in subtropical forest. *Biol. Fertil. Soils* **2016**, *52*, 353–365. [CrossRef]

27. Chen, J.; Luo, Y.; Li, J.; Zhou, X.; Cao, J.; Wang, R.W.; Wang, Y.; Shelton, S.; Jin, Z.; Walker, L.M. Costimulation of soil glycosidase activity and soil respiration by nitrogen addition. *Glob. Change Biol.* **2017**, *23*, 1328–1337. [CrossRef]
28. Looby, C.I.; Treseder, K.K. Shifts in soil fungi and extracellular enzyme activity with simulated climate change in a tropical montane cloud forest. *Soil Biol. Biochem.* **2018**, *117*, 87–96. [CrossRef]
29. Schimel, J.; Balser, T.C.; Wallenstein, M. Microbial stress-response physiology and its implications for ecosystem function. *Ecology* **2007**, *88*, 1386–1394. [CrossRef]
30. García-Palacios, P.; Crowther, T.W.; Dacal, M.; Hartley, I.P.; Reinsch, S.; Rinnan, R.; Rousk, J.; Van den Hoogen, J.; Ye, J.; Bradford, M.A. Evidence for large microbial-mediated losses of soil carbon under anthropogenic warming. *Nat. Rev. Earth Environ.* **2021**, *2*, 507–517. [CrossRef]
31. Luan, J.; Liu, S.; Chang, S.X.; Wang, J.; Zhu, X.; Liu, K.; Wu, J. Different effects of warming and cooling on the decomposition of soil organic matter in warm–temperate oak forests: A reciprocal translocation experiment. *Biogeochemistry* **2014**, *121*, 551–564. [CrossRef]
32. Qi, R.; Li, J.; Lin, Z.; Li, Z.; Li, Y.; Yang, X.; Zhang, J.; Zhao, B. Temperature effects on soil organic carbon, soil labile organic carbon fractions, and soil enzyme activities under long-term fertilization regimes. *Appl. Soil Ecol.* **2016**, *102*, 36–45. [CrossRef]
33. Wang, H.; Liu, S.; Schindlbacher, A.; Wang, J.; Yang, Y.; Song, Z.; You, Y.; Shi, Z.; Li, Z.; Chen, L. Experimental warming reduced topsoil carbon content and increased soil bacterial diversity in a subtropical planted forest. *Soil Biol. Biochem.* **2019**, *133*, 155–164. [CrossRef]
34. Campbell, J.L.; Mitchell, M.J.; Groffman, P.M.; Christenson, L.M.; Hardy, J.P. Winter in northeastern North America: A critical period for ecological processes. *Front. Ecol. Environ.* **2005**, *3*, 314–322. [CrossRef]
35. Meng, C.; Tian, D.; Zeng, H.; Li, Z.; Chen, H.Y.; Niu, S. Global meta-analysis on the responses of soil extracellular enzyme activities to warming. *Sci. Total Environ.* **2020**, *705*, 135992. [CrossRef]
36. Rinnan, R.; Michelsen, A.; Bååth, E. Long-term warming of a subarctic heath decreases soil bacterial community growth but has no effects on its temperature adaptation. *Appl. Soil Ecol.* **2011**, *47*, 217–220. [CrossRef]
37. Brzostek, E.R.; Finzi, A.C. Seasonal variation in the temperature sensitivity of proteolytic enzyme activity in temperate forest soils. *J. Geophys. Res. Biogeosci.* **2012**, *117*, 1018. [CrossRef]
38. Kivlin, S.N.; Treseder, K.K. Soil extracellular enzyme activities correspond with abiotic factors more than fungal community composition. *Biogeochemistry* **2014**, *117*, 23–37. [CrossRef]
39. Sinsabaugh, R.L.; Hill, B.H.; Follstad Shah, J.J. Ecoenzymatic stoichiometry of microbial organic nutrient acquisition in soil and sediment. *Nature* **2009**, *462*, 795–798. [CrossRef]
40. Liu, J.; Xia, H.; Wang, J.; Zhang, W. Bioactive Characteristics of Soil Microorganisms in Different-aged Orange(Citrus reticulate) Plantations. *Agric. Sci. Technol.* **2012**, *13*, 1277–1281.
41. Hu, W.; Tan, J.; Shi, X.; Lock, T.R.; Kallenbach, R.L.; Yuan, Z. Nutrient addition and warming alter the soil phosphorus cycle in grasslands: A global meta-analysis. *J. Soils Sediments* **2022**, *22*, 2608–2619. [CrossRef]
42. Wu, Z.; Dijkstra, P.; Koch, G.W.; Peñuelas, J.; Hungate, B.A. Responses of terrestrial ecosystems to temperature and precipitation change: A meta-analysis of experimental manipulation. *Glob. Change Biol.* **2011**, *17*, 927–942. [CrossRef]
43. Zhang, Y.; Dong, S.; Gao, Q.; Liu, S.; Ganjurjav, H.; Wang, X.; Su, X.; Wu, X. Soil bacterial and fungal diversity differently correlated with soil biochemistry in alpine grassland ecosystems in response to environmental changes. *Sci. Rep.* **2017**, *7*, 1–10. [CrossRef] [PubMed]
44. Zhang, X.; Shen, Z.; Fu, G. A meta-analysis of the effects of experimental warming on soil carbon and nitrogen dynamics on the Tibetan Plateau. *Appl. Soil Ecol.* **2015**, *87*, 32–38. [CrossRef]
45. Geng, Y.; Baumann, F.; Song, C.; Zhang, M.; Shi, Y.; Kühn, P.; Scholten, T.; He, J. Increasing temperature reduces the coupling between available nitrogen and phosphorus in soils of Chinese grasslands. *Sci. Rep.* **2017**, *7*, 1–10. [CrossRef]
46. Santos, F.; Abney, R.; Barnes, M.; Bogie, N.; Ghezzehei, T.A.; Jin, L.; Moreland, K.; Sulman, B.N.; Berhe, A.A. The role of the physical properties of soil in determining biogeochemical responses to soil warming. In *Ecosystem Consequences of Soil Warming*; Elsevier: Amsterdam, The Netherlands, 2019; pp. 209–244.
47. Wang, Q.K.; Wang, S.L.; Liu, Y.X. Responses to N and P fertilization in a young Eucalyptus dunnii plantation: Microbial properties, enzyme activities and dissolved organic matter. *Appl. Soil Ecol.* **2008**, *40*, 484–490. [CrossRef]
48. Dijkstra, F.A.; Pendall, E.; Morgan, J.A.; Blumenthal, D.M.; Carrillo, Y.; LeCain, D.R.; Follett, R.F.; Williams, D.G. Climate change alters stoichiometry of phosphorus and nitrogen in a semiarid grassland. *New Phytol.* **2012**, *196*, 807–815. [CrossRef] [PubMed]
49. Zhu, J.; Li, M.; Whelan, M. Phosphorus activators contribute to legacy phosphorus availability in agricultural soils: A review. *Sci Total Environ* **2018**, *612*, 522–537. [CrossRef] [PubMed]
50. Dong, C.; Wang, W.; Liu, H.; Xu, X.; Zeng, H. Temperate grassland shifted from nitrogen to phosphorus limitation induced by degradation and nitrogen deposition: Evidence from soil extracellular enzyme stoichiometry. *Ecol. Indic.* **2019**, *101*, 453–464. [CrossRef]
51. Jiang, Y.; Rocha, A.V.; Rastetter, E.B.; Shaver, G.R.; Mishra, U.; Zhuang, Q.; Kwiatkowski, B.L. C–N–P interactions control climate driven changes in regional patterns of C storage on the North Slope of Alaska. *Landsc. Ecol.* **2016**, *31*, 195–213. [CrossRef]
52. Guan, P.; Yang, J.; Yang, Y.; Wang, W.; Zhang, P.; Wu, D. Land conversion from cropland to grassland alleviates climate warming effects on nutrient limitation: Evidence from soil enzymatic activity and stoichiometry. *Glob. Ecol. Conserv.* **2020**, *24*, e1328. [CrossRef]
53. Li, J.; Shangguan, Z.; Deng, L. Dynamics of soil microbial metabolic activity during grassland succession after farmland abandonment. *Geoderma* **2020**, *363*, 114167. [CrossRef]
54. Peng, X.; Wang, W. Stoichiometry of soil extracellular enzyme activity along a climatic transect in temperate grasslands of northern China. *Soil Biol. Biochem.* **2016**, *98*, 74–84. [CrossRef]

55. Rieke, E.L.; Cappellazzi, S.B.; Cope, M.; Liptzin, D.; Mac Bean, G.; Greub, K.L.; Norris, C.E.; Tracy, P.W.; Aberle, E.; Ashworth, A. Linking soil microbial community structure to potential carbon mineralization: A continental scale assessment of reduced tillage. *Soil Biol. Biochem.* **2022**, *168*, 108618. [CrossRef]
56. Cui, Y.; Bing, H.; Fang, L.; Jiang, M.; Shen, G.; Yu, J.; Wang, X.; Zhu, H.; Wu, Y.; Zhang, X. Extracellular enzyme stoichiometry reveals the carbon and phosphorus limitations of microbial metabolisms in the rhizosphere and bulk soils in alpine ecosystems. *Plant Soil* **2021**, *458*, 7–20. [CrossRef]
57. Nishina, K.; Ito, A.; Beerling, D.J.; Cadule, P.; Ciais, P.; Clark, D.B.; Falloon, P.; Friend, A.D.; Kahana, R.; Kato, E. Quantifying uncertainties in soil carbon responses to changes in global mean temperature and precipitation. *Earth Syst. Dyn.* **2014**, *5*, 197–209. [CrossRef]
58. Exbrayat, J.; Pitman, A.J.; Zhang, Q.; Abramowitz, G.; Wang, Y. Examining soil carbon uncertainty in a global model: Response of microbial decomposition to temperature, moisture and nutrient limitation. *Biogeosciences* **2013**, *10*, 7095–7108. [CrossRef]
59. Cui, L.; Li, X.; Lin, J.; Guo, G.; Zhang, X.; Zeng, G. The mineralization and sequestration of soil organic carbon in relation to gully erosion. *Catena* **2022**, *214*, 106218. [CrossRef]

Disclaimer/Publisher's Note: The statements, opinions and data contained in all publications are solely those of the individual author(s) and contributor(s) and not of MDPI and/or the editor(s). MDPI and/or the editor(s) disclaim responsibility for any injury to people or property resulting from any ideas, methods, instructions or products referred to in the content.

forests

MDPI

Article

Inter- and Intraspecific Variation Patterns of Leaf Phenotypic Traits in Two Sympatric Pine Species

Yuan Yang [1,†], Meng Hu [1,†], Mingyang Fan [1], Lu Wang [1], Ting Lv [1], Huanchao Zhang [2], Kewang Xu [1], Yifan Duan [1] and Yanming Fang [1,*]

[1] Co-Innovation Center for Sustainable Forestry in Southern China, Key Laboratory of State Forestry and Grassland Administration on Subtropical Forest Biodiversity Conservation, College of Biology and the Environment, Nanjing Forestry University, Nanjing 210037, China
[2] College of Forestry, Nanjing Forestry University, Nanjing 210037, China
* Correspondence: jwu4@njfu.edu.cn; Tel.: +86-25-8542-7428
† These authors contributed equally to this work.

Abstract: Individual persistence under changing climate conditions can be aided by phenotypic plasticity. Needle morphology reflects pine species' adaptation to their habitats, and adaptive plasticity is beneficial to pine survival. As two closely related pines, *Pinus massoniana* Lamb. and *Pinus hwangshanensis* W. Y. Hsia sympatrically occur in the subtropical region of China, forming hilly forests (i.e., subtropical evergreen needleleaf forests) at lower elevations and montane forests (i.e., temperate evergreen needleleaf forests) at medium and high elevations. However, little is known about the intraspecific phenotypic variation patterns of the two pine species and their relationship with environmental factors. Here, we investigated the interspecific and intraspecific variation patterns of needle traits in the two sympatric pine species, focusing on six traits—i.e., leaf length, leaf thickness, leaf width, leaf area, specific leaf area, and leaf dry matter content—as well as the relationship between needle traits and environmental factors. We found significant phenotypic trait differences among populations of each species. Except for leaf length and leaf width, variation within species was greater than variation between species in the needle traits measured. Even more intriguingly, the leaf size traits (i.e., length, width, thickness) were more conservative than the leaf economic traits (i.e., specific leaf area and leaf dry matter content). In other words, the intraspecific variability of the former was weaker than that of the latter. The nature of *P. massoniana* needle traits was mainly shaped by latitude, while the needle traits of *P. hwangshanensis* were significantly affected by annual precipitation. Therefore, phenotypic plasticity may be an essential mechanism for the two pine species to better cope with changing external conditions. The intraspecific variation patterns found in the two pine species and the relationships between traits and environmental factors can provide substantial scientific data for large-scale exploration of intraspecific phenotypic variation in pine species and their breeding practice.

Keywords: phenotypic variation; needle traits; plasticity; interspecific and intraspecific; *Pinus massoniana* Lamb.; *Pinus hwangshanensis* W. Y. Hsia

check for updates

Citation: Yang, Y.; Hu, M.; Fan, M.; Wang, L.; Lv, T.; Zhang, H.; Xu, K.; Duan, Y.; Fang, Y. Inter- and Intraspecific Variation Patterns of Leaf Phenotypic Traits in Two Sympatric Pine Species. *Forests* **2022**, *13*, 2014. https://doi.org/10.3390/f13122014

Academic Editor: Stéphane Maury

Received: 18 October 2022
Accepted: 24 November 2022
Published: 29 November 2022

Publisher's Note: MDPI stays neutral with regard to jurisdictional claims in published maps and institutional affiliations.

Copyright: © 2022 by the authors. Licensee MDPI, Basel, Switzerland. This article is an open access article distributed under the terms and conditions of the Creative Commons Attribution (CC BY) license (https://creativecommons.org/licenses/by/4.0/).

1. Introduction

Understanding phenotypic variation (i.e., the measurable or observable variation in a trait) or phenotypic plasticity (i.e., the ability of a given genotype to express different phenotypes in different environmental circumstances) is necessary to investigate a trait's function and fitness, as well as its ecology and evolution [1,2]. Among other hypotheses, phenotypic plasticity is assumed to facilitate evolution via 'buying time', 'plasticity-led evolution', and 'non-genetic evolution' [3]. Environmental phenotypic change precedes evolutionary adaptation, according to the 'Plasticity-first' hypothesis, which uses a mechanism similar to 'buying time', [4]. However, a thorough review of related literature reveals

that plasticity can both support and impede evolutionary change, and that it is not always adaptive but can also be neutral or even maladaptive [5].

Conversely, several eco-evolutionary mechanisms—such as dispersal, selection, plasticity, and (epi)genetic mutations—can influence how phenotypic variation is expressed in unexpected contexts or under environmental stress [2]. Empirical studies, reciprocal transplanting strategies, and standard garden experiments have demonstrated that genetic or epigenetic characteristics [6] and environmental factors (e.g., geography, climate, and soil) [7] affect plants' phenotypic variation. Despite this, empirical studies on phenotypic variation in plants (i.e., incredible natural populations) are greatly limited.

Pines are a dominant species in forests of the Northern Hemisphere [8] and form large-scale coniferous forests in Asia, Europe, and North America. With 111 species divided into 2 subgenera, 4 sections, and 11 subsections, the genus *Pinus* enjoys a rich species diversity and an intricate evolutionary history [9]. With the deepening of global changes in climate and biodiversity, pines are facing many challenges, including death from drought stress [10] and disease attacks [11]. Undoubtedly, observing phenotypic variation is critical for delving deeply into pine trees' strategies and mechanisms for coping with global changes.

Among the pine species, *P. massoniana* and *P. hwangshanensis* are two genetically closely related taxa that belong to the subgenus *Pinus*, section *Pinus*, and subsection *Pinus*. Here, *P. hwangshanensis* is treated as an independent species after being merged with *P. taiwanensis*—a species found in Taiwan [12]. The evolutionary events of these pines are related to climate and geography. On the other hand, these two pine species are considered to have distinct ecological characteristics and form coniferous forests with different properties. *P. massoniana* is a pioneer species that forms a subtropical evergreen needleleaf forest [13], whereas *P. hwangshanensis* is a pioneer or climax species that forms a temperate evergreen needleleaf forest [14]. More interestingly, the horizontal ranges of *P. massoniana* (27°55′~32°30′ N, 102°40′~109°55′ E) and *P. hwangshanensis* (22°48′~31°48′ N, 112°30′~122°30′ E) are highly overlapped. However, there are noticeable differences in their elevation distribution. Generally, the boundary is 700 m, with *P. hwangshanensis* at the medium and high elevations and *P. massoniana* at the low elevations [15]. It is known that plants' functional traits are expected to change as altitude changes, with plants at higher altitudes having smaller and thicker leaves than plants at lower altitudes [16].

Phenotypic variation in physiology and growth has been observed in pine species populations for needle traits such as leaf length, leaf width, leaf thickness [17], epidermis thickness with cuticle, resin duct diameter [18], stomatal row density, specific leaf area [19], and leaf area [20]. Meanwhile, existing research has reported that needle length, needle length–width ratio, the biomass of needles, and needle longevity follow a precise longitude and latitude pattern [21,22], and that hydraulic efficiency traits exist in a pattern along the altitudinal gradient [23]. However, the results demonstrated that in garden experiments, conifer traits associated with cold and drought resistance may be affected by a combination of genotype and environment [24]. Moreover, it has been emphasized that multiple analytical approaches have led to the conclusion that the environment has an overwhelming impact on survival and growth [25]. Since the two viewpoints are still inconclusive, we focused on the effects of the environment on the needle traits of *P. hwangshanensis* and *P. massoniana*.

When studying phenotypic variation, it is important to note that plants frequently exhibit substantial intraspecific variation in leaf traits—especially in species with heterogeneous environments, along environmental gradients, and with wide ranges [26]. Relevant data show that up to 40% of total variation in some plant traits occurs within species [27]. With increasing altitude, needle length decreases, and leaf dry matter content decreases predictably [28]. Indeed, intraspecific variation arises from heritable differences and plasticity [29], as in the case of *Pinus pinaster* Ait., which has evolved to adapt to its local environment, resulting in high genetic differentiation among populations, along with geographically highly structured intraspecific variation in quantitative traits and neutral

genetic variation [30]. Based on previous studies, we explored the sources of variation in *P. hwangshanensis* and *P. massoniana* through empirical studies.

Two species of pine trees from different elevation gradients on five mountains were selected for the present study, and a total of six leaf morphological traits—leaf length (LL), leaf thickness (TL), leaf width (DL), leaf area (LA), specific leaf area (SLA), and leaf dry matter content (LDMC)—were determined for various groups of pine needles. LL, TL, DL, and LA are traits that are related to needle size and are intuitive trait indicators; SLA is indicative of leaf biomass, and LDMC reflects the efficiency of resource utilization and the environmental adaptation strategy [31]. By using a broad survey of needle structure, we tested the following hypotheses: (1) the six needleleaf traits of the two pine species have a wide range of variation, with LDMC plasticity being significantly higher in *P. hwangshanensis* than in *P. massoniana*; (2) the total variation in most needle leaf traits of the two pine species has higher intraspecies variation than interspecies variation; and (3) the needle leaf morphological traits of the two pine species are influenced by different environmental factors, among which latitude and annual precipitation are the most significant.

2. Materials and Methods

2.1. Study Area and Sampling

The study areas were located in Jiangxi, Anhui, and Zhejiang, China; these provinces are among the core ranges of *P. hwangshanensis* and *P. massoniana*. In order to investigate the impact of elevation on the leaf phenotypic traits of two closely related pines, we identified five mountains as the objects of investigation. *P. massoniana* and *P. hwangshanensis* are located at low and high elevations, respectively. Five different populations for each pine—namely, Mt. Sanqingshan (SQS, 1820 m above sea level), Mt. Lushan (LS, 1474 m), Mt. Jinggangshan (JGS, 1779 m), Mt. Huangshan (HS, 1864 m), and Mt. Tianmushan (TMS, 1506 m)—were involved in our investigation (Figure 1). All five mountains are located in the central subtropical zone, belonging to the subtropical monsoon climate; the climate varies significantly vertically due to the influence of elevation, and the soils are yellow loam, red loam, yellow–brown loam, and other types, mostly related to elevation changes [32–34].

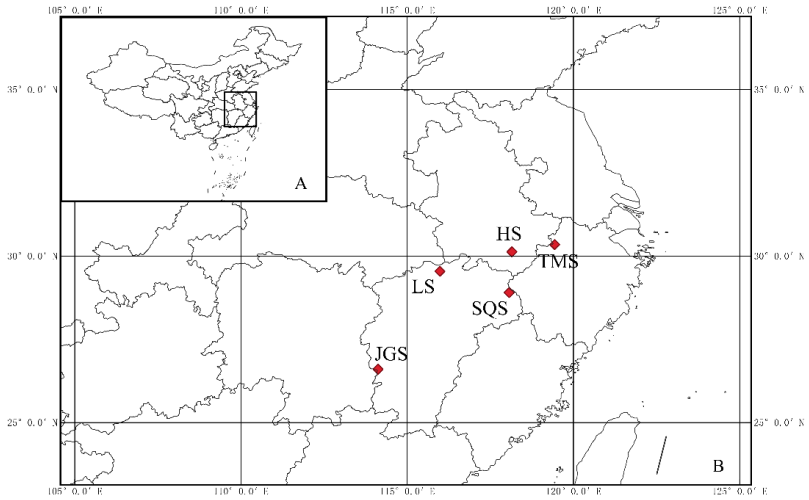


Figure 1. (**A**) The core distribution of *P. massoniana* and *P. hwangshanensis* in Jiangxi, Anhui, and Zhejiang, China. (**B**) The population locations of the two pine species. The codes and corresponding populations are SQS (Mt. Sanqingshan, Jiangxi), LS (Mt. Lushan, Jiangxi), JGS (Mt. Jinggangshan, Jiangxi), HS (Mt. Huangshan, Anhui), and TMS (Mt. Tianmushan, Zhejiang).

The geographic locations for each population are shown in Table 1. According to the elevation gradients of the two pine species, two or three sites (i.e., elevations) were selected for each population of the two pine species. A 20 × 50 m quadrat was set up for each site.

The number of sites was 20 and 15 for *P. massoniana* and *P. hwangshanensis*, respectively (Tables 1 and S1).

Table 1. The geographic locations and main meteorological factors of the sample populations of *P. massoniana* and *P. hwangshanensis*.

Population	Abbreviation	Longitude (°E)	Latitude (°N)	Annual Average Temperature (°C)	Annual Average Precipitation (mm)
Mt. Sanqingshan, Jiangxi	SQS	118°00′~118°06′	28°52′~28°57′	11	1860
Mt. Lushan, Jiangxi	LS	115°50′~116°10′	29°28′~29°45′	12	2024
Mt. Jinggangshan, Jiangxi	JGS	113°39′~114°23′	26°27′~26°40′	17	1890
Mt. Huangshan, Anhui	HS	116°49′~118°59′	29°13′~31°05′	14	2583
Mt. Tianmushan, Zhejiang	TMS	118°36′~120°06′	29°52′~30°55′	14	1870

Needle samples were collected from 60 *P. massoniana* individuals and 44 *P. hwangshanensis* individuals. Three mature individuals of *P. massoniana* and *P. hwangshanensis* with a similar diameter at breast height (DBH) were selected for each site, and fresh needles were randomly sampled from different directions around the tree crowns. The needles were mixed and sealed in a zip-lock bag and then returned to the laboratory for determination of their morphological characteristics.

2.2. Measurements

Ten fascicles of needles were selected randomly from each sampled tree for the measurement of LL, DL, and TL. LL was measured with a metric ruler with an accuracy of 0.1 cm; DL and TL were measured using an outside micrometer with an accuracy of 0.01 mm. An electronic balance was used to measure the saturated fresh weight and dry weight of the leaves, with an accuracy of 0.0001 g. The term 'saturated fresh weight of leaves' refers to the mass of fresh needles that have been immersed in distilled water for 36 h and then extracted after being dried on the surface. Following the aforementioned determination, the needles were dried in an oven at 70 °C until the mass remained constant, and the dry weight of the leaves was then measured. Then, the leaf area (LA), specific leaf area (SLA), and leaf dry matter content (LDMC) were calculated separately.

Referring to the method of Zhang et al. [35], the needle trait indices were calculated as follows:

$$\text{Area of sin gle cambered surface of a needle } (S_{\text{SCS}}):\ S_{\text{SCS}} = \frac{\pi \times \text{DL} \times \text{LL}}{2} \quad (1)$$

$$\text{Leaf area } (S_{LA}):\ S_{LA} = \frac{\pi \times \text{DL} \times \text{LL}}{2} + \text{DL} \times \text{LL} \quad (2)$$

$$\text{Specific leaf area } (S_{SLA}):\ S_{SLA} = \frac{\text{leaf area}}{\text{leaf dry mass}} \quad (3)$$

$$\text{Leaf dry matter content } (C_{LDMC}):\ C_{LDMC} = \frac{\text{leaf dry mass}}{\text{saturated fresh mass}} \times 100\% \quad (4)$$

2.3. Data Analysis

Means, coefficients of variation (CVs), and standard deviations for each trait among the populations were estimated. Data from each single needle measurement were used to conduct analysis of variance.

We log-transformed the data for all needle traits and performed a nested ANOVA using the lme [36] and varcomp [37] functions in R [38], in the following increasing order: individuals, elevations, populations, and species. The code was as follows (e.g., LL):

LL < - lme (log10 (LL) ~1, random = ~1 | species/population/elevation, data = E, method = "REML")

mLL < - varcomp (LL, TRUE, cum = FALSE)

The same model was applied to TL, DL, LA, SLA, and LDMC, only replacing LL with these traits in the R code. REML refers to a restricted maximum likelihood method in the 'lme' function of R (version 4.2.1).

Clustering analysis among populations of *P. massoniana* and *P. hwangshanensis* was performed using the average method in R by the unweighted pair group method with arithmetic mean (UPGMA). The average values of each needle trait were used for cluster analysis. In order to investigate the effects of external factors (geographic and environmental) on the needle traits of the two pine species, redundancy (RDA) analysis was used. The environmental and geographic data for each sampling site were collected by searching WorldClim (http://www.worldclim.org/, accessed on 20 September 2022), using three geographic factors (latitude, longitude, and elevation) and two environmental factors (annual average temperature and annual precipitation). The statistical analysis of this study was completed in SPSS 25.0 and R 4.2.1 [39].

3. Results

3.1. Variation of Needle Traits in the Two Pine Species

The mean values of seven needle morphological traits of *P. massoniana* and *P. hwangshanensis* were significantly different between the populations (Tables 2 and 3). The variation coefficients of morphological traits of *P. massoniana* ranged from 4.11% to 25.85%, and the average variation coefficients of LL, LA, and LDMC were relatively small, while TL, DL, and SLA showed a great range of variation. Additionally, the fluctuation in needle traits of *P. hwangshanensis* was marked with variation coefficients of 4.94~94.80%. LDMC and TL showed significant variation, while the average variation of the other traits was slight. Interestingly, according to the boxplot, seven needle traits within a mountain were markedly different between the *P. massoniana* population and the *P. hwangshanensis* population, and such patterns occurred on all five mountains (Table S1, Figure 2).

Table 2. Mean values, coefficients of variance (CV%), and analysis of variance of needle traits in *P. massoniana*. The population abbreviations are the same as in Table 1. Numbers in bold symbolize statistical significance.

Traits	SQS		LS		JGS		HS		TMS		ANOVA	
	Mean	**CV%**	**Mean**	**CV%**	**Mean**	**CV%**	**Mean**	**CV%**	**Mean**	**CV%**	***F***	***p* (>*F*)**
LL (cm)	11.305	13.48	13.574	17.89	15.638	11.05	13.658	15.98	14.189	11.09	140.600	<0.01
TL (mm)	0.404	4.11	0.423	9.04	0.416	9.62	0.466	15.07	0.403	15.39	62.402	<0.01
DL (cm)	0.079	7.10	0.088	14.15	0.081	11.95	0.080	8.48	0.075	18.98	56.719	<0.01
LA (cm^2)	2.288	16.00	3.075	20.98	3.255	20.11	2.798	19.33	2.731	22.72	87.540	<0.01
SLA (cm^2/g)	149.348	20.46	140.607	19.39	164.363	17.06	137.186	15.37	167.568	25.85	50.105	<0.01
LDMC (g/g)	0.443	16.85	0.455	18.91	0.439	18.12	0.532	14.09	0.402	17.52	83.717	<0.01

Abbreviations: SQS, Mt. Sanqingshan; LS, Mt. Lushan; JGS, Mt. Jinggangshan; HS, Mt. Huangshan; TMS, Mt. Tianmushan.

3.2. Sources of Needle Traits' Variation in the Two Pine Species

The four levels of species, populations, elevations, and individuals had different effects on the variation of the seven functional leaf traits (Figure 3). Except for LDMC, the sources of variation for the needle leaf traits consisted mainly of interspecific and intraspecific contributions. Most of the variation between populations was smaller than the variation within populations for most of the measured needle traits. The variation in LL and DL was mainly derived from interspecific variation, with contributions of 61.48% and 55.73%, respectively. Compared with the other four traits, intraspecies variation contributed more to LA and SLA. The variation in TL was mainly due to intraspecific variation (35.84%),

followed by interspecific variation (29.50%). Elevation contributed the most to LDMC (63.79%).

Table 3. Mean values, coefficients of variance (CV%), and analysis of variance of needle traits in *P. hwangshanensis*. The population abbreviations are the same as in Table 1. Numbers in bold symbolize statistical significance.

Traits	SQS		LS		JGS		HS		TMS		ANOVA	
	Mean	CV%	Mean	CV%	Mean	CV%	Mean	CV%	Mean	CV%	*F*	*p* (>*F*)
LL (cm)	9.477	20.84	8.623	19.52	11.438	10.31	9.763	17.96	9.671	14.14	58.209	<0.01
TL (mm)	0.427	4.94	0.477	10.36	0.498	9.13	0.466	19.51	0.540	8.89	97.383	<0.01
DL (cm)	0.094	8.66	0.099	10.64	0.104	11.29	0.094	13.63	0.106	9.94	50.904	<0.01
LA (cm^2)	2.289	22.94	2.190	20.17	3.066	16.20	2.370	26.23	2.662	20.86	61.234	<0.01
SLA (cm^2/g)	142.461	17.61	121.316	20.69	129.870	15.83	120.501	19.83	117.189	16.31	27.646	<0.01
LDMC (g/g)	0.474	21.74	0.485	21.18	0.249	94.80	0.515	16.30	0.461	84.71	22.928	<0.01

Abbreviations: SQS, Mt. Sanqingshan; LS, Mt. Lushan; JGS, Mt. Jinggangshan; HS, Mt. Huangshan; TMS, Mt. Tianmushan.

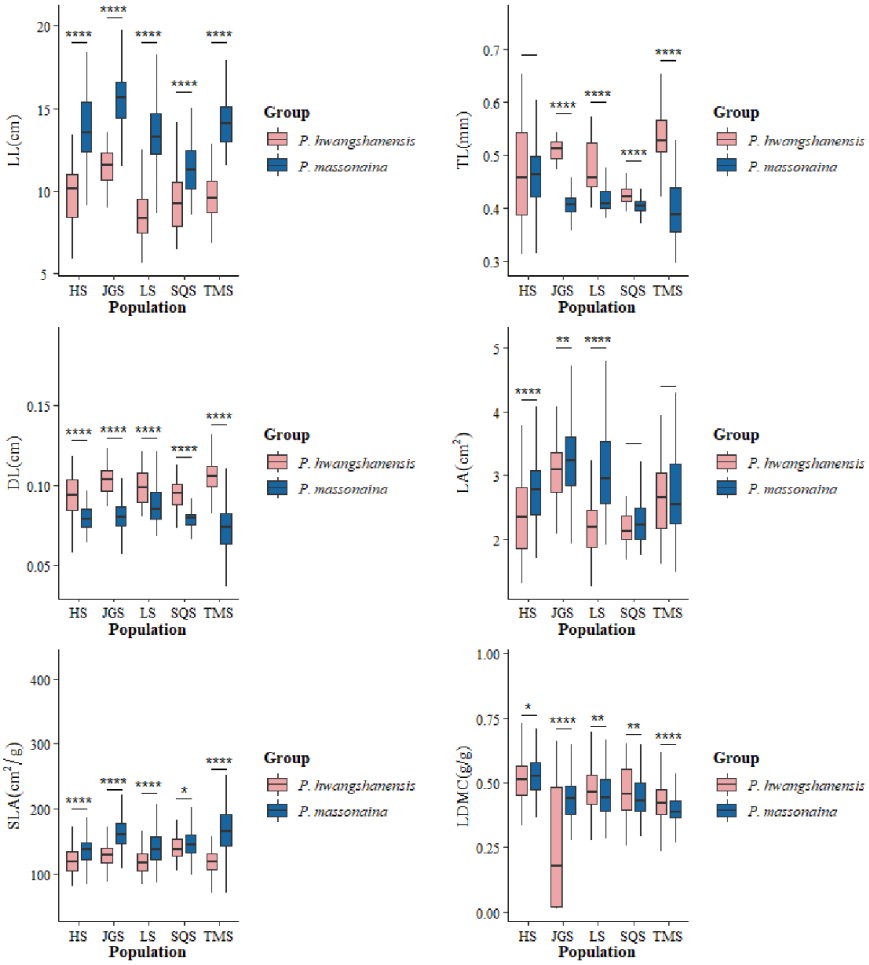


Figure 2. Boxplots of the needle traits in each population between two pine species. The population abbreviations are the same as in Table 1. The three upper, middle, and lower lines represent the 75th, 50th, and 25th percentile values of the variables, respectively. * Significant differences ($p < 0.05$) exist in the populations between *P. massoniana* and *P. hwangshanensis* (** $p < 0.01$, **** $p < 0.0001$). Abbreviations: SQS, Mt. Sanqingshan; LS, Mt. Lushan; JGS, Mt. Jinggangshan; HS, Mt. Huangshan; TMS, Mt. Tianmushan.

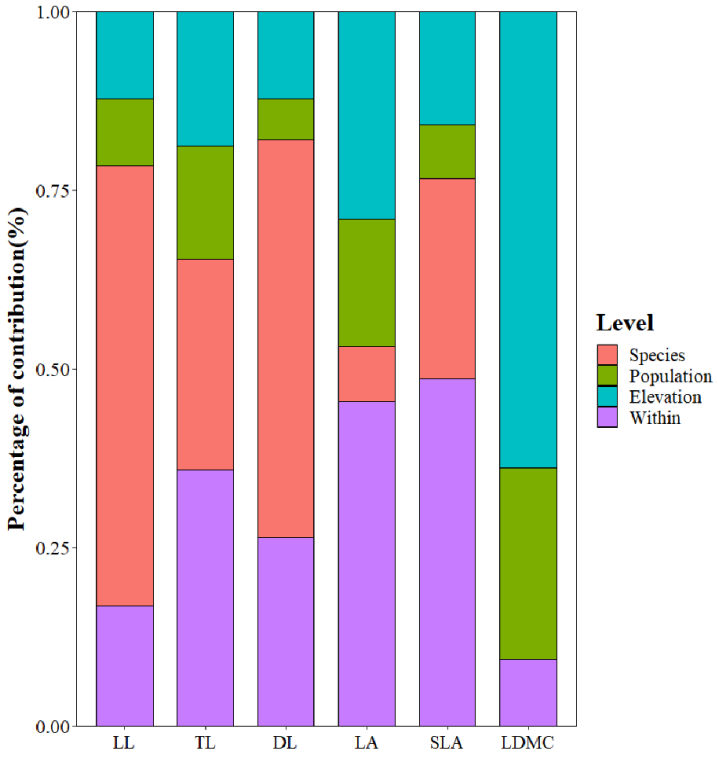


Figure 3. Variance partitioning of needle traits at different levels and between species across geographic populations.

3.3. Cluster Analysis

The two species were divided into two groups by cluster analysis (Figure 4), except for JGS clustered into another group. For *P. massoniana*, the populations in LS and HS were clustered into one group, and the populations in TMS and JGS were clustered into another group. Similar results occurred in *P. hwangshanensis*, where the populations in LS and HS (i.e., the high-latitude populations) were clustered into one group.

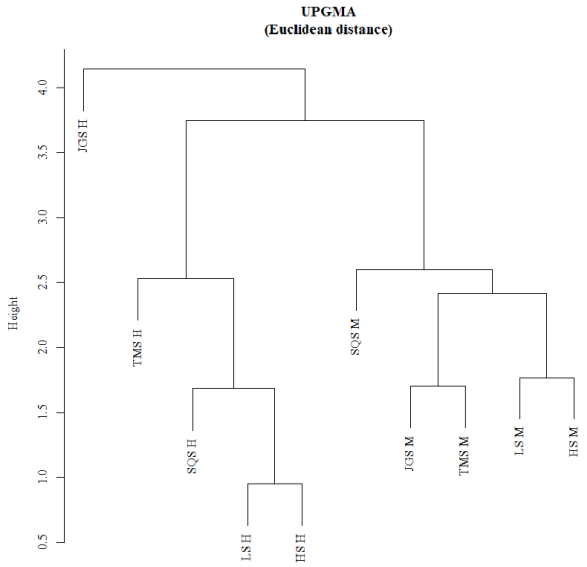
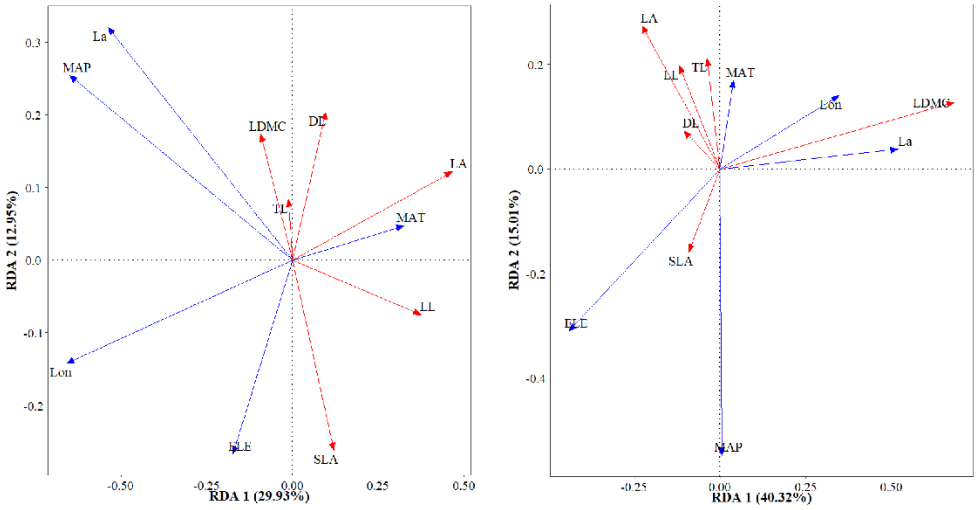


Figure 4. Cluster analysis based on needle traits in five populations of *P. massoniana* and *P. hwangshanensis*. Abbreviations: SQS, Mt. Sanqingshan; LS, Mt. Lushan; JGS, Mt. Jinggangshan; HS, Mt. Huangshan; TMS, Mt. Tianmushan. M, *P. massoniana*; H, *P. hwangshanensis*.

3.4. Redundancy Analysis

The results of the RDA analysis showed that the first three RDA ranking axes included 44.65% of the information on needle traits and their corresponding geographic variables for *P. massoniana*, and latitude (La) had more influence on the distribution of needle traits than other factors (Figure 5a). On the other hand, the first three ordination axes in Figure 5b explain 62.01% of the information of *P. hwangshanensis* needle traits and their corresponding environmental variables. Annual precipitation (MAP) had the greatest influence on the distribution of needle traits.



(**a**) (**b**)

Figure 5. Redundancy analysis based on needle traits of (**a**) *P. massoniana* and (**b**) *P. hwangshanensis*. Abbreviations: Lon: longitude, La: latitude, ELE: elevation, MAT: annual average temperature, MAP: annual precipitation.

4. Discussion

4.1. Phenotypic Variation and Plasticity

The study of needle traits in *P. massoniana* and *P. hwangshanensis* revealed a wide range of phenotypic variation (Tables 2 and 3). Furthermore, *P. massoniana* had less variation than *P. hwangshanensis*—for example, the variation in the leaf dry matter content of *P. hwangshanensis* was pronounced (up to 98.4%). The latest histological studies also proved that *P. hwangshanensis* differed significantly from *P. massoniana* in the formulation phase [40]. Stapley et al. [41] proposed that phenotypic variability was one of the foundations in determining the intrinsic factors that define species and their biogeography, and that adaptation in any species requires phenotypic variation in traits [1,42]. In fact, nearly all traits will be influenced by plasticity [5]. Physiological changes, on the other hand, are thought to be central to phenotypic variation, and because of physiology's systemic nature and sensitivity to environmental changes, the division of labor between traits could be regulated by these changes—particularly the endocrine system [43]. That is, divergence in phenotypic plasticity could result from physiological mechanisms with a genetic basis. This allows us to have a more in-depth discussion of phenotypic variation and phenotypic plasticity.

In the present study, the coefficient of variation of needle traits was used to characterize the ability of plasticity; the average coefficients of variation of LL, TL, and DL were lower than those of LA, SLA, and LDMC, indicating the low plasticity in LL, DL, and TL. Despite the fact that our study did not calculate the phenotypic plasticity index (PPI) [44], the coefficient of variation produced results that were consistent with it [45]. Based on 20 morphological and anatomical needle traits and 10 geographic populations of *Pinus tabuliformis*, Zhang et al. [46] reported that the inter-population heritability of LL, TL, and DL was greater than 0.8, indicating good genetic stability. Meanwhile, they had low levels of plasticity and small coefficients of variation when compared to other traits.

4.2. Phenotypic Variation Patterns of Leaf Traits among and within Species

Conifers are widely assumed to be typical wind-pollinated species, with chloroplast DNA that is primarily inherited paternally via pollen [47]. However, evidence has suggested that geographical barriers may result in low levels of differentiation between populations by limiting the pollen dispersal [48]. A similar conclusion was reached by Meng et al. [49], who reported that the genetic diversity of most needle traits was found to be most abundant within the population of *Pinus tabuliformis* in 18 needle traits. Xie et al. [50] used SRAP markers to study five endemic *Pinus* taxa from China (*Pinus tabulaeformis*, *P. tabulaeformis* var. *mukdensis*, *P. tabulaeformis* f. *shekanensis*, *Pinus massoniana*, and *Pinus henryi*), which showed more genetic diversity within taxa, rather than between taxa.

When investigating genetic variability and adaptive differentiation in conifers, it is well known that variation in needle variability traits is a useful visual indicator [51,52]. Within populations of *Pinus yunnanensis*, the proportion of phenotypic variation in nearly all needle traits was greater than 50%. In other words, trees within populations accounted for the vast majority of total variation [53]. Based on the phenotypic variation of needle traits in *Pinus tabuliformis*, Zhang et al. [46] found that more variation was expressed within populations. Similar results were obtained in our study (Figure 3), which demonstrated that the intraspecific components were generally higher than interspecific components in most of the measured needle traits. However, different needle traits showed different levels of variation within species; intraspecific trait variation (ITV) was relatively high for morphological traits linked to the leaf economics spectrum (e.g., leaf N and P, SLA, LDMC) [54], but low for traits related to leaf size (i.e., LL, TL, DL), which are typically considered to be independent of the leaf economics spectrum but have been linked with adaptation to broad climatic gradients [55].

Additionally, it has been demonstrated that intraspecific variation could have consequences that are comparable to or even greater than those of interspecific variation [27], and that genetics and habitat divergence are the primary forces behind phenotypic variation within species [56].

4.3. Adaptive Phenotypes in the Context of Changing External Factors

Researchers began to understand as early as the middle of the 20th century that environmental changes in a variety of morphological and physiological traits could precede and facilitate genetic changes [57]. Levis and Pfennig [58] underlined the dual function of environmental change as a generator and then selector of phenotypic variation, which reoriented how we think of the 'plasticity-led evolution hypothesis'. In other words, by enabling organisms to react appropriately and immediately to environmental variation, plasticity may confer a special evolutionary benefit [3]. As a result, environmental variation is essential in phenotypic plasticity as well as evolutionary adaptation.

Phenotypic trait variation and genetic architecture are highly influenced by geographic and environmental variations—particularly those linked to photoperiod and temperature (e.g., latitude, longitude, and elevation) [6]. Our study's RDA analysis showed that the two pine species' needle traits were affected by various environmental factors to various degrees (Figure 5). Elevation had a significant impact on needle traits, and the results of earlier investigations [53,59] were consistent in that LL and LDMC showed a negative correlation with altitude. Since *P. hwangshanensis* populations are distributed at higher elevations, they are subjected to more severe winter stress than *P. massoniana* populations, which are found at lower elevations. Thus, their needles are thicker and shorter to withstand the stress of strong winds and snow [60]. In addition, trees that are located at high altitudes face a lack of available water, leading to drought stress [61], and the lower leaf area minimizes stomatal transpirational water loss. Moreover, due to the short growing season at high altitudes and the tendency for soil moisture to freeze in winter—resulting in root uptake—MAP is extremely crucial for this species. *P. hwangshanensis*, on the other hand, had a higher level of plasticity in LDMC than *P. massoniana*, which can be attributed to nutrient deficiencies and low-temperature stresses caused by increased elevation. Cluster analysis could support the

peculiar latitude patterns that SLA and LDMC show in *P. massoniana* and *P. hwangshanensis* (Figure 4). SLA decreased as latitude increased, while LDMC increased as latitude increased. Due to the fact that SLA is associated with plants' growth rates and ecological strategies, it was discovered that *Pinus koraiensis* has smaller LDMC and larger SLA at low latitudes [61]. The greater the SLA, the more effectively leaves photosynthesize in order to adapt to changing habitats [62]. The investment in defense against low temperatures increases with latitude [63]. Based on 'leaf economic spectrum theory' [54], we could conclude that both *P. massoniana* and *P. hwangshanensis* were typical 'slow investment-return'-type species. However, our findings indicated that the resource trade-off strategies of the two pine species differed markedly.

P. massoniana and *P. hwangshanensis* share a common geological history across the mainland, which accounts for their similar levels of genetic diversity [64]. Due to the presence of refugees during the ice ages, climatic changes might have low impacts on these populations at mid-latitudes. Therefore, *P. massoniana* was able to achieve population expansion, while population decline has only recently started, indicating that its population was dealing with serious survival issues [48]. In cold biomes, where the climate is changing most rapidly, the ability of a species to adjust its phenotypes under new circumstances is vital [7].

5. Conclusions

In sum, the needle traits of *P. massoniana* and *P. hwangshanensis* displayed significant heterogeneity, whereas the leaf size traits displayed more consistent heritability between populations. Likewise, the variation of all needle traits within populations was greater than that between populations, suggesting that both genetics and environment played a role in the intraspecific phenotypic variation of the needles. The variation of needle traits was affected by different environmental factors (i.e., longitude, latitude, elevation, temperature, and precipitation), reflecting the adaptability of the traits to the heterogeneous environment. Limited by knowledge, this study is the first to systematically report the intraspecific and interspecific variation patterns of needle traits in multiple populations of *P. hwangshanensis*. Our findings might provide a theoretical reference for the adaptive evolution and breeding practice of Pinaceae.

Supplementary Materials: The following supporting information can be downloaded at: https://www.mdpi.com/article/10.3390/f13122014/s1, ID 502, Dataset name: "Table S1", Table S1: Needle trait indicators of different populations of *P. massoniana* and *P. hwangshanensis*.

Author Contributions: Conceptualization, Y.Y., M.H., K.X. and Y.F.; data curation, L.W. and T.L.; formal analysis, T.L., H.Z. and Y.D.; funding acquisition, Y.D., K.X. and Y.F.; investigation, Y.Y., M.H., L.W., M.F. and Y.F.; methodology, Y.Y., M.H., H.Z. and Y.F.; project administration, Y.D., K.X. and H.Z.; resources, M.F. and M.H.; software, T.L.; validation, L.W.; writing—original draft, Y.Y.; writing—review and editing, L.W., T.L. and Y.F. All authors have read and agreed to the published version of the manuscript.

Funding: This work was supported by the Special Foundation for National Science and Technology Basic Resources Investigation of China (2019FY202300 to Y.F.).

Data Availability Statement: All data used in this study are available in the Supplementary Materials.

Acknowledgments: We thank all reviewers who provided valuable comments for this paper. We are grateful to Huang Kexin for help with sample collection.

Conflicts of Interest: The authors declare no conflict of interest.

References

1. Sultan, S. Phenotypic Plasticity as An Intrinsic Property of Organism. In *Phenotypic Plasticity & Evolution*; Pfennig, D.W., Ed.; CRC Press: London, UK; New York, NY, USA, 2021; pp. 1–24.
2. Thompson, M.J.; Capilla-Lasheras, P.; Dominoni, D.M.; Reale, D.; Charmantier, A. Phenotypic variation in urban environments: Mechanisms and implications. *Trends Ecol. Evol.* **2022**, *37*, 171–182. [CrossRef]

3. Pfennig, D.W. Key Questions about Phenotypic Plasticity. In *Phenotypic Plasticity & Evolution*; Pfennig, D.W., Ed.; CRC Press: London, UK; New York, NY, USA, 2021; pp. 55–88.
4. Levis, N.A.; Pfennig, D.W. Evaluating 'Plasticity-First' Evolution in Nature: Key Criteria and Empirical Approaches. *Trends Ecol. Evol.* **2016**, *31*, 563–574. [CrossRef] [PubMed]
5. Hendry, A.P. Key Questions on the Role of Phenotypic Plasticity in Eco-Evolutionary Dynamics. *J. Hered.* **2016**, *107*, 25–41. [CrossRef] [PubMed]
6. Diouf, I.; Derivot, L.; Koussevitzky, S.; Carretero, Y.; Bitton, F.; Moreau, L.; Causse, M. Genetic basis of phenotypic plasticity and genotype x environment interactions in a multi-parental tomato population. *J. Exp. Bot.* **2020**, *71*, 5365–5376. [CrossRef] [PubMed]
7. Henn, J.J.; Buzzard, V.; Enquist, B.J.; Halbritter, A.H.; Klanderuds, K.; Maitner, B.S.; Michaletz, S.T.; Potschs, C.; Seltzer, L.; Telford, R.J.; et al. Intraspecific Trait Variation and Phenotypic Plasticity Mediate Alpine Plant Species Response to Climate Change. *Front. Plant Sci.* **2018**, *9*, 1548. [CrossRef]
8. Richardson, D.M.; Rundel, P.W.; Jackson, S.T.; Teskey, R.O.; Aronson, J.; Bytnerowicz, A.; Wingfield, M.J.; Proches, S. Human impacts in pine forests: Past, present, and future. *Annu. Rev. Ecol. Evol. Syst.* **2007**, *38*, 275–297. [CrossRef]
9. Gernandt, D.S.; Lopez, G.G.; Garcia, S.O.; Liston, A. Phylogeny and classification of Pinus. *Taxon* **2005**, *54*, 29–42. [CrossRef]
10. Ferriz, M.; Martin-Benito, D.; Canellas, I.; Gea-Izquierdo, G. Sensitivity to water stress drives differential decline and mortality dynamics of three co-occurring conifers with different drought tolerance. *For. Ecol. Manag.* **2021**, *486*, 118964. [CrossRef]
11. Drenkhan, R.; Ganley, B.; Martin-Garcia, J.; Vahalik, P.; Adamson, K.; Adamcikova, K.; Ahumada, R.; Blank, L.; Braganca, H.; Capretti, P.; et al. Global Geographic Distribution and Host Range of *Fusarium circinatum*, the Causal Agent of Pine Pitch Canker. *Forests* **2020**, *11*, 724. [CrossRef]
12. Zheng, W.J. *Sylva Sinica*; Chien, S.S., Chen, H.Y., Eds.; China Forestry Publishing House: Beijing, China, 1983; pp. 297–299.
13. Yu, S.X.; Li, Y.; Wang, Y.F.; Zhou, C.F. The vegetation classification and its digitized map of Heishiding Nature Reserve, Guangdong. I.The distribution of the vegetation type and formation. *Act Sci. Nat. Univ. Sunyasen* **2000**, *39*, 61–66.
14. Wang, L.P.; Zhou, Z.D. On the Positional Problem of the *Pinus Taiwanensis* Forest in the Vegetation Altitude Belts of Mt. Lushan. *Chin. J. Plant Ecol.* **1989**, *13*, 28–35.
15. Tong, Z.K.; Fan, Y.R. Dividing the distribution area of *Pinus taiwanensis* based on climatic and ecologic factors. *J. Cent. South For. Univ.* **1993**, *13*, 81–87.
16. Urbaniak, L.; Chudzinska, E.; Faferek, S. Differentiation of *Pinus sylvestris* populations of the Tatra Mts and the Tuchola forest expressed in the needle anatomical traits. *Dendrobiology* **2008**, *60*, 35–43.
17. Bozkurt, A.E.; Coskuncelebi, K.; Terzioglu, S. Population variability of scots pine (*Pinus sylvestris* L.) in Turkey according to the needle morphology. *Sumar. List* **2021**, *145*, 347–354. [CrossRef]
18. Popovic, V.; Nikolic, B.; Lucic, A.; Rakonjac, L.; Jovanovic, D.S.; Miljkovic, D. Morpho-anatomical trait variability of the Norway spruce (*Picea abies* (L.) Karst.) needles in natural populations along elevational diversity gradient. *Trees-Struct. Funct.* **2022**, *36*, 1131–1147. [CrossRef]
19. Flores, A.; Climent, J.; Pando, V.; Lopez-Upton, J.; Alia, R. Intraspecific Variation in Pines from the Trans-Mexican Volcanic Belt Grown under Two Watering Regimes: Implications for Management of Genetic Resources. *Forests* **2018**, *9*, 71. [CrossRef]
20. Jankowski, A.; Wyka, T.P.; Zytkowiak, R.; Nihlgard, B.; Reich, P.B.; Oleksyn, J. Cold adaptation drives variability in needle structure and anatomy in *Pinus sylvestris* L. along a 1900 km temperate-boreal transect. *Funct. Ecol.* **2017**, *31*, 2212–2223. [CrossRef]
21. Nobis, M.P.; Traiser, C.; Roth-Nebelsick, A. Latitudinal variation in morphological traits of the genus Pinus and its relation to environmental and phylogenetic signals. *Plant Ecol. Divers.* **2012**, *5*, 1–11. [CrossRef]
22. Viveros-Viveros, H.; Camarillo-Luna, A.R.; Saenz-Romero, C.; Aparicio-Renteria, A. Altitudinal variation in morphological traits of *Pinus patula* populations from Oaxaca state, Mexico, and its use in the zoning. *Bosque* **2013**, *34*, 173–179.
23. Taneda, H.; Funayama-Noguchi, S.; Mayr, S.; Goto, S. Elevational adaptation of morphological and anatomical traits by Sakhalin fir (*Abies sachalinensis*). *Trees-Struct. Funct.* **2020**, *34*, 507–520. [CrossRef]
24. Donnelly, K.; Cavers, S.; Cottrell, J.E.; Ennos, R.A. Genetic variation for needle traits in Scots pine (*Pinus sylvestris* L.). *Tree Genet. Genomes* **2016**, *12*, 40. [CrossRef]
25. Taibi, K.; del Campo, A.D.; Aguado, A.; Mulet, J.M. The effect of genotype by environment interaction, phenotypic plasticity and adaptation on *Pinus halepensis* reforestation establishment under expected climate drifts. *Ecol. Eng.* **2015**, *84*, 218–228. [CrossRef]
26. Bussotti, F.; Pollastrini, M.; Holland, V.; Brüggemann, W. Functional traits and adaptive capacity of European forests to climate change. *Environ. Exp. Bot.* **2015**, *111*, 91–113. [CrossRef]
27. Fraser, L.H. TRY-A plant trait database of databases. *Glob. Chang. Biol.* **2020**, *26*, 189–190. [CrossRef] [PubMed]
28. O'Sullivan, K.S.W.; Vila-Cabrera, A.; Chen, J.C.; Greenwood, S.; Chang, C.H.; Jump, A.S. High intraspecific trait variation results in a resource allocation spectrum of a subtropical pine across an elevational gradient. *J. Biogeogr.* **2022**, *49*, 668–681. [CrossRef]
29. Matesanz, S.; Horgan-Kobelski, T.; Sultan, S.E. Phenotypic Plasticity and Population Differentiation in an Ongoing Species Invasion. *PLoS ONE* **2012**, *7*, e44955. [CrossRef]
30. Bucci, G.; Gonzalez-Martinez, S.C.; Le Provost, G.; Plomion, C.; Ribeiro, M.M.; Sebastiani, F.; Alia, R.; Vendramin, G.G. Range-wide phylogeography and gene zones in *Pinus pinaster* Ait. revealed by chloroplast microsatellite markers. *Mol. Ecol.* **2007**, *16*, 2137–2153. [CrossRef]
31. Wilson, P.; Thompson, K.; Hodgson, J. Specific leaf area and leaf dry matter content as alternative predictors of plant strategies. *New Phytol.* **1999**, *143*, 155–162. [CrossRef]

32. Gong, J.; Lu, L.; Jin, X.L.; Nan, W.; Liu, F. Impacts of tourist disturbance on plant communities and soil properties in Huangshan Mountain scenic area. *Acta Ecol. Sin.* **2009**, *29*, 2239–2251.
33. Li, X.H.; Song, M.Z.; Liang, T.J. Characteristics of wild vine resources in Lushan Mountain and their landscape application. *J. South. Agric.* **2013**, *44*, 994–998.
34. Ren, R.F.; Xie, H.S.; Jian, Z.H.; Xu, Y.K.; Zhang, J. Soil Geoligy and Geochemistry Characteristics in the Tianmu Mountain Area Zhejiang Province. *J. Earth Sci. Environ.* **2008**, *30*, 49–53.
35. Zhang, K.; Hou, J.H.; He, N.P. Leaf functional trait distribution and controlling factors of *Pinus tabuliformis*. *Acta Ecol. Sin.* **2017**, *37*, 736–749.
36. Bates, D.; Machler, M.; Bolker, B.M.; Walker, S.C. Fitting Linear Mixed-Effects Models Using lme4. *J. Stat. Softw.* **2015**, *67*, 1–48. [CrossRef]
37. Qu, L.; Guennel, T.; Marshall, S.L. Linear Score Tests for Variance Components in Linear Mixed Models and Applications to Genetic Association Studies. *Biometrics* **2013**, *69*, 883–892. [CrossRef] [PubMed]
38. Messier, J.; McGill, B.J.; Lechowicz, M.J. How do traits vary across ecological scales? A case for trait-based ecology. *Ecol. Lett.* **2010**, *13*, 838–848. [CrossRef]
39. R Core Team. R: A Language and Environment for Statistical Computing. R Foundation for Statistical Computing: Vienna, Austria. Available online: http://www.r-project.org/index.html (accessed on 13 October 2022).
40. Jin, W.T.; Gernandt, D.S.; Wehenkel, C.; Xia, X.M.; Wei, X.X.; Wang, X.Q. Phylogenomic and ecological analyses reveal the spatiotemporal evolution of global pines. *Proc. Natl. Acad. Sci. USA* **2021**, *118*, e2022302118. [CrossRef]
41. Stapley, J.; Reger, J.; Feulner, P.G.D.; Smadja, C.; Galindo, J.; Ekblom, R.; Bennison, C.; Ball, A.D.; Beckerman, A.P.; Slate, J. Adaptation genomics: The next generation. *Trends Ecol. Evol.* **2010**, *25*, 705–712. [CrossRef]
42. Savolainen, O.; Pyhäjärvi, T.; Knürr, T. Gene flow and local adaptation in trees. *Annu. Rev. Ecol. Evol. Syst.* **2007**, *38*, 595–619. [CrossRef]
43. Ledón-Rettig, C.C.; Ragsdale, E.J. Physiological Mechanisms and the Evolution of Plasticity. In *Phenotypic Plasticity & Evolution*; Pfennig, D.W., Ed.; CRC Press: London, UK; New York, NY, USA, 2021; pp. 113–137.
44. Bohnke, M.; Bruelheide, H. How do evergreen and deciduous species respond to shade?—Tolerance and plasticity of subtropical tree and shrub species of South-East China. *Environ. Exp. Bot.* **2013**, *87*, 179–190. [CrossRef]
45. Chen, J.; Zhang, X.J.; Li, Q.Y.; Tao, J.P. Relationships between competition intensity and leaf phenotypic plasticity of woody plants in subalpine forests on different slope. *Acta Ecol. Sin.* **2022**, *42*, 1788–1797.
46. Zhang, M.; Meng, J.; Zhang, Z.; Zhu, S.; Li, Y. Genetic Analysis of Needle Morphological and Anatomical Traits among Nature Populations of *Pinus Tabuliformis*. *J. Plant Stud.* **2017**, *6*, 62. [CrossRef]
47. Robledo-Arnuncio, J.J. Wind pollination over mesoscale distances: An investigation with Scots pine. *New Phytol.* **2011**, *190*, 222–233. [CrossRef] [PubMed]
48. Ge, X.J.; Hsu, T.W.; Hung, K.H.; Lin, C.J.; Huang, C.C.; Huang, C.C.; Chiang, Y.C.; Chiang, T.Y. Inferring Multiple Refugia and Phylogeographical Patterns in *Pinus massoniana* Based on Nucleotide Sequence Variation and DNA Fingerprinting. *PLoS ONE* **2012**, *7*, e43717. [CrossRef]
49. Meng, J.X.; Chen, X.Y.; Huang, Y.J.; Wang, L.M.; Xing, F.Q.; Li, Y. Environmental contribution to needle variation among natural populations of *Pinus tabuliformis*. *J. For. Res.* **2019**, *30*, 1311–1322. [CrossRef]
50. Xie, Q.; Liu, Z.H.; Wang, S.H.; Li, Z.Q. Genetic diversity and phylogenetic relationships among five endemic *Pinus* taxa (Pinaceae) of China as revealed by SRAP markers. *Biochem. Syst. Ecol.* **2015**, *62*, 115–120. [CrossRef]
51. Lexer, C.; Fay, M.F. Adaptation to environmental stress: A rare or frequent driver of speciation? *J. Evol. Biol.* **2005**, *18*, 893–900. [CrossRef]
52. Tobler, M.; Palacios, M.; Chapman, L.J.; Mitrofanov, I.; Bierbach, D.; Plath, M.; Arias-Rodriguez, L.; de Leon, F.J.G.; Mateos, M. Evolution in extreme environments: Replicated phenotypic differentiation in livebearing fish inhabiting sulfidic springs. *Evolution* **2011**, *65*, 2213–2228. [CrossRef] [PubMed]
53. Xu, Y.L.; Woeste, K.; Cai, N.H.; Kang, X.Y.; Li, G.Q.; Chen, S.; Duan, A. Variation in needle and cone traits in natural populations of *Pinus yunnanensis*. *J. For. Res.* **2016**, *27*, 41–49. [CrossRef]
54. Wright, I.J.; Reich, P.B.; Westoby, M.; Ackerly, D.D.; Baruch, Z.; Bongers, F.; Cavender-Bares, J.; Chapin, T.; Cornelissen, J.H.C.; Diemer, M.; et al. The worldwide leaf economics spectrum. *Nature* **2004**, *428*, 821–827. [CrossRef]
55. Craine, J.M.; Ocheltree, T.W.; Nippert, J.B.; Towne, E.G.; Skibbe, A.M.; Kembel, S.W.; Fargione, J.E. Global diversity of drought tolerance and grassland climate-change resilience. *Nat. Clim. Chang.* **2013**, *3*, 63–67. [CrossRef]
56. Jordan, L.; He, R.C.; Hall, D.B.; Clark, A.; Daniels, R.F. Variation in loblolly pine ring microfibril angle in the Southeastern United States. *Wood Fiber Sci.* **2007**, *39*, 352–363.
57. Bateman, K.G. The genetic assimilation of four venation phenocopies (Reprinted). *J. Genet.* **2005**, *84*, 227–257. [CrossRef] [PubMed]
58. Levis, N.A.; Pfennig, D.W. Innovation and Diversification Via Plasticity-Led Evolution. In *Phenotypic Plasticity & Evolution*; Pfennig, D.W., Ed.; CRC Press: London, UK; New York, NY, USA, 2021; pp. 211–240.
59. Lopez, R.; Climent, J.; Gil, L. Intraspecific variation and plasticity in growth and foliar morphology along a climate gradient in the Canary Island pine. *Trees-Struct. Funct.* **2010**, *24*, 343–350. [CrossRef]

60. Groover, A. Gravitropisms and reaction woods of forest trees—evolution, functions and mechanisms. *New Phytol.* **2016**, *211*, 790–802. [CrossRef] [PubMed]
61. Poorter, H.; Niinemets, U.; Poorter, L.; Wright, I.J.; Villar, R. Causes and consequences of variation in leaf mass per area (LMA): A meta-analysis. *New Phytol.* **2009**, *182*, 565–588. [CrossRef]
62. Marshall, J.D.; Monserud, R.A. Erratum: Foliage height influences specific leaf area of three conifer species. *Can. J. For. Res.-Rev. Can. Rech. For.* **2003**, *33*, 1591. [CrossRef]
63. Dong, Y.C.; Liu, Y.H. Response of Korean pine's functional traits to geography and climate. *PLoS ONE* **2017**, *12*, e0184051. [CrossRef]
64. Chiang, T.Y.; Schaal, B.A. Phylogeography of plants in Taiwan and the Ryukyu archipelago. *Taxon* **2006**, *55*, 31–41. [CrossRef]

forests

MDPI

Article

Photosynthetic Processes and Light Response Model Fitting of *Quercus acutissima Carruth.* and *Quercus variabilis Bl.* in the Changjiang River Delta, China

Cunxin Ruan [1,2], Haibo Hu [1,2,*], Can Cheng [1,2], Pei Fang [2], Xichuan Jia [2], Zhaoming Wu [3] and Li Zhu [3]

1 Co-Innovation Center for the Sustainable Forestry in Southern China, Nanjing Forestry University, Nanjing 210037, China
2 Key Laboratory of Soil and Water Conservation and Ecological Restoration in Jiangsu Province, Nanjing Forestry University, Nanjing 210037, China
3 Wuxi Branch, Bureau of Investigation on Hydrologic Water Resources, Wuxi 214100, China
* Correspondence: huhb2000@aliyun.com

Abstract: Plants have the capacity to fix CO_2 through photosynthesis. To reveal the photosynthetic processes of *Quercus acutissima Carruth.* and *Quercus variabilis Bl.*, their net photosynthetic rates were quantified during the early and peak growing seasons. To evaluate forest photosynthetic efficiencies, the photosynthetic light response curves of *Q. acutissima* and *Q. variabilis* were fitted by the rectangular hyperbola model (RHM), non-rectangular hyperbola model (NHM), and modified rectangular hyperbola model (Ye model). The results revealed the following: (1) All daily variation curves of the net photosynthetic rate, stomatal conductivity, and transpiration rate were single-peaked. The peak times of the *Q. acutissima* and *Q. variabilis*' net photosynthetic rates appeared at 12:00 a.m. during the early growing season and 10:00 a.m. during the peak growing season. (2) The photosynthetic capacities of both *Q. acutissima* and *Q. variabilis* during peak growing seasons were higher than during the early growing season. (3) The net photosynthetic rate was found to be positively correlated with stomatal conductivity, the transpiration rate, and photosynthetically active radiation, and it was negatively correlated with the intercellular CO_2 concentration. (4) The Ye model provided the best fit for the light response curves of *Q. acutissima* and *Q. variabilis* when compared with the rectangular hyperbola and nonrectangular hyperbola models. The photosynthetic performance of *Q. acutissima* was superior to that of *Q. variabilis*; thus, it can be employed as a priority tree species in carbon sink forests.

Keywords: photosynthetic rate; photosynthetic efficiency; photosynthetic light response model; *Q. acutissima*; *Q. variabilis*

check for updates

Citation: Ruan, C.; Hu, H.; Cheng, C.; Fang, P.; Jia, X.; Wu, Z.; Zhu, L. Photosynthetic Processes and Light Response Model Fitting of *Quercus acutissima Carruth.* and *Quercus variabilis Bl.* in the Changjiang River Delta, China. *Forests* **2022**, *13*, 2010. https://doi.org/10.3390/f13122010

Academic Editor: Ilona Mészáros

Received: 12 October 2022
Accepted: 24 November 2022
Published: 28 November 2022

Publisher's Note: MDPI stays neutral with regard to jurisdictional claims in published maps and institutional affiliations.

Copyright: © 2022 by the authors. Licensee MDPI, Basel, Switzerland. This article is an open access article distributed under the terms and conditions of the Creative Commons Attribution (CC BY) license (https://creativecommons.org/licenses/by/4.0/).

1. Introduction

Photosynthesis is a biological process that absorbs CO_2 and releases O_2 to balance their concentrations in the ambient atmosphere [1]. Through photosynthesis, forests serve as an important carbon sink for terrestrial ecosystems by fixing CO_2 [2]. Photosynthetic parameters are essential indicators for the evaluation of forest photosynthetic efficiencies. The photosynthetic light response method is an important research technique in plant physiology [3]. From light response curves, photosynthetic parameters such as the maximum net photosynthetic rate, light saturation point, light compensation point, dark respiration rate, and apparent quantum efficiency can be obtained. The photosynthesis of plants is also affected by their physiology (e.g., stomatal conductivity) and environmental factors (e.g., photosynthetically active radiation) [4–6]. As plants grow, the environment, as well as their own physiological conditions, are altered. Subsequently, their photosynthetic capacities change during different growing seasons. Thus, it is critical to elucidate the photosynthetic processes of plants and their impact factors during different growing seasons.

The main models for fitting photosynthetic light response curves include the rectangular hyperbola model (RHM), the nonrectangular hyperbola model (NHM), the Ye-modified model (modified rectangular hyperbola model, YZP), the exponential model, etc. The rectangular hyperbola model was proposed by Baly in 1935, who described the relationship between photosynthesis and irradiance thusly: the net photosynthetic rate increases sharply with greater photosynthetically active radiation under low light intensities and slowly with greater photosynthetically active radiation at moderate light intensities [7]. The rectangular hyperbola model has been applied to simulate the light response curve of *Ziziphus jujuba* V*ar*., *Populus Euramericana* C*v*., and *Pinus pinea* L. and achieved good results [8–10]. The nonrectangular hyperbola model was proposed by Thornley in 1976 based on the rectangular hyperbola model with the addition of curvilinear angle (θ) to adjust the curvature of the curve [11]. Lang found that the nonrectangular hyperbola was the best model for fitting the light response curve of *Prunus sibirica* L., *Hippophae rhamnoides* L., and *Pinus tabulaeformis* Carr. [12]. The modified rectangular hyperbola model was proposed by Ye in 2007, which was based on the rectangular hyperbola model with the addition of a limiting parameter (β) to handle photosynthetic inhibition data. Li discovered that the modified rectangular hyperbola model could well fit the photosynthetic light response curve under a wide range of soil water conditions [13]. The rectangular hyperbola and nonrectangular hyperbola models are good at fitting the light compensation point and apparent quantum efficiency. The photosynthetic parameters fitted by the Ye model describe not only the light response characteristics but also the molecular photosynthetic pigment characteristics [14] and reproduce the light response trends of electron transport and CO_2 absorption [15]. Previous studies on photosynthetic light response curves showed that there were differences in fitting the photosynthetic parameters of the same plant using different models. Thus, it is of particular importance to select the optimal light response model to investigate the photosynthetic attributes of plants [16]. For this study, based on earlier research and our preliminary validations [17,18], we selected rectangular hyperbola, nonrectangular hyperbola, and Ye-modified models to fit the light response curves.

Quercus acutissima Carruth. and *Quercus variabilis* Bl. are widespread across warm temperate and subtropical regions of China. They are important, highly adaptable tree species with strong water conservation and excellent carbon sequestration capacities. These trees are extensively distributed throughout the Yangtze River Delta region and are broadly accepted by researchers as carbon sink trees [19,20]. The Yangtze River Delta region is an important area affected by acid rain, with a 57.12% acid precipitation frequency [21]. Most previous studies into the photosynthetic parameters of *Quercus acutissima* and *Quercus variabilis* involved saplings [22,23], some of which were concentrated in arid and high-temperature regions [24]. Further, they were situated in regions that were less affected by acid rain, while leaf photosynthesis was impacted by acid rain to a certain extent [25]. It is very important to understand the photosynthetic capacities of *Quercus acutissima* and *Quercus variabilis* in this region.

For this study, we continuously observed the photosynthetic diurnal variations of *Q. acutissima* and *Q. variabilis* in the Changjiang River Delta region for different growing seasons and simulated their photosynthetic light response curves using the rectangular hyperbola, nonrectangular hyperbola, and Ye models. This study endeavored to explore the photosynthetic processes and relationships between photosynthesis and ecophysiologicalfactors. Secondly, we aimed to select an optimal model to simulate the light response curves of *Q. acutissima* and *Q. variabilis*. Finally, we selected highly photosynthetically efficient *Quercus* spp. plants. Our results revealed the photosynthetic capacities of oak forests in the Yangtze Delta region and evaluated the photosynthetic efficiencies of individual oak trees. Further, this study provided a scientific basis to support the further study of forest carbon fixation in acid rain-impacted areas.

2. Materials and Methods

2.1. Site Description

This study was conducted at the Changjiang River Delta Forest Ecosystem National Positioning Station (E119°12′03″, N32°07′48″, 332.6 m) of the State Forestry and Grassland Administration. The site inhabits the middle foothills of Hollow Green Mountain, with a 20° southeast slope, in Jurong City, Jiangsu Province, East China (Figure 1), under a north subtropical monsoon climate. The mean annual temperature in this area is 15.2 °C, the mean frost-free period is 233 d, and the mean annual precipitation is 1055.6 mm. The soil is yellow-brown loam at pH 4.76 [26]. The dominant tree species are sawtooth oak (*Q. acutissima*) and oriental oak (*Q. variabilis*), with a small population of maple (*Liquidamdar formosara*), Chinese pistache (*Pistacia chinensis*), etc. The basic characteristics of the forest stands are shown in Table 1.

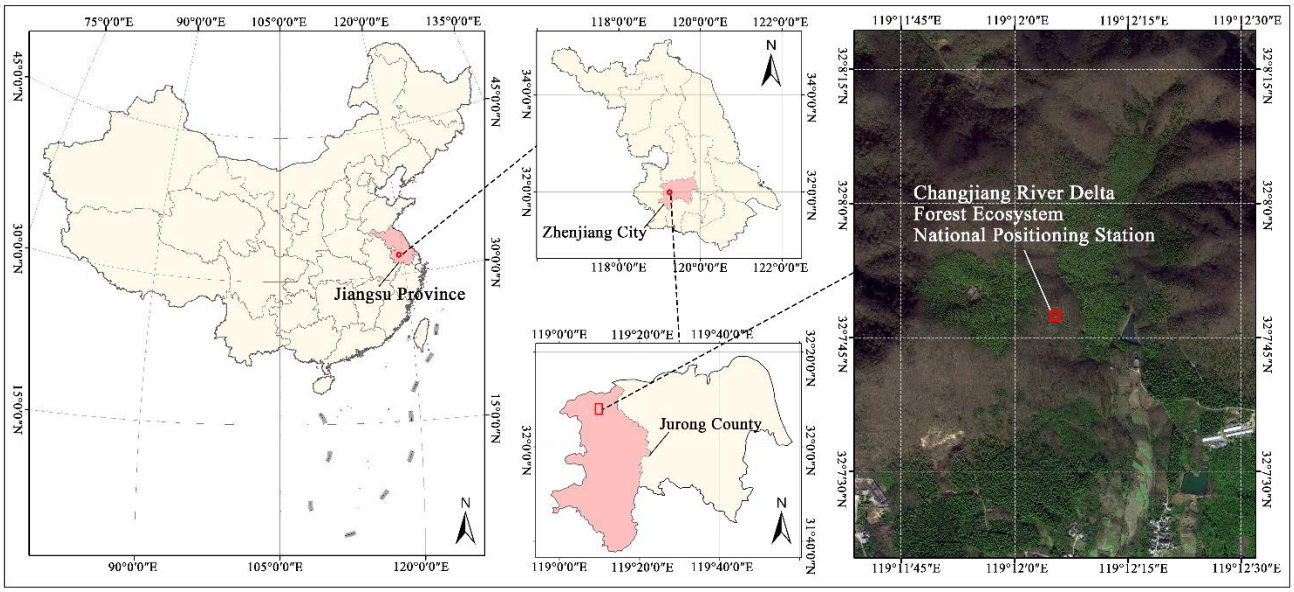


Figure 1. Study site location map. The study site is in Jurong County, Zhenjiang City, Jiangsu Province, China. Red rectangle identifies the sampling site. Because the remote sensing satellite map was obtained in the winter, it appears brown in the red rectangle.

Table 1. Basic characteristics of sample stands. Three sample squares of 20 m × 20 m were set up, wherein every 27 trees was measured.

Tree Species	*Q. acutissima*	*Q. variabilis*
Forest age/years	65	65
Tree height/m	19.24	17.78
Diameter/cm	26.64	25.08
Crown/m	4.6	4.1
Density/plants·hm^{-2}	325	350
Crown density	0.5	0.47

Note: The forest survey was implemented according to the National Standard of the People's Republic of China's "Long-term positioning observation method of forest ecosystem" (GB/T33027-2016).

2.2. Climate Observation

The climate was observed continuously for 24 h every day for the entire year. The main meteorological factors observed at the experimental site were photosynthetically active radiation (PAR) (μmol m^{-2} s^{-1}) and air temperature (°C). The photosynthetically active radiation was measured using a radiation sensor SK01-DP2 (MIDDLETON SOLAR Inc., Melbourne, VIC, Australia), while the air temperature was quantified with a thermo-

hygrometer HMP155A (VAISALA Inc., Helsinki, Finland), which were both at 20 m above the ground surface (observation tower).

2.3. Measurement of Photosynthetic Characteristics and Light Response Curve

From 20 to 28 April and 6 to 14 July (both with clear skies), photosynthetic characteristic measurements were obtained every two hours from 6:00 a.m. to 18:00 p.m. using a portable photosynthesizer LI-6400 (LI-COR Inc., Lincoln, OR, USA). Three healthy and fully expanded leaves were selected from the middle of the canopies of six standard *Q. acutissima* and *Q. variabilis* trees with height and diameter at breast height close to average values. The net photosynthetic rate, intercellular CO_2 concentration, transpiration rates, and stomatal conductivities were measured simultaneously. Finally, the arithmetic averages of the measurements were used as photosynthetic data for the early peak growing season (20 April to 30 May) and the peak growing season (1 July to 30 August), respectively. During the early growing season, the temperature ranged from 15 to 25 °C, air humidity from 34% to 50%, CO_2 concentration from 375 to 398 μmol mol^{-1}, and PAR from 1 to 1300 μmol m^{-2} s^{-1}. During the peak growing season, the temperature ranged from 20 to 35 °C, air humidity from 45% to 91%, CO_2 concentration from 370 to 398 μmol mol^{-1}, and PAR from 1 to 1600 μmol m^{-2} s^{-1}.

According to numerous studies, the most sensitive time for plant photosynthesis in response to light intensity is between 9:00 a.m. and 11:00 a.m. [27–29]. Consequently, for this study, we selected three leaves from three healthy *Q. acutissima* and *Q. variabilis* trees and made measurements from 9:00 a.m. to 11:00 a.m. each day under clear skies from 6 to 14 July. The sample chamber conditions were controlled, with the leaf temperature set at 25 °C, relative air humidity set at 60%, atmospheric CO_2 concentration set at 400 μmol mol^{-1}, an airflow rate of about 500 μmol s^{-1}, and light radiation intensities set at 0, 10, 20, 50, 100, 200, 400, 600, 800, 1000, 1200, 1400, 1600, 1800, and 2000 μmol m^{-2} s^{-1}. Once the light intensities were adjusted, the leaves remained in the sample chamber for two min, with measurement times no less than two minutes.

2.4. Fitting Model of the Photosynthetic Light Response Curve

The photosynthetic light response curves of *Q. acutissima* and *Q. variabilis* were fitted using the rectangular hyperbola, nonrectangular hyperbola, and Ye models. The net photosynthetic rates and photosynthetically active radiation curves were quantified [30], while the maximum net photosynthetic rate, light compensation point, light saturation point, and dark respiration rate were estimated from the curve trend as the measured values of the characteristic parameters of light responses [12,31].

The rectangular hyperbola model (RHM) equation was expressed as follows:

$$P_n = \frac{\alpha I P_{n\max}}{\alpha I + P_{n\max}} - R_d \quad (1)$$

where P_n is the net photosynthetic rate (μmol m^{-2} s^{-1}), α is the initial quantum efficiency, I is the photosynthetic active radiation intensity (μmol m^{-2} s^{-1}), P_{nmax} is the maximum net photosynthetic rate at light saturation (μmol m^{-2} s^{-1}), and R_d is the dark respiration rate (μmol m^{-2} s^{-1})

The nonrectangular hyperbolic model (NHM) equation was expressed as follows:

$$P_n = \frac{\alpha I + P_{n\max} - \sqrt{(\alpha I + P_{n\max})^2 - 4\alpha\theta I P_{n\max}}}{2\theta} - R_d \quad (2)$$

where θ is the optical response curve angle of the curvature, with the other letters referring to the same as above.

The Ye model (the modified rectangular hyperbola model, YZP) equation was expressed as follows:

$$P_n = \alpha \frac{1 - \beta I}{1 + \gamma I} I - R_d \quad (3)$$

where β is the photoinhibition coefficient (m^2 s μmol^{-1}), γ is the light saturation coefficient (m^2 s μmol^{-1}), and the other letters have the same meanings as above.

The light saturation points, I_s (μmol m^{-2} s^{-1}), for the rectangular hyperbola and nonrectangular hyperbola models were calculated using the equation below [32]. First, a linear regression of the photosynthetic active radiation, I, from 0 to 200 (μmol m^{-2} s^{-1}) and the net photosynthetic rate, P_n, were used to obtain the apparent quantum efficiency (AQE) and dark respiration rate (R_d), with the equation expressed as follows:

$$P_n = \mathrm{m} \times I - \mathrm{R_d} \tag{4}$$

where P_n is the net photosynthetic rate (μmol m^{-2} s^{-1}), slope m is apparent quantum efficiency, and the R_d is the dark respiration rate (μmol m^{-2} s^{-1}).

Then, the light saturation point, I_s, was calculated with Equation (4):

$$I_\mathrm{s} = \frac{P_{n\max} + R_\mathrm{d}}{m} \tag{5}$$

where P_{nmax} is the max net photosynthetic rate (μmol m^{-2} s^{-1}), m is apparent quantum efficiency, and R_d is dark respiration rate (μmol m^{-2} s^{-1}).

The light saturation point, I_s, in the Ye model was expressed as follows:

$$I_s = \frac{\sqrt{(\beta+\gamma)/\beta} - 1}{\gamma} \tag{6}$$

where the net photosynthetic rate P_n is 0, and the light compensation point (I_c) (mol m^{-2} s^{-1}) is the photosynthetically active radiation. As a result, for the RHM, NHM, and YZP models, the P_n was set to 0 to obtain the respective I_c values.

The formula of the light compensation point for the rectangular hyperbola model was expressed as follows:

$$I_\mathrm{c} = \frac{R_d P_{n\max}}{\alpha(P_{n\max} - R_d)} \tag{7}$$

The formula of the light compensation point for the nonrectangular hyperbolic model was expressed as follows:

$$I_\mathrm{c} = \frac{P_{n\max} R_d - \theta R_d^2}{\alpha(P_{n\max} - R_d)} \tag{8}$$

The formula of the light compensation point, for the Ye model was expressed as follows:

$$I_\mathrm{c} = \frac{\alpha - R_d\gamma - \sqrt{(\alpha - R_d\gamma)^2 - 4\alpha\beta R_d}}{2\alpha\beta} \tag{9}$$

The maximum net photosynthetic rate equation for the Ye model was expressed as follows:

$$P_{n\max} = \alpha\left(\frac{\sqrt{\beta+\gamma} - \sqrt{\beta}}{\gamma}\right)^2 - R_d \tag{10}$$

2.5. Model Evaluation

To evaluate the goodness of fit for the three models, the root-mean-square error (*RMSE*), mean absolute percentage error (*MAPE*), and determination coefficient (R^2) were calculated using empirical formulae. The determination coefficient was established by fitting the light response curve with Matlab 2020, while the *RMSE* and *MAPE* were calculated using the equations below [33]:

$$RMSE = \sqrt{\frac{1}{n}\sum_{i=1}^{n}(Y_{m,i} - Y_{0,i})^2} \quad (11)$$

where $Y_{m,i}$ is the predicted value of the model, and $Y_{0,i}$ is the observed value, as shown below:

$$MAPE = \frac{1}{n}\sum_{i=1}^{n}\left|\frac{Y_{m,i} - Y_{0,i}}{Y_{0,i}}\right| \times 100\% \quad (12)$$

2.6. Data Analysis

The net photosynthetic rate and eco-physiological factor data were processed using Excel 2017 and SPSS (V 19, Armonk, NY, USA) for correlation analysis. Origin software(Version 2018, Northampton, MA, USA) was employed to plot the dynamic photosynthetic daily change characteristics and photosynthetic light response curves. Matlab software (Version 2020, Natick, MA, USA) was employed to build the rectangular hyperbola, nonrectangular hyperbola, and Ye models.

3. Results

3.1. Diurnal Dynamics of Photosynthetic Parameters

3.1.1. Diurnal Variations of Net Photosynthetic Rates

The daily trend of the net photosynthetic rates of *Q. acutissima* and *Q. variabilis* was a single-peaked curve for both the early and peak growing seasons, as shown in Figure 2A. During the early growing season, the peak net photosynthetic rates of *Q. acutissima* and *Q. variabilis* were 4.40 and 4.07 μmol m^{-2} s^{-1}, respectively, and the peak time appeared at 12:00 a.m. During the peak growing season, the peak net photosynthetic rates of *Q. acutissima* and *Q. variabilis* were 6.87 and 5.05 μmol m^2 s^{-1}, respectively, and the peak time appeared at 10:00 a.m. The peak net photosynthetic rate during the peak growing season occurred two hours earlier than during the early growing season, and the mean daily net photosynthetic rates of both *Q. acutissima* and *Q. variabilis* during the peak growing season were higher than during the early growing season. The average daily net photosynthetic rate of 1.94 μmol m^2 s^{-1} was higher than that of *Q. variabilis* (1.86 μmol m^{-2} s^{-1}) during the early growing season but not significant ($p = 0.12$). During the peak growing season, the average daily net photosynthetic rate of *Q. acutissima* was 4.16 μmol m^{-2} s^{-1}, compared with 3.10 μmol m^{-2} s^{-1} for *Q. variabilis*.

3.1.2. Diurnal Variation of Transpiration Rate

Plant transpiration is intimately linked to photosynthesis, which facilitates carbon assimilation and the diffusion and transportation of CO_2 from the ambient atmosphere to leaf flesh cells. As illustrated in Figure 2D, the daily trends of *Q. acutissima* and *Q. variabilis* transpiration were consistent with the photosynthetic rate (both in a single-peaked pattern), whereas the peak transpiration rate for *Q. acutissima* occurred at 12:00 at 0.80 mol m^{-2} s^{-1} during the early growing season, with a daily mean transpiration rate of 0.377 mol m^{-2} s^{-1}. The peak transpiration rate of *Q. variabilis* also occurred at 12:00 a.m. at 0.67 mol m^2 s^{-1}, whereas the daily mean transpiration rate was 0.36 mol m^{-2} s^{-1}. The peak transpiration rate for *Q. acutissima* appeared at 12:00 at 0.06 mol m^{-2} s^{-1}, and the daily mean transpiration rate was 1.11 mol m^{-2} s^{-1} during the peak growing season. The peak transpiration rate for *Q. variabilis* occurred at 12:00 a.m. at 0.05 mol m^{-2} s^{-1}, and the mean daily transpiration rate was 0.91 mol m^{-2} s^{-1}. The daily mean transpiration rates of *Q. acutissima* and *Q. variabilis* during the peak growing season were higher than those of the early growing season, with the transpiration rate of *Q. acutissima* being higher than that of *Q. variabilis*.

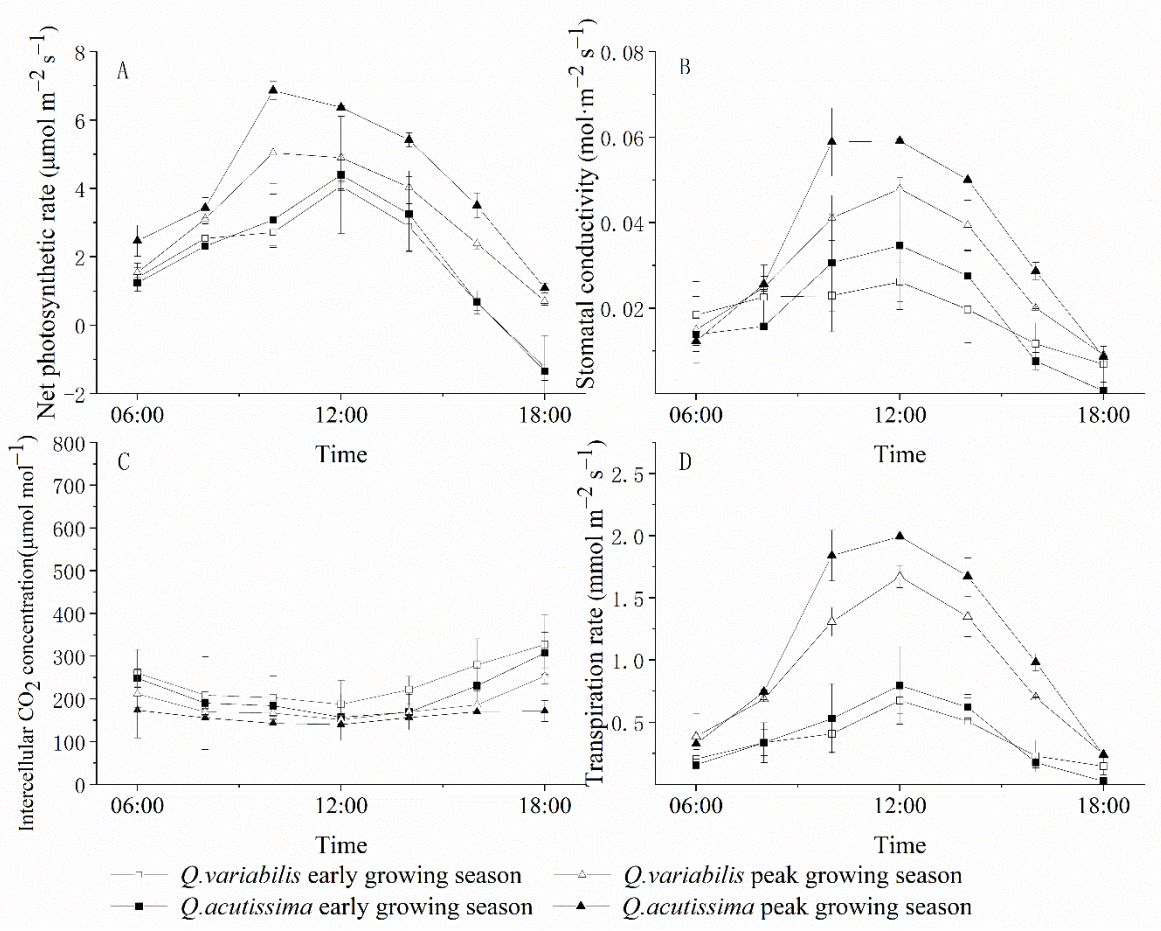


Figure 2. Diurnal variation of photosynthetic characteristics of *Quercus acutissima Carruth.* and *Quercus variabilis Bl.* during early and peak growing seasons. (**A**) Diurnal variation of net photosynthetic rate (μmol m^{-2} s^{-1}). (**B**) Diurnal variation of stomatal conductivity (mol m^{-2} s^{-1}). (**C**) Diurnal variation of intercellular CO_2 concentration μmol mol^{-1}. (**D**) Diurnal variation of transpiration rate (mmol m^{-2} s^{-1}).

3.1.3. Diurnal Variation of Stomatal Conductivity

Stomata are the channels through which CO_2 and water ingress and egress leaves, where stomatal conductivity reflects the capacity of leaves to exchange CO_2 and water with the ambient environment. The daily variation of stomatal conductivity was unimodal (Figure 2B) and corresponded to the daily trend of the net photosynthetic and transpiration rates. The daily average stomatal conductivities of *Q. acutissima* and *Q. variabilis* were lower during the early growing season than during the peak growing season. At 12:00 a.m., the peak stomatal conductivity of *Q. acutissima* was 0.03 mol m^{-2} s^{-1}, whereas that of *Q. variabilis* was 0.03 mol m^{-2} s^{-1}. The peak stomatal conductivity of *Q. acutissima* was 0.06 mol m^{-2} s^{-1} at 12:00 a.m. and 0.05 mol m^{-2} s^{-1} at 12:00 a.m. during the peak growing season. The mean daily stomatal conductivity for *Q. acutissima* was 0.02 mol m^{-2} s^{-1} and 0.02 mol m^{-2} s^{-1} for *Q. variabilis* during the early growing season. During the peak growing season, the mean daily stomatal conductivity was 0.03 mol m^2 s^{-1} for *Q. acutissima* and 0.03 mol m^{-2} s^{-1} for *Q. variabilis*.

3.1.4. Diurnal Variation of Intercellular CO_2

Intercellular CO_2 is the primary raw material for photosynthesis in leaves, where its concentration reflects its strength. As shown in Figure 2C, the daily intercellular variations in CO_2 exhibited a trend of being low in the afternoon and high in the morning and evening during both the early growth and peak seasons. Figure 2 reveals that, as the solar radiation

increased, leaf photosynthesis commenced, after which the intercellular CO_2 concentration gradually decreased to reach its low point at midday. The lowest CO_2 concentrations for *Q. acutissima* and *Q. variabilis* were 157.18 and 187.25 μmol mol^{-1}, respectively, during the early growing season and 140.25 and 151.70 μmol mol^{-1}, respectively, during the peak growing season. The concentration of intercellular CO_2 steadily increased as photosynthesis weakened in the afternoon. During the early growing season, the average intercellular CO_2 concentrations for *Q. acutissima* and *Q. variabilis* were 212.36 and 241.27 μmol mol^{-1}, respectively. During the peak growing season, the intercellular CO_2 concentrations for *Q. acutissima* and *Q. variabilis* were 158.61 and 187.01 μmol mol^{-1}, respectively. The concentration of intercellular CO_2 for *Q. variabilis* was higher than that of *Q. acutissima* during both the early and peak growing seasons. Furthermore, with more robust photosynthesis, the intercellular CO_2 concentration was lower. As shown in Figure 2C, the intercellular CO_2 concentrations of *Q. acutissima* and *Q. variabilis* reached a valley at 10:00 a.m., in conjunction with the peaking net photosynthetic rate.

3.1.5. Correlation Analysis of Net Photosynthetic Rate and Eco-Physiological Factors

We observed physiological indicators such as the net photosynthetic rate, stomatal conductivity, and transpiration rate, as well as associated environmental factors, including photosynthetically active radiation (PAR) and temperature, during the early and peak growing seasons. To better comprehend how the net photosynthetic rate responded to eco-physiological factors, it was correlated with the stomatal conductivity, intercellular CO_2 concentration, transpiration rate, photosynthetically active radiation, and air temperature (Table 2). The net photosynthetic rate was found to be significantly positively correlated with the stomatal conductivity, transpiration rate, and photosynthetically active radiation ($p < 0.01$); significantly negatively correlated with the intercellular CO_2 concentration ($p < 0.01$); and insignificantly correlated with the temperature ($p < 0.05$). The strongest correlation was found between the net photosynthetic rate and stomatal conductivity, and the correlation coefficient increased over time. The correlation coefficient between the net photosynthetic rate and stomatal conductivity was 0.89 during the early growing season and 0.98 during the peak growing season, which indicated that the stomatal conductivity had an increased effect on the net photosynthetic rate during the peak growing season. During both the early and peak growing seasons, the correlation coefficient between the net photosynthetic rate and transpiration rate of *Q. acutissima* was greater than that of *Q. variabilis*, which was consistent with the response pattern of the net photosynthetic rate on the stomatal conductivity of *Q. acutissima*. The correlation coefficients between the net photosynthetic rate and stomatal conductivity for *Q. acutissima* and *Q. variabilis* were greater than those between the net photosynthetic rate and photosynthetically active radiation. This implied that the stomatal conductivity had a greater impact on the net photosynthetic rate than the photosynthetically active radiation.

Table 2. Correlation coefficients between net photosynthetic rate and eco-physiological factors during different growing seasons. PAR: photosynthetically active radiation. Significant values are indicated: **, $p < 0.01$.

Species	Growing Period	Stomatal Conductivity	Internal CO_2 Concentration	Transpiration Rate	Air Temperate	PAR
Q. acutissima	Early	0.890 **	−0.789 **	0.854 **	0.202	0.789 **
	Peak	0.980 **	−0.650 **	0.968 **	0.258	0.626 **
Q. variabilis	Early	0.748 **	−0.737 **	0.617 **	0.281	0.510 **
	Peak	0.942 **	−0.776 **	0.944 **	0.295	0.598 **

3.1.6. Photosynthetic Light Response Model and Photosynthetic Parameters

The dynamic variations in the photosynthetic light response curve for the three models were similar when the PAR was <200 μmol m^{-2} s^{-1} (Figure 3B–D). Specifically, the net

photosynthetic rate increased rapidly with greater photosynthetically active radiation, and the predicted values fitted by the three models were close to those measured. When the PAR was >200 μmol m^{-2} s^{-1}, the imitative effects of the three photosynthetic light response models on the light response curves were varied. In the Ye model, the net photosynthetic rates of *Q. acutissima* and *Q. variabilis* gradually decreased when the PAR exceeded the light saturation point (Figure 3D). In the rectangular hyperbola model, the net photosynthetic rate increased slightly as the PAR increased (Figure 3B). whereas in the nonrectangular hyperbola model, the light response curve trended to smoothing. Changes in the photosynthetic light response curve predicted by the Ye model were consistent with the measured curves when the PAR was >200 μmol m^{-2} s^{-1} (Figure 3A,D).

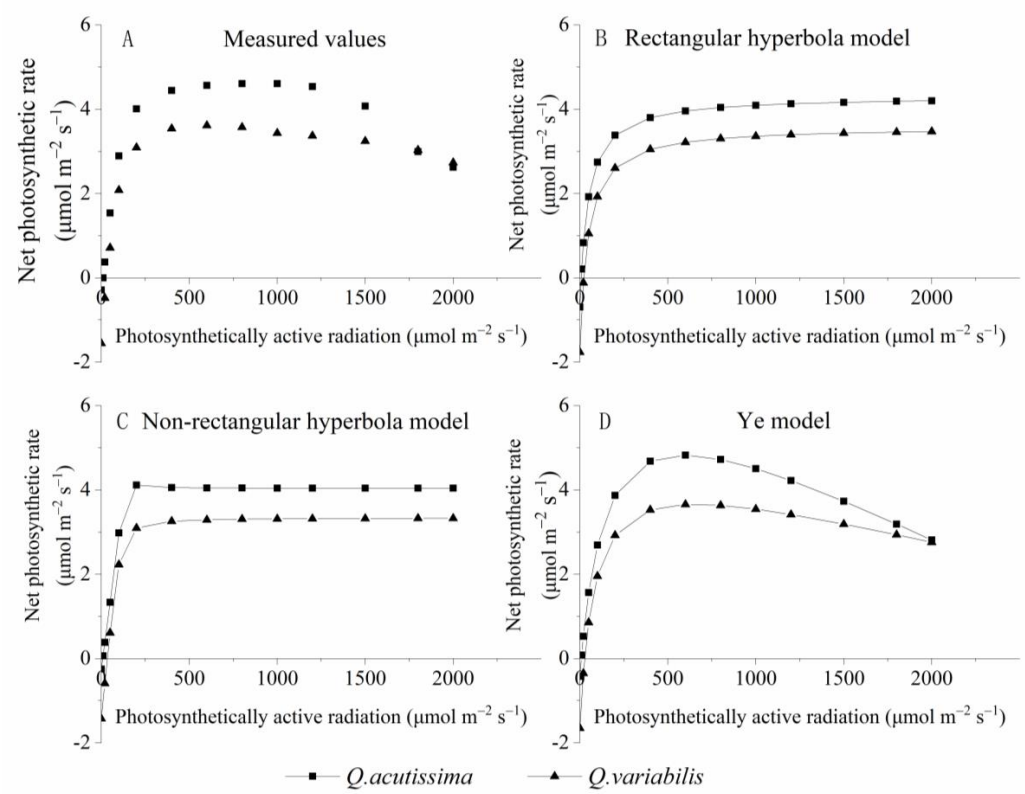


Figure 3. Photosynthetic light response curves of *Q. acutissima* and *Q. variabilis*. (**A**) Scatter of measured values (**B**) Simulative curve of Rectangular hyperbola model (**C**) Simulative Curve of non-rectangular hyperbola model (**D**) Simulative curve of Ye model.

The light saturation point refers to the light intensity when the photosynthetic intensity of a plant reaches its peak. According to Table 3, the light saturation points (LSP) of the measured curves for *Q. acutissima* and *Q. variabilis* were 783.33 and 666.67 μmol m^{-2} s^{-1}, respectively. The ANOVA revealed that the light saturation point of *Q. acutissima* was significantly greater than that of *Q. variabilis* ($p < 0.05$), which meant that *Q. acutissima* utilized more light energy than *Q. variabilis*. The light saturation points of the rectangular hyperbola and nonrectangular hyperbola models for *Q. acutissima* were 62.965% and 78.78%, respectively, which were lower than the measured values, while that of the Ye model was 24.10% lower than the measured values. The light saturation points of the rectangular hyperbola and nonrectangular hyperbola models for *Q. variabilis* were 45.53% and 60.057% lower than the measured values, respectively, while that of the Ye model was 8.62% lower than those measured. This indicated that the light saturation points of the Ye model were closer to the measured values and had a better fit.

Table 3. Photosynthetic parameters of *Quercus acutissima Carruth.* and *Quercus variabilis Bl.* fitted by the three models. Different lowercase letters (i.e., a, b, c) in the same column indicate a significant difference between different models of the same species ($p < 0.05$). Different capital letters (i.e., A, B, C) in the same column indicate a significant difference between different species of the same model ($p < 0.05$). RHM: rectangular hyperbola model; NHM: nonrectangular hyperbola model; YZP: Ye model; LSP: light saturation point; LCP: light compensation point; R_d: dark respiration; and the same below.

Species	Models	LSP/μmol m^{-2} s^{-1}	LCP/μmol m^{-2} s^{-1}	R_d/μ mol m^{-2} s^{-1}	P_{nmax}/μmol m^{-2} s^{-1}	*MAPE*/%	*RMSE*	R^2
Q. acutissima	RHM	296.28bA	7.24aA	0.68cA	5.00aA	20.47	0.68	0.85
	NHM	169.77aA	7.67aA	0.24aA	4.29aA	17.86	0.56	0.90
	YZP	607.24cA	8.14abA	0.42bA	4.85aA	15.37	0.20	0.99
	Measured value	783.33dA	9.86bA	0.29aA	4.65aA	—		
Q. variabilis	RHM	326.84aA	22.67aB	1.76aB	5.36bA	27.18	0.37	0.95
	NHM	239.65aA	34.55aB	1.43aB	4.78abA	25.38	0.24	0.98
	YZP	651.69bA	27.53aB	1.65aB	3.67aB	24.37	0.10	0.99
	Measured value	666.67bB	26.00aB	1.55aB	3.630aB	—		

The minimum light intensity required by plants for photosynthesis is defined as the light compensation point. As shown in Table 3, the light compensation point (LCP) predicted by the rectangular hyperbola model for *Q. acutissima* was 7.24 μmol m^{-2} s^{-1}; for the nonrectangular hyperbola model, it was 7.68 μmol m^{-2} s^{-1}. These values were 26.55 % and 22.18% lower than the measured LCP (9.86 μmol m^{-2} s^{-1}), respectively. The light compensation point predicted by the Ye model (8.14 mol m^{-2} s^{-1}) was 17.51% lower than the measured value. The LCP predicted by the rectangular hyperbola model for *Q. variabilis* was 12.82% lower than the measured value. Further, the LCP predicted by the nonrectangular hyperbola and Ye models were 32.89% and 5.88% higher, respectively, than the measured value.

For this study, the respiration rate value at a light intensity of zero was used as the measured dark respiration rate. Because of ignoring the photorespiration, the actual dark respiration rate was greater than or equal to the measured respiration rate. The predicted dark respiration rates of the three models for *Q. variabilis* were not significantly different from the measured values. However, for *Q. acutissima*, only the predicted dark respiration rate of the nonrectangular hyperbola model was closer to the measured values, while the predicted dark respiration rates of the rectangular hyperbola and Ye models were 137.02% and 43.94% higher, respectively, than the measured values. According to Table 3, the dark respiration rate of *Q. acutissima* was significantly lower than that predicted or measured for *Q. variabilis* ($p < 0.05$), which was 81.39% lower than for *Q. variabilis*. In the Ye model, *Q. acutissima* had a 74.86% lower dark respiration rate than *Q. variabilis*, where the lower the dark respiration rate, the less CO_2 content was released. This meant that, under the same conditions, *Q. acutissima* had a higher carbon storage capacity than *Q. variabilis*.

The highest net photosynthetic rate was the critical parameter in defining the photosynthetic potential. For the rectangular hyperbola and Ye models of *Q. acutissima*, the maximum net photosynthetic rates predicted were 7.68% and 4.30% greater, respectively, than the measured values. However, there were difference between photosynthetic parameters predicted by different models. The predicted maximum net photosynthetic rate of the rectangular hyperbola model was 47.63% significantly higher than that measured for *Q. variabilis* ($p < 0.05$). While, the predicted maximum net photosynthetic rates of the nonrectangular hyperbola and Ye models were 31.57% ($p = 0.08$) and 1.02% ($p= 0.95$) higher than the measured values, respectively. The measured maximum net photosynthetic rate of *Q. acutissima* was 28.02% higher than that of *Q. variabilis* ($p < 0.05$). Similarly, the maximum net photosynthetic rate of *Q. acutissima* predicted by the Ye model was considerably higher than that of *Q. variabilis* ($p < 0.05$).

The imitative effects of the three models were tested via three indicators, including the root-mean-square error (*RMSE*), mean absolute percentage error (*MAPE*), and coefficient of determination (R^2). The *RMSE* measures the differences between the observed and predicted values and reflects the dispersion of errors. The *MAPE* characterizes the average errors of multiple predictions for evaluating the fitting accuracy of the model to the existing data, while R^2 can determine the degree of model fitting. The lower the *MAPE* and *RMSE*, the closer the R^2 is to one, which indicates a better fit. The *RMSE* of the fitted curves of the three *Q. variabilis* models were 0.37, 0.25, and 0.10, respectively, while the *RMSE* of the fitted curves of the three models for *Q. acutissima* were 0.678, 0.57, and 0.20 respectively. The *RMSE* of the Ye model was the smallest of the three models. In terms of the model-fitting accuracy for the *Q. acutissima* and *Q. variabilis* light response curves, the Ye model had the best fitting accuracy for *Q. acutissima* with an error rate of 15.37%, followed by the nonlinear hyperbolic model with an error rate of 17.86%. The Ye model had the best fitting accuracy for *Q. variabilis* with an error rate of 24.37%, followed by the nonlinear hyperbolic model (25.38%). The R^2 values for all three models of *Q. variabilis* were greater than 0.90, whereas the R^2 for the fitted curve of *Q. acutissima* was 0.99 in the Ye model. In summary, the Ye model performed better than the rectangular hyperbola and the non-rectangular hyperbola models in terms of fitting the photosynthetic parameters (e.g., maximum net photosynthetic rate, light saturation point, and light compensation point). Further, its model evaluation index *RMSE* was lower, the R^2 was closer to one, and the fitting accuracy was higher. This signified that the Ye model was better suited for fitting the net photosynthetic light response curves of *Q. acutissima* and *Q. variabilis*.

4. Discussion

4.1. Relationships between Photosynthetic Rates and Eco-Physiological Factors

During the early and peak growing seasons, diurnal changes in the net photosynthetic rates of *Q. acutissima* and *Q. variabilis* were unimodal, which was consistent with Zhao et al. and Fan et al. [34,35], but they diverged from the study of Wang et al. [33]. These researchers thought that this was due to the stomatal conductivity, which limited the availability of CO_2 at higher temperatures [36]. During the peak growing season, the net photosynthetic rates of *Q. acutissima* and *Q. variabilis* were significantly greater than during the early growing season, which was consistent with the changes in leaf stomatal conductivity. The main factor that influenced the net photosynthetic rates of *Q. acutissima* and *Q. variabilis* was stomatal conductivity. Table 1 shows that the correlation coefficients between the stomatal conductivities and net photosynthetic rates of *Q. acutissima* and *Q. variabilis* were 0.89 and 0.75, respectively, during the early growing season, which increased to 0.98 and 0.94 during the peak growing season. This was consistent with the study of Liang, who found that the stomatal factor was the primary driver behind changes in the net photosynthetic rate [37]. Stomatal conductivity steadily increased with stomatal expansion from the early to peak growing seasons, which stimulated photosynthesis [38]. Atmospheric temperatures, vapor pressure deficits, and relative humidity can affect stomatal opening and closing [39] and indirectly affect the net photosynthetic rate. In addition to stomatal factors, stomatal opening and closing had an indirect impact on the photosynthetic rate. Photosynthetic active radiation in conjunction with stomatal factors were important external factors that influenced the net photosynthetic rates of *Q. acutissima* and *Q. variabilis*. Wu et al. discovered that photosynthetically active radiation had a greater impact on sunny plants such as *Q. acutissima* and Pinus sylvestris [40]. This was due to photosynthetically active radiation that induced the generation of adenosine triphosphate (ATP) and nicotinamide adenine dinucleotide phosphate (NADPH), which assimilated carbon in the dark reaction stage [41]. The photosynthetic rate and intercellular CO_2 concentrations were negatively associated, which indicated that more intense photosynthesis consumed additional CO_2. This was because the intercellular CO_2 concentrations affected the photochemical efficiency of photosystem II [42]. The photosynthetic rate was significantly positively correlated with the transpiration rate, which was consistent with the study of Kim [43]. As stomata conductivity reflects the

extent to which stomata open, both photosynthesis and transpiration employ stomata as channels. Thus, both of them increased with higher stomata conductivity.

4.2. Comparison of Photosynthesis–Light Response Models

Currently, the rectangular hyperbola, nonrectangular hyperbola, and Ye models are the most commonly utilized photosynthesis light response models [44], and they play important roles in fitting photosynthetic light response curves, while also predicting photosynthetic parameters [9]. The Ye model can accurately reflect the inhibition of the net photosynthetic rate with higher light intensities during photosynthesis in *Q. acutissima* and *Q. variabilis*, while the rectangular hyperbola and nonrectangular hyperbola models cannot indicate the inhibition of photosynthesis under strong light conditions [45]. This is due to the mathematical expressions for the rectangular hyperbola and nonrectangular hyperbola models lacking the asymptote of the poles [46]. Thus, they cannot simulate the decreasing photosynthetic rate under higher light intensities. Conversely, the Ye model is based on the rectangular hyperbola model with the addition of correction parameters to bring the fitted curve closer to the actual measurement [30]. Deng et al. discovered that the Ye model fitted the *Q. variabilis* photosynthesis–light response curve better than the rectangular hyperbola or nonrectangular hyperbola models [22].

Since photosynthetic parameters reflect the capacity of plants to utilize light energy [45], the adaptabilities of the three models to the light response curves of *Q. acutissima* and *Q. variabilis* were compared. Both the rectangular hyperbola and nonrectangular hyperbola models had lower light saturation points than the actual curve, which was consistent with the studies of Xu and Xi [47,48]. This was due to the light saturation points of the rectangular hyperbola and nonrectangular hyperbola models not being directly obtainable, which had to be calculated using Richardson's hypothetical empirical formula [49]. The light saturation point of *Q. acutissima* predicted by the Ye model was significantly lower than the measured value, while the predicted light saturation point of *Q. variabilis* was not significantly different from the measured value. This indicated that the prediction of the light saturation point of *Q. variabilis* using the Ye model was superior to that of *Q. acutissima*. The prediction of the light compensation point (LCP) for *Q. acutissima* and *Q. variabilis* via the three models revealed differences. The LCP of *Q. acutissima* predicted by the Ye model was closer to the measured curve than that of the rectangular hyperbola and nonrectangular hyperbola models, while the LCP of *Q. variabilis* predicted by the three models was not significantly different from that of the measured value. The differences between the models may have been due to the smaller LCP of *Q. acutissima*, which was more photonically sensitive under low light conditions [50]. The dark respiration rate of *Q. acutissima* predicted by the nonrectilinear hyperbolic model was closer to the measured value, while the dark respiration rates predicted by the rectangular hyperbola and Ye models were significantly larger than the measured values. This signified that the prediction of the dark respiration rate of *Q. acutissima* by the nonrectilinear hyperbolic model was better than those projected by the rectangular hyperbola and Ye models. The predicted dark respiration rates of *Q. variabilis* using the three models were not significantly different from the measured values, which indicated that all three models were suitable for fitting the *Q. variabilis* dark respiration rate.

4.3. Comparison of Net Photosynthetic Rates with Other Regions

In this study, the net photosynthetic rate of *Q. variabilis* was similar to that of the Funiu Mountain area but lower than that of this species on Taihang Mountain and other regions [49]. The net photosynthetic rate of *Q. acutissima* in this study was closer to that of Nanjing, Chuzhou, and Wanyuan [34,51] but lower than that of Fei County, Kunming [52]. According to Table 4, we found that higher precipitation translated to a lower net photosynthetic rate. Following 15 years of continuous observation of terrestrial ecosystems in Qinghai and Tibet, Xu et al. discovered that the net primary productivity decreased with higher precipitation [53]. Wang et al. found that the net photosynthetic rate of *Q. variabilis*

in northern habitats (Beijing) was significantly higher than in southern habitats (Yunnan), which received more precipitation [54]. Furthermore, acid rain had a significant impact on the net photosynthetic rate. Kunming, which has the same annual average temperature and precipitation, has a higher net photosynthetic rate than Nanjing and Jurong, which might have been due to the pH of the rainfall. Acid rain had a positive effect on the leaf photosynthetic rate when the pH was above 5.0 and had a negative effect when below this level [25]. It is known that the annual average precipitation pH value was 4.87 in the Changjiang River Delta [21] and 7.28 in Kunming city [55]. Thus, it was obvious that the pH of precipitation can inhibit photosynthesis in the oak forests of the Changjiang River delta. Differences in the photosynthetic capacities of *Q. variabilis* in different regions were also influenced by latitude. Xiong et al. discovered that latitude had a significant impact on *Q. variabilis* photosynthesis [56]. Liu et al. also found that, at high latitudes, *Q. variabilis* had higher dark respiration rates, whereas, at low latitudes, it had higher maximum net photosynthetic rates and lower light compensation points [57]. This was thought to be attributed to increases in the chlorophyll and nitrogen contents of *Q. variabilis* leaves with increasing latitude.

Table 4. Comparison of net photosynthetic rates of *Q. acutissima* and *Q. variabilis* in different regions. These data were obtained during July and August.

Species	Area	Daily MEAN Net Photosynthetic Rate/μmol·m^{-2}·s^{-1}	Annual Rainfall/mm	Mean Annual Temperature/°C	Precipitation pH	Latitude/N	Climatic Zone	Reference
Q.variabilis	Funiu Mountain	3.26	1100	12~14.1	-	32°45′	Temperate	[49]
	Taihang Mountain	7.62	641.7	12.4~14.3	5.13	35°01′	Temperate	[35]
	Beijing	7.72	669.1	10.8	5.21	40°29′	Temperate	[54]
	Jurong	3.10	1055	15.2	4.87	32°07′	Subtropics	This study
Q.acutissima	Kunming	6.20	1035	15	7.80	-	Subtropics	[52]
	Feixian	6.79	856.4	20	5.35	117°96′	Temperate	[51]
	Chuzhou	3.65	1050	15	5.06	118°08	Subtropics	[51]
	Wanyuan	3.67	1100	15	4.74	108°06′	Subtropics	[51]
	Nanjing	4.47	1100	15.1	4.87	31°35′	Subtropics	[34]
	Jurong	4.16	1055	15.2	4.87	31°59′	Subtropics	This study

4.4. Comparison of Photosynthetic Parameters between Q. acutissima and Q. variabilis

The daily average net photosynthetic rate of *Q. acutissima* was significantly greater than that of *Q. variabilis* during the early and peak growing seasons, and its maximum net photosynthetic rate (referring to photosynthetic potential) was also greater than that of *Q. variabilis*. This indicated that *Q. acutissima* possessed a stronger photosynthetic capacity and superior carbon sequestration efficiency. As the trees grew, the photosynthetic capacity of *Q. acutissima* differed even more significantly from that of *Q. variabilis*. The light compensation point reflects the photosynthetic capacity of plants under low light conditions. The light compensation point of *Q. acutissima* was significantly smaller than that of *Q. variabilis*, which implied that the photosynthetic capacity of *Q. acutissima* was superior under low light conditions. The dark respiration rate is an important parameter that characterizes plant respiration, where the higher the value, the more CO_2 is released. The dark respiration rate of *Q. acutissima* was 0.289 mol m^{-2} s^{-1}, which was significantly lower than that of *Q. variabilis* (1.553 mol m^{-2} s^{-1}). This suggested that the number of carbohydrates consumed by *Q. acutissima* was smaller than that of *Q. variabilis*. Specifically, when all other conditions were equivalent, the quantity of CO_2 fixed by *Q. acutissima* was greater than that of *Q. variabilis*. In summary, *Q. acutissima* had a higher photosynthetic carbon sequestration capacity than *Q. variabilis*, which makes it a priority candidate species for carbon sink forests.

5. Conclusions

By synthesizing data from photosynthetic processes and fitting the photosynthetic light response curves, we assessed the photosynthetic characteristics of *Q. acutissima* and *Q. variabilis* and their photosynthetic efficiencies. Our results indicated the following: (1) The photosynthetic capacities of *Q. acutissima* and *Q. variabilis* significantly increase with their growth. (2) Stomatal conductivity was the most important physiological factor that affected photosynthesis in *Q. acutissima* and *Q. variabilis*, where photosynthetically active radiation was the most critical environmental factor. (3) The Ye model was the optimal model for fitting the light response curves of *Q. acutissima* and *Q. variabilis*. (4) The photosynthetic efficiency of *Q. acutissima* was higher than that of *Q. variabilis*; thus, it can serve as a priority species for carbon sink forests in the Changjiang River delta region. In the future, investigations into the processes and kinetics of acid rain that affect the photosynthesis of *Q. acutissima* and *Q. variabilis* need to be conducted, as does an evaluation of carbon fixation capacities in acid rain areas.

Author Contributions: Conceptualization, C.R. and H.H.; methodology, C.R.; software, C.R.; validation, C.R. and H.H.; formal analysis, C.R.; investigation, C.R., C.C., P.F., X.J., Z.W. and L.Z.; resources, C.R. and H.H.; data curation, C.R., C.C., P.F. and X.J.; writing—original draft preparation, C.R.; writing—review and editing, C.R. and H.H.; visualization, C.R.; supervision, H.H., Z.W. and L.Z.; project administration, C.R., H.H., Z.W. and L.Z.; funding acquisition, H.H. All authors have read and agreed to the published version of the manuscript.

Funding: This research was funded by a special fund project for Technology Innovation in Carbon Peak Carbon-Neutral in 2021 (BE2022305), the National Positioning Observation and Research Station of Forest Ecosystem in Yangtze River Delta (2020132077), and the Technical Collaboration Project on Soil Carbon and Nitrogen Migration Monitoring and Ecological Service Function of Soil and Water Conservation in Hilly Areas of Wuxi City (JSJGWXCG2022-09).

Institutional Review Board Statement: Not applicable.

Informed Consent Statement: Not applicable.

Data Availability Statement: The data that support the findings of this study are available in the supplementary material of this article.

Acknowledgments: We would like to thank Chan Wang and Xin Zhang for their assistance with field experiments and data collection. We also appreciate the technical support of the Xiashu Forest Farm.

Conflicts of Interest: The authors declare no conflict of interest. The funders had no role in the design of the study; in the collection, analyses, or interpretation of the data; in the writing of the manuscript; or in the decision to publish the results.

References

1. Tomimatsu, H.; Tang, Y. Effects of high CO_2 levels on dynamic photosynthesis: Carbon gain, mechanisms, and environmental interactions. *J. Plant Res.* **2016**, *129*, 365–377. [CrossRef]
2. Shi, X.; Wang, T.; Lu, S.; Chen, K.; He, D.; Xu, Z. Evaluation of China's forest carbon sink service value. *Environ. Sci. Pollut. Res. Int.* **2022**, *29*, 44668–44677. [CrossRef] [PubMed]
3. Zhou, H.; Yu, Q.; Kuang, Q.; Wang, W.; Wang, F.; Xu, H.-l. Light response of cut-flower Chrysanthemum cultivars. *J. Food Agric. Environ.* **2013**, *11*, 865–867.
4. Bhusal, N.; Bhusal, S.J.; Yoon, T.-M. Comparisons of physiological and anatomical characteristics between two cultivars in bi-leader apple trees (*Malus* × *domestica* Borkh.). *Sci. Hortic.* **2018**, *231*, 73–81. [CrossRef]
5. Shimada, R.; Takahashi, K. Diurnal and seasonal variations in photosynthetic rates of dwarf pine Pinus pumila at the treeline in central Japan. *Arct. Antarct. Alp. Res.* **2022**, *54*, 1–12. [CrossRef]
6. Jiang, Z.H.; Wang, C.S.; Zhang, J.; Yue, Y.; Li, S.W. Online monitoring and analysis of plant photosynthetic physiology and environmental factors. *Appl. Mech. Mater.* **2013**, *241*, 75–80. [CrossRef]
7. Schechter, P.L.; Wynne, R.A. Even Simpler Modeling of Quadruply Lensed Quasars (and Random Quartets) Using Witt's Hyperbola. *Astrophys. J.* **2019**, *876*, 9–12. [CrossRef]
8. Calama, R.; Puertolas, J.; Madrigal, G.; Pardos, M. Modeling the environmental response of leaf net photosynthesis in *Pinus pinea* L. natural regeneration. *Ecol. Model.* **2013**, *251*, 9–21. [CrossRef]

9. Fang, L.; Zhang, S.; Zhang, G.; Liu, X.; Xia, X.; Zhang, S.; Xing, W.; Fang, X. Application of Five Light-Response Models in the Photosynthesis of *Populus* × *Euramericana* cv. 'Zhonglin46' Leaves. *Appl. Biochem. Biotechnol.* **2015**, *176*, 86–100. [CrossRef]
10. Xia, J.B.; Zhang, G.C.; Wang, R.R.; Zhang, S.Y. Effect of soil water availability on photosynthesis in *Ziziphus jujuba* var. *spinosus* in a sand habitat formed from seashells: Comparison of four models. *Photosynthetica* **2014**, *52*, 253–261. [CrossRef]
11. Park, K.S.; Bekhzod, K.; Kwon, J.K.; Son, J.E. Development of a coupled photosynthetic model of sweet basil hydroponically grown in plant factories. *Hortic. Environ. Biotechnol.* **2016**, *57*, 20–26. [CrossRef]
12. Lang, Y.; Wang, M.; Zhang, G.C.; Zhao, Q.K. Experimental and simulated light responses of photosynthesis in leaves of three species under different soil water conditions. *Photosynthetica* **2013**, *51*, 370–378. [CrossRef]
13. Li, Y.L.; Liu, X.G.; Hao, K.; Yang, Q.L.; Yang, X.Q.; Zhang, W.H.; Cong, Y. Light-response curve of photosynthesis and model fitting in leaves of Mangifera indica under different soil water conditions. *Photosynthetica* **2019**, *57*, 796–803. [CrossRef]
14. Ye, Z.P.; Suggett, D.J.; Robakowski, P.; Kang, H.J. A mechanistic model for the photosynthesis-light response based on the photosynthetic electron transport of photosystem II in C3 and C4 species. *New Phytol.* **2013**, *199*, 110–120. [CrossRef] [PubMed]
15. Yuan, M.; Qu, L.; Wang, X.; Qian, Q.; Yang, W.; Wang, T.; Kong, H.; Jiang, G.; Chong, K. Research Advances on Plant Science in China in 2013. *Chin. Bull. Bot.* **2014**, *49*, 347.
16. Li, X.; Lu, Y.; Huang, A.; Yuan, R.; Li, J.; Hu, D.; Zhong, Q.; Cheng, D. Light response model fitting and photosynthetic characteristics of ten different fern species in subtropics. *Acta Ecol. Sin.* **2022**, *42*, 3333–3344.
17. Huang, Z.J.; Fan, Z.L.; Huang, Y.-T.; Quan, Q.M. Photoresponse Curve Model Research and Correlation Analysis of Euphorbia marginata. *Res. J. Biotechnol.* **2017**, *12*, 258–264.
18. Pan, H.; Feng, Y.; Li, Y. The comparison of light responses among four species of *Calligonum* L. in early autumn. In Proceedings of the 3rd International Conference on Agricultural and Biological Sciences (ABS 2017), Qingdao, China, 26–29 June 2017.
19. Han, M.K.; Kim, K.J.; Yang, K.C. Comparison of carbon storages, annual carbon uptake and soil respiration to planting types in urban park—The case study of Dujeong park in Cheonan city. *Korean J. Environ. Ecol.* **2014**, *28*, 142–148. [CrossRef]
20. Sun, S.; Che, T.; Li, H.; Wang, T.; Ma, C.; Liu, B.; Wu, Y.; Song, Z. Water and carbon dioxide exchange of an alpine meadow ecosystem in the northeastern Tibetan Plateau is energy-limited. *Agric. For. Meteorol.* **2019**, *275*, 283–295. [CrossRef]
21. Li, Q.y.; Liu, X.; Zhang, J.C. Changing trends of acid rain types in the Yangtze River Delta region. *J. Nanjing For. Univ. (Nat. Sci. Ed.)* **2021**, *45*, 168–174.
22. Deng, Y.P.; Lei, J.P.; Pan, L.; Wang, X.R. Model fitting of photosynthetic light-response curves in different Quercus variabilis provenances and its parameter comparison. *Chin. J. Ecol.* **2016**, *35*, 387–394.
23. Xu, F.; Guo, W.h.; Xu, W.h.; Wang, R.q. Effects of light intensity on growth and photosynthesis of seedlings of Quercus acutissima and Robinia pseudoacacia. *Acta Ecol. Sin.* **2010**, *30*, 3098–3107.
24. Xiong, S.; Wang, Y.; Chen, Y.; Gao, M.; Zhao, Y.; Wu, L. Effects of Drought Stress and Rehydration on Physiological and Biochemical Properties of Four Oak Species in China. *Plants* **2022**, *11*, 679. [CrossRef] [PubMed]
25. Dong, D.; Du, E.; Sun, Z.; Zeng, X.; de Vries, W. Non-linear direct effects of acid rain on leaf photosynthetic rate of terrestrial plants. *Environ. Pollut.* **2017**, *231*, 1442–1445. [CrossRef]
26. Guo, G.; Li, X.; Zhu, X.; Xu, Y.Y.; Dai, Q.; Zeng, G.R.; Lin, J. Effect of Forest Management Operations on Aggregate-Associated SOC Dynamics Using a Cs-137 Tracing Method. *Forests* **2021**, *12*, 859. [CrossRef]
27. Chen, X.; Sun, J.; Lyu, M.; Wang, M.; Hu, D.; Zhong, Q.; Cheng, D. Prediction of photosynthetic light-response curves using traits of the leaf economics spectrum for 75 woody species: Effects of leaf habit and sun-shade dichotomy. *Am. J. Bot.* **2021**, *108*, 423–431. [CrossRef]
28. Duan, L.M.; Yan, X.; Liu, T.X.; Wang, G.L.; Tong, X. Photosynthetic physiological characteristics of artificial populus in semi-arid area under multiple scenarios. *J. Soil Water Conserv.* **2019**, *33*, 213–220.
29. Lykins, S.; Scammon, K.; Lawrence, B.T.; Melgar, J.C. Photosynthetic light response of floricane leaves of erect blackberry cultivars from fruit development into the postharvest Period. *Hortscience* **2021**, *56*, 347–351. [CrossRef]
30. Ye, Z.P.; Yu, Q. Comparison of new and several classical models of photosynthesis in response to irradiance. *J. Plant Ecolygy (Chin. Version)* **2008**, *32*, 1356–1361.
31. Wang, H.Z.; Han, L.; Xu, Y.L.; Niu, J.L.; Yu, J. Simulated photosynthetic responses of Populus euphratica during drought stress using light-response models. *Acta Ecol. Sin.* **2017**, *37*, 2315–2324.
32. Yu, Q.; Wang, Q.Y.; Liu, Z.G.; Zhang, M.R.; Zhang, S.Z.; Shen, Y.M. Comparison of the light response models of photosynthesis in leaves of Magnolia sinostellata under different light intensity and moisture conditions. *Chin. J. Ecol.* **2018**, *37*, 898–905.
33. Wang, X.; Tong, X.; Zhang, J.; Meng, P.; Xie, H.; Hu, H.; Li, J. Effects of photosynthesis on soil respiration of *Quercus variabilis* plantation in southern Taihang Mountain of northern China. *J. Beijing For. Univ.* **2021**, *43*, 66–76.
34. Zhao, W.R.; Liu, X.; Zhang, J.C.; Wang, Y.X.; Wang, J.P.; Zhuang, J.Y. Photosynthesis transpiration, the carbon fixation and oxygen release, and the cooling and humidificant capacity of typical tree species in Nanjing suburban. *Sci. Silvae Sin.* **2016**, *52*, 31–38.
35. Fan, Y.; Hu, N.; Ding, S.; Lu, X. Physiological and ecological characteristics of photosynthesis of *Quercus variabilis* of different development stages in the funiu mountain national nature reserve. *J. Ecol. Rural Environ.* **2015**, *31*, 684–689.
36. Zhang, Y.J.; Meinzer, F.C.; Qi, J.H.; Goldstein, G.; Cao, K.F. Midday stomatal conductance is more related to stem rather than leaf water status in subtropical deciduous and evergreen broadleaf trees. *Plant Cell Environ.* **2013**, *36*, 149–158. [CrossRef] [PubMed]
37. Liang, G.; Bu, J.; Zhang, S.; Jing, G.; Zhang, G.; Liu, X. Effects of drought stress on the photosynthetic physiological parameters of Populusxeuramericana "Neva". *J. For. Res.* **2019**, *30*, 409–416. [CrossRef]

38. Wu, B.J.; Liu, Y.J.; Jiang, C.D.; Shi, L. Effects of stomatal development on leaf temperature during leaf expansion. *Plant Physiol. J.* **2015**, *51*, 119–126.
39. Ruan, C.X.; Hu, H.B.; Ji, J.; Ma, B.; Liu, X.L. Transpiration regulations and responses to climate factors of Quercus acutissima and Quercus variabilis in the Changjiang River delta area. *J. Soil Water Conserv.* **2021**, *35*, 338–344.
40. Wu, T.G.; Zeng, G.Q.; Xiao, Y.G.; Yao, J.; Yu, M.K.; Cheng, X.R.; Wang, C. Daily variation of photosynthesis of six tree species under Pinus elliotii forest and their relations with environmental factors. *J. Nanjing For. Univ. (Nat. Sci. Ed.)* **2011**, *35*, 135–138.
41. Feng, L.G.; Feng, Z.; Zhao, L.Y.; Sheng, L.X. Comparison of photosynthetic characteristics between wild plants and cultivars of Rosa rugosa. *Sci. Silvae Sin.* **2007**, *43*, 31–36.
42. Bhusal, N.; Kim, H.S.; Han, S.-G.; Yoon, T.-M. Photosynthetic traits and plant—Water relations of two apple cultivars grown as bi-leader trees under long-term waterlogging conditions. *Environ. Exp. Bot.* **2020**, *176*, 141–153. [CrossRef]
43. Kim, D.-H.; Jung, J.-Y.; Lee, C.-H.; Park, B.-D.; Bae, K.-H.; Kim, K.W.; Kim, P.-G. Effect of transpiration on the physiological vitality of Zelkova serrata. *For. Sci. Technol.* **2020**, *16*, 154–160. [CrossRef]
44. Leng, H.B.; Qin, J.; Ye, K.; Feng, S.C.; Gao, K. Comparison of light response models of photosynthesis in Nelumbo nucifera leaves under different light conditions. *J. Appl. Ecol.* **2014**, *25*, 2855–2860.
45. Chen, Z.Y.; Luo, F.Y.; Peng, Z.S.; Yu, M.Q. Comparison between modified exponential model and common models of light-response curve. *J. Plant Ecol. (Chin. Version)* **2012**, *36*, 1277–1285. [CrossRef]
46. Ye, Z.P. A review on modeling of responses of photosynthesis to light and CO_2. *J. Plant Ecol. (Chin. Version)* **2010**, *34*, 727–740.
47. Xu, G.C.; Luo, W.B.; Li, H.W.; Xu, Y.Q.; Ji, R.C.; Li, G.L.; Lin, Z.M.; Qiu, S.X.; Tang, H. Light response model and photosynthetic parameters of colored potatoes. *Fujian J. Agric. Sci.* **2020**, *35*, 691–698.
48. Xie, F.; Yan, Q.Q.; Yang, F.; Hou, Y.L. Photosynthetic Light Response Curve and Its Model Fitting of Sophora davidii from Different Provenances. *J. Temp. For. Res.* **2020**, *3*, 44–49.
49. Richardson, A.D.; Berlyn, G.P. Changes in foliar spectral reflectance and chlorophyll fluorescence of four temperate species following branch cutting. *Tree Physiol.* **2002**, *22*, 499–506. [CrossRef]
50. Sui, X.-l.; Mao, S.-l.; Wang, L.-h.; Zhang, B.-x.; Zhang, Z.-x. Effect of Low Light on the Characteristics of Photosynthesis and Chlorophyll a Fluorescence During Leaf Development of Sweet Pepper. *J. Integr. Agric.* **2012**, *11*, 1633–1643. [CrossRef]
51. Wang, B.; Yu, M.-K.; Sun, H.-J.; Cheng, X.-R.; Shan, Q.-H.; Fang, Y.-M. Photosynthetic characters of *Quercus acutissima* from different provenances under effects of salt stress. *Chin. J. Appl. Ecol.* **2009**, *20*, 1817–1824.
52. Chen, D.; Ou, G.; Chen, J.; Liu, G.; Li, Q.; Zhang, S.; Zhen, Y. Effects of different weather conditions on photosynthetic characteristics of juvenile plantations of four afforestation tree species in Yunnan Province. *J. Southwest For. Univ.* **2016**, *36*, 32–38.
53. Xu, J.; Chen, H.; Shang, S.; Yang, H.; Zhu, G.; Liu, X. Response of net primary productivity of Tibetan Plateau vegetation to climate change based on CEVSA model. *Arid Land Geogr.* **2020**, *43*, 592–601.
54. Wang, X.; Gao, W.; Liu, J.; Ni, Y.; Qu, L.; Zhao, X.; Yang, W.; Deng, Y.; Jiang, Z. Effects of habitat change on the photosynthetic characteristics of *Quercus variabilis* seedlings. *Acta Ecol. Sin.* **2016**, *36*, 8062–8070.
55. Huang, L.J.; Wang, D.X.; Wang, J.P. Characteristics and variations analysis on chemical composition of atmospheric precipitation of Kunming. *Environ. Sci. Surv.* **2022**, *41*, 46–48.
56. Xiong, D. Study on the Environmental Response to Ecophysiological Features of *Quercus variabilis* Seedlings. Master's Thesis, Huazhong Agricultural University, Wuhan, China, 2011.
57. Liu, J.F.; Xiao, W.F.; Xiong, D.P.; Lei, J.P.; Wang, P.C. Comparison on the physio-ecological characteristics of *Quercus variabilis* seedlings from various latitude sites. *Bull. Bot. Res.* **2011**, *31*, 467–471.

forests

MDPI

Article

Comparative Analysis of Codon Usage Patterns in Chloroplast Genomes of Cherries

Yan-Feng Song [1,2], Qing-Hua Yang [1,2], Xian-Gui Yi [1,2], Zhao-Qing Zhu [3], Xian-Rong Wang [1,2] and Meng Li [1,2,4,*]

[1] Co-Innovation Center for Sustainable Forestry in Southern China, College of Biology and the Environment, Nanjing Forestry University, Nanjing 210037, China
[2] Cerasus Research Center, College of Biology and the Environment, Nanjing Forestry University, Nanjing 210037, China
[3] Shanghai Jishi Landscape Co., Ltd., Shanghai 200080, China
[4] Key Laboratory of National Forestry and Grassland Administration on Subtropical Forest Biodiversity Conservation, College of Biology and the Environment, Nanjing Forestry University, Nanjing 210037, China
* Correspondence: limeng@njfu.edu.cn

Abstract: Synonymous codon usage bias (SCUB) analysis is an effective method to explore species specificity, evolutionary relationships and mRNA translation, as well as to discover novel genes, which are important for understanding gene function and molecular phylogeny. Cherries (*Prunus* subg. *Cerasus*) are flowering plant germplasm resources for edible and ornamental purposes. In this study, we analyzed the codon usage patterns of the 36 chloroplast genomes to provide a scientific basis for elucidating the evolution of subg. *Cerasus*. The results showed that the average GC content was 0.377, the average GC3 was 0.298, and the average ENC value was 49.69. Neutral-plot analysis, ENC-plot analysis, and PR2-plot analysis all indicated that natural selection was the main factor of codon usage bias in subg. *Cerasus*, whereas correlation analysis showed that gene expression level and GC1 also affect the codon usage pattern. The codon usage pattern was consistent across 36 species, and 30 high-frequency codons were identified, with preference for A/T endings; there were 23 optimal codons, and only GAU was identified in all individuals; structural differences existed between the clustering tree based on RSCU values and the phylogenetic tree based on CDS, elucidating the importance of locus mutations and no-preference codons in phylogenetic reconstruction. This study describes for the first time the SCUB pattern and characterization of subg. *Cerasus* chloroplast genomes and provides a new insight to explore the phylogeny of this subgenus.

Keywords: *Prunus*; *Cerasus*; plastid genome; codon usage; phylogeny

check for updates

Citation: Song, Y.-F.; Yang, Q.-H.; Yi, X.-G.; Zhu, Z.-Q.; Wang, X.-R.; Li, M. Comparative Analysis of Codon Usage Patterns in Chloroplast Genomes of Cherries. *Forests* **2022**, *13*, 1891. https://doi.org/10.3390/f13111891

Academic Editor: Tadeusz Malewski

Received: 22 September 2022
Accepted: 5 November 2022
Published: 10 November 2022

Publisher's Note: MDPI stays neutral with regard to jurisdictional claims in published maps and institutional affiliations.

Copyright: © 2022 by the authors. Licensee MDPI, Basel, Switzerland. This article is an open access article distributed under the terms and conditions of the Creative Commons Attribution (CC BY) license (https://creativecommons.org/licenses/by/4.0/).

1. Introduction

The triplet codons perform a fundamental role in protein translation, and the transfer of genetic information from mRNA to protein is a basic link in maintaining the viability of the organism. All amino acids are encoded by two to six codons, except for methionine and tryptophan, which are encoded by only one codon [1,2]. Codons encoding the same amino acid are considered as synonymous codons. In the matter of the process of protein translation, different species tended to use one or more specific synonymous codons called synonymous codon usage bias (SCUB) [3,4]. According to previous studies, protein translation efficiency, tRNA abundance, gene drift, and expression level have all been associated with SCUB, but natural selection and genes mutation are the most important factors [5–9].

Chloroplast is the main organelle used to execute photosynthesis activities and metabolic reactions in green plants. Compared with the nuclear genome, the chloroplast genome in angiosperms is a circular DNA molecule which has a highly conserved genomic structure with a small size, single-parental inheritance, and low nucleotide substitution rate; hence, it is widely used as molecular evidence for phylogenetic analysis and

species identification [10–14]. With the rapid development of high-throughput sequencing technology, massive plants taxon chloroplast genomes have been sequenced, offering the research of chloroplast genome codon with a database.

With the popularity of next-generation genome sequencing technologies, the study of plant genome codons is increasing. However, most studies on plant codon preferences have been conducted only in single species, and comparison of interspecific codon usage patterns is lacking. Cherry is a generic term for *Prunus* subg. *Cerasus* species, which contains approximately 50 species that mainly occupy temperate and subtropical regions of the northern hemisphere [15–19]. Cherries offer a variety of edible drupes and ornamental plants with economic value to human society and thus have great potential for development and application. However, frequent interspecific hybridization and sympatric speciation have yielded little knowledge of the phylogeny of subg. *Cerasus* or the evolutionary forces driving the evolutionary process. At present, numerous studies on the synonymous codon preference of plant chloroplast genomes have been reported, such as Poaceae [20], Magnoliaceae [21], Asteraceae [22], Euphorbiaceae [13], Fragaria [23], and others. In this study, we combined 24 published chloroplast genomes of subg. *Cerasus* and 12 self-assembled plastomes to systematically analyze the synonymous codon usage patterns of subg. *Cerasus* species and reveal the phylogenetic relationships of this taxon, aiming to provide new insights into the evolution of the cherry chloroplast genome as well as scientific information and stable data for the application and conservation of germplasm resources basis.

2. Materials and Methods

2.1. Sampling, DNA Isolation and Sequencing

In order to address the issue of unrepresentative samples in previous studies [24,25], we newly sampled and sequenced the plastome of 12 subg. *Cerasus* species in this study, namely *Prunus clarofolia* (31°20′52.52″ N, 109°58′46.35″ E), *P. conadenia* (28°39′36.84″ N, 97°27′54.05″ E), *P. discoidea* (30°4′14.08″ N, 118°5′25.54″ E), *P. jamasakura* (34°45′53.7″ N, 135°42′10.5″ E), *P. mahaleb* (42°18′23.58″ N, 71°7′19.38″ W), *P. mugus* (27°35′52.81″ N, 98°39′9.62″ E), *P. polytricha* (31°19′29.22″ N, 109°59′2.76″ E), *P. sargentii* (42°9′17.21″ N, 140°9′57.19″ E), *P. schneideriana* (28°18′31.76″ N, 119°18′6.41″ E), *P. serrula* (25°46′30.23″ N, 102°20′30.58″ E), *P. setulose* (34°29′33.52″ N, 103°40′6.34″ E) and *P. yunnanenesis* (23°40′8.88″ N, 106°12′46.74″ E). These fresh mature leaves collected from robust individuals of the wild subg. *Cerasus* species were packed into labeled tea bags and immediately placed in silica gel for drying and storage.

Total Genomic DNA was extracted from each of subg. *Cerasus* plants using a DNeasy Plant Mini Kit (Qiagen Co., Hilden, Germany) following the manufacturer's protocol. The extracted DNA was quantified in NanoDrop ND1000 (Thermo Fisher Scientific, Waltham, MA, USA; quality cutoff, OD 260/280 ratio between 1.7–1.9) and visualized in a 1% agarose-gel electrophoresis for the quality check. Illumina paired-end (PE) libraries (read length: 2 × 125 bp) with insert sizes of 270 to 700 bp for each of subg. *Cerasus* species were constructed and sequenced on MiSeq platform (Illumina Inc., San Diego, CA, USA) by Nanjing Genepioneer Biotechnologies Inc. (Nanjing, China). We removed poor-quality reads (PHRED score of <20) using the quality trim function implemented in CLC Assembly Cell package v. 4.2.1 (CLC Inc., Aarhus, Denmark).

The average clean PE reads for each sample was 3.54 Gb (Phred score > 20), and we subsequently assembled de novo these clean reads using the GetOrganelle pipeline [26]. The assembled chloroplast genomes were annotated by the web application GeSeq (https://chlorobox.mpimp-golm.mpg.de/geseq.html (accessed on 29 April 2022) [27]. Another 24 subg. *Cerasus* plastomes were downloaded from the National Center for Biotechnology Information (NCBI). All samples are listed in Table S1. The coding sequences (CDS) of each species were extracted by Phylosuite v1.2.2 [28].

We filtered coding sequences less than 300 bp and removed duplicate genes and stop codons, and a total of 58 shared CDSs in 36 subg. *Cerasus* species were enumerated for subsequent analysis.

2.2. Codon Composition

We analyzed RSCU (relative synonymous codon usage), ENC (effective number of codons) and CAI (codon adaptation index) of selected protein-coding genes using CodonW v1.4.2 (http://codonw.sourceforge.net/ (accessed on 3 May 2022) and calculated the GC content of the first base of codon (GC1), the second base of codon (GC2), the third base of codon (GC3), and total GC content (GC). The RSCU were calculated as Equation (1):

$$RSCU = \frac{x_{ij}}{\sum_j^{n_i} x_{ij}} n_i \quad (1)$$

where x_{ij} represents the frequency of codon j encoding the i-th amino acid and n_i is the number of synonymous codons encoding the i-th amino acid. If the RSCU value of a codon is equal to 1, it reflects no codon usage bias, instead, the RSCU value reflects the frequency of usage deviation from other codons.

2.3. Neutrality Plot

In the neutral graph, the average values of GC1 and GC2 of each gene were regarded as GC12, which were ordinate; GC3 values were seen as abscissa. Finally, we line-fit the scatter points in the diagram. Often, when the regression coefficient is closer to 1, the SCUB is more affected by the base mutation; the number closer to 0 is greater affected by natural selection.

2.4. Analysis of ENC-Plot

ENC values are used to analyze the extent to which codon usage deviates from random selection, which depicts the extent to which synonymous codons are used unevenly in a specific gene or genome in a given species, ranging from 20 to 61. If the value is greater than 35, it indicates that the use of codons has high bias and vice versa. We plotted scatters with ENC content as ordinate and GC3 values as horizontal coordinates and draw standard curve. The expected values of *ENC* were calculated according to Equation (2):

$$ENC = 2 + GC3s + \frac{29}{GC3s^2 + (1 - GC3s^2)} \quad (2)$$

When mutational pressure has a significant effect on codon usage patterns, ENC values lie on or near the expected curve. On the contrary, when influenced by natural selection and other factors, ENC values are well below the expected curve.

2.5. PR2-Plot

Previous studies have witnessed that the third base of the codon is a critical factor affecting its preference; we chose the third base of the codon to A3/(A3 + T3) as the ordinate, and G3/(G3 + C3) for the horizontal coordinates to draw a PR2-plot diagram to explore whether its preference is related to natural selection or other factors [29].

2.6. Correlation Analysis

Correspondence analysis comparing the usage patterns of 59 codons (excluding codons encoding Met, Trp and three stop codons) led to a series of orthogonal axes that can be used to demonstrate codon usage variation in the chloroplast genome of cherries. Based on SCUB of genes in a multidimensional space of 59 axes, it is possible to derive the distribution of genes, as well as the largest fraction of gene variation, and in this regard to analyze the main factors of codon variation. The codon usage variations in 36 subg. *Cerasus* species were investigated with correspondence analysis based on RSCU using CodonW v1.4.2 [30].

The correlation between the first four axes and each codon usage parameters was analyzed by SPSS v 25.0.

2.7. Optimal Codons

We sorted the 58 protein coding sequences that were filtered from highest to lowest ENC values, then selected the first 10% and the last 10% genes to establish a high–low bias library and calculated the ΔRSCU value (RSCU high − RSCU low). If the RSCU > 1 and ΔRSCU > 0.08, then this codon was defined as high expression superior codon for this species [31].

2.8. Cluster and Phylogenetic Analysis

In order to explore the relationship between the SCUB of plastomes in subg. *Cerasus* plants and its phylogenetic relationship, we conducted a cluster analysis of 36 subg. *Cerasus* in R v3.6.3 using RSCU values as variables, calculated as "Euclidean distance," and plotted the cluster spectrum [32]. We also reconstructed a phylogenetic tree based on 58 CDS sequences using a maximum likelihood method with 1000 bootstrap replications [33]. The tested outgroups were *Ulmus chenmoui* and *Ziziphus jujuba*, both downloaded from NCBI (Genbank accession number: MG581403 and KU351660).

3. Results

3.1. Base Composition Characteristics

As shown in Table 1, the average number of codons in 36 species was 26,165, of which *P. conadenia* had the lowest number (25,205) and *P. pseudocerasus* had the highest number (26,575). The average content of GC1, GC2, GC3 and GC content of CDS sequences were 0.454, 0.377, 0.298 and 0.377 respectively. The results indicated that the three codon bases were biased towards A (adenine) and T (thymine). The GC contents of all tested chloroplast genomes were consistent with GC1 > GC2 > GC3 (Figure 1). The average ENC value was 49.69, the minimum ENC value of *P. fruticosa* was 49.61, and the highest value of *P. discoidea* was 49.76 (Figure 2). All ENC values of this taxon were greater than 49, reflecting weak codon bias overall. The CAI value of all species was 0.166, except *P. conadenia* which was 0.167.

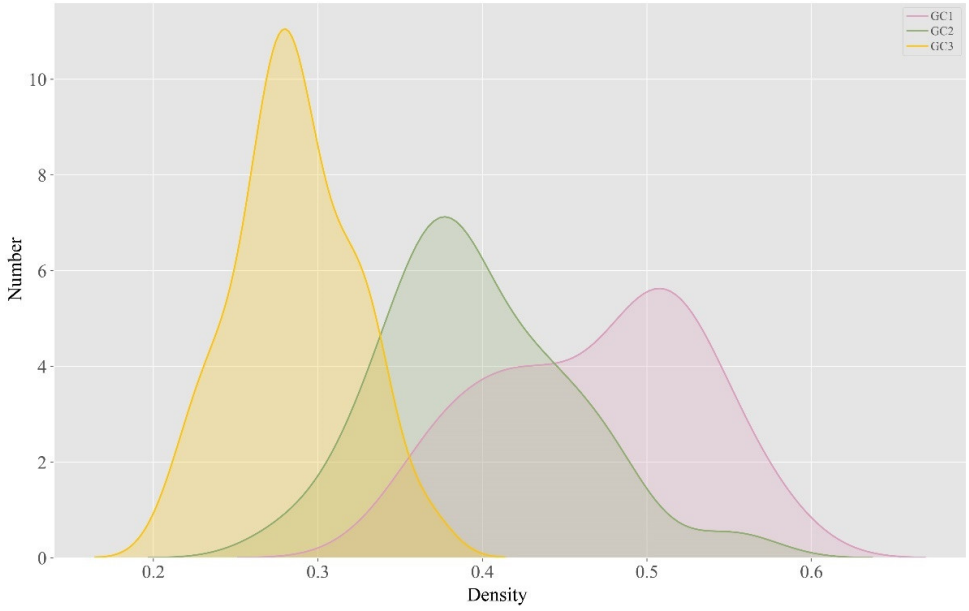


Figure 1. The kernel density curve of GC1, GC2 and GC3. The x-axis represents the density of GC1, GC2 and GC3 contents in all test CDS, and the y-axis indicates the relative quantity.

Table 1. Codon features of 36 subg. *Cerasus* chloroplast genomes.

Species	Codon No.	CG1	CG2	CG3	GC	ENC	CAI
Prunus apetala	26158	0.4529	0.3765	0.2982	0.3760	49.71	0.166
Prunus avium	26162	0.4541	0.3770	0.2978	0.3770	49.66	0.166
Prunus campanulata	26157	0.4542	0.3770	0.2984	0.3770	49.69	0.166
Prunus cerasoides	26172	0.4542	0.3767	0.2979	0.3770	49.68	0.166
Prunus clarofolia	26209	0.4545	0.3768	0.2981	0.3770	49.69	0.166
Prunus conadenia	25205	0.4560	0.3762	0.2974	0.3770	49.67	0.167
Prunus conradinae	26490	0.4535	0.3762	0.2988	0.3770	49.73	0.166
Prunus dielsiana	26151	0.4543	0.3769	0.2984	0.3770	49.70	0.166
Prunus discoidea	26525	0.4533	0.3760	0.2991	0.3770	49.76	0.166
Prunus emarginata	26163	0.4542	0.3769	0.2976	0.3770	49.66	0.166
Prunus fengyangshanica	26163	0.4542	0.3767	0.2984	0.3770	49.71	0.166
Prunus fruticosa	26166	0.4537	0.3766	0.2971	0.3760	49.61	0.166
Prunus itosakura	26152	0.4546	0.3770	0.2982	0.3770	49.69	0.166
Prunus jamasakura	26160	0.4541	0.3769	0.2982	0.3770	49.68	0.166
Prunus jingningensis	26165	0.4542	0.3770	0.2983	0.3770	49.69	0.166
Prunus kumanoensis	26158	0.4543	0.3770	0.2982	0.3770	49.68	0.166
Prunus leveilleana	26158	0.4543	0.3770	0.2983	0.3770	49.69	0.166
Prunus mahaleb	26218	0.4547	0.3771	0.2980	0.3770	49.67	0.166
Prunus matuurae	26156	0.4540	0.3769	0.2986	0.3770	49.72	0.166
Prunus maximowiczii	26158	0.4543	0.3768	0.2984	0.3770	49.71	0.166
Prunus mugus	25990	0.4552	0.3775	0.2977	0.3770	49.67	0.166
Prunus pensylvanica	26162	0.4544	0.3769	0.2980	0.3770	49.68	0.166
Prunus polytricha	26220	0.4543	0.3769	0.2984	0.3770	49.70	0.166
Prunus pseudocerasus	26575	0.4535	0.3761	0.2988	0.3770	49.73	0.166
Prunus rufa	26171	0.4541	0.3769	0.2979	0.3770	49.67	0.166
Prunus sargentii	26153	0.4543	0.3770	0.2981	0.3770	49.67	0.166
Prunus schneideriana	26224	0.4543	0.3769	0.2985	0.3770	49.70	0.166
Prunus serrula	26217	0.4544	0.3769	0.2983	0.3770	49.69	0.166
Prunus setulosa	26227	0.4539	0.3769	0.2980	0.3770	49.67	0.166
Prunus speciosa	26164	0.4540	0.3769	0.2983	0.3770	49.69	0.166
Prunus spontanea	26158	0.4543	0.3770	0.2984	0.3770	49.70	0.166
Prunus subhirtella	26152	0.4546	0.3770	0.2982	0.3770	49.69	0.166
Prunus takesimensis	26158	0.4543	0.3770	0.2983	0.3770	49.69	0.166
Prunus verecunda	26158	0.4544	0.3770	0.2983	0.3770	49.69	0.166
Prunus yedoensis	26152	0.4546	0.3770	0.2982	0.3770	49.69	0.166
Prunus yunnanensis	26003	0.4551	0.3774	0.2977	0.3770	49.66	0.166

3.2. Neutrality Plot Analysis

In order to determine the main factors influencing the SCUB of chloroplast genome, we carried out a neutral plot analysis of 36 subg. *Cerasus* species. As shown in Figure 3, GC12 and GC3 were scattered distribution. GC12 was 0.2852–0.5432, and GC3 was 0.2074–0.3661. The regression coefficient was between 0.1331 and 0.2455, where *P. conradinae* was 0.1331, which was most influenced by natural selection; *P. conadenia* was 0.2455, which was least affected by natural selection. These results suggested that the SCUB of subg. *Cerasus* chloroplast genomes were mainly influenced by natural selection.

Neutrality plot analysis reflects only the factors that influence codon usage patterns; consequently, further analysis of the degree of influence of mutational pressure and natural selection is necessary.

3.3. ENC-Plot Analysis, PR2-Plot Analysis and Correlation Analysis

As shown in Figure 4a, the genes of 36 subg. *Cerasus* species were scattered on both sides of the expected curve, with most genes not near or below the expected curve and a few genes with ENC values less than 35. These results also demonstrated that natural selection is the dominant factor of SCUB of chloroplast genome in subg. *Cerasus* plants.

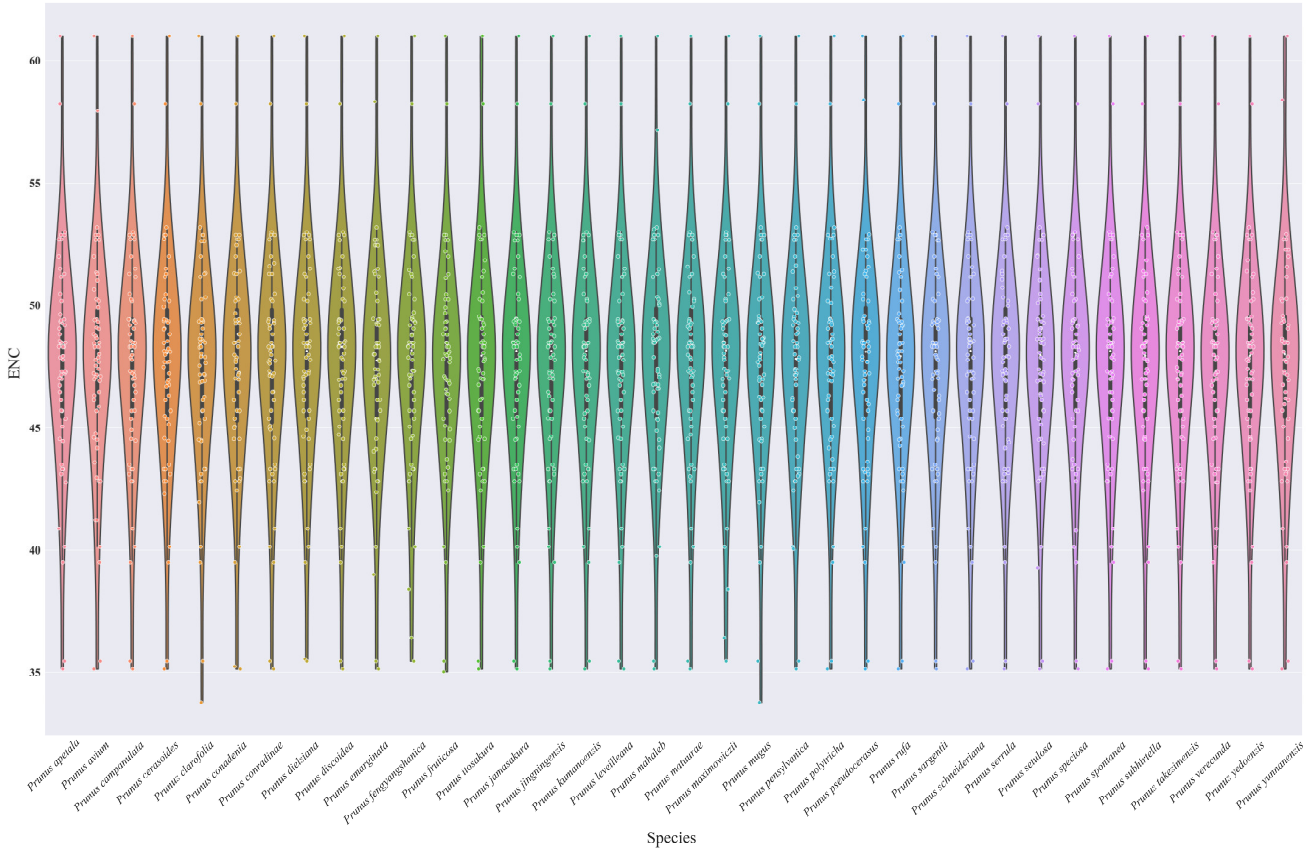


Figure 2. The ENC values of chloroplast genes in subg. *Cerasus* species. The x-axis represents 36 sub. *Cerasus* accessions, and the y-axis indicates the ENC value for all CDS in each species.

We performed a parity check analysis on the relationship between the third base of the codons of all the tested genes of 36 subg. *Cerasus* plants (Figure 4b). The diagram displayed that tested genes were unevenly distributed in four regions, with a large number of genes located in the bottom right, which meant that T was used more frequently than A, and G (guanine) was greater than C (cytosine). Overall, the frequency of A/T and G/C use in the chloroplast genomes of subg. *Cerasus* was asymmetrical and was influenced not only by mutational pressure as well as by natural selection and other factors. This result further validated the effect of natural selection on SCUB in the cherries.

We analyzed the correspondence patterns of 36 subg. *Cerasus* chloroplast genes based on RSCU values. The Axis 1 was the major factor in causing the variation, responsible for about 10% of total variation in all tested subg. *Cerasus* species, with each subsequent axis explaining a decreasing amount of the variation. Based on Pearson correlation analysis, the Axis 1 was significantly correlated with GC1, GC3, GC12, GC, CAI and ENC ($p < 0.01$) (see Table 2), which means that the base composition greatly affected the codon usage bias. GC1 and CAI value were likely to affect the patterns of codon usage, and significantly correlated with COA axes (except Axis 3). This suggested that the first base of codon and the gene expression level were likely involved in some subg. *Cerasus* chloroplast genomes. Furthermore, there were no obvious characteristics of the distribution of subg. *Cerasus* chloroplast genes (Figure 4c).

3.4. High-Frequency Codon and Optimal Codon

The RSCU value of 36 subg. *Cerasus* genome sequences was calculated using CodonW, and high-frequency codons (RSCU > 1) were counted (Supplementary Table S2 and Figure 5). In 36 tested plants, except for the UUG encoded L (leucine) ending in G, the other codons ended in A (13) or T (16), indicating that codon ending in A/T were used more frequently. At amino acid levels, UUA, which also encodes L, showed strong preference in

all subg. *Cerasus* species. We also sorted the ENC values of all tested chloroplast genes in 36 species, picked out five high-value and five low-value genes to build a library, and then selected the codons that met the conditions as the optimal codons (Supplementary Table S3 and Figure 6).

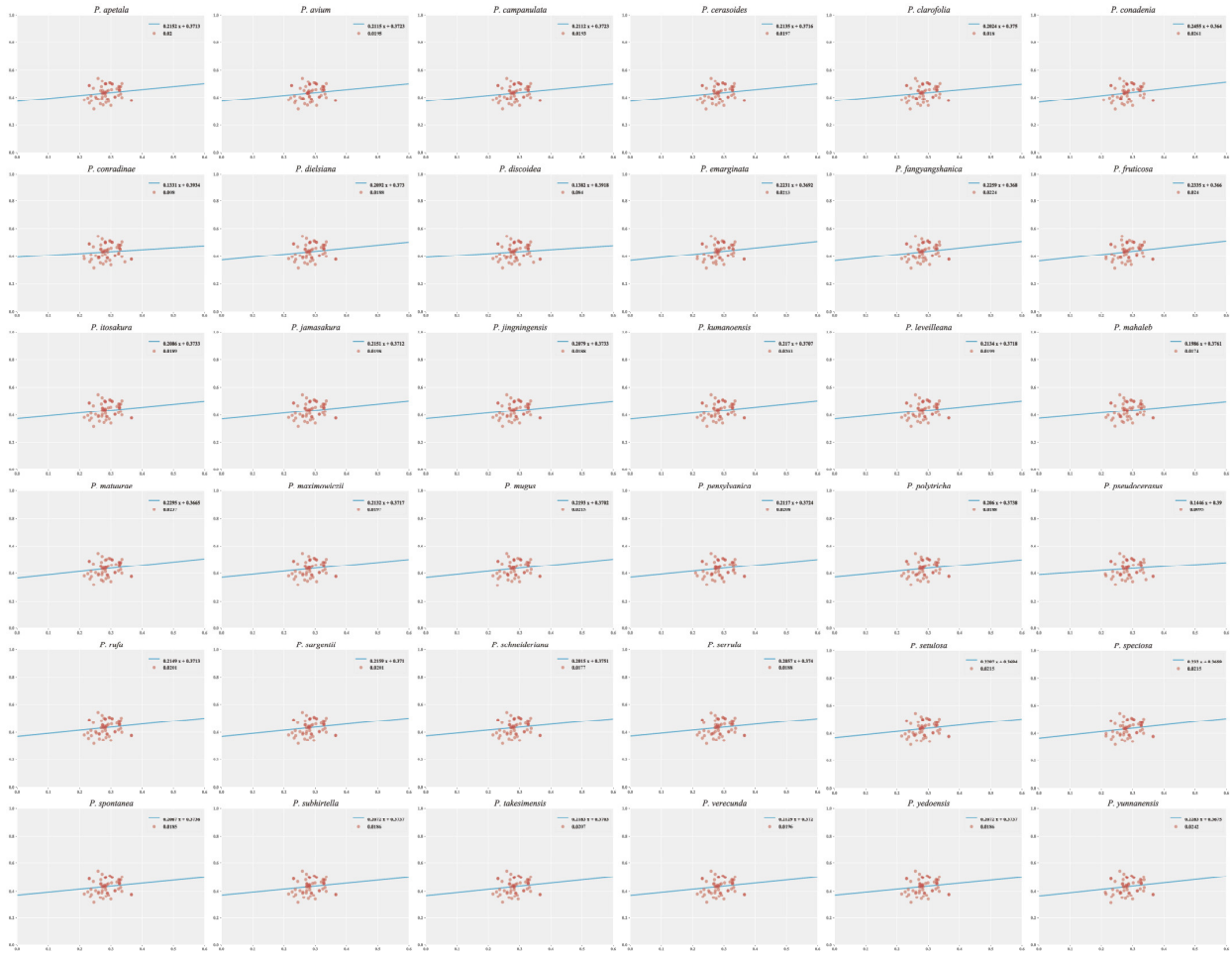


Figure 3. Neutrality plot analysis of 36 subg. *Cerasus* species.

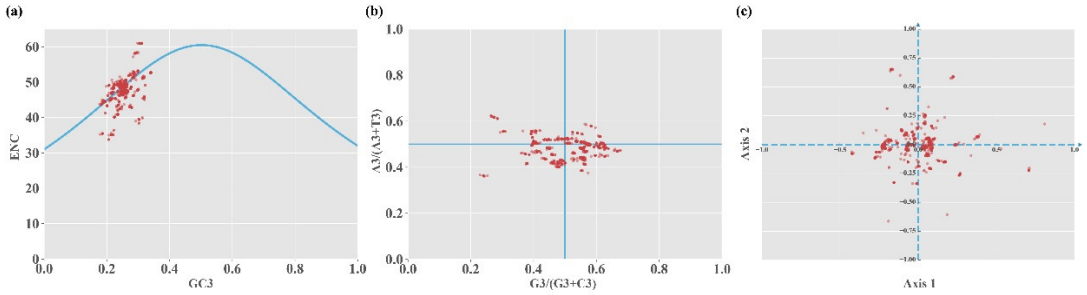


Figure 4. Related plotting analysis of codon usage frequency, with red dots representing protein-coding genes of 36 subg. *Cerasus* species. (**a**) ENC-plot analysis based on the concatenated coding sequences, the x-axis represents the GC3 value of CDS and the y-axis represents its ENC value; (**b**) PR2-plot analysis, the x-axis denotes the value of G3/(G3 + C3) and the y-axis denotes the value of A3/(A3 + T3); (**c**) correspondence analysis of the RSCU values of subg. *Cerasus* species, each point on the plot corresponds to the coordinates on the first and second-principal axes produced by the COA.

Table 2. The correlation coefficients between the axes and codon usage indices of chloroplast genes in 36 subg. *Cerasus* species.

	GC1	GC2	GC3	GC12	GC	CAI	ENC
Axis 1	−0.141 **	0.035	−0.103 **	−0.066 **	−0.091 **	−0.130 **	−0.071 **
Axis 2	−0.074 **	0.026	−0.030	−0.030	−0.037	0.147 **	−0.055 *
Axis 3	−0.023	0.042	−0.023	0.009	0.002	−0.050 *	−0.107 **
Axis 4	−0.050 *	−0.098 **	0.094 **	−0.084 **	−0.049 *	0.077 **	0.034

Notes. * $p < 0.05$. ** $p < 0.01$.

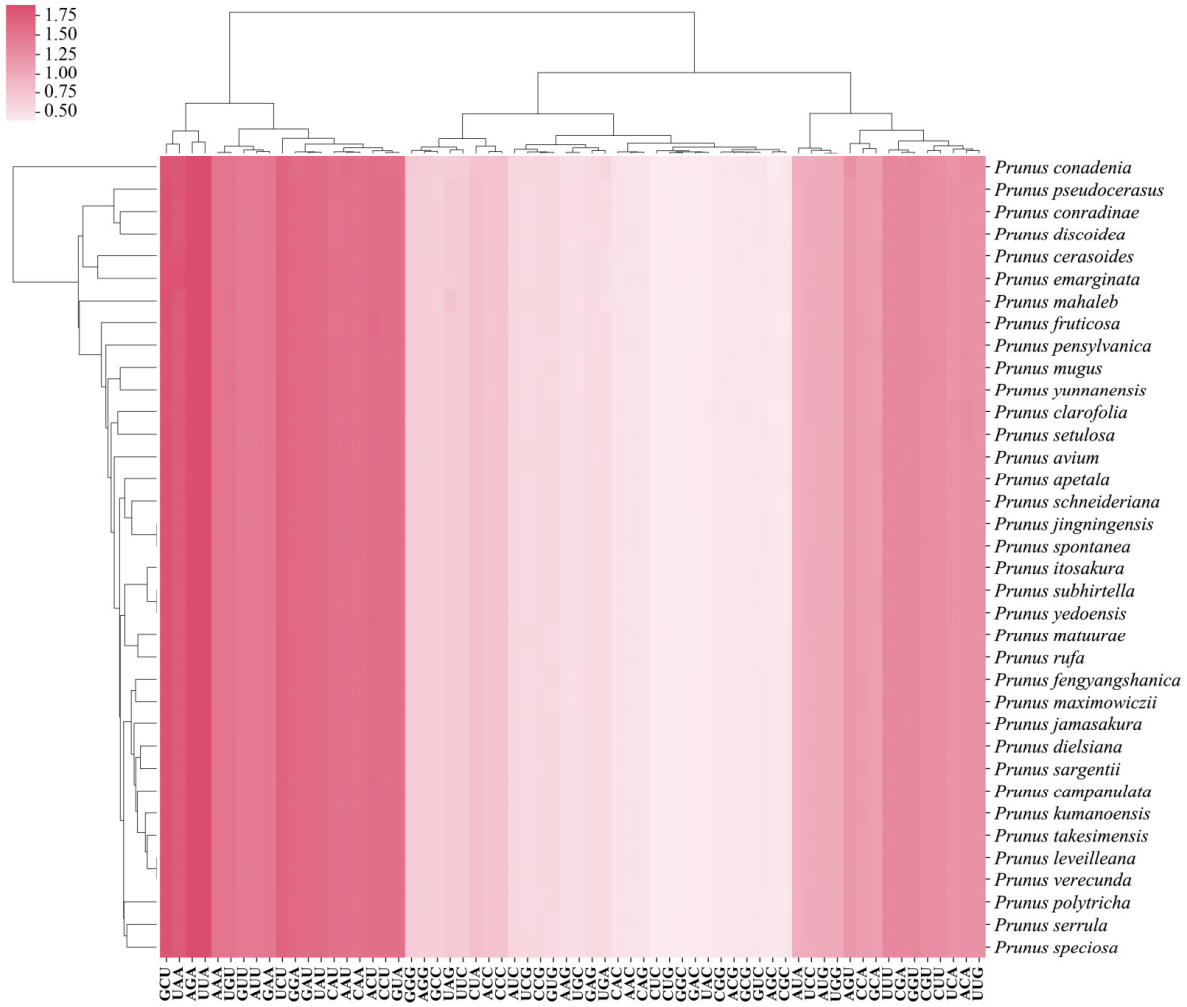


Figure 5. The codon usage of 36 subg. *Cerasus* based on RSCU values of chloroplast genes. The x-axis indicates the triplet codons, and the y-axis represents the 36 subg. *Cerasus* accessions.

A total of 23 optimal codons encoded 12 amino acids were counted, among which 17 ended in A/T, accounting for 73.9%. The results manifested that there were significant differences in the optimal codons of 36 subg. *Cerasus* chloroplast genomes. *P. emarginata* had the most optimal codons, which was 11, while *P. itosakura* had the least number, which was 6. Of 12 species with 7 optimal codons, *P. cerasoides*, *P. kumanoensis*, *P. leveilleana*, *P. rufa*, *P. subhirtella* and *P. yedoensis* harbored the same composition of optimal codons, which were: ACC, AGU, CCU, CGU, GAU, GCC, GCU, UCC and UCU. Among 14 species with 8 optimal codons, ACC, AGA, AGU, CCU, CGU, GAU, GCC and UCU were the optimal codons of *P. clarofolia* and *P. mugus*. Secondly, *P. fengyangshanica*, *P. jingningensis*, *P. matuurae*, *P. maximowiczii*, *P. sargentii*, *P. speciosa*, *P. spontanea*, *P. takesimensis* and *P. verecunda* had the same optimal codon composition, but the difference from the former was that AAU

replaced AGA. Moreover, only one GAU encoding aspartic acid was the common optimal codon of all subg. *Cerasus* species.



Figure 6. Optimal codon analysis of 36 subg. *Cerasus* species. The x-axis indicates the optimal codon and its corresponding encoded protein, and the y-axis represents the 36 subg. *Cerasus* accessions. Dark block positions indicate optimal codons in each species.

3.5. Cluster and Phylogenetic Analysis

Based on the RSCU values of 36 subg. *Cerasus* plastome genomes, we constructed a hierarchical diagram (Supplementary Table S2 and Figure 7a). The result of cluster analysis revealed that 36 subg. *Cerasus* species were divided into 4 clusters, of which only one species in Cluster IV was *P. conadenia*, and the other three clusters contained 10, 22, and 3 species, respectively. Intriguingly, in contrast to the arborescence structure of the cluster analysis, the CDS-based phylogeny split into five clades exhibiting a completely different topology (Figure 7b). *P. mahaleb* placed basal in subg. *Cerasus* and formed a separate branch that was Clade I; Clade II contained 2 species, namely *P. rufa* and *P. cerasoides*; Clade III and Clade IV included 5 and 7 species, respectively; Clade V gathered the largest number of species of wild cherries, with 21.

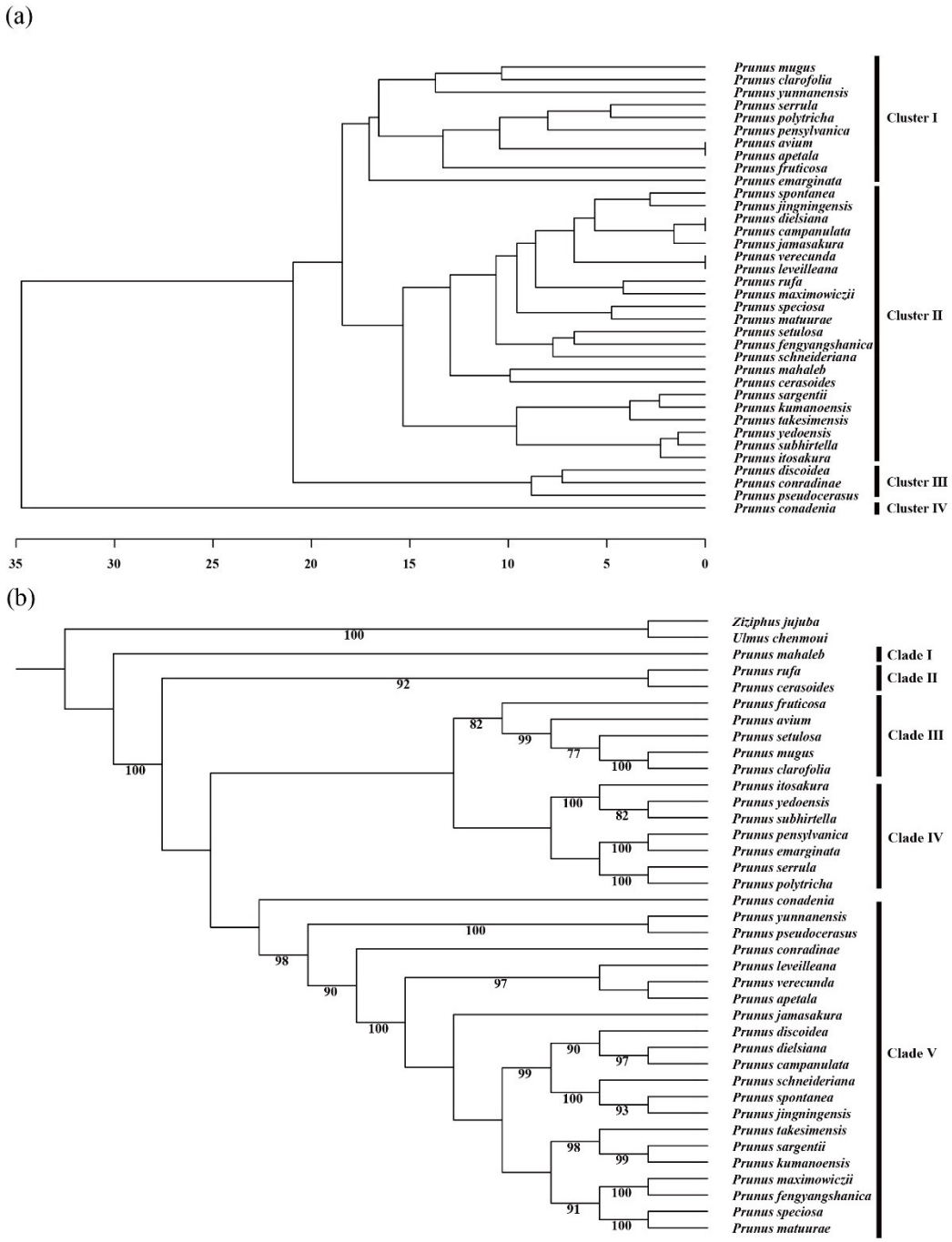


Figure 7. (**a**) Cluster of 36 subg. *Cerasus* chloroplast genomes based on RSCU values; (**b**) CDS-based reconstruction of a phylogenetic tree of subg. *Cerasus*.

4. Discussion

In general, the codon usage bias not only reflects the origin, evolution, and mutation patterns of species or genes, but also has conspicuous implications for gene function and expression [8,13,34]. The substitution in the third base of codon may not instantly alter the corresponding encoded amino acids, but they directly reflect the patterns of codon usage [35,36]. Our analysis results were consistent with most angiosperms codon bias: the GC content of subg. *Cerasus* chloroplast genome was 0.377 and the preferred ending with base A/T; all tested species appeared to have a weak codon preference (ENC value > 49) (Table 1 and Figure 2) [13,22,37]. In case codon preference is affected by natural selection, GC3 value tend to be distributed in a small range in the diagram, and GC12 have no

significant correlation with GC3. We observed a regression line with a lower slope in the 36 species, and also found the regression coefficients were close to 0 (Figure 3), which suggested that natural selection played an important role in codon usage bias in chloroplast genomes of subg. *Cerasus* plants. ENC-plot and PR2-plot analysis both proved that natural selection was the main factor influencing codon preference (Figure 4a,b). Apart from mutations and natural selection, we demonstrated that gene expression levels and the first base of codon also affected codon preferences through COA based on RSCU values (Table 2 and Figure 4c) [38]. 36 subg. *Cerasus* genomes encompassed 30 identical high-frequency codons, and the third base was generally biased towards A/T (Table S2 and Figure 5). On the contrary, the number of interspecies optimal codons ranged 6 from 11 and the only shared codon was GAU (Figure 6). Therefore, the reason for the difference between optimal codon and synonymous codon was that the former was affected by ENC and expression level of different genes.

The results of gene annotation in this study indicated that the least number of codons in *P. conadenia* was directly caused by the absence of the *ndh*B gene, which indirectly led to the clustering into a separate branch. In previous studies, it was found that functional genes missing in chloroplasts were transferred to the nucleus, such as the *inf*A gene in Arabidopsis, *Lotus* [39], and *Elaeagnus* [40], and the *rpl*22 gene in *Castanea* and *Passiflora* [41]. *ndh*B belongs to NADH dehydrogenase and is involved in electron transfer and oxidative phosphate processes. We investigated globally that there is no *ndh*B deletion in any other cherries. Why is the *ndh*B gene only missing in *P. conadenia*? Is it a functional gene transfer or substitution similar to the above case that occurred? At present, we are relatively poorly characterized about the biology of *P. conadenia* with this narrow distribution and further research is needed.

Previous studies have shown that the clustering hierarchical diagram based on SCUB cannot accurately reflect the real phylogenetic relationship. Compared with our phylogenetic tree based on CDS sequences, the cluster tree only reflected some interspecific relationships and provided limited supports for genetic relationships of subg. *Cerasus*. We speculate that the conflict between the topology of the clustering tree and the phylogenetic tree is due to the omission of low to medium preference codons. The CDS-based phylogenetic tree is more affected by base substitutions because it includes some non-preferred codons that also play an important role in phylogenetic relationships and would otherwise fail to reconstruct reliable genetic relationship of species.

5. Conclusions

In this study, we systematically compared the patterns of synonymous codon usage in the subg. *Cerasus* chloroplast genomes, which were all affected by natural selection rather than mutation, and the gene expression level and GC1 also contributed to some extent. In addition, clustering analysis based on RSCU values was not optimal, for which we reconstructed a reliable phylogeny based on CDS and speculated that the former was caused by the absence of the no-preference codons. Overall, we provide a new insight into the evolution of subg. *Cerasus* chloroplast genome in terms of SCUB, which will help to further explore molecular evolutionary mechanisms and optimize the expression levels of exogenous genes in the future.

Supplementary Materials: The following supporting information can be downloaded at: https://www.mdpi.com/article/10.3390/f13111891/s1, Table S1: Genbank accession numbers of 36 subg. *Cerasus* species; Table S2: RSCU value of 36 subg. *Cerasus* species; Table S3: The optimal codons of 36 subg. *Cerasus* chloroplast genome.

Author Contributions: Conceptualization, Y.-F.S. and M.L.; methodology, Y.-F.S.; software, Y.-F.S.; validation, Y.-F.S. and Q.-H.Y. and M.L.; formal analysis, Y.-F.S.; investigation, Y.-F.S. and Q.-H.Y.; resources, X.-G.Y. and Z.-Q.Z.; data curation, Y.-F.S.; writing—original draft preparation, Y.-F.S.; writing—review and editing, M.L.; visualization, Y.-F.S.; supervision, M.L.; project administration,

M.L. and X.-R.W.; funding acquisition, X.-R.W. All authors have read and agreed to the published version of the manuscript.

Funding: This research was funded by grants from Key Modern Agriculture Project of Science and Technology Department of Jiangsu Province, China (Grant No. BE2020343).

Data Availability Statement: Not applicable.

Acknowledgments: We appreciate the assistance of Cheng Zhang (Nanjing Forestry University) during the experiments and data analyses.

Conflicts of Interest: The authors declare no conflict of interest.

References

1. Buhr, F.; Jha, S.; Thommen, M.; Mittelstaet, J.; Kutz, F.; Schwalbe, H.; Rodnina, M.V.; Komar, A.A. Synonymous Codons Direct Cotranslational Folding toward Different Protein Conformations. *Mol. Cell* **2016**, *61*, 341–351. [CrossRef] [PubMed]
2. Zhou, Z.; Dang, Y.; Zhou, M.; Li, L.; Yu, C.-H.; Fu, J.; Chen, S.; Liu, Y. Codon usage is an important determinant of gene expression levels largely through its effects on transcription. *Proc. Natl. Acad. Sci. USA* **2016**, *113*, E6117–E6125. [CrossRef] [PubMed]
3. Long, S.; Yao, H.; Wu, Q.; Li, G. Analysis of compositional bias and codon usage pattern of the coding sequence in Banna virus genome. *Virus Res.* **2018**, *258*, 68–72. [CrossRef]
4. Wang, H.; Meng, T.; Wei, W. Analysis of synonymous codon usage bias in helicase gene from Autographa californica multiple nucleopolyhedrovirus. *Genes Genom.* **2018**, *40*, 767–780. [CrossRef] [PubMed]
5. Romero, H.; Zavala, A.; Musto, H. Codon usage in Chlamydia trachomatis is the result of strand-specific mutational biases and a complex pattern of selective forces. *Nucleic Acids Res.* **2000**, *28*, 2084–2090. [CrossRef]
6. Hunt, R.C.; Simhadri, V.L.; Iandoli, M.; Sauna, Z.E.; Kimchi-Sarfaty, C. Exposing synonymous mutations. *Trends Genet.* **2014**, *30*, 308–321. [CrossRef]
7. Pop, C.; Rouskin, S.; Ingolia, N.T.; Han, L.; Phizicky, E.M.; Weissman, J.S.; Koller, D. Causal signals between codon bias, mRNA structure, and the efficiency of translation and elongation. *Mol. Syst. Biol.* **2014**, *10*, 770. [CrossRef]
8. Quax, T.E.F.; Claassens, N.J.; Söll, D.; van der Oost, J. Codon Bias as a Means to Fine-Tune Gene Expression. *Mol. Cell* **2015**, *59*, 149–161. [CrossRef]
9. López, J.L.; Lozano, M.J.; Lagares, A.; Fabre, M.L.; Draghi, W.O.; Del Papa, M.F.; Pistorio, M.; Becker, A.; Wibberg, D.; Schlüter, A.; et al. Codon Usage Heterogeneity in the Multipartite Prokaryote Genome: Selection-Based Coding Bias Associated with Gene Location, Expression Level, and Ancestry. *mBio* **2019**, *10*, e00505-19. [CrossRef]
10. Daniell, H.; Lin, C.-S.; Yu, M.; Chang, W.-J. Chloroplast genomes: Diversity, evolution, and applications in genetic engineering. *Genome Biol.* **2016**, *17*, 134. [CrossRef]
11. Kwak, S.-Y.; Lew, T.T.S.; Sweeney, C.J.; Koman, V.B.; Wong, M.H.; Bohmert-Tatarev, K.; Snell, K.D.; Seo, J.S.; Chua, N.-H.; Strano, M.S. Chloroplast-selective gene delivery and expression in planta using chitosan-complexed single-walled carbon nanotube carriers. *Nat. Nanotechnol.* **2019**, *14*, 447–455. [CrossRef] [PubMed]
12. Hishamuddin, M.S.; Lee, S.Y.; Ng, W.L.; Ramlee, S.I.; Lamasudin, D.U.; Mohamed, R. Comparison of eight complete chloroplast genomes of the endangered *Aquilaria* tree species (Thymelaeaceae) and their phylogenetic relationships. *Sci. Rep.* **2020**, *10*, 13034. [CrossRef]
13. Wang, Z.; Xu, B.; Li, B.; Zhou, Q.; Wang, G.; Jiang, X.; Wang, C.; Xu, Z. Comparative analysis of codon usage patterns in chloroplast genomes of six Euphorbiaceae species. *PeerJ* **2020**, *8*, e8251. [CrossRef]
14. Wu, Z.; Liao, R.; Yang, T.; Dong, X.; Lan, D.; Qin, R.; Liu, H. Analysis of six chloroplast genomes provides insight into the evolution of *Chrysosplenium* (Saxifragaceae). *BMC Genom.* **2020**, *21*, 621. [CrossRef] [PubMed]
15. Koehne, E. *Prunus* L. In *Plantae Wilsonianae*; Sargent, C.R., Ed.; Dioscorides Press: Portland, OR, USA, 1913; Volume 2, pp. 196–282.
16. Rehder, A. *Manual of Cultivated Trees and Shrubs Hardy in North America Exclusive of the Subtropical and Warmer temperate Regions*; MacMillan: New York, NY, USA, 1940.
17. Krüssmann, G. Cultivated broad-leaved trees and shrubs. In *Timber Press*; Timber Press: Portland, OR, USA, 1986; Volume 3.
18. Lu, L.T.; Ku, T.C.; Li, C.L.; Chen, S.X. Rosaceae (3) Prunoideae. In *Flora Reipublicae Popularis Sinicae, Tomus 38*; Yü, T.T., Ed.; Science Press: Beijing, China, 1986; pp. 1–133.
19. Wang, X.R. *An Illustrated Monograph of Cherry Cultivars in China*; Science Press: Beijing, China, 2014.
20. Zhang, Y.; Nie, X.; Jia, X.; Ding, C.; Biradar, S.; Le, W.; Che, X.; Song, W. Analysis of codon usage patterns of the chloroplast genomes in the Poaceae family. *Aust. J. Bot.* **2012**, *60*, 461–470. [CrossRef]
21. Ji, K.; Song, X.; Chen, C.; Li, G.; Xie, S. Codon Usage Profiling of Chloroplast Genome in Magnoliaceae. *J. Agric. Sci. Technol.* **2020**, *22*, 52–62.
22. Nie, X.; Deng, P.; Feng, K.; Liu, P.; Du, X.; You, F.M.; Song, W. Comparative analysis of codon usage patterns in chloroplast genomes of the Asteraceae family. *Plant Mol. Biol. Rep.* **2014**, *32*, 828–840. [CrossRef]
23. Liu, H.; Xiong, R.; Ni, Y.; Wei, L.; Sun, J.; Wang, G.; Zhang, Y.; Gao, Y. Comparative Analysis of Codon Usage Patterns in Chloroplast Genomes of *Fragaria* Species. *Mol. Plant Breed.* **2021**, 1–23.

24. Shi, S.; Li, J.; Sun, J.; Yu, J.; Zhou, S. Phylogeny and Classification of *Prunus sensu lato* (Rosaceae). *J. Integr. Plant Biol.* **2013**, *55*, 1069–1079. [CrossRef]
25. Zhang, S.-D.; Jin, J.J.; Chen, S.Y.; Chase, M.W.; Soltis, D.E.; Li, H.-T.; Yang, J.-B.; Li, D.-Z.; Yi, T.-S. Diversification of Rosaceae since the Late Cretaceous based on plastid phylogenomics. *New Phytol.* **2017**, *214*, 1355–1367. [CrossRef]
26. Jin, J.-J.; Yu, W.-B.; Yang, J.-B.; Song, Y.; dePamphilis, C.W.; Yi, T.-S.; Li, D.-Z. GetOrganelle: A fast and versatile toolkit for accurate de novo assembly of organelle genomes. *Genome Biol.* **2020**, *21*, 241. [CrossRef] [PubMed]
27. Tillich, M.; Lehwark, P.; Pellizzer, T.; Ulbricht-Jones, E.S.; Fischer, A.; Bock, R.; Greiner, S. GeSeq—Versatile and accurate annotation of organelle genomes. *Nucleic Acids Res.* **2017**, *45*, W6–W11. [CrossRef] [PubMed]
28. Zhang, D.; Gao, F.; Jakovlić, I.; Zou, H.; Zhang, J.; Li, W.X.; Wang, G.T. PhyloSuite: An integrated and scalable desktop platform for streamlined molecular sequence data management and evolutionary phylogenetics studies. *Mol. Ecol. Resour.* **2020**, *20*, 348–355. [CrossRef] [PubMed]
29. Sueoka, N. Near Homogeneity of PR2-Bias Fingerprints in the Human Genome and Their Implications in Phylogenetic Analyses. *J. Mol. Evol.* **2001**, *53*, 469–476. [CrossRef] [PubMed]
30. Wang, H.-X.; Liu, H.; Moore, M.J.; Landrein, S.; Liu, B.; Zhu, Z.-X.; Wang, H.-F. Plastid phylogenomic insights into the evolution of the Caprifoliaceae *s.l.* (Dipsacales). *Mol. Phylogenet. Evol.* **2020**, *142*, 106641. [CrossRef]
31. Liu, Q.; Xue, Q. Comparative studies on codon usage pattern of chloroplasts and their host nuclear genes in four plant species. *J. Genet.* **2005**, *84*, 55–62. [CrossRef]
32. Suzuki, R.; Shimodaira, H. Pvclust: An R package for assessing the uncertainty in hierarchical clustering. *Bioinformatics* **2006**, *22*, 1540–1542. [CrossRef]
33. Nguyen, L.-T.; Schmidt, H.A.; Von Haeseler, A.; Minh, B.Q. IQ-TREE: A Fast and Effective Stochastic Algorithm for Estimating Maximum-Likelihood Phylogenies. *Mol. Biol. Evol.* **2015**, *32*, 268–274. [CrossRef]
34. Tuller, T.; Waldman, Y.Y.; Kupiec, M.; Ruppin, E. Translation efficiency is determined by both codon bias and folding energy. *Proc. Natl. Acad. Sci. USA* **2010**, *107*, 3645. [CrossRef]
35. Gu, W.; Zhou, T.; Ma, J.; Sun, X.; Lu, Z. The relationship between synonymous codon usage and protein structure in *Escherichia coli* and *Homo sapiens*. *Biosystems* **2004**, *73*, 89–97. [CrossRef]
36. Wang, B.; Yuan, J.; Liu, J.; Jin, L.; Chen, J.-Q. Codon Usage Bias and Determining Forces in Green Plant Mitochondrial Genomes. *J. Integr. Plant Biol.* **2011**, *53*, 324–334. [CrossRef] [PubMed]
37. Tang, D.; Wei, F.; Cai, Z.; Wei, Y.; Khan, A.; Miao, J.; Wei, K. Analysis of codon usage bias and evolution in the chloroplast genome of *Mesona chinensis* Benth. *Dev. Genes Evol.* **2021**, *231*, 1–9. [CrossRef] [PubMed]
38. Hershberg, R.; Petrov, D.A. Selection on codon bias. *Annu. Rev. Genet.* **2008**, *42*, 287–299. [CrossRef] [PubMed]
39. Jansen, R.K.; Cai, Z.; Raubeson, L.A.; Daniell, H.; Depamphilis, C.W.; Leebens-Mack, J.; Müller, K.F.; Guisinger-Bellian, M.; Haberle, R.C.; Hansen, A.K.; et al. Analysis of 81 genes from 64 plastid genomes resolves relationships in angiosperms and identifies genome-scale evolutionary patterns. *Proc. Natl. Acad. Sci. USA* **2007**, *104*, 19369–19374. [CrossRef] [PubMed]
40. Choi, K.S.; Son, O.G.; Park, S. The Chloroplast Genome of *Elaeagnus macrophylla* and *trn*H Duplication Event in Elaeagnaceae. *PLoS ONE* **2015**, *10*, e0138727. [CrossRef]
41. Jansen, R.K.; Saski, C.; Lee, S.-B.; Hansen, A.K.; Daniell, H. Complete Plastid Genome Sequences of Three Rosids (*Castanea*, *Prunus*, *Theobroma*): Evidence for At Least Two Independent Transfers of *rpl*22 to the Nucleus. *Mol. Biol. Evol.* **2011**, *28*, 835–847. [CrossRef]

forests

MDPI

Article

Tempo and Mode of Floristic Exchanges between Hainan Island and Mainland Asia: A Case Study of the *Persea* Group (Lauraceae)

Xuejie Huo, Zhi Yang, Yinfeng Xie and Yong Yang *

Center for Sustainable Forestry in Southern China, College of Biology and the Environment, Nanjing Forestry University, 159 Longpan Road, Nanjing 210037, China
* Correspondence: yangyong@njfu.edu.cn

Abstract: The origin of island biodiversity has been a topic of interest in biogeography. Two main hypotheses were suggested to explain the floristic origin of Hainan Island: ancient vicariance vs. recent dispersal. The *Persea* group of Lauraceae was used to examine their origin on Hainan Island. A data matrix including five genera and 49 species was assembled, phylogenetic trees of the *Persea* group were reconstructed using both maximum likelihood and Bayesian inference methods, and a relaxed molecular clock in BEAST was used to estimate the divergence time of the *Persea* group. The results showed that the *Persea* group diverged from its sister clade in the Eocene, and that the endemic and common species of Hainan Island and mainland Asia originated relatively late during the Miocene–Pleistocene. Species of the *Persea* group on Hainan may have arrived from mainland Asia via dispersal or originated via dispersal–isolation–divergence during the Miocene and Pleistocene. The results favor the dispersal hypothesis for the origin of the flora of Hainan Island and negate the vicariance hypothesis.

Keywords: biogeography; flora; Hainan Island; Lauraceae; origin; *Persea* group

check for updates

Citation: Huo, X.; Yang, Z.; Xie, Y.; Yang, Y. Tempo and Mode of Floristic Exchanges between Hainan Island and Mainland Asia: A Case Study of the *Persea* Group (Lauraceae). *Forests* **2022**, *13*, 1722. https://doi.org/10.3390/f13101722

Academic Editor: David Kenfack

Received: 27 September 2022
Accepted: 18 October 2022
Published: 19 October 2022

Publisher's Note: MDPI stays neutral with regard to jurisdictional claims in published maps and institutional affiliations.

Copyright: © 2022 by the authors. Licensee MDPI, Basel, Switzerland. This article is an open access article distributed under the terms and conditions of the Creative Commons Attribution (CC BY) license (https://creativecommons.org/licenses/by/4.0/).

1. Introduction

Hainan Island is the largest tropical island in China. It is located south of Guangdong and Guangxi across the Qiongzhou Strait, east of Vietnam across the Beibu Gulf, and north of the Philippines, Malaysia, and Brunei [1]. The island is mountainous in the middle and slopes to the coast in all directions. It has a characteristic tropical monsoon climate (annual mean temperature: 22–26 °C), adequate light (annual mean hours: 2166 h), and abundant rain (annual mean precipitation: 2000–2400 mm) due to its geographic location [2]. The complex topography and favorable hydrothermal conditions have fundamentally shaped the rich floristic diversity [3].

The flora of Hainan has a strong tropical character [4]. Around 62.8% of the 196 families are tropical in nature. At the genus level, tropical elements account for 80.5%, while temperate elements are relatively low in proportion [3]. Hainan is rich in endemic species, 592 species endemic to China are on Hainan. Most of them are in the four mountainous areas of Wuzhi Shan, Jianfeng Ling, Bawang Ling, and Diaoluo Shan [4–6]. Around 2078 species are common to Asia in general.

Two hypotheses were proposed to explain the tempo and mode of the floristic origin of Hainan, although all studies agree that the flora of the island is continental in origin. Ancient vicariance is one hypothesis to explain the floristic origin of Hainan since the island was once connected to Vietnam and Guangxi, China, in the Eocene, then moved and rotated to the southeast to finally reach its present position [1,3]. The other hypothesis contends that the flora of Hainan was due to recent dispersal and frequent floristic exchanges with the Asian mainland [7–10]. These hypotheses have not been tested by phylogenetic studies based on molecular dating analyses.

Lauraceae are one of the early diverged lineages of angiosperms. Fossils of the family can be traced back to the mid-Cretaceous and have also been recorded in the Eocene flora of Hainan [11–13]. The family has fleshy fruits that are dispersed by birds, among other factors. It is mainly tropical and pantropical, and contains over 3000 species worldwide [14]. The family has the highest species diversity among characteristic tree families in Hainan [1,3] with 122 species and infraspecific taxa in 16 genera. Many species of Lauraceae are also dominant [15]. Within the family, the *Persea* group, with five genera, *Alseodaphne*, *Alseodaphnopsis*, *Dehaasia*, *Machilus*, and *Phoebe*, is well represented in the flora of Hainan. These genera contain species pairs between Hainan and continental Asia, thus providing an ideal opportunity to examine the hypotheses on the floristic origin of Hainan.

To test these hypotheses, we reconstructed a phylogeny of the *Persea* group based on extensive sampling of species on Hainan and mainland Asia and estimated the divergence time of the species. We expected the divergence time between Hainan and the adjoining Asian mainland to be earlier than the Eocene under the tectonic drift and vicariance hypothesis, but later than the Eocene under the recent dispersal hypothesis.

2. Materials and Methods

2.1. Taxon Sampling

We selected 49 species from five genera of the *Persea* group, with *Persea* excluded because it is not native to Hainan. Six species from three genera (*Lindera*, *Litsea*, *Neolitsea*) of the core Lauraceae were chosen as outgroups based on recent molecular studies of Lauraceae [16,17]. Two nuclear fragments, including the nuclear ribosomal internal transcribed spacer (nrITS) and the second intron of the *LEAFY* gene (*LEAFY* intron II), were selected for phylogenetic reconstruction [18]. GenBank accession numbers for nrITS and *LEAFY* intron II sequences are listed in Table 1.

Table 1. GenBank accession numbers for nrITS and *LEAFY* sequences.

Taxon	nrITS	*LEAFY*
Ingroups		
Alseodaphne huanglianshanensis H.W.Li & Y.M.Shui	HQ697182	HQ697007
Alseodaphne semecarpifolia Nees	HQ697184	HQ697015
Alseodaphnopsis andersonii (King ex Hook. f.) H.W. Li & J. Li	FM957793	HQ697002
Alseodaphnopsis hainanensis (Merr.) H.W. Li & J. Li	MG188587	HQ697006
Alseodaphnopsis maguanensis L.Li & J.Li	MN906900	MN906896
Alseodaphnopsis petiolaris (Meisn.) H.W.Li & J.Li	FM957796	HQ697008
Alseodaphnopsis putaoensis L.Li, Y.H.Tan & J.Li	MN906902	MN906898
Alseodaphnopsis rugosa (Merr. & Chun) H.W.Li & J.Li	MG188584	HQ697011
Alseodaphnopsis sichourensis (H.W.Li) H.W.Li & J.Li	MG188597	MG188626
Alseodaphnopsis ximengensis H.W.Li & J.Li	MG188591	MG188599
Dehaasia hainanensis Kosterm.	FJ719308	HQ697025
Dehaasia incrassata (Jack) Nees	HQ697186	HQ697028
Machilus breviflora (Benth.) Hemsl.	FJ755434	HQ697041
Machilus decursinervis Chun	AY934893	HQ697044
Machilus duthiei King ex Hook.f	FJ755425	HQ697055
Machilus gamblei King ex Hook.f	FJ755422	HQ697037
Machilus gongshanensis H.W.Li	FJ755416	HQ697047
Machilus grijsii Hance	FJ755420	HQ697048
Machilus kwangtungensis Y.C.Yang	FJ755424	HQ697051
Machilus leptophylla Hand.-Mazz.	FJ755430	HQ697053
Machilus minutiflora (H.W.Li) L.Li, J.Li & H.W.Li	HQ697208	HQ697147
Machilus monticola S.K.Lee	FJ755418	HQ697056
Machilus nanmu (Oliv) Hemsl.	FJ755409	HQ697066
Machilus oculodracontis Chun	HQ697188	HQ697059
Machilus oreophila Hance	FJ755423	HQ697063
Machilus phoenicis Dunn	FJ755413	HQ697064
Machilus platycarpa Chun	FJ755421	HQ697067
Machilus pomifera (Kosterm.) S.K.Lee	FJ755432	HQ697069

Table 1. *Cont.*

Taxon	nrITS	*LEAFY*
Machilus robusta W.W.Sm.	FJ755426	HQ697071
Machilus salicina Hance	FJ755428	HQ697073
Machilus salicoides S.K.Lee	FJ755433	HQ697074
Machilus shweliensis W.W.Sm.	FJ755414	HQ697075
Machilus thunbergii Siebold & Zucc.	HQ697190	HQ697081
Machilus yunnanensis Lecomte	FJ755415	HQ697083
Phoebe angustifolia Meisn.	HQ697201	HQ697124
Phoebe tavoyana Hook.f.	HQ697202	HQ697130
Phoebe formosana (Hayata) Hayata	HQ697205	HQ697136
Phoebe hungmoensis S.K.Lee	HQ697206	HQ697137
Phoebe lanceolata (Nees) Nees	FJ755410	HQ697141
Phoebe macrocarpa C.Y.Wu	FJ755408	HQ697142
Phoebe megacalyx H.W.Li	HQ697207	HQ697144
Phoebe neurantha (Hemsl) Gamble	HQ697209	HQ697151
Phoebe puwenensis W.C.Cheng	HQ697210	HQ697152
Outgroups		
Lindera erythrocarpa Makino	HQ697215	HQ697167
Lindera megaphylla Hemsl.	HQ697216	HQ697171
Litsea auriculata S.S.Chien & W.C.Cheng	HQ697217	HQ697174
Litsea verticillata Hance	HQ697218	HQ697175
Neolitsea cambodiana Lecomte	HQ697219	HQ697176
Neolitsea howii C.K.Allen	HQ697220	HQ697178

2.2. Phylogenetic Analyses

The nrITS and *LEAFY* intron II sequences were aligned with the program MAFFT (Version 7.471, Tokyo, Japan) [19] and edited manually using BioEdit (Version 7.0.9.0, Wooster, OH, USA) [20]. Ambiguously aligned fragments of two alignments were removed in batches using Gblocks (Version 0.91b, Barcelona, Spain) [21]. The sequences were concatenated and analyzed further. The best-fit partition model was chosen for the dataset (nrITS and *LEAFY* intron II) with ModelFinder [22] based on the Bayesian information criterion (BIC). Phylogenetic analyses were performed using the maximum likelihood (ML) and Bayesian inference (BI) methods. ML phylogenies were inferred using IQ-TREE (Version 1.6.8, Vienna, Austria) [23] under the edge-linked partition model for 5000 ultrafast bootstraps [24], and the Shimodaira–Hasegawa-like approximate likelihood ratio test [25]. BI phylogenies were inferred using MrBayes (Version 3.2.6, Stockholm, Sweden) [26], and the Markov chain Monte Carlo (MCMC) algorithm was run for 500,000 generations with a sampling frequency of every 500 generations. The initial 25% of sampled data were discarded as burn-in. Branch support of the BI tree was determined as Bayesian posterior probabilities (BPs).

2.3. Divergence Time Estimation

The combined dataset of the BI tree was used for molecular dating analyses with BEAST (Version 2.6.6, Auckland, New Zealand) [27]. We used BEAUti (Version 2.6.6, Auckland, New Zealand) [27] to import the dataset, set the substitution model as GTR, implemented the relaxed clock log-normal, and applied a Birth–Death Model. We ran the analysis for 40,000,000 Markov Chain Monte Carlo (MCMC) generations with a sampling frequency of every 4000 generations. TRACER (Version 1.7.2, Edinburgh, UK) [28] was used to calculate the log file's stationarity. After removing the first 10% of trees as burn-in, we generated a maximum clade credibility (MCC) tree in TreeAnnotator (Version 2.6.3, Edinburgh, UK) [28] and visualized it in FigTree (Version 1.4.2, Guangzhou, China) [29,30].

We used two macrofossils to calibrate divergence time estimates: *Alseodaphne changchangensis* JH Jin & JZ Li from the Eocene Changchang Formation of the Changchang Basin of Hainan [12] and *Machilus maomingensis* JH Jin & B Tang from the Eocene Youganwo Formation of the Maoming Basin of Guangdong, southern China [13]. We followed Li et al. [29]

in using *Alseodaphne changchangensis* to calibrate the crown node of the *Persea* group [A: age 37–49 million years ago (Ma)] and applied parameters including a log-normal prior distribution with an offset of 37 Ma, a mean of 1.8, and a standard deviation of 0.35. We used *Machilus maomingensis* to calibrate the stem age of *Machilus* (B: age 33.7–33.9 Ma) following Li et al. [29] and applied parameters including a uniform prior distribution with an offset of 0, a lower of 33.7, and an upper of 33.9 (Table 2).

Table 2. Fossil reference points used in this study.

Node	Calibration Fossil	Minimum Age (MA)	Prior Distribution	Prior Parameters	2.5/Median/97.5% Quantiles (Ma)
A: crown node of the *Persea* group	*Alseodaphne changchangensis*	37–49	log-normal	offset:37; M:1.8; SD:0.35	40/43/49
B: steam node of the *Machilus*	*Machilus maomingensis*	33.7–33.9	uniform	offset:0; Lower:33.7; Upper:33.9	33.7/33.8/33.9

3. Results

3.1. Sequence Characters and Phylogenetic Analyses

3.1.1. Sequence Characters

The numbers of variable sites and parsimony-informative (PI) sites of the nrITS dataset were 114 bp (23.1%) and 72 bp (14.5%), respectively (Table 3). The aligned length of the LEAFY intron II was 625 bp, with 24.2% and 16.7% variable and PI sites, respectively (Table 3). The aligned length of the combined nrITS and *LEAFY* intron II was 1088 bp, with 30.3% and 14.4% variable and PI sites, respectively (Table 3).

Table 3. Characteristics of separate and concatenated sequence datasets and the model selected for ML/BI analysis.

Datasets	No. of Taxa	No. of Sites	No. of Variable/Parsimony-Informative Sites	ML Analysis	BI Analysis
nrITS	49	496	114/72	TPM2u+F+R3	TPM2u+F+R3
LEAFY	49	625	231/96	HKY+F+G4	HKY+F+G4
Combined	49	1088	330/157	Partitioned	Partitioned

3.1.2. Phylogenetic Analyses

The ML tree based on the nrITS and *LEAFY* intron II sequences (Figure 1) showed that the *Persea* group was monophyletic and divided into four clades with very high support (BS: 100; PP: 1). In the *Machilus* clade, *M. pomifera* and *M. monticola*, both endemic to Hainan, were grouped with *M. pomifera* and *M. salicoides* from southern China (BS: 100; PP: 1), while the phylogenetic position of *M. monticola* was not resolved. *Machilus grijsii*, distributed on Hainan and in southeastern China, grouped with *M. platycarpa* and *M. yunnanensis* from southwest China and the Indochina peninsula (BS: 98; PP: 1); *Machilus nanmu* was the earliest diverged species within *Machilus* (BS: 92, PP: 1). In the *Alseodaphne* and *Dehaasia* clade, *Alseodaphne* and *Dehaasia* were mixed together with moderate to high support (BS: 87, PP: 0.99). *Alseodaphnopsis* constituted a small clade, in which *Alseodaphnopsis hainanensis* from Hainan was sister to *Alseodaphnopsis putaoensis* from Southeast Asia (BS: 100, PP: 1). *Alseodaphnopsis rugosa* from Hainan was sister to *Alseodaphnopsis maguanensis* from Yunnan. In the *Phoebe* clade, *P. hungmoensis* from Hainan was clustered with species from Yunnan and adjacent countries, including *P. puwenensis*, *P. tavoyana*, *P. megacalyx*, and *P. macrocarpa*, with moderate to high support (BS: 89, PP: 0.99).

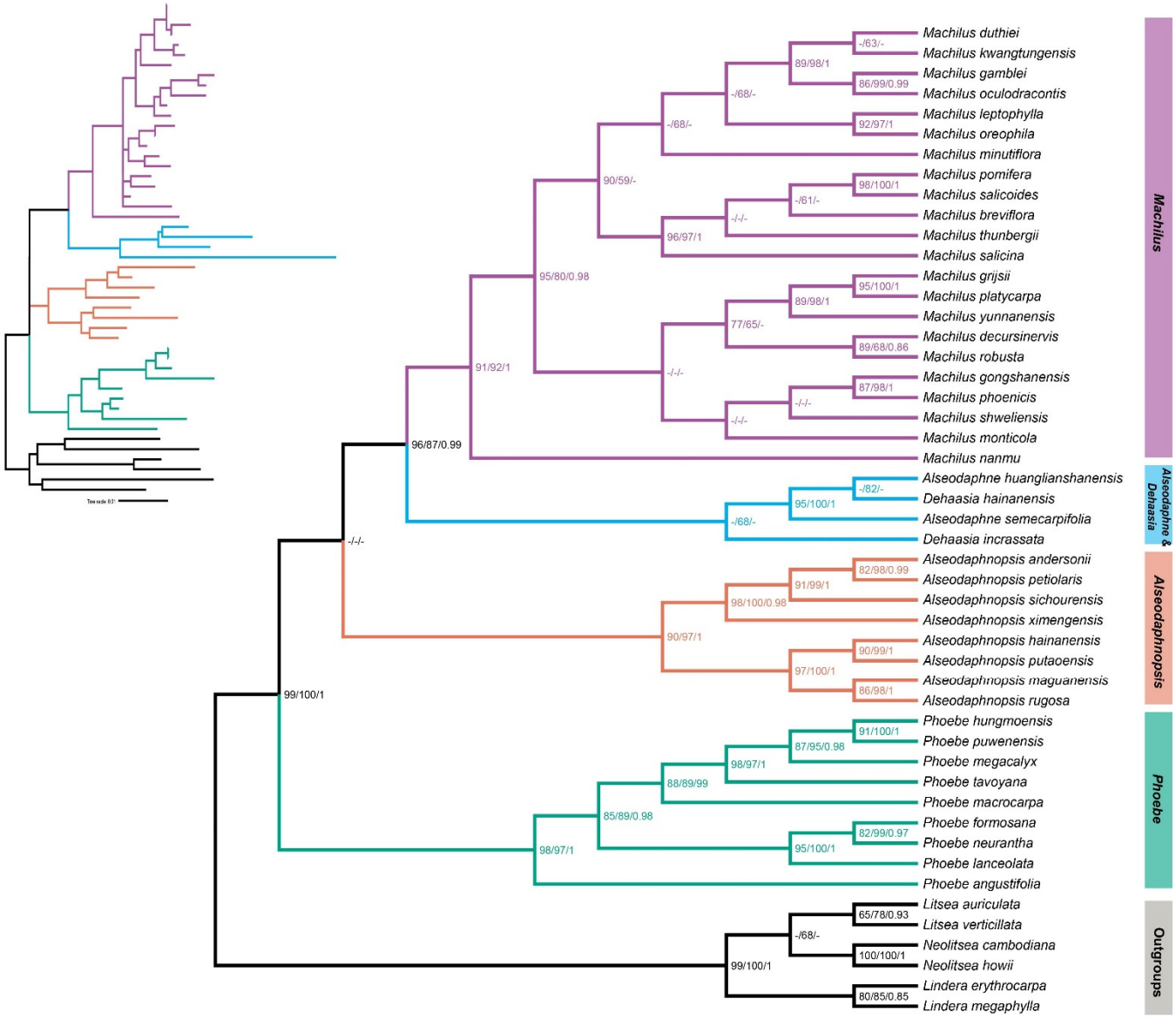


Figure 1. Maximum likelihood (ML) tree of the *Persea* group based on nrITS + *LEAFY* intron II. Numbers of nodes indicate support values of Shimodaira–Hasegawa-like approximate likelihood ratio test (SH-aLRT)/ML bootstrap support (BS)/Bayesian inference (BI) posterior probability (PP). "–" represents nodes with SH-aLRT/BS/PP support < 50%/0.8.

3.2. Divergence Times

The stem and crown ages of the *Persea* group were estimated to be 48.3 Ma (95% highest posterior density (HPD): 40.6–61.3) and 42.3 Ma (95% HPD: 39.6–46.3), respectively (Figure 2). *Alseodaphnopsis* was the earliest diverged lineage within the *Persea* group. The stem and crown ages were 42.7 Ma (95% HPD: 39.6–46.3) and 31.1 Ma (95% HPD: 22.6–40.1), respectively. The stem and crown ages of *Phoebe* were 40.2 Ma (95% HPD: 36.1–44.3), and 28.0 Ma (95% HPD: 18.7–37.3), respectively. The stem and crown ages of *Alseodaphne–Dehaasia* were estimated to be 33.8 Ma (95% HPD: 33.7–33.9) and 23.8 Ma (95% HPD: 17.4–29.9), respectively. The stem age of *Machilus* was the same as *Alseodaphne–Dehaasia*. The crown age was 25.8 Ma (95% HPD: 19.5–32.1).



Figure 2. Time tree of the *Persea* group on Hainan based on nrITS and *LEAFY* intron II inferring from BEAST analysis. Letters in empty circles indicate fossil calibrations; species with asterisk (*) means occurring on Hainan; Hainan Island endemic species are highlighted in red; black bars show 95% confidence interval.

Endemism on Hainan arose around 13.5 Ma. *Alseodaphnopsis hainanensis*, the earliest diverged endemic species on Hainan, split from *Alseodaphnopsis putaoensis* around 13.5 Ma (95% HPD: 6.8–21.4). *Alseodaphnopsis rugosa* (Hainan endemic) split from its sister species around 12.1 Ma (95% HPD: 4.9–20.2). *Alseodaphnopsis putaoensis* and *Alseodaphnopsis maguanensis* are in Burma and Yunnan, China, respectively. *Dehaasia hainanensis*, which is endemic to Hainan, diverged from *Alseodaphne semecarpifolia* around 11.8 Ma (95% HPD: 6.1–18.4). *Machilus monticola* diverged from its sister species in Yunnan around 11.1 Ma (95% HPD: 8.1–17.9). The divergence time for *M. pomifera* was 3.4 Ma (95% HPD: 0.9–6.5); *M. pomifera* is sister to a

small clade, including *M. salicoides*, *M. breviflora*, *M. salicina*, and *M. thunbergii* of mainland China and Southeast Asia.

4. Discussion

Hainan was thought to be separated from the mainland (Beibu Gulf) due to Eocene plate tectonic movement, which fundamentally impacted the origin of the flora of Hainan [3,31]. Based on paleomagnetism and volcanism evidence, Zhu [31] proposed that the flora of Hainan originated via ancient vicariance in the Eocene. Our dating results suggest that species of the *Persea* group on Hainan originated in the Miocene and later, showing a dispersal–isolation–divergence pattern [32]. The split between mboxemphAlseodaphnopsis hainanensis and its sister species *Alseodaphnopsis putaoensis* represents the earliest divergence, which was estimated to have occurred around 13.5 Ma. *Machilus pomifera* (endemic to Hainan) diverged from its sister, *M. salicoides*, around 3.4 Ma. That divergence was the latest event. However, the estimated divergence time for the endemic species of Hainan from sister species was later than the geographic time of separation of Hainan Island from the mainland. We therefore hypothesize that species of the *Persea* group on Hainan may have been derived from mainland Asia via multiple dispersal events followed by isolation and speciation. Divergence of the species pairs between Hainan and the mainland occurred at different times in the Neogene. All of these divergence events between species pairs on Hainan and the Asian mainland occurred in the Miocene or later, which negates the ancient vicariance hypothesis but supports the dispersal hypothesis on the origin of the Hainan flora. Additionally, it appears that endemism on Hainan originated via a dispersal–isolation–divergence pattern.

Our findings are corroborated by a number of recent studies on the divergence time of Hainan endemic species in other families, including Dipterocarpaceae, Magnoliaceae, Podocarpaceae, and Theaceae. The Dipterocarpaceae are thought to have migrated from India to SE China via SE Asia. The species endemic to Hainan (*Hopea hainanensis*) diverged around 23.0 Ma [33,34]. Dong et al. found that *Michelia shiluensis* (Magnoliaceae), an endemic species on Hainan, split from its sister species around 8 Ma [35]. Klaus et al. suggested that *Dacrydium pectinatum* and *Podocarpus annamiensis*, two endemic species on Hainan, diverged around 12.5 Ma and 10 Ma, respectively [36]. Yu et al. indicated that *Polyspora hainanensis* (Theaceae), endemic on Hainan, diverged from its sister species around 3.8 Ma [37]. These studies showed that the endemic species of Hainan evolved multiple times since the early Miocene, thereby supporting the hypothesis of recent dispersal rather than ancient vicariance as the origin of the Hainan flora.

Different mechanisms may have contributed to the origin of the endemic flora of Hainan. Geological events have provided opportunities for floristic exchange between Hainan and the Asian mainland. Periodic land bridges during the Pleistocene connected Hainan and southern China, allowing for frequent exchanges [38,39]. *Cycas taiwaniana* of Hainan, Guangdong, and Fujian, diverged quite recently [40,41] and may have migrated between the mainland and Hainan when a land bridge was available. Plants with fleshy fruits, e.g., Lauraceae, may have entered Hainan via bird dispersal. A large number of avian fossils have been recorded from Miocene strata in Zhaotong, Yunnan Province [42]. Finally, ocean currents may have provided an additional mechanism for floristic exchange, e.g., *Cocos nucifera*, between Hainan and mainland Asia, including Southeast Asia and southern China.

5. Conclusions

The tempo and mode of floristic exchanges between Hainan and mainland Asia are complicated. We conducted phylogeny and molecular dating of the *Persea* group of Lauraceae to test the competing hypotheses of the origin of the flora of Hainan and concluded that the endemic species originated via multiple recent dispersal events, but not due to ancient vicariance. However, it should be acknowledged that we provided only a study of plants with easily dispersable fleshy fruits. To better understand the origin

of the flora of Hainan, further phylogenetic/phylogenomic and molecular dating and biogeographic studies are encouraged.

Author Contributions: Y.Y. conceived the idea. X.H. and Y.Y. designed the research. X.H. and Z.Y. collected data and performed analyses. X.H. drafted the manuscript, X.H., Z.Y., Y.X. and Y.Y. revised and finalized the manuscript. All authors have read and agreed to the published version of the manuscript.

Funding: This work was supported by the National Natural Science Foundation, China (31970205) and the *Metasequoia* funding of the Nanjing Forestry University.

Data Availability Statement: Not applicable.

Acknowledgments: We thank David E. Boufford of the Harvard University Herbaria for his kind help with English.

Conflicts of Interest: The authors declare no conflict of interest.

References

1. Yang, X.B. *Hainan Vegetation*; Science Press: Beijing, China, 2019; Volume 2, pp. 1–20.
2. *Hainan Province Chronicles • Land Chronicles*; Nan Hai Publishing Co.: Haikou, China, 2007; Volume 2, pp. 9–24.
3. Zhu, H. Biogeographical evidences help revealing the origin of Hainan Island. *PLoS ONE* **2016**, *11*, e0151941. [CrossRef] [PubMed]
4. Zhu, Z.X.; Harris, A.J.; Nizamani, M.M.; Thornhill, A.H.; Scherson, R.A.; Wang, H.F. Spatial phylogenetics of the native woody plant species in Hainan, China. *Ecol. Evol.* **2021**, *11*, 2100–2109. [CrossRef]
5. Jiang, Y.X.; Wang, B.; Zang, R.G. *Biodiversity and Its Formation Mechanism of Tropical Forest in Hainan Island*; Science Press: Beijing, China, 2002; Volume 1, pp. 114–122.
6. Francisco-Ortega, J.; Wang, F.G.; Wang, Z.S.; Xing, F.W.; Liu, H.; Xu, H.; Xu, W.X.; Luo, Y.B.; Song, X.Q.; Gale, S.; et al. Endemic seed plant species from Hainan Island: A checklist. *Bot. Rev.* **2010**, *76*, 295–345. [CrossRef]
7. Zhang, C.C.; Liu, L.F. Angiosperms of Hainan Island. *Acta Sci. Nat. Univ. Sunyatseni* **1983**, *1983*, 69–76.
8. Miu, R.H. The gymnosperms of Hainan Island. *Acta Sci. Nat. Univ. Sunyatseni* **1986**, *1986*, 59–65.
9. Wu, D.L.; Xing, F.W.; Ye, H.G.; Li, Z.X.; Chen, B.H. Floristic geography of seed plants on islands in the South China Sea. *J. Trop. Subtrop. Bot.* **1996**, *4*, 1–22.
10. Jin, J.H.; Shen, R.J.; Liao, W.B. Analysis of the families of Cenozoic spermatophytic flora in Hainan Island. *Acta Bot. Boreali–Occident. Sin.* **2008**, *28*, 2125–2131. [CrossRef]
11. Drinnan, A.N.; Crane, P.R.; Friis, E.N.; Pedersen, K.R. Lauraceous flowers from the Potomac Group (Mid–Cretaceous) of Eastern North America. *Bot. Gaz.* **1990**, *151*, 370–384. [CrossRef]
12. Li, J.Z.; Qiu, J.; Liao, W.B.; Jin, J.H. Eocene fossil *Alseodaphne* from Hainan Island of China and its paleoclimatic implications. *Sci. China Ser. D Earth Sci.* **2009**, *52*, 1537–1542. [CrossRef]
13. Tang, B.; Han, M.; Xu, Q.; Jin, J. Leaf cuticle microstructure of *Machilus maomingensis* sp. nov. (Lauraceae) from the Eocene of the Maoming Basin, South China. *Acta Geol. Sin. (Engl. Ed.)* **2016**, *90*, 1561–1571. [CrossRef]
14. Li, S.G. *Flora Reipublicae Popularis Sinicae*; Science Press: Beijing, China, 1982; Volume 124, pp. 1–26.
15. Zhu, H. Families and genera of seed plants in relation to biogeographical origin on Hainan Island. *Biodivers. Sci.* **2017**, *25*, 816–822. [CrossRef]
16. Mo, Y.Q.; Li, L.; Li, J.W.; Rohwer, J.G.; Li, H.W.; Li, J. *Alseodaphnopsis*: A new genus of Lauraceae based on molecular and morphological evidence. *PLoS ONE* **2017**, *12*, e0186545. [CrossRef] [PubMed]
17. Li, L.; Li, J.; Rohwer, J.G.; van der Werff, H.; Wang, Z.H.; Li, H.W. Molecular phylogenetic analysis of the *Persea* group (Lauraceae) and its biogeographic implications on the evolution of tropical and subtropical amphi-Pacific disjunctions. *Am. J. Bot.* **2011**, *98*, 1520–1536. [CrossRef] [PubMed]
18. Zhao, M.L.; Song, Y.; Ni, J.; Yao, X.; Tan, Y.H.; Xu, Z.F. Comparative chloroplast genomics and phylogenetics of nine *Lindera* species (Lauraceae). *Sci. Rep.* **2018**, *8*, 423–439. [CrossRef]
19. Katoh, K.; Standley, D.M. MAFFT multiple sequence alignment software version 7: Improvements in performance and usability. *Mol. Biol. Evol.* **2013**, *30*, 772–780. [CrossRef]
20. Hall, T.A. BioEdit: A user-friendly biological sequence alignment editor and analysis program for Windows 95/98/NT. *Nucleic Acids Symp.* **1999**, *41*, 95–98. [CrossRef]
21. Talavera, G.; Castresana, J. Improvement of phylogenies after removing divergent and ambiguously aligned blocks from protein sequence alignments. *Syst. Biol.* **2007**, *56*, 564–577. [CrossRef]
22. Kalyaanamoorthy, S.; Minh, B.Q.; Wong, T.K.F.; von Haeseler, A.; Jermiin, L.S. ModelFinder: Fast model selection for accurate phylogenetic estimates. *Nat. Methods* **2017**, *14*, 587–589. [CrossRef]
23. Nguyen, L. –T.; Schmidt, H.A.; von Haeseler, A.; Minh, B.Q. IQ–TREE: A fast and effective stochastic algorithm for estimating maximum–likelihood phylogenies. *Mol. Biol. Evol.* **2015**, *32*, 268–274. [CrossRef]

24. Minh, B.Q.; Nguyen, M.A.T.; von Haeseler, A. Ultrafast approximation for phylogenetic bootstrap. *Mol. Biol. Evol.* **2013**, *30*, 1188–1195. [CrossRef]
25. Guindon, S.; Dufayard, J.F.; Lefort, V.; Anisimova, M.; Hordijk, W.; Gascuel, O. New algorithms and methods to estimate maximum–likelihood phylogenies: Assessing the performance of PhyML 3.0. *Syst. Biol.* **2010**, *59*, 307–321. [CrossRef] [PubMed]
26. Ronquist, F.; Teslenko, M.; van der Mark, P.; Ayres, D.L.; Darling, A.; Höhna, S.; Larget, B.; Liu, L.; Suchard, M.A.; Huelsenbeck, J.P. MrBayes 3.2: Efficient Bayesian phylogenetic inference and model choice across a large model space. *Syst. Biol.* **2012**, *61*, 539–542. [CrossRef] [PubMed]
27. Bouckaert, R.; Heled, J.; Kühnert, D.; Vaughan, T.; Wu, C.H.; Xie, D.; Suchard, M.A.; Rambaut, A.; Drummond, A.J. BEAST 2: A software platform for Bayesian evolutionary analysis. *PLoS Comput. Biol.* **2014**, *10*, e1003537. [CrossRef]
28. Rambaut, A.; Drummond, A.J.; Xie, D.; Baele, G.; Suchard, M.A. Posterior summarisation in Bayesian phylogenetics using Tracer 1.7. *Syst. Biol.* **2018**, *67*, 901–904. [CrossRef]
29. Li, H.; Liu, B.; Davis, C.C.; Yang, Y. Plastome phylogenomics, systematics, and divergence time estimation of the *Beilschmiedia* group (Lauraceae). *Mol. Phylogenet. Evol.* **2020**, *151*, 106901. [CrossRef]
30. Xiao, T.W.; Yan, H.F.; Ge, X.J. Plastid phylogenomics of tribe Perseeae (Lauraceae) yields insights into the evolution of East Asian subtropical evergreen broad–leaved forests. *BMC Plant Biol.* **2022**, *22*, 32. [CrossRef]
31. Zhu, H. On the biogeographical origin of Hainan Island in China. *Plant Sci. J.* **2020**, *38*, 839–843. [CrossRef]
32. Masaoki, T. Vicariance and dispersal in the differentiation of vocalization in the Ryukyu Scops Owl *Otus elegans*. *Ibis* **2011**, *153*, 779–788. [CrossRef]
33. Cvetković, T.; Hinsinger, D.D.; Thomas, D.C.; Wieringa, J.J.; Velautham, E.; Strijk, J.S. Phylogenomics and a revised tribal classification of subfamily Dipterocarpoideae (Dipterocarpaceae). *Taxon* **2022**, *22*, 85–102. [CrossRef]
34. Wang, J.H.; Moore, M.J.; Wang, H.; Zhu, Z.X.; Wang, H.F. Plastome evolution and phylogenetic relationships among Malvaceae subfamilies. *Gene* **2021**, *765*, 145103. [CrossRef]
35. Dong, S.S.; Wang, Y.L.; Xia, N.H.; Liu, Y.; Liu, M.; Lian, L.; Li, N.; Li, L.F.; Lang, X.A.; Gong, Y.Q.; et al. Plastid and nuclear phylogenomic incongruences and biogeographic implications of *Magnolia s.l.* (Magnoliaceae). *J. Syst. Evol.* **2021**, *60*, 1–15. [CrossRef]
36. Klaus, K.V.; Matzke, N.J. Statistical comparison of trait–dependent biogeographical models indicates that Podocarpaceae dispersal is influenced by both seed cone traits and geographical distance. *Syst. Biol.* **2020**, *69*, 61–75. [CrossRef] [PubMed]
37. Yu, X.Q.; Gao, L.M.; Soltis, D.E.; Soltis, P.S.; Yang, J.B.; Fang, L.; Yang, S.X.; Li, D.Z. Insights into the historical assembly of East Asian subtropical evergreen broadleaved forests revealed by the temporal history of the tea family. *New Phytol.* **2017**, *215*, 1235–1248. [CrossRef] [PubMed]
38. Jiang, X.L.; Gardner, E.M.; Meng, H.H.; Deng, M.; Xu, G.B. Land bridges in the Pleistocene contributed to flora assembly on the continental islands of South China: Insights from the evolutionary history of *Quercus championii*. *Mol. Phylogenet. Evol.* **2018**, *132*, 36–45. [CrossRef] [PubMed]
39. Lin, S.L.; Chen, L.; Peng, W.X.; Yu, J.H.; He, J.K.; Jiang, H.S. Temperature and historical land connectivity jointly shape the floristic relationship between Hainan Island and the neighbouring landmasses. *Sci. Total Environ.* **2021**, *769*, 144629. [CrossRef]
40. Mankga, L.T.; Yessoufou, K.; Mugwena, T.; Chitakira, M. The cycad genus *Cycas* may have diversified from Indochina and occupied its current ranges through vicariance and dispersal events. *Front. Ecol. Evol.* **2020**, *8*, 44. [CrossRef]
41. Feng, X.Y.; Wang, X.H.; Chiang, Y.C.; Jian, S.G.; Gong, X. Species delimitation with distinct methods based on molecular data to elucidate species boundaries in the *Cycas taiwaniana* complex (Cycadaceae). *Taxon* **2021**, *70*, 477–491. [CrossRef]
42. Zhang, G.J.; Ji, X.P.; Jablonski, N.G.; Su, D.F.; Wang, X.B.; Yang, X.; Li, Z.H.; Fu, L.Y. Stratigraphic significance of the avian fauna from late Miocene of Zhaotong region, Yunnan Province. *Acta Palaeontol. Sin.* **2013**, *52*, 281–287. [CrossRef]

forests

MDPI

Article

Variation Characteristics of Soil Organic Carbon Storage and Fractions with Stand Age in North Subtropical *Quercus acutissima* Carruth. Forest in China

Wenbin Deng [1,2,†], Xia Wang [1,2,†], Haibo Hu [1,2,*], Mengdie Zhu [1,2], Jianyu Chen [1,2], Shuai Zhang [1,2], Can Cheng [1,2], Ziyi Zhu [1,2], Chaoming Wu [3] and Li Zhu [3]

[1] Co-Innovation Center for the Sustainable Forestry in Southern China, Nanjing Forestry University, Nanjing 210037, China
[2] Key Laboratory of Soil and Water Conservation and Ecological Restoration in Jiangsu Province, Nanjing 210037, China
[3] Wuxi Branch, Bureau of Investigation on Hydrologic Water Resources, Wuxi 214100, China
* Correspondence: hhb@njfu.com.cn
† These authors contributed equally to this work.

Abstract: Soil labile organic carbon sensitively reflects subtle changes in the soil carbon pool and is an important aspect of forest soil carbon pool research. However, little is known regarding soil labile organic carbon storage and its dynamic changes during the development of *Quercus acutissima* Carruth. forests. Consequently, we investigated the dynamic changes in soil organic carbon and its labile organic carbon fraction stocks at soil depths of 0–10 cm, 10–20 cm, and 20–40 cm along a 17-year-old, 26-year-old, and 65-year-old chronosequence in *Quercus acutissima* forests. We found that stand age significantly impacted particulate organic carbon (POC), light fraction organic carbon (LFOC), and soil organic carbon (SOC). The POC, LFOC, and SOC contents at different soil depths exhibited an increasing trend with stand age, which could be described by simple linear regression. However, there was no noteworthy difference in the soil water-soluble organic carbon (WSOC) content between different stand ages. Moreover, the 17-year-old, stand had higher POC, LFOC, and WSOC to SOC ratios. Soil nutrients significantly affected organic carbon and fractions, which revealed that POC, LFOC, WSOC, and SOC were remarkably positively correlated with alkaline hydrolysis nitrogen (AN) and available phosphorus (AP) ($p < 0.05$). Furthermore, WSOC, POC, LFOC, and SOC were significantly positively correlated with available potassium (AK) ($p < 0.05$). POC, LFOC, and SOC storage in the 0–40 cm soil layer increased with stand development, while WSOC storage decreased at 65a. In addition, LFOC stocks accounted for the highest proportion of organic carbon stocks. Our results indicated that the development of *Quercus acutissima* forests was a process of carbon sink; however, the soil organic carbon activity was high, and the soil structure was unstable during the early development stage.

Keywords: soil labile organic carbon; soil carbon pool; *Quercus acutissima* forests; chronosequence

check for updates

Citation: Deng, W.; Wang, X.; Hu, H.; Zhu, M.; Chen, J.; Zhang, S.; Cheng, C.; Zhu, Z.; Wu, C.; Zhu, L. Variation Characteristics of Soil Organic Carbon Storage and Fractions with Stand Age in North Subtropical *Quercus acutissima* Carruth. Forest in China. *Forests* **2022**, *13*, 1649. https://doi.org/10.3390/f13101649

Academic Editor: Keryn Paul

Received: 31 August 2022
Accepted: 5 October 2022
Published: 8 October 2022

Publisher's Note: MDPI stays neutral with regard to jurisdictional claims in published maps and institutional affiliations.

Copyright: © 2022 by the authors. Licensee MDPI, Basel, Switzerland. This article is an open access article distributed under the terms and conditions of the Creative Commons Attribution (CC BY) license (https://creativecommons.org/licenses/by/4.0/).

1. Introduction

Since the Industrial Revolution, the concentration of CO_2 in the ambient atmosphere has cumulatively increased by 50%, from 278 ppm before the Industrial Revolution to 417 ppm in June 2022 [1]. Global warming due to increased atmospheric CO_2 concentrations, leads to ocean warming, glacial retreat, rising sea levels, and extreme weather events that alter natural cycles worldwide [2]. As the largest carbon pool in terrestrial ecosystems, the continuous exchange of carbon between the soil carbon pool and ambient atmosphere significantly affects the global carbon cycle and climate [3,4]. Approximately 30.7% of Earth's land area is covered by forests (2016) [5], and more than two-thirds of the carbon in forest ecosystems is sequestered in soils and associated peat deposits [6]. Therefore,

small modifications in the organic carbon pools of forest soils can translate to changes in atmospheric CO_2 concentrations; thus, forests play a unique role in the reduction in atmospheric carbon dioxide concentrations [7,8] and play a critical role in regulating the global carbon cycle and mitigating global warming.

Forest-based warming mitigation strategies will play a key role toward achieving the rapid and deep net-emissions reductions required to prevent catastrophic climate change [9]. Differences in the canopy densities, stand structures, and vegetation compositions of forests across age sequences can lead to variations in the soil microclimate, as well as the quantity and quality of aboveground and belowground litter inputs [10–12]. Consequently, this can alter soil nutrient cycling and carbon flows due to complex plant-soil interactions, which leads to considerable uncertainties in the relationship between the ages of trees and carbon stocks for individual stands [13,14]. Although the variable characteristics of soil carbon storage have been investigated in independent studies of carbon storage for stands of different ages (e.g., 0 to 8-year-old *Eucalyptus* plantations [15]; 29 to 46-year-old Dragon spruce forests [7]; 0 to 110-year-old Scots pine [16]; and 40 to 120-year-old secondary tropical forests [17]), the dynamic changes related to stand age were complex. Consequently, detailed data are required to elucidate changes in the carbon stocks of soil at different developmental stages in forest ecosystems of specific regions. This, to provide a theoretical basis for the improved assessment of the balance between terrestrial and atmospheric carbon.

Studies have indicated that the stability of soil organic carbon depends on interactions between soil aggregates and soil resident minerals [18] and is positively correlated with the labile organic carbon input rate [19]. Soil labile organic carbon (LOC) is a mixture of organic matter that has high availability, and is easily decomposed and utilized by soil microorganisms, which can also directly supply nutrients to plants [20]. As soil labile organic carbon is extremely sensitive to changes in the soil environment, even minor shifts in soil ecosystems will alter its content; thus, it is often employed as an indicator for the evaluation of soil quality and environmental changes [21]. Labile fractions, such as water-soluble organic carbon (WSOC), light fraction organic carbon (LFOC), and particulate organic carbon (POC), are characterized by their easy decomposition and a brief turnover period [22]. Thus, they are typically considered as sensitive indices for changes in soil organic carbon that result from the dynamic responses of vegetation. Soil WSOC is comprised of various soluble organic residues, is the primary available material and energy source for soil microorganisms, and a potential source of carbon sequestration in soils [23], which is generally regarded as the most unstable fraction of soil organic carbon [24]. Therefore, soil WSOC plays an essential role in the accumulation of soil nutrients [25]. Soil POC consists of plant residues, seeds, and microbial debris, which are not enclosed within soil microaggregates [26]. Soil LOC fractions possess the attributes of easy mineralization, easy decomposition, and a short turnover period [22]. Since labile organic carbon can directly participate in the transformation of soil biochemistry and quickly respond to changes in soil organic matter, it is often utilized as an indicator to measure changes in soil carbon pools [27].

As a major contributor to ecosystem functionality, *Quercus acutissima* Carruth. is regarded as an indicator species for the localized assessment of forest health [28]. It is not only one of the most abundant Quercus species in East Asia; it can also adapt to an extensive range of ecological conditions and is widely distributed across China (18° N to 41° N, 91° E to 123° E) [29], spanning an estimated 7451.5 km^2 [30]. *Quercus acutissima* is a pioneer tree species of barren mountains and hills, as well as a pioneer tree species for soil and water conservation, which, in addition to having high ecological, economic, and landscape value [31], is used as timber, fuelwood, charcoal, and acorn production [32]. In the context of global climate change and multifunctional forest management, much research has been conducted on the cultivation technology, development and utilization, physiological and ecological characteristics, and genetic diversity of *Quercus acutissima* [33–36]. However, during the development of *Quercus acutissima* forests the dynamic changes in soil organic

carbon storage and organic carbon fractions, particularly those in labile organic carbon, remain poorly understood. Thus, the purpose of this study was to reveal the influences of stand age on changes in soil labile organic carbon and organic carbon storage and determine the key factors that affect soil labile organic carbon during *Quercus acutissima* development. Furthermore, this study assumed that the growth of *Quercus acutissima* stands was conducive to the accumulation of soil organic carbon.

2. Materials and Methods

2.1. Study Area

The study area is in the Xiashu and Jurong Forest Farms in Jurong City (32°07′ N, 119°12′ E), Jiangsu Province, China (Figure 1). The climate here is a subtropical humid monsoon with an average annual temperature of 15.5 °C and annual precipitation of 1126.4 mm (1969–2018). The average annual relative humidity is 79%, whereas the frost-free period is 233 days. The parent soil material is Quaternary Xiashu Formation (Q_3x) loess-like sediments, which is primarily a yellow-brown soil and mountain yellow-brown soil. The thickness of the soil layer is generally 40–60 cm, and the soil texture is medium to heavy, with a pH of between 4.5 and 5.0. The forest vegetation is derived from the subtropical evergreen broad-leaved forest area of China, and the zonal vegetation is a deciduous broadleaved mixed forest. The experimental site is a natural secondary forest dominated by *Quercus acutissima*, with several *Quercus aliena* var. *acutiserrata*, and *Quercus variabilis* scattered sporadically. The main shrubs include *Rosa multiflora*, *Fortunearia sinensis*, *Callicarpa cathayana*, *Ilex cornuta*, and *Symplocos paniculata*, etc., whereas the herbs mainly include *Parthenocissus tricuspidata*, *Adiantum capillus-veneris*, and so on.

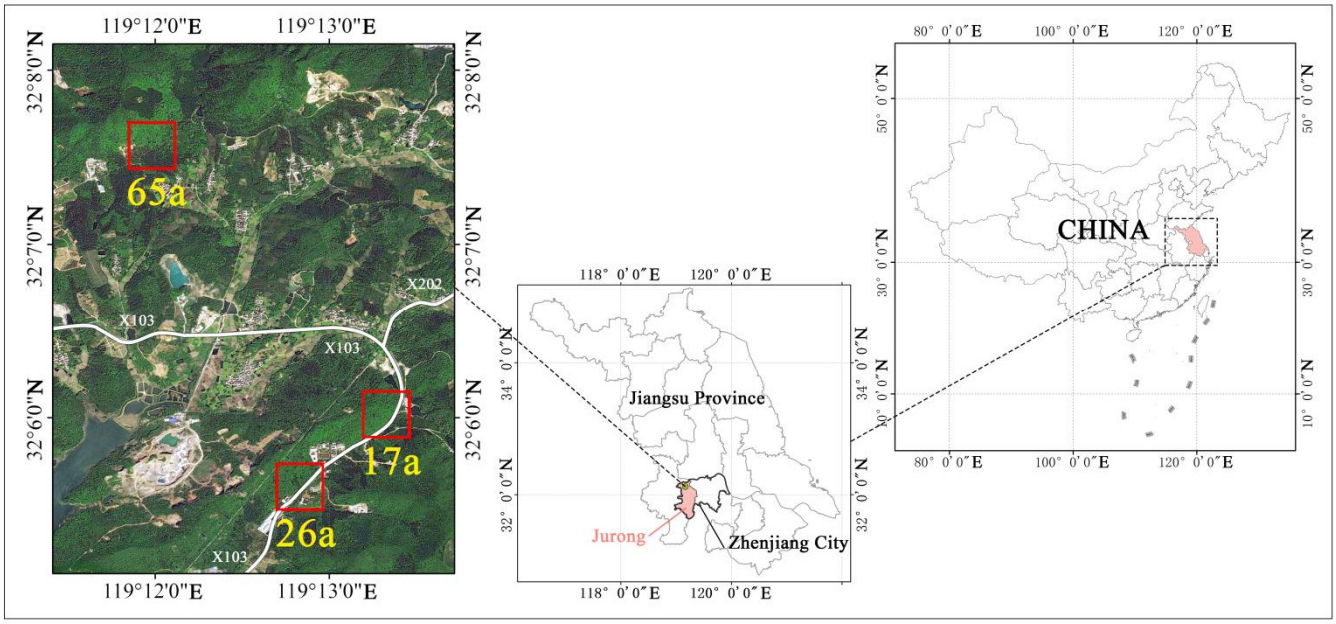


Figure 1. Location of the study site. 17a, 17-year-old stand; 26a, 26-year-old stand; 65a, 65-year-old stand.

2.2. Experimental Design and Sampling

Three differently aged *Quercus acutissima* forest stands were selected (young forest (17-years-old, 17a), half-mature forest (26-years-old, 26a), and mature forest (65-years-old, 65a)). Three experimental plots (20 m × 20 m) were selected according to their slope positions (e.g., upper, middle, and lower) in each forest stand, for a total of nine sample plots that were established, with an inter-plot distance of >20 m. Trees in the *Quercus acutissima* forest sample plots were measured; the diameters at breast height (DBH) and tree heights were recorded; and the overall stand topographies and characteristics were investigated (Table 1). We collected three soil sub-samples with a "diagonal" type distribution at each depth (i.e.,

0–10 cm, 10–20 cm, 20–40 cm) in each plot and mixed the three sub-samples of each plot to a composite soil sample and sifted through a 2 mm sieve to remove plant tissue, roots and gravel. Following natural air-drying and grinding, the physicochemical properties, organic carbon, and labile organic carbon fractions of the soil were analyzed.

Table 1. Basic characteristics of sampling plots studied.

Sample Plot Number	Stand Age/(a)	Stand Density/ (Tree·m^{-2})	Slope Gradient/(°)	Slope Aspect	Diameter at Breast Height/(cm)	Height/(m)	Canopy Density/(%)
1	17	975	30	Southeast	10.2	8.60	48
2	17	700	34	Southeast	10.7	8.85	45
3	17	300	40	Southeast	14.2	10.31	35
4	26	775	8	North	13.4	9.94	80
5	26	825	8	North	15.2	10.63	80
6	26	600	8	North	14.2	10.31	75
7	65	225	28	Southeast	28.6	15.25	55
8	65	325	31	Southeast	26.9	14.73	45
9	65	350	28	Southeast	25.3	14.20	47

2.3. Soil Physical and Chemical Analyses

The soil texture was analyzed using a Laser Particle Analyzer (Microtrac Inc., North Largo, FL, USA), and the gravel volume percentage was measured via the Archimedes method. The soil bulk density (BD) was determined using the cutting ring (Ø50.46 mm × 50 mm high) method. The soil pH was quantified using the glass electrode technique, and the air-dried soil-to-water ratio was l:2.5 (*m*:*v*). The alkaline hydrolysis nitrogen (AN), available potassium (AK), and available phosphorus (AP) contents of soil were measured using the alkali-diffusion, ammonium acetate extraction-flame photometer [37], and hydrochloric acid-sulfuric acid extraction and molybdenum-antimony anti-colorimetric methods, respectively.

2.4. Soil Organic Carbon and Labile Organic Carbon Analyses

The soil organic carbon (SOC) was determined using the potassium dichromate external heating oxidation-ferrous sulfate titration technique [38]. A 5 mL volume of 0.8 M $K_2Cr_2O_7$ and 5 mL of H_2SO_4 were added to 0.1 g of air-dried soil and passed through a 0.149 mm sieve, which was then boiled in an oil bath at 170–180 °C for five min and cooled, after which an indicator was added and titrated with 0.2 M $FeSO_4$.

The soil particulate organic carbon (POC) was determined using the method of [39]. A 20 g volume of air-dried soil was dispersed by shaking overnight in 100 mL solution of sodium hexametaphosphate (5 g/L). The soil mixture was then passed through a 0.053 mm sieve and rinsed repeatedly with distilled water. The sieve residue (i.e., the particulate organic matter portion, >0.053 mm) was dried and weighed. Subsequently, the organic carbon content of the particulate organic matter was determined.

The soil water-soluble organic carbon (WSOC) was determined by modifying the technique described by Yang et al. [40], through extraction with deionized water (the mass ratio of water to soil was 2:1), after which the suspension was shaken at 210 rpm for 1 h, and then centrifuged at 3000 rpm for 15 min. The supernatant was filtered through a 0.45-μm polycarbonate membrane, and the filtrate was assessed using an automatic TOC analyzer (TOC-L CPH CN200, Shimadzu, Kyoto, Japan).

The soil light fraction organic carbon (LFOC) was fractionated using a method modified from McLauchlan and Hobbie [41]. A 10 g volume of air-dried soil was sifted through a 2 mm sieve and placed in 50 mL of a NaI solution with a specific gravity of 1.7 g/cm^3. The soil was ultrasonically dispersed and following centrifugation the upper layer of the suspension was carefully passed through a 0.45-μm polycarbonate membrane. The NaI solution of a single sample was recovered via suction filtration, washed with a $CaCl_2$ solution to separate the light portion, repeatedly rinsed with deionized water, and then dried in a 60 °C oven for 48 h to a constant weight and weighed. The above process was

typically repeated two to three times, where the sum of the light groups separated multiple times was the number of light groups. The light soil group samples were passed through a 0.149 mm sieve and their organic carbon content was determined using the acid dichromate wet oxidation technique.

2.5. Stock Calculation of SOC and Fractions

The SOC and fraction storage ($t \cdot hm^{-2}$) was calculated using the following equation:

$$S(t \cdot hm^{-2}) = \sum_{i}^{n} H_i \times BD_i \times C_i \times (100 - G_i) \times 10^{-3} \quad (1)$$

where S is the storage of SOC or fraction ($t \cdot hm^{-2}$), H_i is the thickness of the i layer (cm), BD_i is the soil bulk density of the i layer ($g \cdot cm^{-3}$), C_i is the organic carbon or fraction content of the i layer ($g \cdot kg^{-1}$), G_i is the volume percentage (%) of gravel with diameters of $\geq$2 mm in the i layer.

2.6. Statistical Analyses

SPSS 22.0 statistical software was employed for the statistical analysis of all data, where the data of each variable were tested by normality and homogeneity. ANOVA was utilized to estimate the impacts of stand age on soil properties and organic carbon components. The LSD test revealed significant differences under $p < 0.05$. Redundancy analysis was used to study the relationships between organic carbon components and soil physicochemical properties for differently aged *Quercus acutissima.* Canoco5.0 and GraphPad Prism9.0 were used for plotting.

3. Results

3.1. Soil Properties

The soil sand, and silt contents of the three stand ages revealed significant differences. The clay content of the 17a stands was significantly lower than that of the 26a and 65a stands, and no significant differences in pH were measured between the three stand ages ($p > 0.05$). The soil BD of the 26a stands was remarkably higher ($p < 0.05$) than the other stand ages. The AN, AP, and AK contents of the 65a stands were higher than those in the 17a and 26a stands and the differences between soil layers were significant, which generally decreased with soil depth. Furthermore, there were no significant differences in the soil mechanical composition, BD, and pH between the soil layers (Table 2).

3.2. Soil Labile Organic Carbon

Soil depth had a significant influence on both soil organic carbon and labile organic carbon. In addition to WSOC, stand age significantly affected POC, LFOC, and SOC, while POC, WSOC, LFOC, and SOC were insensitive to the interactive impacts of stand age and soil depth (Table 3).

The POC content at different soil depths increased with stand age, which could be described by simple linear regression (Figure 2A). In the 17 to 65-years-old stands, the POC content within the 0–10 cm soil layer increased from 4.74 $g \cdot kg^{-1}$ to 9.68 $g \cdot kg^{-1}$; the 10–20 cm soil layer increased from 2.34 $g \cdot kg^{-1}$ to 6.53 $g \cdot kg^{-1}$; and the 20–40 cm soil layer increased from 0.59 $g \cdot kg^{-1}$ to 2.81 $g \cdot kg^{-1}$ (Figure 2A). The POC/SOC ratio within the 20–40 cm soil layer increased linearly by 6.40%, while the 0–10 cm and 10–20 cm soil layers did not exhibit an obvious trend with stand age (Figure 3A). Moreover, the ratio was higher in 17a and 65a, albeit the difference was not significant.

Table 2. Soil physical and chemistry properties of different stand ages. When $p < 0.05$, different capital letters represent differences between forest ages in the same soil layer, whereas different lowercase letters represent differences between soil layers at the same forest age. BD, bulk density; AN, alkaline hydrolysis nitrogen; AP, available phosphorus; AK, available potassium (mean ± SE, n = 3).

Stand Age (a)	**17**			**26**			**65**		
Soil depth (cm)	0–10	10–20	20–40	0–10	10–20	20–40	0–10	10–20	20–40
Sand (%)	63.75 ± 16.35 Aa	77.35 ± 8.15 Aa	59.40 ± 18.65 Aa	23.65 ± 19.78 Ba	27.23 ± 14.59 Ba	22.94 ± 7.18 Ba	40.81 ± 4.60 Ca	43.05 ± 2.87 Ca	38.89 ± 6.72 Ca
Silt (%)	34.15 ± 15.29 Aa	21.02 ± 7.23 Aa	36.72 ± 16.71 Aa	67.13 ± 15.72 Ba	64.52 ± 11.95 Ba	69.26 ± 6.41 Ba	50.31 ± 4.11 Ca	45.45 ± 3.65 Ca	52.91 ± 5.51 Ca
Clay (%)	2.11 ± 2.13 Aa	1.64 ± 0.92 Aa	3.88 ± 2.32 Aa	9.19 ± 4.16 Ba	8.18 ± 3.38 Ba	7.79 ± 1.36 Ba	8.87 ± 2.79 Ba	11.50 ± 3.46 Ba	8.20 ± 4.65 Ba
BD ($g \cdot cm^{-3}$)	1.35 ± 0.03 Aa	1.44 ± 0.18 Aa	1.38 ± 0.10 Aa	1.47 ± 0.02 Ba	1.70 ± 0.05 Ba	1.71 ± 0.05 Ba	1.32 ± 0.09 Aa	1.20 ± 0.33 Aa	1.28 ± 0.28 Aa
pH	4.68 ± 0.48 Aa	4.72 ± 0.16 Aa	4.47 ± 0.12 Aa	4.72 ± 0.05 Aa	4.60 ± 0.29 Aa	4.60 ± 0.03 Aa	4.48 ± 0.12 Aa	4.44 ± 0.10 Aa	4.52 ± 0.13 Aa
AN ($mg \cdot kg^{-1}$)	105.00 ± 32.08 Aa	72.33 ± 10.69 Ab	42.00 ± 7.00 Ac	119.00 ± 14.00 Aa	70.00 ± 7.00 Ab	53.67 ± 8.08 Ac	212.33 ± 32.33 Ba	135.33 ± 21.39 Bb	100.33 ± 10.69 Bc
AP ($g \cdot kg^{-1}$)	6.86 ± 1.76 Aa	8.48 ± 0.98 Ab	6.43 ± 2.15 Ac	10.27 ± 1.49 Aa	4.72 ± 0.71 Ab	2.71 ± 0.26 Ac	15.76 ± 4.22 Ba	7.82 ± 2.00 Bb	4.68 ± 2.20 Bc
AK ($mg \cdot kg^{-1}$)	155.42 ± 58.04 Aa	168.17 ± 23.01 Aa	133.56 ± 19.10 Aa	218.4 ± 13.34 Bb	193.75 ± 15.45 Bb	185.42 ± 15.62 Bb	226.73 ± 23.11 Bc	189.35 ± 5.32 Bc	201.74 ± 33.32 Bc

Note: International system, Stand 0.02–2 mm, Silt 0.002–0.02 mm, Clay <0.002 mm.

Table 3. Effects (F-ratio, *p*-values) of stand age, soil depth, and their interactions on the concentration of soil carbon fractions. SOC, soil organic carbon; POC, particulate organic carbon; WSOC, soil water-soluble organic carbon; LFOC, light fraction organic carbon. * represents statistical significance, in which ** $p < 0.01$, and *** $p < 0.001$.

Index	**Stand Age**		**Soil Depth**		**Stand Age × Soil Depth**	
	F Value	***p* Value**	**F Value**	***p* Value**	**F Value**	***p* Value**
POC	18.006	<0.001 ***	40.953	<0.001 ***	1.643	0.207
WSOC	0.349	0.710	12.739	<0.001 ***	1.291	0.311
LFOC	10.046	0.001 **	7.968	0.003 **	0.336	0.850
SOC	11.098	0.001 **	7.863	0.004 **	0.245	0.909

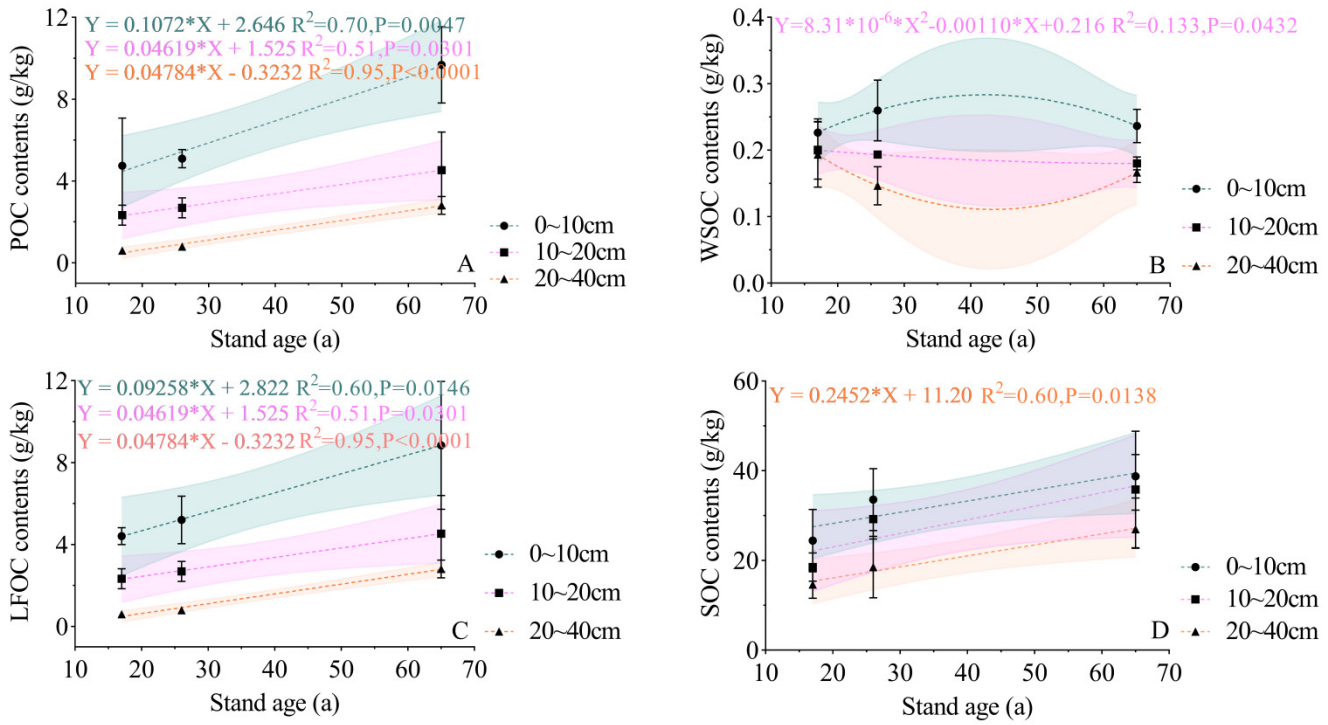


Figure 2. Variations in soil labile organic carbon with stand age. particulate organic fraction (POC, (**A**)); soil water-soluble organic carbon (WSOC, (**B**)); light fraction organic carbon (LFOC, (**C**)); soil organic carbon (SOC, (**D**)) (mean ± SD, n = 3).

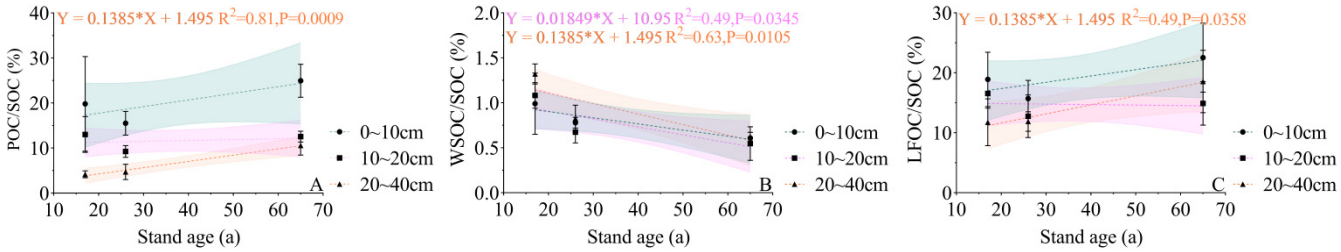


Figure 3. Ratio of soil labile organic carbon fractions and organic carbon in differently aged *Quercus acutissima* forests. Ratio of particulate organic carbon and organic carbon (POC/SOC, (**A**)); Ratio of soil water-soluble organic carbon and organic carbon (WSOC/SOC, (**B**)); Ratio of light fraction organic carbon and organic carbon (LFOC/SOC, (**C**)) (mean ± SD, n = 3).

There was no significant difference in the soil WSOC content between stand ages (Table 3). The WSOC content within the 10–20 cm and 20–40 cm soil layers generally decreased with stand development, and the change trend within the 0–10 cm soil layer was not obvious (Figure 2B). Contrary to POC, the proportion of WSOC to SOC had a significantly negative correlation with stand age, and the proportion tended to increase with the greater soil depth (Figure 3B).

The tendency of the soil LFOC changes was akin to that of the POC, which increased with the changing chronosequence (Figure 2C). Moreover, the LFOC and POC had a good linear relationship (Figure 4B). The LFOC concentration within the 0–10 cm, 10–20 cm, and 20–40 cm soil layers of the 65a stands was 2.0, 1.8, and 3.0 times that of the 17a stands, respectively (Figure 2C). The ratio of LFOC to SOC within the upper soil layer (0–20 cm) was lowest in the 26a stands (12.75%), while the ratio of LFOC to SOC in the deeper soil layer (20–40 cm) increased during stand development (Figure 3C).

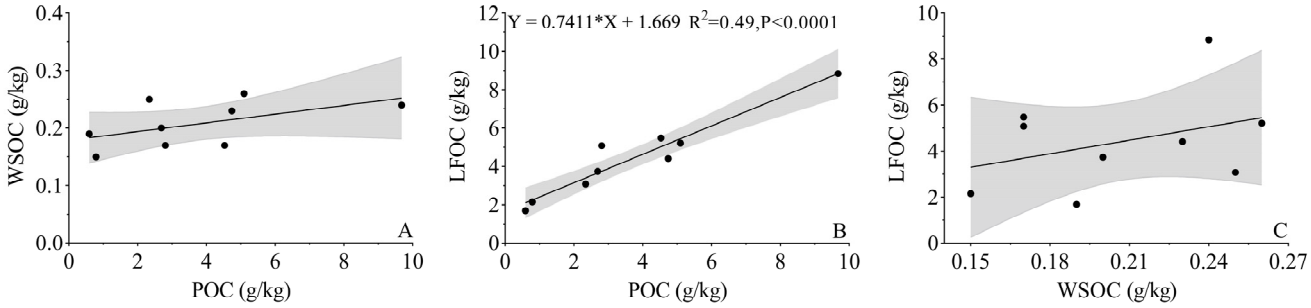


Figure 4. Relationships between labile organic carbon fractions in *Quercus acutissima* forest. Relationships between soil water-soluble organic carbon (WSOC) and particulate organic carbon (POC) (**A**); Relationships between light fraction organic carbon (LFOC) and particulate organic carbon (POC) (**B**); Relationships between light fraction organic carbon (LFOC) and soil water-soluble organic carbon (WSOC) (**C**).

During stand development, the SOC content increased significantly; 65a stands were roughly 1.6–1.9 fold and 1.2–1.5 fold higher than the 17a and 26a stands, respectively. Furthermore, compared with the 0–10 cm soil layer, the SOC concentration was higher than those in the 10–20 cm and 20–40 cm soil layers (Figure 2D).

3.3. Factors Affecting Composition of Soil Labile Organic Carbon

The redundancy analysis revealed the relationships between the physicochemical soil properties and organic carbon and labile organic carbon in differently aged *Quercus acutissima* forests (Figure 5). Axis 1 and 2 accounted for 62.13% and 11.2% of the total variation in soil organic carbon and its labile fractions, respectively. The POC, WSOC, LFOC, and SOC exhibited a notably positive correlation with AN and AP ($p < 0.05$). The POC, LFOC, and SOC were positively correlated with AK, whereas WSOC was not. Only clay had a significant relationship with LFOC and SOC ($p < 0.05$). Additionally, there were no significant relationships between the POC, WSOC, LFOC, SOC and sand, silt, BD, and pH.

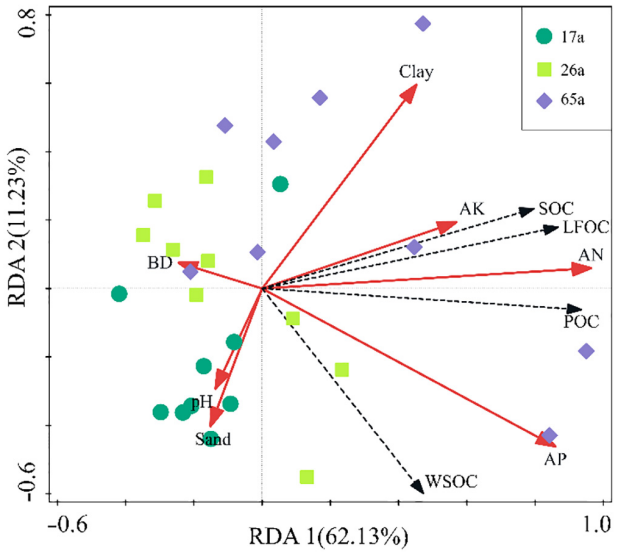


Figure 5. Redundancy analysis screening of soil physicochemical properties (red arrows) affecting the soil carbon fraction (black arrows). SOC, soil organic carbon; POC, particulate organic carbon; WSOC, soil water-soluble organic carbon; LFOC, light fraction organic carbon; BD, bulk density; AN, alkaline hydrolysis nitrogen; AP, available phosphorus; AK, available potassium; 17a, 17-year-old stand; 26a, 26-year-old stand; 65a, 65-year-old stand.

3.4. Soil Carbon Storage

As revealed from the results, POC, LFOC, and SOC storage within the 0–40 cm soil layer increased with stand development, while WSOC storage decreased in the 65a stand (Figure 6). The SOC and labile organic carbon fraction content was significantly reduced with depth. However, this was not reflected in the SOC and labile organic carbon fraction stocks due to changes in the soil gravel volume percentage and bulk density, and carbon stocks did not change markedly with soil depth. The POC storage values of the 0–40 cm soil layer in the 26a and 65a stands were 1.28 and 2.42 times higher, respectively, than that in the 17a stands (Figure 6A). The total WSOC storage ranged from 0.80 to 0.93 t·hm^2 across the chronosequence (Figure 6B). The soil LFOC storage in the 0–40 cm soil depth of the 26a and 65a stands was 42.60% and 130.86% higher, respectively, than those in the 17a stands (Figure 6C). The SOC storage within the 0–40 cm soil layer in the 17a, 26a, and 65a stands was 73.37, 124.33, and 137.60 t·hm^2, respectively (Figure 6D). The proportion of POC, WSOC, and LFOC fraction storage to SOC storage was 9.46%–16.26%, 0.60%–1.12%, and 13.38%–18.81%, respectively.

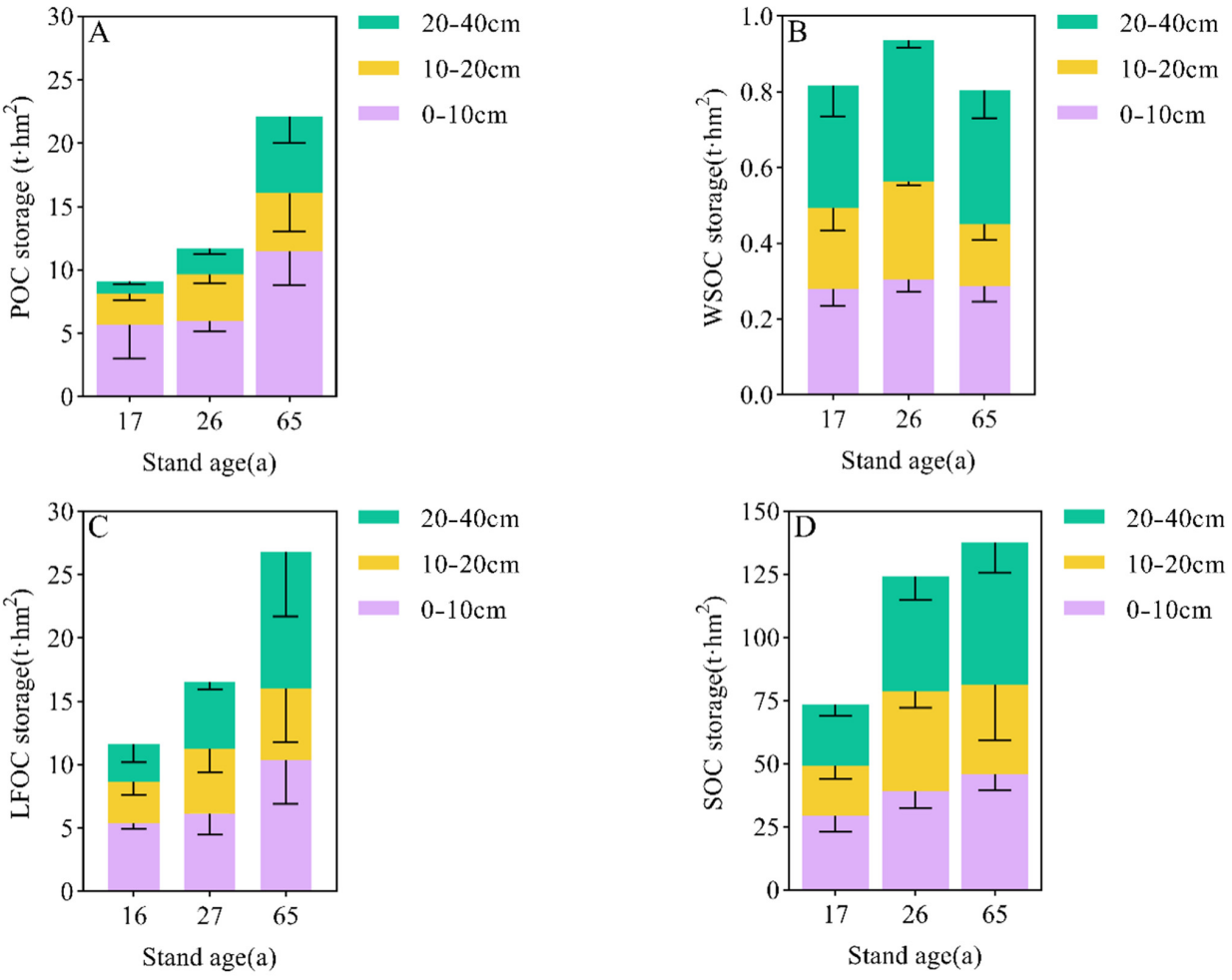


Figure 6. Soil carbon storage of three age groups. particulate organic fraction (POC, A);soil water-soluble organic carbon (WSOC, B); light fraction organic carbon (LFOC, C); soil organic carbon (SOC, D) (mean ± SD, n = 3).

4. Discussion

4.1. Variations in SOC Content and Labile Organic Carbon Fractions across Forest Ages

This study found that stand age and soil depth notably affected changes in soil carbon (Table 3). Since numerous studies found that soil depth significantly impacted the SOC content and labile organic carbon fractions, which decreased with greater soil depth [12,42],

it does not appear in the discussion of this study. Stand age is related to the structure of forests, which can regulate the soil microenvironment and quantity of plant litter [10]; thus, the influence of the distribution of soil carbon fractions during stand development remains uncertain.

The primary sources of POC include microbial biomass debris, residual roots, stubble biomass, and animal manure [43]. LFOC is typically comprised of soil organic matter, which includes mainly animal and plant residues, mycelium, spores, monosaccharides, polysaccharides, and hemilignin [44,45]. For one thing, plant litter inputs are an important source of soil carbon, and aboveground litter tends to be enriched during stand development [46]. For another, as stands develop, soil microbial communities gradually become highly efficient and parsimonious, while the quantity, activities, and related intermediates of soil microbes increase [47]. Furthermore, in this study, the soil AP, AN, and AK generally increased with stand development (Table 2), where relationships between the soil AP, AN, AK, POC, WSOC, LFOC, and SOC concentrations were significantly positively correlated (Figure 5). This indicated that soil nutrients provided an adequate material guarantee for the metabolic activities of soil microorganisms during stand development. Therefore, the LFOC and POC contents tended to increase during the stand development stage, which could be well fitted by a linear function, while the contents of WSOC decreased with the stand development; thus, the correlation with stand age was not obvious (Figure 2). On one hand, litter residue inputs and root exudates were the main sources of soil WSOC [48,49], and the root biomass of *Quercus acutissima* forest decreased with stand development [50], which was consistent with the changing WSOC content with stand age (Figure 2B). Conversely, WSOC is a type of organic carbon in the soil that can be dissolved in water by extraction, which includes simple organic molecules such as carbohydrates, amino acids, and small proteins [51]. Moreover, WSOC is more mobile and robust during rainy summers [52]; therefore, it is less impacted by stand age.

LOC/SOC are generally considered as indicators of changes in soil nutrient status [53,54] and organic carbon dynamics [55], which can indirectly reflect the stability and resilience of carbon pools in forest ecosystems [11]. The ratio of soil labile organic carbon to total organic carbon can better reflect the status of the soil labile organic carbon pool. The higher the proportion of labile organic carbon in the total soil carbon, the greater the activity of soil carbon, and the lower its stability [56]. During stand development, except for WSOC, the proportions of POC and LFOC were higher in the 17a and 65a stands; however, the difference was not obvious (Figure 3A,C), which indicated that their soil organic carbon activities were high and carbon pool stability was low. While the WSOC:SOC ratio showed a decreasing trend, it was also found to be larger in the 17a stand (Figure 3B), which may have been due to the relatively high WSOC content. This meant that the soil structure in the early stage of *Quercus acutissima* forest development was unstable, and SOC was more easily depleted.

4.2. Effects of Stand Age on Soil Carbon Storage

The average organic carbon stock of 111.17 $Mg \cdot hm^{-2}$ reported in this study was within the average range of from 96 to 344 $Mg \cdot hm^{-2}$, which was reported from tropical, temperate, and boreal forest ecosystems [57]. Furthermore, the increase in soil carbon stocks with stand age in this study was similar to that reported for the first few decades following Pine, Masson pine, and Chinese fir afforestation [14,58,59]. This also validated our hypothesis that the development of *Quercus acutissima* stands was beneficial for the accumulation of soil organic carbon. Several studies revealed that soil carbon storage decreased with a greater stand age than half-mature forests [14,59]. Although the WSOC storage of our study illustrated this rule, carbon stocks of nearly-mature (40–50a) and overly-mature forests (>70a) were not investigated. Therefore, it remains unknown whether total organic carbon stocks and other labile organic carbon stocks continue to increase after middle-age in *Quercus acutissima* forests. Changes observed in the SOC pool with stand age indicated that stand age controlled biological processes in this ecosystem. The insignificant differences in carbon storage between the half-mature and mature forests in this research suggested that

the SOC pool was approaching the carrying capacity of forest soil C [59]. It may have been that the carbon inputs from litter and the forest floor can be balanced by increased carbon outputs driven by microbial decomposition, which results in relatively stable soil carbon pools over a chronosequence [60].

Changes in the SOC storage: length of period ratio may be employed as indicators to estimate the rates of increase or decrease in SOC storage [14,61]. There are significant variations in the rate and temporal duration required for carbon accumulation in soil, which are related to the productivity of restored vegetation, physical and biological conditions in the soil, and the history of SOC inputs and physical disturbances [62]. In this study, for *Quercus acutissima* forests from 17 to 26 years and 26 to 65 years, the increasing rates of SOC, POC, and LFOC storage within the 0–40 cm soil layer decreased from 566.16 to 34.04 $g \cdot m^{-2} \cdot a^{-1}$, 28.23 to 26.79 $g \cdot m^{-2} \cdot a^{-1}$, and 54.99 to 26.30 $g \cdot m^{-2} \cdot a^{-1}$, respectively (Figure 6). These results showed that the increased rate of carbon storage in the later stage development of *Quercus acutissima* forests was lower than that during early-stage development. This may have been due to a considerable increase in the biomass of litter during the early stage of *Quercus acutissima* forest development, which promoted nutrient cycling in the young *Quercus acutissima* forest soil [63]. Moreover, related studies indicated that stand age may have the greatest impact on soil carbon storage during the first 10–30 years, and there were other factors that could not be included in our analysis [19,64,65]. Most of the reported rates of change in SOC stocks were typically in orders of magnitude, where the rate of increase in soil organic carbon stocks in the 17–26a *Quercus acutissima* forest of this study was higher than that for the 18–28a *Pinus massoniana* forest soil 0–40 cm (124 $g \cdot m^{-2} \cdot a^{-1}$) [66]. Furthermore, the rate of increase for soil LFOC storage was significantly higher than that of other soil organic carbon fractions, which signified that soil LFOC sensitively reflected the dynamic changes in soil organic carbon storage during *Quercus acutissima* forest development. He et al. [14] found that the soil carbon storage within the 0–20 cm soil layer in a Chinese fir forest increased from 0 to 17 years, and then decreased from 17 to 26 years; thus, the soil carbon storage changed from carbon sink to carbon source in 17 years. In this study, due to the lack of carbon storage data for near-mature forests (40–50a) and over-mature forests (>70a), it was not explored whether the soil carbon pool would transition from a carbon sink to a carbon source during the growth and development of the *Quercus acutissima* forest; thus, further investigations are required.

5. Conclusions

This study elucidated that the LFOC and POC contents showed an increasing trend during the development stage of forest stands, which could be well fitted to a linear function, while WSOC showed an opposite trend. During the stand development stage, the proportion of POC, WSOC, and LFOC in SOC in the 17a stand was relatively high, which indicated that the soil organic carbon activity was high, but the carbon pool stability was low during the early stage of *Quercus acutissima* forest stand development. With stand development, the POC, LFOC, and SOC carbon storage were increased; however, the increased rate of carbon storage during the latter stage of *Quercus acutissima* forest development was lower than that during the early stage. This indicated that the development of the *Quercus acutissima* forest involved a carbon sink process. Due to the lack of carbon storage data for near-mature forests (40–50a) and over-mature forests (>70a) in this paper, further research is required. Simultaneously, the soil LFOC storage capacity rate was significantly higher than that of other soil organic carbon fractions, which indicated that soil LFOC could sensitively reflect dynamic changes in soil organic carbon storage during the development of *Quercus acutissima* forests.

Author Contributions: Conceptualization, writing—original draft, review and editing, X.W., W.D. and H.H.; methodology and data curation, M.Z.; formal analysis and software, J.C.; investigation, S.Z., C.C. and Z.Z.; visualization, X.W. and W.D.; project administration, C.W. and L.Z.; funding acquisition and supervision, H.H. All authors have read and agreed to the published version of the manuscript.

Funding: This study was funded by Special fund project for technology innovation on Carbon Peak Carbon-neutral in 2021, Jiangsu Province (Grant No. BE2022305); Project of National positioning observation and research of forest ecosystem in Yangtze River Delta supported by State Forestry and Grassland Administration (Grant No. 2020132077); Technical Collaboration Project on Soil Carbon and Nitrogen Migration Monitoring and Ecological Service Function of Soil and Water Conservation in Hilly Areas of Wuxi City (Grant No. JSJGWXCG2022-09).

Data Availability Statement: Not applicable.

Acknowledgments: We would like to thank all the colleagues who participated in this research in one way or another during the experiments but were not included in the final authors' list.

Conflicts of Interest: The authors declare that they have no conflict of interest.

References

1. Dlugokencky, E.; Tans, P. Trends in Atmospheric Carbon Dioxide, National Oceanic & Atmospheric Administration, Earth System Research Laboratory (NOAA/ESRL). 2022. Available online: https://gml.noaa.gov/ccgg/trends/global.html (accessed on 18 September 2022).
2. IPCC. *Climate Change 2001: The Scientific Basis*; Cambridge University Press: Cambridge, UK, 2001.
3. Dib, A.E.; Johnson, C.E.; Driscoll, C.T.; Fahey, T.J.; Hayhoe, K. Simulating effects of changing climate and CO_2 emissions on soil carbon pools at the Hubbard Brook experimental forest. *Glob. Change Biol.* **2014**, *20*, 1643–1656. [CrossRef] [PubMed]
4. Gabriel, C.E.; Kellman, L.; Prest, D. Examining mineral-associated soil organic matter pools through depth in harvested forest soil profiles. *PLoS ONE* **2018**, *13*, e0206847. [CrossRef]
5. World Bank. Forest Area (% of Land Area). Available online: https://data.worldbank.org/indicator/AG.LND.FRST.ZS (accessed on 12 May 2022).
6. Dixon, R.K.; Brown, S.; Houghton, P.A. Carbon pools and flux of global forest ecosystem. *Science* **1994**, *263*, 185–190. [CrossRef] [PubMed]
7. Cao, J.J.; Gong, Y.F.; Adamowski, J.F.; Deo, R.C.; Zhu, G.F.; Dong, X.G.; Zhang, X.F.; Liu, H.B.; Xin, C.L. Effects of stand age on carbon storage in dragon spruce forest ecosystems in the upper reaches of the Bailongjiang River basin, China. *Sci. Rep.* **2019**, *9*, 3005. [CrossRef] [PubMed]
8. Guo, G.; Li, X.; Zhu, X.; Xu, Y.Y.; Dai, Q.; Zeng, G.R.; Lin, J. Effect of forest management operations on aggregate-associated SOC dynamics using a ^{137}Cs tracing method. *Forests* **2021**, *12*, 859. [CrossRef]
9. Erb, K.H.; Haberl, H.; Le-Noë, J.; Tappeiner, U.; Tasser, E.; Gingrich, S. Changes in perspective needed to forge "no-regret" forest-based climate change mitigation strategies. *GCB Bioenergy* **2022**, *14*, 246–257. [CrossRef] [PubMed]
10. Lucas-Borja, M.E.; Hedo, J.; Cerdá, A.; Candel-Pérez, D.; Viñegla, B. Unravelling the importance of forest age stand and forest structure driving microbiological soil properties, enzymatic activities and soil nutrients content in Mediterranean Spanishblack pine (*Pinus nigra* Ar. ssp. *salzmannii) forest. Sci. Total Environ.* **2016**, *562*, 145–154. [CrossRef]
11. Zhang, Y.; Tigabu, M.; Yi, Z.; Li, H.; Zhuang, Z.; Yang, Z. Soil parent material and stand development stage effects on labile soil C and N pools in Chinese fir plantations. *Geoderma* **2019**, *338*, 247–258.
12. Wang, C.Q.; Xue, L.; Jiao, R.Z. Soil organic carbon fractions, C-cycling associated hydrolytic enzymes, and microbial carbon metabolism vary with stand age in *Cunninghamia lanceolate* (Lamb.) Hook plantations. *For. Ecol. Manag.* **2021**, *482*, 118887. [CrossRef]
13. Mujuru, L.; Gotora, T.; Velthorst, E.J.; Nzamangara, J.; Hoosbeek, M.R. Soil carbon and nitrogen sequestration over an age sequence of *Pinus patula* plantations in Zimbabwean Eastern Highlands. *For. Ecol. Manag.* **2014**, *313*, 254–265. [CrossRef]
14. He, X.X.; Huang, Y.Z.; Zhang, Q.C.; Ye, S.M.; Wang, S.Q. Distribution of organic carbon fractions in soil aggregates in Chinese fir plantations with different stand ages. *Ecol. Process.* **2021**, *10*, 49. [CrossRef]
15. Du, H.; Zeng, F.P.; Peng, W.X.; Wang, K.L.; Zhang, H.; Liu, L.; Song, T.Q. Carbon storage in a *Eucalyptus* plantation chronosequence in Southern China. *Forests* **2015**, *6*, 1763–1778. [CrossRef]
16. Uri, V.; Kukumägi, M.; Aosaar, J.; Varik, M.; Becker, H.; Aun, K.; Lõhmus, K.; Soosaar, K.; Astover, A.; Uri, M.; et al. The dynamics of the carbon storage and fluxes in Scots pine (*Pinus sylvestris*) chronosequence. *Sci. Total Environ.* **2022**, *817*, 152973. [CrossRef] [PubMed]
17. Jones, I.L.; De-Walt, S.J.; Lopez, O.R.; Bunnefeld, L.; Pattison, Z.; Dent, D.H. Above and belowground carbon stocks are decoupled in secondary tropical forests and are positively related to forest age and soil nutrients respectively. *Sci. Total Environ.* **2019**, *697*, 133987. [CrossRef]

18. Cui, J.; Li, Z.X.; Liu, Z.T.; Ge, B.M.; Fang, C.M.; Zhou, C.L.; Tang, B.P. Physical and chemical stabilization of soil organic carbon along a 500-year cultived soil chronosequence originating from estuarine wetlands: Emporal patterns and land use effects. *Agric. Ecosyst. Environ.* **2014**, *196*, 10–20. [CrossRef]
19. Bradford, M.A.; Fierer, N.; Reynolds, J.F. Soil carbon stocks in experimental mesocosms are dependent on the rate of labile carbon.; nitrogen and phosphorusinputs to soils. *Funct. Ecol.* **2008**, *22*, 964–974. [CrossRef]
20. Janzen, H.H.; Campbell, C.A.; Brandt, S.A.; Lafond, G.P.; Townley-Smith, L. Light-fraction organic matter in soils from long-trem crop rotations. *Soil Sci. Soc. Am. J.* **1992**, *56*, 1799–1806. [CrossRef]
21. Wang, J.Y.; Song, C.C.; Wang, X.W.; Song, Y.Y. Changes in labile soil organic carbon fractions in wetland ecosystems along a latitudinal gradient in Northeast China. *Catena* **2012**, *96*, 83–89. [CrossRef]
22. Li, J.; Wen, Y.; Li, X.; Li, Y.; Yang, X.; Lin, Z.; Song, Z.; Cooper, J.M.; Zhao, B. Soil labile organic carbon fractions and soil organic carbon stocks as affected by long-term organic and mineral fertilization regimes in the North China Plain. *Soil Tillage Res.* **2018**, *175*, 281–290. [CrossRef]
23. Monteith, D.T.; Stoddard, J.L.; Evans, C.D.; de-Wit, H.A.; Forsius, M.; Hogasen, T.; Wilander, A.; Skjelkvale, B.L.; Jeffries, D.S.; Vuorenmaa, J.; et al. Dissolved organic carbon trends resulting from changes in atmospheric deposition chemistry. *Nature* **2007**, *450*, 537–541. [CrossRef]
24. Embacher, A.; Zsolnay, A.; Gattinger, A.; Munch, J.C. The dynamics of water extractable organic matter (WEOM) in common arable topsoils: II. Influence of mineral and combined mineral and manure fertilization in a Haplic Chernozem. *Geoderma* **2008**, *148*, 63–69. [CrossRef]
25. Spohn, M.; Novák, T.J.; Incze, J.; Giani, L. Dynamics of soil carbon, nitrogen, and phosphorus in calcareous soils after land-use abandonment—A Chronosequence Study. *Plant Soil.* **2015**, *401*, 185–196. [CrossRef]
26. Cadisch, G.; Imhof, H.; Urquiaga, S.; Boddey, R.M.; Giller, K.E. Carbon turnover ($\delta^{13}C$) and nitrogen mineralization potential of particulate light soil organic matter after rainforest clearing. *Soil Biol. Biochem.* **1996**, *28*, 1555–1567. [CrossRef]
27. Zhao, S.; Ta, N.; Li, Z.; Yang, Y.; Zhang, X.; Liu, D.; Zhang, A.F.; Wang, X.D. Varying pyrolysis temperature impacts application effects of biochar on soil labile organic carbon and humic fractions. *Appl. Soil. Ecol.* **2018**, *123*, 484–493. [CrossRef]
28. Zilliox, C.; Gosselin, F. Tree species diversity and abundance as indicators of understory diversity in French mountain forests: Variations of the relationship in geographical and ecological space. *For. Ecol. Manag.* **2014**, *321*, 105–116. [CrossRef]
29. Zhang, X.; Li, Y.; Fang, Y. Geographical distribution and prediction of potential ranges of *Quercus acutissima* in China. *Acta Bot. Boreali-Occident. Sin.* **2014**, *34*, 1685–1692.
30. Li, Y.C.; Li, Y.Q.; Wang, L.; Yu, H.Y.; Zhang, X.; Liu, P. Resource investigation and distribution pattern of *Quercus variabilis* Blume and *Quercus acutissima* Carr. as woody energy plant in China. *For. Resour. Manag.* **2013**, *1*, 94–101.
31. Guo, L.M.; Ni, R.Q.; Kan, X.L.; Lin, Q.Z.; Mao, P.L.; Cao, B.H.; Gao, P.; Dong, J.W.; Mi, W.D.; Zhao, B.P. Effects of precipitation and soil moisture on the characteristics of the seedling bank under *Quercus acutissima* forest plantation in Mount Tai, China. *Forests* **2022**, *13*, 545. [CrossRef]
32. Liu, Z.L.; Yu, M.K.; Ma, Y.; Tang, L.Z.; Fang, S.Z. A trend surface analysis of geographic variation in the traits of seeds and seedlings from different *Quercus acutissima* provenances. *Acta Ecol. Sin.* **2011**, *31*, 6796–6804.
33. Liu, X.; Tang, Y.Z.; Cheng, X.F.; Jia, Z.H.; Li, C.; Ma, S.L.; Zhai, L.; Zhang, B.; Zhang, J.C. Comparison of changes in soil moisture content following rainfall in different subtropical plantations of the Yangtze River Delta Region. *Water* **2021**, *13*, 914. [CrossRef]
34. Xiong, S.F.; Wang, Y.D.; Chen, Y.C.; Gao, M.; Zhao, Y.X.; Wu, L.W. Effects of drought stress and rehydration on physiological and biochemical properties of four oak species in China. *Plants* **2022**, *11*, 679. [CrossRef]
35. Gao, J.; Liu, Z.L.; Zhao, W.; Tomlinson, K.W.; Shang-Wen, X.; Zeng, Q.Y.; Wang, X.R.; Chen, J. Combined genotype and phenotype analyses reveal patterns of genomic adaptation to local environments in the subtropical oak Quercus acutissima. *J. Syst. Evol.* **2020**, *59*, 541–556. [CrossRef]
36. Cheng, X.R.; Yuan, H.J.; Xing, W.L.; Wang, Y.D.; Yu, M.K. Effects of provenance and initial planting density on growth and wood properties in young sawtooth oak (*Quercus acutissima*) plantations. *Eur. J. For. Res.* **2020**, *139*, 1067–1078. [CrossRef]
37. Kong, Y.; Ma, N.L.; Yang, Y.; Lai, Y.; Feng, Z.; Shao, X.; Xu, X.; Zhang, D. Examining CO_2 and N_2O Pollution and Reduction from Forestry Application of Pure and Mixture Forest. *Environ. Pollut.* **2020**, *265*, 114951. [CrossRef] [PubMed]
38. Nelson, D.W.; Sommers, L.E. Total carbon.; organic carbon and organic matter. In *Methods of Soil Analysis*; Sparks, D.L., Ed.; Madison Press: Madison, FL, USA, 1996; pp. 961–1010.
39. Garten, C., Jr.; Post, W.M., III.; Hanson, P.J.; Cooper, L.W. Forest soil carbon inventories and dynamics along an elevation gradient in the Southern Appalachian Mountains. *Biogeochemistry* **1999**, *45*, 115–145. [CrossRef]
40. Yang, C.M.; Ou, Y.Z.; Yang, L.Z.; Dong, Y.H. Organic carbon fractions and aggregate stability in an aquatic soil as influenced by agricultural land uses in the Northern China Plain. *Acta Ecol. Sin.* **2006**, *26*, 4148–4155.
41. McLauchlan, K.K.; Hobbie, S.E. Comparison of labile soil organic matter fractionation techniques. *Soil Sci. Soc. Am. J.* **2004**, *68*, 1616–1625. [CrossRef]
42. Li, W.; Zheng, Z.C.; Li, T.X.; Zhang, X.Z.; Wang, Y.D.; Yu, H.Y.; He, S.Q.; Liu, T. Effect of tea plantation age on the distribution of soil organic carbon fractions within water-stable aggregates in the hilly region of Western Sichuan, China. *Catena* **2015**, *133*, 198–205. [CrossRef]
43. Plante, A.F.; Conant, R.T.; Carlson, J.; Greenwood, R.; Shulman, J.M.; Haddix, M.L.; Paul, E.A. Decomposition temperature sensitivity of isolated soil organic matter fractions. *Soil Biol. Biochem.* **2010**, *42*, 991–1996. [CrossRef]

44. Christensen, B.T. *Physical Fractionation of Soil and Organic Matter in Primary Particle Size and Density Separates*; Advances in Soil Science: New York, NY, USA, 1992; pp. 1–90.
45. Christensen, B.T. Physical fractionation of soil and structural and functional complexity in organic matter turnover. *Eur. J. Soil Sci.* **2001**, *52*, 345–353. [CrossRef]
46. Zhu, Y.F.; Hu, H.B.; Xu, N.; Zhang, S.H. The distributing characteristics of aboveground biomass and carbon storage of Quercus acutissima plantation with different ages. *China For. Sci. Technol.* **2014**, *28*, 20–24.
47. Li, J.W.; Sun, X.Q.; Li, M.; Zou, J.Y.; Bian, H.F. Effects of stand age and soil organic matter quality on soil bacterial and fungal community composition in *Larix gmelinii* plantations, Northeast China. *Land. Degrad. Dev.* **2022**, *33*, 1249–1259. [CrossRef]
48. Muller, M.; Alewell, C.; Hagedorn, F. Effective retention of litter-derived dissolved organic carbon in organic layers. *Soil Biol. Biochem.* **2009**, *41*, 1066–1074. [CrossRef]
49. Wickland, K.P.; Neff, J.C.; Aiken, G.R. Dissolved organic carbon in Alaskan Boreal Forest: Sources, chemical characteristics, and biodegradability. *Ecosystems* **2007**, *10*, 1323–1340. [CrossRef]
50. Yang, B.; Xue, W.Y.; Yu, S.C.; Zhou, J.Y.; Zhang, W.H. Effects of stand age on biomass allocation and allometry of *Quercus Acutissima* in the Central Loess Plateau of China. *Forests.* **2019**, *10*, 41. [CrossRef]
51. Bolan, N.S.; Baskaran, S.; Thiagarajan, S. An evaluation of the methods of measurement of dissolved organic carbon in soils, manures, sludges, and stream water. *Commun. Soil Sci. Plant Anal.* **2008**, *27*, 2723–2737. [CrossRef]
52. Liu, T.R.; Peng, D.L.; Tan, Z.J.; Guo, J.P.; Zhang, Y.X. Effects of stand density on soil respiration and soil labile organic carbon and their influence mechanism in Larix Principis-Rupprechtii plantations. *Ecol. Process.* **2021**, *10*, 44. [CrossRef]
53. Bastida, F.; Moreno, J.L.; Hernández, T.; García, C. The long-term effects of the management of a forest soil on its carbon content, microbial biomass and activity under a semi-arid climate. *Appl. Soil. Ecol.* **2007**, *37*, 53–62. [CrossRef]
54. Mattsson, T.; Kortelainen, P.; Räike, A. Export of DOM from boreal catchments: Impacts of land use cover and climate. *Biogeochemistry* **2005**, *76*, 373–394. [CrossRef]
55. Marschner, B.; Kalbitz, K. Controls of bioavailability and biodegradability of dissolved organic matter in soils. *Geoderma* **2003**, *113*, 211–235. [CrossRef]
56. Xu, X.; Zhou, Y.; Ruan, H.H.; Wang, J.S. Temperature sensitivity increases with soil organic carbon recalcitrance along an elevational gradient in the Wuyi Mountains, China. *Soil Biol. Biochem.* **2010**, *42*, 1811–1815. [CrossRef]
57. Lal, R. Soil carbon sequestration to mitigate climate change. *Geoderma* **2004**, *123*, 1–22. [CrossRef]
58. Peichl, M.; Arain, M.A. Above-and belowground ecosystem biomass and carbon pools in an age-sequence of temperate pine plantation forest. *Agric. For. Meteorol.* **2006**, *140*, 51–63. [CrossRef]
59. Justine, M.F.; Yang, W.; Wu, F.; Khan, M.N. Dynamics of biomass and carbon sequestration across a chronosequence of masson pine plantations. *J. Geophys. Res. Biogeosci.* **2017**, *122*, 578–591. [CrossRef]
60. Yang, Y.H.; Luo, Y.Q.; Finzi, A.C. Carbon and nitrogen dynamics during forest stand development: A global synthesis. *New Phytol.* **2011**, *190*, 977–989. [CrossRef]
61. Su, Y.Z.; Liu, W.J.; Yang, R.; Chang, X.X. Changes in soil aggregate, carbon, and nitrogen storages following the conversion of cropland to alfalfa forage land in the marginal oasis of northwest China. *Environ. Manag.* **2009**, *43*, 1061–1070. [CrossRef]
62. Post, W.M.; Kwon, K.C. Soil carbon sequestration and land-use change: Processes and potential. *Glob. Chang. Biol.* **2000**, *6*, 317–327. [CrossRef]
63. Bradshaw, A.D. The reconstruction of ecosystems: Presidential address to the British ecological society. *J. Appl. Ecol.* **1983**, *20*, 1–17. [CrossRef]
64. Batterman, S.A.; Hedin, L.O.; van-Breugel, M.; Ransijn, J.; Craven, D.J.; Hall, J.S. Key role of symbiotic dinitrogen fixation in tropical forest secondary succession. *Nature* **2013**, *502*, 224–227. [CrossRef] [PubMed]
65. Berenguer, E.; Ferreira, J.; Gardner, T.A.; Aragão, L.E.O.C.; De Camargo, P.B.; Cerri, C.E.; Durigan, M.; De-Oliveira, R.C.; Vieira, I.C.G.; Barlow, J. A large-scale field assessment of carbon stocks in human-modified tropical forests. *Glob. Chang. Biol.* **2014**, *20*, 3713–3726. [CrossRef]
66. Ali, A.; Ahmad, A.; Akhta, R.K.; Teng, M.; Zeng, W.; Yan, Z.; Zhou, Z. Patterns of biomass, carbon, and soil properties in Masson pine (*Pinus massoniana* Lamb) plantations with different stand ages and management practices. *Forests* **2019**, *10*, 645. [CrossRef]

forests

MDPI

Article

Nitric Acid Rain Increased Bacterial Community Diversity in North Subtropical Forest Soil

Meijia Zhou, Haibo Hu *, Jinlong Wang, Ziyi Zhu and Yuanyuan Feng

Co-Innovation Center for Sustainable Forestry in Southern China, Key Laboratory of Soil and Water Conservation and Ecological Restoration in Jiangsu Province, Nanjing Forestry University, Nanjing 210037, China
* Correspondence: huhb2000@aliyun.com

Abstract: Nitric acid rain (NAR) seriously affects the biogeochemical cycles of forest communities' ecosystems. However, the effects of NAR on the composition and diversity of the soil bacterial community remain unclear. In this study, a typical subtropical forest of *Quercus acutissima* was selected and simulated spraying of NAR at pH 2.5 (AR2.5), 3.5 (AR3.5), and 4.5 (AR4.5) was implemented to investigate the response of the forest soil bacterial communities to NAR. The results showed that the total number of OTUs of soil bacteria in AR2.5 and AR3.5 treatments was 1.11 and 1.23 times that in the control treatment without NAR (CK), respectively. Acidobacteria, Proteobacteria, and Actinobacteria were the dominant phyla in the subtropical forest, accounting for more than 80% of the community's relative abundance. Concurrently, simulated NAR changed the relative abundance of *Rhodanobacter* significantly, which could be an indicator of soil bacterial community structure under NAR stress. Moreover, the Chao1, Shannon, and Simpson indices of strong acid rain treatments (i.e., AR2.5 and AR3.5) increased by 9.55%–22.5%, 3.6%–7.43%, and 0.15%–0.26%, respectively, compared to CK. Redundancy and correlation analysis illustrated that the phylum level structure of the bacterial community was significantly affected by soil total carbon, total nitrogen, and ammonium nitrogen. Our findings contribute to a better understanding of the effects of NAR on soil microbial communities and potential soil element cycling in north subtropical forests.

Keywords: nitric acid rain; subtropical forest; soil; bacterial community; diversity

check for updates

Citation: Zhou, M.; Hu, H.; Wang, J.; Zhu, Z.; Feng, Y. Nitric Acid Rain Increased Bacterial Community Diversity in North Subtropical Forest Soil. *Forests* **2022**, *13*, 1349. https://doi.org/10.3390/f13091349

Academic Editor: Choonsig Kim

Received: 1 July 2022
Accepted: 23 August 2022
Published: 25 August 2022

Publisher's Note: MDPI stays neutral with regard to jurisdictional claims in published maps and institutional affiliations.

Copyright: © 2022 by the authors. Licensee MDPI, Basel, Switzerland. This article is an open access article distributed under the terms and conditions of the Creative Commons Attribution (CC BY) license (https://creativecommons.org/licenses/by/4.0/).

1. Introduction

Acid rain (AR) pollution has been a global concern since the industrial revolution. Although the harm of AR to human health and ecosystem functions has been alleviated by strict control of SO_2, AR types are gradually changing with the increase in NO_X and NH_3 emissions, and the environmental pollution caused by AR is still serious [1,2]. The proportion of nitric acid rain (NAR) in the Yangtze River Delta region of China is gradually increasing and it has become one of the regions with the highest risk of being eroded by NAR in the world [3]. The increase in H^+ and NO_3^- contents in AR [4,5] leads to severe leaching of K, Ca, Na, and other base ions [6], which directly or indirectly causes changes in the soil microbial community [7]. Considering the increased risk of AR erosion, the impact on global forest ecosystems and soil microorganisms is worth studying.

Forest soil microorganisms are one of the most critical components of the ecosystem [8], and also a sensitive index of forest ecosystem response to environmental stress [9]. Soil bacteria grow rapidly and decompose vigorously. Studies have shown that the relative abundance of Acidobacteria, Actinobacteria, and Proteobacteria of soil bacteria in forest ecosystems is relatively high [10–12], and Acidobacteria and Actinobacteria have the ability to decompose lignin and cellulose [13]. Most studies [14,15] showed that the relative abundance of Acidobacteria was significantly negatively correlated with soil pH, but Jones et al. [16] found that some subgroups of Acidobacteria were significantly positively correlated with soil pH. Wang et al. [17] found that simulated AR treatment improved the

diversity of the bacterial community in early rice soil. Moreover, Liu et al. [18] found that AR with high acidity would increase the biomass of soil bacteria in the early stage. These studies indicate that the effects of AR on soil bacterial communities in a forest ecosystem are restricted by many factors.

The soil bacterial community is the highest proportion of soil microorganisms, and cycling drives all of the biogeochemical cycles in soils [19]. Bacteria mediate nitrogen (N) fixation in forest ecosystems [20], and N can be obtained from a series of organic compounds such as chitin in the polysaccharides of fungal mycelium in forest soil and amino acids and proteins in the dead organic matter [21]. Gao et al. [13] found that pH, total nitrogen (TN), and water content were the main factors affecting bacterial community structure by studying *Betula platyphylla*, a pioneer species in the succession process of the natural secondary forest ecosystem. Cong et al. [15] found a correlation between soil ammonium nitrogen (NH_4^+-N) and nitrate nitrogen (NO_3^--N) and soil bacteria by studying forest soil microorganisms in different climatic zones. Horner-Devine et al. [22] found that changes in soil ammonium ion concentration (NH_4^+) affect bacterial community composition. Wang et al. [23] found that the C/N ratio, soil pH, and organic carbon (C) were the key environmental factors affecting soil bacterial diversity.

However, the effects of NAR on soil bacterial community diversity and structural composition, as well as its regulatory factors, remain unclear. We hypothesized that H^+ and NO_3^- carried by NAR into forest soil would reduce the pH value of forest soil, thus affecting the diversity and structural characteristics of the soil bacterial community. In order to test this hypothesis, a typical north subtropical forest of *Quercus acutissima* was selected, and three NAR treatments (AR2.5, AR3.5, and AR4.5) were set in the test site with pH gradients (pH = 2.5, 3.5, and 4.5). The goals of this study were: (1) to study the response of soil bacterial community structure to NAR, (2) to study the response of soil bacterial community diversity to NAR, and (3) to study the relationship between soil environmental factors and bacterial community under NAR stress. This study provides a theoretical basis for exploring the response of the soil microbial community to NAR stress in north subtropical forest ecosystems.

2. Materials and Methods

2.1. Study Site

This study was conducted at the Yangtze River Delta Forest Ecological Station (32°7′49″ N, 119°12′7″ E) in Zhenjiang, Jiangsu Province, China. This area is home to a monsoon season, having an average yearly rainfall of 1184.3 mm at pH 5.15, with 15.1 °C as the average yearly temperature [24]. The soil texture is medium or heavy soil (Q_{3x}) [25], whereas the altitude of the experimental site is 180 m. The tree stands were mainly *Q. acutissima* with a mean age of ~70 years. The soil pH, total carbon (TC), TN, C/N, dissolved organic carbon (DOC), and alkali-hydrolyzable nitrogen (AN) were 4.53, 17.43 g·kg^{-1}, 1.53 g·kg^{-1}, 11.37, 85.93 mg·kg^{-1}, and 109.88 mg·kg^{-1}, respectively.

2.2. Experimental Treatments

In December 2020, 12 quadrats (3 m × 3 m) were randomly set in a *Q. acutissima* forest, designated as CK (pH = 6.5), AR4.5 (pH = 4.5), AR3.5 (pH = 3.5), and AR2.5 (pH = 2.5) treatments, with three replicates for each treatment. The NAR was prepared used using a master batch of 0.5 mol L^{-1} H_2SO_4 and 0.5 mol L^{-1} HNO_3 with a molar mass ratio of 1:5 [26]. Localized rainfall data for 2011–2021 quantified the average monthly precipitation, the intensity of which fluctuated occasionally (Figure 1). The contents of soil total N added to each plot under different treatments from December 2020 to November 2021 were shown in Table A1. Moreover, the configured NAR were sprayed onto the sample plots on the 15th day of each month from December 2020 to November 2021 (Figure 1). At the same time, the control area was sprayed with an identical amount of tap water (pH = 6.5).

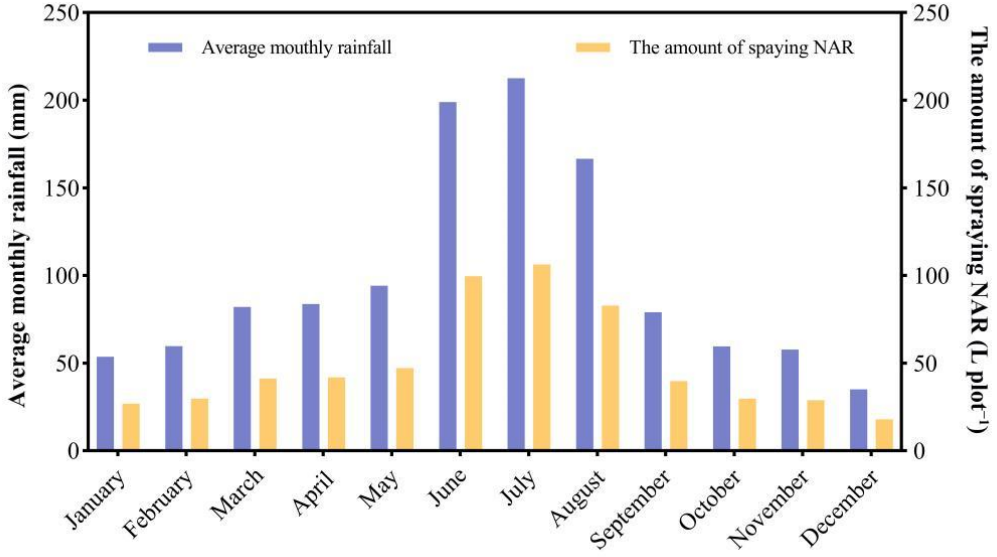


Figure 1. Average monthly rainfall and spraying amounts of NAR at the test plots. 2/3 of the average monthly rainfall from 2011 to 2021 was established as the total annual spraying amount per square meter, and 1/12 was taken as the monthly spraying amount per square meter. The amount of spraying at a given plot was calculated by the monthly spraying amount × 9 m^2 (the area of a single plot).

2.3. Soil Collection and Chemical Analysis

On 30 November 2021, topsoil samples (0~10 cm depth) were collected using the five-point sampling method. One portion of these samples was stored in a dry ice incubator (−80 °C) for later use to quantify the resident bacteria. The other portion was employed to quantify the fresh soil's chemical attributes. One-half was stored at 4 °C, whereas the other half (following the removal of debris such as stones and fallen leaves) was dried naturally and screened (2 mm) for the determination of soil nutrient indices. Soil pH was measured using a pH meter (Sartorius Gmb H: Gottingen, Germany). Soil TN and TC concentrations were determined with an elemental analyzer (Vario EL III, Elementar: Langenselbold, Germany). Soil DOC concentration was quantified using a K_2SO_4 extraction method. Soil AN concentration was measured via an alkaline hydrolysis diffusion technique. Soil NO_3^--N concentration was quantified by spectrophotometry, and the NH_4^+-N was measured via (indophenol blue) colorimetry.

2.4. Extraction and Sequencing of Soil Bacterial DNA

Soil microbial DNA was extracted from the samples using primers from an E.Zn.A.®Soil DNA Kit (Omega Bio-Tek: Norcross, GA, USA). Soil bacterial V3–V4 region underwent PCR amplification. Amplicons were extracted using 2% agarose gel and then refined with an AxyPrep DNA Gel Extraction kit (Axygen Biosciences: Union City, CA, USA). The pure PCR products were then quantified via Qubit® 3.0 (Life Invitrogen: Carlsbad, CA, USA) software. According to Illumina genomic DNA library preparation procedures, the polymerized DNA products were integrated into Illumina peer libraries. Subsequently, the amplicon library was double-terminal sequenced using the Illumina Novaseq 6000 platform (GenePioneer Co. Ltd.: Nanjing, China) (2 × 250).

2.5. Analysis Methods

R (V3.6.2) (R Development Core Team, NZ) was utilized to develop the Venn diagram and count the number of shared and unique bacterial OTUs in the four samples. GraphPad Prism 9 was employed to plot the stacked histogram of the top 20 species abundance at the bacterial phyla and genus levels. MOTHUR software (V1.30.2) (University of Michigan, Stateof Michigan, MI, USA) was used to calculate α diversity (Chao1, Shannon, Simp-

son, and Goods_coverage indices). The effects of different treatments on soil bacterial communities were tested based on Principal Coordinates analysis (PCoA) of Bray–Curtis distance using the "Vegan" package. SPSS 21.0 (SPSS Inc., Chicago, IL, USA) was used for one-way ANOVA and multiple comparative analysis (LSD), with the significance level set as $p < 0.05$. Correlations between ecological factors and the α-diversity of soil resident bacterial populations were tested using Pearson correlation analysis. Soil ecological factor and bacterial community redundancy analysis (RDA) proceeded using Canoco 5 software (Microcomputer Power, Ithaca, NY, USA).

3. Results

3.1. Effects of NAR on Soil Nutrient Contents

Soil pH under the AR2.5 treatment significantly decreased by 0.17 units compared with the CK treatment (Table 1). In contrast to the CK, soil TC, TN, and NH_4^+-N contents under the AR3.5 and AR2.5 treatments significantly decreased by 10.3%–22.4%, 13.1%–19.6%, and 7.0%–18.2%, respectively. Conversely, soil DOC and AN contents under the AR2.5 treatment significantly increased by 31.8% and 17.4%, respectively, compared with the CK treatment. Moreover, there were negligible differences in the C/N under all the treatment groups compared with CK.

Table 1. Soil nutrient contents under different treatments.

Treatments	pH	TC g·kg^{-1}	TN g·kg^{-1}	C/N	DOC mg·kg^{-1}	AN mg·kg^{-1}	NO_3^--N mg·kg^{-1}	NH_4^+-N mg·kg^{-1}
CK	4.53 ± 0.11 a	1.74 ± 0.08 a	1.53 ± 0.06 a	11.4 ± 0.2 a	85.9 ± 10.8 b	110 ± 5 b	15.5 ± 1.1 ab	7.10 ± 0.16 a
AR2.50	4.36 ± 0.06 b	1.35 ± 0.07 c	1.23 ± 0.06 c	11.0 ± 0.2 a	113 ± 4.3 a	129 ± 9 a	17.2 ± 0.8 a	5.81 ± 0.19 c
AR3.50	4.45 ± 0.06 ab	1.56 ± 0.08 b	1.33 ± 0.15 bc	11.8 ± 0.9 a	99.9 ± 9.2 ab	118 ± 2 b	16.1 ± 0.9 a	6.60 ± 0.34 b
AR4.50	4.50 ± 0.08 ab	1.76 ± 0.07 a	1.47 ± 0.06 ab	11.9 ± 0.3 a	96.5 ± 10.9 ab	114 ± 2 b	14.2 ± 0.9 b	6.57 ± 0.24 b

Data are mean ± standard error. Lowercase letters represent significant differences in soil nutrient contents under different NAR treatments ($p < 0.05$). TC: total carbon; TN: total nitrogen; C/N: total carbon/total nitrogen ratio; DOC: dissolved organic carbon; AN: alkali-hydrolyzable nitrogen; NO_3^--N: nitrate nitrogen; NH_4^+-N: ammonium nitrogen. CK: control without acid rain; AR2.5: Acid rain at pH 2.5; AR3.5: Acid rain at pH 3.5; AR4.5: Acid rain at pH 4.5.

3.2. Changes in Soil Bacterial Community Composition

The overall number of bacterial OTUs increased with NAR inputs (Figure 2a). Specifically, the total number of bacterial OTUs was 4165 across all treatments. Among them, there were 1921 OTUs common to all treatments, which accounted for about 46.1% of the total. The distribution of fungal OTUs unique to CK was the lowest, which accounted for 2.88% of the overall OTUs. The dissemination of soil fungal OTUs exclusive of the AR3.5 treatment was the highest, accounting for ~9.24% of the total. Moreover, the total numbers of bacterial OTUs under the AR2.5 and AR3.5 treatments were ~1.11 and 1.23 times that of the CK treatment, respectively.

There were 21 known phyla of bacteria identified among all treatments (Figure 2b). Among them, the relative abundances of Acidobacteria, Proteobacteria, Actinobacteria, Chloroflexi, Gemmatimonadetes, Planctomycetes, Bacteroidetes, WPS-2, Armatimonadetes, and Elusimicrobia in CK were 43.8%, 33.1%, 7.05%, 4.40%, 2.07%, 2.38%, 1.65%, 1.07%, 1.81%, and 1.33%, respectively. These were the predominant bacterial phyla in the *Q. acutissima* forest soil (relative abundance > 1%). Notably, the cumulative relative abundances of Acidobacteria, Proteobacteria, and Actinobacteria were over 80%. In contrast to the CK, AR2.5 and AR3.5 treatments had lower relative abundances of Acidobacteria and Actinobacteria, but a higher relative abundance of Proteobacteria. Concurrently, the relative abundances of Gemmatimonadetes, Planctomycetes, and Bacteroidetes under the AR3.5 treatment significantly increased by 48.3, 18.9, and 51.4% compared to CK treatment.

As shown in Figure 2c, the relative abundance of *Acidibacter*, *Candidatus*, *Solibacter*, *Acidothermus*, and *Bryobacter* under the CK treatment were 2.70%, 1.98%, 1.86%, and 1.59%, respectively, which could be used as indicator genera for the north subtropical forest

(relative abundance > 1%). The spraying of NAR significantly altered the soil bacteria genera. Compared to CK, there was a comparative decrease in the relative abundances of *Acidibacter* and *Acidothermus*, albeit an increase in the relative abundances of *Rhodanobacter* and *Ellin6067* under AR2.5 and AR3.5 treatments. Specifically, the relative abundance of *Acidibacter* and *Acidothermus* under the AR2.5 and AR3.5 treatments were significantly decreased by 17.5%–23.2% and 25.9%–29.6% related to CK. The relative abundances of *Rhodanobacter* and *Ellin6067* in AR2.5 and AR3.5 were 2.3–2.9 and 3.5–2.6 times higher than those of the CK, respectively.

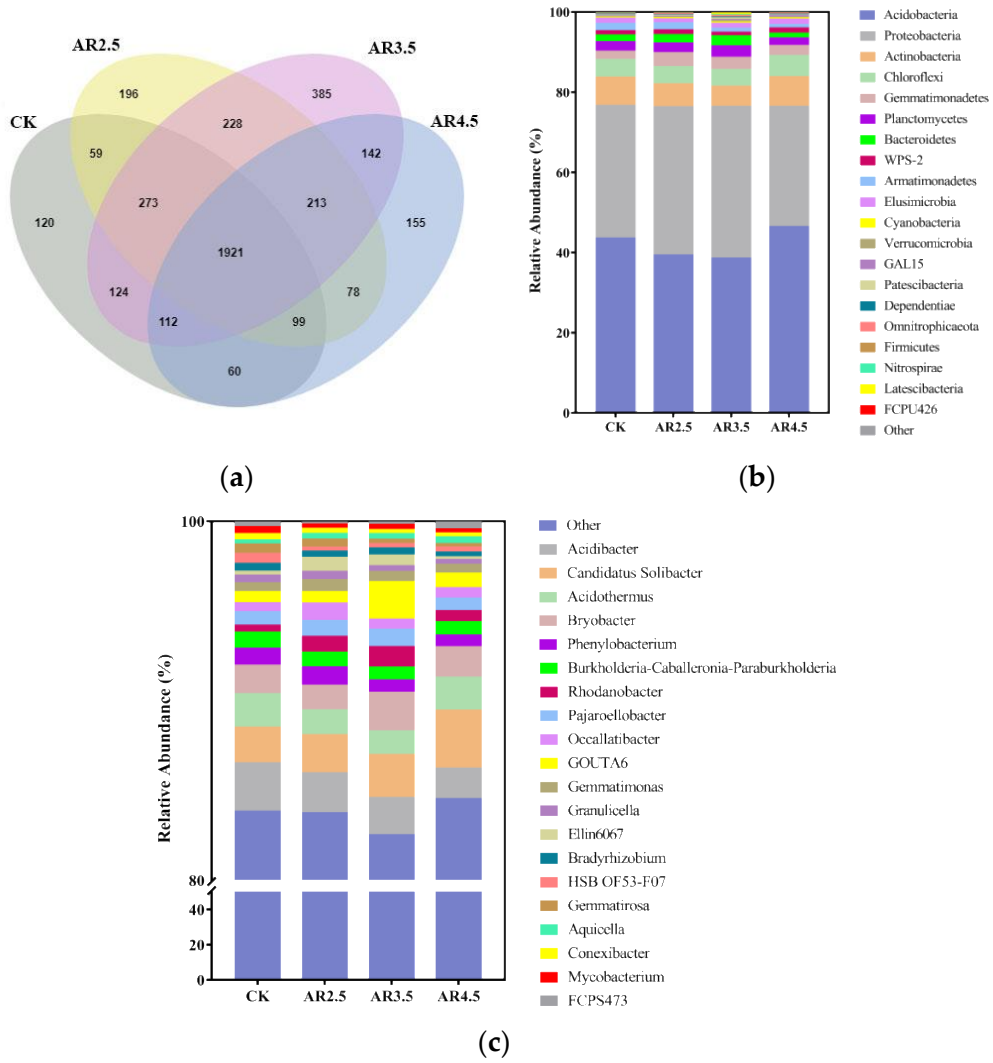


Figure 2. Venn of bacterial OTUs (**a**), community composition at the phyla of soil bacteria (**b**), and community composition at the genus of soil bacteria (**c**) of all treatments. Black dots exist in the set, black dots with a line between them represent intersections, and gray dots do not exist in the intersections. CK: control without acid rain; AR2.5: Acid rain at pH 2.5; AR3.5: Acid rain at pH 3.5; AR4.5: Acid rain at pH 4.5.

3.3. Changes in Soil Bacterial Community Diversity

As shown in Table 2, the α-diversity indexes of AR2.5 and AR3.5 treatments were significantly higher than those of CK. In particular, the Chao1, Shannon, and Simpson indices in AR2.5 and AR3.5 treatments increased by 9.55%–22.5%, 3.60%–7.43%, and 0.15%–0.26%, compared with CK treatment. However, the Goods_coverage index of AR3.5 treatments was less than that of CK and AR4.5 treatments.

Table 2. Soil bacterial community α-diversity indexes under different treatments.

	Chao1	Shannon	Simpson	Goods_Coverage
CK	2472 ± 73 c	8.61 ± 0.07 c	0.9930 ± 0.0006 c	0.9937 ± 0.0002 a
AR2.50	2733 ± 80 b	8.92 ± 0.05 b	0.9945 ± 0.0003 b	0.9931 ± 0.0003 ab
AR3.50	3027 ± 70 a	9.25 ± 0.06 a	0.9956 ± 0.0005 a	0.9928 ± 0.0004 b
AR4.50	2465 ± 96 c	8.56 ± 0.05 c	0.9920 ± 0.0003 d	0.9936 ± 0.0005 a

Data are mean ± standard error. Lowercase letters represent significant differences in soil bacterial community α-diversity indexes under different NAR treatments ($p < 0.05$). CK: control without acid rain; AR2.5: Acid rain at pH 2.5; AR3.5: Acid rain at pH 3.5; AR4.5: Acid rain at pH 4.5.

Principal coordinate (PCoA) analysis (Figure 3) based on Bray–Curtis distance showed that the first two axes of the principal coordinate explained the total variance contribution rate of 64.9%. These two principal components (PC1 and PC2) were the main contributors to the difference in bacterial community composition in forest soil under NAR. The first axis (PC1) and the second axis (PC2) explained 38.3% and 26.6%, respectively. The structure of the soil bacteria community in CK and AR4.5 treatments was concentrated in the positive half axis of the first axis, while that in AR2.5 and AR3.5 treatments was concentrated in the negative half axis of the first axis. At the same time, AR3.5 was concentrated in the positive half axis of the second axis, and AR2.5 was concentrated in the negative half axis of the second axis, indicating significant differences between groups.

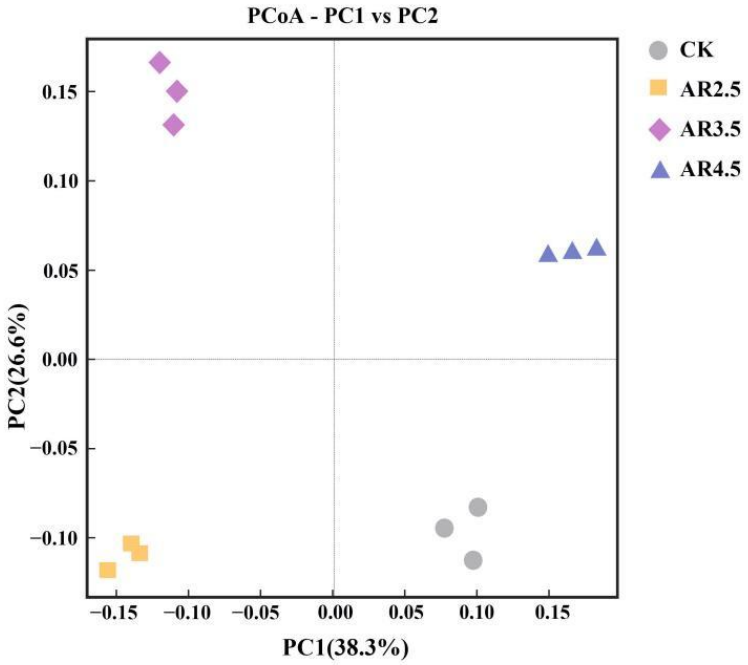


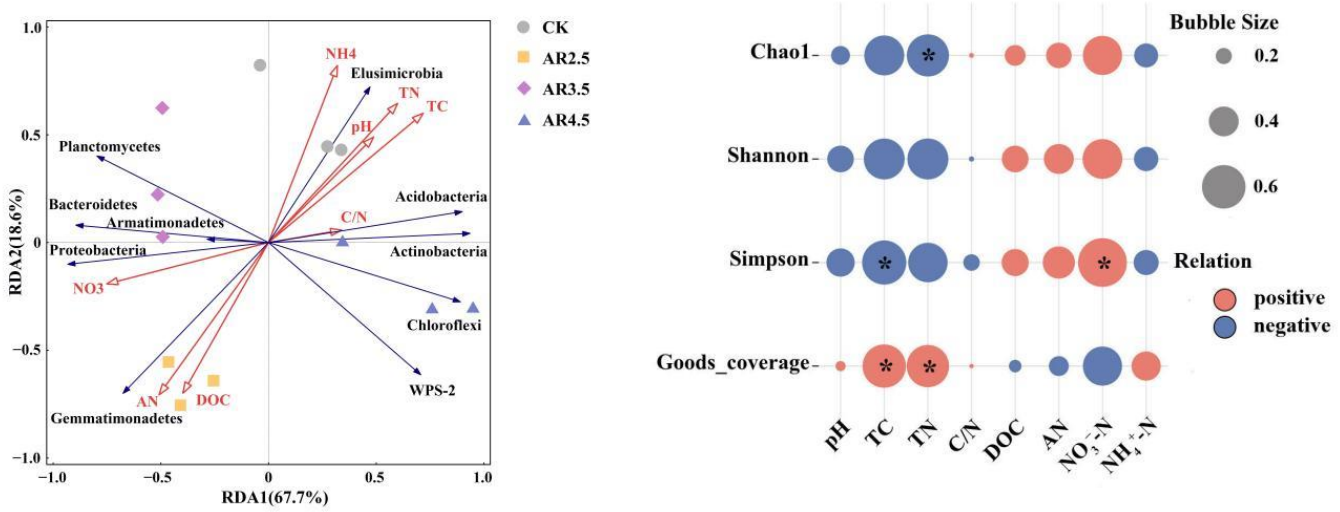
Figure 3. Principal Coordinate Analysis (PCoA) of structure of soil bacteria community. CK: control without acid rain; AR2.5: Acid rain at pH 2.5; AR3.5: Acid rain at pH 3.5; AR4.5: Acid rain at pH 4.5. Each point in the figure represents different treatments. The closer the point distance is, the more similar the bacterial community structure is. The farther the point distance is, the more obvious the difference in bacterial community structure is.

3.4. Response of Soil Bacterial Community to Soil Environmental Factors

According to the redundancy analysis of soil bacterial community structure and soil environmental factors of the *Q. acutisana* forest (Figure 4a), the explanation rate of the first two ranking axes reached 86.3%, the first axis explained 67.7% of the variables, and the second axis explained 18.6% of the variables. Soil TC ($F = 6$, $p = 0.01$) and NH_4^+-N ($F = 3.6$, $p = 0.026$) were the significant factors affecting soil bacterial community structure, with the explanatory rates of 37.6% and 19%, respectively. Gemmatimonadetes were positively

correlated with soil AN, DOC, and NO_3^--N. Concurrently, Acidobacteria, Actinobacteria, and Elusimicrobia were positively correlated with soil pH, TN, TC, and NH_4^+-N.

Correlation analysis results (Figure 4b) showed that the Chao1 index was significantly negatively correlated with soil TN (R = 0.580, $p < 0.05$). The Simpson index was negatively correlated with soil TC (R = 0.610, $p < 0.05$) but was positively correlated with NO_3^--N (R = 0.677, $p < 0.\ 05$). The goods_coverage index was positively correlated with TC (R = 0.598) and TN (R = 0.583, $p < 0.\ 05$).



(**a**) (**b**)

Figure 4. (**a**) Redundancy Analysis (RDA) of the effects on the soil bacterial community and soil environmental factors. (**b**) Bubble plot: Correlation analysis of soil chemical properties and bacterial community α-diversity indexes. The size of the circle indicates the size of the correlation coefficient. * indicate significant difference at $p < 0.05$. TC: total organic carbon; TN: total nitrogen; C/N: total carbon/total nitrogen ratio; DOC: dissolved organic carbon; AN: alkali-hydrolyzable nitrogen; NO3: nitrate nitrogen; NH4: ammonium nitrogen. CK: control without acid rain; AR2.5: Acid rain at pH 2.5; AR3.5: Acid rain at pH 3.5; AR4.5: Acid rain at pH 4.5.

4. Discussion

4.1. Effects of NAR Stress on Soil Bacterial Community Structure

Bacterial communities are extensively dispersed in forest soils and have vital roles in forest ecosystems and soil nutrient cycling [27]. Xia et al. [27] studied bacterial populations in various types of forest soils in Eastern China and found that Actinobacteria and Acidobacteria phyla were the most prevalent. Fierer et al. [28] studied different ecological communities, such as forests, grasslands, tundra, and deserts, and observed that Acidobacteria, Actinobacteria, Bacteroidetes, and Proteobacteria were prevalent across all communities. Other studies [10–12] revealed relatively high Acidobacteria, Actinobacteria, and Proteobacteria populations in forest ecosystems. Acidobacteria can degrade complex lignin and cellulose. In the case of cellulose, it facilitates the generation of acetic acid and hydrogen under hypoxic conditions [29], thereby improving soil nutrient status [30]. Actinobacteria are a group of Gram-positive bacteria, some of which secrete enzymes that decompose lignin and cellulose [13]. Moreover, most of the autogenous and symbiotic nitrogen-fixing microorganisms are derived from Proteobacteria [31]. Our results revealed that phyla with relatively high populations in the CK and simulated NAR groups included Acidobacteria, Proteobacteria, Actinobacteria, Chloroflexi, Gemmatimonadetes, Planctomycetes, Bacteroidetes, WPS-2, Armatimonadetes, and Elusimicrobia (Figure 2b).

Among them, the relative abundances of Acidobacteria, Proteobacteria, and Actinobacteria accounted for more than 80%, indicating that they might be the dominant soil bacteria phylum in the north subtropical forest. These findings are consistent with the results of Lauber et al. [32] and Liu et al. [33], who reported that the most abundant phylum was Acidobacteria. It may be due to the fact that Acidobacteria, Proteobacteria, and Actinobacteria are highly adaptable to diverse environments with more extensive ecological niches [13]. Additionally, potent NAR treatments (i.e., AR2.5 and AR3.5) reduced Acidobacteria and Actinobacteria populations (Figure 2b). This was in contrast to Jones et al. [16], who reported that the populations of soil residing in Acidobacteria were augmented at a lower soil pH [14,15]. This may be related to the differences in the responses of various Acidobacteria subclasses to environmental soil attributes [34]. For instance, the comparative population of Acidobacteria increased with a higher soil N content [35]. Moreover, the reduced population of Actinobacteria might be related to soil pH and it might generally decrease at lower pH [28,36]. Further, the population of Proteobacteria and Gemmatimonadetes treated with AR2.5 and AR3.5 increased at lower pH, which is partially consistent with the results of Wang et al. [17].

The results of this study at the genus level (Figure 2c) revealed that *Acidibacter*, *Candidatus*, *Solibacter*, *Acidothermus*, and *Bryobacter* under the CK treatment could be used as indicator genera of north subtropical forest soil (relative abundance > 1%). However, simulated NAR altered the soil bacteria genus structure. Compared with CK, the AR2.5 and AR3.5 treatments were observed to decrease the *Acidibacter* and *Acidothermus* populations yet enhance the population of *Rhodanobacter* and *Ellin6067*. Among them, the relative abundance of *Rhodanobacter* changed significantly under NAR spraying, which may be employed as a marker for changes in the structure of soil bacterial communities. *Rhodanobacter* is an acid-tolerant genus that can maintain the pH within its cells by adjusting its functions under the influence of AR to maintain its biological activities [17]. This may be one of the reasons behind the increased relative abundance of *Rhodanobacter* in soil treated with NAR in this study.

4.2. Effects of NAR Stress on Bacterial Community Diversity in Forest Soil

The potency and variety of bacterial communities have vital roles in the cycling of nutrients and the ecological balance of forest soils [37,38]. The simulated NAR treatments altered the variety of soil resident bacterial communities in *Q. acutissima* forests. The results indicated (Table 2) that strong NAR treatments (AR2.5 and AR3.5) substantially improved the Chao1, Shannon, and Simpson indices of the bacterial communities in forest soils. Particularly, the AR3.5 treatment induced the greatest richness and evenness in bacterial communities. This was similar to the research results of Wang et al. [17] and Liu et al. [18], contrary to the findings of Wang et al. [39]. Wang et al. [39] found that the growth of bacterial communities was inhibited with greater AR treatment intensity, thereby reducing soil bacterial diversity. However, Wang et al. [17] observed that simulated AR treatments improved the diversity of soil bacterial communities in the early rice season, and the community diversity under the pH 3.5 treatment group was the highest. Liu et al. [18] found that AR with high acidity increased the biomass of soil bacteria in the early stage. This might be due to the fact that the stimulating effects of NAR fertilization were higher than the inhibiting effects of acidity, which improved the soil's bacterial diversity and richness. Moreover, the evenness of soil bacteria was significantly impacted by strong AR, which may have been due to the inhibition of the growth of some bacteria under AR stress, which reduced the richness of the bacteria. However, most bacteria adapted to the acidic environment grew rapidly, which impacted the soil bacterial community even considerably in the *Q. acutissima* forest [39].

4.3. Interactions between Soil Bacterial Communities and Soil Environmental Factors under NAR Stress

Ecological factors have potent influences on the distribution of soil-residing bacterial communities [40], where soil nitrogen is closely related to bacterial community diversity and structural changes [41,42]. Gao et al. [13] observed that TN was the primary factor that affected the structures of bacterial communities, which was strongly correlated with Acidobacteria, Gemmatimonadetes, Actinobacteria, Proteobacteria, and Planctomycetes populations. Cong et al. [15] reported on the relationship between the soil NH_4^+-N and NO_3^--N and soil bacteria by studying forest soil microorganisms in different climatic zones. Horner-Devine et al. [22] found that modified soil NH_4^+ affected the compositions of bacterial communities. Redundancy analysis in this study (Figure 4a) revealed that NH_4^+-N was a significant driver that impacted the structures of bacterial communities in the soil. Correlation analysis (Figures 4b and A1) found that TN was strongly associated with the comparative richness of the Chao1 index, Acidobacteria, Proteobacteria, Actinobacteria, Gemmatimonadetes, and Elusimicrobia. This suggested that TN was the primary driver that impacted the diversity and phylum level structures of bacterial communities. Concurrently, NH_4^+-N was significantly correlated with Gemmatimonadetes and Elusimicrobia, while NO_3^--N was negatively correlated with Actinobacteria, which aligned with earlier studies. This may have been due to bacteria serving as the main facilitator of nitrogen fixation [20] and mineral weathering, which led to the leaching of inorganic nutrients within forest ecosystems [43]. Previous studies found that there were denitrification genes in certain strains of Acidobacteria, Actinobacteria, and other bacteria [44,45]. The addition of NAR inhibits the relative abundance of Acidobacteria and Actinobacteria, which may have affected the denitrification process. Furthermore, NO_3^- carried by NAR is a substrate for denitrification and an inhibitor of N_2O reductase [46], which can also affect the soil nitrogen cycle.

Forest soil stores two-thirds of all terrestrial C [47], where the degradation of lignin and cellulose by soil microorganisms is a key process that regulates the C cycle in the soil system, which influences the ratio between C mineralization and immobilization [47]. Acidobacteria and Actinobacteria play critical ecological roles in the degradation of plant biomass polysaccharides in acidic forest soils [48,49]. The results of redundancy analysis in this study (Figure 4a) indicated that TC was the main influencing factor that drove community structure and diversity patterns. The results of correlation analysis (Figure A1) showed that TC was significantly positively associated with Acidobacteria, whereas TC and DOC were strongly associated with Gemmatimonadetes and Elusimicrobia, which was similar to the research results of Zhao et al. [50]. Therefore, TC is the main influencing factor that drives the diversity and structural distribution of soil bacterial communities [40].

5. Conclusions

In this study, simulated nitric acid rain (NAR) increased the Chao1, Shannon, and Simpson indices, and altered the structure of soil bacterial communities in a north subtropical typical forest (*Quercus acutissima*). The strong acid rain treatments (i.e., AR2.5 and AR3.5) reduced the relative abundances of Acidobacteria and Actinobacteria, whereas enhanced the relative abundances of Proteobacteria and Gemmatimonadetes. At the same time, *Rhodanobacter* can be used as an indicator of soil bacterial community structure under NAR stress. Moreover, the diversity and structural compositions of soil bacterial communities were strongly impacted by the soil's total carbon, total nitrogen, and ammonium nitrogen under NAR stress. This research provides a hypothetical foundation for exploring the reactions of communities of soil bacteria under NAR stress in typical forest ecosystems in north subtropical regions. It is suggested that future research should focus more intently on the long-term effects of NAR on soil microorganisms.

Author Contributions: Conceptualization, M.Z. and Y.F.; methodology, H.H.; software, M.Z.; validation, M.Z., H.H. and Y.F.; formal analysis, M.Z.; investigation, J.W.; resources, Z.Z.; data curation, M.Z.; writing—original draft preparation, M.Z.; writing—review and editing, H.H. and Y.F.; visualization, M.Z.; supervision, Z.Z.; project administration, H.H.; funding acquisition, H.H. All authors have read and agreed to the published version of the manuscript.

Funding: This research was funded by Positioning research project of forest ecological system in Yangtze River delta of National Forestry and Grassland Administration, grant number 2021132068; Special fund project for technology innovation on Carbon Peak Carbon-neutral in 2021, Jiangsu Province, grant number BE2022305, and Technical support and collaboration project from Wuxi Water Conservancy Bureau, grant number 2107116.

Institutional Review Board Statement: Not applicable.

Informed Consent Statement: Not applicable.

Data Availability Statement: The data that support the findings of this study are available from the authors upon reasonable request.

Conflicts of Interest: The authors declare no conflict of interest.

Appendix A

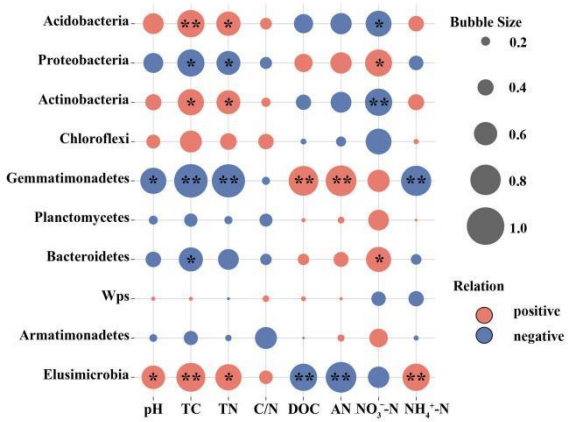


Figure A1. Correlation analysis of soil bacterial community structure characteristics and soil chemical properties. ** and * indicate significant difference at $p < 0.01$ and $p < 0.05$. TC: total organic carbon; TN: total nitrogen; C/N: total carbon/total nitrogen ratio; DOC: dissolved organic carbon; AN: alkali-hydrolyzable nitrogen; NO_3^--N: nitrate nitrogen; NH_4^+-N: ammonium nitrogen.

Table A1. The contents of soil total N added to each plot under different treatments from December 2020 to November 2021.

	January	February	March	April	May	June	July	August	September	October	November	December
CK	0.00	0.00	0.00	0.00	0.00	0.00	0.00	0.00	0.00	0.00	0.00	0.00
AR2.5	0.42	0.47	0.65	0.66	0.74	1.57	1.67	1.30	0.63	0.47	0.45	0.28
AR3.5	0.28	0.31	0.43	0.44	0.49	1.05	1.12	0.87	0.42	0.31	0.30	0.19
AR4.5	0.14	0.16	0.22	0.22	0.25	0.52	0.56	0.43	0.21	0.16	0.15	0.09

Note: the unit of N content is g/plot. When NAR was applied, fine adjustments would be made according to the actual situation in the field.

References

1. Zhao, Y.; Duan, L.; Xing, J.; Larssen, T.; Nielsen, C.P.; Hao, J. Soil Acidification in CHINA: Is Controlling SO2 Emissions Enough? ACS Publications: Washington, DC, USA, 2009.
2. Janssens, I.A.; Dieleman, W.; Luyssaert, S.; Subke, J.; Reichstein, M.; Ceulemans, R.; Ciais, P.; Dolman, A.J.; Grace, J.; Matteucci, G. Reduction of forest soil respiration in response to nitrogen deposition. *Nat. Geosci.* **2010**, *3*, 315–322. [CrossRef]
3. Li, Q.; Liu, X.; Zhang, J. Changing trends of acid rain types in the Yangtze River Delta region. *J. Nanjing For. Univ.* **2021**, *45*, 168. (In Chinese)

4. Wang, C.; Fang, Y.; An, W.; Zeng, C.; Wang, W.; Sardans, J.; Fernández-Martínez, M.; Peñuelas, J. Acid rain mediated nitrogen and sulfur deposition alters soil nitrogen, phosphorus and carbon fractions in a subtropical paddy. *Catena* **2020**, *195*, 104876. [CrossRef]
5. Xiao, S.; Wang, G.G.; Tang, C.; Fang, H.; Duan, J.; Yu, X. Effects of one-year simulated nitrogen and acid deposition on soil respiration in a subtropical plantation in China. *Forests* **2020**, *11*, 235. [CrossRef]
6. Singh, A.; Agrawal, M. Acid rain and its ecological consequences. *J. Environ. Biol.* **2007**, *29*, 15.
7. Xu, H.; Zhang, J.; Ouyang, Y.; Lin, L.; Quan, G.; Zhao, B.; Yu, J. Effects of simulated acid rain on microbial characteristics in a lateritic red soil. *Environ. Sci. Pollut. Res.* **2015**, *22*, 18260–18266. [CrossRef]
8. Liu, X.; Zhang, B.; Zhao, W.; Wang, L.; Xie, D.; Huo, W.; Wu, Y.; Zhang, J. Comparative effects of sulfuric and nitric acid rain on litter decomposition and soil microbial community in subtropical plantation of Yangtze River Delta region. *Sci. Total Environ.* **2017**, *601*, 669–678. [CrossRef]
9. Kumar, U.; Shahid, M.; Tripathi, R.; Mohanty, S.; Kumar, A.; Bhattacharyya, P.; Lal, B.; Gautam, P.; Raja, R.; Panda, B.B. Variation of functional diversity of soil microbial community in sub-humid tropical rice-rice cropping system under long-term organic and inorganic fertilization. *Ecol. Indic.* **2017**, *73*, 536–543. [CrossRef]
10. Kurth, F.; Zeitler, K.; Feldhahn, L.; Neu, T.R.; Weber, T.; Krištůfek, V.; Wubet, T.; Herrmann, S.; Buscot, F.; Tarkka, M.T. Detection and quantification of a mycorrhization helper bacterium and a mycorrhizal fungus in plant-soil microcosms at different levels of complexity. *BMC Microbiol.* **2013**, *13*, 205. [CrossRef]
11. Uroz, S.; Ioannidis, P.; Lengelle, J.; Cébron, A.; Morin, E.; Buee, M.; Martin, F. Functional assays and metagenomic analyses reveals differences between the microbial communities inhabiting the soil horizons of a Norway spruce plantation. *PLoS ONE* **2013**, *8*, e55929. [CrossRef]
12. Yuan, Y.; Si, G.; Wang, J.; Luo, T.; Zhang, G. Bacterial community in alpine grasslands along an altitudinal gradient on the Tibetan Plateau. *FEMS Microbiol. Ecol.* **2014**, *87*, 121–132. [CrossRef] [PubMed]
13. Gao, X.H.; Li, M.; Lu, P.; Lü, G.F.; Niu, Y.F. Bacterial community in the rhizosphere soil of Betula platyphylla in the Daqing Mountains, Hohhot. *Acta Ecol. Sin.* **2019**, *39*, 3586–3596.
14. Griffiths, R.I.; Thomson, B.C.; James, P.; Bell, T.; Bailey, M.; Whiteley, A.S. The bacterial biogeography of British soils. *Environ. Microbiol.* **2011**, *13*, 1642–1654. [CrossRef] [PubMed]
15. Cong, W.; Yu, J.J.; Yu, H.M.; Ding, Y.; Zhang, Y.G. Diversity and community assembly of forest soil microorganisms in different climatic zones. *Sci. Silv. Sin.* **2022**, *58*, 70–79. (In Chinese)
16. Jones, R.T.; Robeson, M.S.; Lauber, C.L.; Hamady, M.; Knight, R.; Fierer, N. A comprehensive survey of soil acidobacterial diversity using pyrosequencing and clone library analyses. *ISME J.* **2009**, *3*, 442–453. [CrossRef]
17. Wang, X.T.; Lan, X.F.; An, W.L.; Xu, X.P.; Wang, W.Q. Effect of simulated acid rain on paddy soil bacterial abundance and diversity in Fuzhou Plain. *Chin. J. Environ. Sci.* **2019**, *39*, 1237–1244.
18. Liu, Z.; Wei, H.; Zhang, J.; Saleem, M.; He, Y.; Zhong, J.; Ma, R. Seasonality regulates the effects of acid rain on microbial community in a subtropical agricultural soil of Southern China. *Ecotoxicol. Environ. Saf.* **2021**, *224*, 112681. [CrossRef]
19. Kuypers, M.M.; Marchant, H.K.; Kartal, B. The microbial nitrogen-cycling network. *Nat. Rev. Microbiol.* **2018**, *16*, 263–276. [CrossRef]
20. Reed, S.C.; Cleveland, C.C.; Townsend, A.R. Functional ecology of free-living nitrogen fixation: A contemporary perspective. *Annu. Rev. Ecol. Evol. Syst.* **2011**, *42*, 489–512. [CrossRef]
21. Lladó, S.; López-Mondéjar, R.; Baldrian, P. Forest soil bacteria: Diversity, involvement in ecosystem processes, and response to global change. *Microbiol. Mol. Biol. Res.* **2017**, *81*, e16–e63. [CrossRef]
22. Horner-Devine, M.C.; Lage, M.; Hughes, J.B.; Bohannan, B.J. A taxa–area relationship for bacteria. *Nature* **2004**, *432*, 750–753. [CrossRef] [PubMed]
23. Wang, L.Y.; Sun, H.Z.; Yang, X. Structure and functional diversity of bacterial community in rhizoshere soil of typical vegetation in the riparian zone along the downstream of Songhua River. *Chin. J. Environ. Sci.* **2022**, *43*, 2182–2191.
24. Lv, Y.; Wang, C.; Jia, Y.; Wang, W.; Ma, X.; Du, J.; Pu, G.; Tian, X. Effects of sulfuric, nitric, and mixed acid rain on litter decomposition, soil microbial biomass, and enzyme activities in subtropical forests of China. *Appl. Soil Ecol.* **2014**, *79*, 1–9. [CrossRef]
25. Wang, X.; Hu, H.B.; Cheng, C.; Zhang, S.; Chen, J.Y.; Lu, H.L. Soil PhytOC sequestration in Quercus acutissima forest in northern subtropics. *J. Zhejiang A F Univ.* **2021**, *38*, 1–9. (In Chinese)
26. Liu, X.; Zhao, W.; Meng, M.; Fu, Z.; Xu, L.; Zha, Y.; Yue, J.; Zhang, S.; Zhang, J. Comparative effects of simulated acid rain of different ratios of SO_4^{2-} to NO_3^- on fine root in subtropical plantation of China. *Sci. Total Environ.* **2018**, *618*, 336–346. [CrossRef]
27. Xia, Z.; Bai, E.; Wang, Q.; Gao, D.; Zhou, J.; Jiang, P.; Wu, J. Biogeographic distribution patterns of bacteria in typical Chinese forest soils. *Front. Microbiol.* **2016**, *7*, 1106. [CrossRef]
28. Fierer, N.; Leff, J.W.; Adams, B.J.; Nielsen, U.N.; Bates, S.T.; Lauber, C.L.; Owens, S.; Gilbert, J.A.; Wall, D.H.; Caporaso, J.G. Cross-biome metagenomic analyses of soil microbial communities and their functional attributes. *Proc. Natl. Acad. Sci. USA* **2012**, *109*, 21390–21395. [CrossRef]
29. Pankratov, T.A.; Kirsanova, L.A.; Kaparullina, E.N.; Kevbrin, V.V.; Dedysh, S.N. Telmatobacter bradus gen. nov., sp. nov., a cellulolytic facultative anaerobe from subdivision 1 of the Acidobacteria, and emended description of Acidobacterium capsulatum Kishimoto et al. 1991. *Int. J. Syst. Evol. Microbiol.* **2012**, *62*, 430–437. [CrossRef]

30. Pankratov, T.A.; Ivanova, A.O.; Dedysh, S.N.; Liesack, W. Bacterial populations and environmental factors controlling cellulose degradation in an acidic Sphagnum peat. *Environ. Microbiol.* **2011**, *13*, 1800–1814. [CrossRef]
31. He, Y.S.; He, T.H.; Feng, Y.Q.; Cui, Q.; Chen, X.Q.; Zhao, M.T.; Qiu, W.J. Characteristics and distribution of soil bacterial of salt marsh tidal wetland in Ordos Platform. *Acta Ecol. Sin.* **2022**, *42*, 3345–3355.
32. Lauber, C.L.; Hamady, M.; Knight, R.; Fierer, N. Pyrosequencing-based assessment of soil pH as a predictor of soil bacterial community structure at the continental scale. *Appl. Environ. Microb.* **2009**, *75*, 5111–5120. [CrossRef] [PubMed]
33. Liu, J.; Sui, Y.; Yu, Z.; Shi, Y.U.; Chu, H.; Jin, J.; Liu, X.; Wang, G. High throughput sequencing analysis of biogeographical distribution of bacterial communities in the black soils of northeast China. *Soil Biol. Biochem.* **2014**, *70*, 113–122. [CrossRef]
34. Navarrete, A.A.; Kuramae, E.E.; de Hollander, M.; Pijl, A.S.; van Veen, J.A.; Tsai, S.M. Acidobacterial community responses to agricultural management of soybean in Amazon forest soils. *FEMS Microbiol. Ecol.* **2013**, *83*, 607–621. [CrossRef] [PubMed]
35. Magill, A.H.; Aber, J.D. Variation in soil net mineralization rates with dissolved organic carbon additions. *Soil Biol. Biochem.* **2000**, *32*, 597–601. [CrossRef]
36. Jeanbille, M.; Buée, M.; Bach, C.; Cébron, A.; Frey-Klett, P.; Turpault, M.P.; Uroz, S. Soil parameters drive the structure, diversity and metabolic potentials of the bacterial communities across temperate beech forest soil sequences. *Microb. Ecol.* **2016**, *71*, 482–493. [CrossRef]
37. Kosolapov, D.B.; Kuschk, P.; Vainshtein, M.B.; Vatsourina, A.V.; Wiessner, A.; Kästner, M.; Müller, R.A. Microbial processes of heavy metal removal from carbon-deficient effluents in constructed wetlands. *Eng. Life Sci.* **2004**, *4*, 403–411. [CrossRef]
38. Nacke, H.; Thürmer, A.; Wollherr, A.; Will, C.; Hodac, L.; Herold, N.; Schöning, I.; Schrumpf, M.; Daniel, R. Pyrosequencing-based assessment of bacterial community structure along different management types in German forest and grassland soils. *PLoS ONE* **2011**, *6*, e17000. [CrossRef]
39. Wang, N.; Wang, C.K.; Pan, X.C.; Bai, C.B. Effects of Simulated Acid Rain on Soil Bacterial Community Diversity in Buffer Zone of Broad-Leaved Forest Invaded by Moso Bamboo. *Res. Environ. Sci.* **2020**, *33*, 1478–1487. (In Chinese)
40. Zeng, Q.; Dong, Y.; An, S. Bacterial community responses to soils along a latitudinal and vegetation gradient on the Loess Plateau, China. *PLoS ONE* **2016**, *11*, e152894.
41. Bell, C.W.; Asao, S.; Calderon, F.; Wolk, B.; Wallenstein, M.D. Plant nitrogen uptake drives rhizosphere bacterial community assembly during plant growth. *Soil Biol. Biochem.* **2015**, *85*, 170–182. [CrossRef]
42. Qin, H.; Li, C.X.; Ren, Q.S. Effects of different land use patterns on soil bacterial and fungal biodiversity in the hydro—Fluctuation zone of the Three Gorges Reservoir region. *Acta Ecol. Sin.* **2017**, *37*, 3494–3504. (In Chinese)
43. Uroz, S.; Oger, P.; Lepleux, C.; Collignon, C.; Frey-Klett, P.; Turpault, M. Bacterial weathering and its contribution to nutrient cycling in temperate forest ecosystems. *Res. Microbiol.* **2011**, *162*, 820–831. [CrossRef] [PubMed]
44. Rösch, C.; Mergel, A.; Bothe, H. Biodiversity of denitrifying and dinitrogen-fixing bacteria in an acid forest soil. *Appl. Environ. Microb.* **2002**, *68*, 3818–3829. [CrossRef]
45. Nelson, M.B.; Martiny, A.C.; Martiny, J.B. Global biogeography of microbial nitrogen-cycling traits in soil. *Proc. Natl. Acad. Sci. USA* **2016**, *113*, 8033–8040. [CrossRef] [PubMed]
46. Dalal, R.C.; Wang, W.; Robertson, G.P.; Parton, W.J. Nitrous oxide emission from Australian agricultural lands and mitigation options: A review. *Soil Res.* **2003**, *41*, 165–195. [CrossRef]
47. Xia, M.; Talhelm, A.F.; Pregitzer, K.S. Fine roots are the dominant source of recalcitrant plant litter in sugar maple-dominated northern hardwood forests. *New Phytol.* **2015**, *208*, 715–726. [CrossRef]
48. Větrovský, T.; Steffen, K.T.; Baldrian, P. Potential of cometabolic transformation of polysaccharides and lignin in lignocellulose by soil Actinobacteria. *PLoS ONE* **2014**, *9*, e89108.
49. Lladó, S.; Žifčáková, L.; Větrovský, T.; Eichlerová, I.; Baldrian, P. Functional screening of abundant bacteria from acidic forest soil indicates the metabolic potential of Acidobacteria subdivision 1 for polysaccharide decomposition. *Biol. Fertil. Soils* **2016**, *52*, 251–260. [CrossRef]
50. Zhao, P.; Bao, J.; Wang, X.; Liu, Y.; Li, C.; Chai, B. Deterministic processes dominate soil microbial community assembly in subalpine coniferous forests on the Loess Plateau. *PeerJ* **2019**, *7*, e6746. [CrossRef]

MDPI AG
Grosspeteranlage 5
4052 Basel
Switzerland
Tel.: +41 61 683 77 34

Forests Editorial Office
E-mail: forests@mdpi.com
www.mdpi.com/journal/forests



Disclaimer/Publisher's Note: The title and front matter of this reprint are at the discretion of the Guest Editors. The publisher is not responsible for their content or any associated concerns. The statements, opinions and data contained in all individual articles are solely those of the individual Editors and contributors and not of MDPI. MDPI disclaims responsibility for any injury to people or property resulting from any ideas, methods, instructions or products referred to in the content.





Academic Open
Access Publishing

mdpi.com

ISBN 978-3-7258-2809-8